

A Decision-level Multi-sensor Data Fusion approach to Land Cover Classification

by

Aidan Magee BSc., MSc.



This thesis is presented in fulfilment of the requirements for the degree of
Doctor of Philosophy

National Centre for Geocomputation
Maynooth University

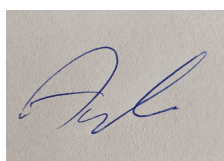
February, 2023

Head of the Department: Prof. Chris Brunson
Supervisors: Prof. Tim McCarthy & Prof. John McDonald

Declaration

This thesis has not been submitted in whole or in part to this or any other university for any other degree and is, except where otherwise stated, the original work of the author.

Signed:

A handwritten signature in blue ink on a light brown background. The signature is stylized and appears to read 'Aidan'.

Aidan Magee

Acknowledgments

I would like to thank my supervisors, Prof Tim McCarthy and Prof John McDonald, for guiding me through the years while undertaking this thesis.

I would like to thank Sean Mannion, and Fearghus Foyle of GeoAerospace for their support and encouragement and for accepting to be the employment partner as part of the Irish Research Council Employment Based Postgraduate Programme to fund the research undertaken as part of my PhD.

I would like to thank Sean O’Kane, Keith Magee, Dr. Nirbhasa Magee, Dr Gourav Misra and Dr. Paul Lewis for taking the time to proofread various parts of the thesis.

I would like to thank Dáire Walsh, and Eduardo Herrera, who has always been available to discuss a matter related to this thesis.

Finally, I would like to thank my partner, Lauren Hennessy, who has shown endless patience over the past few years. Her encouragement, support, and hours spent proofreading has been fundamental to the completion of this thesis.

The research presented in the thesis was funded through the Irish Research Council Employment Based Postgraduate Programme with GeoAerospace Ltd. serving as the Employment Partner.



Abstract

In recent years there has been an increased demand for frequently updated Land Cover Classification (LCC) products. With ever greater numbers of Earth Observation (EO) and Remote Sensing (RS) platforms capturing data, the combined utilisation of data from multiple platforms has the potential to improve both the accuracy and frequency of LCC product updates through a process known as sensor fusion. This thesis examines how the fusion of RS sensors with diverse imaging characteristics can overcome challenges encountered when generating an annual LCC product. To undertake this examination, the technical specifications for the Second Generation Corine Land Cover (CLC+) Backbone raster product and its application on the island of Ireland is used as a case study for evaluating the use of mono-platform and sensor-fused RS datasets for LCC. A review of Machine Learning (ML) techniques in this thesis highlighted key factors crucial to achieving high-accuracy classification along with the proposal of a high-accuracy rapid inference Light Fully Convolutional Neural Network (LFCNN) architecture. This review also highlighted challenges when performing LCC on the island of Ireland, such as frequent cloud cover that can reduce the availability of optical satellite data, preventing the widespread use of high-accuracy multi-temporal ML classification. In this thesis, the application of a decision-level fusion approach is demonstrated as a means of mitigating the issue of frequent cloud cover and ensuring full classification coverage while also increasing classification accuracy. The versatility of a decision-level fusion approach was further demonstrated through the fusion of aerial and satellite RS data to improve LCC in complex non-homogeneous regions such as urban environments. The findings of this research have direct implications not only for performing LCC on the island of Ireland but throughout Europe and beyond, with clear recommendations provided for the generation of LCC products using EO and RS data.

Contents

1	Introduction	1
1.1	Land Cover Classification	2
1.1.1	Earth Observation and Land Cover Classification	3
1.1.2	Machine Learning and Land Cover Classification	4
1.2	LCC Datasets in Ireland	6
1.2.1	Co-ORdinated INformation on the Environment (CORINE)	8
1.2.2	Second Generation Corine Land Cover (CLC+)	9
1.3	Gaps in Current Knowledge in the Field of Land Cover Classification (LCC)	11
1.3.1	Suitability of mono-platform Machine Learning (ML) techniques for annual LCC on the island of Ireland	11
1.3.2	Sensor fusion with variable data availability	12
1.3.3	Decision-level fusion of Satellite and Aerial data	13
1.4	Research Questions	14
1.5	Structure of this Thesis.	16
2	Current State of the Art - Literature Review	18
2.1	Introduction	18
2.2	Challenges using Earth Observation for Land Cover Classification	19
2.2.1	Spectral and Radiometric Resolution	19
2.2.2	Spatial Resolution	23
2.2.3	Temporal Resolution	25
2.3	Spectral Based LCC	29
2.3.1	Spectral Based ML Techniques	31
2.3.1.1	Random Forest (RF)	31
2.3.1.2	Artificial Neural Network (ANN)	33
2.3.1.3	Support Vector Machine (SVM)	34
2.4	Spatial Based LCC	35
2.4.1	Patch-to-Point	35
2.4.2	Patch-to-Patch	37
2.4.3	Object-Based Classification	39
2.5	Temporal LCC	40
2.5.1	Multi-dimensional Techniques	40
2.5.2	Temporal Ensemble Techniques	41
2.5.3	Time Series Analysis	42
2.5.3.1	Recurrent Neural Network	42
2.5.3.2	Time-series CNN	44
2.6	Sensor Fusion LCC	45
2.6.1	Pixel-level Fusion	46

2.6.2	Feature-level Fusion	48
2.6.3	Decision-level Fusion	50
2.6.4	Sensor Fusion with partially Missing Data	53
2.7	Suitability of ML Techniques for CLC+ Backbone Raster Product	55
2.7.1	Pixel-Based Requirement	56
2.7.2	Sensor and Multi-temporal Requirements	56
2.7.3	Spatial Resolution Requirement	58
2.8	Summary	60
3	Evaluation of ML Techniques for Satellite based LCC	62
3.1	Introduction	62
3.2	Data	63
3.2.1	Study Area	63
3.2.2	Satellite Data	65
3.2.2.1	Sentinel-1	65
3.2.2.2	Sentinel-2	67
3.2.2.3	Landsat-8	68
3.2.3	Clipping and Resampling	70
3.2.4	Labelled Data	70
3.3	Methodology	77
3.3.1	Data Preparation for ML	77
3.3.1.1	Point Dataset Preparation	77
3.3.1.2	Patch-to-Point Dataset Preparation	79
3.3.1.3	Temporal Data Preparation	79
3.3.1.4	Normalisation of Data	80
3.3.2	ML Techniques to be Evaluated	81
3.3.2.1	RF and SVM Hyperparameter Selection	82
3.3.2.2	ANN and LSTM Structure	82
3.3.2.3	LCNN and LFCNN	83
3.3.2.4	1DCNN and 3DLFCNN	86
3.3.2.5	Activation Functions and Training Parameters	90
3.3.3	Evaluation Process	91
3.3.3.1	Overall Accuracy	91
3.3.3.2	F1 Score	91
3.3.3.3	Comparative Assessment	91
3.3.3.4	Confusion Matrix	92
3.3.3.5	Model Coverage	93
3.4	Results	96
3.4.1	Independent Platform Results	96
3.4.1.1	Sentinel-2	96
3.4.1.2	Landsat-8	98
3.4.1.3	Sentinel-1	98
3.4.2	Platform Comparative Results	99
3.4.3	Confusion Matrices and Classification Examples	102
3.4.4	Model Coverage	108
3.5	Discussion	110
3.5.1	Prediction Probability and Accuracy	112
3.5.2	Impact of Incorporating Temporal Information	119

3.5.2.1	Temporal Information in Point-based Techniques	119
3.5.2.2	Monthly Observation Requirement	121
3.5.3	Impact of Incorporating Spatial Information	123
3.5.3.1	Inference times of LFCNN and 3DLFCNN architectures	124
3.5.4	Assessing the spatial relationship of classification results	127
3.5.5	Data Quality	129
3.5.5.1	Label Data Quality	129
3.5.5.2	Cloud Cover	131
3.5.5.3	Image Co-registration	133
3.5.5.4	Exclusion of Shrub Class	133
3.6	Conclusion	134
4	Satellite Sensor Fusion LCC	137
4.1	Introduction	137
4.2	Sensor Fusion Comparative Assessment	138
4.2.1	Pixel-Level Fusion	139
4.2.2	Decision-Level Fusion	141
4.2.3	Evaluation Process	142
4.2.4	Results	143
4.3	Variable Data Availability Fusion Assessment	148
4.3.1	Fusion Techniques	148
4.3.1.1	Ordered Fusion	148
4.3.1.2	Voting Fusion	152
4.3.1.3	Probability Fusion	153
4.3.1.4	Multi-ML model Fusion	154
4.3.2	Assessment Criteria	154
4.3.3	Results	156
4.3.3.1	Limiting SVM Fused Average Computational Cost	159
4.3.4	Confusion Matrix and Classification Examples	163
4.4	Conclusion	167
5	Combined Satellite-Aerial Data Fusion	169
5.1	Introduction	169
5.2	Aerial Data Classification	170
5.2.1	Aerial Data	171
5.2.2	Labelled Data	173
5.2.3	ML Architecture	176
5.3	Satellite-Aerial Class-Corresponding Fusion	177
5.3.1	Class Constrained Fusion (Class-Con Fusion)	177
5.3.2	Corresponding Probability Fusion (Cor-Prob Fusion)	178
5.3.3	Classification and Resampling	179
5.3.4	Assessment Methodology	179
5.4	Results	182
5.4.1	Aerial Classification Results	182
5.4.2	Satellite-Aerial Fusion Results	184
5.5	Discussion	186
5.5.1	Spatially Derived Sparsely Vegetated Class	189
5.5.2	Aerial Data Classification Issues	190
5.5.2.1	Misclassification of Water	191

5.5.2.2	Misclassification of Non-Vegetated areas	193
5.6	Conclusion	194
6	Conclusion	196
6.1	Introduction	196
6.2	Main Findings	198
6.2.1	Research Question 1: Suitability of ML for Mono-platform Satellite-derived Annual LCC	198
6.2.2	Research Question 2: Multi-sensor Satellite data Fusion using Sensor Data Inputs that Vary in Terms of Availability	199
6.2.3	Research Question 3: Satellite-Aerial Data Fusion	200
6.2.4	Summary of Contributions	201
6.3	Recommendations and Future Work	202
6.3.1	Refinement of LFCNN architecture	203
6.3.2	Decision-level vs Feature-level Fusion	203
6.3.3	Satellite-Aerial Fusion for Sparsely Vegetated Regions	204
6.3.4	Alternative Label Data Sources	204
6.3.5	Fusion of Alternative Data Sources	205
6.3.6	Recommendations for the practical implementation of annual LCC on the island of Ireland.	206
6.3.7	Future LCC Requirements	209
6.4	Final Remarks	210
A	Satellite Data	233
A.1	Sentinel-1 Images	233
A.2	Sentinel-2 Images	246
A.3	Landsat-8 Images	284
B	Chapter 3 Results	291
B.1	Sentinel-1 Results	292
B.2	Sentinel-2 Results	295
B.3	Landsat-8 Results	304
B.4	Sentinel-1 Results With Shrub	306
B.5	Sentinel-2 Results With Shrub	308
B.6	Landsat-8 Results With Shrub	312
C	Chapter 4 Results	314
C.1	Sensor Fusion Comparative Results	314
C.1.1	Pixel-Level fusion	315
C.1.1.1	Fusion with Annually Averaged data	315
C.1.1.2	Fusion with Half-Yearly Averaged data	319
C.1.1.3	Fusion with Seasonally Averaged data	323
C.1.1.4	Fusion with Monthly Averaged data	324
C.1.2	Decision-Level Fusion	325
C.1.2.1	Preliminary analysis of Decision-Level fusion techniques	326
C.1.2.2	Sentinel-2 and Sentinel-1	326
C.1.2.3	Sentinel-2 and Landsat-8	330
C.1.2.4	Landsat-8 and Sentinel-1	338
C.1.2.5	Sentinel-2 Landsat-8 and Sentinel-1	339

C.2 Variable Data Fusion Assessment Results	347
D Chapter 5 Aerial Surveys	353

List of Figures

1.1	Illustrative example passive and active remote sensing, Source: Grinds-GIS (2015).	3
1.2	Plot of papers related to LCC using EO and ML from 1992 to 2021 on the Web of Science database.	5
1.3	Conceptual design showing the interlinked elements required to deliver improved European land monitoring (CLC+ product suite), Source: Kleeschulte et al. (2019).	10
1.4	Conceptual illustration for mono-platform satellite LCC.	11
1.5	Conceptual illustration for multi-platform satellite LCC.	12
1.6	Conceptual illustration for multi-platform satellite and aerial LCC.	13
2.1	Spectral response function of conventional cameras Canon EOS 500D (Top Left) and Nikon D5000 (Top Right) and multi-spectral cameras Mini-MCA6 (Bottom Left) and Sequoia (Bottom Right), Source: Fastie (2015); Deng et al. (2018).	21
2.2	Illustration of spectral reflectance of water soil and green vegetation, Source: GIS Homework (2021).	21
2.3	Sentinel-2B 10m GSD captured (2018-09-05) over Maynooth University (Left), aerial imagery 0.04m GSD capture (2018-09-03) over Maynooth (Right).	23
2.4	NDVI derived from Sentinel-2 over a year. Red = cultivated land, blue = build-up area and green = grassland, Source: Peressutti (2018).	26
2.5	An example of a unique non-persistent event captured by (a) Sentinel-2A (2018-04-21) in image and circled in red. (b) Sentinel-2A (2018-05-16) image (c) and Microsoft Bing Imagery (www.bing.com/maps/aerial) for reference.	27
2.6	Sentinel-2 image over Dublin, Ireland (01/06/2020) true colour image (top left), MNDWI (top right) and MNDWI threshold with a threshold of zero (bottom).	30
2.7	Example illustration of random forest structure.	32
2.8	Example illustration of artificial neural network.	33
2.9	Example illustration of support vector machine structure.	34
2.10	Illustration of an example CNN structure.	36
2.11	Illustration of an example FCNN structure.	38
2.12	Example of the impact of employing object-based techniques on the ‘noise’ in classification output over Carrick-on-Suir, Tipperary Ireland. Sentinel-2 true colour image (left), pixel-based random forest classification (centre), object-based random forest classification.	40

2.13	Illustration of the four different RNN model categories, Source: Raschka and Mirjalili (2017).	43
2.14	Illustration of the basic structure of the three different fusion categories.	46
2.15	Illustration of the steps involved in performing pixel-level fusion.	46
2.16	Illustration of the steps involved in performing feature-level fusion.	49
2.17	Illustration of the steps involved in performing decision-level fusion.	50
3.1	Geographic extent of study areas. Base map: Microsoft Bing imagery (www.bing.com/maps/aerial).	64
3.2	Illustration of Sentinel-1 satellite, Source: ESA (2021b).	65
3.3	Illustration of Sentinel-2 satellite, Source: ESA (2021c).	68
3.4	Illustration of Landsat-8 satellite, Source: EROS (2013).	69
3.5	Impact of removing shrub label locations from rasterised label dataset.	76
3.6	Point count per class for all regions (a) before and (b) after applying filtering steps to correct for class imbalance.	78
3.7	Illustrative example of ANN architecture.	83
3.8	Illustration of LCNN 5×5 architecture.	84
3.9	Illustration of LFCNN 9×9 architecture.	85
3.10	Illustration of example confusion matrix.	92
3.11	Illustration of example normalised confusion matrix.	93
3.12	Illustrative example of annual Sentinel-2 a) observation count and b) area meeting the six observation count threshold over the assessed Galway region.	94
3.13	Confusion matrix for Sentinel-2 seasonally averaged 3DLFCNN 9×9 .	103
3.14	Confusion matrix for Sentinel-1 monthly averaged 1DCNN.	104
3.15	Confusion matrix for Landsat-8 half-yearly averaged 3DLFCNN 9×9 .	105
3.16	Classification examples over Glengarriff harbour, Co. Cork using the best model for (a) Sentinel-2, (b) Landsat-8 (c) Sentinel-1.	106
3.17	Classification examples over Dunboyne, Co. Meath using the best model for (a) Sentinel-2, (b) Landsat-8 (c) Sentinel-1.	107
3.18	Probability threshold vs accuracy and available sample points for Sentinel-1 monthly averaged 1DCNN 12 .	112
3.19	Probability threshold vs accuracy and available sample points for Sentinel-2 seasonally averaged 3DLFCNN 9×9 .	113
3.20	Probability threshold vs accuracy and available sample points for Landsat-8 half-yearly averaged 3DLFCNN 9×9 .	113
3.21	Probability threshold vs accuracy and available sample points per class for Sentinel-1 monthly averaged 1DCNN 12 .	116
3.22	Probability threshold vs accuracy and available sample points per class for Sentinel-2 seasonally averaged 3DLFCNN 9×9 .	117
3.23	Probability threshold vs accuracy and available sample points per class for Landsat-8 half-yearly averaged 3DLFCNN 9×9 .	118
3.24	Illustrative examples of the coverage with the requirement of a) and c) six observations and b) and d) six months of observations over the Galway region.	122
3.25	Illustrate example of the UNET architecture as proposed by Ronneberger et al. (2015).	126

3.26	Illustration of correctly classified sample points (Green) and misclassified points (Red) from the Dublin test datasets for (a) Sentinel-2 seasonally averaged 3DLFCNN9×9 (b) Landsat-8 half-yearly averaged 3DLFCNN9×9 (c) Sentinel-1 monthly averaged 1DCNN12	128
3.27	Example of poor Copernicus Urban Atlas classification with annual averaged Sentinel 2A&B imagery as a base map.	130
3.28	Comparison of seasonally averaged Senintel-2 3DLFCNN9×9 classification to a mislabelled area.	131
3.29	Sentinel-2 true colour image over Greystones with cloud mask (orange) from ‘MSK_CLOUDS_B00.gml’ file.	132
3.30	Comparison of Sentinel-2A captured 2018-07-02 (left), Annually averaged Sentinel-2A&B imagery (right) over Maynooth.	133
3.31	Confusion matrix for Sentinel-2 seasonally averaged SVM including the <i>Wood shrubs/bushes</i> class.	134
4.1	Illustration of a pixel-level and decision-level fusion workflows.	138
4.2	Example illustration of Full Model Ordered fusion.	150
4.3	Example illustration of Class Order Fusion.	151
4.4	Probability threshold vs accuracy and available sample points for Sentinel-2 seasonally averaged 3DLFCNN9×9.	152
4.5	Probability threshold vs accuracy and available sample points for Landsat-8 half-yearly averaged 3DLFCNN9×9.	152
4.6	Confusion matrix for the full-SVM averaging approach on the SVM Fused fusion set.	164
4.7	Classification examples over Glengarriff harbour, Co Cork that were generated from the three highest accuracy mono-platform models and using the Full-SVM Averaging Fusion approach.	165
4.8	Classification examples over Dunboyne, Co. Meath that were generated from the three highest accuracy mono-platform models and using the Full-SVM averaging fusion approach.	166
5.1	Cessna 172 with sensor pod wing attachment.	171
5.2	The location of aerial survey sites. Base map: Microsoft Bing Imagery (www.bing.com/maps/aerial).	172
5.3	Aerial Labels for a) Maynooth and b) Waterford Airport sites.	175
5.4	Illustration of Modified UNET architecture.	176
5.5	Illustration of satellite-aerial fusion steps.	177
5.6	Aggregated labels generated for satellite classification assessment in Chapter 3 over a) Maynooth and b) Waterford Airport.	180
5.7	Modified labels for satellite-aerial assessment over a) Maynooth and b) Waterford Airport.	181
5.8	Classification output of UNET model for Maynooth and Waterford Airport using aerial RGB Data.	183
5.9	Results of performing Class-Con satellite-aerial fusion using S2SE prior classification.	185
5.10	Illustration of classification change due to satellite-aerial Class-Con fusion relative to satellite-only S2SE classification.	187
5.11	Example of <i>Permanent Herbaceous</i> with some visible bare ground resulting in misclassification as <i>Sparsely Vegetated</i>	189

5.12	Comparison of <i>sparsely vegetated</i> class derived by (b probability vs (c proportion of <i>Permanent Herbaceous</i> or <i>Non-Vegetated</i> class during resampling.	190
5.13	Examples of four water bodies from the aerial dataset with notably different appearances.	191
5.14	Example of b) UNET misclassification and its impact on c) Class-Confusion and d) Cor-Prob fusion.	192
5.15	Non-Vegetation misclassification examples for Maynooth top and Waterford bottom.	193
6.1	Conceptual illustration for mono-platform satellite LCC.	198
6.2	Conceptual illustration for multi-platform satellite LCC.	199
6.3	Conceptual illustration for multi-platform satellite and aerial LCC. . . .	200

List of Tables

1.1	EO derived Copernicus datasets available from land.copernicus.eu.	6
1.2	Evolution of CORINE land cover, Source: Büttner et al. (2021).	8
2.1	ML category definitions used in literature review.	19
2.2	Resolution characteristics definitions.	20
2.3	Examples of satellite spatial resolution and image footprint, Source: Satellite Imaging Corporation (2021); NASA (2021a).	24
2.4	Spectral indices for Sentinel-2 satellite data Sources: Henrich and Brüser (2021); Du et al. (2016).	31
3.1	Sentinel-2 band spectral ranges and spatial resolutions, Source: ESA (2021a).	68
3.2	Landsat-8 band spectral ranges, Source: Ihlen (2019).	69
3.3	CLC+ nomenclature, Source: Kleeschulte et al. (2019).	71
3.4	List of data sources used for the generation of aggregated labels datasets.	72
3.5	Features form each data sources that are aggregated together to their respective Second Generation Corine Land Cover (CLC+) class.	73
3.6	Month ranges used for the generation of half-yearly and seasonally averaged datasets.	79
3.7	List of ML techniques to be assessed in mono-platform comparative analysis.	81
3.8	Details of LCNN architectures examined in the mono-platform comparative assessment.	84
3.9	Details of LFCNN architectures examined in the mono-platform comparative assessment.	86
3.10	Details of 1DCNN architectures examined in the mono-platform comparative assessment.	87
3.11	Details of half-yearly averaged 3DLFCNN architectures examined in the mono-platform comparative assessment.	88
3.12	Details of seasonally averaged 3DLFCNN architectures examined in the mono-platform comparative assessment.	89
3.13	Detail of minimum observation requirements for each temporal dataset. .	95
3.14	Sentinel-2 results using all available label points. The highest test data weighted F1 and OA for each prepared dataset are highlighted with text in bold.	97
3.15	Landsat-8 results using all available label points. The highest test data weighted F1 and OA for each prepared dataset are highlighted with text in bold.	98

3.16	Sentinel-1 results using all available label points. The highest test data weighted F1 and OA for each prepared dataset are highlighted with text in bold.	99
3.17	Sentinel-2 comparative results. The highest test data F1/OA in each column are highlighted with text in bold.	100
3.18	Landsat-8 comparative results. The highest test data F1/OA in each column are highlighted with text in bold.	100
3.19	Cross-Platform comparative results. The highest test data F1/OA in each column are highlighted with text in bold.	101
3.20	Sentinel-2 model coverage for each temporal dataset calculated by the area meeting minimum observation requirements set out in Table 3.13.	108
3.21	Landsat-8 model coverage for each temporal dataset calculated by the area meeting minimum observation requirements set out in Table 3.13.	108
3.22	Sentinel-2 and Landsat-8 combined model coverage for each temporal dataset calculated by the area meeting minimum observation requirements set out in Table 3.13.	109
3.23	List of the mono-platform ML models obtaining the highest Test F1 score for each class.	110
3.24	Test dataset label points available for each comparative assessments.	111
3.25	Percentage of remaining test points at desired target accuracy as a result of probability thresholding. The highest value in each column are highlighted with text in bold.	114
3.26	Estimate of the percentage of area from prediction at a desired target accuracy as a result of probability thresholding. The highest value in each column are highlighted with text in bold.	115
3.27	Results of performing classification using an Support Vector Machine (SVM) with annually averaged Sentinel-2 data that has been generated with set numbers of observations.	119
3.28	Results of comparative assessment only using point-based ML techniques.	120
3.29	Model coverage for each platform and temporal dataset calculated by a requirement for a total of six observations as set out in Table 3.13.	123
3.30	Model coverage for each platform and temporal dataset calculated by a requirement for six months with observations.	123
3.31	Comparison of model inference times for point-based and patch to point LFCNN based ML techniques.	125
4.1	Datasets to be tested with pixel-level fusion techniques.	140
4.2	ML techniques to be assessed for use with pixel-level fused satellite data.	140
4.3	List of mono-platform satellite models (prior models) to be used for decision-level fusion.	141
4.4	Results of comparative assessment of fusion techniques for annually averaged data. The highest test data weighted F1 and OA are highlighted with text in bold.	143
4.5	Results of comparative assessment of fusion techniques for half-yearly averaged data. The highest test data weighted F1 and OA are highlighted with text in bold.	143

4.6	Results of comparative assessment of fusion techniques for seasonally averaged data. The highest test data weighted F1 and OA are highlighted with text in bold.	144
4.7	Results of comparative assessment of fusion techniques for six monthly averaged data. The highest test data weighted F1 and OA are highlighted with text in bold.	144
4.8	Results of comparative assessment of mono-platform and pixel-level fused data with point-based ML techniques. The highest test data weighted F1 and OA for each prepared dataset are highlighted with text in bold. . . .	146
4.9	Decision-level fusion models resulting in negative change in weighted F1 score. Change is calculate relative to the unfused Sentinel-2 seasonally averaged 3DLFCNN9×9 (S2SE).	147
4.10	List of decision-level fusion approaches and the variations of those techniques that will be evaluated in variable data fusion assessment.	149
4.11	List of fusion sets used in the variable data availability fusion assessment.	154
4.12	Percentage of sample points that can be classified by non-fused prior models in the S2AN-reduced dataset.	155
4.13	Percentage of sample points that can be classified by non-fused prior models in the 25%-reduced dataset.	155
4.14	Fusion assessment results using the S2AN-reduced dataset. The highest test data weighted F1 and OA for each fusion set are highlighted with text in bold.	156
4.15	Fusion assessment results using the 25%-reduced dataset. The highest test data weighted F1 and OA for each fusion set are highlighted with text in bold.	158
4.16	Model filtering assessment results on S2AN-reduced dataset. The highest test data weighted F1 and OA for each target model assessment are highlighted with text in bold.	162
4.17	Results of comparative assessment of Full-SVM averaging and Dual-SVM averaging to and SVM model using five different combinations of prior models. The highest test data weighted F1 and OA for each target model assessment are highlighted with text in bold.	162
5.1	Aerial survey details.	172
5.2	Aerial classes along with the definitions and corresponding satellite classes.	174
5.3	List of satellite prior models to be fused.	179
5.4	F1 and OA results of aerial data classification using UNET architecture.	182
5.5	Results for satellite only classification. The highest weighted F1 and OA for each site are highlighted with text in bold.	184
5.6	Results for Class-Con satellite-aerial fusion. The highest weighted F1 and OA for each site are highlighted with text in bold.	184
5.7	Results for Cor-Prob satellite-aerial fusion. The highest weighted F1 and OA for each site are highlighted with text in bold.	184
5.8	Classification change due to satellite-aerial Class-Con fusion relative to satellite only classification.	186
A.1	Sentinel-1 Satellite Images used in Chapter 3 comparative assessment. . .	233
A.2	Sentinel-2 Satellite Images used in Chapter 3 comparative assessment. . .	246
A.3	Landsat-8 Satellite Images used in Chapter 3 comparative assessment. . .	284

B.1	Sentinel-1 Model Results.	292
B.2	Sentinel-2 Model Results.	295
B.3	Landsat-8 Model Results.	304
B.4	Sentinel-1 Model Results including shrub class.	306
B.5	Landsat-8 Model Results including shrub class.	312
C.1	Results of Pixel-level Fusion using Annually Averaged data. Δ result calculated relative to LFCNN9 \times 9 using Annually Averaged Sentinel-2 data.	315
C.2	Results of Pixel-level Fusion using Half-Yearly Averaged data. Δ result calculated relative to 3DLCNN9 \times 9 using Half-Yearly averaged S2 data.	319
C.3	Results of Pixel-level Fusion using Seasonally Averaged data. Δ result calculated relative to 3DLCNN9 \times 9 using Seasonally averaged S2 data.	323
C.4	Results of Pixel-level Fusion using Monthly Averaged data. Δ result calculated relative to 1DCNN6 using Monthly averaged S2.	324
C.5	Prior Model List.	325
C.6	Preliminary analysis of decision-level fusion methodologies using all prior models	326
C.7	Results of Decision-level Fusion Sentinel-2 and Sentinel-1 prior models using an SVM.	327
C.8	Results of Decision-level Fusion Sentinel-2 and Landsat-8 prior models using an SVM.	330
C.9	Results of Decision-level Fusion Landsat-8 and Sentinel-1 prior models using an SVM.	338
C.10	Results of Decision-level Fusion of Sentinel-2 Landsat-8 and Sentinel-1 prior models using SVM.	339
C.11	Results of Decision-level Fusion using the Sentinel Only Fusion Set on S2AN-reduced dataset.	348
C.12	Results of Decision-level Fusion using the Mono-Platform Fusion Set on S2AN-reduced dataset.	349
C.13	Results of Decision-level Fusion using the SVM Fused Fusion Set on the S2AN-reduced dataset.	350
C.14	Results of Decision-level Fusion using the Mono-Platform Fusion Set on the 25%-reduced dataset.	351
C.15	Results of Decision-level Fusion using the SVM Fused and Mono Platform Fusion Set on the 25%-reduced dataset.	352

Acronyms

ANN Artificial Neural Network.

CLC Corine Land Cover.

CLC+ Second Generation Corine Land Cover.

CNN Convolutional Neural Network.

CORINE Co-ORdinated INformation on the Environment.

DN Digital Numbers.

DSM Digital Surface Model.

EO Earth Observation.

ESA European Space Agency.

FCNN Fully Convolutional Neural Network.

GSD Ground Sampling Distance.

LCC Land Cover Classification.

LCNN Light Convolutional Neural Network.

LFCNN Light Fully Convolutional Neural Network.

LiDAR Light Detection and Ranging.

LSTM Long-Short Term Memory.

LUCAS Land Use/Cover Area frame Survey.

ML Machine Learning.

MLP Multilayer Perceptron.

MNDWI Modified Normalised Difference Water Index.

NDVI Normalized Difference Vegetation Index.

OA Overall Accuracy.

PTO Probability Thresholding Ordered.

RADAR Radio Detection and Ranging.

RF Random Forest.

RNN Recurrent Neural Network.

RS Remote Sensing.

SAR Synthetic Aperture Radar.

SVM Support Vector Machine.

UAV Unmanned Aerial Vehicle.

Chapter 1

Introduction

Earth Observation (EO) involves monitoring the physical, chemical and biological systems of the Earth's surface (EU Science Hub, 2022). The utilisation of Remote Sensing (RS) technologies for EO, such as imagery captured from satellites, aircraft, and Unmanned Aerial Vehicles (UAVs), makes EO data a valuable source of information for the production of Land Cover Classification (LCC) datasets (Chaves et al., 2020). Machine Learning (ML) techniques have increasingly been used as an effective tool to process and extract useful information from the increasing volumes of EO data (Salcedo-Sanz et al., 2020). Many of the RS platforms have different sensor characteristics, and the inclusion of data from each sensor (*sensor fusion*) can be used as an effective means of leveraging the unique information from each sensor to improve the analysis of an object or phenomenon (Chang and Bai, 2018). However, there are significant challenges to overcome when incorporating data from sensors with differing spatial, spectral and temporal resolutions. This thesis will examine how the fusion of RS sensors, with diverse imaging characteristics can overcome challenges encountered when performing LCC. These challenges include the issue of frequent cloud cover that can reduce the availability of optical satellite EO data and the challenge of performing EO derived LCC in complex non-homogeneous regions such as in urban environments. In particular, this thesis will examine how sensor fusion can be used to overcome these challenges to improve LCC in Northern European regions such as on the island of Ireland.

This chapter will provide an introduction to the field of LCC outlining (*i*) the role

of EO and ML technologies, (ii) the existing LCC datasets available for the island of Ireland, and, (iii) the current gaps in the field of EO and ML derived LCC that will be addressed in this thesis. The research objectives addressed in this thesis will then be presented along with the three key research questions. Finally, the structure of this thesis will be outlined along with a brief summary of the contents of each chapter.

1.1 Land Cover Classification

Land cover can be defined as “the type of feature present on the surface of the Earth” (Lillesand et al., 2014, p. 213) or the “observed (bio)physical cover of the Earth’s surface” (FAO, 2022a, para. 1). Examples of this include lakes, grassland, pavements and bare rock. This should not be confused with *Land use* which is defined as “the human activity or economic activity associated to that land” (Lillesand et al., 2014, p. 213) or the “activities and inputs people undertake in a certain land cover type to maintain it or produce change” (FAO, 2022b, para. 1). Examples include sports facilities, schools, commercial developments or residential developments. As per their definitions, land cover and land use are related but are distinct terms (Vali et al., 2020; FAO, 2022a). For example, residential land use could have a ‘building’ land cover, however not every building is used for residential use.

Monitoring of land cover and land cover change provides substantial benefits to many sectors such as forestry, agriculture, mining industries, etc. (Belward and Skøien, 2015; Dabija et al., 2021; Li et al., 2020a; Stehman and Foody, 2019). Land cover mapping is also vital to the study of environmental and climate change (Congalton et al., 2014). In recent years the issue of climate change has proven particularly important as Ireland is required to report annual greenhouse gas emissions to the United Nations Framework Convention on Climate Change (UNFCCC) (Cawkwell et al., 2017). Developing and maintaining an up to date and accurate land cover and habitat mapping programme would enable the identification of carbon sequestration opportunities, as well as adaptation options (Brennan and Tubridy, 2017).

1.1.1 Earth Observation and Land Cover Classification

EO makes extensive use of RS technologies. RS is the science of obtaining information using a device without making contact with the surface, area or phenomena being observed (Chang and Bai, 2018). The first aerial photograph was captured from a tethered balloon over Paris in 1858, marking the beginning of the use of cameras to capture information about the Earth's surface remotely (Lillesand et al., 2014). However, it was not until the mid-1940s that RS was used for large-scale land cover and land use classification achieved through mapping the United States using aerial photography (Vali et al., 2020; Marschner, 1950). RS sensors used in EO, record information about a surface or phenomenon by recording the electromagnetic energy that has been reflected from that surface or phenomenon. RS sensors can be passive or active. Passive sensors rely on an external source for the generation of electromagnetic energy. In most cases, this source of electromagnetic energy is the sun. On the other hand, an active RS sensor transmits energy to the surface and records the reflected energy (Shunlin and Jindi, 2020). Figure 1.1, provides an illustrative example of the difference between passive and active sensors.

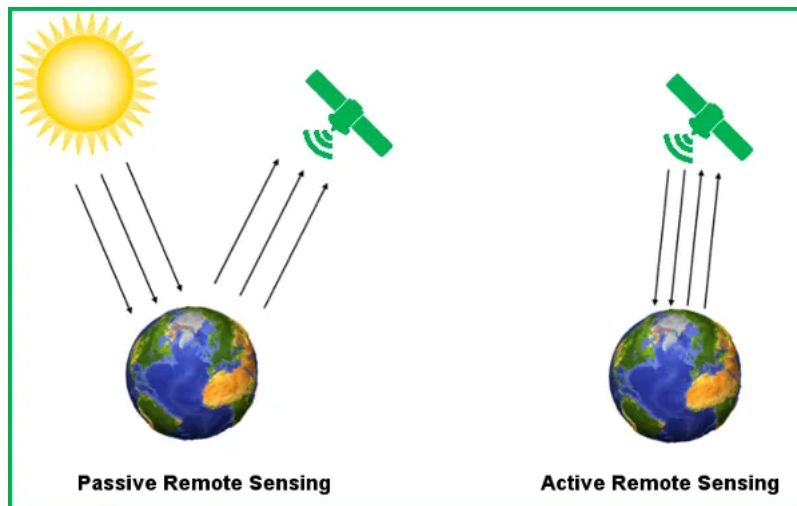


Figure 1.1: Illustrative example passive and active remote sensing, **Source:** GrindsGIS (2015).

Both passive and active RS sensors can be deployed to numerous platforms, including satellite, aircraft and UAVs, making them suitable for capturing accurate and up to date data for LCC. The information obtained from RS platforms has three main components; a spectral component which is the electromagnetic energy recorded by the sensor, a spatial

component which is the change in spectral information across the observed area and a temporal component which is the change in the spectral and spatial components over time. LCC derived from EO can be viewed as being a function of these three components and therefore can be expressed as:

$$LCC \ni \{Spectral, Spatial, Temporal\} \quad (1.1)$$

The use of RS technology enables the capture of this spectral, spatial and temporal information of land cover in a more cost-effective manner than traditional land surveying and as a result, has become the primary source for the generation of most modern LCC datasets (Congalton et al., 2014; Yan et al., 2015).

1.1.2 Machine Learning and Land Cover Classification

Early techniques for the conversion of remotely sensed imagery into land cover datasets involved the manual photointerpretation of imagery (Lillesand et al., 2014; European Environment Agency, 1995). However, with advancements in computer processing and in ML, there have been significant improvements in the accuracy and automation of the generation of LCC datasets (Vali et al., 2020; Aguilera, 2020). ML is the label ascribed to a wide range of data analytical techniques which are capable of extracting patterns from raw data without parameters needing to be explicitly defined by humans (Goodfellow et al., 2016). While the difference between traditional statistics and ML is not well defined, statistical techniques rely on the analyst's prior knowledge for the choice of the correct models to use. However, most ML techniques require no prior knowledge of the data's structure (Bzdok et al., 2018). Additionally, ML techniques can outperform traditional statistical methods, particularly in situations where there is an abundance of label data to fit (train) the ML models (Aguilera, 2020). There is an estimated 5 Petabytes of EO data collected each year (Salcedo-Sanz et al., 2020). Traditional statistical methods may be unsuitable for processing this volume of data which is set to increase as more RS platforms are deployed. ML on the other hand, have been demonstrated as an effective means of extracting patterns out of 'big data' (Salcedo-Sanz et al., 2020; Bzdok et al.,

2018). As a result of the benefits of using ML over traditional statistical techniques, numerous studies have examined the use of ML in a broad range of EO applications, including the monitoring of surface temperature and drought monitoring, water quality assessment, vegetation biomass, and land cover and land use classification (Salcedo-Sanz et al., 2020; Ali et al., 2015). Since the early 1990s, there has been a significant increase in the number of studies examining the use of ML techniques for LCC. Figure 1.2 illustrates the number of papers identified on the Web of Science database (www.webofscience.com) related to LCC using EO and ML. As illustrated in Figure 1.2, there has been a steady increase in the number of papers related to LCC using EO and ML. This result was obtained using the following search query:

(ALL=(“land cover classification”) AND (ALL=(“machine learning”) OR ALL=(“Deep learning”) OR ALL=(“Neural Network”) OR ALL=(“CNN”) OR ALL=(“support vector machine”) OR ALL=(“svm”) OR ALL=(“random forest”))) AND (ALL=(“remote sensing”) OR ALL=(“earth observation”) OR ALL=(“satellite”) OR ALL=(“aerial”) OR ALL=(“UAV”))

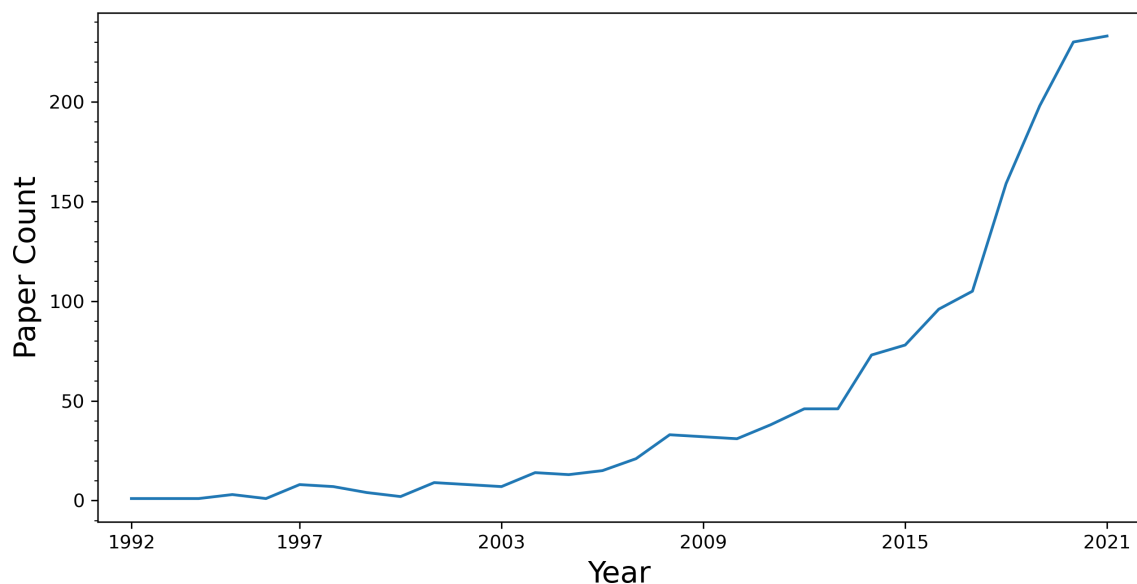


Figure 1.2: Plot of papers related to LCC using EO and ML from 1992 to 2021 on the Web of Science database.

1.2 LCC Datasets in Ireland

At the time of writing, Ireland has no national land cover map. However, there are other land cover and land use datasets generated for larger global or European monitoring which cover the island of Ireland. Global LCC datasets include the 100m resolution Copernicus Global Land Cover 2019 datasets and the 10m resolution ESA World Cover 2020 dataset (Green and Zimmermann, 2021). Copernicus has also released additional land cover datasets produced from satellite imagery using a combination of ML and interactive rule-based classification available from land.copernicus.eu and are listed in Table 1.1.

Table 1.1: EO derived Copernicus datasets available from land.copernicus.eu.

Dataset	Description
Imperviousness	A product mapping the built-up areas and sealed soil density ranging from 0-100%.
Forest Type	A product mapping the density of tree cover and its dominant leaf type.
Grassland	A product mapping the presence or absence of grassland vegetation.
Water & Wetness	A product mapping permanent water; temporary water; permanent wetness and temporary wetness.
Small Woody Features	A product mapping woody linear features with a minimum width of 20m and a minimum length of 50m, and small patchy woody elements with an area of between 200m ² and 5000m ²

Another example of a European wide dataset is the JRC EU Crop Map 2018, a 10m resolution map of areas under crop and their crop types, including grasslands. The JRC EU Crop Map 2018 is an EO derived dataset generated using ML which was trained using the Land Use/Cover Area frame Survey (LUCAS) dataset. The LUCAS dataset is an important Europe wide land cover dataset (Ballin et al., 2018). However, unlike each of the datasets discussed so far that provide LCC over a large area, the LUCAS dataset consists of land cover labels for point location in a 4km² grid structure. Each point is manually defined using in situ observations or manual photointerpretation. The LUCAS dataset was originally developed in 2001 and was intended to provide early crop

estimates for the European Commission. In 2006, the focus of sampling changed from just an agricultural land survey to encompass a more general survey of land cover and land use. With the LUCAS dataset consisting of point samples in a 4km² grid structure, this dataset is unsuitable as a national land cover dataset due to its low spatial resolution. Low-resolution datasets such as this can result in the misrepresentation of the cover of some land coverage classes. (Brennan and Tubridy, 2017)

Datasets generated at a European level are not always suitable for use as a national land cover dataset. As a result, these datasets commonly include land cover classes that are inappropriate for a National Land Cover dataset for Ireland. For example, in Pan-European datasets such as the EU Crop Map 2018 and the LUCAS dataset, the classification schema contains many land cover classes not present on the island of Ireland. In addition, ML derived datasets such as those listed in Table 1.1 and in the JRC EU Crop Map 2018 are trained and validated on European-wide datasets. Therefore, additional validation of the data on a national Level needs to be undertaken for it to be used as a national dataset.

In response to the absence of a national land cover map, a joint project between the Ordnance Survey Ireland (OSI) and the Environmental Protection Agency (EPA) was undertaken for the generation of the first national land cover map intended to be published in 2022 (Green and Zimmermann, 2021). The first dataset will be generated for the 2018 reference year and designed as a baseline for monitoring future land cover change (Commins, 2021). Utilising both satellite and aerial imagery along with additional sectoral data such as the PRIME 2 dataset, this national land cover map provides a more robust and higher resolution national land cover dataset than currently available (EPA, 2022). For this project, a national land cover classification system for Ireland was developed, ensuring compatibility with European land cover and land use reporting (NPWS, 2017).

1.2.1 Co-ORdinated INformation on the Environment (CORINE)

In the absence of a national LCC dataset, the Co-ORdinated INformation on the Environment (CORINE) land cover mapping series is the most detailed land cover dataset currently available in Ireland (Brennan and Tubridy, 2017). CORINE is a Pan European Land Use and Land Cover monitoring programme. Established in 1985 by the European Community, that aimed to develop geo-spatial datasets on environmental information that were standardised and comparable across Europe (EPA, 2021; European Environment Agency, 1995). The first classification dataset released was for the year 1990 and was intended as an initial snapshot upon which future classification schemes could be compared. Since then, additional datasets have been released for 2000, 2006, 2012 and 2018. Each dataset following the original 1990 release also included a land cover change dataset (Büttner et al., 2021). While the CORINE classification scheme has not changed with successive releases of the CORINE datasets, the definition of each class has been updated to remove ambiguity between classes (Büttner and Kosztra, 2017; Kosztra et al., 2019). Additional differences between subsequent CORINE data releases included the spaceborne RS data used for each assessment, the resulting geometric accuracy and the overall production time in generating the datasets (Büttner et al., 2021). Table 1.2 outlines some of the changes between each iteration of the CORINE dataset.

Table 1.2: Evolution of CORINE land cover, **Source:** Büttner et al. (2021).

	CLC 1990	CLC 2000	CLC 2006	CLC 2012	CLC 2018
Satellite data	Landsat-4/5 (single date) (in a few cases Landsat MSS)	Landsat-7 ETM (single date)	SPOT-4 and/or IRS LISS III (dual date)	IRS,SPOT -4/7 and RapidEye (dual date)	Sentinel-2 and Landsat-8 for gap filling (dual date)
Time Consistency	1986-1996	2000 +/- 1 year	2006 +/- 1 year	2011-2012	2017-2018
Geometric accuracy of satellite images	$\leq 50\text{m}$	$\leq 25\text{m}$	$\leq 25\text{m}$	$\leq 25\text{m}$	$\leq 10\text{m}$
Production Time	10 years	5 years	3 years	2 years	1.5 years

Designed as a pan-European dataset, there are some limitations which make it unsuitable for some applications (Brennan and Tubridy, 2017). One such limitation is the 25ha minimum mapping unit. This minimum mapping unit is designed to work for spatial analysis at scales of 1:100,000. However, for applications including urban planning, forest management or risk assessments, higher scales of 1:50,000 to 1:10,000 are usually required. In addition the minimum mapping unit of 25ha is unsuitable for mapping some land cover classes and may result in the underrepresentation of some classes (Ovejero-Campos et al., 2019). The minimum mapping unit of 25ha can cause additional issues in countries such as Ireland where the unique makeup of highly varied landscape and small field parcels results in particular classes which cannot viably be mapped (Brennan and Tubridy, 2017). While nomenclature definitions have been updated for clarity, nevertheless, issues have still arisen due to mixed classes. An example of a mixed class that could be represented by two independent land cover classes is the class ‘Land principally occupied by agriculture, with significant areas of natural vegetation’. The ambiguity of classes such as this can result in different interpretations of the class in different regions or indeed, by different analysts (Aune-Lundberg and Strand, 2021).

1.2.2 Second Generation Corine Land Cover (CLC+)

In recognition of the limitations with the CORINE system, in 2017 the Environment Information and Observation Network (EIONET) Action Group on Land Monitoring in Europe (EAGLE Group) was tasked with the development of the Second Generation Corine Land Cover (CLC+). At the time of writing, the first CLC+ dataset is still in production (Copernicus, 2021) and will be produced for 2018 to be compatible with the CORINE 2018 dataset (Kleeschulte et al., 2019). CLC+ system has four main elements: Backbone, Core, Instance and Legacy. CLC+ Backbone consists of a vector and raster product generated from a combination of geospatial and EO data. CLC+ Core is an all-in-one data container for environmental land monitoring information according to the EAGLE data model. CLC+ Instance is the ‘nominal’ endpoint or final product in the establishment of the CLC+ product suite. And finally CLC+ Legacy, is a dataset derived

from the CLC+ Instance and is designed for back-compatibility with the first generation CORINE datasets.

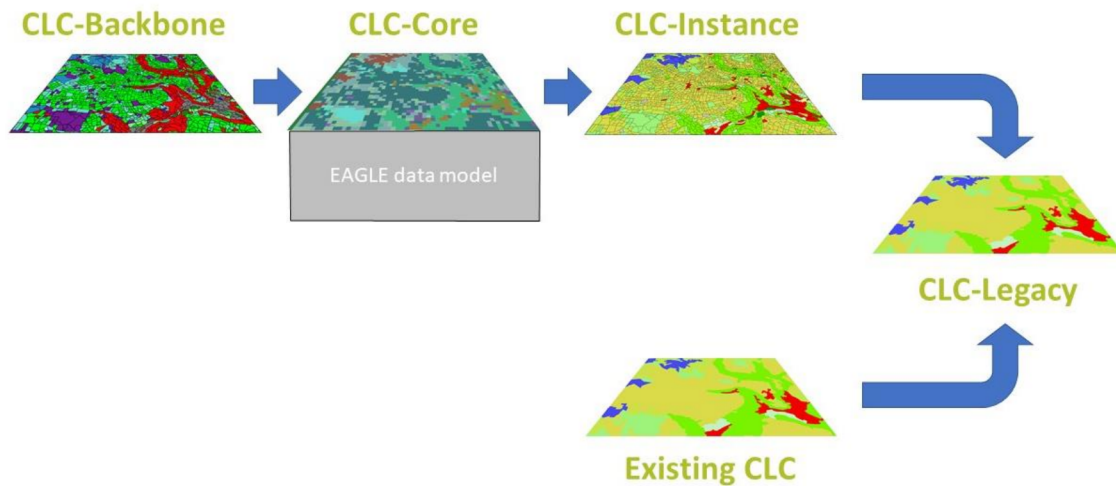


Figure 1.3: Conceptual design showing the interlinked elements required to deliver improved European land monitoring (CLC+ product suite), **Source:** Kleeschulte et al. (2019).

CLC+ Backbone

Of the four CLC+ elements, CLC+ Backbone is the only element that is primarily derived from EO data. CLC+ Backbone has two data outputs, a *Raster Product* and a *Vector Product*.

Raster product

The raster product is to be generated by a pixel-based methodology with 12 land cover classes and a 10m spatial resolution. The primary data source for this dataset is Sentinel-2 satellite imagery. However, due to the lack of availability of Sentinel-2 data, it is recommended that Sentinel-1 and Landsat-8 satellite data be used where required as suitable supplementary data to aid in classification.

Vector Product

The Vector Product is to be generated using a combination of known linear segments ‘Hard bones’ and image segmentation to identify natural boundaries in the landscape ‘Soft bones’. The generation of Soft bone segments is achieved using multi-temporal

data from Sentinel-2 along with mono-temporal Very High Resolution (VHR) satellite imagery. Finally, each segment is assigned a classification derived from classified pixels of the Raster Product under each segment (Kleeschulte et al., 2019)

1.3 Gaps in Current Knowledge in the Field of LCC

Despite the rapid growth in the number of studies examining the use ML for EO derived LCC, gaps in the current state of knowledge were identified during the literature review conducted as part of this thesis.

1.3.1 Suitability of mono-platform ML techniques for annual LCC on the island of Ireland

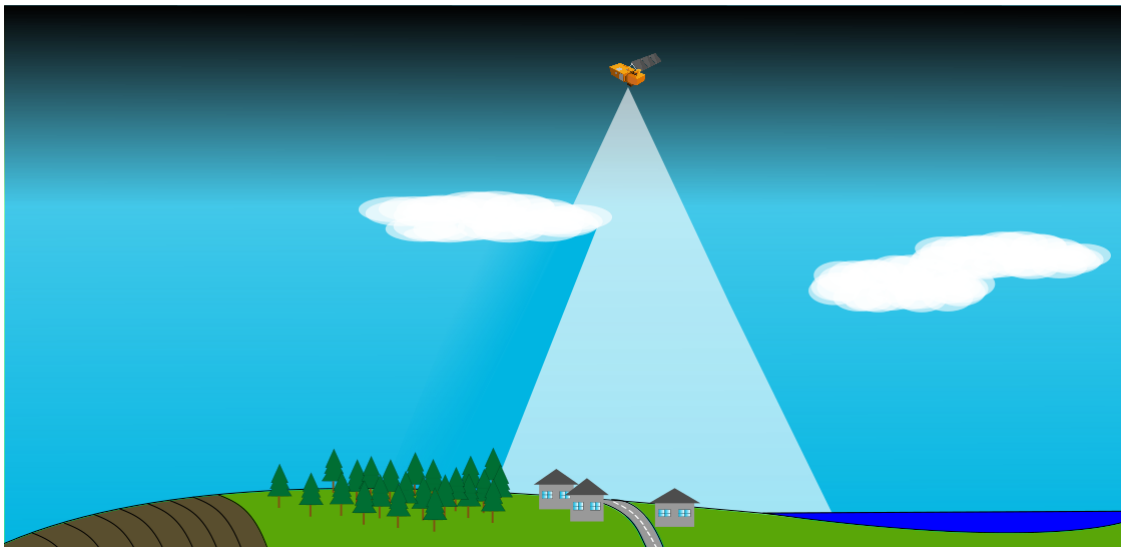


Figure 1.4: Conceptual illustration for mono-platform satellite LCC.

Along with the increase in the studies examining the use of ML for LCC, there is an increase in demand for EO derived LCC products (Macarringue et al., 2022). Demand is also increasing for more frequently updated LCC products. In a workshop on CORINE Land Cover+ in Brussels in November 2017, almost a quarter of member state representatives indicated the desire for a yearly updated product (Kleeschulte et al., 2019). If annually updated products are generated, the use of data captured outside the target

year may not be suitable. Despite the increased number of satellite RS platforms capturing data, obtaining sufficient optical satellite data to perform multi-temporal LCC using intra-annual data from a single platform can be challenging (Griffiths et al., 2019). The use of intra-annual mono-platform data can be particularly challenging in a region with frequent cloud cover such as Ireland, which has 100% cloud cover over 50% of the time (Met Éireann, 2021). Therefore, an examination of the suitability of ML techniques for intra-annual mono-platform LCC in a region with frequent cloud cover is required. The suitability of any analytical technique is largely dependent on the application. Therefore, to assess the suitability of ML techniques for the generation of an annual LCC product, the guidelines for the generation of the CLC+ Backbone raster product will be used as the reference to determine technique suitability.

1.3.2 Sensor fusion with variable data availability

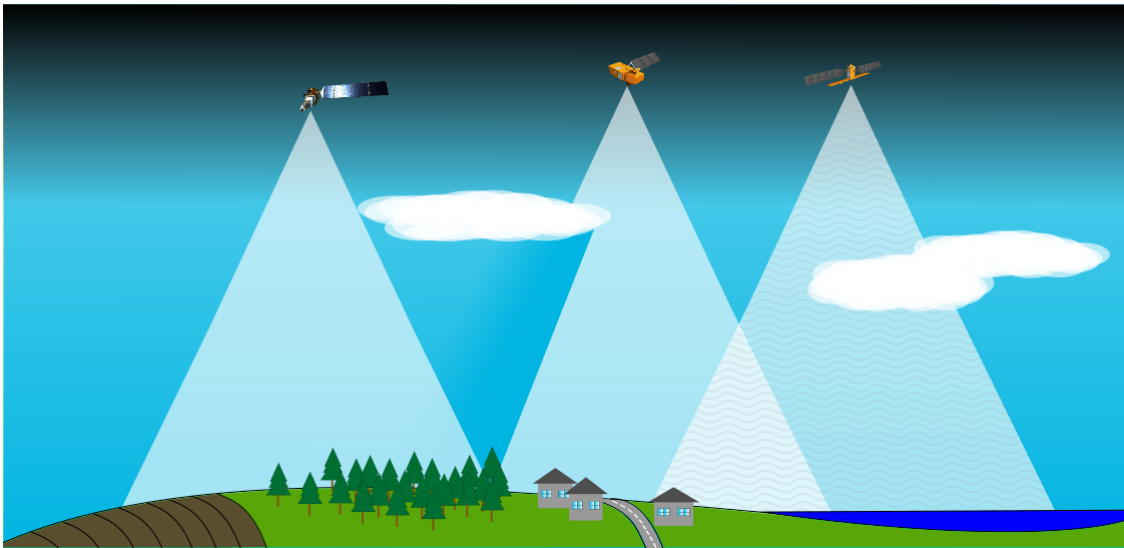


Figure 1.5: Conceptual illustration for multi-platform satellite LCC.

The use of data from multiple satellite platforms can be a useful means of improving classification coverage and accuracy. For example, where the platforms have similar characteristics, techniques such as gap-filling and harmonisation can be employed to overcome this issue of missing data as a result of cloud cover (Griffiths et al., 2019; Zhong et al., 2019). However, where there are significant areas of missing data, these techniques may not be suitable (El Fellaoui et al., 2016). As a result of cloud cover, it is not

always possible to ensure that for a given sensor there will be consistent data coverage across a large area. This issue is further compounded when fusing data from multiple sensors. Therefore, methodologies used for satellite data fusion in such situations need to be robust enough for a fusion where the data available varies across the assessed region. While there have been some studies that have examined this subject, such as by Salberg and Jenssen (2012) and Useya and Chen (2018), further investigation into this topic is required.

1.3.3 Decision-level fusion of Satellite and Aerial data

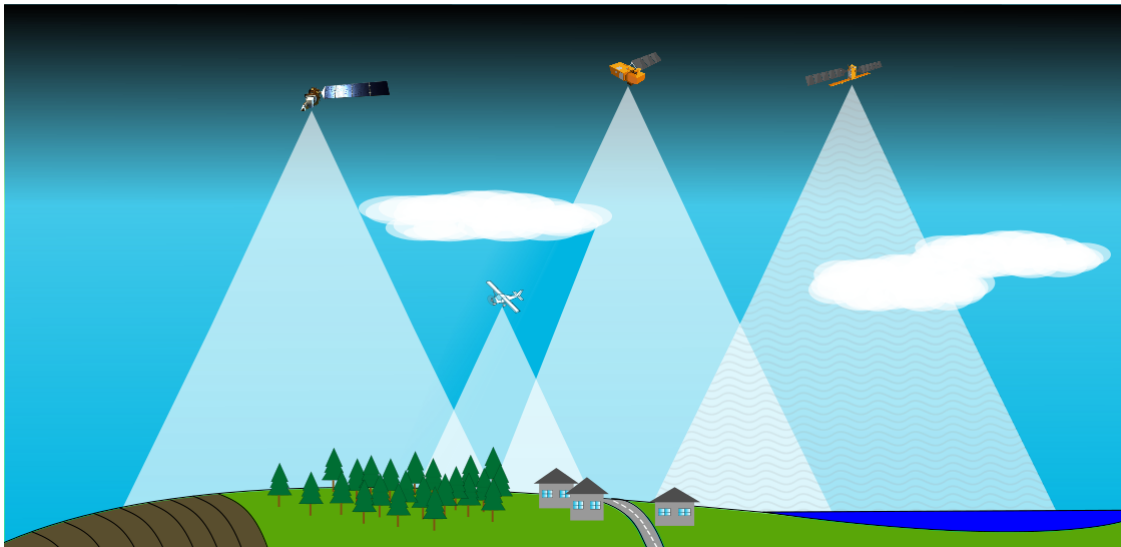


Figure 1.6: Conceptual illustration for multi-platform satellite and aerial LCC.

Another area where there is a significant gap in the current literature is in the fusion of satellite and aerial data to improve the accuracy of LCC. The use of high-resolution imagery for LCC has significant benefits (Kannoja and Jaiswal, 2018). However, its capture for large scale surveying is expensive compared to the use of satellite data. This issue is further exacerbated when multiple observations are required for multi-temporal analysis. Alternatively, the fusion of high-resolution aerial and multi-temporal satellite data can be performed to leverage unique information provided by each platform. During the literature review conducted as part of this thesis, the majority of papers focus on the pixel-level fusion of image data from two sources. Pixel-level fusion involves combining data from each image which can then be used as input data for a model (Chang and

Bai, 2018). However, significant challenges can be encountered with fusing data with significantly different spectral, spatial and temporal resolutions. This issue is further exacerbated when attempting to fuse data from multiple satellite platforms with aerial data. In such a situation, a decision-level fusion approach may be more suitable. In decision-level fusion, classification is performed on each platform independently before being combined to make a final classification output (Le Bris et al., 2019). Under a decision-level fusion approach, the classification of multi-platform satellite data can be performed independently to the aerial data before applying a fusion technique. While undertaking the literature review for this thesis, no papers were identified that utilised a decision-level fusion approach to fuse satellite and aerial data for LCC. Therefore, there is significant scope for further investigation into this topic.

1.4 Research Questions

This thesis will explore the following questions to address the identified gaps in current knowledge:

Question 1

What ML techniques are suitable for mono-platform satellite-derived annual LCC on the island of Ireland?

With the field of ML encompassing a wide range of data analytical techniques, addressing this question will involve the identification of state of the art ML techniques used for LCC in the existing literature. These techniques will be assessed for the classification of data on the island of Ireland with suitability defined not only by classification accuracy but also by the impact of cloud cover on the classification coverage of the technique. These techniques will be assessed using data from three satellite platforms: Sentinel-1, Sentinel-2 and Landsat-8. In addition, these techniques will be used as a baseline to determine the effectiveness of sensor-fusion techniques.

Question 2

How can a multi-sensor satellite data fusion approach be employed where frequent cloud cover results in differences in sensor data availability over the area that is being assessed?

With the issue of frequent cloud cover identified as a potential issue for LCC over the island of Ireland, the incorporation of data from multiple satellites may be an appropriate methodology to overcome this issue. However, there are various methods of performing data fusion. Therefore, the suitability of these techniques needs to be assessed to identify if they are appropriate in regions with frequent cloud cover.

Question 3

Can aerial data be used to further improve the accuracy of multi-sensor satellite-derived LCC?

The use of aerial RS data can contribute important information about land cover through the use of high-resolution imagery. With the ability of light aircraft to fly beneath the cloud cover, it may be particularly suited for capturing high-resolution data for a region with frequent cloud cover. However, the inclusion of high-resolution aerial data into multi-temporal multi-model satellite classification poses many challenges which need to be addressed.

1.5 Structure of this Thesis.

This thesis consists of six further chapters with the following structure:

Chapter 2: Current State of the Art - Literature Review

In this chapter, the challenges of performing LCC using EO technologies are examined. As part of this examination, existing techniques are identified in the literature to overcome these challenges. This chapter also presents the role of ML in the generation of LCC data and highlights the gaps in the current knowledge. This chapter also examines the suitability of ML techniques for the generation of the CLC+ LCC datasets and how they relate to the challenges identified in performing LCC.

Chapter 3: Evaluation of ML Techniques for Satellite based LCC

In this chapter, a comparative assessment of ML techniques is performed to determine their suitability for performing EO derived LCC on the island of Ireland. As part of this comparative assessment, the impact of frequent cloud cover on model coverage and accuracy is also assessed.

Chapter 4: Satellite Sensor Fusion LCC

This chapter examines the application of satellite sensor fusion to improve the accuracy and coverage of LCC on the island of Ireland. This assessment is conducted in two parts; a comparative assessment between pixel-level and decision-level fusion techniques and an assessment of fusion techniques where the availability of satellite data varies across the assessed region.

Chapter 5: Combined Satellite-Aerial Data Fusion

In this chapter, decision-level fusion is used and examined for the fusion of non-temporal high-resolution aerial data and multi-temporal and multi-platform satellite data. As the aerial data is mono-temporal, a simplified classification schema is required for its classification. The simplified classes are generated such that they could be related to the satellite class schema before performing fusion. The

satellite-aerial fusion technique presented in this chapter demonstrates how fusion can be performed despite the significant difference in the characteristics of each data source.

Chapter 6: Conclusion

This chapter provides a concise summary of the work undertaken in this thesis and identifies the key contributions of this research. It also highlights challenges encountered when undertaking this thesis and identifies topics for future work. Finally, it concludes with some last remarks on this thesis.

Chapter 2

Current State of the Art - Literature Review

2.1 Introduction

This chapter outlines the current state of the art in ML techniques for LCC using EO technologies. In particular, this chapter will examine techniques suitable for the generation of the CLC+ Backbone raster product for mapping land cover over geographic regions impacted by frequent cloud cover. This chapter will be structured into seven sections. **Section 2.2** will outline the challenges associated with utilising EO data for LCC. **Sections 2.3 to 2.6** will provide an in-depth review of ML techniques that can be employed for LCC using EO data. The ML techniques reviewed in this chapter will be discussed in the context of four modelling categories: Spectral-based LCC, Spatial-based LCC, Temporal LCC and Sensor Fusion LCC. It should be noted that not all ML techniques fit neatly into any one of these categories, with many techniques containing elements from one or more of these categories. The ML modelling categories and associated definitions for each category are specified below in Table 2.1.

Table 2.1: ML category definitions used in literature review.

LCC Category	Category Focus
Spectral-based	ML techniques that primarily rely on spectral information within an image.
Spatial-based	ML techniques that leverage the spatial relationship between pixels within an image.
Temporal	ML techniques that utilise the variations in the spectral or spatial information in the image over time.
Sensor Fusion	ML techniques combining data collected from multiple sources or different sensors.

Finally, **Section 2.7** will examine the requirements for the generation of CLC+ and will assess the suitability of ML techniques for the generation of CLC+ Backbone raster product.

2.2 Challenges using Earth Observation for Land Cover Classification

With EO playing a central role in modern LCC, it is important to understand the factors that may impact the accuracy of using EO data for LCC. The factors that impact the accuracy of LCC using EO will be discussed in this study in terms of the fundamental resolution characteristics of the EO data namely; spectral, radiometric, spatial and temporal resolution (Chang and Bai, 2018). The definition of each resolution type is provided in Table 2.2.

2.2.1 Spectral and Radiometric Resolution

For RS sensors, their spectral resolution is typically defined by the number of distinct spectral wavelength ranges known as *bands*, while the sensor’s radiometric resolution relates to its sensitivity and ability to record differences in the signal strength received by the sensor (Chang and Bai, 2018). Sensors capable of recording information from about five to twelve bands are commonly referred to as multi-spectral sensors, while sensors that can capture a much higher number of bands (typically tens to hundreds of

Table 2.2: Resolution characteristics definitions.

Resolution Type	Definition
Spectral	The ability to differentiate signals captured at different spectral ranges in the electromagnetic spectrum (Chang and Bai, 2018).
Radiometric	The ability to record differences in the strength of the signal being recorded (Ihlen, 2019).
Spatial	The ability to identify spatial differences in the objects or phenomenon being detected. This is normally recorded as pixel size or Ground Sampling Distance (GSD) (Lillesand et al., 2014).
Temporal	The ability to detect the temporal change in an object or phenomenon being recorded. This usually is recorded as the frequency of data capture (ESA, 2015).

bands) are referred to as hyperspectral sensors (Adão et al., 2017). In contrast, consumer-grade cameras capture three spectral ranges, Red, Green and Blue (RGB). These image sensors, commonly use a Bayer filter on a single imaging chipset, comprising a number of Red, Green Blue digital receptors and are designed to reproduce the human perceptual quality of a scene rather than produce accurate spectral recordings (Yang et al., 2014; Nguyen et al., 2014). The difference between the spectral sensitivity of a consumer-grade camera and a multi-spectral camera is illustrated in Figure 2.1.

In addition, many consumer-grade cameras commonly record each band with an 8 bit (256 grey levels) radiometric resolution (Lillesand et al., 2014). This is in comparison to the Sentinel-2 multi-spectral sensor, which records spectral information with a 12 bit (4,096 grey levels) radiometric resolution (ESA, 2015). The use of sensors with a high spectral and radiometric resolution is important in EO, as the reflected electromagnetic energy from a surface can provide information about the object or phenomenon being observed (Emery and Camps, 2017). Figure 2.2 provides an illustrated example of how the reflectance of three land cover types may differ depending on the wavelength being observed. Sensors used for EO are not limited to the capture of optical data. For example, Radio Detection and Ranging (RADAR) is a widely used EO technique. This technique involves the transmission of radio waves of a wavelength between 0.5cm to 100cm. After reflecting off a surface, the retuned signal’s strength, polarization, and phase are recorded.

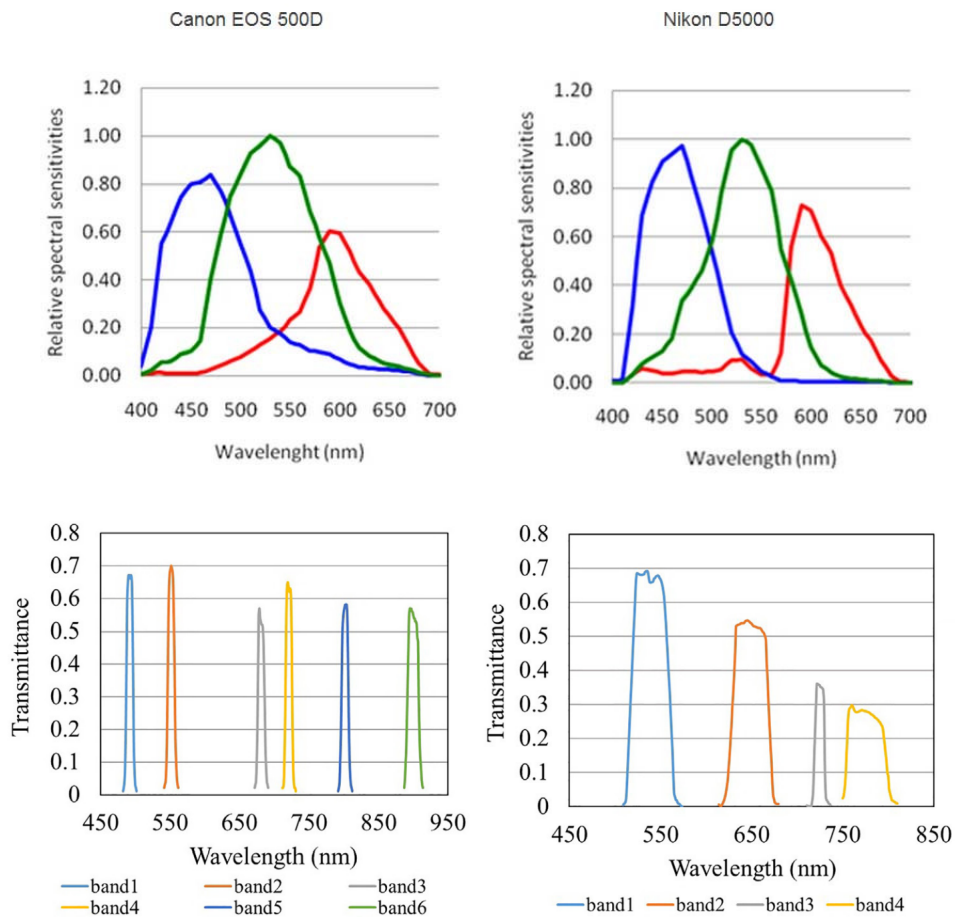


Figure 2.1: Spectral response function of conventional cameras Canon EOS 500D (Top Left) and Nikon D5000 (Top Right) and multi-spectral cameras Mini-MCA6 (Bottom Left) and Sequoia (Bottom Right), **Source:** Fastie (2015); Deng et al. (2018).

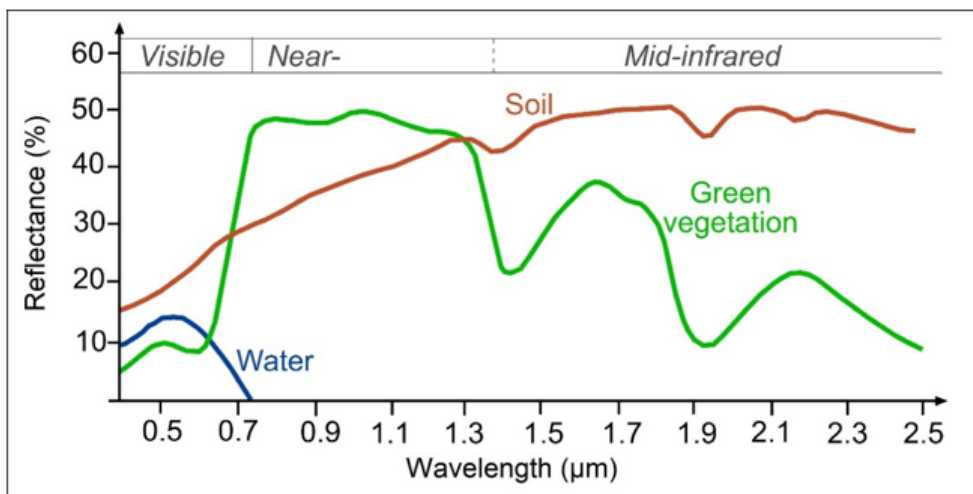


Figure 2.2: Illustration of spectral reflectance of water soil and green vegetation, **Source:** GIS Homework (2021).

Platforms such as Sentinel 1, TerraSAR-X and RADARSAT-2 used a technique known as Synthetic Aperture Radar (SAR) for increased spatial resolution (Chang and Bai, 2018).

While increasing the spectral resolution of a sensor can have a significant benefit to the generation of LCC data, there are limits to spectral range and resolution that can be recorded. The biggest limitation to the spectral resolution is that narrowing the spectral range reduces the energy that is recorded by the sensor. This reduction in the signal recorded by the sensor can increase the impact of noise in the data recorded by the sensor (Rasti et al., 2018). The use of multiple sensors with differing spectral resolutions can increase the information recorded about an object or platform. However, for some applications, the different but sometimes overlapping spectral resolutions of each platform and sensor can make comparing data recorded from each sensor challenging. For this reason, data collected from ‘twinned’ satellite platforms such as Sentinel-1 A&B, Sentinel-2 A&B and Pleiades 1A&1B aim to have almost identical spectral and radiometric resolutions between satellite pairs (ESA, 2012b, 2015; Coeurdevey and Gabriel-Robez, 2012). To aid cross platform analysis, spectrally harmonized datasets have been generated. One such example is the ‘The Harmonized Landsat and Sentinel-2 surface reflectance’ dataset. In this product, Sentinel-2 data has been spectrally adjusted to match the Landsat-8 spectral resolution (Claverie et al., 2018). Harmonization between sensors can also be achieved by converting spectral data from each data source to a common format. Sagan et al. (2019) demonstrated this approach through the application of spectral indices. They were able to demonstrate that imagery captured from a UAV mounted with a Parrot Sequoia multi-spectral camera could be used in conjunction with WorldView-3 multi-spectral imagery for high temporal crop monitoring. However, as outlined in this paper, there are minor differences in the spectral resolution of each sensor which will be incorporated into the calculated spectral indices. In this study, the researchers aimed to collect data from similar dates for both the satellite and UAV platform. However, no concurrent surveys were captured to assess if spectral indices calculated for each platform are comparable.

As electromagnetic energy passes through the atmosphere, this energy can be absorbed or scattered by gasses. The degree by which this interaction occurs is dependent

on the energy’s wavelength. Therefore, to obtain accurate spectral information from the data recorded by RS sensors, this interaction with the atmosphere needs to be accounted for. This is particularly important when recording the change in an object’s spectral response over time (Shunlin and Jindi, 2020). A number of atmospheric correction techniques have been developed for different sensors and conditions. After performing atmospheric correction of optical data, the signal recorded by the sensor represents the surface radiance or reflectance of the recorded object or phenomenon (ESA, 2015; Ihlen, 2019). The need for atmospheric correction is not consistent across all RS sensors. Some SAR platforms such as Sentinel-1 are not affected by atmospheric conditions including cloud cover (d’Andrimont et al., 2021).

2.2.2 Spatial Resolution

When deciding whether a sensor is suitable for a given application, a key factor is its spatial resolution (Baghdadi and Zribi, 2017). The spatial resolution of RS data is commonly represented by its Ground Sampling Distance (GSD). GSD is the area on a surface represented by a single pixel in the image. Depending on the LCC application, the spatial resolution of the data can be a significant limiting factor to generating accurate LCC data. For example, in Figure 2.3 all buildings in the 0.04m resolution aerial imagery can be visually identified. However, in the 10m resolution Sentinel-2 imagery, many smaller buildings could not be visually separated from one another.



Figure 2.3: Sentinel-2B 10m GSD captured (2018-09-05) over Maynooth University (Left), aerial imagery 0.04m GSD capture (2018-09-03) over Maynooth (Right).

Table 2.3: Examples of satellite spatial resolution and image footprint, **Source:** Satellite Imaging Corporation (2021); NASA (2021a).

Platform	Maximum GSD	Image Footprint
Worldview 4	0.31m	13.1km ²
Pleiades 2	0.5m	20km ²
RapidEye	5m	77km ²
Sentinel-2	10m	290km ²
Landsat-8	15m	185km ²
MODIS	250m	2330km ²

While a high spatial resolution can significantly improve classification accuracies, platforms and sensors capturing high-resolution data tend to have a much smaller overall spatial coverage over the ground surface (Zhu et al., 2010). Table 2.3 provides a comparison between the spatial resolution and image coverage of five optical satellites.

Higher spatial resolution imagery not only helps in delineating the boundary between classes but also improves classification accuracy when used with ML techniques specifically designed to take the spatial relationship of data into account (Kannoja and Jaiswal, 2018). With the use of medium to low-resolution imagery, boundaries between objects may not be well defined. As a result, pixels along this boundary may contain a mix of spectral information from both objects (Li et al., 2019; Shunlin and Jindi, 2020). However, obtaining higher resolution aerial or UAV imagery can dramatically increase the cost of data capture, data storage and the computational cost of processing the data (Véstias, 2019).

Further challenges are encountered when analysing data captured from multiple platforms with different spatial resolutions. For example, in a 10cm GSD aerial image, 10,000 pixels would cover the same area as a single Sentinel 2 pixel with a GSD of 10m. To account for this difference, data from one platform can be interpolated to match the spatial resolution of the other. While this process is normally performed to reduce the resolution of the high-resolution data source to match the lower resolution data source, techniques such as pansharpening can be employed to increase the spatial resolution of an image. When performing pansharpening, a high-resolution image is used as a reference to improve the spatial resolution of the another image (Chang and Bai, 2018). Platforms such

as the Landsat-8 and Pleiades contain a specific panchromatic sensor that can be used to pansharpen the lower resolution multi-spectral imagery (Satellite Imaging Corporation, 2021; Ihlen, 2019; Coeurdevey and Gabriel-Robez, 2012). More recently ML enabled super-resolution techniques have been developed that can be used to improve the spatial resolution of an image. Shao et al. (2019) and Isa et al. (2021) demonstrated how a ML enabled super-resolution approach can be used to increase the resolution of Landsat-8 data from 30m GSD to 10m GSD. Their papers also demonstrated that these techniques could be used to spectrally harmonise Landsat-8 data to that of Sentinel-2. While the application of a super-resolution approach may have some benefits in particular situations, it is essential to understand the limitations of this technique. As this approach effectively approximates the target sensor’s spectral and spatial resolution, anomalies are likely to occur where the input sensor has insufficient information for this purpose. This limitation is recognised in the paper by Isa et al. (2021), where due to the absence of a band with a similar wavelength range in the input Landsat 8 data, the model was unable to reliably predict band 10 of Sentinel-2. In the study by Shao et al. (2019), the super-resolution of the Landsat 8 data was achieved by utilising multiple Sentinel-2 observations from similar dates as auxiliary information to aid in the super-resolution. As recognised in the paper, this approach may not be viable if there are insufficient Sentinel-2 observations due to cloud cover. Attempts to apply the super-resolution approach without using the auxiliary Sentinel-2 data resulted in significantly lower classification results. Given these results, the model may overly rely on the Sentinel-2 auxiliary information to determine the spectral information for the predicted output rather than rely on the Landsat-8 information. The reliance on the Sentinel-2 auxiliary information may result in anomalies in the predicted output where there are significant changes over the observed area between the capture of the auxiliary information and the target Landsat-8 date.

2.2.3 Temporal Resolution

Temporal resolution refers to the frequency of data capture over a specific area of the land surface. Accounting for temporal variability can be particularly useful when classi-

ifying vegetation cover, as the spectral response can change for different vegetation types depending on the time of year (Kovačević et al., 2020; Nogueira et al., 2019). An example of temporal variation is illustrated in Figure 2.4. This plot displays Normalized Difference Vegetation Index (NDVI) values for three land cover classes using Sentinel-2 data. An NDVI from Sentinel-2 data is calculated using the following formula (Henrich and Brüser, 2021):

$$NDVI = \frac{\rho_{NIR} - \rho_{Red}}{\rho_{NIR} + \rho_{Red}} \quad (2.1)$$

where (ρ_{Red}) is the reflectance from the Red band and (ρ_{NIR}) is the reflectance from the near-infrared band.

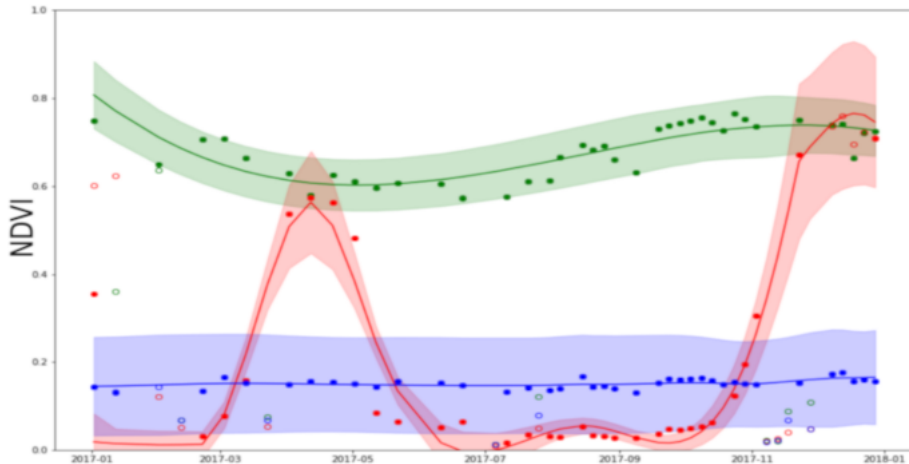


Figure 2.4: NDVI derived from Sentinel-2 over a year. Red = cultivated land, blue = build-up area and green = grassland, **Source:** Peressutti (2018).

An additional consideration is that some phenomena that indicate land cover types such as seasonal lakes (turlough) are only visible using RS at certain times of the year (Walsh et al., 2021). Utilising temporal information can also help mitigate the influence of unique non-persistent events that may impact LCC accuracy. Unique non-persistent events can include extreme weather events such as flooding or human activities. An example of a non-persistent event is visible in Figure 2.5. In this instance, during the capture of the Sentinel-2 image on the 21st April 2018, slurry was in the process of being spread on established grassland. As the owner of the farmland highlighted in Figure 2.5, the agricultural practices of the land are known to the author. Typical farm management

activities such as this may temporally change the spectral reflectance from the surface and as a result may negatively impact the spectral analysis.

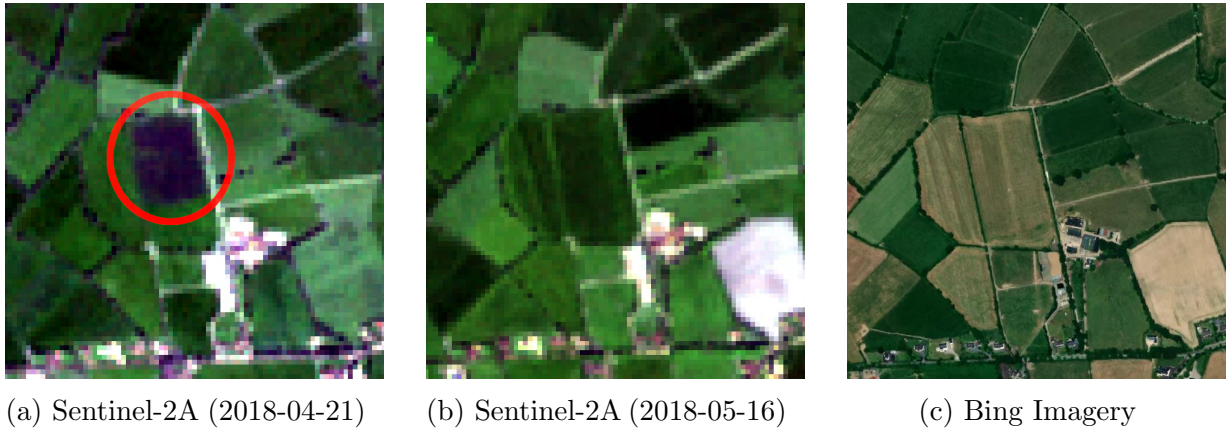


Figure 2.5: An example of a unique non-persistent event captured by (a) Sentinel-2A (2018-04-21) in image and circled in red. (b) Sentinel-2A (2018-05-16) image (c) and Microsoft Bing Imagery (www.bing.com/maps/aerial) for reference.

While there are many benefits to the use of temporal information for LCC there are many challenges that can be encountered through its application. One such challenge is obtaining sufficient optical satellite observations over the target region. While the number of EO platforms has significantly increased over recent years, obtaining sufficient optical satellite imagery remains one of the most significant challenges for temporal analysis in regions with frequent cloud cover (Huang et al., 2020) such as Ireland. Where a small area of a region undergoing assessment has missing data due to cloud cover, gap-filling techniques can be used. These gap-filling techniques include global linear histogram matching or matrix completion (El Fellaoui et al., 2016). Gap-filling techniques can be particularly useful when performing analysis over a large area as some temporal ML techniques require that all data points being analysed have identical observation counts and dates (Zhong et al., 2019). However, these gap-filling techniques may not be suitable where there are significant areas of the assessed region that have missing data due to cloud cover. If two regions have a different number of observations, two independent models may need to be trained for each respective region (Salberg and Jenssen, 2012).

One potential solution to address the challenge of limited temporal resolution as a result of frequent cloud cover, is to include data captured from multiple platforms. However, as already discussed, there are additional challenges when performing analysis

using data sources which have different spectral and spatial characteristics. Some SAR platforms may be a viable alternative in regions with frequent cloud cover. This is due to the fact that cloud cover has a minimal impact on the wavelength that some SAR systems operate (Emery and Camps, 2017). Capturing data using an aircraft or UAVs can be used as another alternative to optical satellite platforms due to their ability to fly beneath cloud cover. However, the cost issue of surveying a large region is further compounded if multiple surveys are required to accommodate multi-temporal analysis. Additionally, variation in the cloud cover during an aerial or UAV survey may result in variable solar irradiance conditions that may negatively impact the quality of captured multi-spectral or hyper-spectral imagery (Wang et al., 2019).

One consideration when performing analysis using multi-temporal data is that the inclusion of additional temporal information can dramatically increase computational requirements and the volume of data to be processed (Kovačević et al., 2020). As a result, a number of techniques have been developed in an attempt to account for this issue. Observations that do not significantly contribute to the model’s prediction accuracy can be excluded through data exploration. This approach can be useful before training a model for cropland cover classification as it has been determined that data collected within specific date ranges are significantly better at aiding discrimination between classes (Valcarce-Diñeiro et al., 2019). Alternatively, a dimensionality reduction approach can be employed to reduce the number of variables used when training a model. When performing dimensionality reduction, the aim is to transform the input variables such that they can be represented by fewer variables while not losing information that might be significant to the analysis. Dimensionality reduction can be achieved through methods such as temporal averaging, the utilisation of spectral indices in place of spectral bands, or performing Principle Component Analysis (PCA). These approaches have been applied in a number of studies such as by Huang et al. (2020), Haarpaintner and Hindberg (2019) and Carrasco et al. (2019). While each of these studies obtains the highest classification accuracy using normalised difference indices, by limiting the analysis to a single spectral index such as NDVI, other spectral information is excluded from the analysis. In each

study, the temporal mean and variance of these indices were examined as input variables. However, as identified by Carrasco et al. (2019), the analysis results can be negatively impacted where there are few observations to calculate the data's temporal mean or variance.

2.3 Spectral Based LCC

Spectral based LCC techniques rely on the pixel values which are recorded as Digital Numbers (DN) within an image for classification. A simple example of how DN values can be used for the classification of images can be demonstrated with the use of thresholding, where a class is assigned to a pixel if its DN value is greater than or less than a defined threshold value. This is represented by the formula:

$$DN'_i = \begin{cases} 1, & DN_i < \theta \\ 0, & DN_i > \theta \end{cases} \quad (2.2)$$

A practical example of using thresholding for classification is illustrated in Figure: 2.6, where a Sentinel-2 image has been classified into land and water. This process was achieved by first calculating a Modified Normalised Difference Water Index (MNDWI) using the following formula (Du et al., 2016):

$$MNDWI = \frac{\rho_{Green} - \rho_{SWIR}}{\rho_{Green} + \rho_{SWIR}} \quad (2.3)$$

where (ρ_{Green}) is the reflectance from the green band and (ρ_{SWIR}) is the reflectance from the short-wavelength infrared band. In the case of data from the Sentinel-2 satellite, the formula is as follows:

$$MNDWI = \frac{\rho_{Band3} - \rho_{Band11}}{\rho_{Band3} + \rho_{Band11}} \quad (2.4)$$

MNDWI takes advantage of the significant difference in how the green and short-wavelength infrared bands are reflected by land and water. Difference indices such as the MNDWI

have values ranging between -1 and 1. In the case of MNDWI, higher values above zero generally correspond to water, while lower values typically correspond to land (Du et al., 2016). The results of applying this threshold are visible in Figure 2.6. While this approach does appear successful at identifying water bodies in the scene, there are a number of locations where land is falsely classified as water.

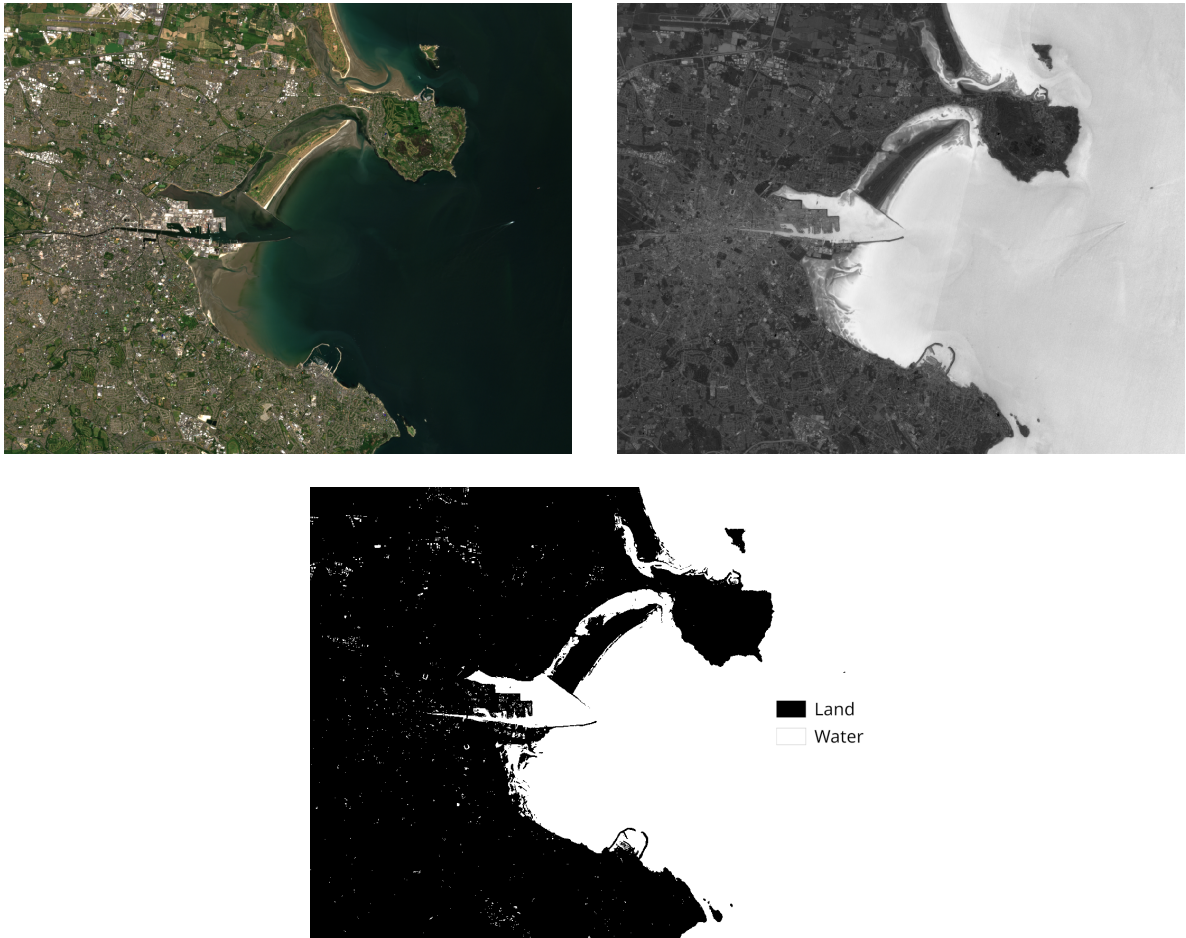


Figure 2.6: Sentinel-2 image over Dublin, Ireland (01/06/2020) true colour image (top left), MNDWI (top right) and MNDWI threshold with a threshold of zero (bottom).

Spectral indices such as MNDWI are used to reduce the spectral information captured across multiple bands to a single value. The output of these indices can then be used in further analysis. Table 2.4 lists a number of spectral indices that have been developed to highlight specific elements of the recorded RS spectral information.

Table 2.4: Spectral indices for Sentinel-2 satellite data **Sources:** Henrich and Brüser (2021); Du et al. (2016)

Indices	Formula
Normalized Difference Vegetation Index (NDVI)	$\frac{\rho_{band8} - \rho_{band4}}{\rho_{band8} + \rho_{band4}}$
Modified Normalised Difference Water Index (MNDWI)	$\frac{\rho_{Band3} - \rho_{Band11}}{\rho_{Band3} + \rho_{Band11}}$
Leaf Chlorophyll Index	$\frac{\rho_{band8} - \rho_{band5}}{\rho_{band8} + \rho_{band4}}$
Soil Composition Index	$\frac{\rho_{band11} - \rho_{band8}}{\rho_{band11} + \rho_{band8}}$
Global Vegetation Moisture Index	$\frac{(\rho_{band9} + 0.1) - (\rho_{band12} + 0.02)}{(\rho_{band9} + 0.1) + (\rho_{band12} + 0.02)}$

2.3.1 Spectral Based ML Techniques

A number of other spectral-based classification techniques, varying in complexity, follow a similar process to the example provided in the preceding section in terms of grouping pixels based on DN values. Three examples of ML techniques used for spectral base classification that will be examined in this section include; Random Forest (RF), Artificial Neural Network (ANN) and Support Vector Machine (SVM).

2.3.1.1 Random Forest (RF)

RF is an ensemble-based ML technique that employs a collection of decision tree models. Using bootstrapped samples from the original training data set, each decision tree is developed by recursively partitioning the data into nodes such that each node contains similar samples. For each partition step, a random subset of the available features is used to determine the optimum partitioning of the samples. This process is repeated until a defined threshold has been met, such as the tree depth. Predictions using a RF model are

achieved by taking the majority vote of all decision trees within the model as illustrated in Figure 2.7. While each decision tree may not produce accurate classification, the overall result of the RF can be much more accurate (Breiman, 2001; Zafari et al., 2019). Additional benefits to implementing RF is its ability to overcome the issue of ‘noise’ in the input data and its ability to handle large datasets (Shunlin and Jindi, 2020; Nitze et al., 2015). A number of papers applying a comparative analysis of ML techniques have identified RF in particular as one of the best-performing spectral-based methodologies for LCC using medium spatial resolution EO imagery (Talukdar et al., 2020; He et al., 2019; Wulder et al., 2018). In the case of the paper by He et al. (2019), RF was utilised with temporal information by including the spectral data from each date as additional input variables. This study demonstrated that RF could outperform models that are specifically designed to be used with temporal data. A significant benefit of utilising RF is the ability to identify the importance of each input variable to the classification result. Identifying the importance of each input variable can enable an analyst to exclude variables that do not contribute to the model, reducing the computational cost of performing classification. Additionally, examining the importance of input variables can provide the analyst insight into the type of data required for future study. In the paper by He et al. (2019), the researchers identified that features derived from March or April were the most significant variables to the classification of winter wheat.

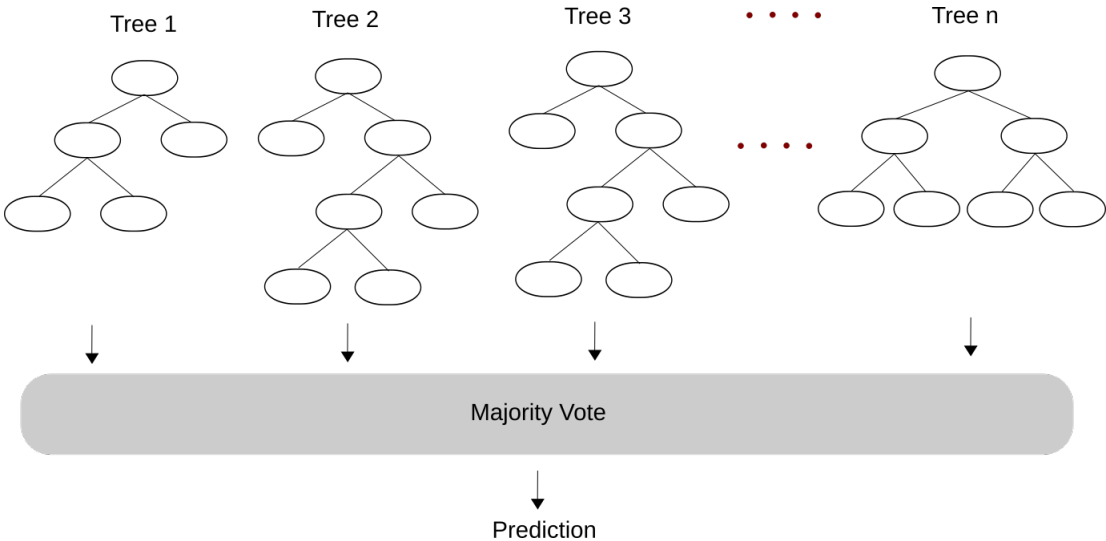


Figure 2.7: Example illustration of random forest structure.

2.3.1.2 Artificial Neural Network (ANN)

ANN, derive their name from the fact that they were first developed as models for neurons in the human brain. Their widespread application is such that they have become the foundation upon which more complicated ML techniques have been developed (Raschka and Mirjalili, 2017). An ANN is composed of layers of nodes. For each node (i) the input values (x) are each multiplied by weights (w). These calculations are summed along with a bias (b) before applying an activation function (S). The output of a neuron (y_i) is given by (Skansi, 2018):

$$y_i = S \left(b_i + \sum_{j=1}^n w_{ij}x_j \right) \quad (2.5)$$

In general, the activation functions are nonlinear in structure and so enable the network to model non-linear relationships in the data. The output from each layer of neurons is input into the next layer. This process is repeated until the end of the network where the output of the final layer is used as the model prediction. Figure 2.8 provides an illustration of an example ANN architecture. The model is trained using a methodology known as backpropagation (Hastie et al., 2017), where the weights and bias of the neurons are updated based on a loss function. Beginning with the last layer of the network, the weights and bias of each neuron in the layer are updated before moving to the previous layer.

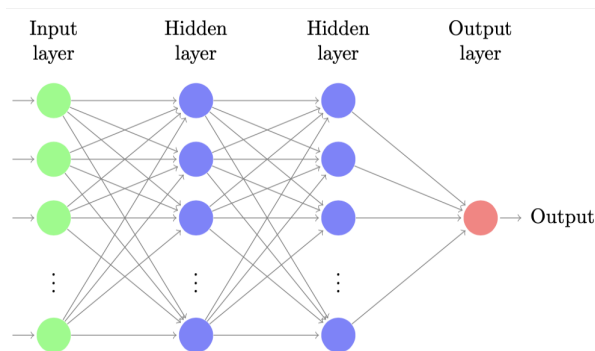


Figure 2.8: Example illustration of artificial neural network.

Over the years, a number of different types ANNs have been developed. One of the simplest forms of ANNs, comprising very few layers is commonly referred to as a

Multilayer Perceptron (MLP). Conversely, ANNs that have a large number of hidden layers fall into the category of deep learning, which has been proven as an extremely powerful tool for modelling complex data (Shunlin and Jindi, 2020). ANNs have appeared in a number of papers comparing ML techniques for LCC (Gašparović and Dobrinić, 2020; Camargo et al., 2019; Talukdar et al., 2020). In these comparisons, ANNs are generally surpassed by other ML techniques. However, ANNs have played a vital role in the development of EO derived LCC as the original foundational structure for other spatial models such as Convolutional Neural Networks (CNNs) and temporal models such as Recurrent Neural Networks (RNNs).

2.3.1.3 Support Vector Machine (SVM)

A SVM functions by defining a hyperplane that is designed to maximise the margin between samples from each class and the hyperplane. An SVM's margin is defined as the sum of the distance to the hyperplane from the closest point in each class. The points on the margin are referred to as support vectors (Zafari et al., 2019; Hastie et al., 2017). Figure 2.9 provides a basic illustration of a SVM for separation of two dimensional data.

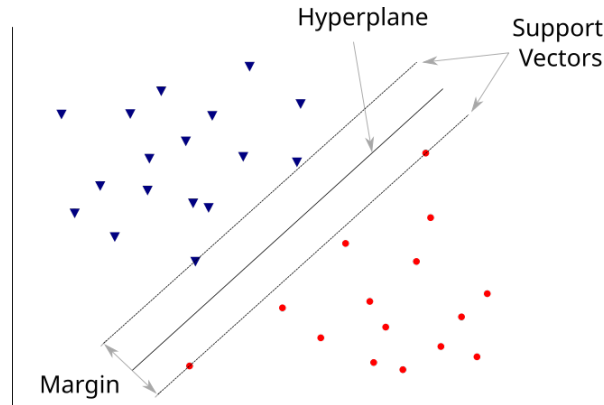


Figure 2.9: Example illustration of support vector machine structure.

SVMs are particularly effective when employed with high dimensional data (Shunlin and Jindi, 2020). While RF is widely used for LCC, for some applications SVMs can provide comparable results. Camargo et al. (2019) conducted a comparative assessment on a variety of pixel-based machine learning techniques for LCC using ALOS-2/PALSAR-2 Polarimetric SAR imagery. Of the ML techniques they evaluated, they observed that

RF, MLP, and SVM obtained the best results with statistically similar Kappa indices for each. A comparative assessment of ML techniques for LCC using SAR data by Gašparović and Dobrinić (2020) found that for single observation classification, SVMs outperformed all other techniques assessed, including RF and ANN. In the study undertaken by Dabija et al. (2021), evaluating the use of Sentinel-2 and Landsat-8 for the classification of Corine Land Cover (CLC) data, it was found that an SVM obtained the highest accuracy results for each respective platform sensor dataset.

2.4 Spatial Based LCC

Spatial Based LCC techniques use the spatial relationship of data within an image to provide additional information, enabling improved classification accuracy (Sharma et al., 2017). A Convolutional Neural Network (CNN) is an example of an ML technique that has been developed to exploit the spatial relationship inherent within an image (Carranza-García et al., 2019). CNNs have a number of similarities to ANNs and are influenced by the understanding of how the brain interprets visual information (Rawat and Wang, 2017). As with ANNs, a number of CNN architectures have been developed. To examine the application of CNNs for LCC, here CNNs will be divided into two broad architectures. The first architecture uses an image patch as an input into the network resulting in a single classification output (Patch-to-Point). In the second type of CNN architecture, the output of the CNN is an image where each pixel is assigned a class (Patch-to-Patch).

2.4.1 Patch-to-Point

Similar to ANNs, a CNN comprises an input layer, a number of hidden layers and an output layer. In CNNs, the hidden layers include *convolutional* and *pooling* layers. Convolutional layers utilise an array of values known as a kernel. For a given pixel in the input image array, the dot product is calculated between the kernel and the pixels neighbouring, equalling the size of the kernel centred at that pixel. This process is repeated for all pixels in the input data enabling the spatial relationship of data within the image

to be taken into account. This process also enables the sharing of parameters across the entire image. The output of each layer is referred to as a feature map (Goodfellow et al., 2016). Pooling Layers are designed to reduce the size of a feature map through the aggregation of values. This process reduces the number of variables and can reduce the impact of spatial distortions and translations in the input data. A common form of pooling is max pooling, where the largest value within its receptive field is selected as the value for the next layer (Rawat and Wang, 2017). In CNNs that are designed to generate a single classification based on an input image, the network performs a number of convolution and pooling of layers before ‘flattening’ the data into a one-dimensional layer and subsequently, the resulting vector is input into a dense neural network (Skansi, 2018). An example of the structure of a CNN is outlined in Figure 2.10.

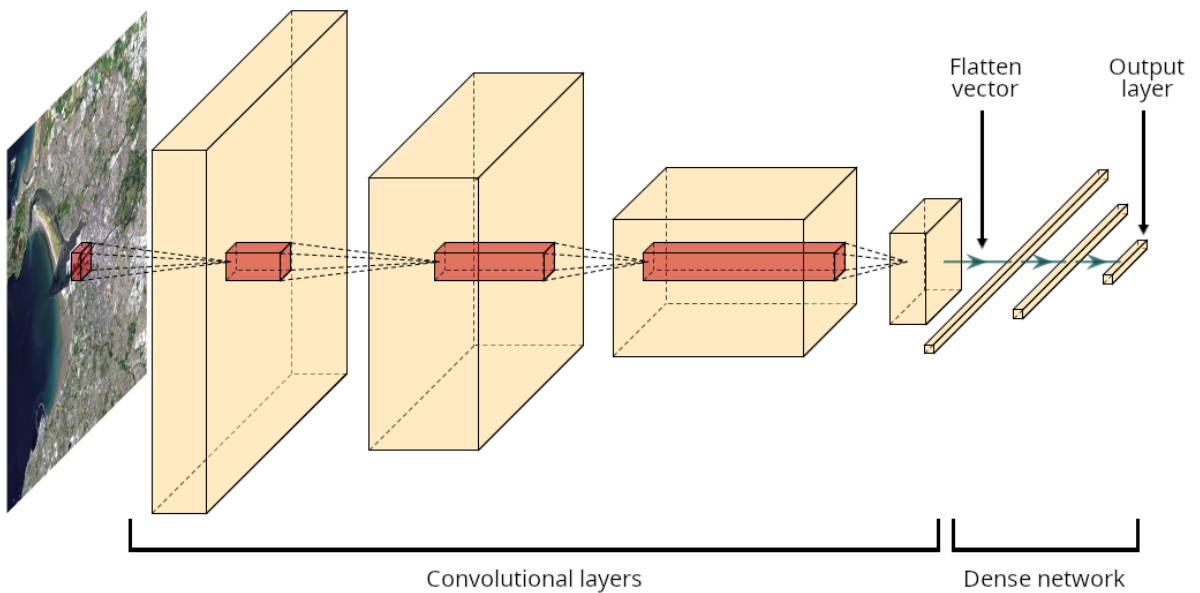


Figure 2.10: Illustration of an example CNN structure.

The resulting output of patch-to-point CNNs is a single classification where the output could either represent a single target pixel or an overall classification known as *scene classification*. Scene classification provides a class that represents a particular feature of the input image patch. Some researchers use the terms ‘land cover’ or ‘land use’ classification when discussing scene classification techniques in contemporary research publications. However, without modification these techniques, in themselves, do not result in a land cover classification map (Ma et al., 2019). Carranza-García et al. (2019)

obtained much higher accuracy results using CNNs, when carrying out a comparison of ML techniques for LCC using k-nearest-neighbours, RF, SVM and CNN. In addition, there study observed that the computation time for performing classification using their CNN model was significantly faster than with RF and SVM. However, this analysis did not appear to account for the fact that their model requires the generation of an input patch for each pixel to be classified. This generation process will result in the creation of highly overlapped input patches for classification over a large area, significantly reducing the computation time.

Song et al. (2019) evaluated the performance of spectral-based and spatial-based ML techniques for LCC using Landsat-8 data. In their study, each of the models, incorporating spatial data, outperformed spectral-based techniques. The researchers also found that the use of a shallow CNN which, they refer to as a Light CNN (LCNN) produced the best results. This study set out to examine models suitable for classification where there are a limited number of sample points to train the model. Additionally, the “deep” CNN (DCNN) which is used in the study for comparison, utilised a small input patch of 5X5 pixels. Therefore, it is unclear if the DCNN architecture or an alternative CNN architecture, utilising larger patch inputs would outperform the LCNN architecture with more sample points. The application of CNNs is not limited to classifying 2D spatial information. Xu et al. (2018) demonstrated how a 3D CNN trained for using Light Detection and Ranging (LiDAR) information can out-perform a 2D CNN using 2D raster information such as a DSM and gridded intensity information derived from LiDAR data. However, as identified in their paper, the application of a 3D-CNN requires a significant volume of training data to ensure accurate classification. Additionally, the issue of LiDAR data occlusion from dense tree cover was identified as a potential source of classification error.

2.4.2 Patch-to-Patch

Patch-to-Patch CNNs generate an image as an output. As these methods calculate the classification of multiple pixels based on the input image, the resulting process can be significantly more computationally efficient than a patch to point method which can

require the generation and classification of highly overlapped image patches to classify the overall image (Wu et al., 2019). These architectures are commonly composed of a series of convolutional pooling layers followed by a series of deconvolution and upscaling layers. As these networks are primarily composed of convolutional layers, they are also known as Fully Convolutional Neural Network (FCNN). Long et al. (2015) presented one of the first implementations of a FCNN capable of achieving pixel-level semantic segmentation. An example of the structure of a FCNN is illustrated in Figure 2.11.

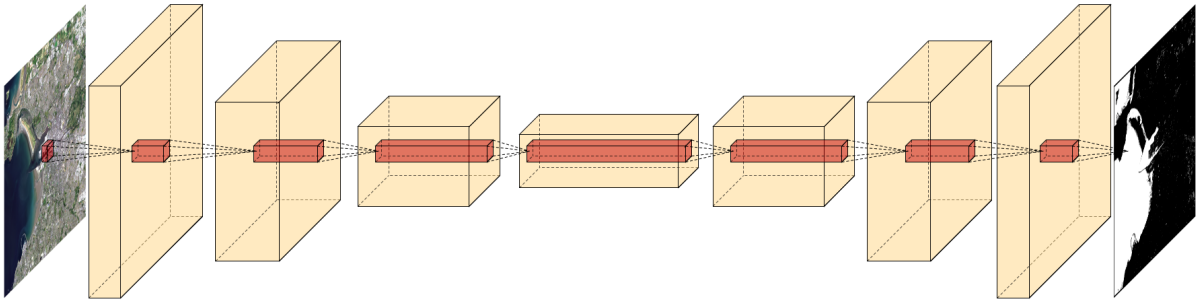


Figure 2.11: Illustration of an example FCNN structure.

Since the publication of the paper by Long et al. (2015), research in this field has dramatically increased, giving rise to the design and development of many novel CNN architectures. The results of a study conducted by Zhang et al. (2020b) revealed that the use of CNN architectures such as SegNet, U-Net, and PSPNet significantly outperformed more traditional ML methods such as SVMs, RF and CART (Classification and regression tree). However, due to the significant number of training variables in the assessed CNN architectures, the authors recognised that a substantially larger number of training variables are required to accurately train such models. Additionally, as these models require a patch model to be trained, the generation of these labels can be substantially more time-consuming. When using CNNs with very high-resolution imagery, it may also be necessary to use a CNN architecture which processes the imagery at different scales. These CNN architectures, also known as multi-scale CNNs are designed to take advantage of the clear boundaries visible in the imagery along with the overall context of the object being classified (Sun et al., 2019; Zhang et al., 2020a). In both papers, the authors propose generating multiple image patches of differing sizes centred at the

location where classification is to be performed. For each patch size, a dense CNN is used to extract features which are then concatenated together for final classification. As a result, the classification process will be significantly slower and require more computational resources than a single scale CNN architecture. However, a comparison of the computation time relative to other CNN architectures is not provided in either paper.

2.4.3 Object-Based Classification

Another approach to integrating spatial information into LCC is through the application of object-based classification. Object-based classification utilises a two-step process. The first step is the grouping of homogeneous and contiguous pixels into segments. A common classification is then assigned to all pixels within that object (De Luca et al., 2019). A large number of segmentation techniques have been developed, including *Watershed Transformation*, *Mean Shift Segmentation* and *Region Adjacency Graph Segmentation*. The choice of which segmentation technique to employ is dependent on the input image and associated application (Hossain and Chen, 2019). Once the segments have been generated, each segment is assigned an independent classification. One approach in assigning a class to a segment is through computing common attributes for each segment such as the average spectral value, the segment size and shape. These variables can then be used as inputs into models such as ANNs, RFs and SVMs (De Luca et al., 2019; Whyte et al., 2018; Hurskainen et al., 2019; Vilar et al., 2020). Alternatively, each generated segment can be used to define the input patch for a CNN (Zhang et al., 2020a; Li et al., 2019). In some instances, the classification of the image is performed independently to the segmentation and a single class is assigned to each segment based on the independently classified pixels within it (Zhou et al., 2019; Kleeschulte et al., 2019; Mugiraneza et al., 2019). One benefit of object-based classification is that it can help reduce the impact of the “noise” effect associated with spectral models (Zhang et al., 2020b). Figure 2.12 provides an illustrated example of this effect and how object-based classification can reduce the impact of noise in a classified output.

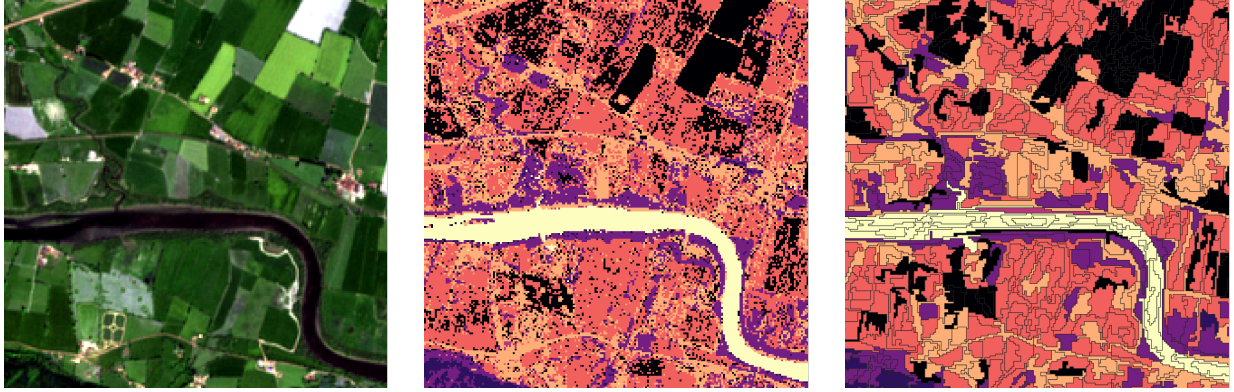


Figure 2.12: Example of the impact of employing object-based techniques on the ‘noise’ in classification output over Carrick-on-Suir, Tipperary Ireland. Sentinel-2 true colour image (left), pixel-based random forest classification (centre), object-based random forest classification.

2.5 Temporal LCC

While techniques discussed so far take advantage of spectral and spatial characteristics of an object or phenomenon at a specific instance in time, temporal analysis utilises the variations in spectral and spatial information over time. These techniques will be explored and analysed under three broad categories; multi-dimensional techniques, temporal ensemble techniques and time-series analysis.

2.5.1 Multi-dimensional Techniques

One of the most straightforward approaches to incorporate temporal information is to simply include the temporal dimension of the data as additional input variables. This approach enables the use of spectral and spatial ML techniques such as RF, ANN, SVM, and CNN. Gašparović and Dobrinić (2020) undertook a comparative assessment on the identification of vegetation using multi-temporal Sentinel-1 imagery. This assessment compared techniques such as RF, SVM, extreme gradient boosting (XGB), MLP, Adaboost.M1 (AB), and extreme machine learning (ELM). This comparative assessment revealed that for the given application, the highest accuracy results could be achieved using an MLP. The study observed that where a single date was used for classification, an SVM outperformed other assessment techniques. The inclusion of multitemporal satellite data increased classification accuracy for each ML technique, with the MLP obtaining

the highest classification result. While the study identifies that increasing the number of satellite observations increases classification accuracy, only a maximum of five Sentinel-1 observations were used per site. The authors conclude that increasing the number of observations may reduce the impact of speckle noise present in SAR data. It is unclear from this study if increasing the number of observations beyond five would further increase classification results.

A number of papers have employed dimensionality reduction techniques before training their models to account for, the high number of input variables that can arise when applying temporal analysis. For example, Huang et al. (2020) applied RF on the temporal mean and variance data values of an NDVI calculated using Sentinel-2 data. Their method was effective in differentiating land cover classes, including forestry, agricultural land, water, wetland and impervious surfaces. This methodology was particularly effective in the target study area as frequent cloud cover made employing other temporal classification methodologies difficult due to insufficient cloud-free data. However, as identified in Section 2.2.3, by relying on a single vegetation index such as NDVI, potentially beneficial information from other spectral bands is excluded from the analysis. Additionally, the accuracy of the calculated mean and variance will be impacted by the number of observations and may negatively impact classification accuracy in an area with frequent cloud cover. The use of RF with temporally averaged data was also examined by Carrasco et al. (2019). These researchers employed a temporal averaging approach to account for missing data due to cloud cover. Their results demonstrated that the use of seasonally averaged data could outperform annually-averaged data. The study also noted that increasing the number of dates included in the temporal average improved the classification accuracy.

2.5.2 Temporal Ensemble Techniques

Another methodology of incorporating temporal information when performing LCC is to apply an ensemble based approach. This approach is achieved by first performing independent classification for each observation date. The output from these classifications

are combined to form a final classification. Mendili et al. (2020) employed this approach by training a CNN using the VGG-16 architecture for each observation date. The output of this model from each observation was concatenated together before being used as an input into another CNN. Only three input dates could be used and only a two-class output could be generated due to the computation requirements involved in the process. As a result, several models may need to be trained if more than two land cover classes are to be classified.

2.5.3 Time Series Analysis

The temporal ML techniques discussed so far exploit temporal information as multi-dimensional data where the order of input variables are, in most instances, inconsequential. However, the order of temporal variation can provide additional information about the relationship between variables (Aggarwal, 2018). Two ML techniques which can be used with time-series data are *Recurrent Neural Networks (RNNs)* and *Time-series CNNs*.

2.5.3.1 Recurrent Neural Network

Recurrent Neural Networks (RNNs) are a family of ANNs designed to process data as a sequence of values. For a given time-series, data is input into the model in the order it occurs in the series. Each iteration of this process is commonly referred to as a time-step. The models generated from each time-step are used as an input to the model at the next time-step along with the next value or set of values in the time-series. This process is repeated for the full length of the sequence. Through this process, each member of the series is processed using the same parameters (Goodfellow et al., 2016). There are four main input and output RNN model structures as illustrated in Figure 2.13.

Primarily driven by research in speech recognition and stock market prediction, RNNs have seen iterative improvements by including techniques such as Long-Short Term Memory (LSTM) or Gated Recurrent Units (GRU). These techniques are designed to overcome some of the challenges of training models with large sequential datasets. These techniques

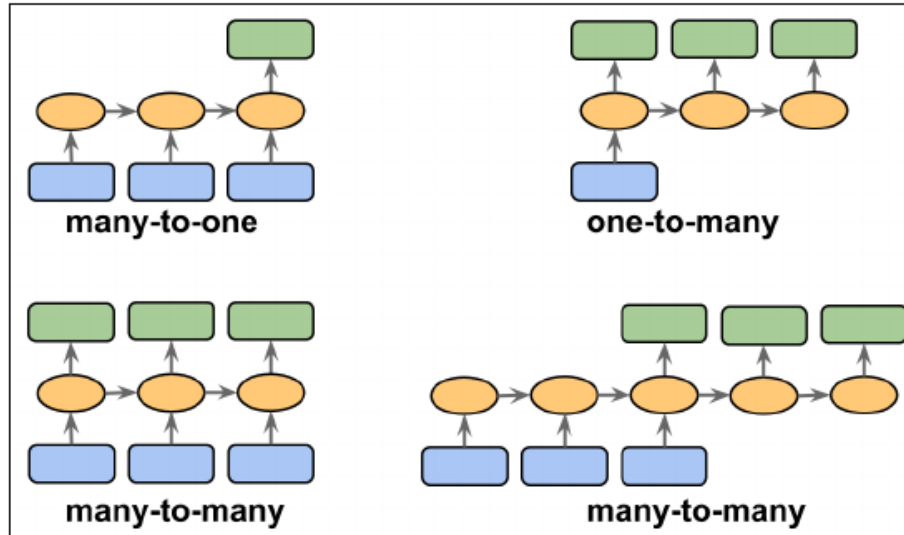


Figure 2.13: Illustration of the four different RNN model categories, **Source:** Raschka and Mirjalili (2017).

also aim to ensure only relevant information is passed on at each time-step (Raschka and Mirjalili, 2017). Rußwurm and Körner (2017), demonstrated that the benefit of time-series analysis for LCC with both an RNN and RNN with LSTM achieve significantly higher classification accuracies when compared with non-temporal methodologies such as CNN and SVM. Ienco et al. (2017) demonstrated how the incorporation of classifiers such as RF and SVM into an RNN with LSTM can further improve LCC accuracy. In their assessment RNN with LSTM out-performed multi-temporal classification with SVM or RF. He et al. (2019) identified that RF slightly outperformed an RNN with using attention-based long short-term memory (A-LSTM) in a comparative assessment for the identification of winter wheat. However, it was observed that classification time was significantly faster using the A-LSTM used with GPU acceleration. While this study identified that classification time is shorter with a LSTM model, the training of RNN based models can be challenging and requires that all data be prepared in an ordered series (Pascanu et al., 2013). Therefore, with a higher classification result and greater ease at training, the application of RF may be more suitable. A CNN can be integrated into an RNN in order to facilitate the inclusion of spatial information into time-series analysis. This approach was examined by Rußwurm and Körner (2018). Their study demonstrated that an RNN based model could be used even when some of the input

data contained cloud cover. This negated the requirement to perform cloud masking before training the model. In their study, it was identified that their model could identify and mask clouds visible in any image in the sequence, thereby negating their impact on the final classification. However, it is unclear from the study if issues would arise where images with significant cloud cover made up a substantial proportion of the time series. Additionally, the authors do not outline the impact of cloud shadow on the classification results.

2.5.3.2 Time-series CNN

An alternative methodology of processing time-series data is through the use of CNNs. Just as CNNs can take advantage of the spatial relationship of data within grid data, CNNs can be adapted such that they are capable of leveraging the temporal data in the form of 3D grid data. In this instance, the third dimension is temporal information and one approach is to use a CNN utilising one dimensional convolutions (*1D-CNN*). However, this approach does not leverage spatial information within the data. In a recent study involving deep learning-based multi-temporal crop classification by Zhong et al. (2019), a 1D-CNN outperformed a number of other techniques including an RNN with LSTM. The successful application of a 1D-CNN was also demonstrated by Zhao et al. (2019) on SAR data for crop detection. The application of time-series analysis is particularly suitable for SAR time-series data due to its cloud penetration capability, and so avoiding gaps in the time-series data. Implementing a CNN utilising three dimensional convolutions (*3D-CNN*) enables the integration of both spatial and temporal information in the ML models. This technique was examined in a recent study by Ji et al. (2018) which demonstrated that a 3D-CNN was capable of outperforming a 2D-CNN for crop classification. Li et al. (2020b) utilised a Multi-Scale Fully Convolutional 3D-CNN designed to exploit the global and local features within each image. In their study, a Multi-Scale Fully Convolutional 3D-CNN outperformed a number of 2D and 3D ML techniques for LCC. While the study examines the computational complexity of the proposed model in terms of training parameters, no detail is provided on the time required to perform classification.

Additionally, the authors outline that a random sampling approach was used for selecting the training, validation and test dataset used in the assessment. However, with a random sampling approach, there is no guarantee of the independence of the test data, as test samples can be selected in close proximity to training samples. Ideally, a stratified random sampling approach should be applied ensuring test sample independence (Kubat, 2017).

2.6 Sensor Fusion LCC

All the ML techniques discussed so far have been focused on data collected from a single sensor or platform. The use of data from a single sensor has the benefit of simplifying the analysis as it can be assumed that all data being used as model inputs comprise of the same structure. However, combining data collected from multiple sources or sensors (*Sensor Fusion*) can significantly increase the information available for the analysis of an object or phenomenon (Chang and Bai, 2018; Salcedo-Sanz et al., 2020). Sensor fusion between image data from different platforms poses a variety of challenges. Each sensor may have different spatial, spectral and radiometric attributes which usually need to be taken into account prior to processing. A variety of methods have been developed to enable sensor fusion modelling techniques. These techniques can be broadly grouped into three categories, *pixel-level*, *feature-level* and *decision-level* (Chang and Bai, 2018; Useya and Chen, 2018; Mahyouba et al., 2019). Fusion at the pixel level is the most direct form of fusion and involves simply including data from each sensor as input variables before training the model. Feature-level fusion is performed by first extracting features from each data source, which are then fused. These features can be extracted prior to training a model and as input variables to the model. Alternatively, the features can be derived and combined within a model's structure. Finally, in a decision-level fusion approach, each data source is classified independently, and the output classifications are fused to provide a final classification (Zhang, 2010). An illustrative example of the structure of the three different fusion categories is illustrated in Figure 2.14.

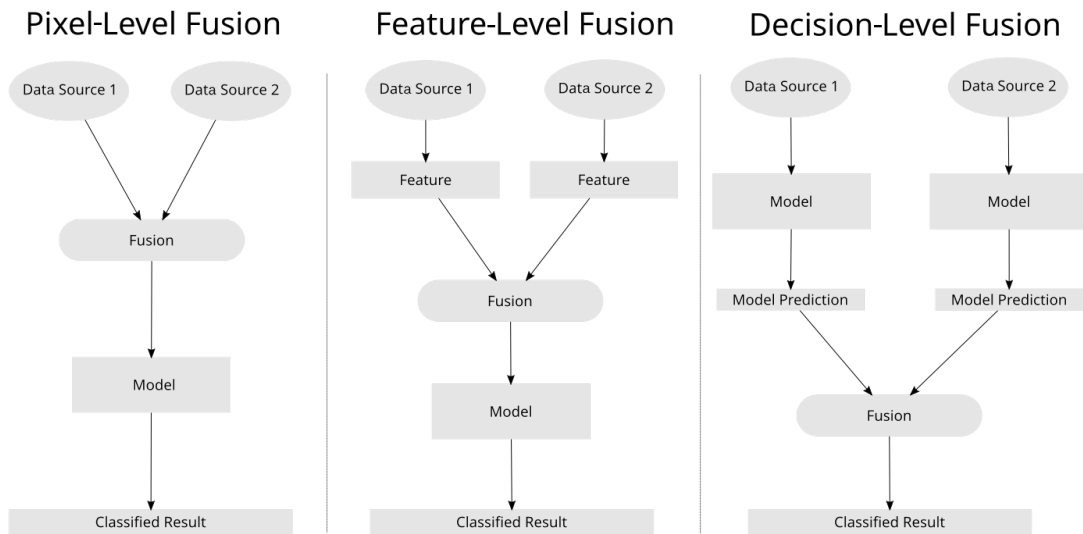


Figure 2.14: Illustration of the basic structure of the three different fusion categories.

2.6.1 Pixel-level Fusion

Pixel-level fusion is one of the most direct forms of sensor fusion, where data from each source is combined into a single image dataset (Zhang, 2010). Figure 2.15 provides an illustrative example of the pixel-level fusion process.

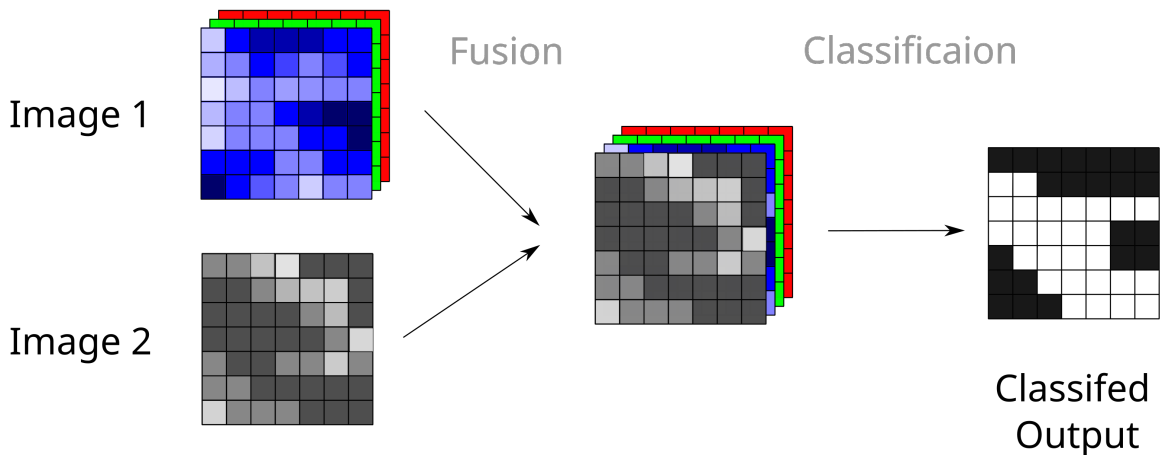


Figure 2.15: Illustration of the steps involved in performing pixel-level fusion.

As already highlighted in this chapter, applying a harmonisation technique can be a valuable methodology to enable pixel-level sensor fusion. However, as a result of spectral harmonisation, useful spectral information in the unharmonised data source may be lost in the process. Additionally, any error in the harmonisation process would propagate to

further analysis stages. An alternative methodology of pixel-level fusion is to simply include the spectral information of each source into the analysis. A study by Barrett et al. (2016) demonstrated that the pixel-level fusion of Sentinel-1 SAR and Sentinel-2 optical data could obtain higher accuracies for the classification of upland vegetation than can be obtained from either source alone. Mercier et al. (2019) demonstrated that using a combination of Sentinel-1 and Sentinel-2 time-series data for LCC over predominantly forested areas in Spain and Brazil provided more accurate classification than that provided by either satellite alone. Their approach was to use a RF classifier and treat data from each source as additional input features in a combined temporal stack. A feature selection step was included to reduce the number of variables used in the analysis. In the study, the increase in accuracy due to the combination of Sentinel-1 and Sentinel-2 was more pronounced over the Spain study area, with Sentinel-2 data alone obtaining similar results over the Brazil study area. One possible reason for this result is the difference in date range and number of Sentinel-1 observations used between the two sites. In the Spain study area, 22 Sentinel-1 observations were used from December 2016 to September 2017, while only 14 observations from November 2016 to December 2017 were used for the Brazilian study area. As a result, the use of Sentinel-1 data alone obtained lower classification results in the Brazil area than in the Spain area. This, in turn, would negatively impact the fused classification results in the Brazil area. Carrasco et al. (2019) also employed an RF model to enable data fusion of Sentinel-1, Sentinel-2 and Landsat-8 data. For classification over the entire study area, the combined data fusion approach obtained higher classification results than from a single sensor alone. However, their approach required that all datasets had a complete temporal dataset series with no missing data. Their study demonstrated that the fused datasets produced higher classification accuracy than individual sensor datasets. During their study, they compared the result of fusion to performing classification utilising two non-temporally aggregated Sentinel-2 observations. In this assessment, the fused dataset obtained almost identical results to using two non-temporally aggregated Sentinel-2 observations. However, due to cloud cover, this comparison could only be conducted over 80% of the study area.

A study by Liu et al. (2019) also examined the fusion of Sentinel-1 and Sentinel-2 data. In their study, they observed that the inclusion of Sentinel-1 data in a RF model significantly increased classification results in comparison to Sentinel-2 data alone. However, only minor improvements in classification accuracy were observed with the inclusion of Sentinel-1 data when training a CNN model. CNN models utilise the spatial relationship between pixels to improve classification accuracy. Due to factors such as speckle noise present in SAR data, Sentinel-1 data may not be suitable for use in a CNN architecture. In the study, segmentation from the fused SAR and optical data was used to refine and improve the accuracy of the generated pixel-level classification map. As outlined in section 2.4.3, the application of object base classification can reduce the impact of noise in the input dataset, such as the speckle noise present in SAR data.

Pixel-level fusion is also a commonly applied methodology for the fusion of satellite data and high-resolution data from aerial or UAV sources. In a literature review conducted by Emilien et al. (2021) two-thirds of identified papers, performing data fusion between satellite and UAV data used a pixel-level fusion technique. A study by Zou et al. (2018) demonstrated the use of pixel-level fusion of GF-1 satellite and UAV data for crop classification.

2.6.2 Feature-level Fusion

Sensor fusion at the feature level occurs after the processing of one or more of the data sources has been undertaken in order to extract relevant object features. For example, an object feature can be either manually defined or generated using one of the input data sources. Relevant information from each source can then be extracted to the object before performing fusion of the data (Chang and Bai, 2018). An illustrative example of the steps involved in performing feature-level fusion is presented in Figure 2.16.

Gevaert et al. (2015) utilised this approach using manually defined features. Their study demonstrated that eight-meter GSD satellite multispectral data from Formosat-2 and 1-meter GSD UAV hyperspectral data can be combined as a spectral–temporal response surface. This spectral–temporal response surface could then be used for fur-

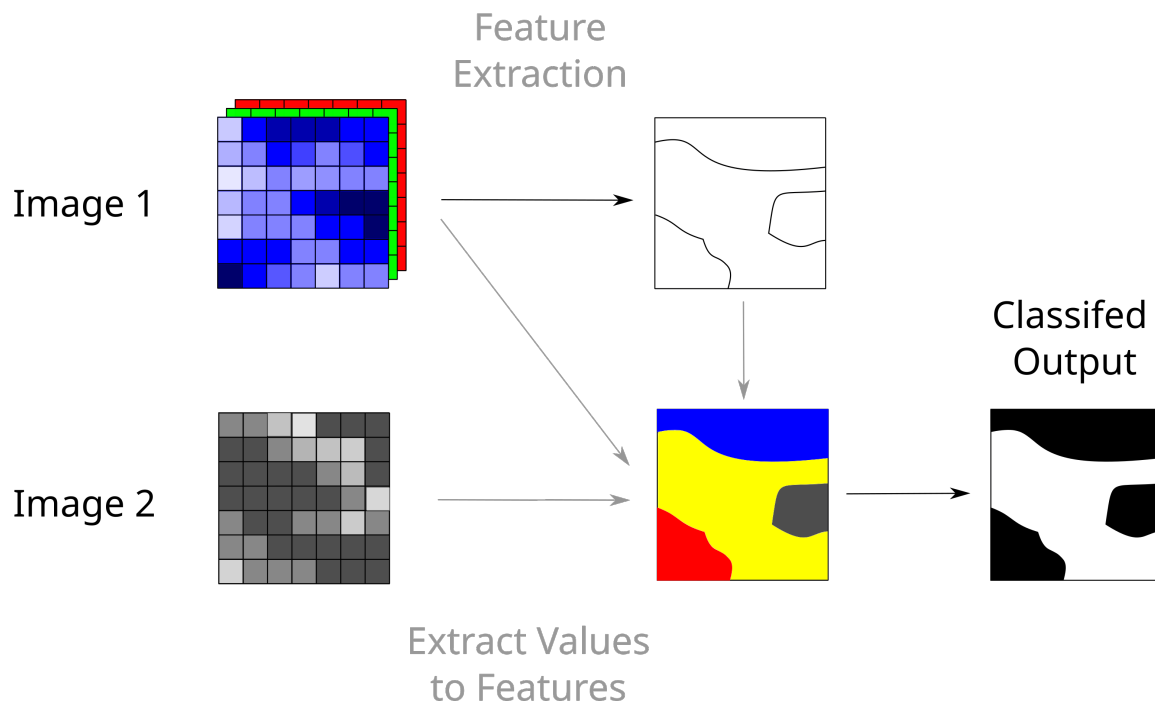


Figure 2.16: Illustration of the steps involved in performing feature-level fusion.

ther analysis of the sample plots. A feature-level fusion technique was developed by Feng et al. (2019) for LCC using Sentinel-1 and 2 multi-temporal data. In this study, a CNN was used for feature extraction for each image at each time-step. Extracted features were then concatenated together before classification. This study also identified issues when attempting to perform classification using a CNN with Sentinel-1 data alone. However, when combined with Sentinel-2 data in their proposed multibranch network, they observed an increase in classification accuracy in comparison to using Sentinel-2 data alone. Rasti and Ghamisi (2020) achieve sensor fusion by transforming data into a low-dimensional subspace where features can be extracted. This fusion approach was examined for two datasets. The first dataset contains hyperspectral, multispectral LiDAR, and very high-resolution RGB images over the University of Houston, USA. The second dataset comprised only hyperspectral and LiDAR data for the city of Trento, Italy. The subspace feature extraction was performed using morphological profiles, which is used to model the spatial dependencies of adjacent pixels. These features were then classified using an RF classifier. Their results demonstrated that a higher classification accuracy could be achieved with fused data when compared with single data source classification.

However, no comparison was undertaken to determine the benefit of performing the proposed subspace feature extraction approach to other sensor fusion approaches, such as pixel-level fusion.

2.6.3 Decision-level Fusion

Decision-level fusion is achieved by first performing independent analysis on each data source, and the results of each model are combined to make an overall decision. Figure 2.17 provides an illustrative example of the decision-level fusion process.

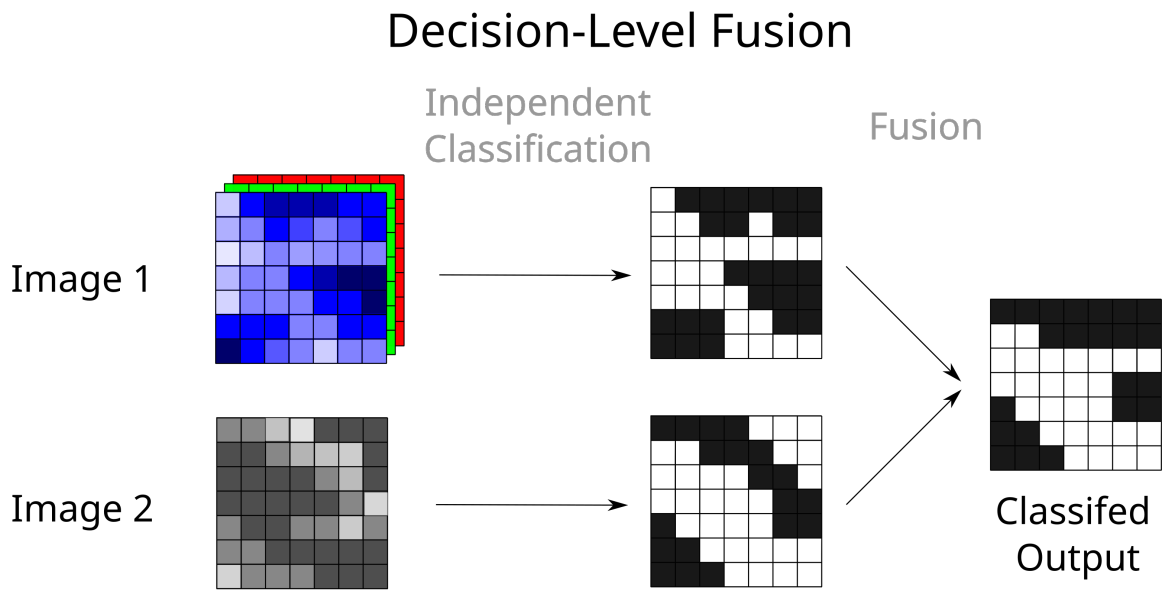


Figure 2.17: Illustration of the steps involved in performing decision-level fusion.

The application of decision-level fusion assumes that each independent analysis will provide unique information about the object or phenomenon being observed, and the fusion seeks to leverage this information from each source (Chang and Bai, 2018; Raschka and Mirjalili, 2017). In comparison to pixel-level and feature-level fusion, the application of decision-level fusion preserve significantly less information at the point of fusion (Gravina et al., 2017). However, decision-level fusion benefits from lower computational costs compared to pixel-level and feature-level fusion, along with enabling the fusion of diverse data types.

Several methodologies can be employed to enable multi-sensor decision-level data fusion. For a hand-crafted approach to fusion, a rules-based fusion approach can be

employed. This approach takes advantage of the interpreter’s knowledge of the data and survey area. A recent study by Zare and Mahmoudi (2019) demonstrated the effectiveness of a rules-based approach for the fusion of optical and SAR data which significantly improved classification accuracy in comparison to classification from a single data source. Applying a rules-based approach to sensor fusion leverages a researcher’s knowledge to improve classification. However, this approach may prove time-consuming, particularly where a significant number of data sources are to be fused.

Several studies have demonstrated the application of *voting* based techniques for data fusion. The classification predicted from each model is counted and the final classification is the class which received the most votes. Useya and Chen (2018) employed a plurality voting methodology for decision-level fusion. In this study, fusion was performed between Landsat-7, Landsat-8 and Sentinel-2 over the Manicaland province in Zimbabwe with a focus on crop classification. Multiple observations were utilised to generate a single mosaic for each platform. The researchers carried out a comparative analysis and demonstrated that the use of a decision-level fusion approach could outperform pixel-level fusion. In addition, it was observed that performing fusion using output from multiple differing ML techniques obtained higher classification results than from a single technique from each data source. This approach to fusion is similar to the concept of ‘weak learners’, where each ML technique will model different features of the input data (Bonaccorso, 2018).

While some studies have assigned equal weights for each vote, when applied to fusing data with significantly different properties, a weighted voting approach may be more suitable (Zhong et al., 2017). Vohra and Tiwari (2020) demonstrated this weighted voting approach for LCC using RGB and hyperspectral data. Their study used the class conditional probabilities of each classifier to assign the weight of each vote. While the EO data used in this study is fused using an object-based fusion approach. In the study an SVM and ANN model were trained from the fused input features. The weighted voting fusion is then employed to fuse the output of the SVM and ANN models obtaining a higher classification result than can be obtained from either model alone. Zhong et al. (2017) employed a Differential Evolution Algorithm to determine the optimum weights for

decision-level fusion of LiDAR and hyperspectral data for LCC. Through this approach, the fusion model is trained to determine the significance that each input should have on the final outcome. The results of the study demonstrate that the optimised weighted voting approach obtained a higher classification approach over unfused methodologies. However, no comparison was given over the results of unweighted fusion or the fusion weighed by model classification probability. Another approach for decision-level fusion is to input the independently classified data from each source into another ML model (Zhang, 2010; Meng et al., 2020). Bigdeli et al. (2014) employed a Naive Bayes model for decision-level fusion of LiDAR and hyperspectral imagery. In their study, SVM models were trained on data from each source independently. This study demonstrated that the application of naive bayes for decision-level fusion could improve classification accuracy over mono-platform classification. However, no details of the efficiency of this approach were provided relative to mono-platform classification. In the paper by Yokoya et al. (2018), a Markov random field classifier was employed to produce a final classification using the class-conditional probabilities of models trained on Sentinel-2, Landsat-8 and Open Street Map Data. However, in this study the proposed architecture performed sensor fusion at the pixel level and the fused data was used to train models using three ML techniques, RF, CNN and gradient boosting machines (GBM). The application of decision-level fusion utilising a Markov random field classifier was used as a means of fusing the output of the three models with the aim of smoothing noise that may be generated from any particular model.

During this literature review, few LCC papers were identified that utilised a decision-level fusion for the fusion of medium spatial resolution images such as those obtained from Landsat-8 and Sentinel-2 with high or very high resolution imagery that can be obtained from aerial and UAV platforms. The fusion of 1.5m resolution mono-temporal Spot6 satellite data and 10m resolution Sentinel-2 satellite data was examined by Wendl et al. (2018). In their study, the Spot6 model was classified using a CNN model, and the multitemporal Sentinel-2 data was classified by a RF model. An SVM fusion model was used to fuse the independent models using class probabilities. A study by Sirmacek and

Unsalan (2010) applied a decision-level fusion approach for the fusion of aerial and Ikonos satellite data. In their study, the independent satellite and aerial probabilities were fused for building detection. This study focused on building location and therefore did not perform LCC. In a review of UAV and satellite synergistic studies, Emilien et al. (2021) noted that while they could not find any studies that performed decision-level fusion between UAV and satellite data, its application, nevertheless, had interesting potential. With only a limited number of papers identified examining the use of decision-level fusion for the fusion of medium spatial resolution and high or very high spatial resolution data, this is a significant gap in current knowledge in this field.

2.6.4 Sensor Fusion with partially Missing Data

While sensor fusion techniques for LCC have been utilised in multiple studies observed during this literature review, few studies were identified that applied sensor fusion in scenarios where one or more of the sensors to be fused are missing across the assessed areas. In many instances, particularly where the ML techniques are utilised for the fusion of multi-sensor data, it is assumed that at each location in the assessed area, the availability of data from each sensor is consistent. Temporal averaging, Gap filling, and sensor harmonisation techniques have been used in studies as potential solutions for small areas of missing data. These techniques were successfully employed in studies such as Carrasco et al. (2019) who employed temporal averaging, Griffiths et al. (2019) who employed a band-wise temporal linear interpolation for gap filling and Nguyen and Henebry (2019) who utilised the Harmonized Landsat-8 and Sentinel-2 (HLS) product for LCC. Many ML techniques such as SVM or ANN require that the number of input variables do not change during training or inference (Han and Kang, 2022). Therefore, changes in the available data across the assessed region pose a significant challenge. A number of techniques have been developed to account for missing data in input models. These techniques include simple replacement methodologies such as zero or mean value replacement (Salberg and Jenssen, 2012).

Alternatively, ML models can be used for the imputation of the missing data values.

A study by Han and Kang (2022), compared multiple methods of value replacement and value imputation techniques on 20 benchmark datasets for machine learning classification. In this study, five techniques for value replacement/imputation were examined. These included both zero and mean value replacement techniques. For value imputation, three ML techniques were examined, the use of a K-Nearest Neighbour (KNN) as proposed by Troyanskaya et al. (2001), the use of a denoising autoencoder as proposed by Gondara and Wang (2018), and the use of a generative adversarial network (GAN) as proposed by (Shang et al., 2017). A significant limitation of each of these techniques is that they rely on other observations to aid in the generation of replacement data. Any change between the reference observation and the target date will not be detected. Additionally, where there is a substantial number of missing observations at one location due to issues such as frequent cloud cover, these approaches may not be suitable. A study by Schneider (2012) examined the use of ML techniques in a region with partially missing sensor data. Multi-temporal models were trained with some missing data to overcome the issue of missing data in the study. The study identified that ML techniques such as SVM and Decision trees could result in accurate classification from multi-temporal Landsat-8 satellite datasets where there is some missing data. However, it was observed the number of missing observations impacted the classification accuracy.

Gap filling and value imputation may be suitable for replacing small gaps in missing data. However, in situations where there are significant regions with missing data or a significant percentage of missing data at a point, these techniques may not be suitable. In such scenarios, the sensor fusion technique utilised needs to be flexible enough to only fuse the available data without imputation of other sensors. One such technique was assessed by Salberg and Jenssen (2012) through the training of a SVM model for each combination of available data. For each location, the appropriate SVM model was used depending on data availability. This approach was observed to outperform techniques such as zero value replacement for missing data and was utilised for the pixel-level fusion of Digital Surface Model (DSM) and multi-temporal Landsat-8 imagery with missing input data due to cloud cover. The comparative assessment by Useya and Chen (2018)

examined the fusion of Landsat-7, Landsat-8 and Sentinel-2 data with significant regions of missing data amongst each platform. In their study, they employed both pixel-level fusion and decision level fusion techniques to ensure full data coverage over the assessed region. During their study, the use of a plurality voting decision-level fusion approach obtained better results than the assessed pixel-level fusion technique. While the study by Useya and Chen (2018) examines the use of decision-level fusion for the fusion of data with variable data availability, this study only examines a single decision-level fusion technique. Given the limited number of studies focusing on addressing the issue of applying fusion in situations where data availability varies across the assessed region, a further examination into this field is required.

2.7 Suitability of ML Techniques for CLC+ Backbone Raster Product

As one of the primary sources for EO derived land cover labelling within CLC+, significant consideration is required to determine suitable methodologies for the generation of the CLC+ Backbone raster product. As outlined in this literature review, there are a variety of ML techniques that can be used for the classification of EO data. However, a number of the techniques discussed may not be suitable for generating this product. These techniques will be reviewed in terms of the CLC+ Backbone raster product requirements set out in the CLC+ Backbone technical specifications (Kleeschulte et al., 2019) and CLC+ Backbone tender specifications (Agency, 2019) in order to assess the suitability of the techniques discussed in preceding sections.

These requirements include:

- The pixel based EO derived requirement.
- The sensor and multi-temporal requirement.
- The resolution requirement.

2.7.1 Pixel-Based Requirement

Despite a number of papers demonstrating the effectiveness of object-based techniques, the requirement for a pixel-based methodology excludes these techniques. This exclusion also encompasses object-based feature-level fusion techniques. One likely reason for this requirement is that the CLC+ Backbone vector product is technically an object-based classification dataset where classes are derived from the independently classified raster dataset. As a result, implementing an object-level classification for the generation of the raster product would be redundant. However, it is not clear if this requirement precludes the application of any spatial based techniques. CNNs such as the Light CNN evaluated by Song et al. (2019) can be used to incorporate spatial data and classify each pixel independently. However, for any adjacent pixels to be classified, the variables used to classify the point are not independent as each generated patch covers highly overlapped areas (Wu et al., 2019). This lack of variable independence for the classification of a pixel is also true for FCNNs. For most FCNN architectures, the class of any pixel in the output patch is dependent on all values in the input patch. However, despite the potential issue of non-independence of variables, a number of assessments have demonstrated the effectiveness of incorporating spatial information into LCC. As such, the application of CNNs for the generation of the CLC+ Backbone raster product should be explored.

2.7.2 Sensor and Multi-temporal Requirements

The recommended EO data source for the generation of the CLC+ Backbone raster product is Sentinel-2. In particular, the technical specification requires that at least six observations within the target reference year be used to enable temporal analysis. Therefore all techniques used in the generation of the raster product must be able to include temporal information in consideration of this requirement. This does not exclude any specific ML architecture discussed in this chapter. However, architectures such as 1D/3D-CNNs or RNNs have been shown to be particularly suited for managing this time-series data (Rußwurm and Körner, 2018; Ienco et al., 2017; Zhao et al., 2019). A significant impact of this requirement is that in regions with frequent cloud cover, obtaining suf-

efficient observation from Sentinel-2's optical sensors may be challenging. In the CLC+ Backbone technical specifications, it was recognized that regions along the Atlantic coast with frequent and high cloud cover may have had few cloud-free satellite images over a given year upon which to use for LCC (Kleeschulte et al., 2019). Ireland is one of the regions in Europe most significantly impacted by the issue of cloud cover. As an island on the northwest of Europe that is strongly influenced by Atlantic low-pressure systems, Ireland has 100% cloud cover 50% of the time (Met Éireann, 2021). One recommendation set out in the technical specifications for dealing with the issue of limited observations is the inclusion of EO data from the year preceding and following the target reference year. This approach does increase the number of available observations to be used in the analysis. However, by broadening the analysis over three years, there is an increased risk that the land cover class may change over the observation period, for example, due to urban development or change in agricultural practices. In addition, changes in the climatic conditions across the three years may also need to be considered. The first CLC+ datasets are being generated for the year 2018. In 2018, Ireland experienced drought conditions for the months of June and July (Moore et al., 2018). With drought conditions uncommon on the island in Ireland, this occurrence may significantly impact the spectral response of vegetation relative to the preceding and following year. The current update cycle of the CLC+ Backbone datasets is expected to be 3-6 years. However, during a workshop on CORINE Land Cover+ in Brussels in November 2017, almost a quarter of member state representatives indicated the desire for a yearly updated product (Kleeschulte et al., 2019). With an increase in demand for up-to-date land cover monitoring, it is likely that the demand for annual updates will increase in the future. If updated annually, the use of satellite imagery outside the target year would result in a significant repeat in the data used across each update. Therefore, the capture and processing of data from within the same target year should be examined for the generation of future CLC+ Backbone datasets.

The application of gap-filling techniques using Landsat-8 data has also been suggested as a recommended methodology to mitigate the issue of limited Sentinel-2 observations

due to frequent cloud cover (Kleeschulte et al., 2019). Sentinel-1 data was also suggested as a means of improving classification accuracies. However, no recommendation was provided for the means of incorporating each of these data sources. There are three categories of sensor fusion; pixel-level, feature-level and decision-level, as outlined in Section 2.6. Pixel-level fusion through a spatial and spectral harmonisation approach can increase the temporal availability of data. However, harmonisation is commonly performed using another optical satellite data such as Landsat-8 which is also affected by frequent cloud cover. For this reason, harmonised Sentinel-2 and Landsat-8 may still not provide sufficient cloud-free observations. In addition, any error in the harmonisation process may negatively impact the overall classification results. Non-harmonised pixel-level fusion and non-object feature-level fusion have been demonstrated to improve classification accuracies. However, with each data source having differing spatial, spectral and temporal resolutions, performing fusion at this level would be challenging. There is an additional challenge in applying fusion techniques where the availability of each data source differs across the assessed regions. With these considerations, a decision-level fusion approach would likely be the most suitable approach to incorporate data from each platform. However, the means and effectiveness of utilising a decision-level fusion approach in a region with frequent cloud cover requires examination.

2.7.3 Spatial Resolution Requirement

The final consideration is the requirement for a 10m resolution output. The recommended EO input is Sentinel-2, which has only four spectral bands with a 10m spatial resolution. The remaining bands have a resolution of 20m and 60m. Therefore, if limiting the input data to only 10m or better resolution, only four Sentinel-2 bands could be used. Additionally, this requirement would exclude the use of Landsat-8 with its 30m resolution bands. The Sentinel-1 Ground Range, Multi-Look, Detected (GRD) product is provided at a 10m spatial resolution. However, the GRD product is derived from the Slant Range, Single-Look Complex (SLC) product. Due to the off nadir observation of SAR the spatial resolution of the SLC product varies across the observation area (Emery and Camps,

2017). Spatial resolution ranges from 5m to 20m for Sentinel-1 when operating in the Interferometric Wide Swath Mode. Therefore, the ability to delineate boundaries may vary across the GRD product. While data-acquisition modes such as Strip Map Mode result in 5m spatial resolution, Interferometric Wide Swath Mode is the default capture mode (Attema et al., 2007). Furthermore, pre-processing steps such as applying a speckle filter to remove ‘noise’ can result in blurring the imagery (Kupidura, 2016). Considering these issues, the inclusion of Landsat-8, Sentinel-1 and non-10m Sentinel-2 resolution bands may negatively impact classification accuracy, particularly at the boundary between land cover classes. One possible solution for this issue is the incorporation of high-resolution imagery into the analysis to help improve classification and minimise the issue of misclassification around class boundaries. While the technical specification mentions the inclusion of high-resolution satellite imagery for the generation of the CLC+ Backbone vector product, there was no mention of its inclusion in the generation of the CLC+ Backbone raster product. One likely reason for this is the difficulty in applying fusion between data with significantly different spatial resolutions. Additionally, sensor fusion techniques may have already been used at the satellite level to overcome the issue of missing data due to frequent cloud cover. Therefore, the further fusion of high-resolution data may pose additional challenges. One possible means of incorporating the high-resolution RS data to prior fused satellite data is through the use of a decision-level fusion technique. In a region with frequent cloud cover, obtaining enough high-resolution optical satellite data over a large area may be quite challenging. One viable alternative is for the inclusion of aerial or UAV data where the aircraft or drone can fly beneath the cloud cover. Incorporating this high-resolution optical imagery into the raster LCC should be explored further as a potential means of improving class delineation, particularly in complex scenes. While undertaking this literature review, no papers were identified that used a decision-level fusion approach to fuse satellite and aerial data for LCC. Therefore, this subject requires further investigation.

2.8 Summary

This chapter explored the key challenges in LCC as well as potential solutions in the current state of the art of ML modelling in terms of how these techniques can be applied to LCC. These challenges and potential solutions were examined and assessed under four fundamental RS characteristics namely; spatial, spectral radiometric and temporal resolution. It was found that increasing the resolution of any one of these RS variables can improve classification accuracies. However, sometimes these improvements can, inadvertently, generate additional issues that need to be addressed. In the process of assessing the challenges associated with each resolution category, a number of ML techniques and in some cases adaptations were highlighted, which were found to significantly improve final classification results. Throughout this chapter, many ML classification techniques were examined from simple spectral thresholding to more advanced time-series and sensor fusion ML techniques. On closer scrutiny, a number of papers were identified that demonstrated that better ML classification results were usually generated when exploiting the spatial or temporal properties of the RS data when compared to model outputs that simply relied on spectral data alone.

This chapter then examined the suitability of ML techniques for the generation of the CLC+ Backbone raster product and, in particular, how well the model outputs matched the requirements set out in the CLC+ technical specifications. This closer examination identified three areas requiring further investigation. The first area requiring further investigation is whether the incorporation of spatial data through the use of CNN architectures increase classification accuracy relative to pixel-based techniques for the generation of the CLC+ Backbone raster product. This issue will be addressed in Chapter 3 and in line with the first research question “What ML techniques are suitable for mono-platform satellite-derived annual LCC on the island of Ireland?”.

The second area requiring further investigation is whether a decision-level sensor fusion approach can be used as an appropriate means of fusing data with differing resolutions and availability across the assessed region. This issue will be examined in Chapter 4 and will be addressed in line with the second research question of this thesis “How

can a multi-sensor satellite data fusion approach be employed where frequent cloud cover results in differences in sensor data availability over the area that is being assessed?”

Finally, the use of a decision-level fusion approach for the fusion of satellite and aerial data is an area requiring further investigation. This subject will be examined in Chapter 5 and will address the third research question in this thesis “Can aerial data be used to further improve the accuracy of multi-sensor satellite-derived LCC?”

Chapter 3

Evaluation of ML Techniques for Satellite based LCC

3.1 Introduction

This chapter will examine the generation of EO derived LCC using ML techniques. In particular, this chapter will examine the challenges associated with performing LCC using a single satellite source as a result of frequent cloud cover on the island of Ireland. This chapter will build upon the work undertaken in Chapter 2 by conducting a comparative analysis of several ML techniques. The techniques to be evaluated in this comparative assessment will be performed on data captured by three satellite platforms, Sentinel-1, Sentinel-2 and Landsat-8. The techniques reviewed in this comparative analysis will be examined based on their suitability for the generation of the CLC+ Backbone raster product. One important requirement set out in the CLC+ technical specifications is that a minimum of six satellite observations should be used for classifications. As outlined in the CLC+ technical specifications, in regions with frequent cloud cover it may not be possible to meet this requirement for all areas. As part of the comparative analysis, the coverage of each technique will also be assessed based on this requirement.

This chapter is structured into four sub-sections in order to carry-out this comparative assessment. **Section 3.2** will outline the regions and data to be used in this evaluation. **Section 3.3** will describe the data preparation methodologies, the ML techniques to be evaluated and will outline the metrics used for assessing the suitability of techniques. **Section 3.4** will detail the results of the study. **Section 3.5** will provide an in-depth analysis of the results and highlight the knowledge learned from this assessment.

3.2 Data

A systematic approach was employed when preparing all data used in this assessment to ensure reproducibility in various data handling and analysis stages. The same geodetic datum and projection system was used for all spatial datasets examined in this study. The use of a common geographic projection system between datasets ensures that all geographic information is comparable between datasets. The correct choice of projection was necessary to minimise the spatial distortions which can occur when attempting to represent the surface of the earth as a two-dimensional object (Bolstad, 2019). The ‘WGS84/UTM29N’ (EPSG:32629) projection was used as the common geodetic framework for this assessment. WGS84/UTM29N is a meter based projection designed for use on data between 12°W and 6°W in the Northern Hemisphere (MapTiler, 2019). This projection was also chosen as it was the default projection provided for much of the satellite EO data used in this assessment.

3.2.1 Study Area

This study was undertaken at seven sites, located across on the island of Ireland. The choice of these locations was primarily determined by the availability of labelled data from the Copernicus Urban Atlas and Copernicus Coastal Zones datasets. A bounding box was created for five of the regions based on the coverage extent of the Copernicus Urban Atlas data available in each region. Two additional target study areas of interest labelled as *Dunglow* and *Glengariff* were also generated. The extent of these two target

study areas was manually defined in areas with sufficient label data coverage from the Coastal Zones dataset.



Figure 3.1: Geographic extent of study areas. Base map: Microsoft Bing imagery (www.bing.com/maps/aerial).

3.2.2 Satellite Data

Only satellite data from a single year will be used to assess the suitability of generating an annual CLC+ Backbone raster product in this assessment. Therefore, 2018 was chosen as the year to collate satellite data for this study. This year was also chosen since it was the target year for the generation of the first CLC+ dataset (Kleeschulte et al., 2019) and labelled land-cover data was also available for 2018.

The three satellite data sources to be used in this comparative assessment are Sentinel-1, Sentinel-2 and Landsat-8. Tables listing all satellite images used in this assessment are presented in Appendix A.

3.2.2.1 Sentinel-1

As part of the European Space Agency (ESA) Sentinel satellite series, Sentinel-1 is an earth observation satellite consisting of a C-band SAR system that transmits and receives electromagnetic energy in both a horizontal and vertical polarisation with a central frequency between 5250-5570 MHz (ESA, 2012a). Presently, there are two Sentinel-1 satellites in orbit, Sentinel-1A and Sentinel-1B (ESA, 2021d). Figure 3.2, provides an illustrative example of a Sentinel-1 satellite.



Figure 3.2: Illustration of Sentinel-1 satellite, **Source:** ESA (2021b).

This platform was primarily designed with the following application in mind:

- monitoring sea-ice zones and the polar environment.
- mapping in support of humanitarian aid in crisis situations.
- surveillance of marine environments.
- monitoring land surface motion risks.
- mapping of land surfaces: forest, water, soil and agriculture.

(ESA, 2012a)

The data used in this research was downloaded from the Copernicus Open Access Hub (scihub.copernicus.eu/dhus) as a ground range detected product processed to a 10m pixel resolution with both VV + VH polarization. Once downloaded, pre-processing of each dataset was undertaken using the following image-processing steps in the ESA SNAP software package.

1. *Radiometric Calibration*

This process was undertaken to account for the systematic variation in the image signal across the sensing area (Lillesand et al., 2014).

2. *Speckle Filter*

RADAR pulses transmitted from RADAR satellites such as Sentinel-1 are transmitted coherently so that transmitted waves oscillate in phase with one another. However, interaction with different objects can change in the phase of the returning data. This change in phase can result in amplification or reduction of other returning signals. This has the result of creating noise (*speckle*) in the captured data (Lillesand et al., 2014). This research is focused on understanding the temporal characteristics from each data source, therefore a multi-look approach for reducing speckle filter was not applied as this requires multiple independent images captured over the same location (Emery and Camps, 2017). A Lee Sigma filter was applied to the data to reduce the impact of the speckle.

3. *Terrain Correction to UTM N29*

Terrain correction uses a known elevation model along with known satellite orbital positions in order to georeference the data to correct for relief displacement caused by elevation variation across the observed area and ensure spatial accuracy (Chang and Bai, 2018). The reference elevation dataset used in this assessment was produced by the Shuttle Radar Topography Mission (SRTM) sensor system.

4. *Convert to Decibels (dB)*

Finally, the image data was converted to a backscattering signal as a log ratio of the transmitted and received signal in decibels (dB) (Lillesand et al., 2014). This step was undertaken to ensure data was comparable between datasets.

3.2.2.2 Sentinel-2

ESA's Sentinel 2 constellation presently comprises of two sun-synchronous near-polar orbiting multi-spectral satellites, Sentinel-2A and Sentinel-2B. Figure 3.3, provides an illustrative example of a Sentinel-2 satellite. The onboard Multi-Spectral Instrument (MSI), is capable of capturing imagery with 13 spectral bands between 433nm and 2202nm. Four of these bands have a spatial resolution of 10m, six bands have a spatial resolution of 20m, and three have a spatial resolution of 60m. Table 3.1 details the spatial and spectral specifications for the Sentinel-2 satellites. While there are minor differences in the spectral resolution between Sentinel-2A and Sentinel-2B (ESA, 2021a), for this assessment, the spectral resolution from each satellite will be treated as identical.

To align with the guidelines outlined in the CLC+ technical specifications, all Sentinel-2 data used in this assessment was atmospherically corrected to bottom of atmosphere reflectance (Kleeschulte et al., 2019). The atmospherically corrected data was downloaded as a L2A product from the Copernicus Open Access Hub (scihub.copernicus.eu/dhus). The selection of image data to download was based on visual observation of the preview images, selecting images which contained cloud-free regions over the areas of interest for the 2018 test-year. Initial cloud cover masks were generated using data provided in the *MSK_CLOUDS_B00.gml* file along with pixels in the file *MSK_CLDPRB_60m.jp2* with



Figure 3.3: Illustration of Sentinel-2 satellite, **Source:** ESA (2021c).

Table 3.1: Sentinel-2 band spectral ranges and spatial resolutions, **Source:** ESA (2021a).

Band Number	S2A		S2B		Spatial Resolution (m)
	Central wavelength (nm)	Bandwidth (nm)	Central wavelength (nm)	Bandwidth (nm)	
1	442.7	21	442.3	21	60
2	492.4	66	492.1	66	10
3	559.8	36	559.0	36	10
4	664.6	31	665.0	31	10
5	704.1	15	703.8	16	20
6	740.5	15	739.1	15	20
7	782.8	20	779.7	20	20
8	832.8	106	833.0	106	10
8b	864.7	21	864.0	22	20
9	945.1	20	943.2	21	60
10	1373.5	31	1376.9	30	60
11	1613.7	91	1610.4	94	20
12	2202.4	175	2185.7	185	20

values above 90, indicating a 90% probability of cloud cover. Visual inspection of each image was then conducted to identify any remaining cloud, cloud shadow, or atmospheric haze within the image that could impact the research results.

3.2.2.3 Landsat-8

Launched in 2013, the Landsat-8 satellite is the eighth satellite launched in the Landsat satellite series, which started with Landsat-1 in 1972. Figure 3.4, provides an illustrative example of the Landsat-8 satellite. Landsat-8 has two onboard EO sensors, the Operational Land Imager (OLI) and the Thermal Infrared Sensor (TIRS). The OLI has eight 30m multi-spectral bands and one 15m resolution panchromatic band. The TIRS has

two 100m resolution bands (Ihlen, 2019). Table 3.2 details the spatial and spectral specifications for the Landsat-8 satellites. Due to the lower resolution and calibration issues with the sensor (Barsi et al., 2017), TIRS data will not be used in this assessment.

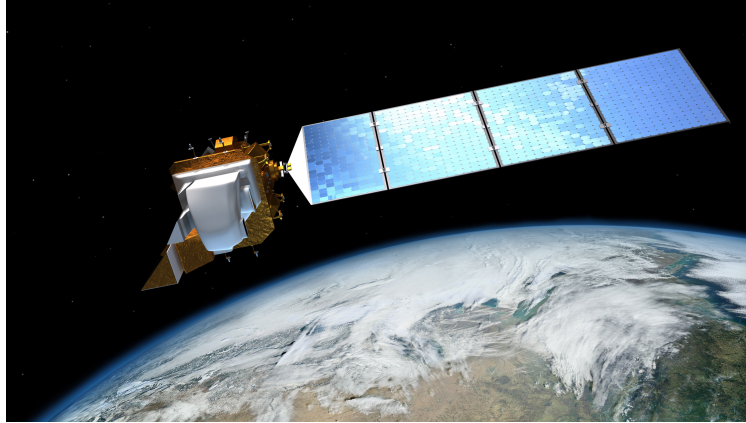


Figure 3.4: Illustration of Landsat-8 satellite, **Source:** EROS (2013).

Table 3.2: Landsat-8 band spectral ranges, **Source:** Ihlen (2019).

Band Number	Band Name	Wavelength Range (nm)	Spatial Resolution (m)
1	Costal/Aerosol	0.435 – 0.451	30
2	Blue	0.452 – 0.512	30
3	Green	0.533 – 0.590	30
4	Red	0.636 – 0.673	30
5	NIR	0.851 – 0.879	30
6	SWIR	1.566 – 1.651	30
7	SWIR2	2.107 – 2.294	30
8	Pan	0.503 – 0.676	15
9	Cirrus	10.60 – 11.19	30
10	TIR-1	11.50 – 12.51	100
11	TIR-2	13.63 – 13.84	100

Landsat-8 data obtained for this assessment was downloaded from the USGS Earth Explorer website (earthexplorer.usgs.gov). As with Sentinel-2 data, the selection of imagery to download was based on visual inspection of all Landsat-8 preview data over the survey areas for 2018, selecting images with cloud-free regions. The Level 2 (L2) Surface Reflectance product was downloaded in order to comply with the requirement for atmospherically corrected data. This product does not include the 15m resolution panchromatic band (Ihlen, 2019) and the Band 9 (*Cirrus*) and therefore these bands were not used in this assessment.

3.2.3 Clipping and Resampling

Each image was clipped to the defined regions shown in Figure 3.1, once each satellite data source had been prepared. During this process, each image was resampled to ensure that the image's minimum and maximum extents were divisible by 10. Resampling was performed using a bilinear interpolation. This process was performed to ensure alignment between the grid structure of each image and the label data used in this assessment.

3.2.4 Labelled Data

The CLC+ Backbone technical specifications define the twelve land cover classes required for the raster product classification dataset. The classification schema for the CLC+ Backbone raster product is detailed in Table 3.3. Examination of LCC datasets, including CORINE 2018, URBAN ATLAS, and LUCAS revealed that the following classes were not identified and reported on the island of Ireland and therefore will be excluded from this assessment:

- Class 4: Woody - broadleaved, evergreen trees
- Class 8: Lichens and mosses
- Class 12: Snow and Ice

In addition to these classes, Class 5: *Woody (shrubs/bushes)* will also be excluded from this assessment. As this class is defined based on elevation, elevation information would be required in this assessment. While it is possible to generate a DSM using Sentinel-1 data, preliminary analysis of the inclusion of a DSM generated using Sentinel-1 data did not improve classification accuracy. One possible reason for this is the poor quality labelled data for shrubs. During preliminary analysis the shrub class was primarily defined using the Copernicus High-res Small Woody 2015 dataset. With satellite data capture for the year 2018, changes to the land cover class may have occurred since 2015. For these aforementioned reasons, classes, 4,5,8 and 12 were excluded from this assessment.

Table 3.3: CLC+ nomenclature, **Source:** Kleeschulte et al. (2019).

No.	Class Name	Description
1	Sealed	All impervious and sealed surfaces. Artificial surfaces such as buildings and artificial constructions, asphalt, concrete, tarmacadam.
2	Woody needle leaved trees	Trees and shrubs with typical needle-shaped leaves. The botanical group Gymnospermae (Ford-Robertson, 1971).
3	Woody broadleaved, deciduous trees	Perennial plants which are leafless for a certain period during the year of the botanical group Angiospermae, with the exception of ginkgo (<i>Ginkgo biloba</i>).
4	Woody broadleaved, evergreen trees	Perennial plants that are never entirely without green foliage of the botanical group Angiospermae, with the exception of ginkgo (<i>Ginkgo biloba</i>).
5	Woody shrubs/bushes	Perennial woody plants with a shrub growth form with height usually less than 8 metres of any leaf type.
6	Permanent herbaceous	Areas of continuous vegetation cover with no bare soil throughout the year. This includes both managed and unmanaged vegetation such as grasslands, or arable areas with a permanent vegetation cover (e.g. fodder crops) or even set-aside land in agriculture.
7	Periodically herbaceous	Areas of land cover which may alternate between bare soil and herbaceous vegetation within one year. Typically this would be a result of managed arable areas.
8	Lichens and mosses	Any type of lichen or mosses. Lichens are composite organisms formed by a symbiotic relationship of a fungus and a photosynthetic partner. Mosses are non-vascular plants in the land plant division Bryophyta. They are small (a few centimetres tall) herbaceous (non-woody) plants that absorb water and nutrients mainly through their leaves and also photosynthesize.
9	Sparsely Vegetated	Sparsely vegetated and unstable areas of stones, boulders, or rubble on steep slopes where the vegetation layer consisting of herbaceous vegetation covers between 10% and 50% of the surface.
10	Non-vegetated	Contains consolidated and unconsolidated materials as well as permanent bare soils, where non-vegetated areas cover $\geq 90\%$ of the land surface. Examples include rock formations, quarries, mineral extraction sites, open pit mines, screes, sand, permanent bare soil.
11	Water	Water in liquid state of aggregation regardless of location, shape, salinity and origin both natural or artificial. This includes rivers, canals, natural lakes, fishponds, man-made reservoirs, pools, irrigation ponds.
12	Snow and ice	Areas covered in snow for at least 90% of observation period or Ice for 100% of the observation period.

With the official CLC+ 2018 Backbone dataset still in production (Copernicus, 2021), no single source of data could be found for the generation of the required land cover labels. For the assessment, multiple data sources were aggregated together to ensure sufficient label data sources for each land cover class. The data sources used for labelled information are listed in Table 3.4.

Table 3.4: List of data sources used for the generation of aggregated labels datasets.

Data Set	Date Obtained
Copernicus Coastal Zones 2018	05/04/2021
Copernicus Urban Atlas 2018	24/03/2020
Copernicus EU-Hydro	16/06/2020
EPA Lake Segments	25/03/2020
Riparian Zones 2012	12/07/2019
Copernicus High-res Forestry 2018	25/03/2020
Copernicus High-res Small Woody 2015	26/04/2020

A systematic approach was applied to aggregate the labelled datasets used in this assessment. The first step was the aggregation of features within each dataset and assigned to their respective CLC+ nomenclature. The feature aggregation from each data source is outlined in Table 3.5. No land cover class was identified in the Copernicus Urban Atlas datasets that could accurately represent a *Sparsely Vegetated* land cover class. As a result of the aggregation of the Copernicus Urban Atlas dataset, Sparsely Vegetated regions were commonly labelled as *Permanent Herbaceous*. Therefore, manual relabelling of *Sparsely Vegetated* was performed using photointerpretation of the 10m resolution

Sentinel-2 and Bing imagery in QGIS. Each dataset was merged after the datasets had been aggregated into the CLC+ classification schema. This data merging was performed by beginning with the manually digitised *Sparsely Vegetated* label and then merging each aggregated dataset in the order appearing in Table 3.5. The dataset to be merged was clipped by existing labels where there was a conflict of labels. Once aggregated, the vector labels from each region were converted to a 10m raster dataset. The extent of the raster was created so that the beginning of each grid location was divisible by 10 for each region. The process was undertaken to ensure the label data grid was directly relatable to each satellite image pixel.

Table 3.5: Features from each data sources that are aggregated together to their respective CLC+ class.

Class Name	Data Source
Sealed	<p data-bbox="549 949 979 981">Copernicus Coastal Zones 2018</p> <p data-bbox="612 987 756 1019">Features:</p> <ul style="list-style-type: none"> <li data-bbox="667 1025 1225 1099">1.1 Urban fabric, industrial, commercial, public, military and private units <li data-bbox="667 1106 1225 1137">1.2.1 Road networks and associated land <li data-bbox="667 1144 1145 1176">1.2.2 Railways and associated land <li data-bbox="667 1182 1161 1214">1.2.3 Port areas and associated land <li data-bbox="667 1220 991 1252">1.3.3 Construction sites <p data-bbox="549 1294 954 1326">Copernicus Urban Atlas 2018</p> <p data-bbox="612 1332 756 1364">Features:</p> <ul style="list-style-type: none"> <li data-bbox="667 1370 1102 1402">11100 Continuous Urban Fabric <li data-bbox="667 1408 1235 1440">11210 Discontinuous Dense Urban Fabric <li data-bbox="667 1447 1378 1478">11220 Discontinuous Medium Density Urban Fabric <li data-bbox="667 1485 1326 1516">11230 Discontinuous Low Density Urban Fabric <li data-bbox="667 1523 1378 1554">11240 Discontinuous Very Low Density Urban Fabric <li data-bbox="667 1561 1015 1592">11300 Isolated Structures <li data-bbox="667 1599 1358 1673">12100 Industrial, commercial, public, military and private units <li data-bbox="667 1680 1278 1711">12210 Fast transit roads and associated land <li data-bbox="667 1718 1198 1749">12220 Other roads and associated land <li data-bbox="667 1756 1158 1787">12230 Railways and associated land <li data-bbox="667 1794 895 1825">12300 Port areas <li data-bbox="667 1832 1002 1863">13300 Construction sites

Features from each data source that are aggregated together to their respective CLC+ class [continued].

Class Name	Data Source
<p>Woody Needle leaved trees (Woody Coniferous)</p>	<p>Copernicus Coastal Zones 2018 Feature: 3.2 Coniferous forest</p> <p>Copernicus High-res Forestry 2018 Feature: Coniferous forest</p>
<p>Woody broadleaved, evergreen trees (Woody Broadleaved)</p>	<p>Copernicus Coastal Zones 2018 Feature: 3.1 Broadleaved forest</p> <p>Copernicus High-res Forestry 2018 Feature: Broadleaved forest</p>
<p>Permanent herbaceous</p>	<p>Copernicus Coastal Zones 2018 Features: 4.0 Grassland 2.2 Permanent crops 1.4 Green urban, sports and leisure facilities 7.1.2.2 Unexploited peat bogs</p> <p>Copernicus Urban Atlas 2018 Feature: 14100 Green urban areas 32000 Herbaceous vegetation associations (natural grassland, moors...) 23000 Pastures</p>
<p>Periodically herbaceous</p>	<p>Copernicus Coastal Zones 2018 Features: 2.1 Arable land</p> <p>Copernicus Urban Atlas 2018 Feature: 21000 Arable land (annual crops)</p>

Features from each data source that are aggregated together to their respective CLC+ class [continued].

Class Name	Data Source
Sparsely vegetated	<p>Copernicus Coastal Zones 2018</p> <p>Features:</p> <p>6.1 Sparsely vegetated areas</p> <p>Manual photo interpretation</p>
Non-vegetated	<p>Copernicus Coastal Zones 2018</p> <p>Features:</p> <p>6.2 Beaches, dunes, river banks</p> <p>6.3 Bare rocks, burnt areas, glaciers and perpetual snow</p> <p>7.2.3 Intertidal flats</p> <p>Copernicus Urban Atlas 2018</p> <p>Feature:</p> <p>13100 Mineral extraction and dump sites</p> <p>33000 Open spaces with little or no vegetation</p>
Water	<p>Copernicus EU-Hydro</p> <p>Features:</p> <p>Canals_p</p> <p>Coastal_p</p> <p>River_Net_p</p> <p>Transit_p</p> <p>InlandWater</p> <p>Riparian Zones 2012</p> <p>Features:</p> <p>9 Rivers and Lakes</p> <p>10 Sea and Ocean</p>

While this assessment is primarily focused on inland LCC, it is noted that some of the labelled datasets for water extend into coastal and ocean waters. The inclusion of this sample data ensures that the trained models are robust to a wide variety of water bodies and could be used in coastal regions without concern for the manual digitising of coastal boundaries.

The exclusion of the *Woody (shrubs/bushes)* from this assessment also meant ensuring removing locations that might represent this class. To exclude these regions, the Copernicus High-res Small Woody 2015 dataset and the *Heathland and Scrub, Lines of Trees and Scrub* and *Transitional Woodland and Scrub* features in the Copernicus Zones dataset were used. This exclusion was achieved by clipping and removing all existing labels except for the *Woody (Needle leaved trees)* and *Woody (Broadleaved, deciduous Trees)* classes. Figure 3.5 illustrates the impact of shrub removal on the rasterised label dataset.



(a) Annually averaged Sentinel-2.



(b) Rasterised labels before shrub removal. (c) Rasterised labels after shrub removal.

Figure 3.5: Impact of removing shrub label locations from rasterised label dataset.

3.3 Methodology

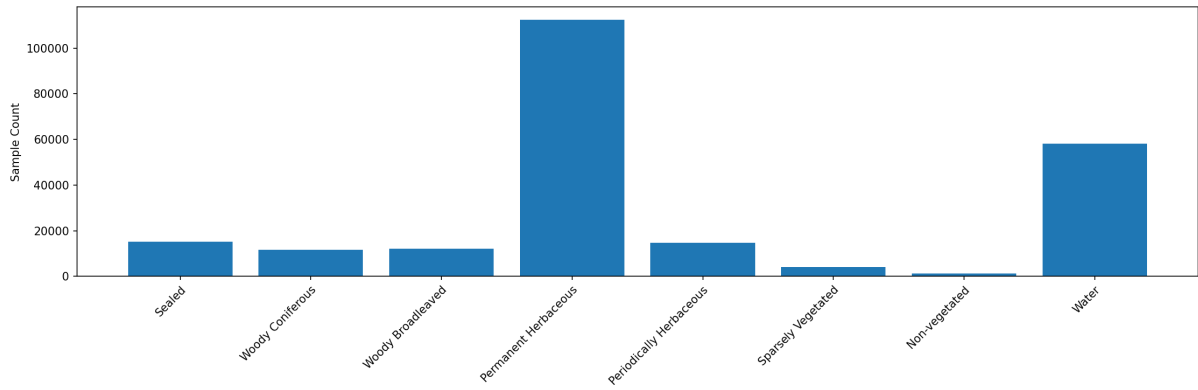
Following the pre-processing steps of the satellite and label data a systematic approach was employed in order to convert the data to a format that could be used to train and test various ML models.

3.3.1 Data Preparation for ML

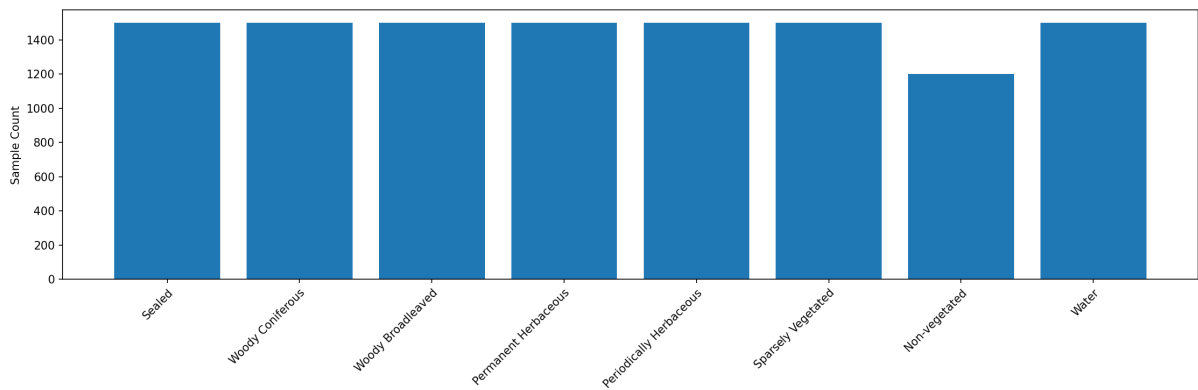
The data used in this assessment was split into three components; training data, validation data and test data. All satellite data from the Dublin region was used as test data for this assessment. Selecting a single region for the test data ensured that it was fully independent of the training and validation data. Dublin was chosen as the region for the test data as it contained sufficient labels of each of the land cover classes to be used in this assessment. The remaining regions were then used to generate the training and validation data. Two different dataset types were created for this study: a Point Dataset and a Patch-to-Point Dataset.

3.3.1.1 Point Dataset Preparation

Random sample points were generated at 10 points per square kilometres for each region used in this study. Points within 100m of each other were removed to ensure that there was no duplication of sample locations. The land cover class at each point location was extracted from the rasterised label files. Examination of the extracted point data revealed class imbalances in the number of points per class. An imbalance in classes can negatively impact classification accuracies (Kubat, 2017; Igual and Seguí, 2017). Points within each class that had greater than 125% of the points in the least frequent class were randomly removed in order to reduce the impact of class imbalance in the point data. While this class balancing is important, it is recognised that this process may result in a proportionally higher cluster of points in regions with less frequently occurring classes. The rebalancing was independently applied to the test data and the combined training and validation data. Figure 3.6, illustrates the total sample point count before and after filtering.



(a) Unfiltered Points.



(b) Filtered Points.

Figure 3.6: Point count per class for all regions (a) before and (b) after applying filtering steps to correct for class imbalance.

After correcting for class imbalance, a stratified random sampling approach was applied to split the non-test data points into the validation and training data, with the validation dataset making up 10% of the available data. A stratified random sampling approach was used to ensure a similar class distribution was available between the training and validation data. Once the training, validation and test data points had been generated, the pixel value and image capture date from each Sentinel-1 image and each cloud and cloud shadow free area of the Sentinel-2 and Landsat-8 images were extracted for each point in the datasets. The inclusion of bands with differing spatial resolutions was examined in more detail since Sentinel-2 imagery consists of bands, processing three different spatial resolutions. For this purpose, three combinations of Sentinel-2 bands were prepared. The first combination included the four 10m bands, the second version included the 10m and 20m bands and the third version included all Sentinel-2 bands.

3.3.1.2 Patch-to-Point Dataset Preparation

For this assessment *Patch-to-Point* datasets were generated to assess the contribution of incorporating spatial information in the analysis. Patch-to-Point datasets contain image *patches* and a single label. For these datasets, the same point locations from the point datasets were used. For each point in the point datasets, an image was clipped from the satellite data centring on the pixel intersecting that point to make the image patch. The size of the patch clipped for the generation of the Patch-to-Point dataset was dependent on the input size of the model. Each non 10m resolution Sentinel-2 band was resampled to 10m using a nearest neighbour sampling approach in order to facilitate the inclusion of Sentinel-2 bands with differing spatial resolutions.

3.3.1.3 Temporal Data Preparation

Temporally averaged versions of both the point and patch-to-point datasets were created to assess the benefits of temporal models. Four temporally averaged datasets were created for each point and patch-to-point dataset. The four temporally averaged datasets include annually-averaged datasets, half-yearly averaged datasets, seasonally averaged datasets and monthly averaged datasets. Meteorological seasons were used as the boundary between seasons temporal ranges for both the half-yearly averaged datasets and seasonally averaged datasets. The winter season was excluded from the seasonally averaged datasets due to the limited number of observations from December to February. Table 3.6 outlines the month ranges applied for both the half-yearly and seasonally averaged datasets.

Table 3.6: Month ranges used for the generation of half-yearly and seasonally averaged datasets.

Averaged Dataset Type	Seasons	Month Ranges
Half-yearly averaged	Spring and Summer Autumn and Winter	March - August September - February
Seasonally averaged	Spring Summer Autumn	March - May June - August September - November

Monthly averaged data prepared for Sentinel-1 enable the generation of a twelve-month temporal stack. However, due to the lack of available optical observations, for Sentinel-2, only a six-monthly averaged temporal stack could be generated. The Sentinel-2 six-monthly averaged temporal stack was generated using the monthly averaged observations from April, May, June, July, September and October. These months were chosen after closer data examination revealed that observations over each region were only available for those six months. Investigation of the samples obtained for Landsat-8 data revealed that due to a limited number of satellite sensor observations, there were insufficient sample points to reliably train and assess the accuracy of Landsat-8 models using seasonally averaged data and monthly averaged data. In addition there were insufficient Landsat-8 observations to confine analysis to areas that have a minimum of six observations. Therefore, a single observation was required for the Landsat-8 annual average and two observations for the Landsat-8 half-year average data.

3.3.1.4 Normalisation of Data

The spectral values of the respective satellite sensor data were scaled between zero and one for each prepared dataset. This was achieved through the conversion of DN values to reflectance values for the Sentinel-2 and Landsat-8 data. This value conversion was achieved using the following formulae:

Sentinel-2 (ESA, 2015):

$$S2_{\rho} = S2_{DN}/10000 \quad (3.1)$$

Landsat-8 (Ihlen, 2019):

$$L8_{\rho} = (L8_{DN} \times 2.75 \times 10^{-05}) - 0.2 \quad (3.2)$$

For Sentinel-1 data, maximum ($S1_{max}$) and minimum ($S1_{min}$) threshold values were set at 10dB and -30dB, respectively. Values above the maximum threshold were set to the maximum threshold value, and values below the minimum threshold were set to the minimum threshold value. This step was undertaken to remove the impact of extreme outliers values on the dataset. All values were then scaled between zero and one using the following formula (Raschka and Mirjalili, 2017):

$$S1_{norm} = \frac{S1_{DN} - S1_{min}}{S1_{max} - S1_{min}} \quad (3.3)$$

3.3.2 ML Techniques to be Evaluated

There are a wide variety of ML techniques that can be applied for LCC using EO data, as noted in Chapter 2. Eight ML techniques are listed in Table 3.7 and were examined for this comparative analysis.

Table 3.7: List of ML techniques to be assessed in mono-platform comparative analysis.

Technique	Abbreviation
Random Forest	RF
Support Vector Machine	SVM
Artificial Neural Network	ANN
Recurrent Neural Network with Long-Short Term Memory	LSTM
Light Convolutional Neural Network	LCNN
Light Fully Convolutional Neural Network	LFCNN
1D Convolutional Neural Network	1DNN
3D Light Fully Convolutional Neural Network	3DLFCNN

Several studies demonstrated the benefit of Patch-to-Patch base CNN techniques (Zhang et al., 2020b; Sun et al., 2019; Zhang et al., 2020a), as outlined in Chapter 2. Patch-to-Patch models generally require fully semantic patch labels with all pixels containing a specific label. The label datasets used in this assessment were generated

using aggregation of multiple datasets and therefore contain regions with no data. Additionally, the exclusion of shrub further increased the areas without data. Consequently, it was not possible to generate sufficient label data to train Patch-to-Patch based models.

RF and SVM models were trained using the python module Sklearn version 0.24.2. All ANN-based architectures were trained using Tensorflow 2.4.2. These architectures include; ANN, LSTM, Light Convolutional Neural Network (LCNN), Light Fully Convolutional Neural Network (LFCNN), 1DCNN and 3DLFCNN.

3.3.2.1 RF and SVM Hyperparameter Selection

The structure of both RF and SVM are outlined in Chapter 2. The choice of hyperparameters for both models was selected using the GridSearchCV module in Sklearn to iterate over a range of hyperparameters. In this process, the hyperparameters with the best results on the validation data were chosen to train the model.

3.3.2.2 ANN and LSTM Structure

For both ANN and LSTM the number of hidden layers and the number of neurons per layer was manually defined for each model. However, after much experimentation, the best performance was observed with an expansion-contraction structure. There are two aspects to the models in this structure: an expansion part and a contraction part. For the expansion part, the number of neurons in each hidden layer is increased relative to the previous layer. In the contraction part of the neural network, each hidden layer decreased the number of neurons relative to the previous layers. In between the expansion and contraction part of the model, a 10% dropout layer is used during training. Dropout is a regulation methodology that helps prevent overfitting and enables the models to develop a degree of redundancy in the network. This is achieved by excluding a percentage of the output of the previous layer at each training step (Aggarwal, 2018). Each trained model had a different number of tuneable variables due to manually defining the number of hidden layers and the number of neurons per layer depending on the input data. Figure 3.7 provides an illustrative example of the ANN structure used in this assessment.

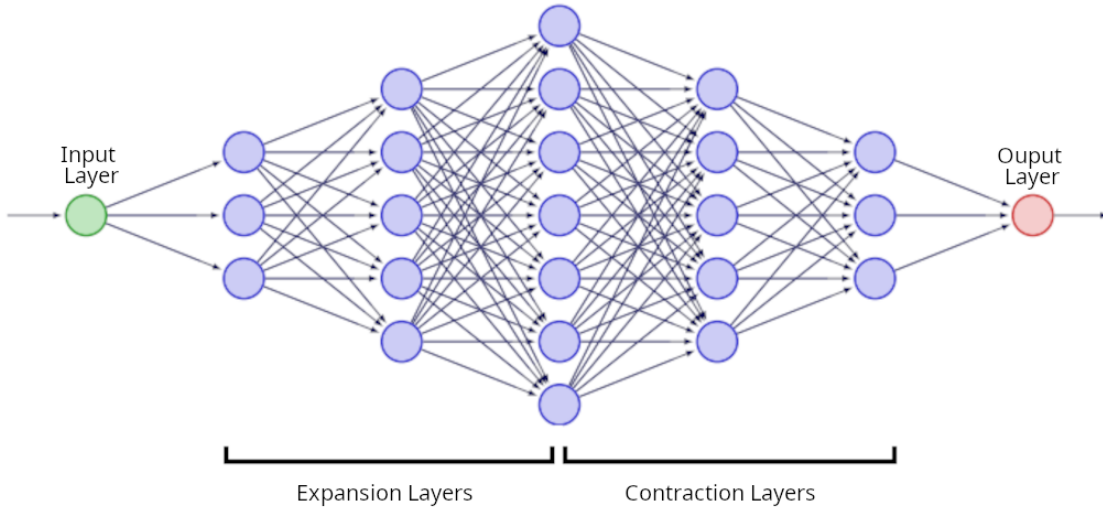


Figure 3.7: Illustrative example of ANN architecture.

3.3.2.3 LCNN and LFCNN

Proposed by Song et al. (2019), Light Convolutional Neural Network (LCNN) is a CNN architecture with two convolutional layers. A patch input array is provided as input to this model and the classification at the centre of the input patch is subsequently computed. In their paper, Song et al. (2019) proposed two architectures, one with a 3×3 input patch size and one with a 5×5 input patch size. Both proposed architectures include 10 feature outputs in the first convolutional layer and 20 feature outputs in the second layer. This output was then flattened into a one-dimensional array. Figure 3.8 provides an illustration of the structure of the LCNN architecture with a 5×5 input patch size (LCNN $_{5 \times 5}$). Table 3.8 outlines the structure both LCNN networks. In a CNN model the number of input bands impacts the number of trainable parameters in the first convolutional layer for each trained model. Each model was trained on data from different platforms with differing numbers of input bands (B).

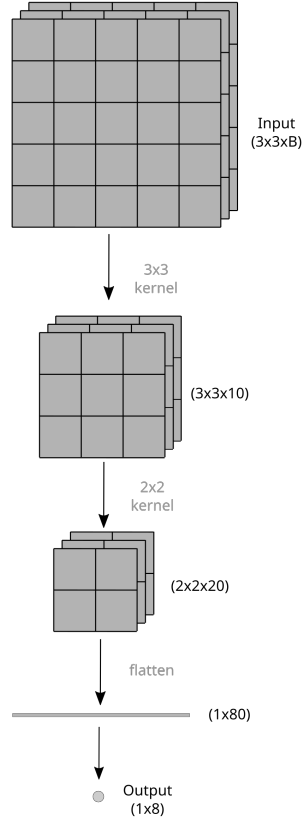


Figure 3.8: Illustration of LCNN5x5 architecture.

The number of trainable parameters in the first convolutional layer (N) is calculated with the following formula (Medium, 2018):

$$N = B * K * O + O \quad (3.4)$$

Where (K) represents the kernel size and (O) represents the number of output features. Therefore, the total number of trainable parameters in each model is given by (N) plus the sum of trainable parameters in each subsequent layer in the model architecture.

Table 3.8: Details of LCNN architectures examined in the mono-platform comparative assessment.

Model Name	Input Shape	Hidden Layers			Trainable Parameters
		kernel size	output features	padding	
LCNN3x3	$3 \times 3 \times B$	3x3	10	Same	$1,468 + N$
		2x2	20	Valid	
LCNN5x5	$5 \times 5 \times B$	3x3	10	Valid	$1,468 + N$
		2x2	20	Valid	

Three additional modified LCNN architectures were proposed and assessed. These networks are designed to use larger input images and have more hidden layers and features per layer. One notable variation in the proposed alternative LCNN architectures is that rather than flattening the output of the convolutional layers, the proposed alternative architectures are designed such that the output of the final convolution layer is a $1 \times 1 \times C$ size where (C) is the number of classes to be classified. During training, this architecture is trained using point information with a shape of $1 \times 1 \times C$. This model will be referred to as an Light Fully Convolutional Neural Network (LFCNN), as the model contains only convolutional layers. The architectural details of each LFCNN model evaluated in this assessment are outlined in Table 3.9. Figure 3.9 provides an illustration of the structure of the LFCNN architecture with a 9×9 input patch size (LFCNN 9×9).

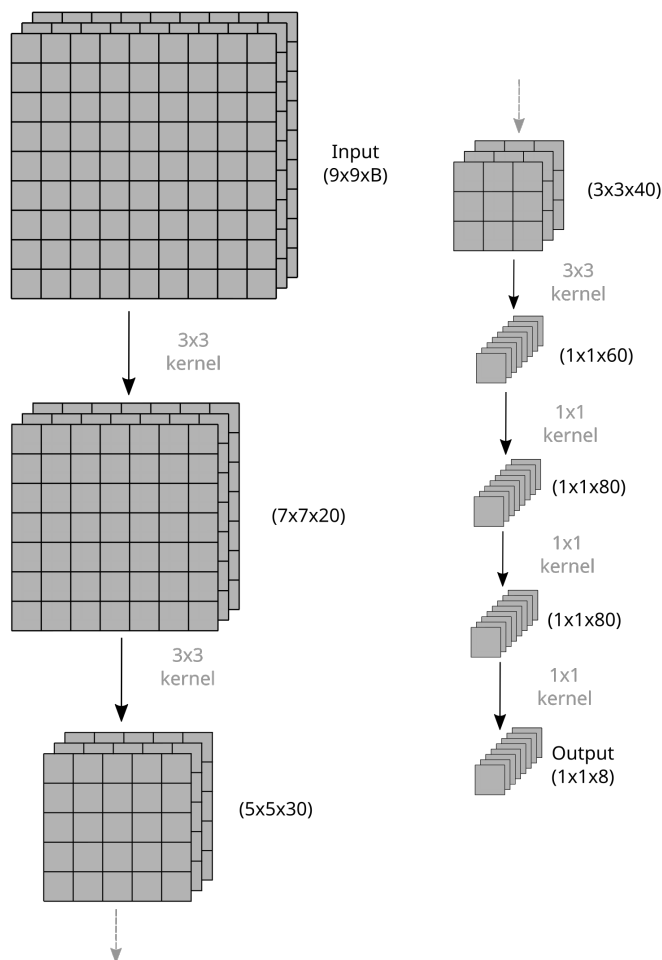


Figure 3.9: Illustration of LFCNN 9×9 architecture.

Table 3.9: Details of LFCNN architectures examined in the mono-platform comparative assessment.

Model Name	Input Shape	Hidden Layers			Trainable Parameters	
		kernel size	output features	padding		
LFCNN9×9	9×9×B	3×3	20	Valid	49,938 + N	
		3×3	30	Valid		
		3×3	40	Valid		
		3×3	60	Valid		
		Dropout 50%				
		1×1	80	Valid		
		1×1	8	Valid		
LFCNN15×15	15×15×B	5×5	20	Valid	139,538 + N	
		3×3	30	Valid		
		3×3	40	Valid		
		3×3	60	Valid		
		Dropout 50%				
		3×3	80	Valid		
		1×1	8	Valid		
LFCNN17×17	17×17×B	5×5	20	Valid	200,988 + N	
		5×5	40	Valid		
		3×3	50	Valid		
		3×3	60	Valid		
		Dropout 50%				
		3×3	70	Valid		
		1×1	8	Valid		

No pooling layers are present in the proposed architectures, and all convolutional layers use a stride of 1. Therefore, the output size of the model scales proportionally with the input patch size. For example, for the LFCNN9×9 architecture, the models can be trained with a 9×9 input patch for the classification of a single pixel (1×1) or point location point. However, with a 2008×2008 input, the model will output the classification for a 2000×2000 patch identical to one where each pixel was classified by the same model using 9×9 input patches for each output pixel.

3.3.2.4 1DCNN and 3DLFCNN

The application of 1DCNN and 3DLFCNN were examined in order to assess the performance of CNNs when used with temporal information inputs. 1DCNN models perform convolution over time. Three 1DCNNs architectures were examined in this assessment

and Table 3.10 outlines the network shape for each architecture. 1DCNN4 was trained using seasonally averaged Sentinel-1 data. 1DCNN6 was trained using Sentinel-2 six-monthly averaged data, and 1DCNN12 was trained using Sentinel-1 for twelve-monthly averaged data.

Table 3.10: Details of 1DCNN architectures examined in the mono-platform comparative assessment.

Model Name	Input Shape	Hidden Layers			Trainable Parameters	
		kernel size	output features	padding		
1DCNN4	$4 \times B$	3	20	Same	$37,708 + N$	
		3	40	Same		
		3	60	Same		
		3	80	Valid		
		2	80	Valid		
		1	8	Valid		
1DCNN6	$6 \times B$	3	20	Same	$82,748 + N$	
		3	20	Same		
		3	40	Same		
		3	60	Same		
		3	80	Same		
		3	80	Valid		
		3	80	Valid		
		2	80	Valid		
		Dropout 10%				
		1	80	Valid		
1	9	Valid				
1DCNN12	$12 \times B$	3	20	Valid	$69,948 + N$	
		3	20	Valid		
		3	40	Valid		
		3	60	Valid		
		3	80	Valid		
		2	80	Valid		
		1	80	Valid		
		1	80	Valid		
		1	80	Valid		
		1	80	Valid		
		1	8	Valid		

Eight 3D CNN architectures were designed and implemented, building upon the LCNN and LFCNN structures to enable the inclusion of temporal information in the analysis. The structure of each model is outlined in Table 3.11 and 3.12.

Table 3.11: Details of half-yearly averaged 3DLFCNN architectures examined in the mono-platform comparative assessment.

Model Name	Input Shape	Hidden Layers			Trainable Parameters
		kernel size	output features	padding	
3DLCNN3×3	$2 \times 3 \times 3 \times B$	1×3×3	10	Same	$3,788 + N$
		2×3×3	20	Valid	
		Reshape to 2D array			
		1×1	8	Valid	
3DLCNN5×5	$2 \times 5 \times 5 \times B$	1×3×3	10	Valid	$3,788 + N$
		2×3×3	20	Valid	
		Reshape to 2D array			
		1×1	8	Valid	
3DLFCNN9×9	$2 \times 9 \times 9 \times B$	1×3×3	20	Valid	$116,028 + N$
		1×3×3	40	Valid	
		1×3×3	60	Valid	
		2×3×3	80	Valid	
		Dropout 50%			
Reshape to 2D array					
		1×1	8	Valid	
3DLFCNN15×15	$2 \times 15 \times 15 \times B$	1×3×3	20	Valid	$200,908 + N$
		1×3×3	40	Valid	
		1×3×3	60	Valid	
		1×3×3	80	Valid	
		2×3×3	80	Valid	
		Dropout 50%			
		Reshape to 2D array			
		1×1	8	Valid	

Table 3.12: Details of seasonally averaged 3DLFCNN architectures examined in the mono-platform comparative assessment.

Model Name	Input Shape	Hidden Layers			Trainable Parameters
		kernel size	output features	padding	
3DLCNN3×3	$3 \times 3 \times 3 \times B$	$3 \times 3 \times 3$	10	Same	$5,588 + N$
		$3 \times 3 \times 3$	20	Valid	
		Reshape to 2D array			
		1×1	8	Valid	
3DLCNN5×5	$3 \times 5 \times 5 \times B$	$2 \times 3 \times 3$	10	Valid	$3,788 + N$
		$2 \times 3 \times 3$	20	Valid	
		Reshape to 2D array			
		1×1	8	Valid	
3DLFCNN9×9	$3 \times 9 \times 9 \times B$	$1 \times 3 \times 3$	20	Valid	$137,628 + N$
		$1 \times 3 \times 3$	40	Valid	
		$2 \times 3 \times 3$	60	Valid	
		$2 \times 3 \times 3$	80	Valid	
		Dropout 50%			
Reshape to 2D array					
		1×1	8	Valid	
3DLFCNN15×15	$3 \times 15 \times 15 \times B$	$1 \times 3 \times 3$	20	Valid	$236,428 + N$
		$1 \times 3 \times 3$	40	Valid	
		$1 \times 3 \times 3$	60	Valid	
		$2 \times 3 \times 3$	80	Valid	
		$2 \times 3 \times 3$	80	Valid	
		Dropout 50%			
		Reshape to 2D array			
		1×1	8	Valid	

3.3.2.5 Activation Functions and Training Parameters

A softmax activation function was used in the final layer for each ANN-based architecture examined in the assessment and is given by the following formula (Bonaccorso, 2018):

$$\text{Softmax}(x)_i = \frac{e^{x_i}}{\sum_{j=1}^n e^{x_j}} \quad (3.5)$$

Where, n is the dimension of the output vector and $\mathbf{x} = [x_1, \dots, x_n]$ is the input vector. The output of a softmax activation function represents a probability distribution for each class (Goodfellow et al., 2016; Bonaccorso, 2018). An argmax operation was then used to convert the model probability outputs to discrete classes, where the highest class probability is assigned as the class for that output. A Rectified Linear Unit (RELU) activation function was used for all other layers in the models. A RELU activation function outputs the input value unchanged for all positive input values. All negative input values have an output of zero. The RELU activation function (Φ) is given by the following formula (Raschka and Mirjalili, 2017):

$$\Phi(x) = \begin{cases} 0, & x < 0 \\ 1, & x > 0 \end{cases} \quad (3.6)$$

Each ANN-based model was trained using a categorical cross-entropy loss function. Categorical cross-entropy loss is calculated using the following formula (Bonaccorso, 2018):

$$CE = - \sum_i^N x_i \log(y_i) \quad (3.7)$$

Where (y) denotes true label and $\mathbf{x} = [x_1, \dots, x_n]$ denotes the model predicted probability. The Adam algorithm was used for gradient-based optimisation with an initial learning rate of 0.0001. The Adam algorithm determines an adaptive learning rate during training and is one of the most widely employed algorithms for updating model weights (Bonaccorso, 2018). An early stopping operation was utilised to stop training where there was no improvement in the validation accuracy after 15 epochs.

3.3.3 Evaluation Process

For this assessment, the performance of each technique was assessed using four metrics, Overall Accuracy (OA), F1 score, confusion matrices and the coverage percentage of each technique.

3.3.3.1 Overall Accuracy

Overall Accuracy (OA) was calculated as a ratio between correct classification and total predictions (Kubat, 2017).

$$OA = \frac{TruePositive + TrueNegative}{TotalSamples} \quad (3.8)$$

3.3.3.2 F1 Score

An F1 score was calculated for each class using the following formula (Raschka and Mirjalili, 2017):

$$F_1 = 2 \frac{precision * recall}{precision + recall} \quad (3.9)$$

$$precision = \frac{tp}{tp + fp} \quad (3.10)$$

$$recall = \frac{tp}{tp + fn} \quad (3.11)$$

Where (tp) is the true positive predictions, (fp) is the false positive predictions and (fn) is the false negative predictions. An overall Weighted F1 score of each model was generated as the average F1 score for each class weighted by the proportion of label points for that class (Pastor-Pellicer et al., 2013; Sklearn, 2020).

3.3.3.3 Comparative Assessment

A preliminary examination of the data revealed differences in the number of label points available to evaluate each model due to the identified issue of cloud cover. Therefore,

the results of this assessment will be presented in two stages to provide an accurate comparison of the performance of each model. In the first stage, the weighted F1 and OA of models from each platform with similarly prepared datasets will be compared. In the second stage, models with the highest test dataset weighted F1 score from the first stage will be selected to perform an in-depth comparison of models from each platform. The labels to be used to calculate the weighted F1 and OA in the second stage will be filtered to those that are common between each model in the comparative assessment.

3.3.3.4 Confusion Matrix

To aid in the interpretation of the results from each model, a confusion matrix was generated for each model. A confusion matrix is a grid matrix identifying the true positive, true negative, false positive and false negative samples for each class (Forsyth, 2018). An example of a confusion matrix is illustrated in Figure 3.10.

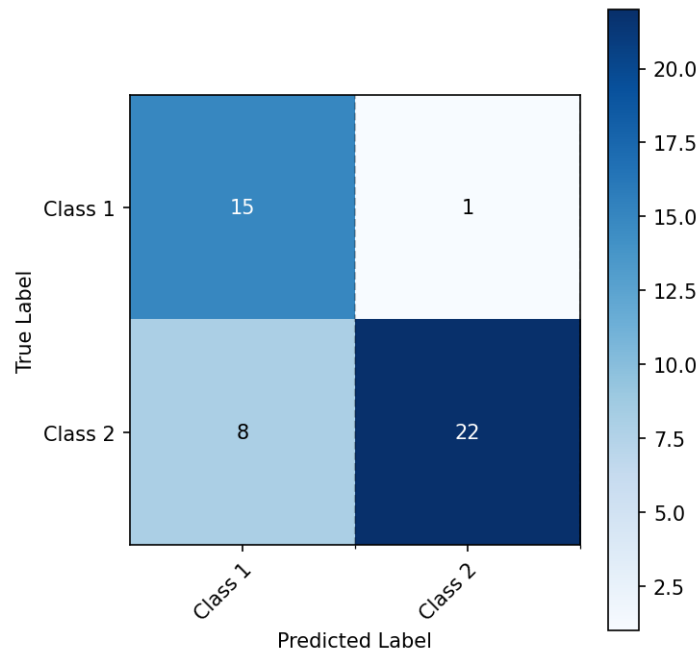


Figure 3.10: Illustration of example confusion matrix.

For this assessment, the values of each confusion matrix were normalised by the number of predictions for that class. Column-wise normalisation by the predicted labels was performed to highlight each predicted classes true and false positives. Normalisation also reduces the impact of differing sample counts between the predicted classes (Gašparović

and Dobrinić, 2020). Figure 3.11. illustrates the impact of this normalisation on data from Figure 3.10 above.

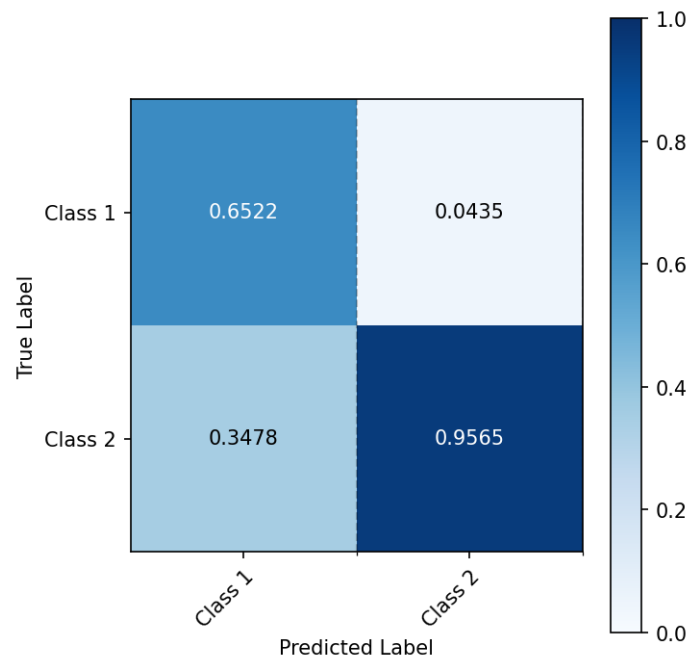
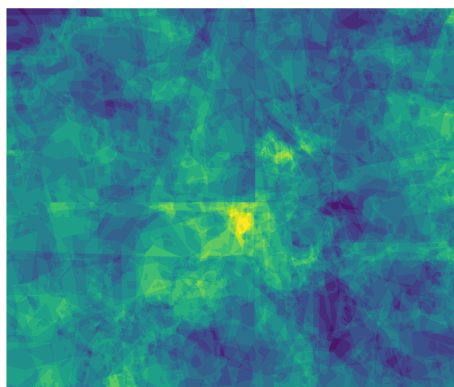
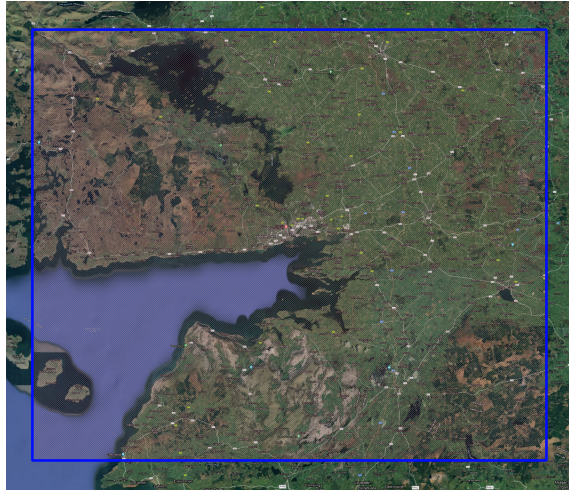


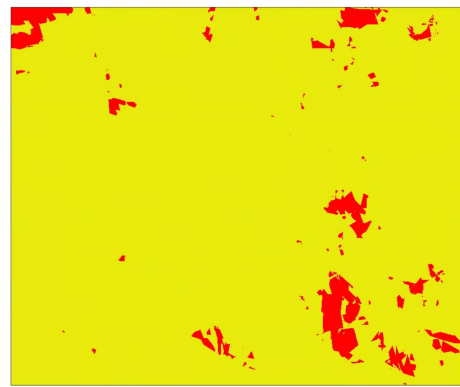
Figure 3.11: Illustration of example normalised confusion matrix.

3.3.3.5 Model Coverage

One of the requirements set out in the CLC+ technical specifications is that a minimum of six satellite observations should be used for classifications. For this assessment, the term coverage will be defined as the percentage of the accessed regions with a minimum of six observations. The coverage of each technique will also be assessed based on this requirement. Figure 3.12 illustrates the total Sentinel-2 observation count over the Galway region and highlights the areas with greater than six observations. As visible in Figure 3.12 not all areas meet this requirement. The technical specifications highlight that it may not be possible to meet this requirement in regions with frequent cloud cover (Kleeschulte et al., 2019).



(a) Observation Count



(b) Observation Threshold

Figure 3.12: Illustrative example of annual Sentinel-2 a) observation count and b) area meeting the six observation count threshold over the assessed Galway region.

As the techniques evaluated in this comparative assessment were undertaken using one of the four different temporally averaged datasets, coverage was determined by the availability of that type of temporal data. For the annually averaged datasets, the requirement was defined as the percentage coverage with a minimum of six observations. For the half-yearly averaged and seasonally averaged datasets the available regions were further filtered to those with equal distribution between the averaging ranges. This required that a minimum of three cloud free observations were required for each half of the year in the half-yearly averaged dataset. Each season must have a minimum of two cloud free observations for the seasonally averaged data for each of the three seasons used in the assessment. Finally, for the monthly averaged datasets a minimum of one observation for each of the selected months was required. Table 3.13, outlines the criteria used to determine the availability for each temporal range.

Table 3.13: Detail of minimum observation requirements for each temporal dataset.

Temporal Dataset	Requirement
Annual Average	Minimum of six observations for the entire year.
Half-Yearly Average	Minimum of three observations for each half of the year.
Seasonally Average	Minimum of two observations for each season.
Monthly Average	Minimum of one observation per month used in the temporal dataset.

The coverage used in this assessment was calculated using the manually digitised cloud masks for both the Sentinel-2 and Landsat-8 data. This requirement is only relevant to the optical imagery from Sentinel-2 and Landsat-8. It can be assumed that Sentinel-1 has 100% coverage due to its ability to capture data both day and night and to penetrate cloud cover.

3.4 Results

A total of 111 models were trained and evaluated as part of this comparative assessment. The weighted F1 and OA of models from each platform will be presented independently in this comparative assessment. A complete list of the results obtained as part of this assessment is, including the F1 score for each class, is presented in Appendix B.

3.4.1 Independent Platform Results

Tables 3.14 to 3.16 displays the validation and test data weighted F1 and OA for models trained using Sentinel-2, Landsat-8 and Sentinel-1 datasets. The results displayed in these tables are calculated using all label points available for the model. Therefore, the results displayed for each platform are only comparable between models using similarly prepared data.

3.4.1.1 Sentinel-2

81 models were generated using Sentinel-2 data. Three combinations of input bands were assessed for each architecture and prepared dataset. A single result will be presented for each architecture and prepared dataset to aid in the interpretation of these results. The results using input variables that obtained the highest test dataset weighted F1 score for each architecture and prepared dataset are presented in Table 3.14. The results for all 81 models generated using Sentinel-2 data are presented in Appendix B. The use of SVM, LFCNN9×9 and LFCNN15×15 all obtained the same weighted F1 score of 0.731 for Sentinel-2 annually averaged data with LFCNN9×9 obtaining a marginally higher OA of 0.736. However, for the half-yearly averaged and seasonally averaged Sentinel-2 datasets, the application 3DLFCNN9×9 outperformed all other models with a weighted F1 score of 0.764 and 0.794, respectively. The highest accuracy results were obtained using the 1DCNN6 architecture for the six monthly averaged datasets with a weighted F1 score of 0.791. However, this result is only marginally better than the results obtained using an SVM with a weighted F1 score of 0.790. No 3DLFCNN based architectures could be trained for the six monthly averaged datasets.

Table 3.14: Sentinel-2 results using all available label points. The highest test data weighted F1 and OA for each prepared dataset are highlighted with text in bold.

Model Name	Variables	Data Preparation	Validation		Test	
			F1	OA	F1	OA
ANN	10m and 20m Bands	Annually Averaged	0.695	0.703	0.720	0.728
RF	All Bands	Annually Averaged	0.667	0.674	0.672	0.677
SVM	10m and 20m Bands	Annually Averaged	0.685	0.692	0.731	0.734
LCNN3×3	10m and 20m Bands	Annually Averaged	0.670	0.678	0.689	0.695
LCNN5×5	10m and 20m Bands	Annually Averaged	0.695	0.700	0.699	0.700
LFCNN9×9	10m and 20m Bands	Annually Averaged	0.729	0.735	0.731	0.736
LFCNN15×15	10m and 20m Bands	Annually Averaged	0.718	0.723	0.731	0.735
LFCNN17×17	10m and 20m Bands	Annually Averaged	0.710	0.714	0.706	0.713
ANN	All Bands	Half-Yearly Averaged	0.713	0.714	0.736	0.725
RF	All Bands	Half-Yearly Averaged	0.688	0.693	0.691	0.678
SVM	10m and 20m Bands	Half-Yearly Averaged	0.704	0.709	0.736	0.734
3DLCNN3×3	10m and 20m Bands	Half-Yearly Averaged	0.677	0.689	0.721	0.726
3DLCNN5×5	10m and 20m Bands	Half-Yearly Averaged	0.724	0.728	0.753	0.756
3DLFCNN9×9	10m and 20m Bands	Half-Yearly Averaged	0.751	0.753	0.764	0.765
3DLFCNN15×15	10m and 20m Bands	Half-Yearly Averaged	0.70	0.705	0.735	0.738
ANN	10m and 20m Bands	Seasonally Averaged	0.732	0.734	0.761	0.762
RF	10m and 20m Bands	Seasonally Averaged	0.705	0.712	0.723	0.729
SVM	10m and 20m Bands	Seasonally Averaged	0.736	0.739	0.757	0.760
3DLCNN3×3	10m and 20m Bands	Seasonally Averaged	0.708	0.716	0.722	0.733
3DLCNN5×5	10m and 20m Bands	Seasonally Averaged	0.738	0.743	0.761	0.763
3DLFCNN9×9	10m and 20m Bands	Seasonally Averaged	0.763	0.766	0.794	0.795
3DLFCNN15×15	10m and 20m Bands	Seasonally Averaged	0.762	0.760	0.762	0.762
ANN	10m and 20m Bands	Six Monthly Averaged	0.702	0.709	0.746	0.756
RF	All Bands	Six Monthly Averaged	0.732	0.738	0.748	0.753
SVM	10m and 20m Bands	Six Monthly Averaged	0.732	0.734	0.790	0.789
LSTM	All Bands	Six Monthly Averaged	0.727	0.731	0.775	0.775
1DCNN6	10m and 20m Bands	Six Monthly Averaged	0.757	0.755	0.791	0.789

For most models, the use of the Sentinel-2 combined 10m and 20m bands resulted in the highest weighted F1 and OA. For some point-based models, the inclusion of all Sentinel-2 bands resulted in minor improvements. However, for all the patch-to-point based models, the use of only the Sentinel-2 10m bands or all Sentinel-2 bands resulted in poorer results relative to the use of the combined 10m and 20m bands.

3.4.1.2 Landsat-8

The results of each Landsat-8 model are presented in Table 3.15. For the Landsat-8 annually averaged data, the best results were obtained using LFCNN9×9, while for the half-yearly averaged data 3DLFCNN9×9 obtained the best results. The LFCNN17×17, 3DLFCNN15×15 and 3DLFCNN17×17 architectures could not be successfully trained using Landsat-8 data.

Table 3.15: Landsat-8 results using all available label points. The highest test data weighted F1 and OA for each prepared dataset are highlighted with text in bold.

Model Name	Variables	Data Preparation	Validation		Test	
			F1	OA	F1	OA
ANN	All Bands	Annually Averaged	0.628	0.635	0.652	0.652
RF	All Bands	Annually Averaged	0.614	0.629	0.595	0.603
SVM	All Bands	Annually Averaged	0.621	0.633	0.640	0.642
LCNN3×3	All Bands	Annually Averaged	0.598	0.606	0.600	0.606
LCNN5×5	All Bands	Annually Averaged	0.618	0.628	0.613	0.623
LFCNN9×9	All Bands	Annually Averaged	0.677	0.681	0.678	0.680
LFCNN15×15	All Bands	Annually Averaged	0.576	0.592	0.538	0.557
ANN	All Bands	Half-Yearly Averaged	0.665	0.676	0.680	0.680
RF	All Bands	Half-Yearly Averaged	0.674	0.687	0.667	0.658
SVM	All Bands	Half-Yearly Averaged	0.702	0.710	0.699	0.702
3DLCNN3×3	All Bands	Half-Yearly Averaged	0.706	0.710	0.717	0.718
3DLCNN5×5	All Bands	Half-Yearly Averaged	0.655	0.66	0.630	0.644
3DLFCNN9×9	All Bands	Half-Yearly Averaged	0.712	0.720	0.726	0.715

3.4.1.3 Sentinel-1

All results presented in Table 3.16 are comparable since all Sentinel-1 temporal datasets had the same sample points. The best results obtained using Sentinel-1 were achieved

using the 1DCNN12 architecture with monthly averaged data. No patch-to-point models could successfully be trained using Sentinel-1 data.

Table 3.16: Sentinel-1 results using all available label points. The highest test data weighted F1 and OA for each prepared dataset are highlighted with text in bold.

Model Name	Variables	Data Preparation	Validation		Test	
			F1	OA	F1	OA
ANN	VV & VH	Annually Averaged	0.439	0.453	0.457	0.479
RF	VV & VH	Annually Averaged	0.504	0.511	0.477	0.482
SVM	VV & VH	Annually Averaged	0.468	0.479	0.447	0.455
ANN	VV & VH	Half-Yearly Averaged	0.491	0.501	0.495	0.505
RF	VV & VH	Half-Yearly Averaged	0.529	0.534	0.522	0.533
SVM	VV & VH	Half-Yearly Averaged	0.530	0.539	0.536	0.545
ANN	VV & VH	Seasonally Averaged	0.525	0.535	0.551	0.569
RF	VV & VH	Seasonally Averaged	0.592	0.597	0.556	0.563
SVM	VV & VH	Seasonally Averaged	0.593	0.597	0.593	0.599
1DCNN4	VV & VH	Seasonally Averaged	0.62	0.623	0.620	0.630
ANN	VV & VH	Monthly Averaged	0.638	0.642	0.609	0.606
RF	VV & VH	Monthly Averaged	0.620	0.626	0.595	0.603
SVM	VV & VH	Monthly Averaged	0.686	0.689	0.642	0.645
LSTM	VV & VH	Monthly Averaged	0.602	0.604	0.600	0.602
1DCNN12	VV & VH	Monthly Averaged	0.691	0.694	0.654	0.653

3.4.2 Platform Comparative Results

The results of the comparative assessment for Sentinel-2 and Landsat-8 models are given in Tables 3.17 and 3.18 respectively. The results of the cross-platform comparative assessment are displayed in Table 3.19.

Table 3.17: Sentinel-2 comparative results. The highest test data F1/OA in each column are highlighted with text in bold.

		Sealed	Woody Coniferous	Woody Broadleaved	Permanent Herbaceous	Periodically Herbaceous	Sparsely Vegetated	Non-vegetated	Water	Weighted F1	OA
LFCNN9×9 Annually Averaged	Train	0.738	0.845	0.640	0.500	0.633	0.771	0.602	0.959	0.709	0.709
	Validation	0.774	0.887	0.699	0.449	0.637	0.743	0.694	0.953	0.729	0.730
	Test	0.738	0.880	0.730	0.512	0.722	0.661	0.521	0.982	0.773	0.774
3DLFCNN9×9 Half-Yearly Averaged	Train	0.803	0.850	0.674	0.589	0.656	0.823	0.662	0.965	0.750	0.750
	Validation	0.808	0.860	0.783	0.581	0.656	0.796	0.633	0.963	0.760	0.762
	Test	0.809	0.893	0.775	0.615	0.760	0.650	0.578	0.980	0.808	0.808
3DLFCNN9×9 Seasonally Averaged	Train	0.790	0.855	0.677	0.593	0.658	0.813	0.674	0.975	0.751	0.753
	Validation	0.772	0.885	0.781	0.612	0.684	0.815	0.659	0.964	0.771	0.772
	Test	0.831	0.881	0.777	0.611	0.755	0.685	0.663	0.978	0.819	0.818
1DCNN6 Six Monthly Averaged	Train	0.851	0.864	0.744	0.635	0.757	0.861	0.820	0.993	0.813	0.810
	Validation	0.733	0.847	0.732	0.574	0.698	0.809	0.680	0.973	0.754	0.751
	Test	0.755	0.831	0.696	0.579	0.757	0.667	0.643	0.985	0.791	0.789

Table 3.18: Landsat-8 comparative results. The highest test data F1/OA in each column are highlighted with text in bold.

		Sealed	Woody Coniferous	Woody Broadleaved	Permanent Herbaceous	Periodically Herbaceous	Sparsely Vegetated	Non-vegetated	Water	Weighted F1	OA
LFCNN9×9 Annually Averaged	Train	0.742	0.839	0.669	0.480	0.590	0.771	0.664	0.979	0.725	0.727
	Validation	0.694	0.821	0.638	0.500	0.524	0.760	0.636	0.994	0.702	0.705
	Test	0.682	0.817	0.716	0.552	0.612	0.256	0.492	0.987	0.702	0.704
3DLFCNN9×9 Half-Yearly Averaged	Train	0.693	0.826	0.593	0.489	0.555	0.764	0.572	0.966	0.692	0.700
	Validation	0.759	0.820	0.596	0.517	0.619	0.740	0.604	0.988	0.712	0.720
	Test	0.695	0.841	0.675	0.626	0.694	0.177	0.525	0.986	0.726	0.715

Table 3.19: Cross-Platform comparative results. The highest test data F1/OA in each column are highlighted with text in bold.

		Sealed	Woody Coniferous	Woody Broadleaved	Permanent Herbaceous	Periodically Herbaceous	Sparsely Vegetated	Non-vegetated	Water	Weighted F1	OA
Sentinel-2 LFCNN9×9 Annually Averaged	Train	0.738	0.828	0.650	0.484	0.663	0.781	0.569	0.965	0.717	0.715
	Validation	0.763	0.889	0.735	0.45	0.652	0.756	0.732	0.968	0.744	0.744
	Test	0.747	0.898	0.719	0.485	0.723	0.098	0.520	0.981	0.774	0.769
Sentinel-2 3DLFCNN9×9 Half-Yearly Averaged	Train	0.812	0.829	0.667	0.586	0.691	0.843	0.682	0.969	0.763	0.762
	Validation	0.775	0.861	0.804	0.581	0.667	0.795	0.629	0.979	0.765	0.765
	Test	0.823	0.918	0.787	0.613	0.773	0.267	0.571	0.979	0.819	0.815
Sentinel-2 3DLFCNN9×9 Seasonally Averaged	Train	0.795	0.840	0.673	0.587	0.686	0.818	0.668	0.978	0.759	0.760
	Validation	0.784	0.901	0.819	0.644	0.702	0.805	0.688	0.968	0.792	0.791
	Test	0.847	0.918	0.785	0.585	0.760	0.059	0.637	0.981	0.823	0.819
Sentinel-2 1DCNN6 Six Monthly Averaged	Train	0.865	0.848	0.742	0.631	0.774	0.865	0.811	0.992	0.818	0.815
	Validation	0.776	0.873	0.762	0.578	0.731	0.842	0.806	0.990	0.795	0.791
	Test	0.766	0.842	0.722	0.569	0.769	0.118	0.656	0.985	0.802	0.804
Landsat-8 LFCNN9×9 Annually Averaged	Train	0.743	0.835	0.675	0.491	0.610	0.765	0.640	0.980	0.721	0.723
	Validation	0.674	0.800	0.679	0.550	0.574	0.760	0.667	0.990	0.711	0.712
	Test	0.793	0.800	0.671	0.456	0.682	0.278	0.542	0.986	0.769	0.775
Landsat-8 3DLFCNN9×9 Half-Yearly Averaged	Train	0.700	0.824	0.585	0.478	0.574	0.762	0.577	0.968	0.687	0.694
	Validation	0.773	0.822	0.667	0.579	0.615	0.736	0.670	0.990	0.731	0.735
	Test	0.772	0.862	0.648	0.492	0.682	0.154	0.527	0.985	0.767	0.763
Sentinel-1 1DCNN12 Monthly Averaged	Train	0.649	0.781	0.649	0.512	0.675	0.684	0.588	0.987	0.698	0.696
	Validation	0.478	0.825	0.679	0.495	0.653	0.734	0.557	0.979	0.684	0.685
	Test	0.665	0.782	0.623	0.518	0.745	0.0	0.413	0.981	0.736	0.734

The best results were obtained using the 3DLFCNN9×9 architecture with seasonally averaged Sentinel-2 data for the Sentinel-2 only and cross-platform comparative assessments. A test dataset weighted F1 of 0.823 and OA of 0.819 were obtained using this architecture when carrying out the cross-platform comparative assessment. 3DLFCNN9×9 produced the best results with a test dataset weighted F1 of 0.726 and OA of 0.715 for the Landsat-8 only comparative assessment.

3.4.3 Confusion Matrices and Classification Examples

Figures 3.13 to 3.15, display the confusion matrices for the best performing model from each platform. Examination of these confusion matrices revealed that there is a high degree of confusion between the *Periodically Herbaceous* and *Permanent Herbaceous* classes. There is over 10% confusion between the two classes for each of the displayed models. In addition, for each model, over 14% of the *Sealed* class predictions were instead classified as *Non-Vegetated*. Figures 3.16 and 3.17 provided an illustrative example of the classification output from the best performing model from each platform.

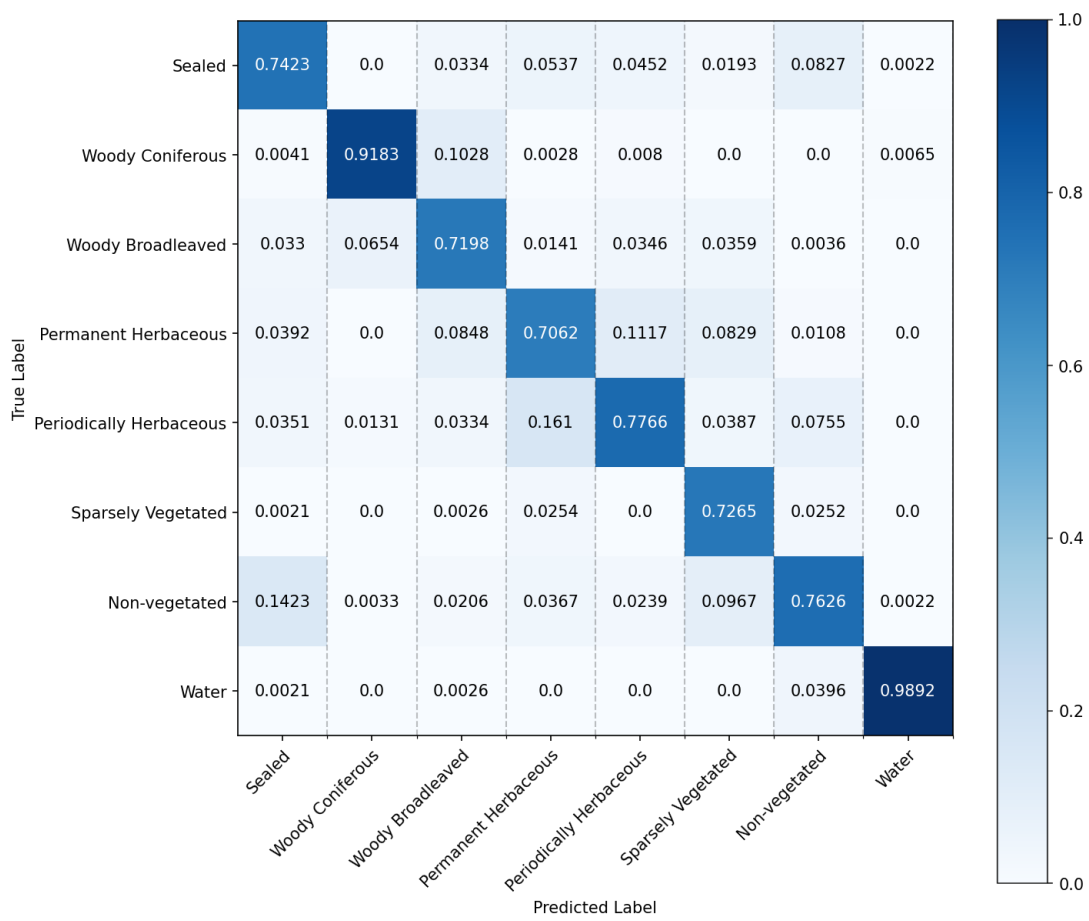


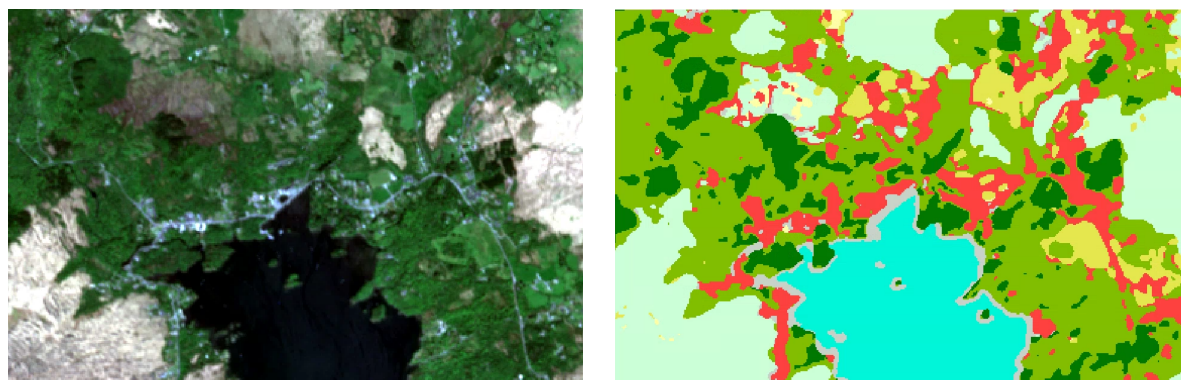
Figure 3.13: Confusion matrix for Sentinel-2 seasonally averaged 3DLFCNN9×9.



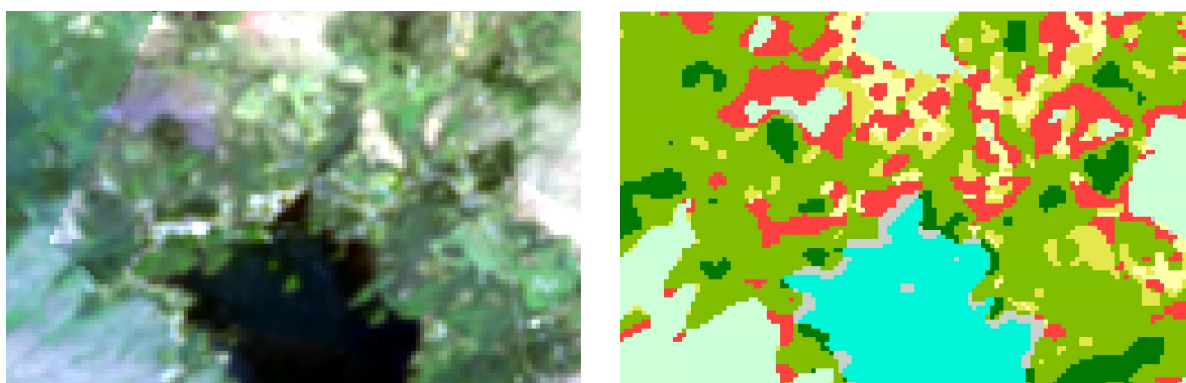
Figure 3.14: Confusion matrix for Sentinel-1 monthly averaged 1DCNN.



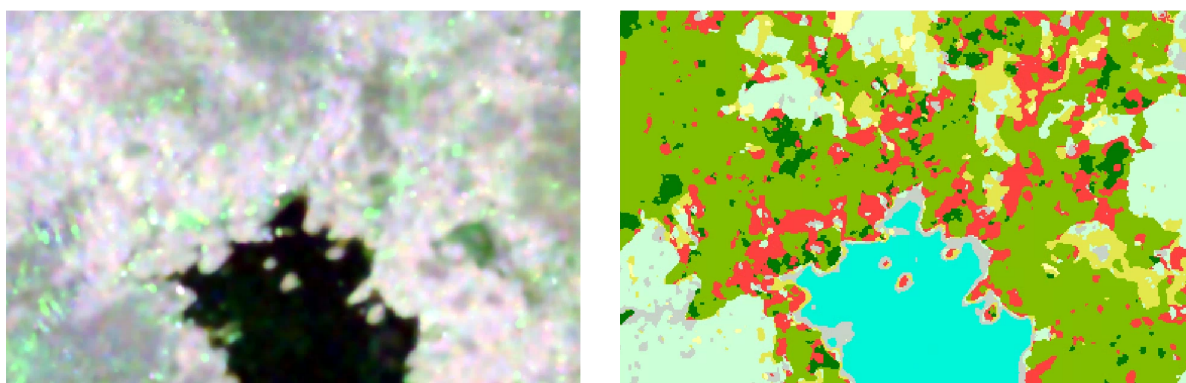
Figure 3.15: Confusion matrix for Landsat-8 half-yearly averaged 3DLFCNN9x9.



(a) Sentinel-2 seasonally averaged 3DLFCNN9×9.



(b) Landsat-8 half-yearly averaged 3DLFCNN9×9.



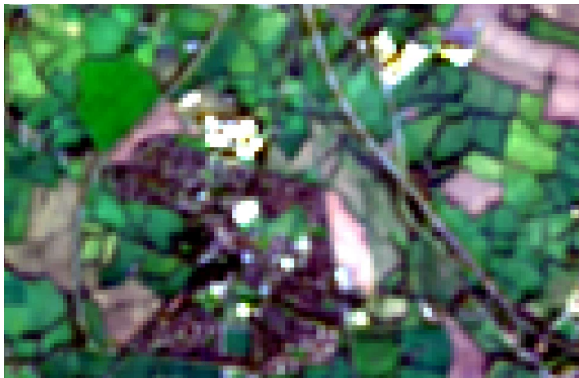
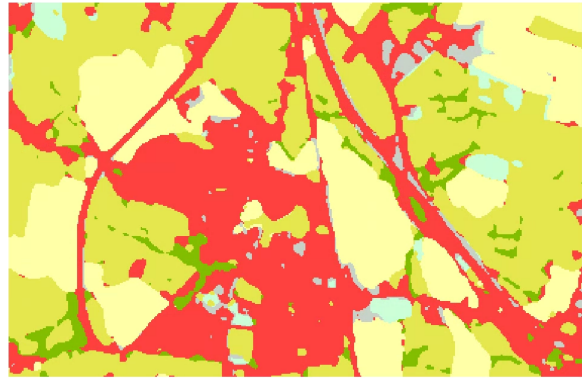
(c) Sentinel-1 monthly averaged 1DCNN12.



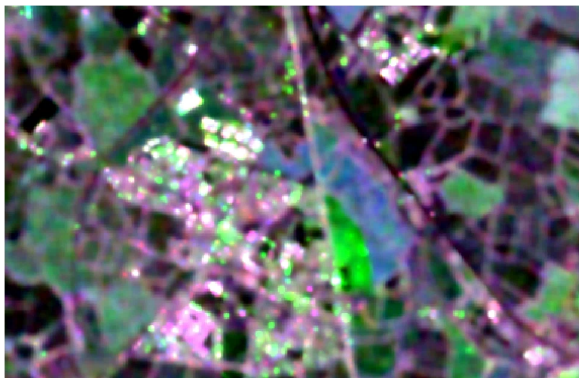
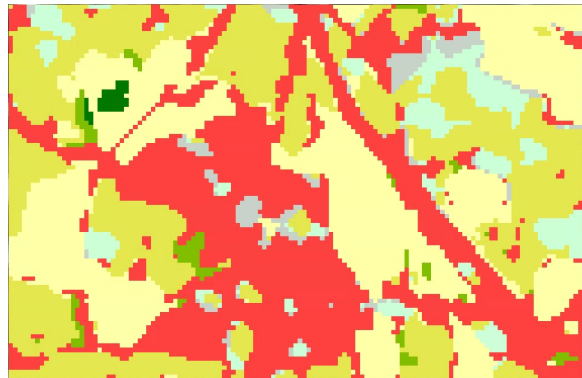
Figure 3.16: Classification examples over Glengarriff harbour, Co. Cork using the best model for (a) Sentinel-2, (b) Landsat-8 (c) Sentinel-1.



(a) Sentinel-2 seasonally averaged 3DLFCNN9×9.



(b) Landsat-8 half-yearly averaged 3DLFCNN9×9.



(c) Sentinel-1 monthly averaged 1DCNN12.

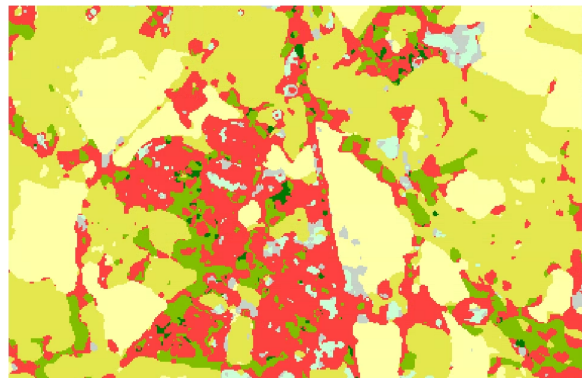


Figure 3.17: Classification examples over Dunboyne, Co. Meath using the best model for (a) Sentinel-2, (b) Landsat-8 (c) Sentinel-1.

3.4.4 Model Coverage

Tables 3.20 and 3.21 outline the coverage of each region for Sentinel-2 and Landsat-8 respectively. In addition, the combined coverage of Sentinel-2 and Landsat-8 is provided in Table 3.22. This fused coverage illustrates the coverage where a harmonised Sentinel-2 and Landsat-8 approach was employed to increase temporal data availability.

Table 3.20: Sentinel-2 model coverage for each temporal dataset calculated by the area meeting minimum observation requirements set out in Table 3.13.

	Annually Averaged	Half-Yearly Averaged	Seasonally Averaged	Six Monthly Averaged
Belfast	99.94%	88.52%	84.90%	30.80%
Cork	99.72%	80.65%	87.69%	53.20%
Dublin	95.64%	69.93%	80.37%	29.48%
Dunglow	94.19%	65.84%	75.59%	1.77%
Galway	95.30%	62.18%	55.44%	12.40%
Glengariff	100.00%	99.47%	97.97%	52.29%
Limerick	99.11%	71.59%	76.32%	19.19%
Waterford	100.00%	96.68%	99.83%	59.46%
Combined	97.55%	76.81%	81.36%	33.37%

Table 3.21: Landsat-8 model coverage for each temporal dataset calculated by the area meeting minimum observation requirements set out in Table 3.13.

	Annually Averaged	Half-Yearly Averaged	Seasonally Averaged
Belfast	11.32%	4.80%	0.71%
Cork	39.82%	28.59%	11.64%
Dublin	12.65%	7.58%	3.12%
Dunglow	12.12%	2.81%	1.22%
Galway	73.54%	7.13%	5.37%
Glengariff	75.75%	61.00%	38.81%
Limerick	31.21%	7.84%	4.04%
Waterford	86.65%	76.40%	42.38%
Combined	36.19%	19.02%	9.90%

Table 3.22: Sentinel-2 and Landsat-8 combined model coverage for each temporal dataset calculated by the area meeting minimum observation requirements set out in Table 3.13.

	Annually Averaged	Half-Yearly Averaged	Seasonally Averaged	Six Monthly Averaged
Belfast	100.00%	96.09%	94.82%	34.67%
Cork	100.00%	99.75%	97.88%	89.79%
Dublin	99.39%	83.53%	87.33%	39.68%
Dunglow	98.43%	66.40%	80.09%	2.54%
Galway	99.60%	81.05%	81.65%	16.75%
Glengariff	100.00%	100.00%	99.80%	81.46%
Limerick	99.86%	84.74%	93.51%	25.03%
Waterford	100.00%	99.98%	99.94%	96.95%
Combined	99.68%	89.16%	91.13%	49.11%

As evident in Tables 3.20 and 3.22, increasing the temporal splits reduces the area where each model type could be employed. This is particularly notable with Landsat-8, which is a single satellite compared to the twin satellites in operation for Sentinel-2. Combining Sentinel-2 and Landsat-8 increased the coverage, however, this still does not result in 100% coverage. For a monthly averaged dataset, the maximum coverage that could be achieved is 49.11%. Of the assessed regions, Dunglow produced the lowest coverage with only 2.54% coverage for the monthly averaged dataset.

3.5 Discussion

The highest comparative weighted F1 score of 0.823 and OA of 0.819 was obtained using a 3DLFCNN9×9 with seasonally averaged Sentinel-2 data. However, this model did not obtain the highest F1 score for each land cover class. Table 3.23 lists the model that obtained the highest F1 score for each class.

Table 3.23: List of the mono-platform ML models obtaining the highest Test F1 score for each class.

Class Name	Model	F1
Sealed	Sentinel-2 Seasonally Averaged 3DLFCNN9×9	0.847
Woody Coniferous	Sentinel-2 Seasonally Averaged 3DLFCNN9×9	0.918
Woody Broadleaved	Sentinel-2 Half-Yearly Averaged 3DLFCNN9×9	0.792
Permanent herbaceous	Sentinel-2 Half-Yearly Averaged 3DLFCNN9×9	0.613
Periodically herbaceous	Sentinel-2 Half-Yearly Averaged 3DLFCNN9×9	0.773
Sparsely Vegetated	Landsat-8 Annually Averaged LFCNN9×9	0.278
Non-vegetated	Sentinel-2 Six Monthly Averaged 3DLFCNN9×9	0.656
Water	Landsat-8 Annually Averaged LFCNN9×9	0.986

Overall, *Water* obtained the highest class F1 scores with all models in the comparative assessments obtaining a F1 score greater than 0.9 for the classification of *Water* on the test dataset. The lowest class F1 score that was obtained on the test dataset was for *Sparsely Vegetated*. However, this result may be misleading as limiting the label points to only those available to all models resulted in only 13 *Sparsely Vegetated* label point locations remaining in the test dataset. Table 3.24 provides the count of available label points in the test dataset available for each comparative assessment.

Table 3.24: Test dataset label points available for each comparative assessments.

	All Label Points	Sentinel-2 Comparative	Landsat-8 Comparative	Cross Platform Comparative
Sealed	481	178	388	163
Woody Coniferous	481	102	251	64
Woody Broadleaved	481	107	323	74
Permanent Herbaceous	481	94	301	73
Periodically Herbaceous	481	145	360	134
Sparsely Vegetated	481	50	31	13
Non- vegetated	385	102	295	91
Water	481	301	451	290
Total	3752	1079	2400	902

It is necessary to examine the training and validation results in order to determine the highest accuracy classification results for the *Sparsely Vegetated* class due to the limited number of test sample points available in the cross-platform comparative assessment. The Sentinel-2 six-monthly averaged 1DCNN obtained the highest F1 score based on the training and validation results. However, the highest test F1 score was obtained using a Sentinel-2 seasonally-averaged 3DLFCNN 9×9 , when the Sentinel-2 comparative assessment results were examined and where more *Sparsely Vegetated* sample points existed. The notable change in the results based on sample availability makes interpreting the results a significant challenge.

Another challenge to interpreting the results of this comparative assessment is that a number of the models produce higher classification accuracies in the test datasets when compared to those with the training and validation dataset. This phenomenon appears to be more frequent in the temporally split Sentinel-2 data. One possible reason for this is that limited sample locations may include more ‘typical’ examples of the classes. This phenomenon exacerbates further the challenge of interpreting results.

3.5.1 Prediction Probability and Accuracy

While the overall accuracy of each model is important, each model can also be examined in terms of the accuracy relative to its predicted probability. For each model trained in this assessment, the prediction probability of each class can be obtained. The relationship between prediction probability and accuracy can be examined by calculating the accuracy of predictions made above a series of probability thresholds. However, these probability thresholds exclude points below the threshold, reducing the number of available sample point locations. Therefore the accuracy for each threshold is calculated in relation to the remaining points above the threshold. Figures 3.18 to 3.20, illustrate the relationship between predicted probability and accuracy of each of the best performing models for each platform using this approach.

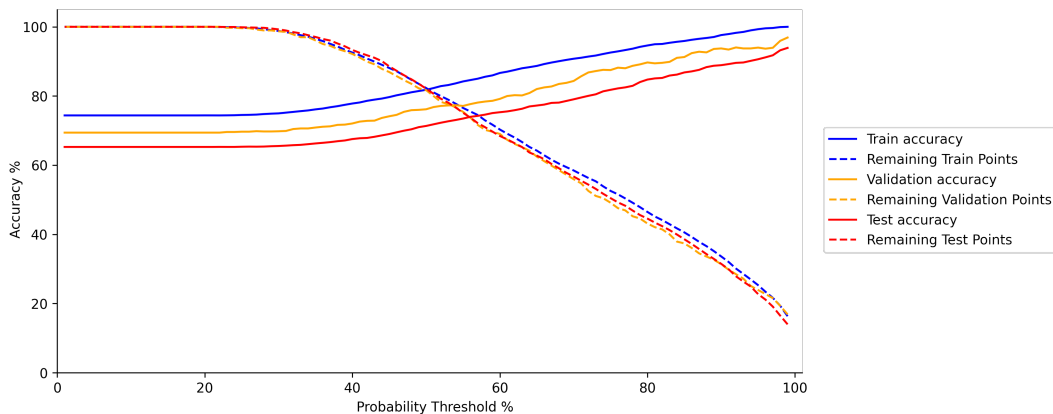


Figure 3.18: Probability threshold vs accuracy and available sample points for Sentinel-1 monthly averaged 1DCNN12.

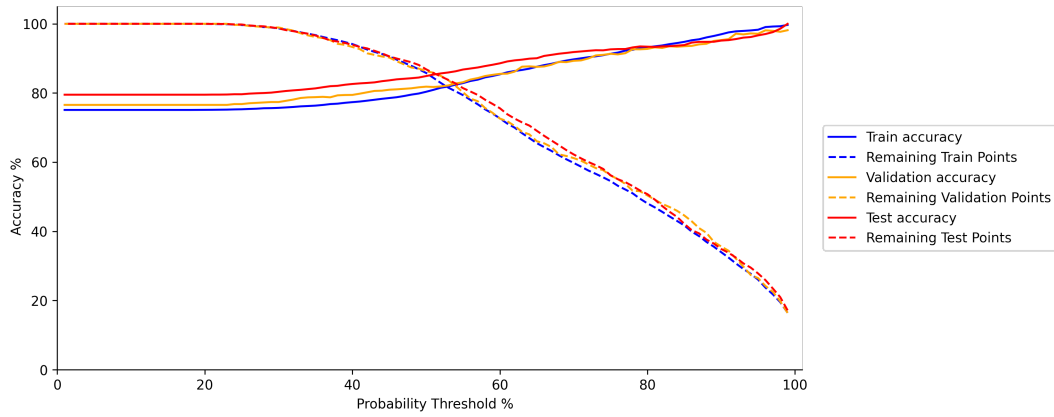


Figure 3.19: Probability threshold vs accuracy and available sample points for Sentinel-2 seasonally averaged 3DLFCNN9×9.

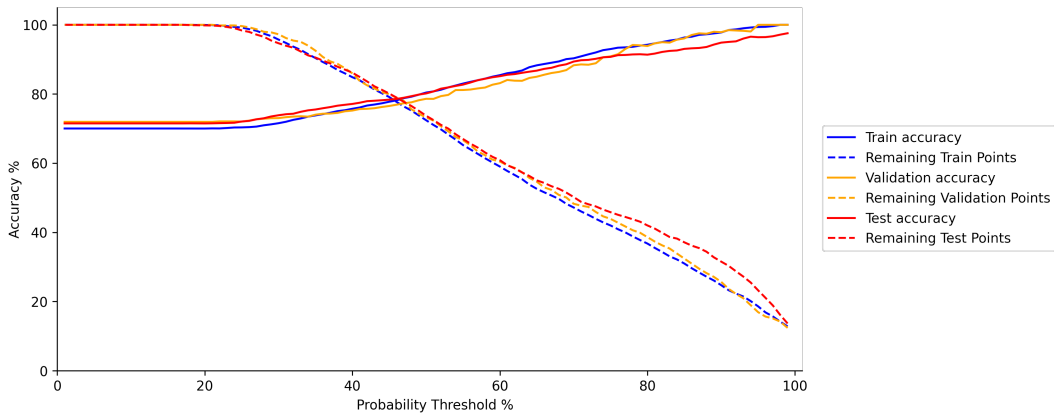


Figure 3.20: Probability threshold vs accuracy and available sample points for Landsat-8 half-yearly averaged 3DLFCNN9×9.

As seen in Figures 3.18 to 3.20, increasing the probability threshold increases the classification accuracy. Using this information, a probability threshold can be set for each model such that the classification results are above a desired accuracy. Table 3.25, details the percentage of remaining test sample points from the comparative assessment after a probability threshold where the models accuracy is above four defined accuracies.

Table 3.25: Percentage of remaining test points at desired target accuracy as a result of probability thresholding. The highest value in each column are highlighted with text in bold.

Target Accuracy	80%	85%	90%	95%
Sentinel-2 LFCNN9×9 Annually Averaged	93.94%	79.78%	68.71%	53.78%
Sentinel-2 3DLFCNN9×9 Half-Yearly Averaged	100%	89.58%	75.33%	56.31%
Sentinel-2 3DLFCNN9×9 Seasonally Averaged	100%	92.98%	78.71%	60.41%
Sentinel-2 1DCNN6 Six Monthly Averaged	100%	87.11%	72.46%	54.01%
Landsat-8 LFCNN9×9 Annually Averaged	96.49%	84.20%	73.56%	55.23%
Landsat-8 3DLFCNN9×9 Half-Yearly Averaged	92.97%	80.24%	68.80%	57.95%
Sentinel-1 1DCNN12 Monthly Averaged	85.60%	74.82%	63.48%	53.48%

The largest remaining sample points with a target accuracy of 95% was obtained using Sentinel-2 seasonally averaged 3DLFCNN9×9. However, as outlined in the methodology, sample points were filtered to ensure a balance between each class. Therefore, the results presented in Table 3.25 are not a true representation of the model coverage over the assessed regions. By predicting the probability output across each region using the satellite raster data and the probability thresholds defined from the sample points, a more accurate estimation of the coverage at the set accuracy ranges can be calculated for each model. The result of this process is displayed in Table 3.26.

Table 3.26: Estimate of the percentage of area from prediction at a desired target accuracy as a result of probability thresholding. The highest value in each column are highlighted with text in bold.

Target Accuracy	80%	85%	90%	95%
Sentinel-2 LFCNN9×9 Annually Averaged	53.73%	43.37%	33.72%	25.99%
Sentinel-2 3DLFCNN9×9 Half-Yearly Averaged	59.27%	42.85%	31.09%	24.88%
Sentinel-2 3DLFCNN9×9 Seasonally Averaged	65.59%	52.30%	36.19%	26.43%
Sentinel-2 1DCNN6 Six Monthly Averaged	30.15%	29.96%	28.76%	26.73%
Landsat-8 LFCNN9×9 Annually Averaged	16.88%	13.24%	11.85%	10.89%
Landsat-8 3DLFCNN9×9 Half-Yearly Averaged	8.56%	7.41%	6.77%	6.26%
Sentinel-1 1DCNN12 Monthly Averaged	77.54%	62.00%	46.29%	31.34%

Based on the results presented in Table 3.26, the largest estimated area for each target accuracy was obtained using Sentinel-1 monthly averaged 1DCNN12. However, these results should only be viewed as an estimate of the spatial coverage. As illustrated in Figures 3.21 to 3.23, the application of probability thresholding impacts each class differently for each model. Therefore, the coverage at a target accuracy threshold would largely depend on the land cover over that area. With each model and sensor having differing estimated coverage and accuracies for each class, these results indicate that a sensor fusion approach may be an appropriate means of maximising classification coverage and accuracy when classifying a geographical region impacted by frequent cloud cover. However, the use of sensor fusion techniques will be explored further in Chapter 4.

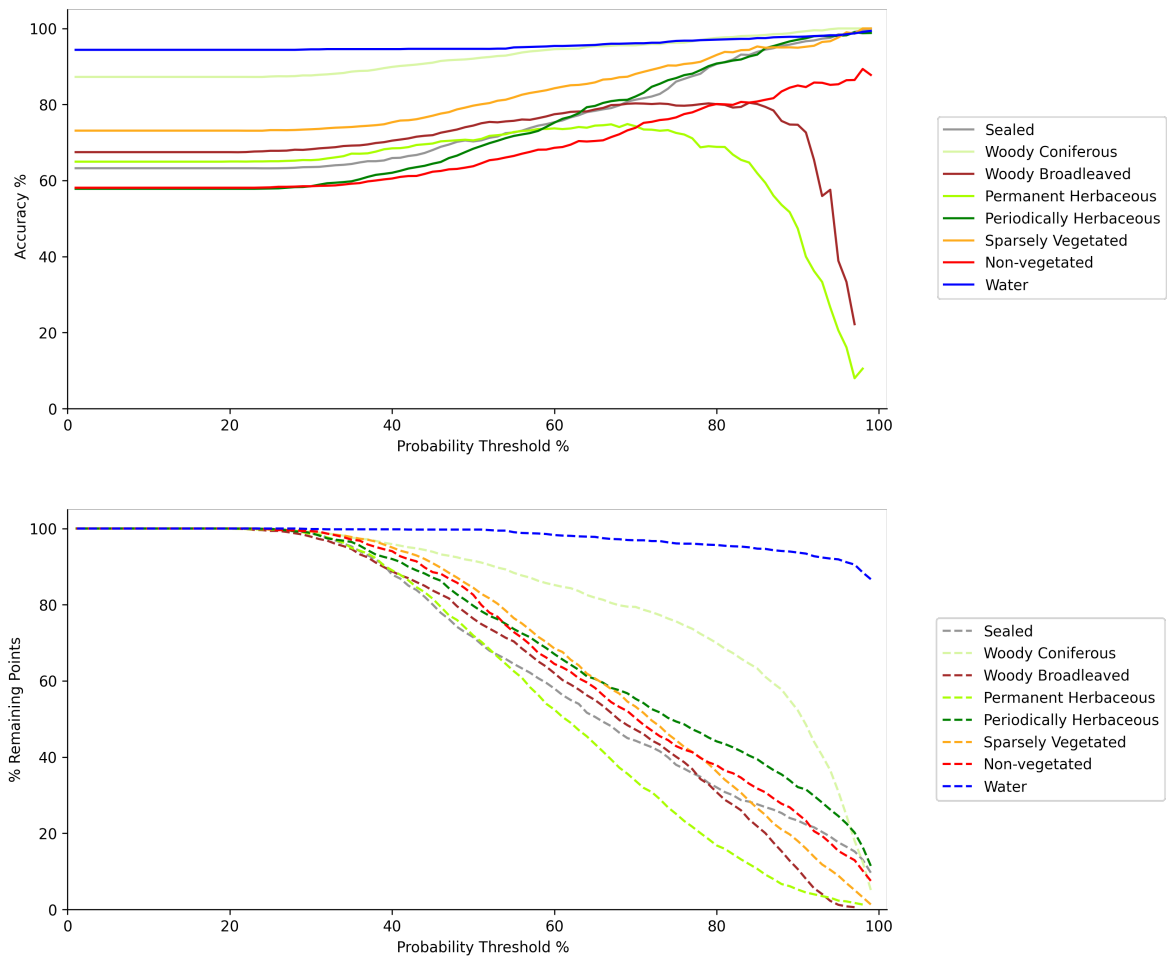


Figure 3.21: Probability threshold vs accuracy and available sample points per class for Sentinel-1 monthly averaged 1DCNN12.

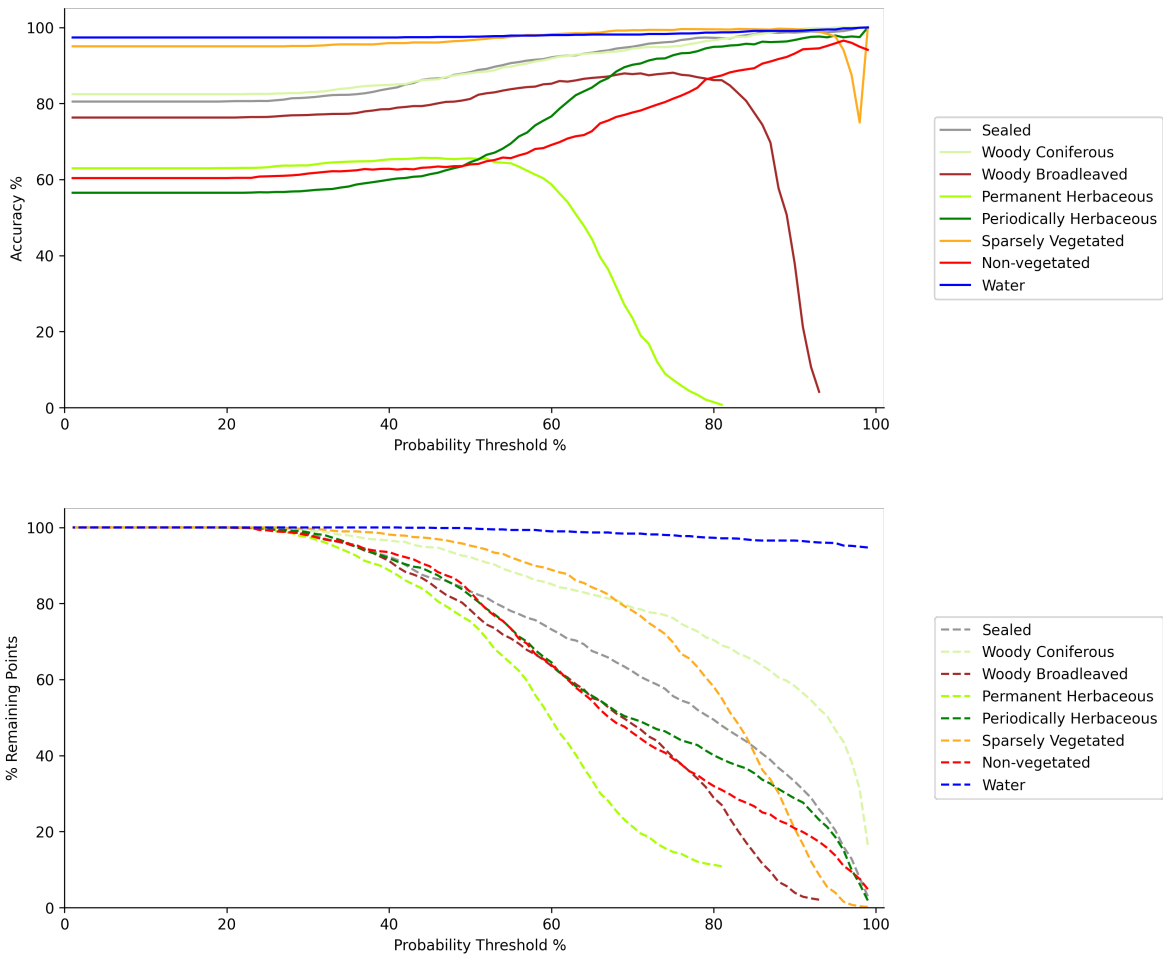


Figure 3.22: Probability threshold vs accuracy and available sample points per class for Sentinel-2 seasonally averaged 3DLFCNN9×9.

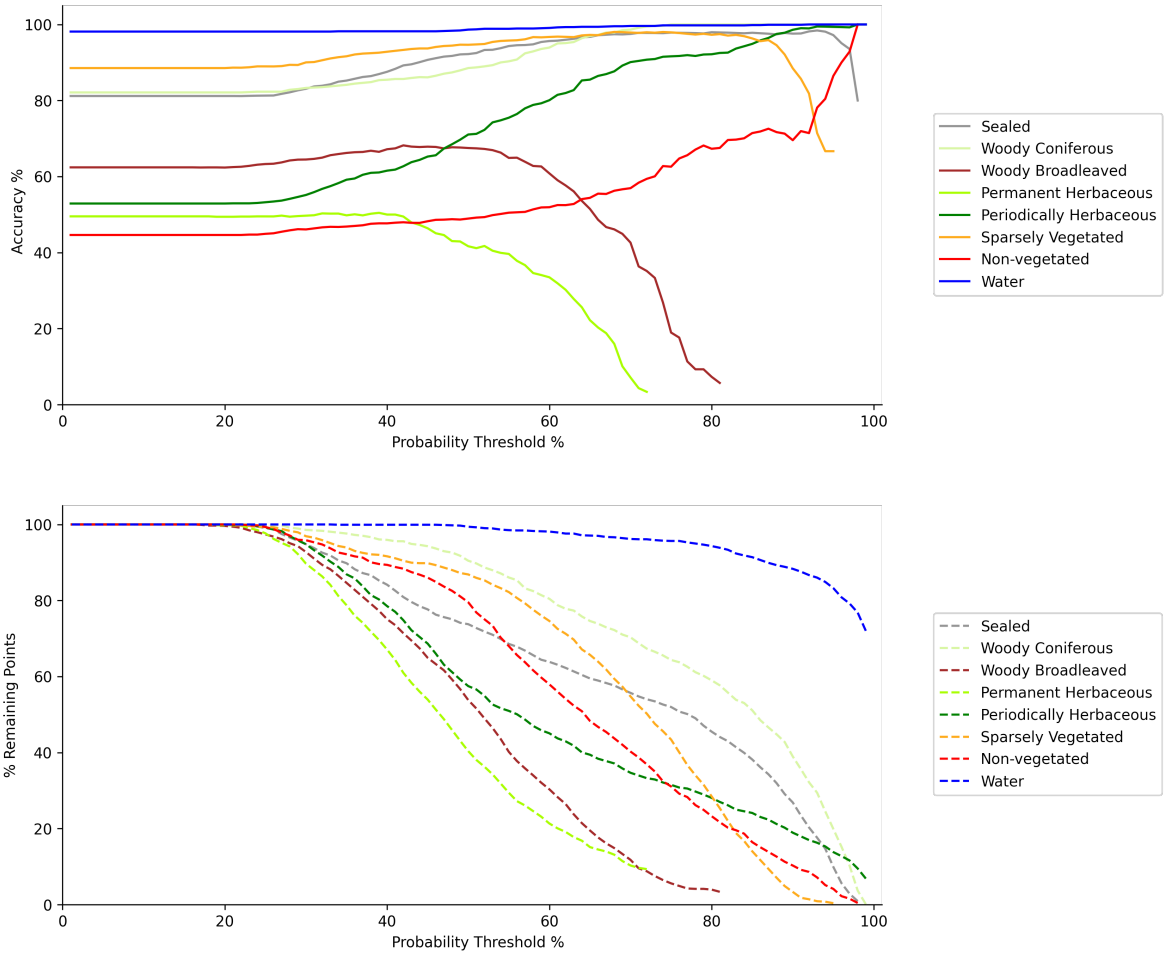


Figure 3.23: Probability threshold vs accuracy and available sample points per class for Landsat-8 half-yearly averaged 3DLFCNN9×9.

Examination of the relationship between probability and per class classification accuracy reveals that the increase in classification accuracy is not proportional among each class. It is also notable that after a given threshold, the accuracy of a class can decrease. For Sentinel-2 seasonally averaged 3DLFCNN9×9 and Landsat-8 half-yearly averaged 3DLFCNN9×9, this phenomenon is most noticeable with the *Permanent Herbaceous* and *Woody Broadleaved* classes. This phenomenon is also visible in the Sentinel-1 monthly averaged 1DCNN12, for the *Sparsely Vegetated* and *Non-vegetated* classes. However, it should be noted that there are fewer sample points available to calculate the overall accuracy at higher thresholds. Therefore, a few misclassified samples disproportionately and negatively impact the classification accuracies.

3.5.2 Impact of Incorporating Temporal Information

The importance of incorporating temporal data became apparent through carrying out this comparative assessment. Increasing the number of temporal splits for each platform resulted in a higher weighted F1 score. Additionally, increasing the number of observations to be averaged improves classification accuracy for the annually-averaged data. Table 3.27 lists the test dataset weighted F1 score with annually averaged data generated using a different number of observations. For each test, the observations to be used as part of the averaging process were randomly selected. The results presented in Table 3.27 were generated from classification using a SVM with annually averaged Sentinel-2 data.

Table 3.27: Results of performing classification using an SVM with annually averaged Sentinel-2 data that has been generated with set numbers of observations.

Observations	Weighted F1	OA
1	0.550	0.560
2	0.626	0.631
3	0.659	0.664
4	0.682	0.685
5	0.694	0.697
6	0.706	0.709

This finding further confirms the requirements set out in the CLC+ technical specifications for a minimum of six satellite observations. Additionally, the impact of observation count on accuracy may provide insight into the reduced accuracy of Landsat-8 models compared to Sentinel-2 models with similarly prepared datasets. It was not possible to apply the minimum observation limit to Landsat-8, as outlined in the methodology, due to the limited number of observations.

3.5.2.1 Temporal Information in Point-based Techniques

The guidelines in the CLC+ technical specifications did not explicitly outline that spatial models such as CNN could not be used for the generation of the Backbone raster product.

However, if the use of spatial models cannot be implemented, a comparison of the point-based techniques using only the spectral-temporal data is required. Table 3.28, lists the highest accuracy Sentinel-2 point-based models from a comparative assessment for each temporal dataset.

Table 3.28: Results of comparative assessment only using point-based ML techniques.

Temporal Preparation	Variables	Model Name	Validation		Test	
			F1	OA	F1	OA
Annually Averaged	Sentinel-2 10m and 20m Bands	SVM	0.696	0.698	0.771	0.773
Half-Yearly Averaged	Sentinel-2 10m and 20m Bands	SVM	0.709	0.710	0.773	0.773
Seasonally Averaged	Sentinel-2 10m and 20m Bands	ANN	0.720	0.721	0.776	0.776
Six Monthly Averaged	Sentinel-2 10m and 20m Bands	1DCNN6	0.755	0.752	0.788	0.786

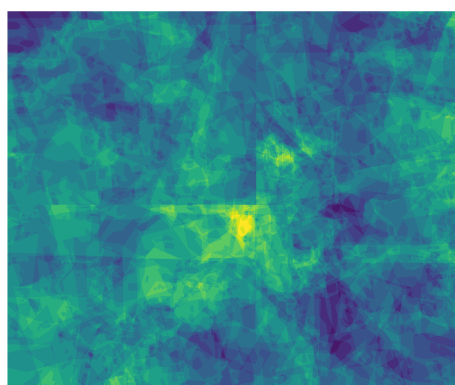
The results of the comparative assessment outline in Table 3.28 convey similar results to the other comparative assessments where models using increased temporal splits have higher classification accuracy. However, one significant difference is that unlike the spatial models, where the best model was obtained with the use of seasonally averaged data, with point-based models, the best models were obtained using six monthly averaged data. Therefore, if the requirements prohibit the use of spatial models such as LFCNN, the application of 1DCNN6 using six monthly averaged data would be recommended for generating LCC datasets. However, as outlined in Table 3.20, the coverage of the six monthly averaged data is very limited and is impacted by the issue of cloud cover.

An additional observation of this comparative assessment is that for each temporal dataset, the application of RF was outperformed by other techniques such as SVM, ANN and 1DCNN. This result contrasts with results obtained in studies by Breiman (2001) and Zafari et al. (2019) that observed better classification results using RF over other point-based techniques. However, overall it was observed the choice of point-based technique had only a minor impact on the results in comparison to the changes in temporal data preparation.

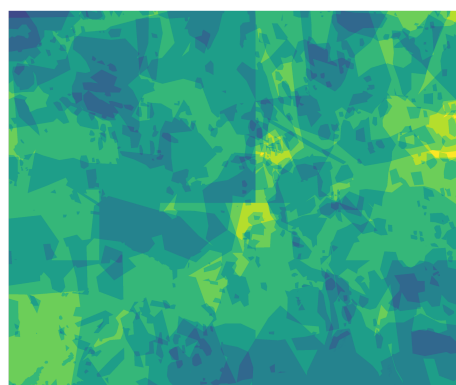
The observation that classification accuracy improves with an increased number of satellite observations in a temporal average and with higher temporal delineation through an increased number of temporal splits is consistent with results obtained by Carrasco et al. (2019). However, this observation is in contradiction with the fact that the highest accuracy model trained during this assessment was a 3DLFCNN 9×9 model trained with seasonally averaged Sentinel-2 10m and 20m band data. While attempts were made to train 3DLFCNN 9×9 models using the six-monthly Sentinel-2 data, this process was largely unsuccessful. One possible reason for this issue is the number of trainable variables in the models. For example, 3DLFCNN 9×9 architectures designed for the six-monthly averaged Sentinel-2 10m and 20m band data had 486,488 trainable parameters. In comparison, the equivalent 3DLFCNN 9×9 model for seasonally averaged Sentinel-2 10m and 20m band data use over 3.5 times fewer trainable parameters at 137,628. Additionally, the 1DCNN6 for six-monthly averaged Sentinel-2 10m and 20m band data has just 83,368 trainable parameters. This issue highlights the challenge of including both spatial and high temporal information into a model.

3.5.2.2 Monthly Observation Requirement

While not explicitly stated in the technical specifications, there are some references in the technical specifications that suggest a requirement for a minimum of ‘six months with observations’ rather than a minimum of six total observations. The application of this increased requirement would significantly reduce the coverage of each dataset. Figure 3.24 provides an illustrative example of the difference in coverage between a requirement of six observations vs a requirement of six months of observations. Tables 3.29 and 3.30 detail the difference in coverage based on each criteria.



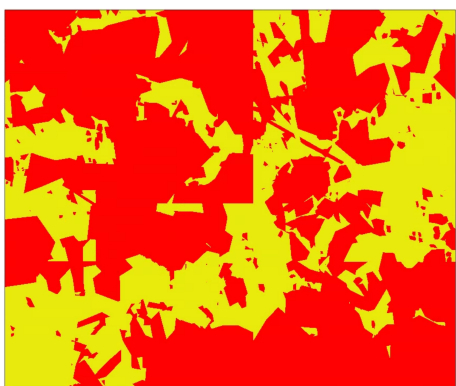
(a) Total Observation Count



(b) Count of Months with Observations



(c) Threshold by Six Total Observations



(d) Threshold by Six Months with Observations

Figure 3.24: Illustrative examples of the coverage with the requirement of a) and c) six observations and b) and d) six months of observations over the Galway region.

Table 3.29: Model coverage for each platform and temporal dataset calculated by a requirement for a total of six observations as set out in Table 3.13.

	Annually Averaged	Half-Yearly Averaged	Seasonally Averaged
Sentinel-2	97.55%	76.81%	81.36%
Landsat-8	36.19%	19.02%	9.90%
Combined Sentinel-2 and Landsat-8	99.68%	89.16%	91.13%

Table 3.30: Model coverage for each platform and temporal dataset calculated by a requirement for six months with observations.

	Annually Averaged	Half-Yearly Averaged	Seasonally Averaged
Sentinel-2	72.11%	37.43%	46.81%
Landsat-8	19.35%	11.85%	6.74%
Combined Sentinel-2 and Landsat-8	85.31%	59.49%	62.23%

As outlined in Tables 3.29 and 3.30, the application of a requirement for six months with observations significantly reduces the coverage of each dataset. The six-monthly averaged dataset was not included in this comparison as, by default, the dataset meets the ‘six months with observations’ requirement. Some months have a greater number of observations proportionally due to seasonal variation in cloud cover. Therefore, the requirement for a minimum of six months with observations would aid in ensuring a greater temporal distribution of observations used for LCC. However, the reduced coverage as a result of this requirement would prevent the classification of significant areas of the assessed regions. Additionally, reducing the coverage of each model can significantly reduce the number of labels available to train a model, which has been identified as a significant challenge such as with the training of the 3DLFCNN architecture with six-monthly averaged data.

3.5.3 Impact of Incorporating Spatial Information

As part of this comparative assessment, it was observed that the inclusion of spatial information in the form of patch-to-point models could improve classification accuracies

relative to the results of point-based techniques. The LFCNN 9×9 and 3DLFCNN 9×9 architectures, in particular, obtained the best results for both Landsat-8 and Sentinel-2. During exploratory analysis for the design of the LFCNN and 3DLFCNN architectures, there was a reduction in classification accuracy for models with greater than six convolutional layers. Additionally, the inclusion of a high percentage dropout layers appeared to aid both the model training and overall classification accuracies. Through this assessment, a number of models were trained to utilise data with different spatial resolutions. All Sentinel-2 models using the 10m and 20m bands combined resulted in higher classification accuracies than with the 10m bands on their own. For some point based techniques, the inclusion of the 60m bands resulted in minor improvement. An example of improved classification as a result of including the 60m bands can be seen with the application of an RF model using annually-averaged Sentinel-2 data. When trained with all bands, the model obtained a test weighted F1 score of 0.672. However, when trained with only the 10m and 20m bands, the model obtained a test weighted F1 score of 0.670. However, for all patch-to-point based techniques, the inclusion of the 60m bands resulted in a reduction in classification accuracies. With a resolution of 30m and with a target prediction resolution of 10m, the difference in spatial resolution is likely a contributing factor to the reduced accuracy of Landsat-8 models relative to comparable Sentinel-2 models.

3.5.3.1 Inference times of LFCNN and 3DLFCNN architectures

One benefit of the LFCNN and 3DLFCNN architectures is that they can be trained on point data but still, be used to output patch images without modification to the model architecture. As a result of their design, the LFCNN and 3DLFCNN are faster at the classification of large raster images relative to the point models. Table 3.31, displays the difference in inference time between the LFCNN 9×9 and 3DLFCNN 9×9 architectures and point based architectures for the prediction of a 2000×2000 raster tile from Sentinel-2 10m and 20m bands data. In this comparison, the SVM and ANN architectures were chosen for the annually-averaged and seasonally averaged point-based models respectively as they were the best performing point-based models identified in the comparative assessment

for their respective temporal datasets. CPU inference times were calculated using an AMD Ryzen 9 5900X 12 Core Processor and GPU inference times were calculated using an NVIDIA RTX 3080.

Table 3.31: Comparison of model inference times for point-based and patch to point LFCNN based ML techniques.

Temporal Data Type	Model	Inference Time (Seconds)	
		CPU	GPU
Annually Averaged	SVM	288.16	N/A
	LFCNN9×9	0.99	0.28
Seasonally Averaged	ANN	39.77	65.17
	3DLFCNN9×9	2.99	0.80

As displayed in Table 3.31, the application of the LFCNN9×9 and 3DLFCNN9×9 models were faster than either point-based technique. The slowest model was the SVM taking over four minutes to generate a prediction. While the use of a GPU reduced the inference time for the LFCNN9×9 and 3DLFCNN9×9 architectures, its use with the ANN models increased the inference time. As training LFCNN and 3DLFCNN architecture require the generation of patch input data, the preparation of data to train the models can take considerably more time to generate than for point models.

The results presented in Table 3.14 outlined that similar classification accuracy can be obtained by the application of both an SVM and LFCNN9×9 model using annually averaged Sentinel-2 data. Therefore, where inference time is important, the application of the LFCNN9×9 architecture would be recommended. However, if inference time is not a consideration, the application of an SVM may be more appropriate for use with annually averaged Sentinel-2 data due to the simpler data preparation workflow of point data over patch-to-point training datasets.

A preliminary assessment of the use of patch-to-patch based techniques was examined through the application of the UNET architecture. UNET is a fully convolutional neural network first proposed by Ronneberger et al. (2015). Figure 3.25 illustrates the structure of the UNET architecture as proposed by Ronneberger et al. (2015). A notable feature of the UNET architecture is the 1x1 convolutional skip connectors that are intended to ensure spatial delineation is maintained in the output segmentation map. As a patch-

to-patch based technique, this model requires fully labelled patches to train the model. The architecture proposed by Ronneberger et al. (2015), outputs a 388×388 label patch. However, this represents a 3.88km^2 area for Sentinel-2 10m resolution data. In ideal conditions where the proposed regions had 100% label coverage, this would result in an estimated 2404 possible unique labels. This is reduced to 267 possible unique labels for the 30m Landsat-8 imagery. With this in mind, modified UNET architectures were examined with much smaller input and output data sizes. However, with models requiring 20×20 patch labels for training, it was still not possible to generate sufficient labels with balanced label classes. As a patch-to-patch based technique, this model requires fully labelled patches to train the model. The architecture proposed by Ronneberger et al. (2015), outputs a 388×388 label patch. However, this represents a 3.88km^2 area for Sentinel-2 10m resolution data. In ideal conditions where the proposed regions had 100% label coverage, this would result in an estimated 2404 possible unique labels. This is reduced to 267 possible unique labels for the 30m Landsat-8 imagery. With this in mind, modified UNET architectures were examined with much smaller input and output data sizes. However, with models requiring 20×20 patch labels for training, it was still not possible to generate sufficient labels with balanced label classes.

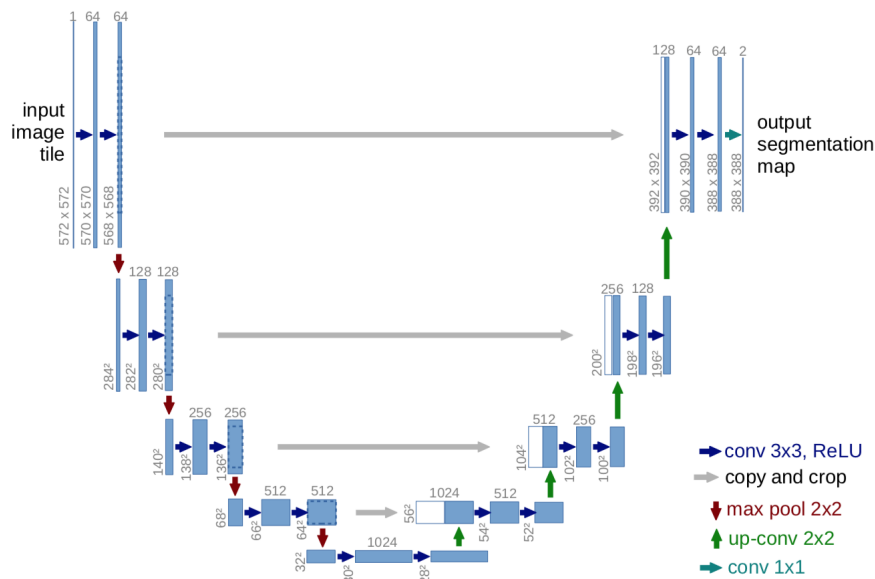
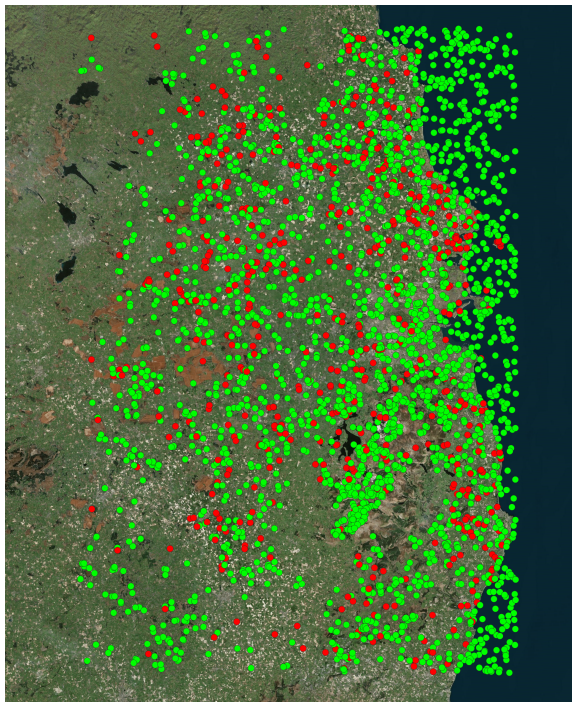


Figure 3.25: Illustrate example of the UNET architecture as proposed by Ronneberger et al. (2015).

3.5.4 Assessing the spatial relationship of classification results

EO data is inherently spatial, so it is important to consider and identify any spatial relationship or autocorrelation that may be present in the data and classification results. However, the nature of the data used in this assessment makes the identification of such properties challenging. For example, the number of observations used for performing classification impacts classification accuracy as detailed in Table 3.27. Additionally, the ability to apply a given model is dependent on the availability of input data. Consequently, the ability to apply high-accuracy models varies across and between regions as outlined in Section 3.4.4. Therefore, the spatial distribution factors that can impact the frequency of cloud cover over a region and, thus, the ability of optical satellite data can impact classification accuracy. These factors could include proximity to the coastline or mountainous regions. A visual assessment of the location of each correctly classified and misclassified test sample point for the best-performing models was performed to examine the spatial relationship of the classification results. Figure 3.26 displays the location of the correct and misclassified point locations for the test datasets for the Sentinel-2 seasonally averaged 3DLFCNN 9×9 , the Sentinel-1 monthly averaged 1DCNN12, and the Landsat-8 half-yearly averaged 3DLFCNN 9×9 models. A notable observation when comparing each image is the large areas of unclassified points visible in the Sentinel-2 seasonally averaged 3DLFCNN 9×9 and the Landsat-8 half-yearly averaged 3DLFCNN 9×9 models. The missing sample points in these areas are a result of insufficient observations to perform classification. This phenomenon appears particularly pronounced over the Wicklow mountains region in the South-East of the assessment area. Other areas where there are comparatively few observation points in each image are due to limited labelled data in those areas. There are also notable clusters of sample points which is a result of label data distribution and the sample point balancing methodology utilised in this assessment as outlined in Section 3.3.1.1. There is no visible pattern in the distribution of misclassified data. However, with an uneven spatial distribution of land cover classes over the assessed area, it is expected that a higher number of misclassified points will occur in a region where there are a larger proportion of classes that the model has low

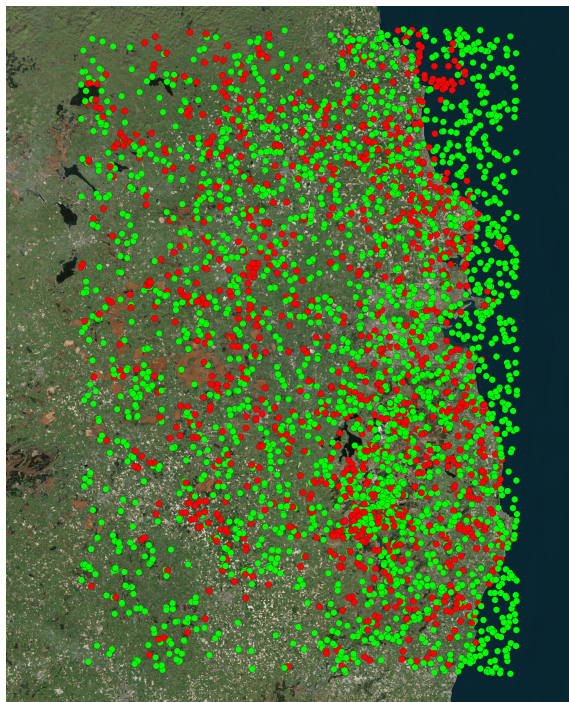
classification accuracy.



(a) Sentinel-2 seasonally averaged 3DLFCNN9×9



(b) Landsat-8 half-yearly Averaged 3DLFCNN9×9



(c) Sentinel-1 monthly averaged 1DCNN12

Figure 3.26: Illustration of correctly classified sample points (Green) and misclassified points (Red) from the Dublin test datasets for (a) Sentinel-2 seasonally averaged 3DLFCNN9×9 (b) Landsat-8 half-yearly averaged 3DLFCNN9×9 (c) Sentinel-1 monthly averaged 1DCNN12

3.5.5 Data Quality

As observed by Zhou et al. (2020) when undertaking LCC using ML techniques, the quality of the data used is as important as the ML techniques used. For this reason, it was essential to evaluate the quality of the data used when training ML models.

3.5.5.1 Label Data Quality

One of the most significant issues encountered when performing this assessment was the acquisition of sufficient high-quality labelled data to perform a reliable comparison of each ML technique. However, potential errors were observed while undertaking a visual inspection of the Copernicus Urban Atlas and the Copernicus Coastal Zones datasets. Figure 3.27, illustrates an example of poor class boundaries in the Copernicus Urban Atlas dataset with a field of Arable crops partially defined as Pastures. This observation coincides with the Copernicus Urban Atlas 2018 Validation Report. In the report, using a ‘blind validation’ approach, an OA of 68.48% was recorded (Wegscheider et al., 2021). The report identifies that this error was not consistent amongst all classes, with an accuracy of 82.14% for urban classes and an accuracy of 66.48% for rural classes. However, it is identified in the report that the blind validation approach can underestimate the accuracy of some classes. An alternative method for assessing accuracy referred to as the ‘positional accuracy’ approach, calculated higher accuracies of 93.61% and 86.64% for urban and rural classes, respectively. In comparison, for the Copernicus Coastal Zones dataset, an OA of 98.24% and 97.70% was calculated for the blind and positional accuracies respectively (Zotti and Mantia, 2021). Given the potential source of error that can be incorporated into the label dataset, the choice of data is important. However, by limiting that choice of label data to locations where high-accuracy labels can be guaranteed, other issues may arise. In the case of the dataset used in the assessment, by excluding any rural classes in the Copernicus Urban Atlas dataset, the classification of any rural classes would be predominantly based on the Copernicus Coastal Zones dataset. As a result, the model would be trained and validated in a near-coastal environment making it unsuitable for inland classification where the characteristics of the classes may differ.

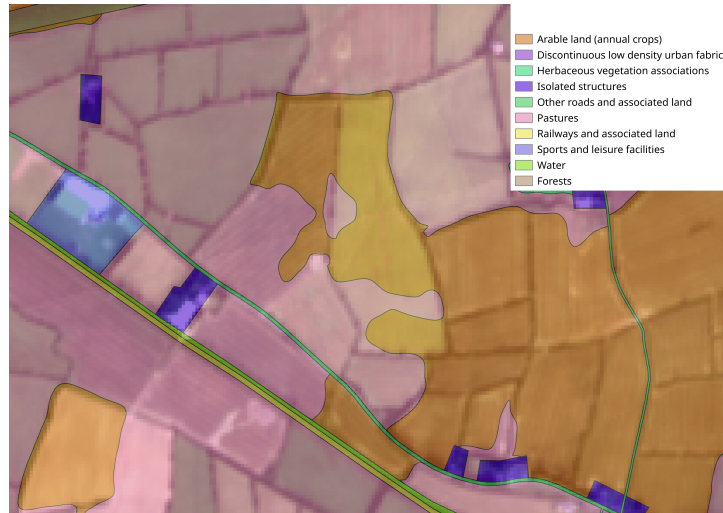


Figure 3.27: Example of poor Copernicus Urban Atlas classification with annual averaged Sentinel 2A&B imagery as a base map.

Examination of the confusion matrices in Figures 3.13 to 3.15, revealed that the *Periodically Herbaceous* and *Permanent Herbaceous* classes exhibited a high degree of confusion. Poor labelling, such as illustrated in Figure 3.27, may be a possible source for this confusion. This issue not only impacts the model during training but also impacts the calculated accuracy results. As is visible in Figure 3.28, the aggregated labels inherited the error from the Copernicus Urban Atlas dataset. In contrast, a 3DLFCNN using seasonally averaged Sentinel-2 data appears to classify a greater proportion of the area correctly. However, if the model was evaluated over this area, a significant proportion of the area would be identified as misclassified. Therefore, the trained models may have a higher classification accuracy than is calculated from the labelled data. However, it is difficult to fully determine the validity of this assertion without a redefinition of the label data. A potential means of maximising the benefit of such datasets is to employ a multistep training approach. Under this approach, a model could be initially trained on the larger volume, but lower accuracy labelled data. Secondary training/model refinement and accuracy validation could then be undertaken on the higher-accuracy label datasets. This approach to model training could mitigate some of the issues identified in this section. However, further investigation beyond the scope of this assessment would be required to determine the accuracy of this approach and if this approach is prone to overfitting to the higher accuracy labels used in the second phase of training.

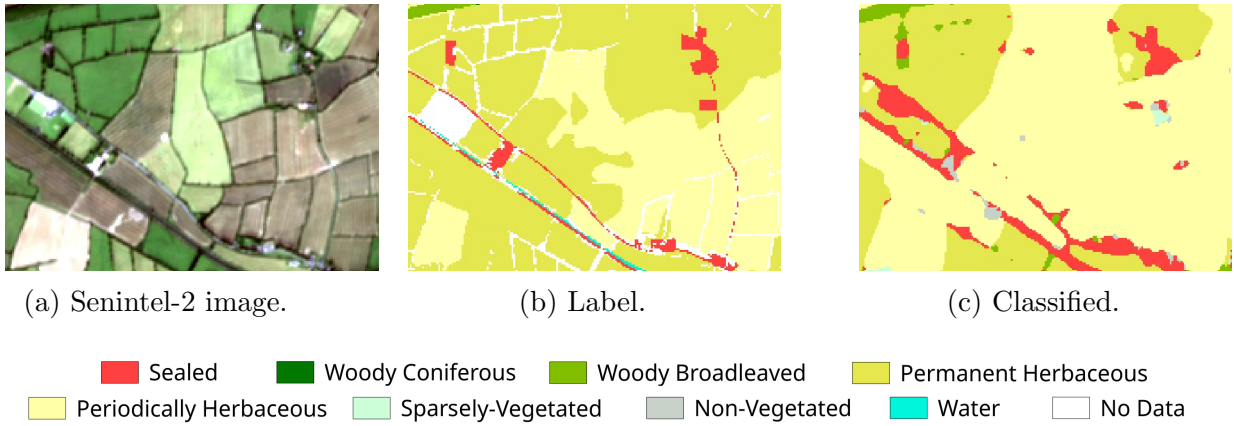


Figure 3.28: Comparison of seasonally averaged Sentinel-2 3DLFCNN9×9 classification to a mislabelled area.

Various other sources of labelled data were examined as potential data sources for this study, including Open Street Maps (OSM), LUCAS and Prime2. Of these alternative datasets, the LUCAS 2018 dataset was the most viable dataset. However, this dataset does not contain a class that would represent the *Sparsely Vegetated* class and therefore could not be used as a complete label dataset. Additionally, sampled in a 2km² grid, there were insufficient sample locations for each class in the assessed regions to train and validate the accuracy of each model.

3.5.5.2 Cloud Cover

While the increase in temporal splits increased classification accuracy, it also reduced the available region where the models could be applied. The models with the highest accuracy were obtained using Sentinel-2 seasonally averaged data. However, these models only have 80.87% coverage. If a harmonised product was generated between the Landsat-8 and Sentinel-2, this coverage could be increased to 90.48%. With results obtained from Sentinel-2 data outperforming those obtained from Landsat-8, it would be advised to harmonise the Landsat-8 data spatially and spectrally to Sentinel-2. However, as identified in Chapter 2, the harmonisation process can introduce errors into the harmonised data that may negatively impact classification accuracy.

For this assessment, cloud masks were manually digitised in QGIS, using the existing cloud masks provided with the data as a reference. The cloud mask provided as part of

the Sentinel-2 L2A is generated using the Sen2COR algorithm (Clerc et al., 2022). As apparent in Figure 3.29, the cloud mask provided as part of the Sentinel-2 L2A product underestimates the cloud coverage. In addition, these cloud masks do not cover cloud shadow, which can also negatively impact the recorded spectral information. The miss identification of the cloud and cloud shadow can be a significant source of error in EO derived analysis (Misra et al., 2020).

A comparative assessment of cloud and cloud shadow detection algorithms for Sentinel-2 imagery was conducted by Tarrío et al. (2020). Their study identified the highest cloud classification OA of 85.1% was obtained from LaSRC algorithm. In the study, Sen2Cor and LaSRC frequently failed to identify cloud shadows. Other assessed techniques were observed to overestimate cloud cover. For these reasons, manual digitisation was performed to ensure that any factors that would negatively impact the results were removed. However, the emphasis on spectral quality may have resulted in an underestimation of the coverage of the models.

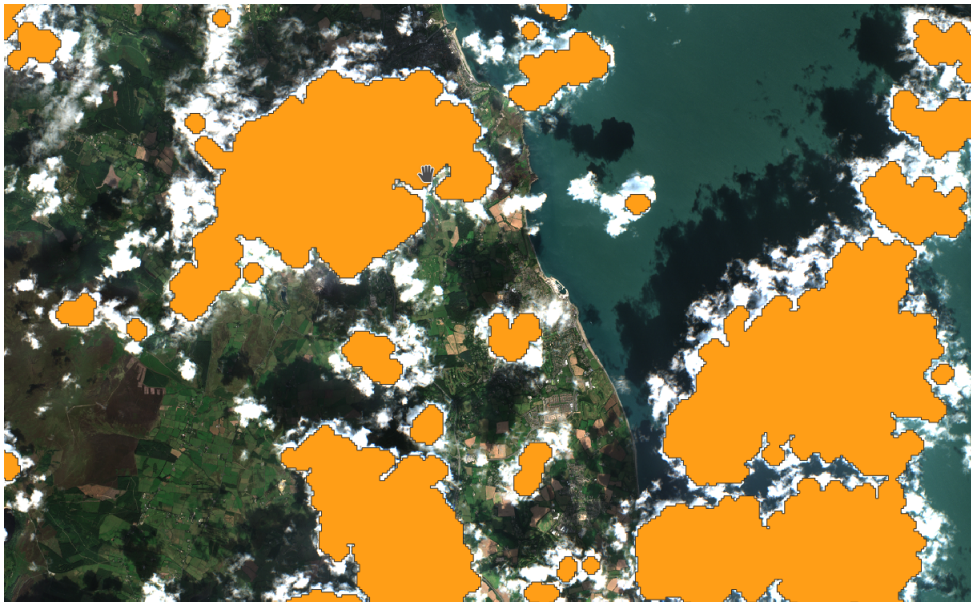


Figure 3.29: Sentinel-2 true colour image over Greystones with cloud mask (orange) from ‘MSK_CLOUDS_B00.gml’ file.

3.5.5.3 Image Co-registration

For this study, additional co-registration of images was not performed as part of the data processing workflow. With significant cloud cover in a number of scenes, it was decided not to perform co-registration as it would have been challenging to detect sufficient features for accurate co-registration of each image. Additionally, as per the CLC+ technical specification, the required positional accuracy should be equal to the Sentinel-2 positional accuracy with no mention of the requirement of additional co-registration (Kleeschulte et al., 2019). Visual inspection of the images also revealed that additional co-registration was not required. Figure 3.30, illustrates the quality of co-registration by comparing field and road boundaries of a single image to an annually-averaged image using up to 16 different images captured over a year.



Figure 3.30: Comparison of Sentinel-2A captured 2018-07-02 (left), Annually averaged Sentinel-2A&B imagery (right) over Maynooth.

3.5.5.4 Exclusion of Shrub Class

As part of this comparative assessment, the *Wood shrubs/bushes* class was excluded due to poor classification accuracies. Figure 3.31, displays the confusion matrix for a Sentinel-2 seasonally averaged SVM model trained on labelled data that included a *Wood shrubs/bushes* class. The *Wood shrubs/bushes* class was defined using the High-res Small woody 2015 dataset and *Heathland and Scrub*, *Lines of Trees and Scrub* and *Transitional Woodland and Scrub* features in the Copernicus Zones dataset for this preliminary assess-

ment. The *Wood shrubs/bushes* class has the lowest classification accuracy of each model, as is evident in the confusion matrix. Additionally, its inclusion reduces the accuracy of a number of other classes.



Figure 3.31: Confusion matrix for Sentinel-2 seasonally averaged SVM including the *Wood shrubs/bushes* class.

3.6 Conclusion

The results of the comparative assessment undertaken in this chapter demonstrate that the most accurate classification results could be obtained using 3DLFCNN9×9 with seasonally averaged Sentinel-2 10m and 20m bands. The proposed LFCNN and 3DLFCNN architectures were demonstrated as effective means of including spatial information with

the models capable of being trained on point data. These models can then be used to classify large raster images faster than other assessed point-based techniques. The inclusion of both spatial and temporal information were identified as significant to ensure high accuracy LCC. Models incorporating spatial information such as LFCNN or LCNN were observed to be particularly important for Landsat-8 and Sentinel-2. However, it could not be utilised with Sentinel-1 data. The inclusion of temporal information was observed to increase the accuracy of each model. The use of the 1DCNN was particularly useful at classifying data with many observation dates, such as with Sentinel-1 monthly averaged data. However, this study highlighted the challenges when performing classification in regions with frequent cloud cover. In particular, two issues were identified when attempting to interpret the results of the comparative assessment. The first issue arises from the limited number of common sample point locations available to each model. The *Sparseley Vegetated* class is the class that is most significantly impacted by this issue resulting in a limited number of test sample point locations by which to assess each model's accuracy. The second issue is that certain models obtain higher classification accuracy in the test datasets than the training and validation dataset. This phenomenon was found to occur more frequently with temporal models where there were fewer test sample points available and therefore may provide misleading results. Therefore, to determine the most suitable techniques, it was essential to examine the training, validation and test dataset results.

By implementing the coverage assessment, it was found that increasing the temporal splits of the data reduces the regions that a given model can be applied to. However, as demonstrated through both the comparative assessment and assessment on the impact of observation count, the inclusion of temporal data is essential to ensure high classification accuracy.

An examination of the relationship between probability threshold and accuracy revealed that by applying a probability threshold, each model could obtain a desired target accuracy. However, this same process significantly reduces the coverage of each model. Based on these results, a model fusion or sensor fusion approach may be a better suited

methodology of maximising coverage while ensuring high classification accuracy, especially in regions affected by frequent cloud cover. A more detailed examination of the benefits of applying a model fusion approach to improve classification accuracy and coverage is examined in Chapter 4.

In summary, this chapter provided the following contributions:

1. LFCNN and 3DLFCNN architectures were proposed as a methodology for a spatial model that can be trained on point data and used for fast inference over a large area. An in-depth comparative assessment of ML techniques was undertaken, with the best results achieved using seasonally averaged Sentinel-2 3DLFCNN 9×9 obtaining a weighted F1 and OA of 0.823 and 0.819, respectively, in a cross-platform comparative assessment.
2. The challenges associated with undertaking a comparative assessment in a region with frequent cloud cover were identified. The model coverage assessment revealed that 100% model coverage could not be obtained using any of the Sentinel-2 or Landsat-8 models with a requirement for a minimum of six observations. The implementation of a fusion-based LCC technique was identified as a potential means of overcoming some of these issues.

Chapter 4

Satellite Sensor Fusion LCC

4.1 Introduction

This chapter explores the potential of implementing multi-sensor fusion techniques in improving LCC accuracy using EO data. In particular, this detailed examination investigates how the application of a decision-level fusion approach can be used as an effective means for sensor fusion where data availability varies across the assessed regions. In Chapter 3, an in-depth comparative assessment of ML techniques for EO derived LCC was conducted for the island of Ireland. This assessment was performed using data from three satellite platforms, Sentinel-1, Sentinel-2 and Landsat-8. Through this comparative assessment it was found that high-accuracy multi-temporal optical satellite models could not be utilised across all areas of the assessed regions, due to the frequent cloud cover. As a result, the area in which these high-accuracy multi-temporal models could be applied was limited.

This chapter will examine whether or not the integration of data from multiple sensors, termed *sensor fusion*, can overcome the limitation observed when performing LCC using a single sensor. The assessment of sensor fusion techniques undertaken in this chapter will be explored in two stages. The first stage will be a comparative assessment between pixel-level fusion and decision-level fusion approaches. This comparative assessment will examine how each fusion approach can be used to improve LCC accuracy and will be undertaken in **Section 4.2**. Following this comparative assessment between

fusion approaches, the second stage, detailed in **Section 4.3**, will examine sensor fusion techniques suitable for the fusion of datasets where data from one or more satellite platforms may not be available over part of the assessed region.

4.2 Sensor Fusion Comparative Assessment

Sensor fusion techniques using image data can be categorised into three broad categories; pixel-level fusion, feature-level fusion and decision-level fusion (Chang and Bai, 2018; Useya and Chen, 2018; Mahyoubia et al., 2019). This comparative assessment was undertaken using two of these techniques; pixel-level fusion and decision-level fusion. In pixel-level fusion, data from each source is combined into a single image dataset. This combined dataset is then used as the input variables to train a model. Decision-level fusion on the other hand, involves the independent classification of data from each platform. The output of this classification process is then combined and used for further analysis (Zhang, 2010). Figure 4.1, provides an illustration of the workflow when implementing both pixel-level and decision-level fusion.

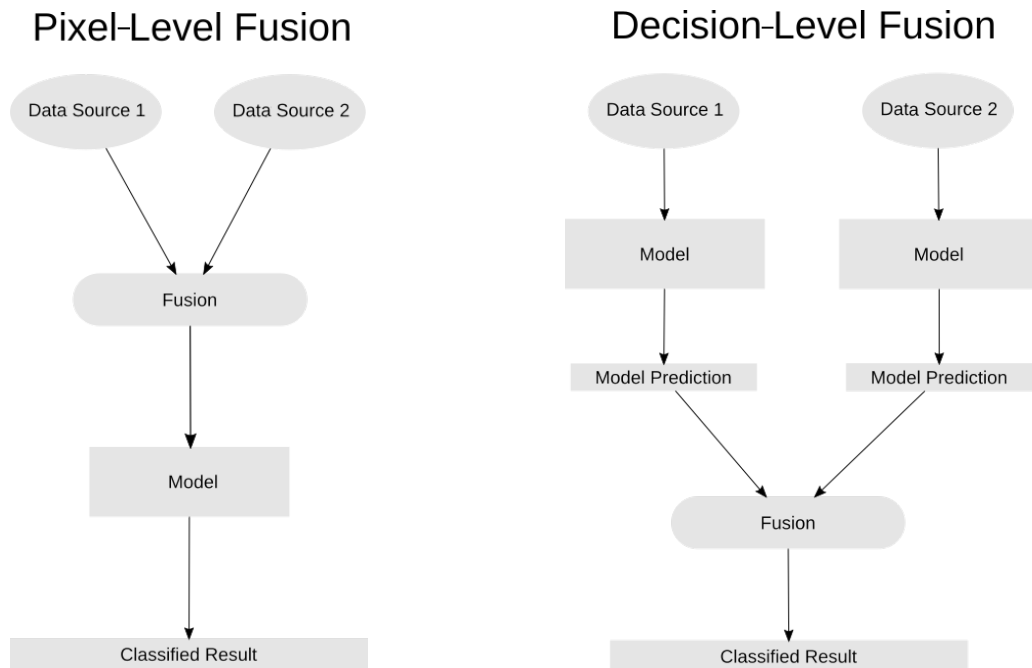


Figure 4.1: Illustration of a pixel-level and decision-level fusion workflows.

The third category of sensor fusion is feature-level fusion. In a feature-level fusion approach, feature objects are extracted from each data source into a common format. These features can be extracted as segmented objects derived from one or more of the data sources or through the conversion of each data source into a common feature space. These features can either be extracted as part of a preprocessing step and used as input data for a ML model or they can be extracted within the model structure itself (Zhang, 2010). As outlined in Chapter 2, object-based feature-level fusion techniques are not suitable for the generation of the CLC+ Backbone raster product. Feature-level fusion techniques where the features are extracted within the model's structure will also be excluded from this comparative assessment as these fusion techniques require the design of specific ML architectures for each of the sensor data combinations. Therefore in a scenario where the available data varies across the application of such an approach may be impractical.

4.2.1 Pixel-Level Fusion

The satellite data prepared as part of the comparative assessment undertaken in Chapter 3 was used to evaluate the pixel-level fusion techniques assessed in this chapter. In Chapter 3, the satellite data from three platforms; Sentinel-1, Sentinel-2 and Landsat-8 were grouped into four temporally aggregated datasets; annually averaged, half-yearly averaged, seasonally averaged, and monthly averaged. Eight combinations of the data were prepared from the three available platforms. Table 4.1 lists the datasets used for pixel-level fusion as part of this assessment. As highlighted in Chapter 3, there were insufficient observations for the inclusion of seasonally averaged and monthly averaged Landsat-8 data. Additionally, the seasonally averaged Sentinel-2 and Sentinel-1 data used in this assessment for pixel-level fusion will not include data from the winter season due to limited data availability. For the six monthly averaged datasets, the six months selected for this dataset are April, May, June, July, September and October. The ML techniques applied to the pixel-level fused datasets are listed in Table 4.2. The details of each ML technique have been outlined in Chapter 3.

Table 4.1: Datasets to be tested with pixel-level fusion techniques.

Platforms Names	Temporal Data Preparation
Sentinel-2 and Landsat-8	Annually Averaged
Sentinel-2, Landsat-8 and Sentinel-1	Annually Averaged
Sentinel-2 and Sentinel-1	Annually Averaged
Sentinel-2 and Landsat-8	Half-yearly Averaged
Sentinel-2, Landsat-8 and Sentinel-1	Half-yearly Averaged
Sentinel-2 and Sentinel-1	Half-yearly Averaged
Sentinel-2 and Sentinel-1	Seasonally Averaged
Sentinel-2 and Sentinel-1	Six Monthly Averaged

Table 4.2: ML techniques to be assessed for use with pixel-level fused satellite data.

Technique	Abbreviation
Random Forest	RF
Support Vector Machine	SVM
Artificial Neural Network	ANN
Recurrent Neural Network with Long-Short Term Memory	LSTM
Light Convolutional Neural Network	LCNN
Light Fully Convolutional Neural Network	LFCNN9×9
1D Convolutional Neural Network	1DNN6
3D Light Fully Convolutional Neural Network	3DLFCNN9×9

4.2.2 Decision-Level Fusion

The first stage in decision-level fusion comprises the independent classification of data from each platform. The models used to classify data from each independent platform will be referred to as *prior models*, and the associated output will be referred to as *prior classification* for the predictor of a single class or *prior probability* for the predicted probability of each class. The prior models to be used as part of the assessment are listed in Table 4.3. Each prior model will be given a simplified acronym for this assessment to aid in interpreting the results.

Table 4.3: List of mono-platform satellite models (prior models) to be used for decision-level fusion.

Platform	Model	Acronym
Sentinel-2	Annually Averaged 10m and 20m bands 3DLFCNN9×9	S2AN
Sentinel-2	Half-Yearly Averaged 10m and 20m bands 3DLFCNN9×9	S2HY
Sentinel-2	Seasonally Averaged 10m and 20m bands 3DLFCNN9×9	S2SE
Sentinel-2	Six Monthly Averaged 10m and 20m bands 1DCNN6	S2MO
Landsat-8	Annually Averaged All Bands LFCNN9×9	L8AN
Landsat-8	Half-Yearly Averaged All Bands 3DLFCNN9×9	L8HY
Sentinel-1	Monthly Averaged All Bands 1DCNN12	S1MO

An SVM will be employed to perform decision-level fusion combining the prior predicted probability from mono-platform models as input variables, providing a single fused category as output. Preliminary experimentation using alternative methods of decision-level fusion were examined, such as the use of ‘Weighted Majority Voting’, the use of ML techniques such as ANN, SVM and RF and by employing ‘Bayesian fusion’ techniques

through the application of prior probability averaging and maximum prior probability selection. The results of this preliminary analysis are presented in Appendix C.1.2.1. The results of the preliminary assessment revealed that the application of prior probability averaging and fusion using an SVM obtained the best results. While both techniques obtained similar results, the use of an SVM model was selected for this comparative assessment. While prior probability averaging obtained comparable results, SVM was selected for this comparative assessment as it formed the basis of multiple fusion techniques that will be examined in Section 4.3 of this Chapter.

4.2.3 Evaluation Process

As identified in Chapter 3, Section 3.3.3.3, an examination of the data revealed differences in the number of label points available to evaluate each model. This is further exacerbated when applying sensor fusion techniques. A preliminary evaluation of the results of performing sensor fusion was undertaken. In this preliminary evaluation for each fused model, the difference in weighted F1 and OA was calculated relative to mono-sensor models trained in Chapter 3. For each pixel-level fused model, the change in weighted F1 and OA was calculated relative to the best mono-sensor model prepared using the same temporally prepared dataset. For the decision-level fusion models, the change in weighted F1 and OA was calculated relative to the highest accuracy Sentinel-2 prior model used in the fusion. The preliminary evaluation results are provided in Appendix C. Following this preliminary assessment, a selection of the pixel-level and decision-level sensor fused models that resulted in the greatest change in weighted F1 and OA relative to mono-sensor models were chosen to be used in a comparative assessment between pixel-level and decision-level fusion techniques.

The land cover labels generated during the comparative assessment in Chapter 3 were used to calculate the weighted F1 and OA of both pixel-level fusion and decision-level fusion techniques.

4.2.4 Results

47 pixel-level fusion models and 101 decision-level fusion models were trained as part of this comparative assessment. A selection of the highest accuracy sensor fused models will be presented in this section. Tables 4.4 to 4.7 outline the results of a direct comparison between the results of pixel-level fusion and decision-level fusion and the unfused models. The results of unfused and pixel-level fusion models presented in Tables 4.4 to 4.7 were selected as the models obtaining the highest test data weighted F1 score for their given temporal dataset. For each comparison, the selection of decision-level fusion techniques was limited to those where the highest accuracy prior models used in its generation was the same as the non-fused model used in the comparison. As highlighted in Chapter 3 Section 3.3.3.3, the sample points available to each model differ due to differences in each model’s data requirement. Therefore, the weighted F1 and OA for each model are only comparable for model results presented within each table.

Table 4.4: Results of comparative assessment of fusion techniques for annually averaged data. The highest test data weighted F1 and OA are highlighted with text in bold.

Fusion Type	Satellite Data / Prior Models	Model	Dataset	Results	
				F1	OA
Unfused	Annually Averaged Sentinel-2 10m and 20m bands	LFCNN9×9	Validation	0.741	0.745
			Test	0.733	0.732
Pixel-level Fused	Annually Averaged Sentinel-1 and Sentinel-2 10m and 20m bands	SVM	Validation	0.736	0.736
			Test	0.765	0.762
Decision-level Fused	S2AN, L8AN and S1MO	SVM	Validation	0.776	0.777
			Test	0.783	0.784

Table 4.5: Results of comparative assessment of fusion techniques for half-yearly averaged data. The highest test data weighted F1 and OA are highlighted with text in bold.

Fusion Type	Satellite Data / Prior Models	Model	Dataset	Results	
				F1	OA
Unfused	Half-Yearly Averaged Sentinel-2 10m and 20m bands	3DLFCNN9×9	Validation	0.750	0.752
			Test	0.769	0.763
Pixel-level Fused	Half-Yearly Averaged Sentinel-1 and Sentinel-2 10m and 20m bands	SVM	Validation	0.734	0.736
			Test	0.774	0.772
Decision-level Fused	S2AN, S2HY L8AN and S1MO	SVM	Validation	0.760	0.760
			Test	0.794	0.793

Table 4.6: Results of comparative assessment of fusion techniques for seasonally averaged data. The highest test data weighted F1 and OA are highlighted with text in bold.

Fusion Type	Satellite Data / Prior Models	Model	Dataset	Results	
				F1	OA
Unfused	Seasonally Averaged Sentinel-2 10m and 20m bands	3DLFCNN9×9	Validation	0.767	0.771
			Test	0.784	0.780
Pixel-level Fused	Seasonally Averaged Sentinel-1 and Sentinel-2 10m and 20m bands	3DLFCNN9×9	Validation	0.770	0.773
			Test	0.780	0.778
Decision-level Fused	S2HY, S2SE L8AN and S1MO	SVM	Validation	0.776	0.777
			Test	0.801	0.800

Table 4.7: Results of comparative assessment of fusion techniques for six monthly averaged data. The highest test data weighted F1 and OA are highlighted with text in bold.

Fusion Type	Satellite Data / Prior Models	Model	Dataset	Results	
				F1	OA
Unfused	Six-Monthly Averaged Sentinel-2 10m and 20m bands	1DCNN6	Validation	0.753	0.748
			Test	0.789	0.787
Pixel-level Fused	Six-Monthly Averaged Sentinel-1 and Sentinel-2 10m and 20m bands	1DCNN6	Validation	0.742	0.7382
			Test	0.796	0.793
Decision-level Fused	S2AN, S2MO L8AN and S1MO	SVM	Validation	0.769	0.763
			Test	0.832	0.832

The results presented in Tables 4.4 to 4.7, illustrate that the application of a decision-level fusion outperforms pixel-level fusion in the assessed regions. In each comparison, the application of the decision-level fusion results in a notable increase in weighted F1 and OA results for both validation and test datasets relative to the unfused model. However, pixel-level fusion obtained mixed results, with some models producing minor improvements on the test dataset relative to the unfused model. However, there was a minor reduction in OA and weighted F1 for the validation dataset in each instance. In each comparison, the best pixel-level fusion results were obtained using Sentinel-1 and Sentinel-2 fused data. The highest pixel-level fused weighted F1 score on the test dataset was obtained using an SVM for the annually averaged and half-yearly averaged datasets. The results obtained from this assessment indicate that the application of pixel-level fusion to include Sentinel-1 or Landsat-8 for spatial models such as LFCNN9×9 or 3DLFCNN9×9 can negatively impact classification results relative to unfused Sentinel-2 data. In Chapter 3, the best mono-platform models for the annually averaged, half-yearly averaged and seasonally averaged data were obtained using LFCNN9×9 and 3DLFCNN9×9 architectures.

These results highlighted the importance of including spatial information when performing classification. The reduction in classification accuracy when utilising spatial models with pixel-level fused data is likely a significant contributing factor to the overall lower classification results obtained from pixel-level fusion techniques relative to decision-level fusion techniques. However, the application of pixel-level fusion improved the classification results obtained from point-based techniques such as SVM, RF and ANN relative to the mono-sensor point-based techniques as outlined in Table 4.8. As illustrated in the results presented in Table 4.8, the application of pixel-level fusion of Sentinel-1 and Sentinel-2 data improved classification accuracy for all point-based techniques, excluding one. The one exception was the application of an LSTM using six-monthly averaged data, which obtained significantly poorer results after pixel-level fusion. The improvement in classification accuracy through the fusion of Sentinel-1 and Sentinel-2 data for LCC was also observed in the study by Mercier et al. (2019). However, in their study, a RF model was the only ML technique examined. For each temporal range, the inclusion of Landsat-8 data resulted in a reduction in classification accuracy relative to the mono-platform Sentinel-2 models. One possible reason for this is that as a multispectral sensor, there is little additional information provided by Landsat-8 that is not otherwise provided by the Sentinel-2 data. In addition, with its lower spatial resolution of 30m, the inclusion of Landsat-8 data at the pixel level would likely result in lower classification accuracy around class boundaries. Carrasco et al. (2019) observed similar results with a lower OA obtained from the fusion of Landsat-8 and Sentinel-2 data than with Sentinel-2 data alone. However, in their study, the fusion of Sentinel-1, Sentinel-2 and Landsat-8 data obtained the best classification results.

Table 4.8: Results of comparative assessment of mono-platform and pixel-level fused data with point-based ML techniques. The highest test data weighted F1 and OA for each prepared dataset are highlighted with text in bold.

Temporal Preparation	Variables	Model Name	Validation		Test	
			F1	OA	F1	OA
Annually Averaged	Sentinel-2 10and20m Bands	ANN	0.695	0.703	0.720	0.728
		RF	0.663	0.670	0.670	0.676
		SVM	0.686	0.693	0.732	0.735
	Sentinel-1 and Sentinel-2 10and20m Bands	ANN	0.701	0.704	0.737	0.733
		RF	0.701	0.706	0.702	0.706
		SVM	0.727	0.730	0.762	0.763
Half-Yearly Averaged	Sentinel-2 10and20m Bands	ANN	0.709	0.713	0.734	0.721
		RF	0.681	0.687	0.684	0.690
		SVM	0.704	0.709	0.736	0.734
	Sentinel-1 and Sentinel-2 10and20m Bands	ANN	0.725	0.729	0.768	0.771
		RF	0.703	0.708	0.727	0.730
		SVM	0.734	0.737	0.779	0.781
Seasonally Averaged	Sentinel-2 10and20m Bands	ANN	0.735	0.739	0.762	0.765
		RF	0.705	0.712	0.723	0.729
		SVM	0.736	0.739	0.757	0.761
	Sentinel-1 and Sentinel-2 10and20m Bands	ANN	0.749	0.752	0.768	0.771
		RF	0.728	0.732	0.740	0.741
		SVM	0.755	0.757	0.787	0.787
Six Monthly Averaged	Sentinel-2 10and20m Bands	ANN	0.702	0.709	0.746	0.756
		RF	0.721	0.728	0.747	0.753
		SVM	0.732	0.734	0.789	0.789
		LSTM	0.687	0.699	0.752	0.758
		1DCNN6	0.757	0.755	0.791	0.789
	Sentinel-1 and Sentinel-2 10and20m Bands	ANN	0.728	0.730	0.781	0.775
		RF	0.766	0.767	0.754	0.753
		SVM	0.766	0.764	0.790	0.788
		LSTM	0.630	0.645	0.679	0.708
		1DCNN6	0.743	0.739	0.797	0.794

A distinct benefit of a decision-level fusion approach over pixel-level fusion is the ability to include data which vary significantly in terms of data-formats into the final analysis. For example, the fusion of the S2AN, S2MO, L8AN and S1MO prior models involves two point-based prior models and two patch-to-point based prior models. In addition, the two patch-to-point prior models are trained using annually averaged data and the two point-based prior models are trained using monthly averaged data. This enables the decision-level fused models to leverage unique information provided by each

independent prior model.

For each decision-level fusion model, the results of fusion were compared to the prior model with the highest F1 score used as input. Of the 101 combinations of prior models assessed, only 4 combinations of prior models resulted in a reduction in the weighted F1 score relative to the compared unfused prior model. In each instance where there was a reduction in the weighted F1, the prior model used for comparison was S2SE. Table 4.9 lists the four models that resulted in a reduction in weighted F1.

Table 4.9: Decision-level fusion models resulting in negative change in weighted F1 score. Change is calculate relative to the unfused Sentinel-2 seasonally averaged 3DLFCNN9×9 (S2SE).

Prior Models	Weighted F1 Change
S2SE, S2HY, S2AN and S1MO	-0.003
S2SE, S2AN and S1MO	-0.002
S2SE and S1MO	-0.018
S2SE and L8AN	-0.008

The largest reduction in weighted F1 for the test dataset was obtained through fusing *S2SE* and *S1MO* prior probabilities with a change in weighted F1 of -0.018. In each instance, the only negative weighted F1 were observed calculated relative to the *S2SE* prior model, which was the highest accuracy mono-platform model trained as part of the comparative assessment undertaken in Chapter 3.

Overall the results of this comparative assessment demonstrate the application of decision-level fusion can outperform pixel-level fusion over the study-region under assessment. These results corroborate the results obtained by Useya and Chen (2018) where they observed that a decision-level fusion approach was more suitable for crop detection than a pixel-level fusion. However, in their study, the focus was on single image composites and did not utilise time-series information.

4.3 Variable Data Availability Fusion Assessment

A significant issue identified in Chapter 3, was that the coverage of each sensor was different across the assessed regions. As a result, there are considerable variations in the data available at any given point in the assessed regions. An additional observation in Chapter 3 was that the method of preparing the temporal data for a given model impacted the model's coverage. This issue is further exacerbated when a decision-level fusion technique is applied, as the fusion model's coverage is dependent on the overlapping coverage of each prior model. In Chapter 2, several techniques were identified which could be used to manage missing data, such as gap filling, value replacement, or value imputation. However, such techniques may not be appropriate in scenarios where there are significant regions with missing data or a significant proportion of the data is missing at a given point. The use of fusion methodologies suitable for the decision-level fusion of data with variable prior model coverage will be assessed in this section. These methodologies will be assessed with the aim of ensuring complete coverage over an assessed region while maximising classification accuracy.

4.3.1 Fusion Techniques

A number of decision-level fusion techniques were evaluated that are best suited for the fusion of datasets with variable input, as a means of overcoming the issue of variable model coverage. Four decision-level fusion approaches were evaluated for this assessment; Ordered Fusion, Voting Fusion, Probability Fusion, Multi-ML model Fusion. Variations of these techniques were evaluated as part of this assessment. A full list of the fusion approaches along with their variations are presented in Table 4.10.

4.3.1.1 Ordered Fusion

Ordered fusion, is a fusion technique also referred to as 'cascading specialists' (Wagner et al., 2011). As identified in Chapter 3, each trained mono-platform model (prior model) has differing classification accuracy and coverage. In ordered fusion, a single model is used to assign the class at any given point. The aim of this fusion approach is to determine

Table 4.10: List of decision-level fusion approaches and the variations of those techniques that will be evaluated in variable data fusion assessment.

Fusion Approach	Variation of Technique
Ordered Fusion	<ul style="list-style-type: none"> • Full Model Ordered <ul style="list-style-type: none"> – F1 Ordered – OA Ordered • Class Ordered • Probability Thresholding Ordered (PTO)
Probability Fusion	<ul style="list-style-type: none"> • Max Probability <ul style="list-style-type: none"> – Model F1 Weighted Max Probability – Class F1 Weighted Max Probability • Average Probability <ul style="list-style-type: none"> – Model F1 Weighted Average Probability – Class F1 Weighted Average Probability
Voting Fusion	Weighted Voting
Multi-ML Model Fusion	N/A

which prior model is to be used for classification at any given point. This process is achieved by performing classification using each prior model in a defined order (Wagner et al., 2011). After performing classification using the first model in the order, some points may not have been classified as they were outside that model’s coverage. The next prior model in the order is then utilised to perform classification within its coverage. This process is repeated with each model in order until all points are classified. Figure 4.2, provides an illustrative example of the steps involved in an ordered fusion approach. For this assessment, the use order for each model was determined by the classification results of the validation dataset.

The order of classification is not limited to entire models, with the possibility of ordering sub-components of models by class or probability ranges. Three approaches to Ordered Fusion were assessed, Full Model Ordered, Class Ordered and Probability Thresholding Ordered (PTO).

Full Model Ordered

In a full model ordered fusion approach, the order of classification is determined by the models' weighted F1 or OA. Figure 4.2 provides an illustrative example of the full model ordered classification process.

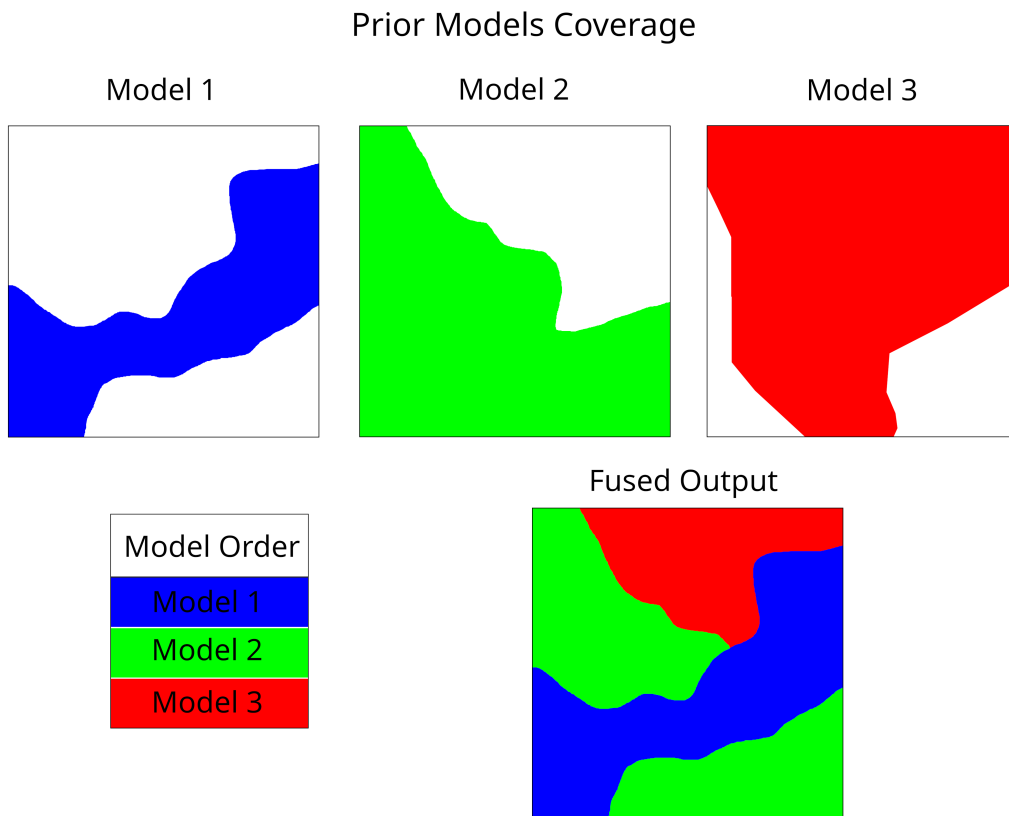


Figure 4.2: Example illustration of Full Model Ordered fusion.

Class Ordered

Each prior model used in this assessment outputs multiclass prior classification. In a class ordered approach, the prior classification of each model is subdivided by class. Each model's prior classification class (MC) is then assigned an ordering using the class

F1 score for that model. Each *MC* prediction is then used in order and only classifies the points for the given class. The process of subdividing by class is designed to leverage the differences in each model’s classification accuracy for each class. Figure 4.3, provides an illustrative example of class ordered classification process.

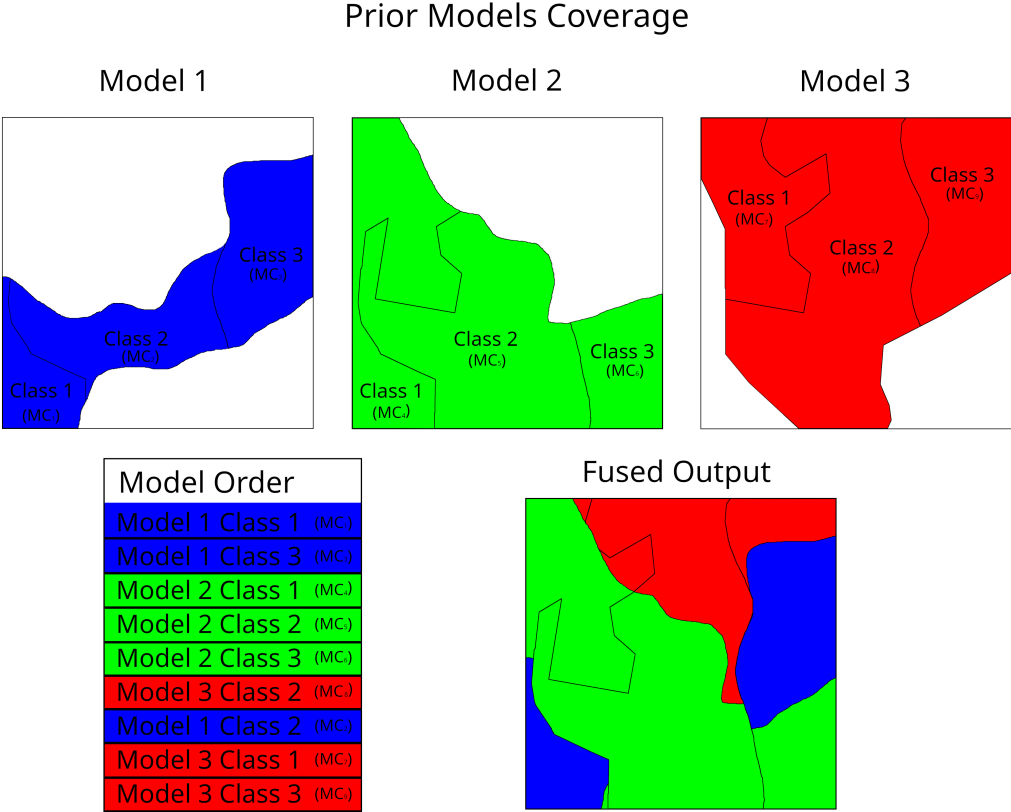


Figure 4.3: Example illustration of Class Order Fusion.

Probability Thresholding Ordered (PTO)

As outlined in Chapter 3, classifications made with a higher class probability tend to have a higher classification accuracy. However, this relationship is not identical between each model. Figures 4.4 and 4.5 illustrates the plot of the relationship between the accuracy of prediction and probability threshold for two models. A probability thresholding approach is proposed to take advantage of this relationship. Similar to the class ordered approach, the prior classification of each model is subdivided. However, in the PTO approach, the prior probability of a model is used to subdivide the model’s prior classification. Proba-

bility threshold ranges were set at intervals of 0.01 such that each prior classification can be divided into a maximum of 100 intervals. For each model, the OA was calculated at each probability threshold interval, and an overall ranking was generated for the probability range subsections from each model. Classification is then performed in order using the ranked probability range subsections.

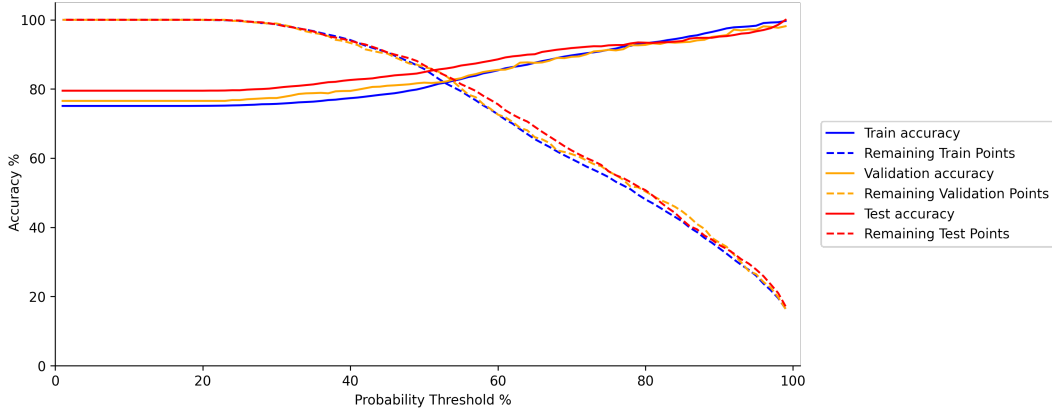


Figure 4.4: Probability threshold vs accuracy and available sample points for Sentinel-2 seasonally averaged 3DLFCNN9×9.

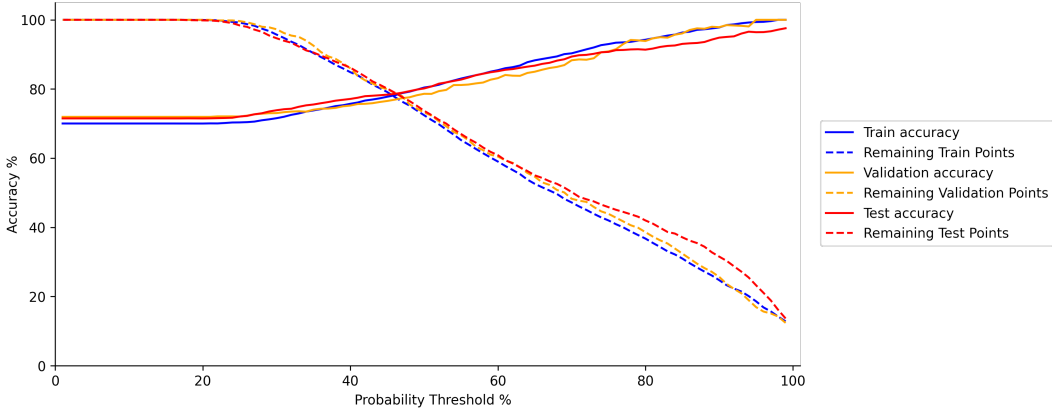


Figure 4.5: Probability threshold vs accuracy and available sample points for Landsat-8 half-yearly averaged 3DLFCNN9×9.

4.3.1.2 Voting Fusion

Voting fusion is a fusion technique where, each prior model (P) generates a discrete classification (d_p) as a vote and the final label ascribed is the class with the most votes (Gravina et al., 2017). A decision can only be guaranteed where there is an odd number of prior models for the classification of classes (Wagner et al., 2011). Therefore, each

class will be weighted (w) by the models OA from the validation dataset to reduce the likelihood of a tie in the vote. In a weighted voting fusion approach, the class (c) that receives the most votes (v) for a given sample (x) is given by (Wagner et al., 2011):

$$v_c(x) = \sum_{p=1}^P w_p d_{p,c}(x) \quad (4.1)$$

4.3.1.3 Probability Fusion

Probability Fusion, also referred to as ‘Bayesian fusion’ techniques explicitly utilise the prior probability of each prior model to assign classification (Le Bris et al., 2019; Gravina et al., 2017). Two approaches to probability fusion were examined as part of this assessment, Max Probability and Average Probability.

Max Probability

Max probability fusion is a technique where the final classification is determined by the highest prior probability of any of the prior models for a given location. Additionally, a variation of the technique was explored by applying a weight to the model’s prior probability before identifying the class with the max probability. Two approaches to applying the weight were examined; a single weight applied to all prior probabilities in the model using the model’s weighted F1 score and an independent weight applied to each class prior probability using the class F1 score. The validation datasets were used to calculate the F1 score weights for each model.

Average probability Fusion

Average probability fusion calculates the average of each prior probability (a) for each prior model (P) to calculate a final classification. As with max probability fusion, this fusion approach can be weighted (w) by the model’s weighted F1 or class F1 score. Therefore, the total weighted support (μ_c) for each class (c) is given by (Wagner et al., 2011):

$$\mu_c(x) = \frac{\sum_{p=1}^P w_p a_{p,c}(x)}{P} \quad (4.2)$$

4.3.1.4 Multi-ML model Fusion

The application of ML models such as SVMs for decision-level fusion, as outlined in Section 4.2, can significantly improve classification accuracy in comparison to the individual prior models. One modelling strategy to exploit ML models over an area with variable data availability is to train a unique SVM model for each combination of the available input dataset. During inference, the model chosen to be used for inference is based on the available prior models at that point. This approach of applying an SVM in a region with missing data was also examined by Salberg and Jenssen (2012).

4.3.2 Assessment Criteria

This assessment will be performed on three combinations of prior models. The use of three different combinations of prior models was undertaken to provide a better understanding of the application of fusion techniques with different datasets. The combination of prior models will be referred to as *fusion sets*. Table 4.11 outlines the prior models included in each fusion set.

Table 4.11: List of fusion sets used in the variable data availability fusion assessment.

Set Name	Description
Sentinel-2 Only	Prior models trained on Sentinel-2 data
Mono-Platform	Prior models trained using data from a single platform
SVM Fused	Decision-level sensor fused models performed using an SVM

Examination of the prior models in each fusion set revealed that it was not possible to classify all sample points using the *Sentinel-2 Only* fusion set. Therefore, the sample points to be classified by each fusion set were reduced such that all fusion sets could classify the same sample points. This process was undertaken to ensure the results of

each model could be compared to a common baseline complete dataset. This reduction in sample points was achieved by ensuring all sample points could be classified using the S2AN prior model. This reduced dataset will be referred to as the S2AN-reduced dataset for this assessment. While the S2AN prior model was capable of classifying all sample points in the S2AN-reduced dataset, other prior models were only suitable for classifying a percentage of this dataset. Table 4.12 outlines the percentage of sample points in the S2AN-reduced dataset that could be classified by each non-fused prior model following criteria for a minimum of six observations set out in the CLC+ Backbone technical specifications. A second dataset was generated to simulate the impact of a reduced number of Sentinel-2 observations. The reduction of Sentinel-2 observations was simulated by identifying the sample points that do not meet the minimum of six observations criteria if a random 25% of the Sentinel-2 observation points were removed. This dataset will be referred to as the 25%-reduced dataset. The impact of this process on the percentage of sample points that Sentinel-2 prior models can classify is outlined in Table 4.13.

Table 4.12: Percentage of sample points that can be classified by non-fused prior models in the S2AN-reduced dataset.

Prior Model	Percentage Cover
S1MO	100%
S2AN	100%
S2HY	77.86%
S2SE	83.15%
S2MO	36.98%
L8AN	18.41%
L8HY	9.07%

Table 4.13: Percentage of sample points that can be classified by non-fused prior models in the 25%-reduced dataset.

Prior Model	Percentage Cover
S2AN	84.51%
S2HY	54.65%
S2SE	50.66%
S2MO	15.08%

4.3.3 Results

The results of applying the assessed fusion techniques on the S2AN-reduced dataset are presented in Table 4.14. For context, the results of applying the Sentinel-2 annually averaged LFCNN9×9 model (S2AN) is included in Table 4.14.

Table 4.14: Fusion assessment results using the S2AN-reduced dataset. The highest test data weighted F1 and OA for each fusion set are highlighted with text in bold.

Set Name	Fusion Technique	Validation		Test	
		F1	OA	F1	OA
Sentinel-2 Annually Averaged LFCNN9×9 (S2AN)	None	0.729	0.735	0.731	0.736
Sentinel-2 Only	F1 Ordered	0.747	0.750	0.770	0.773
	OA Ordered	0.752	0.753	0.773	0.774
	Class F1 Ordered	0.769	0.772	0.761	0.765
	PTO	0.756	0.759	0.768	0.773
	Weighted Voting	0.761	0.763	0.782	0.784
	Max Probability	0.753	0.756	0.772	0.777
	Model F1 Weighted Max Probability	0.754	0.758	0.774	0.778
	Class F1 Weighted Max Probability	0.743	0.753	0.766	0.774
	Average Probability	0.766	0.769	0.783	0.786
	Model F1 Weighted Average Probability	0.767	0.771	0.784	0.786
Class F1 Weighted Average Probability	0.765	0.771	0.777	0.783	
Mono-Platform	F1 Ordered	0.752	0.753	0.773	0.774
	OA Ordered	0.751	0.755	0.781	0.783
	Class F1 Ordered	0.770	0.771	0.754	0.754
	PTO	0.760	0.763	0.765	0.769
	Weighted Voting	0.766	0.769	0.785	0.787
	Max Probability	0.750	0.754	0.769	0.772
	Model F1 Weighted Max Probability	0.754	0.758	0.772	0.775
	Class F1 Weighted Max Probability	0.746	0.754	0.756	0.764
	Average Probability	0.766	0.768	0.790	0.791
	Model F1 Weighted Average Probability	0.770	0.772	0.789	0.791
Class F1 Weighted Average Probability	0.764	0.769	0.784	0.788	
SVM Fused	F1 Ordered	0.775	0.777	0.791	0.792
	OA Ordered	0.780	0.782	0.777	0.776
	Class F1 Ordered	0.792	0.795	0.765	0.765
	PTO	0.774	0.778	0.798	0.799
	Weighted Voting	0.773	0.774	0.799	0.798
	Max Probability	0.778	0.782	0.794	0.795
	Model F1 Weighted Max Probability	0.777	0.781	0.798	0.799
	Class F1 Weighted Max Probability	0.755	0.764	0.787	0.792
	Average Probability	0.779	0.781	0.805	0.805
	Model F1 Weighted Average Probability	0.779	0.781	0.805	0.805
	Class F1 Weighted Average Probability	0.769	0.774	0.805	0.807
Multi-ML model	0.771	0.773	0.793	0.792	

The results presented in this section contain the weighted F1 score and OA of each technique for the validation and test datasets. The full results of performing each fusion technique used in this assessment are presented in Appendix C. The results presented in Table 4.14 demonstrate that the application of each of the average probability fusion techniques on the SVM Fused fusion set obtained the highest weighted F1 score of 0.805. The application of a class F1 weighted average probability fusion approach obtained a marginally higher OA of 0.807 than the model F1 weighted and unweighted average probability fusion techniques. In addition, the application of the model F1 weighted and unweighted average probability fusion approaches obtained the highest classification results for the Sentinel-2 only, and Mono-Platform Fusion sets, respectively. These results indicated that the application of weightings did not significantly improve classification accuracy. In section 3.5.1 the relationship between prediction probability and classification accuracy was established. Therefore, further application of weights to the prior probabilities may not be necessary.

Overall the application of order based techniques was outperformed by average probability fusion. In addition, the results revealed no clear best order based methodology. Model OA ordering obtained better results than other order fusion techniques in the Sentinel-2 and mono-platform fusion sets. However, in the SVM fused fusion set, the Model F1 order and PTO fusion techniques outperformed the Model OA ordered approach. One potential reason for this inconsistency and the relatively poor performance of the ordered fusion techniques relative to other assessed fusion techniques is the difficulty in reliably calculating a comparable order ranking between each model. As identified in Chapter 3, there is a significant reduction in the number of samples available to compute the accuracy metrics when performing a comparative assessment between models with differing coverage. This issue is further exacerbated when calculating class-specific F1 scores. This difficulty is a likely contributing factor to the poor performance of the Class F1 ordered fusion approach. In this assessment, the validation dataset was used to determine model order. As this dataset has fewer overall sample points than the test dataset, this issue is likely further exacerbated by the issue demonstrated in Chapter 3. During a

preliminary examination of fusion techniques, the use of the training dataset to calculate the model order was examined as a dataset with more sample points. However, it was observed that for most techniques, the use of the validation dataset outperformed the use of the training dataset when calculating the model order.

Table 4.15, provides the results of performing the coverage assessment on the 25%-reduced dataset. Due to the reduced Sentinel-2 coverage, the Sentinel-2 only fusion set could not classify all data points and therefore was not used in this assessment. Additionally, SVM fused models alone could not classify all sample points for the same reason. Therefore, a joint mono-platform and SVM fused fusion set was assessed.

Table 4.15: Fusion assessment results using the 25%-reduced dataset. The highest test data weighted F1 and OA for each fusion set are highlighted with text in bold.

Set Name	Fusion Technique	Validation		Test	
		F1	OA	F1	OA
Mono-Platform	F1 Ordered	0.727	0.731	0.760	0.761
	OA Ordered	0.738	0.742	0.764	0.765
	Class F1 Ordered	0.747	0.750	0.734	0.733
	PTO	0.738	0.741	0.745	0.747
	Weighted Voting	0.746	0.749	0.766	0.768
	Max Probability	0.725	0.728	0.744	0.747
	Model F1 Weighted Max Probability	0.727	0.731	0.745	0.748
	Class F1 Weighted Max Probability	0.720	0.728	0.735	0.743
	Average Probability	0.748	0.750	0.762	0.763
	Model F1 Weighted Average Probability	0.748	0.750	0.763	0.763
Class F1 Weighted Average Probability	0.734	0.740	0.761	0.764	
SVM Fused and Mono-Platform	F1 Ordered	0.758	0.759	0.780	0.780
	OA Ordered	0.757	0.759	0.778	0.778
	Class F1 Ordered	0.774	0.776	0.771	0.772
	PTO	0.753	0.756	0.776	0.778
	Weighted Voting	0.757	0.758	0.788	0.787
	Max Probability	0.753	0.756	0.779	0.780
	Model F1 Weighted Max Probability	0.753	0.756	0.784	0.786
	Class F1 Weighted Max Probability	0.738	0.745	0.771	0.776
	Average Probability	0.759	0.760	0.791	0.791
	Model F1 Weighted Average Probability	0.760	0.760	0.791	0.790
	Class F1 Weighted Average Probability	0.756	0.759	0.791	0.792
Multi-ML model	0.751	0.753	0.780	0.779	

The results of the 25%-reduced dataset assessment presented in Table 4.15 convey similar results to those obtained for the S2AN-reduced dataset in Table 4.14. In Table 4.15, the highest weighted F1 score of 0.791 was obtained by each of the average probability fusion techniques. The application of class F1 weighted average probability fusion obtained the highest OA of 0.792. As with the assessment on the S2AN-reduced dataset, the application of weightings to average probability fusion only resulted in a minor improvement and was not consistent across fusion sets. One notable difference in the 25%-reduced dataset assessment is that the best results for the mono-sensor fusion set was obtained with the use of a voting fusion approach with a minor improvement over Model F1 Weighted Average Probability fusion results.

Overall examination of the results reveals that applying unweighted average probability fusion with SVM fused models is the most suitable technique. While not obtaining the highest classification accuracy in the assessment, only minor differences were observed with the inclusion of weightings. Additionally, as already highlighted, errors in the calculation of weightings based on the test or validation data may negatively impact the classification results. The results of this assessment also demonstrate that applying unweighted average probability fusion with SVM fused models can outperform the use of voting fusion as utilised in the study by Useyá and Chen (2018) and the use of a Multi-ML model approach as utilised in the study by Salberg and Jenssen (2012).

4.3.3.1 Limiting SVM Fused Average Computational Cost

While the application of average probability fusion with SVM fused models was identified as a suitable methodology for fusion over the assessed region, with over 101 models to fuse, its application is computationally expensive. With each SVM fused model utilising a combination of prior models, the number of prior model combinations (T) can be calculated by the following formula (Heumann et al., 2016):

$$T = \sum_{k=2}^n {}^n C_k = \sum_{k=2}^n \frac{n!}{k!(n-k)!} \quad (4.3)$$

Where (n) denotes the total number of prior models and (k) denotes the number of prior models to be combined. For the seven mono-sensor prior models, there are a total of 120 model combinations that can be generated. As a number of those combinations only combine prior models using the same sensor, only 101 combinations were generated. If additional sensors were included in the fusion, the number of combinations would increase significantly and thus the computational requirement. For the combination of eight models, there would be 247 possible combinations, and for nine, there would be 502. This significant increase makes the application of a full combination SVM probability averaged approach computationally expensive for the fusion of data from multiple satellites.

With the aim of limiting the impact of this issue, an exploratory analysis was performed to identify if comparable results could be obtained by averaging a significantly lower number of models. For this purpose, three methodologies were examined to reduce the number of SVM model prior probability outputs to be averaged; *Top F1 Filtering* approach, a *Max Model per Point Filtering* approach and a *Dual-SVM Averaging* approach.

Top F1 Filtering

In the top F1 filtering approach, the SVM fused models to be averaged were limited to the models that were used in the Model F1 Order fusion approach. The assumption of this approach is that these models are the highest accuracy SVM models while still providing full coverage over the assessed region.

Max Model per Point Filtering

Under this approach for each point, a maximum number of SVM fused models were used to generate an average. Three max values were examined 3, 5 and 10. The models to be used for each point were the models with the highest weighted F1 score.

Dual-SVM Averaging

Under the dual-SVM averaging approach, the models to be averaged were limited to SVM

models that had utilised just two prior models as an input. In a dual-SVM averaging approach, the formula in Equation 4.3 to calculate the total number of combinations to be averaged can be simplified to:

$$T = \frac{n!}{2(n-2)!} \quad (4.4)$$

The results of limiting the number of SVM fused models to be averaged are displayed in Table 4.16. The averaging of all 101 SVM fused model prior probabilities will be referred to as *full-SVM averaging*. These results revealed that applying the dual-SVM averaging approach can produce a comparable weighted F1 score to the application of full-SVM averaging while only requiring 14 SVM fused models to be averaged. An additional benefit to this approach is that the number of SVM fused model prior probabilities to be averaged is known prior to training. For the assessed regions, only 14 SVM fused model prior probabilities needed to be trained when employing dual-SVM averaging. In contrast, the use of the top F1 filtering and max model per point filter approaches require the training of an SVM fused model for each prior model combination before identification of the SVM fused model prior probabilities to be averaged. Therefore, the use of a dual-SVM averaging approach can significantly reduce the complexity of the fusion workflow. One possible reason that the application of a dual-SVM averaging approach can obtain results comparable to full-SVM averaging is that with each SVM using pairs of prior models, sufficient information about the relationship between each prior model is extracted to be used in the averaging fusion. In addition, as the prior models are not weighted or filtered by F1 or OA, this approach is not impacted by the miscalculation of weights as identified in Section 4.3.3. To further corroborate the results presented in Table 4.16, the application of the dual-SVM averaging approach was compared to the top 6 SVM fused models. The results of this comparative assessment is presented in Table 4.17. The result of this assessment demonstrates that the application of the dual-SVM averaging approach can obtain comparable results to both the target SVM fused model and a full-SVM averaging approach using all prior models used to generate the target SVM.

Table 4.16: Model filtering assessment results on S2AN-reduced dataset. The highest test data weighted F1 and OA for each target model assessment are highlighted with text in bold.

Filtering Technique	Validation			Test		
	F1	OA	Models used	F1	OA	Models used
Full-SVM averaging	0.779	0.781	101	0.805	0.805	101
Top F1 filtering	0.775	0.777	11	0.787	0.786	11
3 Max model per point	0.771	0.774	38	0.794	0.794	40
5 Max model per point	0.769	0.772	52	0.793	0.793	53
10 Max model per point	0.772	0.776	72	0.798	0.797	72
Dual-SVM averaging	0.771	0.773	14	0.805	0.804	14

Table 4.17: Results of comparative assessment of Full-SVM averaging and Dual-SVM averaging to and SVM model using five different combinations of prior models. The highest test data weighted F1 and OA for each target model assessment are highlighted with text in bold.

Target Model	Fusion Technique	Validation		Test	
		F1	OA	F1	OA
S2AN S2MO L8AN L8HY S1MO	Target model	0.821	0.819	0.842	0.846
	Full-SVM averaging	0.790	0.787	0.841	0.845
	Dual-SVM averaging	0.806	0.803	0.841	0.844
S2AN S2HY S2SE L8HY S1MO	Target model	0.809	0.810	0.805	0.805
	Full-SVM averaging	0.796	0.796	0.811	0.809
	Dual-SVM averaging	0.782	0.782	0.812	0.809
S2HY S2SE L8AN L8HY S1MO	Target model	0.810	0.810	0.803	0.802
	Full-SVM averaging	0.800	0.801	0.809	0.807
	Dual-SVM averaging	0.793	0.793	0.821	0.817
S2HY S2SE L8HY S1MO	Target model	0.805	0.805	0.806	0.805
	Full-SVM averaging	0.796	0.796	0.805	0.804
	Dual-SVM averaging	0.786	0.786	0.810	0.808
S2AN S2HY S2MO L8AN	Target model	0.771	0.765	0.822	0.822
	Full-SVM averaging	0.781	0.775	0.829	0.830
	Dual-SVM averaging	0.792	0.788	0.822	0.823

4.3.4 Confusion Matrix and Classification Examples

Figure 4.6 displays the confusion matrix for the full-SVM averaging approach. Figures 4.7 and 4.8, provide illustrative examples of the classification results from full-SVM averaging approach alongside classification from the best mono-platform models generated in Chapter 3. Examining the images presented in Figures 4.7 and 4.8, reveals that the application of the Full-SVM averaging fusion approach results in relatively minor changes over the given areas. One potential reason is that the S2SE model is the highest-accuracy mono-platform model. Therefore, the application of sensor fusion did not significantly improve the classification of the given areas. Additionally, as previously presented in Table 4.9, the application of some SVM fused models results in a reduction in classification accuracy relative to the S2SE model. The application of Full-SVM averaging fusion approach appears to result in rougher boundaries between classes and with the addition of smaller fragmented class segments than present in the data classified with the S2SE model. With similar small fragmented features present in the S1MO classified map, its inclusion in the fused data may be a significant contributing factor to its occurrence. Despite this issue, the inclusion of S1MO appears to aid in correcting areas originally misclassified as *Sparsely Vegetated* in both the S2SE and L8HY classification maps. In Figure 4.8, several areas are misclassified as *Sparsely Vegetated* in the classification maps from S2SE and L8HY models. However, these areas appear to be correctly classified in both the S1MO and Full-SVM fused classification maps.

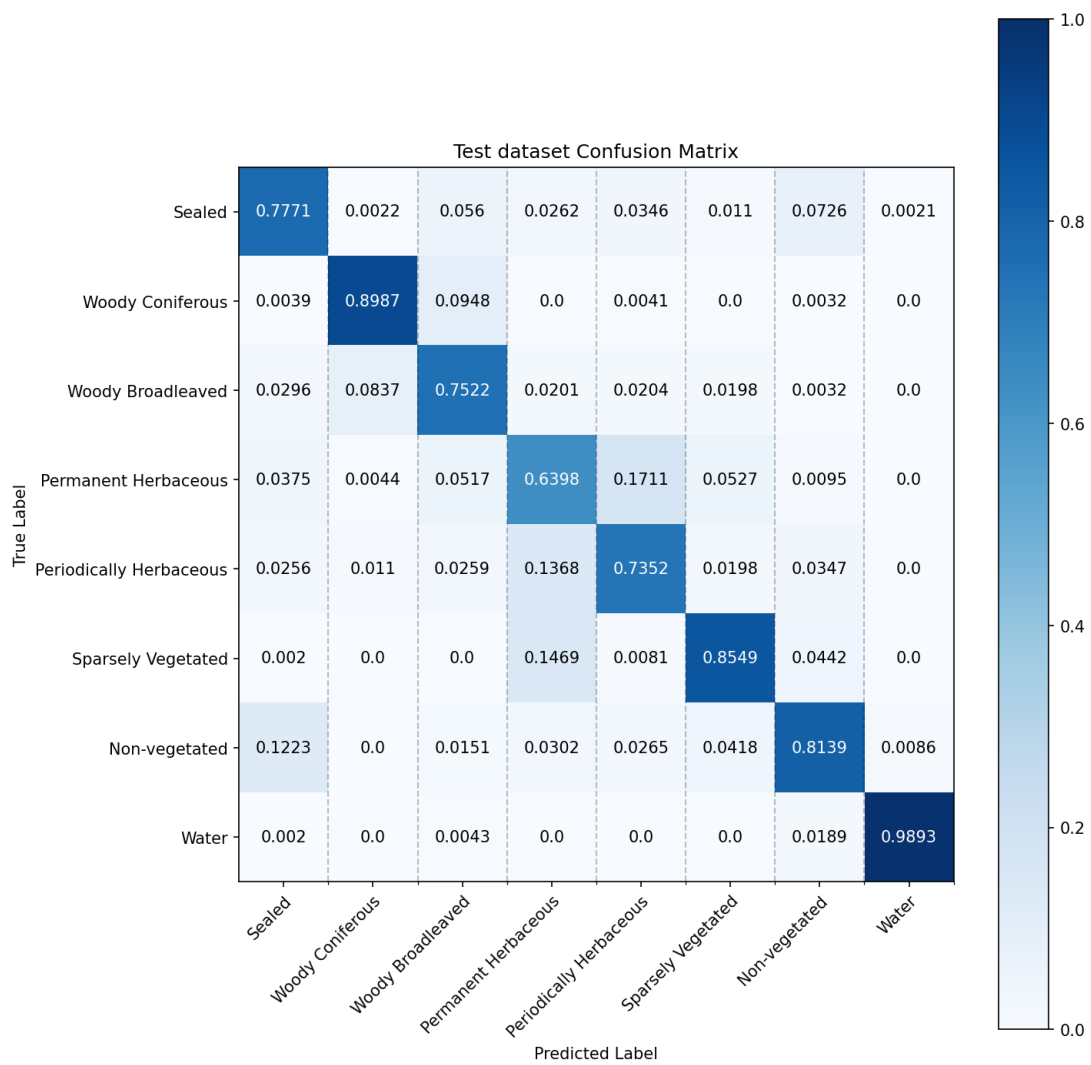


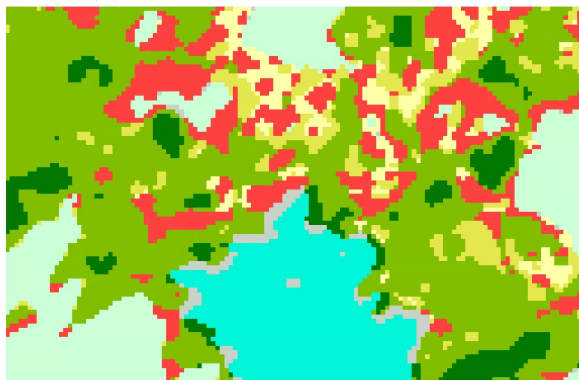
Figure 4.6: Confusion matrix for the full-SVM averaging approach on the SVM Fused fusion set.



(a) Sentinel-2 true colour image.



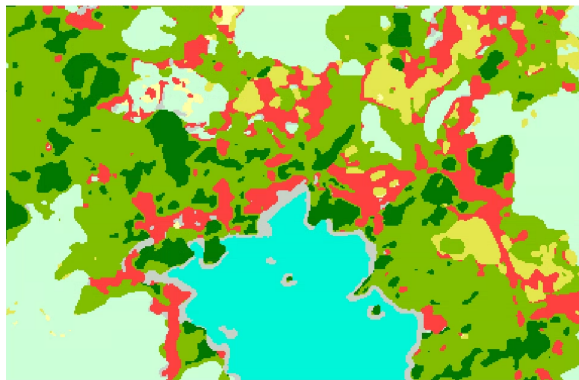
(b) Label



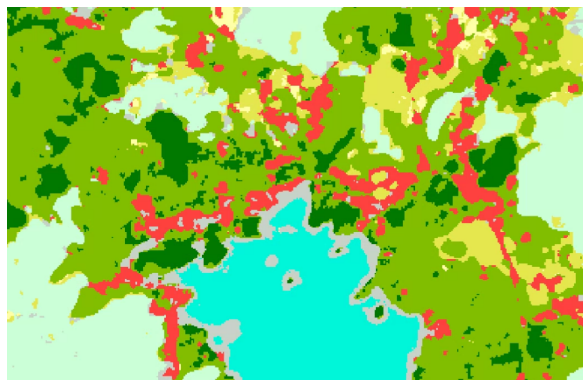
(c) Landsat-8 half-yearly averaged 3DLFCNN9x9 (L8HY).



(d) Sentinel-1 monthly averaged 1DCNN12 (S1MO).



(e) Sentinel-2 seasonally averaged 3DLFCNN9x9 (S2SE).



(f) Full-SVM averaging fusion approach.



Figure 4.7: Classification examples over Glengarriff harbour, Co Cork that were generated from the three highest accuracy mono-platform models and using the Full-SVM Averaging Fusion approach.

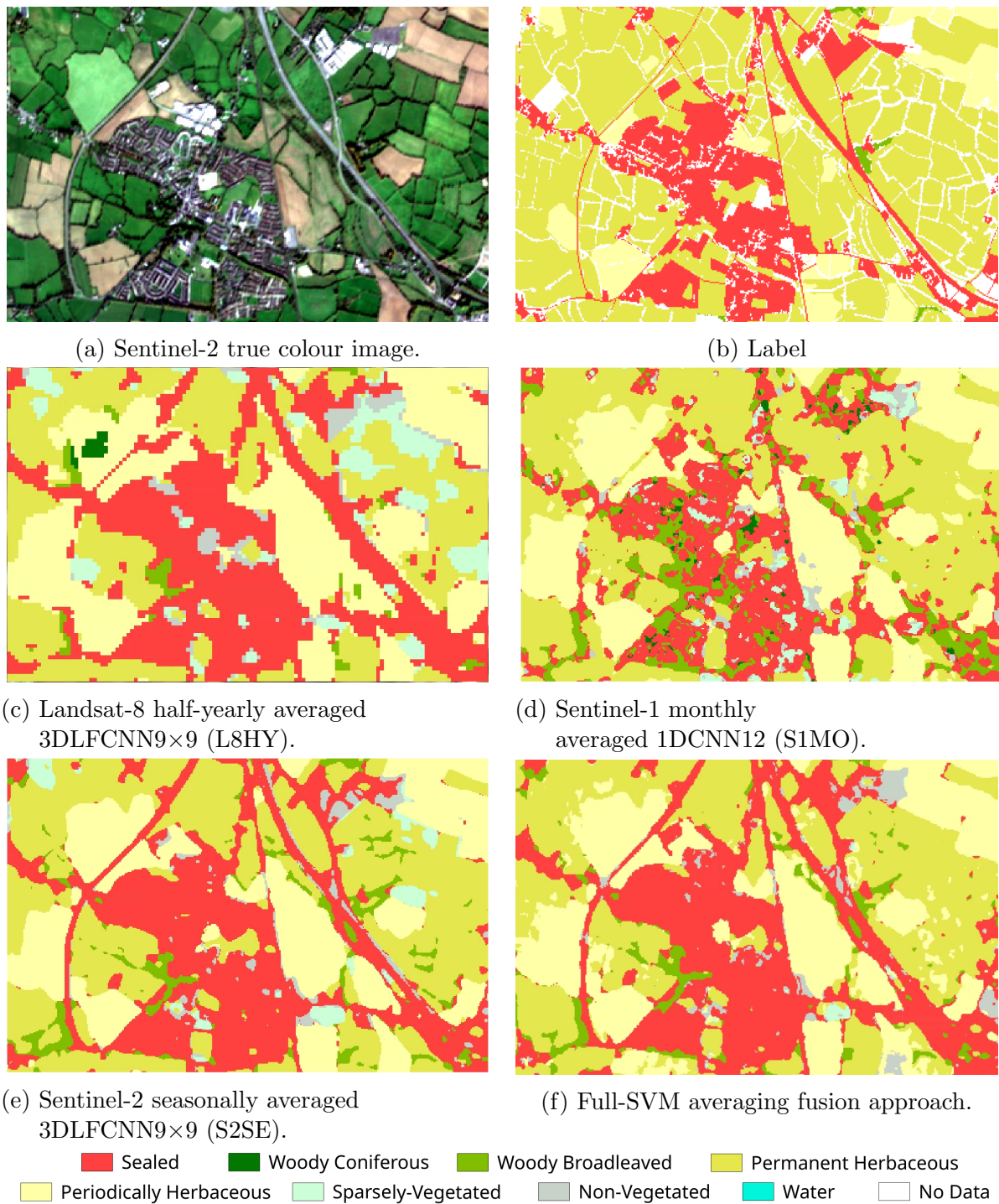


Figure 4.8: Classification examples over Dunboyne, Co. Meath that were generated from the three highest accuracy mono-platform models and using the Full-SVM averaging fusion approach.

4.4 Conclusion

This chapter demonstrates that the accuracy of satellite-derived classification can be improved by applying decision-level sensor fusion techniques. A comparative assessment evaluating the performance of pixel-level fusion and decision-level fusion using a SVM was performed. In this assessment, decision-level fusion obtained higher classification accuracy. The evaluation also revealed that a decision-level fusion approach is more suitable for fusing distinctly different datasets. An assessment of multiple decision-level fusion techniques was undertaken to determine their suitability in the context of variable data availability. The results of this assessment demonstrated that the highest accuracy results could be obtained by generating a SVM fused model for each combination of prior models before applying average probability fusion. While the inclusion of weights to average probability fusion obtained slightly higher classification results, this increase in classification accuracy was minor and not consistent across each dataset used in the experimental evaluation. One significant issue identified in this assessment was that for the seven prior models, 101 SVM fused combinations were generated. As a result, the application of average probability fusion on the SVM fused models would be computationally prohibitive. However, during this assessment, comparable results could be obtained using average probability fusion on SVM models, which only utilised two prior models each. Therefore, only 14 SVM fused models would need to be trained.

Key contributions:

1. The undertaking of a comparative assessment demonstrated that decision-level fusion could outperform pixel-level fusion. For example, A 1DCNN6 architecture trained with pixel-level fused of six monthly averaged Sentinel-1 and Sentinel-2 data obtained an F1 and OA of 0.796 and 0.793, respectively. However, in the same comparative assessment, the decision level fusion of four prior models, S2AN, S2MO, L8AN and S1MO, using an SVM obtained a weighted F1 and OA of 0.832. In particular decision-level fusion was observed to be suitable for the fusion of data with significantly different compositions. The results of this comparative assess-

ment revealed that the application of decision-level fusion is an appropriate means of fusing data in a scenario where data availability varies across the assessed region and was examined further in the variable data availability fusion assessment.

2. The application of average probability fusion for each combination of SVM fused model (Full-SVM averaging) was demonstrated to obtain high accuracy classification for fusion over an area with variable data availability. Applying prior probability weightings using the model's class F1 score obtained the highest test dataset weighted F1 and OA of 0.805 and 0.807, respectively. However, the benefit of applying weights to the prior probabilities was not deemed sufficient, given the potential risk posed by identified issues when calculating the weightings. Therefore, the application of unweighted average probability fusion was recommended for performing data fusion. Full-SVM averaging provides a robust methodology for the fusion of the data, which can be applied to the fusion of any combination of EO data captured over an assessed region. This technique is particularly suited for application on the island of Ireland, where frequent cloud cover results in significant variation in the availability of optical satellite data.
3. The application of dual-SVM averaging was proposed as a lower computation approach of fusion that can obtain comparable results to full-SVM averaging. Using a dual-SVM averaging approach, a test dataset weighted F1 and OA of 0.805 and 0.804, respectively, was obtained. The lower computation requirement may be even more consequential where data from a significant number of satellite platforms is to be included in the analysis.

Chapter 5

Combined Satellite-Aerial Data Fusion

5.1 Introduction

In this chapter, a decision-level fusion approach combining both satellite and aerial data is examined. The approach extends the work of Chapters 3 and 4 by leveraging the complementary strengths of each platform. In particular, this chapter will examine how the inclusion of high-resolution aerial data can be used to improve the classification accuracy of satellite-derived LCC.

The spatial resolution of the data used for performing classification was identified as a significant factor impacting classification accuracy in both the literature review conducted in Chapter 2 and the comparative assessment of satellite-derived LCC undertaken in Chapter 3. In Chapter 2, it was identified that high-resolution imagery enabled accurate delineation of class boundaries and was required to identify specific land cover classes. However, as the size of the region under consideration grows, obtaining high spatial resolution imagery can be challenging (Zhu et al., 2010). This issue is further exacerbated where analysis requires the capture and collation of multi-temporal RS information. One of the key findings in Chapter 3, was the requirement for multi-temporal data in order to produce high accuracy satellite-derived LCC. Therefore, mono-temporal high spatial

resolution data alone would be insufficient for the classification of land cover types that are inherently temporal such as the *Periodically Herbaceous* class. Given the challenges of obtaining multi-temporal high-resolution data, the application of a sensor fusion approach has the potential to leverage information from high spatial resolution aerial data along with the multi-temporal information of the satellite data. Chapter 4 demonstrated that applying a decision-level fusion approach enabled the fusion of data from varying sources possessing differing spatial, spectral and temporal resolutions. An additional benefit of utilising a decision-level fusion approach is that this technique enables multi-satellite sensor fusion to be performed independent of satellite-aerial fusion.

As reported in Chapter 3, frequent cloud cover can significantly hinder the collection of useful optical satellite data. The ‘Very High Resolution Image Mosaic 2018’ dataset released by Copernicus on the 7th October 2021 provides an almost complete coverage 2m resolution dataset across Europe. However, the imagery used to generate this dataset was captured over a three year period between 2017-2019 (Copernicus, 2022). The overall aim of this thesis, as outlined in Chapter-1, is to examine methodologies that enable the generation of higher-quality, annual LCC datasets. Therefore, capturing all data relevant to generating a LCC within the target year is essential. Light aircraft and UAVs have the potential to offer a suitable and effective alternative to high-resolution satellites with their inherent ability to fly below most instances of cloud in Ireland.

This Chapter is laid out as follows; **Section 5.2** will outline the data and methodology used to classify the aerial data in order to examine how decision-level satellite-aerial fusion can improve LCC. **Section 5.3** will describe the decision-level fusion technique under examination and outline how this technique will be evaluated. **Section 5.4** will report on the results of this assessment. Finally, **Section 5.5** will provide an in-depth discussion of the results and highlight the key findings of this decision-level fusion technique.

5.2 Aerial Data Classification

The proposed methodology involves the application of a decision-level fusion approach for the fusion of aerial and satellite prior classifications. The required prior satellite clas-

sifications were computed using the technique discussed in Chapters 3 & 4. To perform satellite-aerial decision-level fusion, independent classification of aerial data was required.

5.2.1 Aerial Data

The aerial imagery used as part of this assessment was captured using a Nikon D800E Camera mounted on a Cessna 172 light aircraft using a sensor pod mounted on the right-wing strut. The sensor pod is a bespoke sensor housing designed to enable various RS cameras and sensors to be fitted to the aircraft, allowing researchers to adjust and configure the sensors prior to flight (Cahalane et al., 2017). Figure 5.1 displays this wing strut mounted sensor pod.



Figure 5.1: Cessna 172 with sensor pod wing attachment.

Optical data was captured across six different sites. LiDAR data was also captured over two of these survey areas. However, since LiDAR data was only captured over two sites there was insufficient data available to reliably train, validate and test the accuracy of its use in a ML model. As such, this LiDAR data was only used during the georectification process (see below). The location and date of each survey are listed in Table 5.1. The spatial resolution of each survey is provided as the survey's GSD. The location of the survey areas to be used in this assessment are delineated in Figure 5.2.

Table 5.1: Aerial survey details.

Site	Date captured	Area (km ²)	Survey GSD
Sroughan	2016-08-16	2.11	0.07m
Horsepasstown	2016-08-16	2.18	0.08m
Twomilebridge	2016-08-16	3.51	0.06m
Rathdown Upper	2016-07-28	1.76	0.06m
Maynooth	2018-09-03 and 2018-08-21	6.72	0.04m
Waterford Airport	2018-09-13	4.812	0.05m

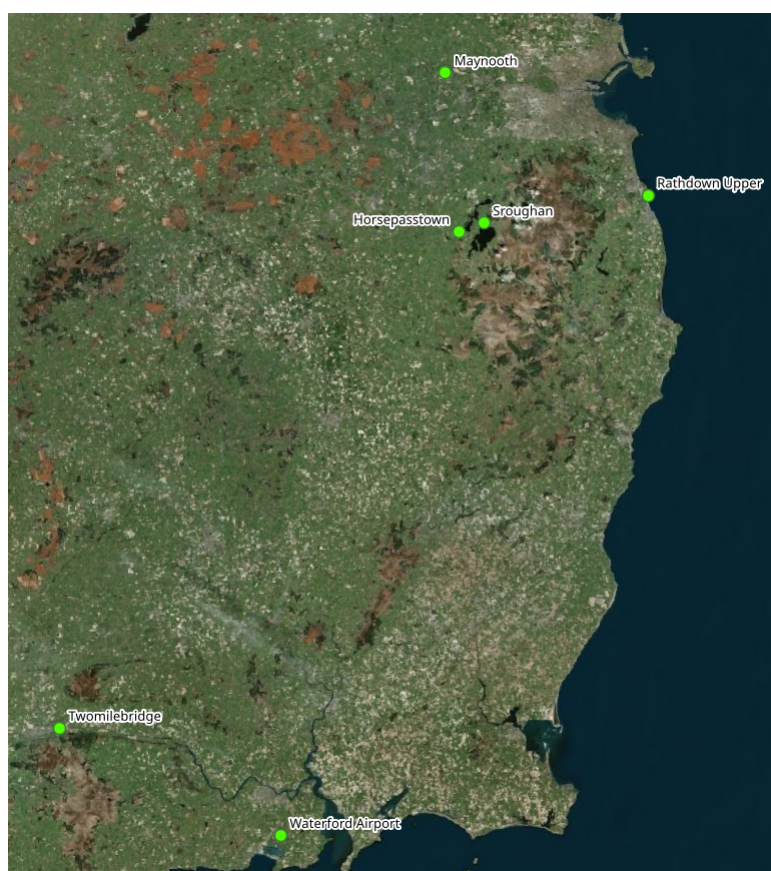


Figure 5.2: The location of aerial survey sites. Base map: Microsoft Bing Imagery (www.bing.com/maps/aerial).

The photogrammetric software Agisoft Metashape V was used to convert the individual images captured over each survey area into a single merged georectified image. The photogrammetric process uses tie point matching to identify common points between images, which are then used to generate a 3-dimensional surface. This surface is then used to correct relief displacement resulting in an orthorectified mosaic (Lillesand et al., 2014;

Förstner and Wrobel, 2016). During orthorectification, ground control points were used to georectify the image. For the Waterford and Maynooth surveys, ground control points were selected from high accuracy LiDAR data captured concurrently as part of these surveys. For the remaining sites, ground control points were selected from features visible in both the aerial-survey and Microsoft Bing imagery (www.bing.com/maps/aerial). Each image was resampled to 0.25m GSD, once orthorectified, using cubic interpolation. During resampling, the minimum and maximum extents of each orthorectified image were set to be divisible by 10, therefore matching the grid structure of the satellite data generated in Chapter 3. The aerial resolution image data comprises pixels that are 0.25m resolution and so divide evenly into the 10m resolution grid structure of the satellite data. Ensuring that aerial data’s raster grid structure aligns to and subdivides the satellite raster grid structure was undertaken to facilitate resampling steps that were performed later in the fusion process. No significant increase in classification accuracy was observed during initial experimentation using higher resolution imagery for the given classes. It is worth noting that the selected resolution is similar to very high-resolution satellite platforms such as WorldView-3 and Pléiades Neo, possessing pixel resolutions of 0.31m and 0.30m GSD respectively (AIRBUS, 2022; ESA, 2022). Therefore, it is expected that comparable results should be obtainable from these platforms.

5.2.2 Labelled Data

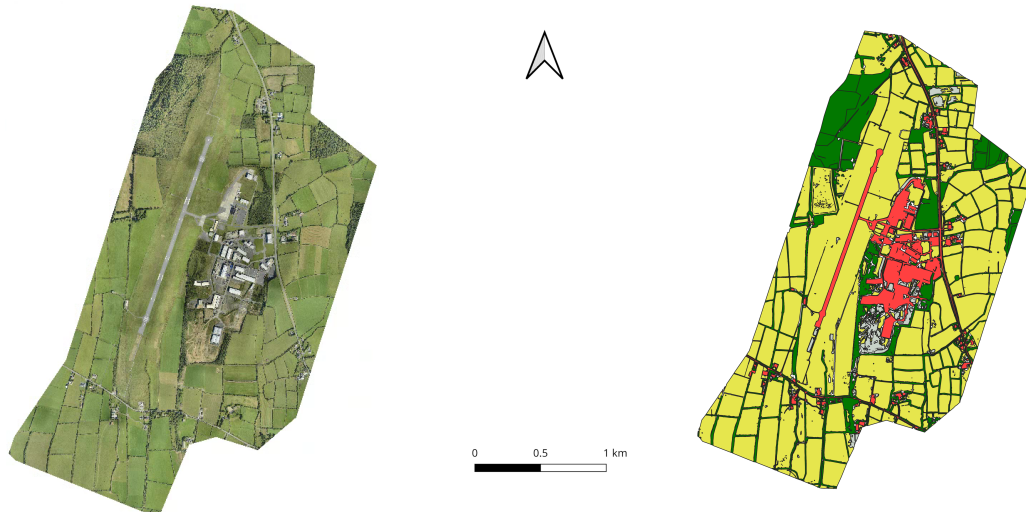
Chapter 4 described how decision-level fusion was performed using prior models, each of which used the same classification structure. However, as the aerial data used in this assessment was captured over a single time period, it would not be possible to reliably differentiate some of the land cover classes such as *Periodically Herbaceous* and *Permanent Herbaceous*. For this reason, a simplified version of the satellite classification schema outlined in Chapter 3 was used for the classification of aerial data. The aerial classification schema was designed such that each aerial class directly corresponded to one or more satellite classes. For example, both the *Woody Coniferous* and *Woody Broadleaved* satellite classes were simplified to the *Woody Vegetation* aerial class. This form of decision-level

fusion will be referred to as *class-corresponding fusion*. Table 5.2, lists the classes that were used for the labelling of aerial data along with the corresponding satellite classes.

Table 5.2: Aerial classes along with the definitions and corresponding satellite classes.

Aerial Classes	Description	Corresponding Satellite class
Woody Vegetation	Any perennial woody plants.	Woody Coniferous and Woody Broadleaved
Herbaceous Vegetation	Annual, biennial or perennial plants that do not have a persistent woody stem above the ground. This includes both managed and unmanaged vegetation such as grasslands and arable crops visible during the time of data capture.	Permanent Herbaceous, Periodically Herbaceous and Sparsely Vegetated
Non-Vegetated	Consolidated and unconsolidated materials as well as bare soils. Examples include rock formations, quarries, mineral extraction sites, open-pit mines, screes, sand, bare soil.	Periodically Herbaceous, Non-Vegetated and Sparsely Vegetated
Sealed	All impervious and sealed surfaces. Artificial surfaces such as buildings and artificial constructions, asphalt, concrete, tarmacadam.	Sealed
Water	Water in a liquid state of aggregation regardless of location, shape, salinity and origin, both natural or artificial. This includes rivers, canals, natural lakes, fishponds, man-made reservoirs, pools, irrigation ponds.	Water

Labels for each survey region were manually digitised as vector data using the open-source geographic information software QGIS. Where available, additional datasets such as open street maps and Prime2 were used as reference material for labelling the data. Figure 5.3, illustrates labels over the Maynooth and Waterford Airport survey areas.



(a) Waterford Airport.



(b) Maynooth.

Herbaceous Vegetation
 Woody Vegetation
 Non-Vegetated
 Sealed
 Water

Figure 5.3: Aerial Labels for a) Maynooth and b) Waterford Airport sites.

The vector labels for each site, once generated, were converted to raster format with a spatial resolution of 0.25m GSD with an equal extent to the orthorectified aerial data for that site. Non-overlapping label patches with a dimension of 100×100 pixels were extracted with corresponding image patches of 284×284 pixels. For this assessment, the Maynooth site was used as the test site for the evaluation of aerial classification results and the remaining sites were used for training and validation. Validation data was generated as a random 10% sample of the non-test data.

5.3 Satellite-Aerial Class-Corresponding Fusion

The methodology proposed in this assessment performs fusion in three steps; *i*) interpolation of satellite prior probabilities to 0.25m GSD, *ii*) fusion of aerial and interpolated satellite data, and *iii*) the resampling of the fused data to the output 10m GSD. Figure 5.5 provides an illustrative overview of the three steps involved in the proposed satellite-aerial fusion methodology.

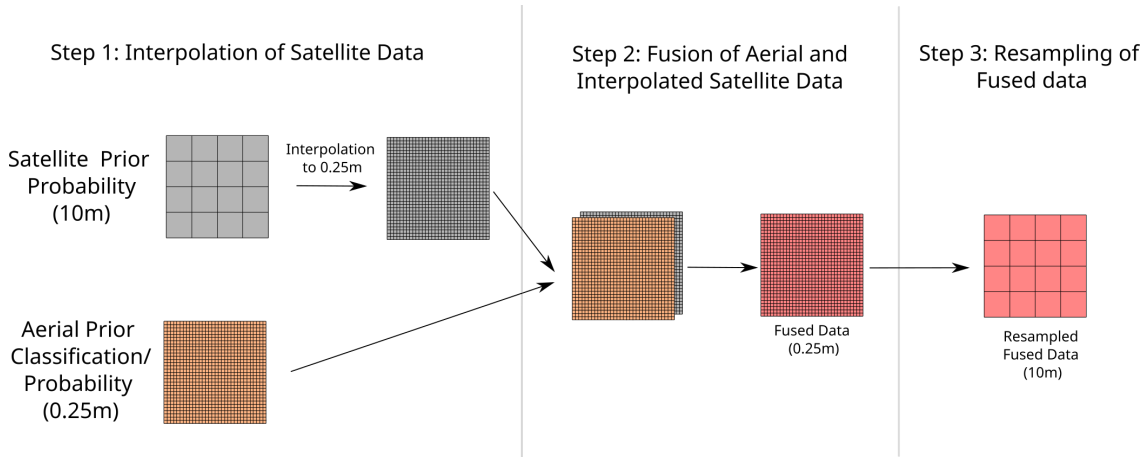


Figure 5.5: Illustration of satellite-aerial fusion steps.

The first step in the proposed satellite-aerial fusion methodology involves the interpolation of the satellite prior probability to 0.25m GSD. This step was achieved using a cubic interpolation methodology.

Two approaches to class-corresponding fusion were examined to undertake the second step in the proposed satellite-aerial fusion methodology; a class constrained fusion (Class-Con Fusion) approach and a corresponding probability fusion (Cor-Prob Fusion) approach.

5.3.1 Class Constrained Fusion (Class-Con Fusion)

Under the Class-Con Fusion approach, the aerial prior classification is used to constrain the location where the satellite classification can be performed. This constrained approach assumes that the aerial data's higher spatial resolution is better suited for the classification of the simplified LCC. Under this approach, the prior satellite probabilities were masked by the corresponding aerial prior class as listed in Table 5.2. For any given

location, the satellite prior probability (S_p) for a given satellite class (S_c) is unchanged where the satellite class is in the set of corresponding satellite classes for the aerial prior classification (A_c) at that given location. Where the satellite class is not in the set of corresponding satellite classes for the aerial prior classification, the satellite prior probability is set to zero. The fused class probability (S'_p) for Class-Con Fusion is given by:

$$S'_p = \begin{cases} S_p, S_c \in A_c \\ 0, S_c \notin A_c \end{cases} \quad (5.1)$$

The *Sealed* and *Water* classes have only one corresponding satellite class. Therefore, the aerial classification is the sole contributor to their classification in the final output.

5.3.2 Corresponding Probability Fusion (Cor-Prob Fusion)

Corresponding probability fusion calculates the product of the satellite prior probability and its corresponding aerial class probability (A_p) as defined in Table 5.2. For satellite classes such with a single corresponding aerial class, the fused class probability is given by:

$$S'_p = S_p \times A_p \quad (5.2)$$

For satellite classes such as *Periodically Herbaceous* that have two corresponding aerial classes, the maximum probability of the corresponding classes (A_{p1}) and (A_{p2}) was first calculated. The product of the maximum aerial class probability and the corresponding satellite prior probability was then calculated. The fused class probability with two corresponding aerial classes is given by:

$$S'_p = S_p \times \max(A_{p1}, A_{p2}) \quad (5.3)$$

5.3.3 Classification and Resampling

Once fused, the class of each pixel was determined by the class with the highest probability, excluding the *Sparsely Vegetated* class. The class to be assigned to each 10m pixel was determined as the mode of classes from the contributing pixels to be resampled. The class description for the *Sparsely Vegetated* class provided in the CLC+ technical specification is as follows; ‘Sparsely vegetated and unstable areas of stones, boulders, or rubble on steep slopes where the vegetation layer consisting of herbaceous vegetation covers between 10% and 50% of the surface.’(Kleeschulte et al., 2019) The *Sparsely Vegetated* class was originally defined for use with 10m resolution satellite datasets. However, at very high spatial resolutions, *Sparsely Vegetated* areas can be considered as either *Permanent Herbaceous* or *Non-Vegetated*. Therefore, the *Sparsely Vegetated* class was assigned to a 10m resolution pixel where over 50% contributing 0.25m pixels were *Non-Vegetated* and between 10% and 50% were the *Permanent Herbaceous* class.

5.3.4 Assessment Methodology

Four satellite prior models were used to assess the performance of satellite-aerial fusion. Three of the prior models were mono-sensor satellite models using Sentinel-1, Sentinel-2 and Landsat-8. Each of these mono-sensor models were selected for this assessment as the highest accuracy model for their respective sensor identified in Chapter 3. The fourth satellite prior model used in this assessment is an SVM decision-level fused model generated in Chapter 4. Table 5.3, lists the prior satellite models to be used for satellite-aerial fusion. Each model will be given a unique acronym to aid in the interpretation of the results.

Table 5.3: List of satellite prior models to be fused.

Satellite Source/Prior model	Model	Acronym
Monthly Averaged Sentinel-1	1DCNN12	S1MO
Seasonally Averaged Sentinel-2	3DLFCNN9×9	S2SE
Annually Averaged Landsat-8	LFCNN9×9	L8AN
S1MO, S2SE & L8AN	SVM	SVM-Fused

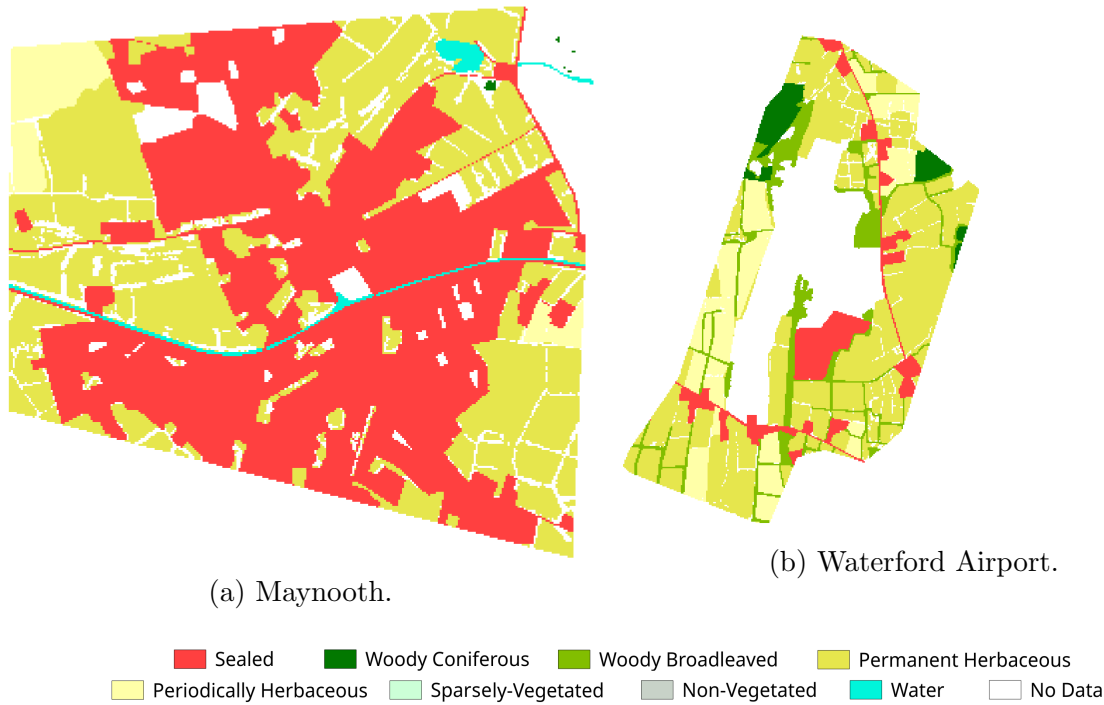


Figure 5.6: Aggregated labels generated for satellite classification assessment in Chapter 3 over a) Maynooth and b) Waterford Airport.

With only two aerial surveys carried out in 2018, both of the Maynooth and Waterford Airport sites were used to assess the impact of implementing satellite-aerial fusion. For both sites, a new label dataset was generated to assess the results of performing satellite-aerial fusion. Note that the labelled dataset generated over these regions in Chapter 3 has significant areas of missing data (see Figure 5.6) and, therefore, could not be used. In the Waterford Airport region, the missing region was defined as *Airports* in the Copernicus Urban Atlas dataset and *Airports and associated land* within the Copernicus Coastal Zones dataset. This class definition does not clearly align to any of the CLC+ Backbone raster product classes and so was excluded in the generation of a label dataset generated for Chapters 3 and 4. Additionally, a visual inspection of the label datasets generated for Chapters 3 and 4 lack the boundary delineation that would be appropriate for this assessment. The new label datasets for this assessment were generated by modifying the labels used to train the aerial UNET model and updating the land cover classes to correspond to the satellite label classes. The updating of the class was achieved using the Chapter 3 label dataset as a reference, along with photo-interpretation of high-resolution aerial imagery and Sentinel-2 imagery. The vector labels were converted to a 10m resolution

raster dataset following initial processing. Conversion to a 10m resolution was achieved by first generating a 10m vector grid. For each square in the vector grid, the class with the largest intersecting area from the vector dataset was assigned to that square. However, where *Non-Vegetated* has the largest intersecting area and *Permanent Herbaceous* consists of between 10% and 50% of the intersecting area, the vector was assigned the class *Sparsely Vegetated*. This gridded vector dataset was then converted to a raster format. The updated label dataset is illustrated in Figure 5.7.

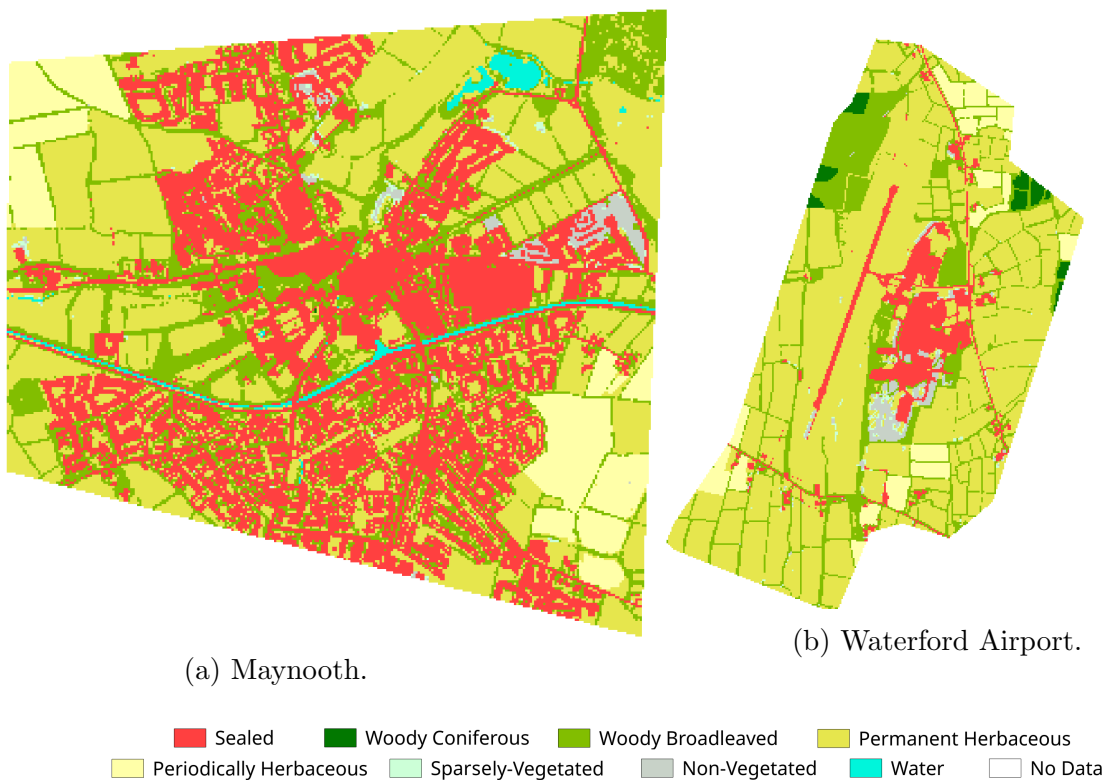


Figure 5.7: Modified labels for satellite-aerial assessment over a) Maynooth and b) Waterford Airport.

5.4 Results

The results of performing classification using a UNET model on aerial data is first presented followed by the second set of results associated with the satellite-aerial fusion techniques.

5.4.1 Aerial Classification Results

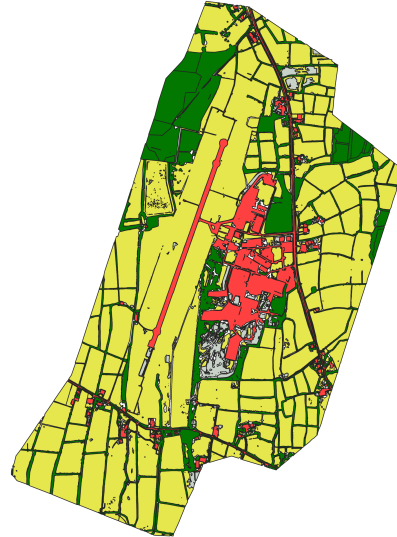
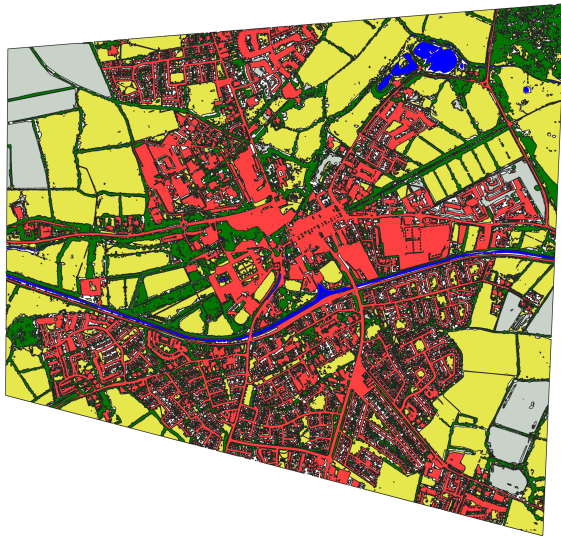
An accuracy of 92.16% and 92.50% was achieved for the training and validation datasets respectively. However, a lower accuracy of 84.70% was obtained for the test data. Table 5.4 lists the F1 score, weighted F1 and OA for each class of each site used in this assessment.

Table 5.4: F1 and OA results of aerial data classification using UNET architecture.

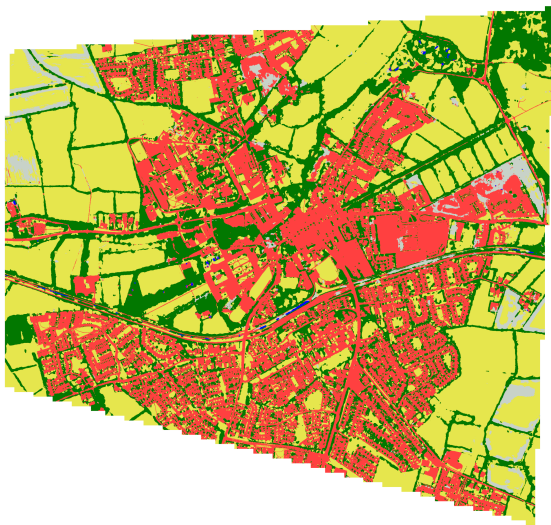
	Woody Vegetation	Herbaceous Vegetation	Non-Vegetated	Sealed	Water	Weighted F1	OA
Maynooth	0.765	0.875	0.625	0.922	0.206	0.843	0.847
Waterford Airport	0.938	0.983	0.780	0.957	N/A*	0.967	0.967
Sroughan	0.908	0.967	0.973	0.916	0.9972	0.9779	0.9775
Horsepasstown	0.953	0.974	0.910	0.954	0.999	0.976	0.976
Twomilebridge	0.963	0.967	0.911	0.971	0.920	0.962	0.962
Rathdown Upper	0.767	0.896	0.920	0.710	0.993	0.924	0.923

* No Water is present at the Waterford Airport site.

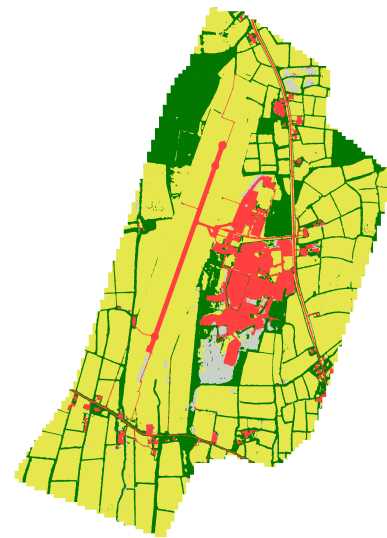
As can be seen in Table 5.4, the lowest F1 score was obtained from the classification of *Water* over the Maynooth Site. The output classification results over both Maynooth and Waterford Airport are detailed in Figure 5.8.



(a) Ground truth labels.



Maynooth.



Waterford Airport.

(b) UNET classification output.

■ Herbaceous Vegetation ■ Woody Vegetation ■ Non-Vegetated ■ Sealed ■ Water

Figure 5.8: Classification output of UNET model for Maynooth and Waterford Airport using aerial RGB Data.

5.4.2 Satellite-Aerial Fusion Results

Table 5.5 lists the weighted F1 and OA for each satellite model. The results of performing satellite-aerial class-corresponding fusion is displayed in Tables 5.6 and 5.7. Figure 5.9 illustrates the results of performing Class-Con satellite-aerial fusion using the S2SE prior model.

Table 5.5: Results for satellite only classification. The highest weighted F1 and OA for each site are highlighted with text in bold.

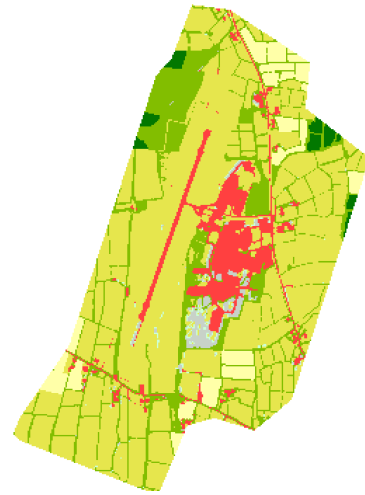
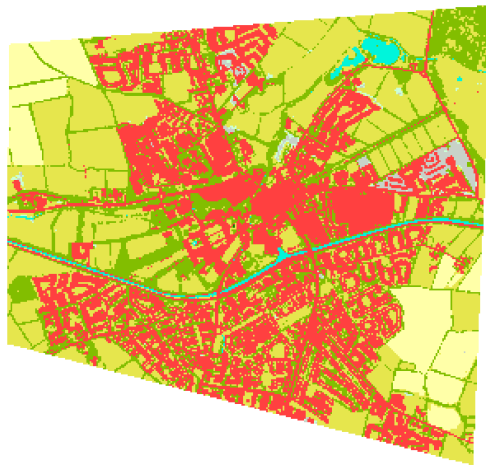
Satellite model	Maynooth		Waterford Airport	
	F1	OA	F1	OA
S1MO	0.460	0.501	0.647	0.663
S2SE	0.654	0.647	0.612	0.640
L8AN	0.322	0.372	0.376	0.435
SVM-Fused	0.601	0.604	0.554	0.593

Table 5.6: Results for Class-Con satellite-aerial fusion. The highest weighted F1 and OA for each site are highlighted with text in bold.

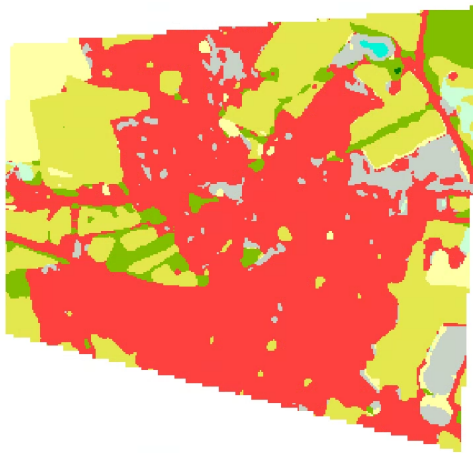
Satellite prior model	Maynooth		Waterford Airport	
	F1	OA	F1	OA
S1MO	0.784	0.7688	0.8456	0.8331
S2SE	0.794	0.789	0.859	0.859
L8AN	0.697	0.681	0.691	0.630
SVM-Fused	0.763	0.755	0.791	0.755

Table 5.7: Results for Cor-Prob satellite-aerial fusion. The highest weighted F1 and OA for each site are highlighted with text in bold.

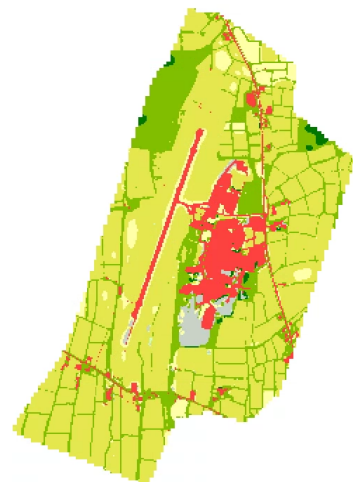
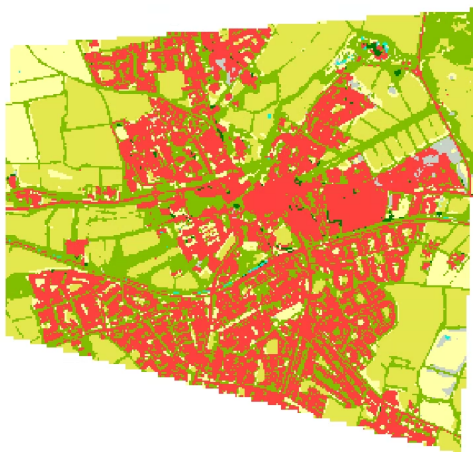
Satellite prior model	Maynooth		Waterford Airport	
	F1	OA	F1	OA
S1MO	0.767	0.752	0.837	0.823
S2SE	0.766	0.769	0.852	0.853
L8AN	0.66	0.641	0.687	0.706
SVM-Fused	0.720	0.719	0.770	0.733



(a) Ground truth labels.



(b) Satellite only classification.



(c) Satellite-aerial fused classification.



Figure 5.9: Results of performing Class-Con satellite-aerial fusion using S2SE prior classification.

The results of this assessment reveal a notable increase in classification accuracy as a result of satellite-aerial class-corresponding fusion for each satellite platform and each fusion type. Overall the highest classification accuracy was obtained using the Class-Con fusion approach with S2SE prior classification. The satellite-aerial fusion of S1MO prior classification resulted in a significant increase in classification accuracy, with fused results only marginally lower than with the S2SE prior model.

5.5 Discussion

This study demonstrates that, aerial data can be fused with satellite data to significantly improve classification accuracy through the use of a decision-level fusion approach. To further examine the impact of satellite-aerial fusion, the change in LCC relative to satellite only classification was examined. The spatial location and distribution of the change in LCC, as a result of satellite-aerial Class-Con fusion relative to the classification output of the S2SE prior model is detailed in Figure 5.10. The classification change illustrated in this image is divided into three categories. Table 5.8 lists the percentage change from each category. The three categories of change are defined as follows:

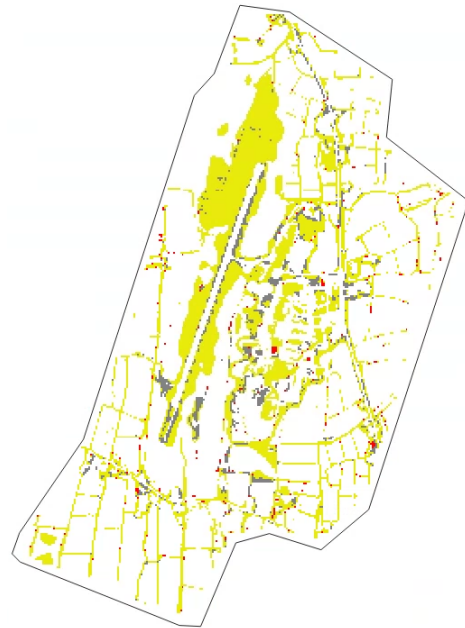
- *Positive Change* : where the fusion corrected a previously misclassified pixel.
- *Negative Change* : where the fusion resulted in the misclassification of a previously correctly classified pixel.
- *Neutral Change* : where both the prior classification and fused classification were incorrect.

Table 5.8: Classification change due to satellite-aerial Class-Con fusion relative to satellite only classification.

	Maynooth	Waterford Airport
Positive Change	15.81%	21.30%
Neutral Change	5.59%	3.42%
Negative Change	1.68%	0.66%



(a) Maynooth.



(b) Waterford.

Unchanged
 Positive Change
 Neutral Change
 Negative Change

Figure 5.10: Illustration of classification change due to satellite-aerial Class-Con fusion relative to satellite-only S2SE classification.

The application of satellite-aerial fusion resulted in significant positive classification change as can be seen in both Figure 5.10 and Table 5.8. Visual inspection of Figures 5.9 and 5.10 reveals that a significant proportion of the change occurs at the boundary of existing classes and with the classification of small linear features misclassified by the satellite data. However, there are examples of larger areas that experienced positive change as a result of satellite-aerial fusion, such as the reclassification of the *Sparsely Vegetated* class to the *Permanent Herbaceous* class in the Waterford Airport site.

One notable observation in this assessment is the relatively poor performance of the SVM-Fused satellite prior model. In Chapter 4, it was observed that the application of SVM decision-level fusion could obtain significantly higher classification accuracy over mono-platform models. However, the SVM-Fused model before satellite-aerial fusion resulted in lower classification accuracy than the S2SE model for both sites and the S1MO model for the Waterford site. The application of satellite-aerial fusion resulted in a significant improvement in the classification accuracy for the SVM-Fused model.

However, for both Class-Con and Cor-Prob Fusion the use of the S2SE and S1MO models outperformed the SVM-Fused model. The application of L8AN resulted in the lowest classification accuracy of both the satellite only classification and the satellite-aerial fused classification. Landsat-8 has the lowest spatial resolution of the three assessed satellite platforms, with a spatial resolution of 30m. This lower spatial resolution is likely a contributing factor to its lower classification results. Additionally, as the L8AN model utilised annually averaged data, it may be less suitable to differentiate temporal classes such as *Periodically Herbaceous* and *Permanent Herbaceous*. The L8AN model is used as one of the prior input models for the SVM-Fused model. Therefore, the poor classification result of the L8AN models over the assessed sites is likely a contributing factor to the results obtained by the SVM-Fused model.

This assessment demonstrated how, through the use of a decision-level fusion approach, aerial data could be used to refine satellite derived LCC. This assessment is not unique in the application of fusion techniques for the fusion of medium and high-resolution imagery. As highlighted in the literature review, the majority of studies performing fusion between medium and high-resolution imagery perform pixel-level fusion. The study by Wendl et al. (2018) performed decision-level fusion using Sentinel-2 multi-temporal imagery and 1.5m resolution mono-temporal Spot-6 satellite data. Alongside the difference in platform and resolution, the use of differing but relatable class schemas between the models to be fused is an important finding in this PhD study. The study by Wendl et al. (2018) demonstrates how high-resolution imagery can be used to improve classification results obtained from medium resolution multi-temporal imagery. While not examined in this study, it is proposed that very high-resolution satellite platforms such as WorldView-3 and Pléiades Neo, with a resolution of 0.31m and 0.30m GSD respectively (AIRBUS, 2022; ESA, 2022) could be used as an alternative to aerial imagery. However, further examination of this topic would be required.

5.5.1 Spatially Derived Sparsely Vegetated Class

The most notable example of reclassification over a large area as a result of satellite-aerial fusion was observed in the Waterford Airport Site. The reclassification occurred over an area originally misclassified as *Sparsely Vegetated*. This area was reclassified as *Permanent Herbaceous* as a result of the fusion process. Examination of the high-resolution imagery in this area reveals a significant proportion of visible bare ground between the vegetation, as visible in Figure 5.11, which may explain the satellite misclassification. However, with the area predominantly vegetated, the *Permanent Herbaceous* class is the correct classification for this area.

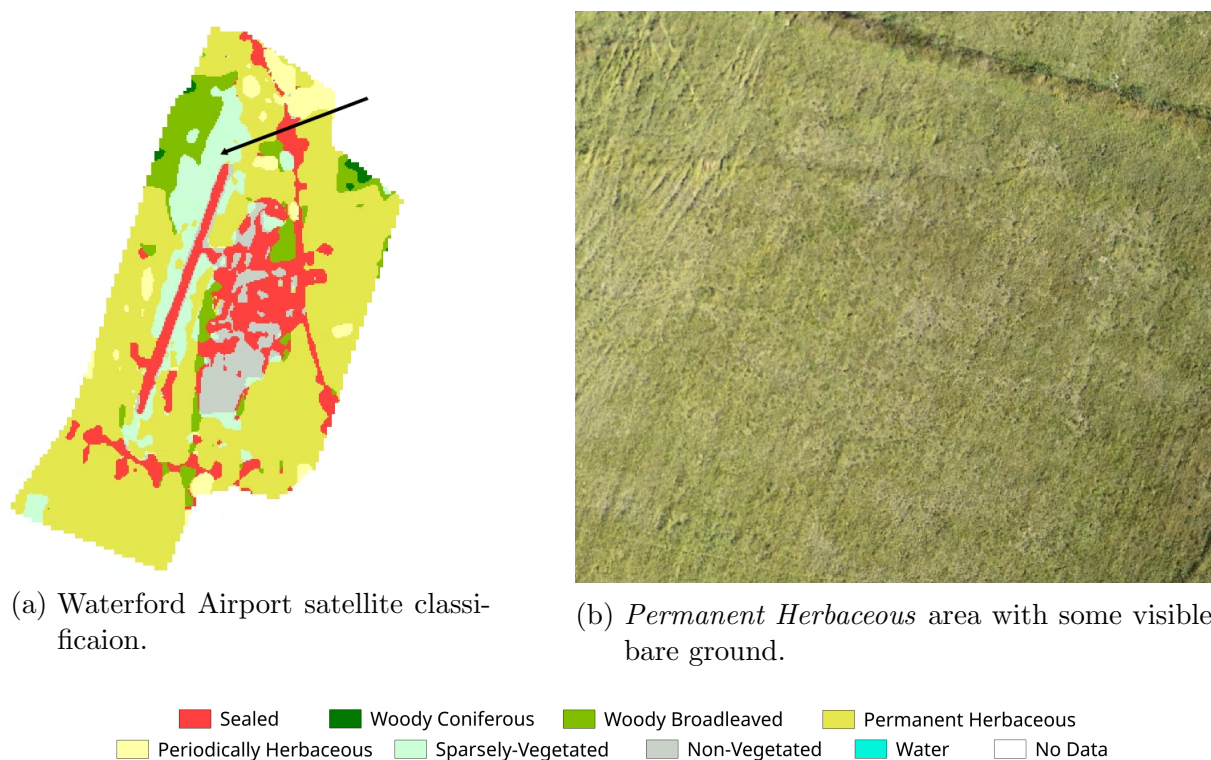


Figure 5.11: Example of *Permanent Herbaceous* with some visible bare ground resulting in misclassification as *Sparsely Vegetated*.

This change in class is a result of the assignment of the *Sparsely Vegetated* class based on the proportions of *Permanent Herbaceous* or *Non-Vegetated* classified pixels during resampling of the fused data from 0.25m data to 10m. The decision to use this approach to derive the *Sparsely Vegetated* class was partially driven by issues encountered when deriving the class based on the satellite prior probability as with other classes. Initial assessments using the satellite prior probability in a similar manner to the *Herbaceous*

Vegetated class resulted in some noticeable misclassifications after fusion. Figure 5.12 illustrates a location which was misclassified as *Sparsely Vegetated* as a result of Class-Con fusion where the *Sparsely Vegetated* class was determined by the satellite prior probability. This misclassification occurred most frequently in urban areas. The mix of artificial surfaces and vegetation in these areas may result in similar spectral properties of the *Sparsely Vegetated* class at a 10m resolution. Therefore, a higher prior probability from satellite models would be expected for the *Sparsely Vegetated* class than for the *Periodically Herbaceous* or *Permanent Herbaceous* classes.

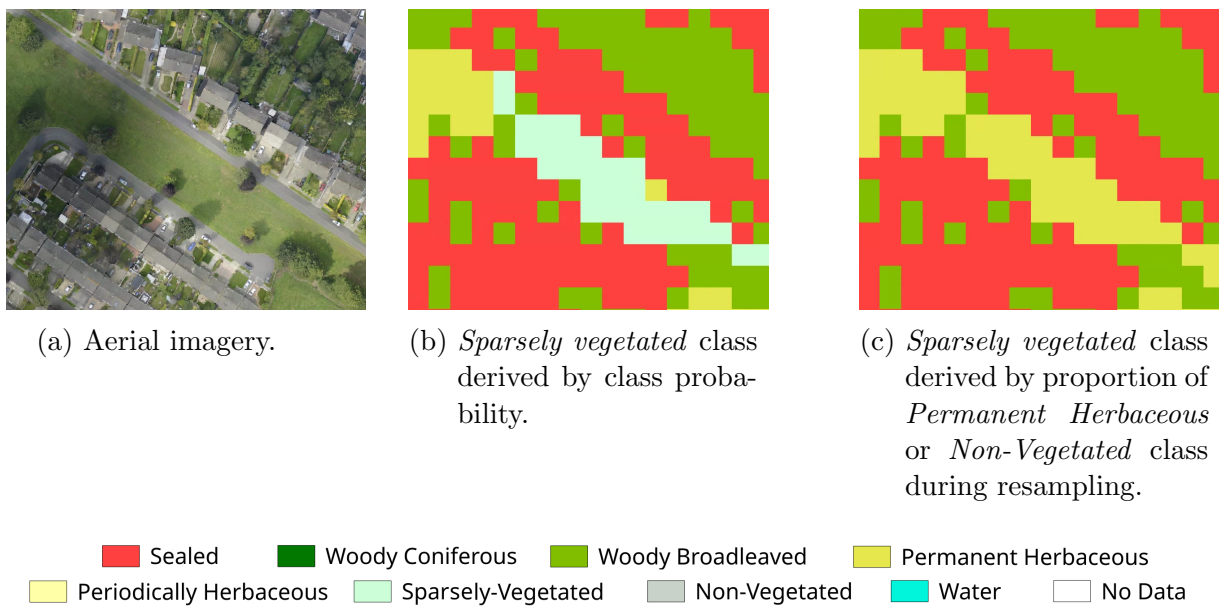


Figure 5.12: Comparison of *sparsely vegetated* class derived by (b) probability vs (c) proportion of *Permanent Herbaceous* or *Non-Vegetated* class during resampling.

It is noted that in regions under assessment, there are very few examples of areas that should be defined as *Sparsely Vegetated*. To fully assess the accuracy of defining *Sparsely Vegetated* class through this methodology, additional surveys over areas containing significant *Sparsely Vegetated* cover would be required to fully assess the benefit of this technique.

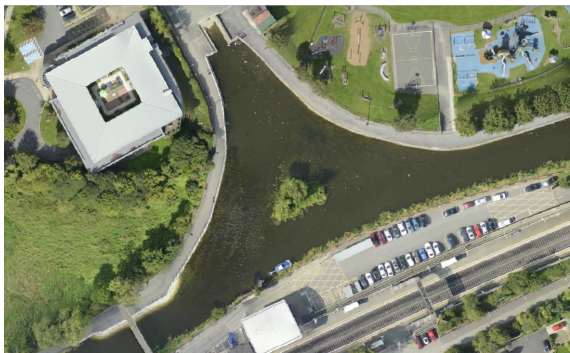
5.5.2 Aerial Data Classification Issues

With the implementation of satellite-aerial fusion resulting in a significant change in classification accuracy over the test regions under assessment, any errors in aerial classi-

fication can significantly impact the fusion results.

5.5.2.1 Misclassification of Water

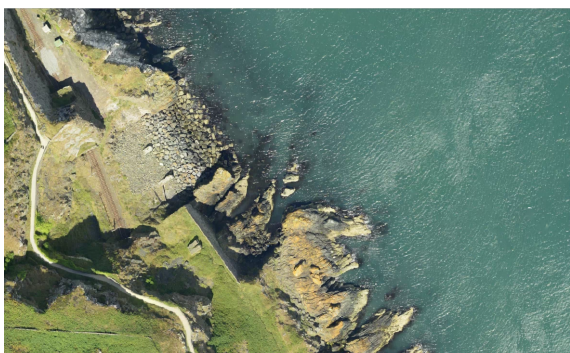
During this assessment, the classification of *Water* over the Maynooth site resulted in the lowest aerial class F1 score. Examination of the locations misclassified over the Maynooth site highlighted a potential reason for this result. Over the Maynooth site, the two main water bodies are the Royal Canal running through the town and a small reservoir to the North-West of the site. Figure 5.13 displays the two water bodies in the Maynooth site along with examples of other water bodies included as part of the training dataset. The appearance of water in the Rathdown Upper site or Horsepasstown site differs significantly from the appearance of the canal or reservoir water in the Maynooth site, as can be seen in Figure 5.13. The reservoir in particular, contains significant vegetation cover within the water body.



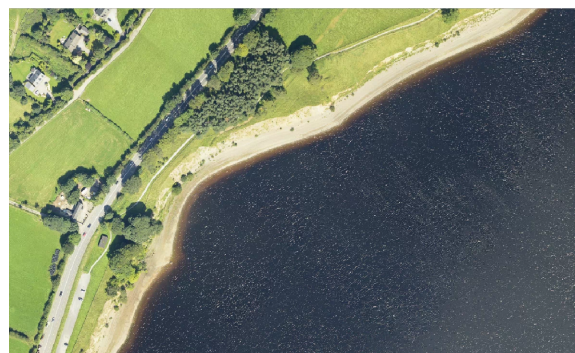
(a) Maynooth Canal.



(b) Maynooth Reservoir.



(c) Rathdown Upper.



(d) Horsepasstown.

Figure 5.13: Examples of four water bodies from the aerial dataset with notably different appearances.

The noticeable difference in visual appearance between the water bodies in the training sites and the water bodies in the Maynooth site is likely a contributing factor to the poor classification results. Additional surveys over canals and similar water bodies would be required to overcome this issue and to ensure the model is suitably trained for their classification. Examination of the satellite only classification reveals the satellite models also misclassified these water bodies. Therefore, the misclassification in the aerial data is not expected to have a significant negative impact on the final classification results. Aerial misclassification such as this is particularly important when employing Class-Con fusion. Under Class-Con fusion both the *Water* and *Sealed* classes are 100% determined by the aerial classification results. Therefore, any misclassification in the aerial data disproportionately impacts the final classification. For instance, Figure 5.14 provides an example of the misclassification of *Herbaceous Vegetation* as *Water* in the aerial data.

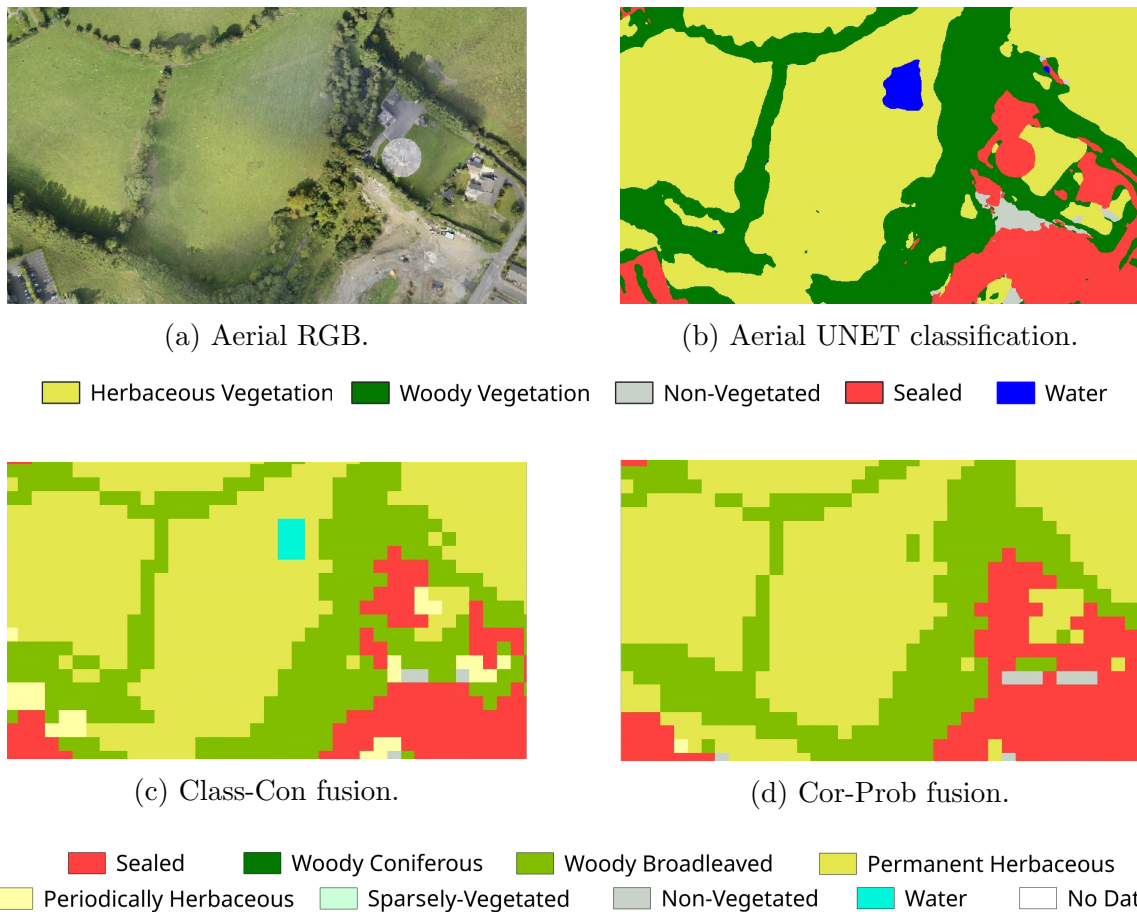


Figure 5.14: Example of b) UNET misclassification and its impact on c) Class-Con fusion and d) Cor-Prob fusion.

As a result of the aerial misclassification, the application of the Class-Con Fusion

resulted in misclassification in the fused data. However, while the application of Cor-Prob fusion resulted in a lower weighted F1 score for the Maynooth site, as is visible in Figure 5.14, its application is less prone to the issue of aerial misclassification.

5.5.2.2 Misclassification of Non-Vegetated areas

The second-lowest aerial classification F1 score obtained on the Maynooth test site was for the *Non-Vegetated* class. This was also the lowest F1 score for the Waterford Airport site. Examining these results reveals that a major contribution to this is the misclassification over arable land. In these instances, *Non-Vegetated* cover was misclassified as *Herbaceous Vegetation*. The misclassification of *Non-Vegetated* land cover as *Herbaceous Vegetation* over arable cropland can be seen in Figure 5.15. Vegetation is visible, at various stages in crop development, in each field as depicted in Figure 5.15. This issue is likely to be prevalent in dynamic cultivated land, especially at the start of the growth season when crops are beginning to sprout and bear leaves. While this issue impacts the calculated F1 score for the aerial classification, it is not expected to negatively impact the fusion results with both classes related to the *Periodically Herbaceous* class.

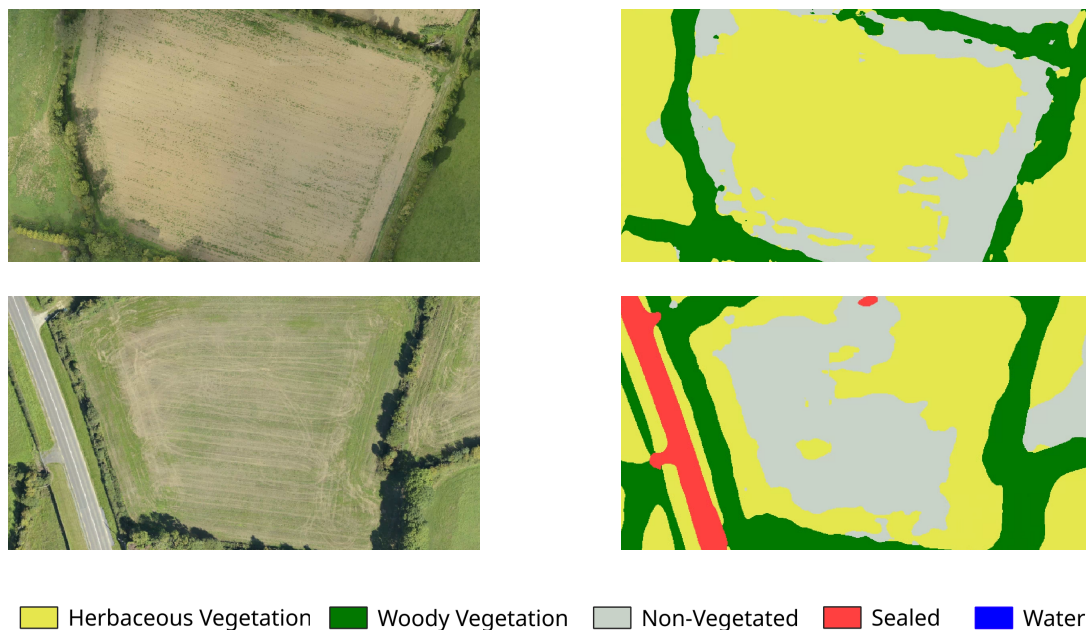


Figure 5.15: Non-Vegetation misclassification examples for Maynooth top and Waterford bottom.

5.6 Conclusion

This chapter demonstrates how high-resolution aerial data can be fused with medium resolution satellite data to improve classification in comparison to satellite only classification. A decision-level fusion approach was used with differing but comparable class schemas for each platform. Aerial classification was performed using a modified UNET model for the classification of five land cover classes. In contrast, satellite prior models were trained to classify eight land cover classes. Overall, higher classification results were obtained using a Class-Con fusion approach with the S2SE prior model. However, it is recognised that under the Class-Con fusion approach, the classification of the *Sealed* and *Water* classes is solely derived from the aerial model. Examination of the results reveals that the classification of the *Sealed* class is noticeably better with aerial data than with any of the assessed satellite models. Under this approach, the classification of the inherently temporal classes is derived based on the multi-temporal satellite data.

Some issues with the classification of water bodies using aerial data were observed over the Maynooth site. While it is expected that this issue may negatively impact classification accuracy, these water bodies were also misclassified by the satellite models. As a result, the misclassification of the aerial data had no negative impact on the classification result.

Key contributions:

1. The demonstration of the class constrained (*Class-Con*) decision-level fusion approach for the fusion of satellite and aerial data. The application of Class-Con fusion improved the weighted F1 score from 0.654 to 0.794 over the Maynooth site and 0.647 to 0.859 over the Waterford Airport site. This approach to fusion enables the incorporation of mono-temporal data to improve classification in a situation with an inherently temporal class. Due to the prohibitive cost of aerial surveys, capturing and including aerial data would otherwise be unviable. This approach to data decision-level fusion can also be utilised for the fusion of high-resolution satellite data along with the multi-temporal satellite data.

-
2. The assignment of the *sparsely vegetated* class during resampling to 10m GSD was also proposed as a potential methodology to more accurately represent classes which are derived based on a proportion of other classes. While further examination would be required, this approach to the classification of the *sparsely vegetated* class may be more appropriate than the use of multi-temporal multi-spectral medium resolution satellite data.

Chapter 6

Conclusion

6.1 Introduction

The generation of high accuracy and frequently updated LCC products pose many challenges. This thesis set out to demonstrate techniques that could be utilised to increase the classification accuracy of an annually generated LCC product using the specification for the generation of the CLC+ Backbone raster product as a guideline. Through the undertaking of the literature review, gaps in the current knowledge were identified. Based on these gaps in knowledge, three research questions were identified:

Question 1: *What ML techniques are suitable for mono-platform satellite-derived annual LCC on the island of Ireland?*

In North Atlantic regions such as on the island of Ireland, frequent cloud cover limits the availability of satellite optical data. As a result, it may not always be possible to capture sufficient optical satellite data to generate accurate LCC products. By addressing this research question, the extent to which frequent cloud cover impacts the generation of LCC products on the island of Ireland could be examined. In addition, addressing this question provided an opportunity to perform a comparative assessment of ML techniques to determine their suitability for the generation of the CLC+ Backbone raster product on the island of Ireland.

Question 2: *How can a multi-sensor satellite data fusion approach be employed where frequent cloud cover results in differences in sensor data availability over the area that is being assessed?*

The use of data from multiple sensors (sensor fusion) has been demonstrated in many studies to improve the accuracy of LCC. However, due to frequent cloud cover, over a large region, there will inevitably be differences in the availability of data from optical satellite platforms. In addressing this question, practical applications of sensor fusion were examined, suitable for a scenario where the availability of input data varies across the assessed region.

Question 3: *Can aerial data be used to further improve the accuracy of multi-sensor satellite-derived LCC?*

During the literature review, few studies were identified examining the fusion of aerial and satellite data for LCC. The ability of aerial data to capture high spatial resolution imagery has the potential to significantly improve classification accuracy, particularly around class boundaries where mixed spectral information from medium spatial resolution satellites may result in misclassification. In addition, light aircraft have the ability to fly beneath cloud cover, which is a trait particularly useful on the island of Ireland. By addressing this research question, this thesis aimed to examine how the benefits of aerial data can be used to improve satellite derived LCC products.

A concise summary of the contributions of this thesis will be provided in **Section 6.2** and potential future work to be carried out will be outlined in **Section 6.3**. Final Remarks will then be provided in **Section 6.4**.

6.2 Main Findings

The contributions of this thesis will be discussed in terms of how they address this thesis's three research questions.

6.2.1 Research Question 1: Suitability of ML for Mono-platform Satellite-derived Annual LCC

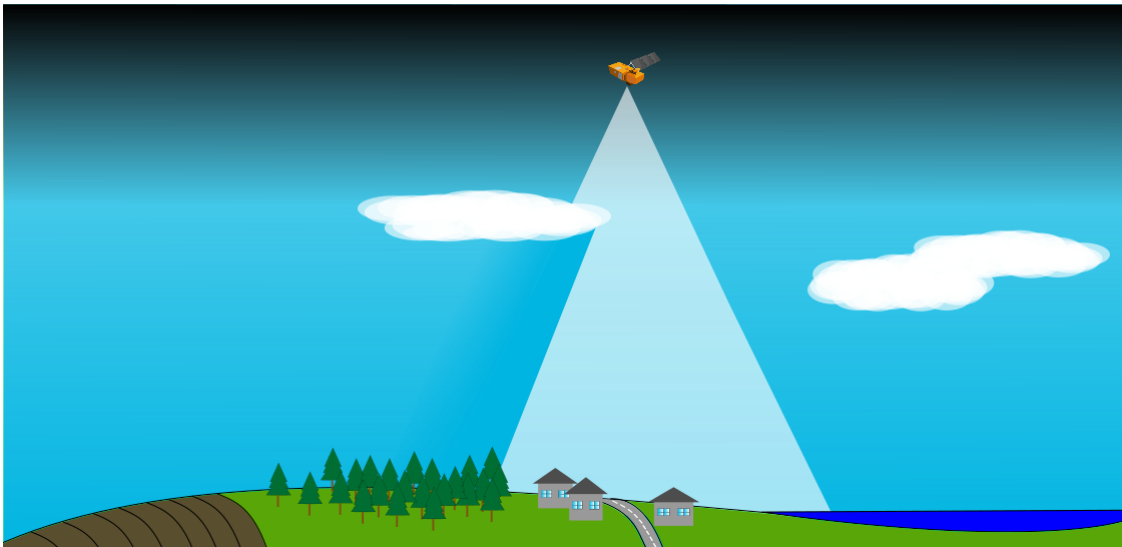


Figure 6.1: Conceptual illustration for mono-platform satellite LCC.

The LFCNN and 3DLFCNN architectures were proposed in Chapter 3 as part of the assessment of ML techniques for the generation of an annual LCC product. These architectures were observed to outperform the point-based techniques such as SVMs, RFs and ANNs on similar datasets. An additional benefit of the proposed architectures is that their application resulted in a substantial reduction in computation time for the classification of large image patches, making them ideal for generating LCC datasets over a large area.

Another contribution of the assessment undertaken in Chapter 3 was the confirmation of results obtained by Carrasco et al. (2019). In both their and this study, it was found that the number of observations used to generate an averaged dataset and the number of temporal splits in the averaged datasets significantly increases classification accuracy.

Finally, in Chapter 3, to assess mono-platform suitability, the percentage area of each

region where each model could be employed (model coverage) was assessed based on the requirement for a minimum of six observation and manually digitised cloud masks. This assessment revealed that none of the assessed techniques were identified to have 100% coverage over all regions. The various LCC modelling techniques explored and developed during the course of this research highlight the critical influence and impact of cloud cover on satellite RS products over North European countries such as Ireland.

6.2.2 Research Question 2: Multi-sensor Satellite data Fusion using Sensor Data Inputs that Vary in Terms of Availability

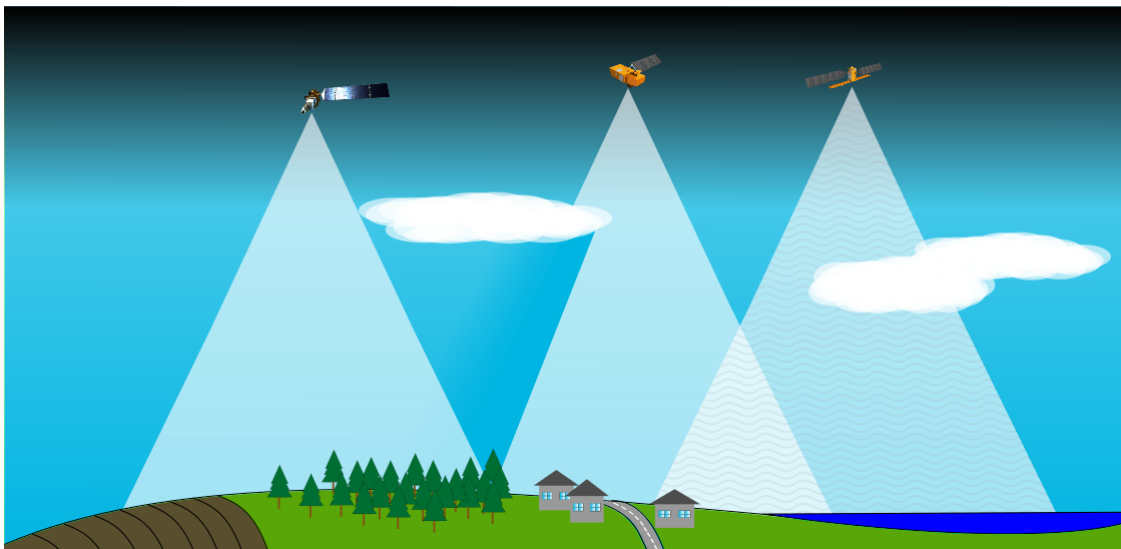


Figure 6.2: Conceptual illustration for multi-platform satellite LCC.

To evaluate multi-sensor satellite data fusion techniques, a two-part assessment was undertaken in Chapter 4. The first part was a comparative assessment of pixel-level and decision-level fusion techniques. The assessment results demonstrated that the application of decision-level fusion could produce better classification results over the assessed region, corroborating the results of a study by Useya and Chen (2018).

The second part of this assessment was the evaluation of several decision-level fusion techniques suitable for fusion over a region with variable data availability. The averaging of prior probabilities from each combination of SVM fused model (Full-SVM averaging)

obtained the highest classification results in this assessment. However, with seven prior models, a total of 101 SVM fused models were trained and used during inference. The averaging of only SVM fusion models that were generated using pairs of prior models (Dual-SVM averaging) was proposed as a means of limiting the number of SVM models to be trained. It was observed that the Dual-SVM averaging approach could obtain comparable results to Full-SVM averaging while only requiring the training of 14 SVM fused models. The proposed approach to fusion was demonstrated not only to be suitable for the generation of high accuracy classification products but may also be suitable for the inclusion of data from additional EO platforms not evaluated in this assessment.

6.2.3 Research Question 3: Satellite-Aerial Data Fusion

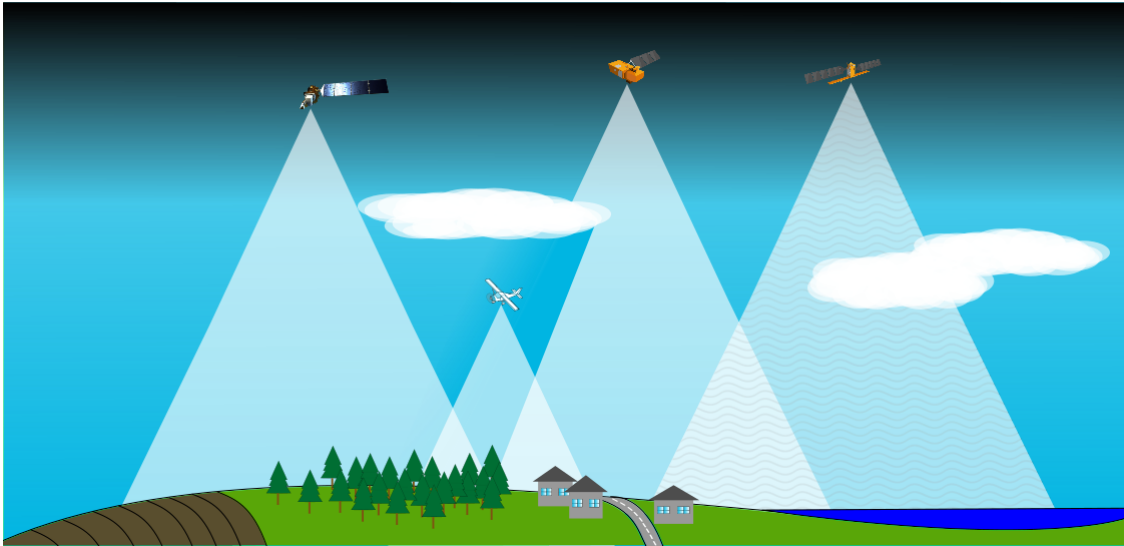


Figure 6.3: Conceptual illustration for multi-platform satellite and aerial LCC.

The use of a decision-level fusion approach for the fusion of satellite and aerial data was examined in Chapter 5. A single aerial survey lacks the temporal information necessary to classify the inherently temporal land cover classes in the CLC+ Backbone raster product. Therefore, a class-corresponding decision-level fusion approach was proposed. A simplified classification structure was derived for the aerial dataset. This simplified classification structure was designed such that each aerial class directly corresponded to one or more satellite classes used in Chapters 3 and 4. Two variations of class-corresponding decision-level fusion were examined; a class constrained fusion approach and a correspond-

ing probability fusion approach. The application of the class constrained fusion approach obtained higher classification accuracy in this assessment. Additionally, the use of high-resolution imagery for assigning the *sparsely vegetated* class during resampling to 10m GSD was also proposed. However, insufficient data was available to comprehensively evaluate this technique. The results of this assessment demonstrated that the proposed satellite-aerial fusion methodology could be implemented as a practical approach that increased classification accuracy over the assessed regions.

6.2.4 Summary of Contributions

1. The proposal and evaluation of the LFCNN and 3DLFCNN architectures. The application of proposed architectures have the following advantages:
 - These ML architectures are suitable for training on sparse point data but can be used for inference of an image output without modification of the architecture.
 - They are computationally faster inference time over large areas than other assessed point-based ML techniques.
 - The LFCNN and 3DLFCNN architectures produce the highest classification accuracies of the mono-platform ML techniques, which were evaluated in this study.
2. The proposal and evaluation of Full-SVM fused averaging and Dual-SVM fused averaging approaches. These proposed fusion methodologies provided the following contributions:
 - These methodologies are suitable for performing multi-sensor data fusion over an area where data available from each platform may differ at each given location.
 - Full-SVM fused averaging obtained the highest classification accuracy of the assessed sensor fusion techniques.

-
- Dual-SVM fused averaging provides a lower computational cost alternative to Full-SVM fused averaging with a minimal reduction in classification accuracy.
3. The proposal and evaluation of a satellite-aerial decision-level fusion approach suitable for the fusion of models with differing but relatable classification schemas ‘class-corresponding fusion’. The application of the proposed satellite-aerial fusion technique had the following benefits:
- The proposed fusion methodology enables the fusion of mono-temporal aerial data with multi-temporal multi-modal satellite data.
 - The application of the proposed fusion methodology resulted in LCC accuracy improvements in the assessed sites relative to classification performed using satellite data alone.
 - The proposed fusion methodology enabled the assignment of the *Sparsely Vegetated* class based on the proportion of *Permanent Herbaceous* and *Non-Vegetated* in contributing pixels when resampling the fused data from 0.25m to 10m. This approach to classifying the *Sparsely Vegetated* class reduced classification error over the assessed sites.
4. Critically assessing and confirmation of the following studies by:
- Carrasco et al. (2019) who identified the relationship between classification accuracy and the number of temporal splits and observation count per split.
 - Useya and Chen (2018) who demonstrated that decision-level fusion can outperform pixel-level techniques for LCC.

6.3 Recommendations and Future Work

The work undertaken in this thesis examined a broad range of ML and sensor fusion techniques for LCC. However, through this work, several topics were identified that require further research and analysis in order to ensure the efficient and timely production of high-quality LCC maps.

6.3.1 Refinement of LFCNN architecture

In Chapter 3, the LFCNN structure was demonstrated to be suitable for high accuracy classification, rapid inference over large areas and training on sparse point data sources. However, there are some limitations to the evaluation undertaken in this thesis that could be addressed in future studies.

An issue identified in Chapter 3 was the difficulty of training a 3DLFCNN architecture using the six-monthly Sentinel-2 data. One possible reason for this issue is the number of trainable variables in the models. The difficulty in training models with a large number of training variables may also explain the difficulty in training LFCNN models with an input patch size greater than 9×9 pixels. This issue may be overcome by simply increasing the size of the training dataset. Alternative approaches to address this issue include modification of the architecture to result in fewer training variables or the application of techniques such as ‘transfer learning’. Transfer learning is the process of pre-training a network or part of a network on an independent dataset before training on the target dataset (Xu et al., 2017).

A significant limitation of the comparative assessment undertaken in Chapter 3 was the lack of a comparison between the LFCNN architecture and other patch-to-patch fully convolutional neural networks. However, due to the issue of obtaining sufficient fully segmented labelled data over the assessed region, it was not possible to train a patch-to-patch fully convolutional neural networks during the comparative assessment undertaken in Chapter 3.

6.3.2 Decision-level vs Feature-level Fusion

While not examined in this thesis, the application of feature-level fusion has significant advantages when performing sensor fusion. In Chapter 4, the utilisation of decision-level fusion was demonstrated to be a practical and high-accuracy methodology for the fusing of data from diverse sources. However, there is a significant degree of information loss in the application of decision-level fusion. In comparison, in both pixel-level and feature-level fusion, significantly more information about the relationship between the

data from each sensor is retained. The primary drawback of the application of feature-level fusion in a region with variable data availability is the requirement to design a specific model architecture for each combination of sensor data to be fused. Additionally, The application of feature-level fusion poses many of the same issues identified during the application of pixel-level fusion, such as the limited number of overlapping sample points. However, further examination would be required to determine if decision-level fusion is more suitable than feature-level fusion over the assessed regions.

6.3.3 Satellite-Aerial Fusion for Sparsely Vegetated Regions

When examining the implementation of satellite-aerial fusion in Chapter 5, the assignment of the *sparsely vegetated* class during resampling to 10m GSD was examined. Under this approach, it was assumed that at a spatial resolution greater than 1m, Sparsely vegetated regions can be re-classified as either *Herbaceous Vegetation* or *Non-vegetated*. When resampling to a 10m resolution, the assignment of the *Sparsely Vegetated* class was then determined based on the proportions of *Herbaceous Vegetation* and *Non-vegetated* pixels to be resampled. While this approach to defining the *Sparsely Vegetated* class was utilised in Chapter 5, it was acknowledged that the regions where this technique was employed were largely devoid of sparsely vegetated cover. Therefore, further studies in regions with significant areas of sparse vegetation are required to fully understand the impact of implementing the proposed satellite-aerial fusion technique.

6.3.4 Alternative Label Data Sources

A significant challenge identified throughout the undertaking of this thesis was obtaining sufficient and accurate labels to train and evaluate the ML models. During this assessment, an aggregated data source methodology was used for the generation of a label datasets. However, it was recognised that this process was not ideal, not only due to identified miss-labelling but due to issues in the correlation between the original label data source and the aggregated label. The primary example of this issue is the lack of a *Periodically Vegetated* class in the original data source. Therefore, the source for the

Periodically Vegetated class in both the Copernicus Coastal Zones 2018 and Copernicus Urban Atlas 2018 datasets was *Arable land*. While periodic vegetation is commonly a result of arable agriculture, the definition of this class encompasses other instances of periodic vegetation which may occur outside of an agricultural setting. Given the challenges posed by aggregated data sources to generate label data suitable for the CLC+ Backbone raster product classification schema, the generation of a bespoke label dataset for this purpose would be required. This process would ensure that for each class, a profile of its spectral, spatial and temporal fingerprint could be generated.

6.3.5 Fusion of Alternative Data Sources

The fusion of sensor data with distinctly different characteristics was examined in this thesis. However, there is a significant number of alternative EO data sources that could be included in a multi-sensor ML fusion analysis for LCC. In theory, the application of a decision-level fusion approach can enable the fusion of almost any additional EO platform data regardless of its spectral or temporal properties. However, some issues may arise where there is significant variations in the spatial characteristics of the platforms. Studies have examined the fusion of low-resolution satellite data such as the Moderate Resolution Imaging Spectroradiometer (MODIS), which has a spatial resolution of 250m to 1km (NASA, 2022) and Visible Infrared Imaging Radiometer Suite (VIIRS), which has a spatial resolution between 250m to 750m (NASA, 2021b) with medium resolution data such as Landsat-8 or Sentinel-2 using pixel-level fusion techniques (Shen et al., 2013; Jia et al., 2014; Shen et al., 2022). However, further research would be required to examine how data from these platforms could be used to improve the generation of an annual LCC product.

The inclusion of a variety of high and very high-resolution sensors and platforms could also be explored. As outlined in Chapter 5, very high-resolution satellite data from platforms such as WorldView-3 and Pléiades Neo may provide comparable results to aerial RGB data. Additionally, both of these satellite platforms provide multispectral data that is likely to improve classification results over RGB imagery. There are also

a variety of additional sensor data that can be captured from aerial or UAV platforms, such as multispectral, hyperspectral or LiDAR data, providing additional information to improve classification accuracy. Determining the benefit of including this additional information in the generation of a CLC+ Backbone raster product is an area where significant research could be conducted.

6.3.6 Recommendations for the practical implementation of annual LCC on the island of Ireland.

Several considerations are needed when examining the practical challenges of generating an annual national land cover dataset for the island of Ireland. These considerations include the spatial resolution of the data, the choice of an appropriate land cover schema, and the challenges of obtaining sufficient label data to generate and validate the accuracy of the dataset.

The spatial resolution of a LCC product significantly impacts many other characteristics of the product, including the choice of classification schema and the data source used for its generation. The national land cover dataset scheduled to be released in 2022 is intended as a high-resolution dataset incorporating high-resolution satellite and aerial data. However, the cost of data capture and the time requirement for its generation and validation impede the generation of an annual product at this resolution. Given this challenge, the generation of a medium-resolution LCC product of around 10m may be more suitable for an annual product. A product of this resolution would facilitate the use of medium-resolution satellites such as Sentinel-1, Sentinel-2 or Landsat-8 in its generation.

The choice of classification schema is one of the most important considerations in the generation of any LCC product. The choice of classification schema not only needs to consider the intended use of the product but also needs to be reliably and accurately discernible using the data used for its generation. Where a classification schema is chosen that is unsuitable for the spatial, spectral or temporal resolution of the input data substantial misclassification may occur. Therefore, the choice of classification schema should account for the limitations of EO data and only include classes that can be accurately clas-

sified from the given EO sources. The *Woody shrub/brush* class is an example of a class in the CLC+ backbone dataset that is challenging to classify using medium-resolution satellite data alone. Preliminary analysis in Chapter 3 using Sentinel-1, Sentinel-2, and Landsat-8 revealed that it was not possible to accurately classify the *Woody shrub/brush* class. It was concluded that as a class primarily defined based on height, height information would be required for its classification. If the *Woody shrub/brush* class was to be included, elevation information would be required from high-resolution SAR satellite sources such as TerraSAR-X or from tri-stereo capable optical satellite platforms such as Pléiades or WorldView-3. Alternatively, aerial platforms capturing LiDAR data or height derived from aerial photogrammetry could also be used as the source of height information. While multiple observations would be required for the derivation of inherently temporal classes, such as the *Periodically Herbaceous* class, a single height measurement for the year would be appropriate for the purpose of defining the *Woody shrub/brush* class. In practice, a classification schema for an annual LCC product could be based on the schema used for the CLC+ Backbone raster product but exclude the *Woody shrub/brush* class. Under this approach, the use of multitemporal medium-resolution data could be used for the classification of all classes of the annual product. For each year that the CLC+ Backbone raster product is to be updated, height data could then be captured and used to reclassify classes such as *Woody Broadleaved* or *Woody Coniferous* based on a defined height threshold.

The use of very high-resolution aerial data was successfully demonstrated in this thesis as a means of improving satellite-derived LCC in complex non-homogenous regions. However, the capture of sufficient aerial data for its application across the island of Ireland is prohibitively expensive. The use of very high-resolution satellite data from platforms such as WorldView-3 and Pléiades Neo could also be used for this purpose. Alternatively, the capture of very high-resolution data could be targeted to known non-homogenous areas identified from the medium-resolution satellite data where its application would result in the greatest improvement in classification accuracy. Additionally, this data does not need to be captured each year as many of the features may not change year to

year. Instead, medium-resolution satellite data could be used to identify regions where significant change may have occurred since the previous surveys, enabling the targeted capture of additional data.

In this thesis, obtaining sufficient and appropriate labelled data was one of the largest challenges encountered when attempting to perform LCC using ML techniques. The production of an annual LCC product using ML techniques would require the generation of an updated labelled dataset for each year. The generation of sufficient land cover labels is exceptionally time-consuming. This is further exacerbated by the generation of fully segmented labels used for the training of patch-to-patch based CNN architectures. Considering this time requirement the generation and annual updating of a point-based label dataset would be recommended. This dataset could be used in conjunction with patch-to-point based CNN architectures for classification such as the LFCNN architecture proposed in this thesis. To further reduce the burden of annually updating labels, the use of LCC or EO data from previous years may also aid in the identification of potential training labels for each year. New label datasets would be required to retrain/refine ML models for each year to account for annual variations in land cover spectral and temporal signatures. Using the previous year's LCC data as a reference and EO data to identify change, it may be possible to indicate the suitability of existing labels and identify potential locations for new LCC labels. However, manual verification of this label data would still be required to ensure data quality.

The collection of in situ data and the manual photointerpretation of imagery are time expensive procedures. Therefore, the application of such manual procedures in an annually generated product should be limited with classification primarily performed using ML from EO data. While there are a wide array of ML techniques, the utilisation of CNN based architectures for optical data has been demonstrated to increase classification accuracy relative to other ML techniques. The increased classification accuracy of CNN was not only demonstrated in this thesis but also identified in several studies presented in the literature view of this thesis. As identified above, a patch-to-point based CNN architecture may be more suitable due to the challenge of obtaining sufficient fully

segmented label data. However, point-based techniques would be recommended where classification is performed using Sentinel-1 data. If no inherently temporal LCC classes are present in the classification schema, the use of annually averaged EO data may be suitable. However, for the classification of inherently temporal LCC classes such as *Periodically Herbaceous*, the use of multi-temporal data and temporal ML techniques would be required. For optical data, the use of 3D CNN architectures would be recommended, while a 1D CNN architecture would be required for classification using Sentinel-1 data.

The increased classification accuracy that can be obtained from utilising multi-sensor data fusion techniques has been demonstrated in this thesis. Therefore, the application of sensor fusion in the generation of any annual LCC product would be recommended. In particular, the application of decision-level fusion techniques would be recommended with its simple but robust workflows that were demonstrated to outperform pixel-level fusion in this thesis. This relatively simplistic workflow is particularly suitable for generating an annual updated LCC product where production time is limited. In addition, the utilisation of a decision-level fusion workflow ensures that alternative EO data sources, where available, could be incorporated into the generation of the annual product with minimal change to the production workflow. The use of a simple probability averaging approach to fusion could be used for decision-level fusion. However, as demonstrated in this thesis, the application of a Full-SVM or Dual-SVM averaging approach would result in higher classification accuracy in the generated product.

6.3.7 Future LCC Requirements

With the increased demand for up-to-date LCC datasets, the type of LCC product and the manner by which it is produced is likely to change over time. As highlighted in Chapter 1, there is currently a demand for the generation of annual LCC products. While in this thesis, it was assumed that an annual product would follow the annual calendar for specific land cover classes, this may not always be the best practice. For the annual classification of crop types or agricultural practices, defining the annual period based on growing seasons may be more appropriate.

While this thesis focused on data captured within a target year, there is potential for using some inter-annual data to further improve classification accuracy and reduce computational cost. One such method would be to use inter-annual data to identify potential changes between years. Under this approach, only regions undergoing substantial change in their spectral, spatial or temporal characteristics would be reclassified. Progressing beyond the generation of an annual LCC product, dynamic LCC products may potentially provide near real-time updates to LCC. In a dynamic LCC product, updates to the product are added as new EO data is captured. This product could identify changes in LCC in near real-time. However, the generation of such a product would pose its own challenges, such as determining an appropriate class schema and the thresholds that would determine at which point classification change would be recorded.

6.4 Final Remarks

Producing accurate, timely LCC maps provides a crucial reference layer to a range of end-users, including farmers, land owners, urban planners and government policymakers, that not only helps optimise land use and food production but also the big global challenges facing our world, including climate change and sustainability. High-quality LCC products can also be used as a base layer for detecting and categorising change over time at the forest, farm, peatland and urban parcel level, which, in turn, can be developed to explore novel methodologies for mapping human activity in terms of land management.

The topics covered in this thesis present novel techniques to improve classification accuracy when performing LCC using EO data. Foremost of these contributions were;

- The proposed LFCNN and 3DLFCNN architectures for high accuracy classification and rapid large scale inference.
- The proposed Full-SVM Fused averaging and Dual-SVM averaging approaches for fusion in situations where there is differences in sensor data availability over the area that is being assessed.

-
- The proposed class-corresponding fusion of aerial and satellite enabling the fusion of mono-temporal aerial data with multi-temporal multi-modal satellite data.

Through these contributions, this thesis adds to current knowledge, providing practical and robust techniques which can be utilised for the generation of an annual LCC product. While the techniques presented in this thesis demonstrated the versatility of EO and ML for LCC, this field is rapidly developing, and significant advancements in the field are likely to occur in the years to come.

Bibliography

- Adão, T., Hruška, J., Pádua, L., Bessa, J., Peres, E., Morais, R., and Sousa, J. J. (2017). Hyperspectral imaging: A review on uav-based sensors, data processing and applications for agriculture and forestry. *Remote Sensing*, 9(11):1110.
- Agency, E. E. (2019). Framework service contract for the copernicus land monitoring services – clc+ backbone production, including raster and vector products based on satellite input data from 2017/2018/2019.
- Aggarwal, C. C. (2018). *Neural networks and deep learning*, volume 10. Springer, Yorktown Heights, NY, USA.
- Aguilera, M. A. Z. (2020). Classification of land-cover through machine learning algorithms for fusion of sentinel-2a and planetscope imagery. In *2020 IEEE Latin American GRSS & ISPRS Remote Sensing Conference (LAGIRS)*, pages 246–253. IEEE.
- AIRBUS (2022). Pléiades neo. [online]. Available at: <https://www.intelligence-airbusds.com/imagery/constellation/pleiades-neo/> (accessed 20 May 2022).
- Ali, I., Greifeneder, F., Stamenkovic, J., Neumann, M., and Notarnicola, C. (2015). Review of machine learning approaches for biomass and soil moisture retrievals from remote sensing data. *Remote Sensing*, 7(12):16398–16421.
- Attema, E., Bargellini, P., Edwards, P., Levrini, G., Lokas, S., Moeller, L., Rosich-Tell, B., Secchi, P., Torres, R., Davidson, M., Snoeij, P., et al. (2007). The radar mission for gmes operational land and sea services. *ESA bulletin*, (131):10–17.

-
- Aune-Lundberg, L. and Strand, G.-H. (2021). The content and accuracy of the corine land cover dataset for norway. *International Journal of Applied Earth Observation and Geoinformation*, 96:102266.
- Baghdadi, N. and Zribi, M. (2017). *Land surface remote sensing in urban and coastal areas*. ISTE Press, London SW19 4EU, UK.
- Ballin, M., Barcaroli, G., Masselli, M., and Scarnó, M. (2018). *Redesign sample for Land Use/Cover Area frame Survey (LUCAS) 2018*. Eurostat.
- Barrett, B., Raab, C., Cawkwell, F., and Green, S. (2016). Upland vegetation mapping using random forests with optical and radar satellite data. *Remote sensing in ecology and conservation*, 2(4):212–231.
- Barsi, J. A., Markham, B. L., Montanaro, M., Gerace, A., Hook, S. J., Schott, J. R., Raqueno, N. G., and Morfitt, R. (2017). Landsat-8 tirs thermal radiometric calibration status. In *Earth Observing Systems XXII*, volume 10402, page 104021G. International Society for Optics and Photonics.
- Belward, A. S. and Skoien, J. O. (2015). Who launched what, when and why; trends in global land-cover observation capacity from civilian earth observation satellites. *ISPRS Journal of Photogrammetry and Remote Sensing*, 103:115–128.
- Bigdeli, B., Samadzadegan, F., and Reinartz, P. (2014). A decision fusion method based on multiple support vector machine system for fusion of hyperspectral and lidar data. *International Journal of Image and Data Fusion*, 5(3):196–209.
- Bolstad, P. (2019). *GIS fundamentals: a first text on geographic information systems*. XanEdu, Ann Arbor, MI, 6th edition.
- Bonaccorso, G. (2018). *Mastering machine learning algorithms: expert techniques to implement popular machine learning algorithms and fine-tune your models*. Packt Publishing Ltd.
- Breiman, L. (2001). Random forests. *Machine learning*, 45(1):5–32.

-
- Brennan, M. and Tubridy, M. (2017). National landcover and habitat mapping programme for ireland use case analysis and economic value study. Report, The Heritage Council, Kilkenny.
- Bzdok, D., Altman, N., and Krzywinski, M. (2018). Statistics versus machine learning. *Nature Methods*, 15(4):233.
- Büttner, G. and Kosztra, B. (2017). CLC2018 technical guidelines. Technical report, European Environment Agency, Spittelauer Lände 5, A-1090 Wien, Austria.
- Büttner, G., Kosztra, B., Maucha, G., Pataki, R., Kleeschulte, S., Hazeu, G., Vittek, M., Schröder, C., and Littkopf, A. (2021). *Copernicus Land Monitoring Service*. European Environment Agency (EEA), Copenhagen K. – Denmark.
- Cahalane, C., Walsh, D., Magee, A., Mannion, S., Lewis, P., and McCarthy, T. (2017). Sensor pods: Multi-resolution surveys from a light aircraft. *Inventions*, 2(1):2.
- Camargo, F. F., Sano, E. E., Almeida, C. M., Mura, J. C., and Almeida, T. (2019). A comparative assessment of machine-learning techniques for land use and land cover classification of the brazilian tropical savanna using alos-2/palsar-2 polarimetric images. *Remote Sensing*, 11(13):1600.
- Carranza-García, M., García-Gutiérrez, J., and Riquelme, J. C. (2019). A framework for evaluating land use and land cover classification using convolutional neural networks. *Remote Sensing*, 11(3):274.
- Carrasco, L., O’Neil, A. W., Morton, R. D., and Rowland, C. S. (2019). Evaluating combinations of temporally aggregated sentinel-1, sentinel-2 and landsat 8 for land cover mapping with google earth engine. *Remote Sensing*, 11(3):288.
- Cawkwell, F., Barrett, B., Nitze, I., Green, S., Black, K., and Hallahan, P. (2017). The irish land mapping observatory: mapping and monitoring land cover, use and change. Research report, Environmental Protection Agency, Johnstown Castle, Co. Wexford, Ireland.

-
- Chang, N.-B. and Bai, K. (2018). *Multisensor data fusion and machine learning for environmental remote sensing*. CRC Press, Boca Raton, Florida.
- Chaves, M. E. D., Picoli, M. C. A., and Sanches, I. D. (2020). Recent applications of landsat 8/oli and sentinel-2/msi for land use and land cover mapping: A systematic review. *Remote Sensing*, 12(18):3062.
- Claverie, M., Ju, J., Masek, J. G., Dungan, J. L., Vermote, E. F., Roger, J.-C., Skakun, S. V., and Justice, C. (2018). The harmonized landsat and sentinel-2 surface reflectance data set. *Remote Sensing of Environment*, 219:145–161.
- Clerc, S., Devignot, O., and Pessiot, L. (2022). S2 mpc level 2a data quality report. Technical report, ESA.
- Coeurdevey, L. and Gabriel-Robez, C. (2012). *Pléiades Imagery User Guide*. Astrium GEO-Information Services, F-31030 Toulouse Cedex 4 - France, 2nd edition.
- Commings, B. (2021). New land-cover map of habitats in development. [online]. Available at:
<https://www.agriland.ie/farming-news/new-land-cover-map-of-habitats-in-development/> (accessed 28 Nov 2022).
- Congalton, R. G., Gu, J., Yadav, K., Thenkabail, P., and Ozdogan, M. (2014). Global land cover mapping: A review and uncertainty analysis. *Remote Sensing*, 6(12):12070–12093.
- Copernicus (2021). CLC+. [online]. Available at:
<https://land.copernicus.eu/pan-european/clc-plus> (accessed 13 August 2021).
- Copernicus (2022). Very high resolution image mosaic 2018. Online.
- Dabija, A., Kluczek, M., Zagajewski, B., Raczko, E., Kycko, M., Al-Sulttani, A. H., Tardà, A., Pineda, L., and Corbera, J. (2021). Comparison of support vector machines and random forests for corine land cover mapping. *Remote Sensing*, 13(4):777.

-
- De Luca, G., N Silva, J. M., Cerasoli, S., Araújo, J., Campos, J., Di Fazio, S., and Modica, G. (2019). Object-based land cover classification of cork oak woodlands using uav imagery and orfeo toolbox. *Remote Sensing*, 11(10):1238.
- Deng, L., Mao, Z., Li, X., Hu, Z., Duan, F., and Yan, Y. (2018). Uav-based multispectral remote sensing for precision agriculture: A comparison between different cameras. *ISPRS journal of photogrammetry and remote sensing*, 146:124–136.
- Du, Y., Zhang, Y., Ling, F., Wang, Q., Li, W., and Li, X. (2016). Water bodies’ mapping from sentinel-2 imagery with modified normalized difference water index at 10-m spatial resolution produced by sharpening the swir band. *Remote Sensing*, 8(4):354.
- d’Andrimont, R., Verhegghen, A., Lemoine, G., Kempeneers, P., Meroni, M., and van der Velde, M. (2021). From parcel to continental scale—a first european crop type map based on sentinel-1 and lucas copernicus in-situ observations. *Remote Sensing of Environment*, 266:112708.
- El Fellah, S., Rziza, M., and El Haziti, M. (2016). An efficient approach for filling gaps in landsat 7 satellite images. *IEEE Geoscience and Remote Sensing Letters*, 14(1):62–66.
- Emery, W. and Camps, A. (2017). *Introduction to satellite remote sensing: atmosphere, ocean, land and cryosphere applications*. Elsevier, The Boulevard, Langford Lane, Kidlington, Oxford OX5 1GB, United Kingdom.
- Emilien, A.-V., Thomas, C., and Thomas, H. (2021). Uav & satellite synergies for optical remote sensing applications: A literature review. *Science of Remote Sensing*, page 100019.
- EPA (2021). Current trends land and soil. [online]. Available at:
<https://www.epa.ie/our-services/monitoring-assessment/assessment/irelands-environment/land-soil/current-trends-land-and-soil/> (accessed 24 November 2021).
- EPA (2022). Land use and land cover. [online]. Available at:
<https://www.epa.ie/our-services/monitoring-assessment/assessment/irelands-environment/land-soil/current-trends-land-and-soil> (accessed 28 Nov 2022).

-
- EROS (2013). Landsat 8 illustration above earth. [online]. Available at:
<https://www.usgs.gov/media/images/landsat-8-illustration-above-earth> (accessed 16 November 2021).
- ESA (2012a). *ESA's radar observatory mission for GMES operational services*. ESA Communications, ESTEC, PO Box 299, 2200 AG Noordwijk, The Netherlands.
- ESA (2012b). *Sentinel-1 ESA's Radar Observatory Mission for GMeS Operational Services*. European Space Agency, 2200 AG Noordwijk, The Netherlands.
- ESA (2015). *Sentinel-2 User Handbook*. European Space Agency, 2nd edition.
- ESA (2021a). Multispectral instrument (msi) overview. [online]. Available at:
<https://sentinel.esa.int/web/sentinel/technical-guides/sentinel-2-msi/msi-instrument>
(accessed 13 August 2021).
- ESA (2021b). Sentinel-1 overview. [Online]. Available at:
<https://sentinels.copernicus.eu/web/sentinel/missions/sentinel-1/overview> (accessed 16 November 2021).
- ESA (2021c). Sentinel-2 operations. [online]. Available at:
https://www.esa.int/Enabling_Support/Operations/Sentinel-2_operation (accessed 16 November 2021).
- ESA (2021d). The sentinel missions. [online]. Available at:
https://www.esa.int/Applications/Observing_the_Earth/Copernicus/The_Sentinel_missions
(accessed 13 October 2021).
- ESA (2022). Worldview-4. [online]. Available at:
<https://earth.esa.int/eogateway/missions/worldview-4> (accessed 20 May 2022).
- EU Science Hub (2022). Earth observation. [online]. Available at:
https://joint-research-centre.ec.europa.eu/scientific-activities/earth-observation_en
(accessed 22 March 2022).

-
- European Environment Agency (1995). Corine land cover. [online]. Available at:
<https://www.eea.europa.eu/publications/COR0-landcover> (accessed 3 January 2021).
- FAO (2022a). Agrovoc multilingual thesaurus, food and agriculture organization of the united nations : Land cover. [online]. Available at:
https://agrovoc.fao.org/browse/agrovoc/en/page/c_37897 (accessed 16 May 2022).
- FAO (2022b). Agrovoc multilingual thesaurus, food and agriculture organization of the united nations : Land use. [online]. Available at:
https://agrovoc.fao.org/browse/agrovoc/en/page/c_4182 (accessed 16 May 2022).
- Fastie, C. (2015). Dual bandpass filters. [online]. Available at:
<https://publiclab.org/notes/cfastie/11-24-2015/dual-band-pass-filters> (accessed 28 November 2021).
- Feng, Q., Yang, J., Zhu, D., Liu, J., Guo, H., Bayartungalag, B., and Li, B. (2019). Integrating multitemporal sentinel-1/2 data for coastal land cover classification using a multibranch convolutional neural network: A case of the yellow river delta. *Remote Sensing*, 11(9):1006.
- Förstner, W. and Wrobel, B. P. (2016). *Photogrammetric computer vision*. Springer.
- Forsyth, D. (2018). *Probability and statistics for computer science*. Springer, Urbana, IL, USA.
- Gašparović, M. and Dobrinić, D. (2020). Comparative assessment of machine learning methods for urban vegetation mapping using multitemporal sentinel-1 imagery. *Remote Sensing*, 12(12):1952.
- Gevaert, C. M., Suomalainen, J., Tang, J., and Kooistra, L. (2015). Generation of spectral–temporal response surfaces by combining multispectral satellite and hyperspectral uav imagery for precision agriculture applications. *IEEE Journal of Selected Topics in Applied Earth Observations and Remote Sensing*, 8(6):3140–3146.

-
- GIS Homework (2021). Remote sensing and its major applications — simplified 2021. [online]. Available at: <https://gishomework.com/remote-sensing-and-its-major-application/> (accessed 25 November 2021).
- Gondara, L. and Wang, K. (2018). Mida: Multiple imputation using denoising autoencoders. In *Pacific-Asia conference on knowledge discovery and data mining*, pages 260–272. Springer.
- Goodfellow, I., Bengio, Y., and Courville, A. (2016). *Deep Learning*. MIT Press.
- Gravina, R., Alinia, P., Ghasemzadeh, H., and Fortino, G. (2017). Multi-sensor fusion in body sensor networks: State-of-the-art and research challenges. *Information Fusion*, 35:68–80.
- Green, S. and Zimmermann, J. (2021). Ireland from abroad, irish land cover and land use mapped internationally. [online]. Available at: <https://storymaps.arcgis.com/stories/5cb8c1ba0de5406384ec86ef5f0e034f> (accessed 28 February 2022).
- Griffiths, P., Nendel, C., and Hostert, P. (2019). Intra-annual reflectance composites from sentinel-2 and landsat for national-scale crop and land cover mapping. *Remote sensing of environment*, 220:135–151.
- GrindsGIS (2015). What is remote sensing. [online]. Available at: <https://grindgis.com/what-is-remote-sensing/know-basics-of-remote-sensing> (accessed 24 March 2022).
- Haarpaintner, J. and Hindberg, H. (2019). Multi-temporal and multi-frequency sar analysis for forest land cover mapping of the mai-ndombe district (democratic republic of congo). *Remote Sensing*, 11(24):2999.
- Han, J. and Kang, S. (2022). Dynamic imputation for improved training of neural network with missing values. *Expert Systems with Applications*, page 116508.

-
- Hastie, T., Tibshirani, R., and Friedman, J. (2017). *The Elements of Statistical Learning*. Springer, 2nd edition.
- He, T., Xie, C., Liu, Q., Guan, S., and Liu, G. (2019). Evaluation and comparison of random forest and a-lstm networks for large-scale winter wheat identification. *Remote Sensing*, 11(14):1665.
- Henrich, V. and Brüser, K. (2021). Index database. [online]. Available at: <https://www.indexdatabase.de/db/s-single.php?id=96> (accessed 03 November 2021).
- Heumann, C., Schomaker, M., et al. (2016). *Introduction to statistics and data analysis*. Springer.
- Hossain, M. D. and Chen, D. (2019). Segmentation for object-based image analysis (obia): A review of algorithms and challenges from remote sensing perspective. *ISPRS Journal of Photogrammetry and Remote Sensing*, 150:115–134.
- Huang, C., Zhang, C., He, Y., Liu, Q., Li, H., Su, F., Liu, G., and Bridhikitti, A. (2020). Land cover mapping in cloud-prone tropical areas using sentinel-2 data: Integrating spectral features with ndvi temporal dynamics. *Remote Sensing*, 12(7):1163.
- Hurskainen, P., Adhikari, H., Siljander, M., Pellikka, P., and Hemp, A. (2019). Auxiliary datasets improve accuracy of object-based land use/land cover classification in heterogeneous savanna landscapes. *Remote sensing of environment*, 233:111354.
- Ienco, D., Gaetano, R., Dupaquier, C., and Maurel, P. (2017). Land cover classification via multitemporal spatial data by deep recurrent neural networks. *IEEE Geoscience and Remote Sensing Letters*, 14(10):1685–1689.
- Igual, L. and Seguí, S. (2017). Introduction to data science. In *Introduction to Data Science*, pages 1–4. Springer.
- Ihlen, V. (2019). *Landsat 8 (L8) Data Users Handbook*. Department of the Interior U.S. Geological Survey, Sioux Falls, South Dakota, 5th edition.

-
- Isa, S. M., Suharjito, Kusuma, G. P., and Cenggoro, T. W. (2021). Supervised conversion from landsat-8 images to sentinel-2 images with deep learning. *European Journal of Remote Sensing*, 54(1):182–208.
- Ji, S., Zhang, C., Xu, A., Shi, Y., and Duan, Y. (2018). 3d convolutional neural networks for crop classification with multi-temporal remote sensing images. *Remote Sensing*, 10(1).
- Jia, K., Liang, S., Zhang, N., Wei, X., Gu, X., Zhao, X., Yao, Y., and Xie, X. (2014). Land cover classification of finer resolution remote sensing data integrating temporal features from time series coarser resolution data. *ISPRS Journal of Photogrammetry and Remote Sensing*, 93:49–55.
- Kannoja, S. P. and Jaiswal, G. (2018). Effects of varying resolution on performance of cnn based image classification: An experimental study. *Int. J. Comput. Sci. Eng.*, 6(9):451–456.
- Kleeschulte, S., Banko, G., Smith, G., Arnold, S., Scholz, J., Pleschberger, C., Kosztra, B., Maucha, G., Valcarcel, N., Delgado, J., and Dufourmont, H. (2019). Technical specifications for implementation of a new land-monitoring concept based on eagle. d3: Draft design concept and clc-backbone, clc-core.
- Kosztra, B., Büttner, G., Hazeu, G., and Arnold, S. (2019). Updated clc illustrated nomenclature guidelines. Technical report, European Environment Agency, Spittelauer Lände 5, 1090, Wien, Austria.
- Kovačević, J., Cvijetinović, Ž., Lakušić, D., Kuzmanović, N., Šinžar-Sekulić, J., Mitrović, M., Stančić, N., Brodić, N., and Mihajlović, D. (2020). Spatio-temporal classification framework for mapping woody vegetation from multi-temporal sentinel-2 imagery. *Remote Sensing*, 12(17):2845.
- Kubat, M. (2017). *An introduction to machine learning*. Springer, Coral Gables, FL, USA, 2nd edition.

-
- Kupidura, P. (2016). Comparison of filters dedicated to speckle suppression in sar images. *International Archives of the Photogrammetry, Remote Sensing & Spatial Information Sciences*, 41.
- Le Bris, A., Chehata, N., Ouerghemmi, W., Wendl, C., Postadjian, T., Puissant, A., and Mallet, C. (2019). Decision fusion of remote-sensing data for land cover classification. In *Multimodal Scene Understanding*, pages 341–382. Elsevier.
- Li, E., Samat, A., Liu, W., Lin, C., and Bai, X. (2019). High-resolution imagery classification based on different levels of information. *Remote Sensing*, 11(24):2916.
- Li, Q., Qiu, C., Ma, L., Schmitt, M., and Zhu, X. X. (2020a). Mapping the land cover of africa at 10 m resolution from multi-source remote sensing data with google earth engine. *Remote Sensing*, 12(4):602.
- Li, R., Zheng, S., Duan, C., and Zhang, C. (2020b). Land cover classification from remote sensing images based on multi-scale fully convolutional network. *arXiv preprint arXiv:2008.00168*.
- Lillesand, T., Kiefer, R. W., and Chipman, J. (2014). *Remote sensing and image interpretation*. John Wiley & Sons, Daryaganj, New Delhi, 6th edition.
- Liu, S., Qi, Z., Li, X., and Yeh, A. G.-O. (2019). Integration of convolutional neural networks and object-based post-classification refinement for land use and land cover mapping with optical and sar data. *Remote Sensing*, 11(6):690.
- Long, J., Shelhamer, E., and Darrell, T. (2015). Fully convolutional networks for semantic segmentation. In *Proceedings of the IEEE conference on computer vision and pattern recognition*, pages 3431–3440.
- Ma, L., Liu, Y., Zhang, X., Ye, Y., Yin, G., and Johnson, B. A. (2019). Deep learning in remote sensing applications: A meta-analysis and review. *ISPRS journal of photogrammetry and remote sensing*, 152:166–177.

-
- Macarringue, L. S., Bolfe, É. L., and Pereira, P. R. M. (2022). Developments in land use and land cover classification techniques in remote sensing: a review. *Journal of Geographic Information System*, 14(01):1–12.
- Mahyoub, S., Fadil, A., Mansour, E., Rhinane, H., and Al-Nahmia, F. (2019). Fusing of optical and synthetic aperture radar (sar) remote sensing data: A systematic literature review (slr). *International Archives of the Photogrammetry, Remote Sensing and Spatial Information Sciences*, 42(4/W12):127–138.
- MapTiler (2019). Epsg:32629. online.
- Marschner, F. (1950). Major land uses in the united states (map scale 1: 5,000,000). *USDA Agricultural Research Service, Washington, DC*, 252.
- Medium (2018). How to calculate the number of parameters in the cnn? [online]. Available at: <https://medium.com/@iamvarman/how-to-calculate-the-number-of-parameters-in-the-cnn-5bd55364d7ca> (accessed 06 June 2022).
- Mendili, L. E., Puissant, A., Chougrad, M., and Sebari, I. (2020). Towards a multi-temporal deep learning approach for mapping urban fabric using sentinel 2 images. *Remote Sensing*, 12(3):423.
- Meng, T., Jing, X., Yan, Z., and Pedrycz, W. (2020). A survey on machine learning for data fusion. *Information Fusion*, 57:115–129.
- Mercier, A., Betbeder, J., Rumiano, F., Baudry, J., Gond, V., Blanc, L., Bourgoin, C., Cornu, G., Marchamalo, M., Pocard-Chapuis, R., et al. (2019). Evaluation of sentinel-1 and 2 time series for land cover classification of forest–agriculture mosaics in temperate and tropical landscapes. *Remote Sensing*, 11(8):979.
- Met Éireann (2021). Sunshine and solar radiation. [online]. Available at: <https://www.met.ie/climate/what-we-measure/sunshine> (accessed 13 May 2021).

-
- Misra, G., Cawkwell, F., and Wingler, A. (2020). Status of phenological research using sentinel-2 data: A review. *Remote Sensing*, 12(17):2760.
- Moore, P., Murphy, A., Downes, P., and Watters, V. (2018). An analysis of the heatwaves and droughts that affected ireland and europe in the summer of 2018. Technical report, Met Éireann.
- Mugiraneza, T., Nascetti, A., and Ban, Y. (2019). Worldview-2 data for hierarchical object-based urban land cover classification in kigali: Integrating rule-based approach with urban density and greenness indices. *Remote Sensing*, 11(18):2128.
- NASA (2021a). Moderate resolution imaging spectroradiometer (modis) specifications. [online]. Available at: modis.gsfc.nasa.gov/about/specifications.php (accessed 26 November 2021).
- NASA (2021b). Visible infrared imaging radiometer suite (viirs). [online]. Available at: <https://www.earthdata.nasa.gov/learn/find-data/near-real-time/viirs> (accessed 03 June 2022).
- NASA (2022). Moderate resolution imaging spectroradiometer (modis) data. [online]. Available at: <https://modis.gsfc.nasa.gov/data/> (accessed 03 June 2022).
- Nguyen, L. H. and Henebry, G. M. (2019). Characterizing land use/land cover using multi-sensor time series from the perspective of land surface phenology. *Remote Sensing*, 11(14):1677.
- Nguyen, R. M., Prasad, D. K., and Brown, M. S. (2014). Training-based spectral reconstruction from a single rgb image. In *European Conference on Computer Vision*, pages 186–201. Springer.
- Nitze, I., Barrett, B., and Cawkwell, F. (2015). Temporal optimisation of image acquisition for land cover classification with random forest and modis time-series. *International Journal of Applied Earth Observation and Geoinformation*, 34:136–146.

-
- Nogueira, K., dos Santos, J. A., Menini, N., Silva, T. S., Morellato, L. P. C., and Torres, R. d. S. (2019). Spatio-temporal vegetation pixel classification by using convolutional networks. *IEEE Geoscience and Remote Sensing Letters*, 16(10):1665–1669.
- NPWS (2017). National landcover & habitat mapping in ireland. [online]. Available at: [https://www.npws.ie/sites/default/files/general/NLCHM Newsletter May 2017.pdf](https://www.npws.ie/sites/default/files/general/NLCHM%20Newsletter%20May%202017.pdf) (accessed 29 Nov 2022).
- Ovejero-Campos, A., Fernández, E., Ramos, L., Bento, R., and Méndez-Martínez, G. (2019). Methodological limitations of clc to assess land cover changes in coastal environments. *Journal of Coastal Conservation*, 23(3):657–673.
- Pascanu, R., Mikolov, T., and Bengio, Y. (2013). On the difficulty of training recurrent neural networks. In *International conference on machine learning*, pages 1310–1318. PMLR.
- Pastor-Pellicer, J., Zamora-Martínez, F., España-Boquera, S., and Castro-Bleda, M. J. (2013). F-measure as the error function to train neural networks. In Rojas, I., Joya, G., and Gabestany, J., editors, *Advances in Computational Intelligence*, pages 376–384, Berlin, Heidelberg. Springer Berlin Heidelberg.
- Peressutti, D. (2018). Introducing eo-learn. [online]. Available at: <https://medium.com/sentinel-hub/introducing-eo-learn-ab37f2869f5c> (accessed 07 May 2020).
- Raschka, S. and Mirjalili, V. (2017). *Python machine learning*. Packt publishing ltd, Livery Place 35 Livery Street Birmingham B3 2PB, UK, 2nd edition.
- Rasti, B. and Ghamisi, P. (2020). Remote sensing image classification using subspace sensor fusion. *Information Fusion*, 64:121–130.
- Rasti, B., Scheunders, P., Ghamisi, P., Licciardi, G., and Chanussot, J. (2018). Noise reduction in hyperspectral imagery: Overview and application. *Remote Sensing*, 10(3):482.

-
- Rawat, W. and Wang, Z. (2017). Deep convolutional neural networks for image classification: A comprehensive review. *Neural computation*, 29(9):2352–2449.
- Ronneberger, O., Fischer, P., and Brox, T. (2015). U-net: Convolutional networks for biomedical image segmentation. In *International Conference on Medical image computing and computer-assisted intervention*, pages 234–241. Springer.
- Rußwurm, M. and Körner, M. (2017). Multi-temporal land cover classification with long short-term memory neural networks. *International Archives of the Photogrammetry, Remote Sensing & Spatial Information Sciences*, 42.
- Rußwurm, M. and Körner, M. (2018). Multi-temporal land cover classification with sequential recurrent encoders. *ISPRS International Journal of Geo-Information*, 7(4):129.
- Sagan, V., Maimaitijiang, M., Sidike, P., Maimaitiyiming, M., Erkbol, H., Hartling, S., Peterson, K., Peterson, J., Burken, J., and Fritschi, F. (2019). Uav/satellite multiscale data fusion for crop monitoring and early stress detection. *International Archives of the Photogrammetry, Remote Sensing and Spatial Information Sciences*, 42:715–722.
- Salberg, A.-B. and Jenssen, R. (2012). Land-cover classification of partly missing data using support vector machines. *International journal of remote sensing*, 33(14):4471–4481.
- Salcedo-Sanz, S., Ghamisi, P., Piles, M., Werner, M., Cuadra, L., Moreno-Martínez, A., Izquierdo-Verdiguier, E., Muñoz-Marí, J., Mosavi, A., and Camps-Valls, G. (2020). Machine learning information fusion in earth observation: A comprehensive review of methods, applications and data sources. *Information Fusion*, 63:256–272.
- Satellite Imaging Corporation (2021). Satellite sensors. [online]. Available at: <https://www.satimagingcorp.com/satellite-sensors/> (accessed 26 November 2021).
- Schneider, A. (2012). Monitoring land cover change in urban and peri-urban areas using dense time stacks of landsat satellite data and a data mining approach. *Remote Sensing of Environment*, 124:689–704.

-
- Shang, C., Palmer, A., Sun, J., Chen, K.-S., Lu, J., and Bi, J. (2017). Vigan: Missing view imputation with generative adversarial networks. In *2017 IEEE International Conference on Big Data (Big Data)*, pages 766–775. IEEE.
- Shao, Z., Cai, J., Fu, P., Hu, L., and Liu, T. (2019). Deep learning-based fusion of landsat-8 and sentinel-2 images for a harmonized surface reflectance product. *Remote Sensing of Environment*, 235:111425.
- Sharma, A., Liu, X., Yang, X., and Shi, D. (2017). A patch-based convolutional neural network for remote sensing image classification. *Neural Networks*, 95:19–28.
- Shen, H., Wu, P., Liu, Y., Ai, T., Wang, Y., and Liu, X. (2013). A spatial and temporal reflectance fusion model considering sensor observation differences. *International journal of remote sensing*, 34(12):4367–4383.
- Shen, Y., Zhang, X., and Yang, Z. (2022). Mapping corn and soybean phenometrics at field scales over the united states corn belt by fusing time series of landsat 8 and sentinel-2 data with viirs data. *ISPRS Journal of Photogrammetry and Remote Sensing*, 186:55–69.
- Shunlin, L. and Jindi, W. (2020). *Advanced remote sensing: terrestrial information extraction and applications*. Academic Press, 125 London Wall, London EC2Y 5AS, United Kingdom, 2nd edition.
- Sirmacek, B. and Unsalan, C. (2010). A probabilistic framework to detect buildings in aerial and satellite images. *IEEE transactions on geoscience and remote sensing*, 49(1):211–221.
- Skansi, S. (2018). *Introduction to Deep Learning: from logical calculus to artificial intelligence*. Springer.
- Sklearn (2020). F1 score. [online]. Available at: https://scikit-learn.org/stable/modules/generated/sklearn.metrics.f1_score.html (accessed 07 January 2022).

-
- Song, H., Kim, Y., and Kim, Y. (2019). A patch-based light convolutional neural network for land-cover mapping using landsat-8 images. *Remote Sensing*, 11(2):114.
- Stehman, S. V. and Foody, G. M. (2019). Key issues in rigorous accuracy assessment of land cover products. *Remote Sensing of Environment*, 231:111199.
- Sun, G., Huang, H., Zhang, A., Li, F., Zhao, H., and Fu, H. (2019). Fusion of multiscale convolutional neural networks for building extraction in very high-resolution images. *Remote Sensing*, 11(3):227.
- Talukdar, S., Singha, P., Mahato, S., Pal, S., Liou, Y.-A., Rahman, A., et al. (2020). Land-use land-cover classification by machine learning classifiers for satellite observations—a review. *Remote Sensing*, 12(7):1135.
- Tarrio, K., Tang, X., Masek, J. G., Claverie, M., Ju, J., Qiu, S., Zhu, Z., and Woodcock, C. E. (2020). Comparison of cloud detection algorithms for sentinel-2 imagery. *Science of Remote Sensing*, 2:100010.
- Troyanskaya, O., Cantor, M., Sherlock, G., Brown, P., Hastie, T., Tibshirani, R., Botstein, D., and Altman, R. B. (2001). Missing value estimation methods for dna microarrays. *Bioinformatics*, 17(6):520–525.
- Useya, J. and Chen, S. (2018). Comparative performance evaluation of pixel-level and decision-level data fusion of landsat 8 oli, landsat 7 etm+ and sentinel-2 msi for crop ensemble classification. *IEEE Journal of Selected Topics in Applied Earth Observations and Remote Sensing*, 11(11):4441–4451.
- Valcarce-Diñeiro, R., Arias-Pérez, B., Lopez-Sanchez, J. M., and Sánchez, N. (2019). Multi-temporal dual-and quad-polarimetric synthetic aperture radar data for crop-type mapping. *Remote Sensing*, 11(13):1518.
- Vali, A., Comai, S., and Matteucci, M. (2020). Deep learning for land use and land cover classification based on hyperspectral and multispectral earth observation data: A review. *Remote Sensing*, 12(15):2495.

-
- Véstias, M. P. (2019). A survey of convolutional neural networks on edge with reconfigurable computing. *Algorithms*, 12(8):154.
- Vilar, P., Morais, T. G., Rodrigues, N. R., Gama, I., Monteiro, M. L., Domingos, T., and Teixeira, R. F. (2020). Object-based classification approaches for multitemporal identification and monitoring of pastures in agroforestry regions using multispectral unmanned aerial vehicle products. *Remote Sensing*, 12(5):814.
- Vohra, R. and Tiwari, K. (2020). Comparative analysis of svm and ann classifiers using multilevel fusion of multi-sensor data in urban land classification. *Sensing and Imaging*, 21(1):1–21.
- Wagner, J., Andre, E., Lingenfelter, F., and Kim, J. (2011). Exploring fusion methods for multimodal emotion recognition with missing data. *IEEE Transactions on Affective Computing*, 2(4):206–218.
- Walsh, E., Bessardon, G., Gleeson, E., and Ulmas, P. (2021). Using machine learning to produce a very high resolution land-cover map for ireland. *Advances in Science and Research*, 18:65–87.
- Wang, S., Baum, A., Zarco-Tejada, P. J., Dam-Hansen, C., Thorseth, A., Bauer-Gottwein, P., Bandini, F., and Garcia, M. (2019). Unmanned aerial system multi-spectral mapping for low and variable solar irradiance conditions: Potential of tensor decomposition. *ISPRS journal of photogrammetry and remote sensing*, 155:58–71.
- Wegscheider, S., Lindmayer, A., and Stumpf, A. (2021). Urban atlas 2018 validation report. Technical report, European Environment Agency.
- Wendl, C., Le Bris, A., Chehata, N., Puissant, A., and Postadjian, T. (2018). Decision fusion of spot6 and multitemporal sentinel2 images for urban area detection. In *IGARSS 2018-2018 IEEE International Geoscience and Remote Sensing Symposium*, pages 1734–1737. IEEE.

-
- Whyte, A., Ferentinos, K. P., and Petropoulos, G. P. (2018). A new synergistic approach for monitoring wetlands using sentinel-1 and 2 data with object-based machine learning algorithms. *Environmental Modelling & Software*, 104:40–54.
- Wu, G., Guo, Y., Song, X., Guo, Z., Zhang, H., Shi, X., Shibasaki, R., and Shao, X. (2019). A stacked fully convolutional networks with feature alignment framework for multi-label land-cover segmentation. *Remote Sensing*, 11(9):1051.
- Wulder, M. A., Coops, N. C., Roy, D. P., White, J. C., and Hermosilla, T. (2018). Land cover 2.0. *International Journal of Remote Sensing*, 39(12):4254–4284.
- Xu, G., Zhu, X., Fu, D., Dong, J., and Xiao, X. (2017). Automatic land cover classification of geo-tagged field photos by deep learning. *Environmental Modelling & Software*, 91:127–134.
- Xu, Z., Guan, K., Casler, N., Peng, B., and Wang, S. (2018). A 3d convolutional neural network method for land cover classification using lidar and multi-temporal landsat imagery. *ISPRS journal of photogrammetry and remote sensing*, 144:423–434.
- Yan, W. Y., Shaker, A., and El-Ashmawy, N. (2015). Urban land cover classification using airborne lidar data: A review. *Remote Sensing of Environment*, 158:295–310.
- Yang, C., Westbrook, J. K., Suh, C. P.-C., Martin, D. E., Hoffmann, W. C., Lan, Y., Fritz, B. K., and Goolsby, J. A. (2014). An airborne multispectral imaging system based on two consumer-grade cameras for agricultural remote sensing. *Remote Sensing*, 6(6):5257–5278.
- Yokoya, N., Ghamisi, P., Xia, J., Sukhanov, S., Heremans, R., Tankoyeu, I., Bechtel, B., Le Saux, B., Moser, G., and Tuia, D. (2018). Open data for global multimodal land use classification: Outcome of the 2017 ieee grss data fusion contest. *IEEE Journal of Selected Topics in Applied Earth Observations and Remote Sensing*, 11(5):1363–1377.
- Zafari, A., Zurita-Milla, R., and Izquierdo-Verdiguier, E. (2019). Evaluating the performance of a random forest kernel for land cover classification. *Remote sensing*, 11(5):575.

-
- Zare, M. L. and Mahmoudi, F. T. (2019). Road recognition based on decision level fusion of sar and optic data. *The International Archives of Photogrammetry, Remote Sensing and Spatial Information Sciences*, 42:665–669.
- Zhang, J. (2010). Multi-source remote sensing data fusion: status and trends. *International Journal of Image and Data Fusion*, 1(1):5–24.
- Zhang, S., Li, C., Qiu, S., Gao, C., Zhang, F., Du, Z., and Liu, R. (2020a). Emmcnn: An etps-based multi-scale and multi-feature method using cnn for high spatial resolution image land-cover classification. *Remote Sensing*, 12(1):66.
- Zhang, X., Han, L., Han, L., and Zhu, L. (2020b). How well do deep learning-based methods for land cover classification and object detection perform on high resolution remote sensing imagery? *Remote Sensing*, 12(3):417.
- Zhao, H., Chen, Z., Jiang, H., Jing, W., Sun, L., and Feng, M. (2019). Evaluation of three deep learning models for early crop classification using sentinel-1a imagery time series—a case study in zhanjiang, china. *Remote Sensing*, 11(22):2673.
- Zhong, L., Hu, L., and Zhou, H. (2019). Deep learning based multi-temporal crop classification. *Remote sensing of environment*, 221:430–443.
- Zhong, Y., Cao, Q., Zhao, J., Ma, A., Zhao, B., and Zhang, L. (2017). Optimal decision fusion for urban land-use/land-cover classification based on adaptive differential evolution using hyperspectral and lidar data. *Remote Sensing*, 9(8):868.
- Zhou, K., Ming, D., Lv, X., Fang, J., and Wang, M. (2019). Cnn-based land cover classification combining stratified segmentation and fusion of point cloud and very high-spatial resolution remote sensing image data. *Remote Sensing*, 11(17):2065.
- Zhou, Q., Tollerud, H. J., Barber, C. P., Smith, K., and Zelenak, D. (2020). Training data selection for annual land cover classification for the land change monitoring, assessment, and projection (lcmapp) initiative. *Remote Sensing*, 12(4):699.

Zhu, X., Chen, J., Gao, F., Chen, X., and Masek, J. G. (2010). An enhanced spatial and temporal adaptive reflectance fusion model for complex heterogeneous regions. *Remote Sensing of Environment*, 114(11):2610–2623.

Zotti, M. and Mantia, C. L. (2021). Production of very high resolution land cover/land use dataset for coastal zones of the reference years 2012 and 2018 final delivery report. Technical report, European Environment Agency.

Zou, Y., Li, G., and Wang, S. (2018). The fusion of satellite and unmanned aerial vehicle (uav) imagery for improving classification performance. In *2018 IEEE International Conference on Information and Automation (ICIA)*, pages 836–841. IEEE.

Appendix A

Satellite Data

Contents

A.1 Sentinel-1 Images	233
A.2 Sentinel-2 Images	246
A.3 Landsat-8 Images	284

All satellite image names provided in Appendix A correspond to the file name when downloaded from the Copernicus Open Access Hub (scihub.copernicus.eu/dhus) in the case of Sentinel-1 and Sentinel-2 data and from the USGS Earth Explorer website (earth-explorer.usgs.gov) for Landsat-8 data.

A.1 Sentinel-1 Images

Table A.1: Sentinel-1 Satellite Images used in Chapter 3 comparative assessment.

S1B_IW_GRDH_1SDV_20180712T064611_20180712T064636_011774_015A92_D13D
S1B_IW_GRDH_1SDV_20181021T180615_20181021T180640_013254_018809_77F6
S1B_IW_GRDH_1SDV_20180101T064607_20180101T064632_008974_01003F_E604
S1A_IW_GRDH_1SDV_20180325T180647_20180325T180712_021175_02466F_950E
S1B_IW_GRDH_1SDV_20180518T180607_20180518T180632_010979_0141A2_20F5
S1B_IW_GRDH_1SDV_20180302T064605_20180302T064630_009849_011CFA_74C7

Sentinel-1 Satellite Images used in Chapter 3 comparative assessment [continued].

S1B_IW_GRDH_1SDV_20181004T064615_20181004T064640_012999_018024_10F1
S1A_IW_GRDH_1SDV_20181120T180657_20181120T180722_024675_02B652_9AF6
S1A_IW_GRDH_1SDV_20180921T180657_20180921T180722_023800_0298AF_A5CE
S1A_IW_GRDH_1SDV_20180617T180652_20180617T180717_022400_026CF2_8E66
S1A_IW_GRDH_1SDV_20180217T180647_20180217T180712_020650_0235CA_B143
S1A_IW_GRDH_1SDV_20180418T180649_20180418T180714_021525_025169_4635
S1B_IW_GRDH_1SDV_20181220T180613_20181220T180638_014129_01A3FE_3CC3
S1B_IW_GRDH_1SDV_20180822T180613_20180822T180638_012379_016D27_5F2A
S1B_IW_GRDH_1SDV_20180805T064613_20180805T064638_012124_01652F_CBBC
S1B_IW_GRDH_1SDV_20180118T180605_20180118T180630_009229_010898_C99A
S1B_IW_GRDH_1SDV_20181203T064614_20181203T064639_013874_019B8D_96B0
S1B_IW_GRDH_1SDV_20180501T064607_20180501T064632_010724_013964_DF26
S1B_IW_GRDH_1SDV_20180206T064605_20180206T064630_009499_01116E_DF3E
S1B_IW_GRDH_1SDV_20181109T064615_20181109T064640_013524_019064_F336
S1A_IW_GRDH_1SDV_20180723T180654_20180723T180719_022925_027CB9_187F
S1B_IW_GRDH_1SDV_20180407T064606_20180407T064631_010374_012E32_1FE6
S1B_IW_GRDH_1SDV_20180606T064609_20180606T064634_011249_014A4E_B213
S1B_IW_GRDH_1SDV_20180910T064614_20180910T064639_012649_017570_E8BB
S1B_IW_GRDH_1SDV_20181109T064640_20181109T064705_013524_019064_EEEC
S1B_IW_GRDH_1SDV_20180703T182154_20180703T182219_011650_0156CE_ED22
S1A_IW_GRDH_1SDV_20181115T064736_20181115T064801_024595_02B363_310D
S1B_IW_GRDH_1SDV_20180326T064630_20180326T064655_010199_01287E_94F2
S1B_IW_GRDH_1SDV_20180805T064638_20180805T064703_012124_01652F_BCF8
S1B_IW_GRDH_1SDV_20181028T064640_20181028T064705_013349_018AED_3E83
S1B_IW_GRDH_1SDV_20200208T064643_20200208T064708_020174_026302_6B8F
S1B_IW_GRDH_1SDV_20180922T064640_20180922T064705_012824_017ACC_2269
S1B_IW_GRDH_1SDV_20180419T064631_20180419T064656_010549_0133C5_00DD

Sentinel-1 Satellite Images used in Chapter 3 comparative assessment [continued].

S1B_IW_GRDH_1SDV_20181121T064640_20181121T064705_013699_0195F0_108A
S1B_IW_GRDH_1SDV_20180104T182153_20180104T182218_009025_0101F7_0B16
S1A_IW_GRDH_1SDV_20180320T064726_20180320T064751_021095_0243D9_617A
S1A_IW_GRDH_1SDV_20180718T064732_20180718T064757_022845_027A2D_F242
S1B_IW_GRDH_1SDV_20180305T182152_20180305T182217_009900_011EBB_FA0B
S1B_IW_GRDH_1SDV_20181203T064639_20181203T064704_013874_019B8D_09AC
S1A_IW_GRDH_1SDV_20180519T064729_20180519T064754_021970_025F6A_C74E
S1B_IW_GRDH_1SDV_20181016T064640_20181016T064705_013174_01857C_8C04
S1B_IW_GRDH_1SDV_20180817T064638_20180817T064703_012299_016A99_E044
S1B_IW_GRDH_1SDV_20180410T182150_20180410T182215_010425_012FDA_4ECC
S1A_IW_GRDH_1SDV_20180119T064727_20180119T064752_020220_022805_2644
S1B_IW_GRDH_1SDV_20180901T182158_20180901T182223_012525_0171AC_9113
S1A_IW_GRDH_1SDV_20180306T181430_20180306T181455_020898_023D9E_C517
S1B_IW_GRDH_1SDV_20181215T064639_20181215T064704_014049_01A143_0D06
S1B_IW_GRDH_1SDV_20181227T064639_20181227T064704_014224_01A711_C19E
S1A_IW_GRDH_1SDV_20180916T064735_20180916T064800_023720_02960A_1D0E
S1B_IW_GRDH_1SDV_20181004T064640_20181004T064705_012999_018024_2997
S1B_IW_GRDH_1SDV_20180910T064639_20180910T064704_012649_017570_82BE
S1B_IW_GRDH_1SDV_20180405T181341_20180405T181406_010352_012D81_07A4
S1B_IW_GRDH_1SDV_20180504T182151_20180504T182216_010775_013B11_FADF
S1B_IW_GRDH_1SDV_20180204T181340_20180204T181405_009477_0110B8_4145
S1B_IW_GRDH_1SDV_20180407T064631_20180407T064656_010374_012E32_D172
S1B_IW_GRDH_1SDV_20180218T064630_20180218T064655_009674_01172A_8A8C
S1B_IW_GRDH_1SDV_20181206T182158_20181206T182223_013925_019D49_ABD7
S1B_IW_GRDH_1SDV_20180618T064635_20180618T064700_011424_014FB3_2ED2
S1B_IW_GRDH_1SDV_20180501T064632_20180501T064657_010724_013964_1914
S1B_IW_GRDH_1SDV_20180314T064630_20180314T064655_010024_0122D0_A696

Sentinel-1 Satellite Images used in Chapter 3 comparative assessment [continued].

S1A_IW_GRDH_1SDV_20180105T181431_20180105T181456_020023_0221C8_46C5
S1B_IW_GRDH_1SDV_20180525T064633_20180525T064658_011074_0144BE_B5AE
S1B_IW_GRDH_1SDV_20180513T064632_20180513T064657_010899_013F0E_277B
S1B_IW_GRDH_1SDV_20180724T064637_20180724T064702_011949_015FE6_9EC5
S1B_IW_GRDH_1SDV_20180817T064703_20180817T064728_012299_016A99_471C
S1B_IW_GRDH_1SDV_20180419T064631_20180419T064656_010549_0133C5_00DD
S1A_IW_GRDH_1SDV_20180704T181416_20180704T181441_022648_027435_4422
S1B_IW_GRDH_1SDV_20180314T064630_20180314T064655_010024_0122D0_A696
S1B_IW_GRDH_1SDV_20180618T064700_20180618T064725_011424_014FB3_A91A
S1A_IW_GRDH_1SDV_20180505T181412_20180505T181437_021773_025929_6F13
S1B_IW_GRDH_1SDV_20180910T064639_20180910T064704_012649_017570_82BE
S1B_IW_GRDH_1SDV_20180525T064633_20180525T064658_011074_0144BE_B5AE
S1B_IW_GRDH_1SDV_20180218T064655_20180218T064720_009674_01172A_1F11
S1A_IW_GRDH_1SDV_20180119T064727_20180119T064752_020220_022805_2644
S1A_IW_GRDH_1SDV_20181207T181419_20181207T181444_024923_02BEDC_878A
S1B_IW_GRDH_1SDV_20180501T064632_20180501T064657_010724_013964_1914
S1B_IW_GRDH_1SDV_20180405T181341_20180405T181406_010352_012D81_07A4
S1B_IW_GRDH_1SDV_20181028T064640_20181028T064705_013349_018AED_3E83
S1B_IW_GRDH_1SDV_20180805T064638_20180805T064703_012124_01652F_BCF8
S1B_IW_GRDH_1SDV_20180504T182151_20180504T182216_010775_013B11_FADF
S1A_IW_GRDH_1SDV_20180105T181431_20180105T181456_020023_0221C8_46C5
S1B_IW_GRDH_1SDV_20180803T181336_20180803T181401_012102_016488_63D5
S1B_IW_GRDH_1SDV_20180218T064630_20180218T064655_009674_01172A_8A8C
S1B_IW_GRDH_1SDV_20180407T064631_20180407T064656_010374_012E32_D172
S1B_IW_GRDH_1SDV_20181016T064640_20181016T064705_013174_01857C_8C04
S1B_IW_GRDH_1SDV_20200208T064643_20200208T064708_020174_026302_6B8F
S1B_IW_GRDH_1SDV_20180204T181340_20180204T181405_009477_0110B8_4145

Sentinel-1 Satellite Images used in Chapter 3 comparative assessment [continued].

S1A_IW_GRDH_1SDV_20180718T064732_20180718T064757_022845_027A2D_F242
S1B_IW_GRDH_1SDV_20180922T064640_20180922T064705_012824_017ACC_2269
S1A_IW_GRDH_1SDV_20180519T064729_20180519T064754_021970_025F6A_C74E
S1B_IW_GRDH_1SDV_20180604T181332_20180604T181357_011227_0149AF_8F00
S1B_IW_GRDH_1SDV_20181215T064639_20181215T064704_014049_01A143_0D06
S1B_IW_GRDH_1SDV_20180618T064635_20180618T064700_011424_014FB3_2ED2
S1A_IW_GRDH_1SDV_20181008T181420_20181008T181445_024048_02A0BD_3278
S1B_IW_GRDH_1SDV_20180305T182152_20180305T182217_009900_011EBB_FA0B
S1B_IW_GRDH_1SDV_20181206T182158_20181206T182223_013925_019D49_ABD7
S1B_IW_GRDH_1SDV_20180908T181338_20180908T181403_012627_0174C9_BB2C
S1B_IW_GRDH_1SDV_20180513T064632_20180513T064657_010899_013F0E_277B
S1A_IW_GRDH_1SDV_20180916T064735_20180916T064800_023720_02960A_1D0E
S1B_IW_GRDH_1SDV_20180724T064637_20180724T064702_011949_015FE6_9EC5
S1A_IW_GRDH_1SDV_20180306T181430_20180306T181455_020898_023D9E_C517
S1B_IW_GRDH_1SDV_20180901T182158_20180901T182223_012525_0171AC_9113
S1B_IW_GRDH_1SDV_20181203T064639_20181203T064704_013874_019B8D_09AC
S1B_IW_GRDH_1SDV_20180419T064656_20180419T064721_010549_0133C5_F1FF
S1B_IW_GRDH_1SDV_20180703T182154_20180703T182219_011650_0156CE_ED22
S1B_IW_GRDH_1SDV_20180326T064630_20180326T064655_010199_01287E_94F2
S1B_IW_GRDH_1SDV_20181121T064640_20181121T064705_013699_0195F0_108A
S1A_IW_GRDH_1SDV_20181115T064736_20181115T064801_024595_02B363_310D
S1B_IW_GRDH_1SDV_20180104T182153_20180104T182218_009025_0101F7_0B16
S1B_IW_GRDH_1SDV_20181107T181338_20181107T181403_013502_018FC0_3C68
S1B_IW_GRDH_1SDV_20180410T182150_20180410T182215_010425_012FDA_4ECC
S1B_IW_GRDH_1SDV_20181227T064639_20181227T064704_014224_01A711_C19E
S1B_IW_GRDH_1SDV_20180817T064638_20180817T064703_012299_016A99_E044
S1B_IW_GRDH_1SDV_20181109T064640_20181109T064705_013524_019064_EEEC

Sentinel-1 Satellite Images used in Chapter 3 comparative assessment [continued].

S1B_IW_GRDH_1SDV_20181016T064705_20181016T064730_013174_01857C_1B2F
S1A_IW_GRDH_1SDV_20180320T064726_20180320T064751_021095_0243D9_617A
S1B_IW_GRDH_1SDV_20181004T064640_20181004T064705_012999_018024_2997
S1B_IW_GRDH_1SDV_20180123T181405_20180123T181430_009302_010AFB_E818
S1B_IW_GRDH_1SDV_20181004T064615_20181004T064640_012999_018024_10F1
S1B_IW_GRDH_1SDV_20180501T064607_20180501T064632_010724_013964_DF26
S1A_IW_GRDH_1SDV_20180318T181455_20180318T181520_021073_024324_DDCB
S1A_IW_GRDH_1SDV_20180926T181510_20180926T181535_023873_029AFC_E7D9
S1B_IW_GRDH_1SDV_20180324T181405_20180324T181430_010177_0127D0_EE1F
S1B_IW_GRDH_1SDV_20180910T064614_20180910T064639_012649_017570_E8BB
S1B_IW_GRDH_1SDV_20180223T065411_20180223T065436_009747_0119A3_9310
S1B_IW_GRDH_1SDV_20180628T181424_20180628T181449_011577_015482_FD4E
S1A_IW_GRDH_1SDV_20180529T181504_20180529T181529_022123_026458_1370
S1B_IW_GRDH_1SDV_20181203T064614_20181203T064639_013874_019B8D_96B0
S1B_IW_GRDH_1SDV_20180407T064606_20180407T064631_010374_012E32_1FE6
S1B_IW_GRDH_1SDV_20180216T181405_20180216T181430_009652_01167C_FEEA
S1B_IW_GRDH_1SDV_20181109T064615_20181109T064640_013524_019064_F336
S1B_IW_GRDH_1SDV_20180606T064609_20180606T064634_011249_014A4E_B213
S1B_IW_GRDH_1SDV_20180206T064605_20180206T064630_009499_01116E_DF3E
S1B_IW_GRDH_1SDV_20181026T181429_20181026T181454_013327_018A40_A84E
S1A_IW_GRDH_1SDV_20180728T181507_20180728T181532_022998_027F08_6C09
S1A_IW_GRDH_1SDV_20180423T181502_20180423T181527_021598_02539D_185D
S1B_IW_GRDH_1SDV_20180302T064605_20180302T064630_009849_011CFA_74C7
S1A_IW_GRDH_1SDV_20181125T181510_20181125T181535_024748_02B901_FA1F
S1B_IW_GRDH_1SDV_20180805T064613_20180805T064638_012124_01652F_CBBC
S1B_IW_GRDH_1SDV_20180101T064607_20180101T064632_008974_01003F_E604
S1B_IW_GRDH_1SDV_20180712T064611_20180712T064636_011774_015A92_D13D

Sentinel-1 Satellite Images used in Chapter 3 comparative assessment [continued].

S1B_IW_GRDH_1SDV_20180827T181427_20180827T181452_012452_016F63_FAAA
S1A_IW_GRDH_1SDV_20180505T181412_20180505T181437_021773_025929_6F13
S1B_IW_GRDH_1SDV_20181227T064639_20181227T064704_014224_01A711_C19E
S1B_IW_GRDH_1SDV_20180604T181332_20180604T181357_011227_0149AF_8F00
S1B_IW_GRDH_1SDV_20180901T182158_20180901T182223_012525_0171AC_9113
S1B_IW_GRDH_1SDV_20181004T064640_20181004T064705_012999_018024_2997
S1B_IW_GRDH_1SDV_20181107T181338_20181107T181403_013502_018FC0_3C68
S1B_IW_GRDH_1SDV_20180218T064655_20180218T064720_009674_01172A_1F11
S1B_IW_GRDH_1SDV_20181206T182158_20181206T182223_013925_019D49_ABD7
S1B_IW_GRDH_1SDV_20180922T064640_20180922T064705_012824_017ACC_2269
S1A_IW_GRDH_1SDV_20180306T181430_20180306T181455_020898_023D9E_C517
S1B_IW_GRDH_1SDV_20180817T064638_20180817T064703_012299_016A99_E044
S1A_IW_GRDH_1SDV_20180105T181406_20180105T181431_020023_0221C8_B853
S1B_IW_GRDH_1SDV_20180419T064656_20180419T064721_010549_0133C5_F1FF
S1A_IW_GRDH_1SDV_20180519T064729_20180519T064754_021970_025F6A_C74E
S1B_IW_GRDH_1SDV_20180410T182150_20180410T182215_010425_012FDA_4ECC
S1B_IW_GRDH_1SDV_20180405T181341_20180405T181406_010352_012D81_07A4
S1B_IW_GRDH_1SDV_20181028T064640_20181028T064705_013349_018AED_3E83
S1B_IW_GRDH_1SDV_20180803T181336_20180803T181401_012102_016488_63D5
S1B_IW_GRDH_1SDV_20180419T064631_20180419T064656_010549_0133C5_00DD
S1B_IW_GRDH_1SDV_20181016T064640_20181016T064705_013174_01857C_8C04
S1B_IW_GRDH_1SDV_20180326T064630_20180326T064655_010199_01287E_94F2
S1B_IW_GRDH_1SDV_20180618T064635_20180618T064700_011424_014FB3_2ED2
S1B_IW_GRDH_1SDV_20180204T181340_20180204T181405_009477_0110B8_4145
S1B_IW_GRDH_1SDV_20180501T064632_20180501T064657_010724_013964_1914
S1A_IW_GRDH_1SDV_20180105T181431_20180105T181456_020023_0221C8_46C5
S1B_IW_GRDH_1SDV_20181121T064640_20181121T064705_013699_0195F0_108A

Sentinel-1 Satellite Images used in Chapter 3 comparative assessment [continued].

S1B_IW_GRDH_1SDV_20200208T064643_20200208T064708_020174_026302_6B8F
S1B_IW_GRDH_1SDV_20180305T182152_20180305T182217_009900_011EBB_FA0B
S1A_IW_GRDH_1SDV_20181001T182219_20181001T182248_023946_029D66_36E8
S1B_IW_GRDH_1SDV_20180703T182154_20180703T182219_011650_0156CE_ED22
S1B_IW_GRDH_1SDV_20181215T064639_20181215T064704_014049_01A143_0D06
S1B_IW_GRDH_1SDV_20180908T181338_20180908T181403_012627_0174C9_BB2C
S1A_IW_GRDH_1SDV_20181207T181419_20181207T181444_024923_02BEDC_878A
S1A_IW_GRDH_1SDV_20180916T064735_20180916T064800_023720_02960A_1D0E
S1B_IW_GRDH_1SDV_20180805T064638_20180805T064703_012124_01652F_BCF8
S1A_IW_GRDH_1SDV_20180802T182217_20180802T182246_023071_028139_1952
S1A_IW_GRDH_1SDV_20181008T181420_20181008T181445_024048_02A0BD_3278
S1B_IW_GRDH_1SDV_20180724T064637_20180724T064702_011949_015FE6_9EC5
S1A_IW_GRDH_1SDV_20180718T064732_20180718T064757_022845_027A2D_F242
S1B_IW_GRDH_1SDV_20180104T182153_20180104T182218_009025_0101F7_0B16
S1B_IW_GRDH_1SDV_20181109T064640_20181109T064705_013524_019064_EEEEC
S1B_IW_GRDH_1SDV_20181016T064705_20181016T064730_013174_01857C_1B2F
S1B_IW_GRDH_1SDV_20180513T064632_20180513T064657_010899_013F0E_277B
S1B_IW_GRDH_1SDV_20180407T064631_20180407T064656_010374_012E32_D172
S1B_IW_GRDH_1SDV_20180910T064639_20180910T064704_012649_017570_82BE
S1B_IW_GRDH_1SDV_20181203T064639_20181203T064704_013874_019B8D_09AC
S1A_IW_GRDH_1SDV_20180306T181405_20180306T181430_020898_023D9E_D33E
S1B_IW_GRDH_1SDV_20180218T064630_20180218T064655_009674_01172A_8A8C
S1B_IW_GRDH_1SDV_20180314T064630_20180314T064655_010024_0122D0_A696
S1A_IW_GRDH_1SDV_20181106T182219_20181106T182248_024471_02AED0_BE52
S1A_IW_GRDH_1SDV_20180203T182213_20180203T182242_020446_022F4C_081D
S1B_IW_GRDH_1SDV_20180817T064703_20180817T064728_012299_016A99_471C
S1A_IW_GRDH_1SDV_20180320T064726_20180320T064751_021095_0243D9_617A

Sentinel-1 Satellite Images used in Chapter 3 comparative assessment [continued].

S1A_IW_GRDH_1SDV_20181115T064736_20181115T064801_024595_02B363_310D
S1A_IW_GRDH_1SDV_20180704T181416_20180704T181441_022648_027435_4422
S1B_IW_GRDH_1SDV_20180525T064633_20180525T064658_011074_0144BE_B5AE
S1A_IW_GRDH_1SDV_20180119T064727_20180119T064752_020220_022805_2644
S1B_IW_GRDH_1SDV_20180618T064700_20180618T064725_011424_014FB3_A91A
S1B_IW_GRDH_1SDV_20180504T182151_20180504T182216_010775_013B11_FADF
S1A_IW_GRDH_1SDV_20180603T182213_20180603T182242_022196_0266A5_CE5D
S1A_IW_GRDH_1SDV_20180802T182217_20180802T182246_023071_028139_1952
S1B_IW_GRDH_1SDV_20180305T182127_20180305T182152_009900_011EBB_4F55
S1B_IW_GRDH_1SDV_20180419T064656_20180419T064721_010549_0133C5_F1FF
S1B_IW_GRDH_1SDV_20180604T181332_20180604T181357_011227_0149AF_8F00
S1B_IW_GRDH_1SDV_20180817T064703_20180817T064728_012299_016A99_471C
S1A_IW_GRDH_1SDV_20180704T181416_20180704T181441_022648_027435_4422
S1A_IW_GRDH_1SDV_20181001T182219_20181001T182248_023946_029D66_36E8
S1A_IW_GRDH_1SDV_20180105T181406_20180105T181431_020023_0221C8_B853
S1B_IW_GRDH_1SDV_20180504T182126_20180504T182151_010775_013B11_9F2C
S1A_IW_GRDH_1SDV_20180306T181405_20180306T181430_020898_023D9E_D33E
S1A_IW_GRDH_1SDV_20180916T064735_20180916T064800_023720_02960A_1D0E
S1B_IW_GRDH_1SDV_20180703T182154_20180703T182219_011650_0156CE_ED22
S1B_IW_GRDH_1SDV_20180305T182152_20180305T182217_009900_011EBB_FA0B
S1B_IW_GRDH_1SDV_20180901T182133_20180901T182158_012525_0171AC_B2A5
S1A_IW_GRDH_1SDV_20180519T064729_20180519T064754_021970_025F6A_C74E
S1A_IW_GRDH_1SDV_20180718T064732_20180718T064757_022845_027A2D_F242
S1B_IW_GRDH_1SDV_20180803T181336_20180803T181401_012102_016488_63D5
S1B_IW_GRDH_1SDV_20180908T181338_20180908T181403_012627_0174C9_BB2C
S1B_IW_GRDH_1SDV_20180218T064655_20180218T064720_009674_01172A_1F11
S1A_IW_GRDH_1SDV_20181207T181419_20181207T181444_024923_02BEDC_878A

Sentinel-1 Satellite Images used in Chapter 3 comparative assessment [continued].

S1B_IW_GRDH_1SDV_20181206T182158_20181206T182223_013925_019D49_ABD7
S1B_IW_GRDH_1SDV_20180703T182129_20180703T182154_011650_0156CE_A750
S1B_IW_GRDH_1SDV_20180504T182151_20180504T182216_010775_013B11_FADF
S1A_IW_GRDH_1SDV_20181008T181420_20181008T181445_024048_02A0BD_3278
S1A_IW_GRDH_1SDV_20180119T064727_20180119T064752_020220_022805_2644
S1A_IW_GRDH_1SDV_20181106T182219_20181106T182248_024471_02AED0_BE52
S1B_IW_GRDH_1SDV_20180104T182128_20180104T182153_009025_0101F7_4CE4
S1B_IW_GRDH_1SDV_20180618T064700_20180618T064725_011424_014FB3_A91A
S1B_IW_GRDH_1SDV_20180901T182158_20180901T182223_012525_0171AC_9113
S1A_IW_GRDH_1SDV_20180203T182213_20180203T182242_020446_022F4C_081D
S1B_IW_GRDH_1SDV_20180204T181340_20180204T181405_009477_0110B8_4145
S1B_IW_GRDH_1SDV_20181016T064705_20181016T064730_013174_01857C_1B2F
S1B_IW_GRDH_1SDV_20180405T181341_20180405T181406_010352_012D81_07A4
S1B_IW_GRDH_1SDV_20181206T182133_20181206T182158_013925_019D49_A204
S1B_IW_GRDH_1SDV_20180410T182125_20180410T182150_010425_012FDA_5845
S1A_IW_GRDH_1SDV_20180505T181412_20180505T181437_021773_025929_6F13
S1B_IW_GRDH_1SDV_20180410T182150_20180410T182215_010425_012FDA_4ECC
S1B_IW_GRDH_1SDV_20180104T182153_20180104T182218_009025_0101F7_0B16
S1A_IW_GRDH_1SDV_20181115T064736_20181115T064801_024595_02B363_310D
S1A_IW_GRDH_1SDV_20180320T064726_20180320T064751_021095_0243D9_617A
S1B_IW_GRDH_1SDV_20181107T181338_20181107T181403_013502_018FC0_3C68
S1A_IW_GRDH_1SDV_20180603T182213_20180603T182242_022196_0266A5_CE5D
S1B_IW_GRDH_1SDV_20181206T182133_20181206T182158_013925_019D49_A204
S1B_IW_GRDH_1SDV_20180504T182151_20180504T182216_010775_013B11_FADF
S1B_IW_GRDH_1SDV_20180817T064703_20180817T064728_012299_016A99_471C
S1B_IW_GRDH_1SDV_20180326T064655_20180326T064720_010199_01287E_5DD2
S1B_IW_GRDH_1SDV_20180125T064656_20180125T064721_009324_010BB1_EF96

Sentinel-1 Satellite Images used in Chapter 3 comparative assessment [continued].

S1B_IW_GRDH_1SDV_20180829T064704_20180829T064729_012474_01700C_BB46
S1B_IW_GRDH_1SDV_20180703T182154_20180703T182219_011650_0156CE_ED22
S1B_IW_GRDH_1SDV_20181121T064705_20181121T064730_013699_0195F0_24E2
S1B_IW_GRDH_1SDV_20180724T064702_20180724T064727_011949_015FE6_BABD
S1A_IW_GRDH_1SDV_20181106T182219_20181106T182248_024471_02AED0_BE52
S1A_IW_GRDH_1SDV_20180916T064735_20180916T064800_023720_02960A_1D0E
S1A_IW_GRDH_1SDV_20180718T064732_20180718T064757_022845_027A2D_F242
S1A_IW_GRDH_1SDV_20180519T064729_20180519T064754_021970_025F6A_C74E
S1B_IW_GRDH_1SDV_20180504T182126_20180504T182151_010775_013B11_9F2C
S1B_IW_GRDH_1SDV_20180630T064701_20180630T064726_011599_015528_DCF6
S1B_IW_GRDH_1SDV_20180922T064705_20180922T064730_012824_017ACC_2CE2
S1B_IW_GRDH_1SDV_20180419T064656_20180419T064721_010549_0133C5_F1FF
S1A_IW_GRDH_1SDV_20180709T182215_20180709T182244_022721_027653_3086
S1B_IW_GRDH_1SDV_20180410T182150_20180410T182215_010425_012FDA_4ECC
S1A_IW_GRDH_1SDV_20180907T182219_20180907T182248_023596_029211_2537
S1B_IW_GRDH_1SDV_20180530T065504_20180530T065529_011147_014721_6233
S1A_IW_GRDH_1SDV_20180802T182217_20180802T182246_023071_028139_1952
S1A_IW_GRDH_1SDV_20180110T182213_20180110T182242_020096_022427_242B
S1B_IW_GRDH_1SDV_20181206T182158_20181206T182223_013925_019D49_ABD7
S1B_IW_GRDH_1SDV_20180305T182127_20180305T182152_009900_011EBB_4F55
S1B_IW_GRDH_1SDV_20180305T182152_20180305T182217_009900_011EBB_FA0B
S1B_IW_GRDH_1SDV_20180703T182129_20180703T182154_011650_0156CE_A750
S1A_IW_GRDH_1SDV_20180603T182213_20180603T182242_022196_0266A5_CE5D
S1A_IW_GRDH_1SDV_20180320T064726_20180320T064751_021095_0243D9_617A
S1A_IW_GRDH_1SDV_20180416T182211_20180416T182240_021496_025081_A4EC
S1A_IW_GRDH_1SDV_20180311T182212_20180311T182241_020971_023FF8_BAD8
S1B_IW_GRDH_1SDV_20180901T182133_20180901T182158_012525_0171AC_B2A5

Sentinel-1 Satellite Images used in Chapter 3 comparative assessment [continued].

S1B_IW_GRDH_1SDV_20180104T182128_20180104T182153_009025_0101F7_4CE4
S1B_IW_GRDH_1SDV_20180901T182158_20180901T182223_012525_0171AC_9113
S1B_IW_GRDH_1SDV_20180218T064655_20180218T064720_009674_01172A_1F11
S1B_IW_GRDH_1SDV_20180618T064700_20180618T064725_011424_014FB3_A91A
S1B_IW_GRDH_1SDV_20180104T182153_20180104T182218_009025_0101F7_0B16
S1B_IW_GRDH_1SDV_20180410T182125_20180410T182150_010425_012FDA_5845
S1A_IW_GRDH_1SDV_20181115T064736_20181115T064801_024595_02B363_310D
S1A_IW_GRDH_1SDV_20181001T182219_20181001T182248_023946_029D66_36E8
S1A_IW_GRDH_1SDV_20180119T064727_20180119T064752_020220_022805_2644
S1A_IW_GRDH_1SDV_20180203T182213_20180203T182242_020446_022F4C_081D
S1B_IW_GRDH_1SDV_20181227T064704_20181227T064729_014224_01A711_481A
S1B_IW_GRDH_1SDV_20181016T064705_20181016T064730_013174_01857C_1B2F
S1B_IW_GRDH_1SDV_20180216T181340_20180216T181405_009652_01167C_E516
S1B_IW_GRDH_1SDV_20180429T181355_20180429T181420_010702_0138B4_623A
S1B_IW_GRDH_1SDV_20180613T063822_20180613T063847_011351_014D75_B790
S1B_IW_GRDH_1SDV_20180414T063818_20180414T063843_010476_013175_07AC
S1B_IW_GRDH_1SDV_20181026T181339_20181026T181404_013327_018A40_CBCE
S1B_IW_GRDH_1SDV_20180719T063824_20180719T063849_011876_015DB8_C720
S1A_IW_GRDH_1SDV_20180728T181442_20180728T181507_022998_027F08_18A7
S1A_IW_GRDH_1SDV_20180926T181420_20180926T181445_023873_029AFC_286D
S1B_IW_GRDH_1SDV_20180108T063819_20180108T063844_009076_010399_CE40
S1B_IW_GRDH_1SDV_20181026T181404_20181026T181429_013327_018A40_27EE
S1A_IW_GRDH_1SDV_20180529T181414_20180529T181439_022123_026458_0E89
S1A_IW_GRDH_1SDV_20181125T181420_20181125T181445_024748_02B901_6C87
S1B_IW_GRDH_1SDV_20181116T063827_20181116T063852_013626_0193A6_BCAA
S1B_IW_GRDH_1SDV_20180213T063818_20180213T063843_009601_0114D5_C7EB
S1B_IW_GRDH_1SDV_20181011T063828_20181011T063853_013101_018347_ED4F

Sentinel-1 Satellite Images used in Chapter 3 comparative assessment [continued].

S1A_IW_GRDH_1SDV_20180529T181439_20180529T181504_022123_026458_FD04
S1B_IW_GRDH_1SDV_20180628T181334_20180628T181359_011577_015482_7D1E
S1A_IW_GRDH_1SDV_20180728T181417_20180728T181442_022998_027F08_69D9
S1B_IW_GRDH_1SDV_20180123T181340_20180123T181405_009302_010AFB_4089
S1A_IW_GRDH_1SDV_20181125T181445_20181125T181510_024748_02B901_F660
S1B_IW_GRDH_1SDV_20180917T063827_20180917T063852_012751_017898_EC7B
S1B_IW_GRDH_1SDV_20180812T063825_20180812T063850_012226_016864_D252
S1B_IW_GRDH_1SDV_20180827T181337_20180827T181402_012452_016F63_6A72
S1B_IW_GRDH_1SDV_20181225T181337_20181225T181402_014202_01A65C_15FC
S1B_IW_GRDH_1SDV_20180309T063818_20180309T063843_009951_012073_39CA
S1B_IW_GRDH_1SDV_20180628T181359_20180628T181424_011577_015482_5A2D
S1B_IW_GRDH_1SDV_20181225T181402_20181225T181427_014202_01A65C_7D36
S1B_IW_GRDH_1SDV_20180429T181330_20180429T181355_010702_0138B4_9AEB
S1B_IW_GRDH_1SDV_20181210T063826_20181210T063851_013976_019EE7_2332
S1A_IW_GRDH_1SDV_20180926T181445_20180926T181510_023873_029AFC_FFA2
S1B_IW_GRDH_1SDV_20180508T063819_20180508T063844_010826_013CB2_534A
S1B_IW_GRDH_1SDV_20180827T181402_20180827T181427_012452_016F63_A9F2

A.2 Sentinel-2 Images

Table A.2: Sentinel-2 Satellite Images used in Chapter 3 comparative assessment.

S2B_MSIL2A_20181224T113459_N0211_R080_T30UUF_20181224T122924
S2B_MSIL2A_20181207T114449_N0211_R123_T30UUF_20181207T153404
S2B_MSIL2A_20181207T114449_N0211_R123_T29UPV_20181207T153404
S2B_MSIL2A_20181207T114449_N0211_R123_T29UPU_20181207T153404
S2B_MSIL2A_20181207T114449_N0211_R123_T29UPA_20181207T153404
S2B_MSIL2A_20181207T114449_N0211_R123_T29UNV_20181207T153404
S2B_MSIL2A_20181207T114449_N0211_R123_T29UNU_20181207T153404
S2B_MSIL2A_20181207T114449_N0211_R123_T29UNA_20181207T153404
S2B_MSIL2A_20181207T114449_N0211_R123_T29UMU_20181207T153404
S2B_MSIL2A_20181207T114449_N0211_R123_T29UMT_20181207T153404
S2B_MSIL2A_20181130T115439_N0211_R023_T29UNV_20181130T155554
S2B_MSIL2A_20181130T115439_N0211_R023_T29UNB_20181130T155554
S2B_MSIL2A_20181130T115439_N0211_R023_T29UNA_20181130T155554
S2B_MSIL2A_20181127T114419_N0211_R123_T29UNU_20181127T124838
S2B_MSIL2A_20181127T114419_N0211_R123_T29UNT_20181127T124838
S2B_MSIL2A_20181127T114419_N0211_R123_T29UMU_20181127T124838
S2B_MSIL2A_20181127T114419_N0211_R123_T29UMT_20181127T154700
S2B_MSIL2A_20181127T114419_N0211_R123_T29UMT_20181127T124838
S2B_MSIL2A_20181120T115359_N0210_R023_T29UMV_20181120T161636
S2B_MSIL2A_20181120T115359_N0210_R023_T29UMT_20181120T161636
S2B_MSIL2A_20181120T115359_N0210_R023_T29ULT_20181120T161636
S2B_MSIL2A_20181110T115359_N0210_R023_T29UPB_20181110T160522
S2B_MSIL2A_20181110T115359_N0210_R023_T29UPA_20181110T160522
S2B_MSIL2A_20181110T115359_N0210_R023_T29UNV_20181110T160522
S2B_MSIL2A_20181110T115359_N0210_R023_T29UNU_20181110T160522

Sentinel-2 Satellite Images used in Chapter 3 comparative assessment [continued].

S2B_MSIL2A_20181110T115359_N0210_R023_T29UNT_20181110T160522
S2B_MSIL2A_20181110T115359_N0210_R023_T29UNB_20181110T160522
S2B_MSIL2A_20181110T115359_N0210_R023_T29UNA_20181110T160522
S2B_MSIL2A_20181110T115359_N0210_R023_T29UMV_20181110T160522
S2B_MSIL2A_20181110T115359_N0210_R023_T29UMU_20181110T160522
S2B_MSIL2A_20181110T115359_N0210_R023_T29UMT_20181110T160522
S2B_MSIL2A_20181104T113319_N0209_R080_T30UUF_20181104T143826
S2B_MSIL2A_20181104T113319_N0209_R080_T29UPV_20181104T143826
S2B_MSIL2A_20181104T113319_N0209_R080_T29UPA_20181104T143826
S2B_MSIL2A_20181028T114349_N0209_R123_T30UUF_20181028T175230
S2B_MSIL2A_20181028T114349_N0209_R123_T29UPV_20181028T175230
S2B_MSIL2A_20181028T114349_N0209_R123_T29UPU_20181028T175230
S2B_MSIL2A_20181028T114349_N0209_R123_T29UPB_20181028T175230
S2B_MSIL2A_20181028T114349_N0209_R123_T29UPA_20181028T175230
S2B_MSIL2A_20181028T114349_N0209_R123_T29UNV_20181028T175230
S2B_MSIL2A_20181028T114349_N0209_R123_T29UNU_20181028T175230
S2B_MSIL2A_20181028T114349_N0209_R123_T29UNT_20181028T175230
S2B_MSIL2A_20181028T114349_N0209_R123_T29UNB_20181028T175230
S2B_MSIL2A_20181028T114349_N0209_R123_T29UNA_20181028T175230
S2B_MSIL2A_20181028T114349_N0209_R123_T29UMV_20181028T175230
S2B_MSIL2A_20181028T114349_N0209_R123_T29UMU_20181028T175230
S2B_MSIL2A_20181028T114349_N0209_R123_T29UMT_20181028T175230
S2B_MSIL2A_20181028T114349_N0209_R123_T29UMA_20181028T175230
S2B_MSIL2A_20181028T114349_N0209_R123_T29ULT_20181028T175230
S2B_MSIL2A_20181021T115359_N0209_R023_T29UNV_20181021T174705
S2B_MSIL2A_20181021T115359_N0209_R023_T29UNU_20181021T174705
S2B_MSIL2A_20181021T115359_N0209_R023_T29UNB_20181021T174705

Sentinel-2 Satellite Images used in Chapter 3 comparative assessment [continued].

S2B_MSIL2A_20181021T115359_N0209_R023_T29UMU_20181021T174705
S2B_MSIL2A_20181018T114349_N0209_R123_T30UUF_20181018T143222
S2B_MSIL2A_20181018T114349_N0209_R123_T29UPV_20181018T143222
S2B_MSIL2A_20181018T114349_N0209_R123_T29UPU_20181018T143222
S2B_MSIL2A_20181018T114349_N0209_R123_T29UPT_20181018T143222
S2B_MSIL2A_20181018T114349_N0209_R123_T29UPB_20181018T143222
S2B_MSIL2A_20181018T114349_N0209_R123_T29UPA_20181018T143222
S2B_MSIL2A_20181018T114349_N0209_R123_T29UNV_20181018T143222
S2B_MSIL2A_20181018T114349_N0209_R123_T29UNU_20181018T143222
S2B_MSIL2A_20181018T114349_N0209_R123_T29UNT_20181018T143222
S2B_MSIL2A_20181018T114349_N0209_R123_T29UNA_20181018T143222
S2B_MSIL2A_20181018T114349_N0209_R123_T29UMV_20181018T143222
S2B_MSIL2A_20181018T114349_N0209_R123_T29UMU_20181018T143222
S2B_MSIL2A_20181018T114349_N0209_R123_T29UMT_20181018T143222
S2B_MSIL2A_20181015T113319_N0209_R080_T30UUG_20181015T163033
S2B_MSIL2A_20181015T113319_N0209_R080_T30UUF_20181015T163033
S2B_MSIL2A_20181015T113319_N0209_R080_T29UPV_20181015T163033
S2B_MSIL2A_20181015T113319_N0209_R080_T29UPU_20181015T163033
S2B_MSIL2A_20181015T113319_N0209_R080_T29UPB_20181015T163033
S2B_MSIL2A_20181015T113319_N0209_R080_T29UPA_20181015T163033
S2B_MSIL2A_20181015T113319_N0209_R080_T29UNU_20181015T163033
S2B_MSIL2A_20181015T113319_N0209_R080_T29UNT_20181015T163033
S2B_MSIL2A_20181011T115359_N0209_R023_T29UMT_20181011T161453
S2B_MSIL2A_20181011T115359_N0209_R023_T29ULT_20181011T161453
S2B_MSIL2A_20181005T113319_N0208_R080_T30UUG_20181005T175906
S2B_MSIL2A_20181005T113319_N0208_R080_T30UUF_20181005T175906
S2B_MSIL2A_20180928T114349_N0208_R123_T29UPU_20180928T192024

Sentinel-2 Satellite Images used in Chapter 3 comparative assessment [continued].

S2B_MSIL2A_20180928T114349_N0208_R123_T29UNV_20180928T192024
S2B_MSIL2A_20180928T114349_N0208_R123_T29UNU_20180928T192024
S2B_MSIL2A_20180928T114349_N0208_R123_T29UMU_20180928T192024
S2B_MSIL2A_20180928T114349_N0208_R123_T29UMT_20180928T192024
S2B_MSIL2A_20180921T115349_N0208_R023_T29UPA_20180921T194601
S2B_MSIL2A_20180921T115349_N0208_R023_T29UNV_20180921T194601
S2B_MSIL2A_20180921T115349_N0208_R023_T29UNU_20180921T194601
S2B_MSIL2A_20180921T115349_N0208_R023_T29UNB_20180921T194601
S2B_MSIL2A_20180921T115349_N0208_R023_T29UNA_20180921T194601
S2B_MSIL2A_20180921T115349_N0208_R023_T29UMV_20180921T194601
S2B_MSIL2A_20180921T115349_N0208_R023_T29UMT_20180921T194601
S2B_MSIL2A_20180918T114339_N0208_R123_T29UPV_20180918T155828
S2B_MSIL2A_20180918T114339_N0208_R123_T29UPU_20180918T155828
S2B_MSIL2A_20180918T114339_N0208_R123_T29UNU_20180918T155828
S2B_MSIL2A_20180918T114339_N0208_R123_T29UNT_20180918T155828
S2B_MSIL2A_20180905T113309_N0208_R080_T29UPV_20180905T175148
S2B_MSIL2A_20180905T113309_N0208_R080_T29UPU_20180905T175148
S2B_MSIL2A_20180905T113309_N0208_R080_T29UPT_20180905T175148
S2B_MSIL2A_20180901T115349_N0208_R023_T29UNU_20180901T201240
S2B_MSIL2A_20180901T115349_N0208_R023_T29UNT_20180901T201240
S2B_MSIL2A_20180901T115349_N0208_R023_T29UMU_20180901T201240
S2B_MSIL2A_20180901T115349_N0208_R023_T29UMT_20180901T201240
S2B_MSIL2A_20180829T114339_N0208_R123_T30UUF_20180829T204905
S2B_MSIL2A_20180829T114339_N0208_R123_T29UPV_20180829T204905
S2B_MSIL2A_20180829T114339_N0208_R123_T29UPU_20180829T204905
S2B_MSIL2A_20180829T114339_N0208_R123_T29UPA_20180829T204905
S2B_MSIL2A_20180829T114339_N0208_R123_T29UNV_20180829T204905

Sentinel-2 Satellite Images used in Chapter 3 comparative assessment [continued].

S2B_MSIL2A_20180829T114339_N0208_R123_T29UNU_20180829T204905
S2B_MSIL2A_20180829T114339_N0208_R123_T29UNB_20180829T204905
S2B_MSIL2A_20180829T114339_N0208_R123_T29UNA_20180829T204905
S2B_MSIL2A_20180819T114339_N0208_R123_T29UPT_20180819T180914
S2B_MSIL2A_20180819T114339_N0208_R123_T29UNT_20180819T180914
S2B_MSIL2A_20180816T113309_N0208_R080_T29UPU_20180816T170436
S2B_MSIL2A_20180812T115359_N0208_R023_T29UNA_20180812T175844
S2B_MSIL2A_20180809T114349_N0208_R123_T30UG_20180809T181140
S2B_MSIL2A_20180809T114349_N0208_R123_T30UUF_20180809T181140
S2B_MSIL2A_20180809T114349_N0208_R123_T29UPV_20180809T181140
S2B_MSIL2A_20180809T114349_N0208_R123_T29UPA_20180809T181140
S2B_MSIL2A_20180809T114349_N0208_R123_T29UNV_20180809T181140
S2B_MSIL2A_20180809T114349_N0208_R123_T29UMU_20180809T181140
S2B_MSIL2A_20180809T114349_N0208_R123_T29UMT_20180809T181140
S2B_MSIL2A_20180730T114349_N0208_R123_T29UPV_20180730T193722
S2B_MSIL2A_20180730T114349_N0208_R123_T29UNV_20180730T193722
S2B_MSIL2A_20180730T114349_N0208_R123_T29UNB_20180730T193722
S2B_MSIL2A_20180730T114349_N0208_R123_T29UMT_20180730T193722
S2B_MSIL2A_20180713T115359_N0208_R023_T29UMU_20180713T174201
S2B_MSIL2A_20180713T115359_N0208_R023_T29UMT_20180713T174201
S2B_MSIL2A_20180710T114349_N0208_R123_T30UG_20180710T173033
S2B_MSIL2A_20180710T114349_N0208_R123_T29UPV_20180710T173033
S2B_MSIL2A_20180710T114349_N0208_R123_T29UPU_20180710T173033
S2B_MSIL2A_20180710T114349_N0208_R123_T29UPT_20180710T173033
S2B_MSIL2A_20180710T114349_N0208_R123_T29UPB_20180710T173033
S2B_MSIL2A_20180710T114349_N0208_R123_T29UPA_20180710T173033
S2B_MSIL2A_20180710T114349_N0208_R123_T29UNV_20180710T173033

Sentinel-2 Satellite Images used in Chapter 3 comparative assessment [continued].

S2B_MSIL2A_20180710T114349_N0208_R123_T29UNU_20180710T173033
S2B_MSIL2A_20180710T114349_N0208_R123_T29UNT_20180710T173033
S2B_MSIL2A_20180710T114349_N0208_R123_T29UMV_20180710T173033
S2B_MSIL2A_20180710T114349_N0208_R123_T29UMU_20180710T173033
S2B_MSIL2A_20180710T114349_N0208_R123_T29UMT_20180710T173033
S2B_MSIL2A_20180707T113319_N0208_R080_T29UPU_20180707T154927
S2B_MSIL2A_20180707T113319_N0208_R080_T29UPT_20180707T154927
S2B_MSIL2A_20180703T115359_N0208_R023_T29UPB_20180703T180433
S2B_MSIL2A_20180703T115359_N0208_R023_T29UPA_20180703T180433
S2B_MSIL2A_20180703T115359_N0208_R023_T29UNV_20180703T180433
S2B_MSIL2A_20180703T115359_N0208_R023_T29UNU_20180703T180433
S2B_MSIL2A_20180703T115359_N0208_R023_T29UNT_20180703T180433
S2B_MSIL2A_20180703T115359_N0208_R023_T29UNB_20180703T180433
S2B_MSIL2A_20180703T115359_N0208_R023_T29UNA_20180703T180433
S2B_MSIL2A_20180703T115359_N0208_R023_T29UMV_20180703T180433
S2B_MSIL2A_20180703T115359_N0208_R023_T29UMU_20180703T180433
S2B_MSIL2A_20180703T115359_N0208_R023_T29UMT_20180703T180433
S2B_MSIL2A_20180703T115359_N0208_R023_T29ULT_20180703T180433
S2B_MSIL2A_20180630T114349_N0208_R123_T30UUG_20180630T173428
S2B_MSIL2A_20180630T114349_N0208_R123_T30UUF_20180630T173428
S2B_MSIL2A_20180630T114349_N0208_R123_T29UPV_20180630T173428
S2B_MSIL2A_20180630T114349_N0208_R123_T29UPU_20180630T173428
S2B_MSIL2A_20180630T114349_N0208_R123_T29UPT_20180630T173428
S2B_MSIL2A_20180630T114349_N0208_R123_T29UPB_20180630T173428
S2B_MSIL2A_20180630T114349_N0208_R123_T29UPA_20180630T173428
S2B_MSIL2A_20180630T114349_N0208_R123_T29UNV_20180630T173428
S2B_MSIL2A_20180630T114349_N0208_R123_T29UNU_20180630T173428

Sentinel-2 Satellite Images used in Chapter 3 comparative assessment [continued].

S2B_MSIL2A_20180630T114349_N0208_R123_T29UNT_20180630T173428
S2B_MSIL2A_20180630T114349_N0208_R123_T29UNB_20180630T173428
S2B_MSIL2A_20180630T114349_N0208_R123_T29UNA_20180630T173428
S2B_MSIL2A_20180630T114349_N0208_R123_T29UMV_20180630T173428
S2B_MSIL2A_20181224T113459_N0211_R080_T30UUF_20181224T122924
S2B_MSIL2A_20181207T114449_N0211_R123_T30UUF_20181207T153404
S2B_MSIL2A_20181207T114449_N0211_R123_T29UPV_20181207T153404
S2B_MSIL2A_20181207T114449_N0211_R123_T29UPU_20181207T153404
S2B_MSIL2A_20181207T114449_N0211_R123_T29UPA_20181207T153404
S2B_MSIL2A_20181207T114449_N0211_R123_T29UNV_20181207T153404
S2B_MSIL2A_20181207T114449_N0211_R123_T29UNU_20181207T153404
S2B_MSIL2A_20181207T114449_N0211_R123_T29UNA_20181207T153404
S2B_MSIL2A_20181207T114449_N0211_R123_T29UMU_20181207T153404
S2B_MSIL2A_20181207T114449_N0211_R123_T29UMT_20181207T153404
S2B_MSIL2A_20181130T115439_N0211_R023_T29UNV_20181130T155554
S2B_MSIL2A_20181130T115439_N0211_R023_T29UNB_20181130T155554
S2B_MSIL2A_20181130T115439_N0211_R023_T29UNA_20181130T155554
S2B_MSIL2A_20181127T114419_N0211_R123_T29UNU_20181127T124838
S2B_MSIL2A_20181127T114419_N0211_R123_T29UNT_20181127T124838
S2B_MSIL2A_20181127T114419_N0211_R123_T29UMU_20181127T124838
S2B_MSIL2A_20181127T114419_N0211_R123_T29UMT_20181127T154700
S2B_MSIL2A_20181127T114419_N0211_R123_T29UMT_20181127T124838
S2B_MSIL2A_20181120T115359_N0210_R023_T29UMV_20181120T161636
S2B_MSIL2A_20181120T115359_N0210_R023_T29UMT_20181120T161636
S2B_MSIL2A_20181120T115359_N0210_R023_T29ULT_20181120T161636
S2B_MSIL2A_20181110T115359_N0210_R023_T29UPB_20181110T160522
S2B_MSIL2A_20181110T115359_N0210_R023_T29UPA_20181110T160522

Sentinel-2 Satellite Images used in Chapter 3 comparative assessment [continued].

S2B_MSIL2A_20181110T115359_N0210_R023_T29UNV_20181110T160522
S2B_MSIL2A_20181110T115359_N0210_R023_T29UNU_20181110T160522
S2B_MSIL2A_20181110T115359_N0210_R023_T29UNT_20181110T160522
S2B_MSIL2A_20181110T115359_N0210_R023_T29UNB_20181110T160522
S2B_MSIL2A_20181110T115359_N0210_R023_T29UNA_20181110T160522
S2B_MSIL2A_20181110T115359_N0210_R023_T29UMV_20181110T160522
S2B_MSIL2A_20181110T115359_N0210_R023_T29UMU_20181110T160522
S2B_MSIL2A_20181110T115359_N0210_R023_T29UMT_20181110T160522
S2B_MSIL2A_20181104T113319_N0209_R080_T30UUF_20181104T143826
S2B_MSIL2A_20181104T113319_N0209_R080_T29UPV_20181104T143826
S2B_MSIL2A_20181104T113319_N0209_R080_T29UPA_20181104T143826
S2B_MSIL2A_20181028T114349_N0209_R123_T30UUF_20181028T175230
S2B_MSIL2A_20181028T114349_N0209_R123_T29UPV_20181028T175230
S2B_MSIL2A_20181028T114349_N0209_R123_T29UPU_20181028T175230
S2B_MSIL2A_20181028T114349_N0209_R123_T29UPB_20181028T175230
S2B_MSIL2A_20181028T114349_N0209_R123_T29UPA_20181028T175230
S2B_MSIL2A_20181028T114349_N0209_R123_T29UNV_20181028T175230
S2B_MSIL2A_20181028T114349_N0209_R123_T29UNU_20181028T175230
S2B_MSIL2A_20181028T114349_N0209_R123_T29UNT_20181028T175230
S2B_MSIL2A_20181028T114349_N0209_R123_T29UNB_20181028T175230
S2B_MSIL2A_20181028T114349_N0209_R123_T29UNA_20181028T175230
S2B_MSIL2A_20181028T114349_N0209_R123_T29UMV_20181028T175230
S2B_MSIL2A_20181028T114349_N0209_R123_T29UMU_20181028T175230
S2B_MSIL2A_20181028T114349_N0209_R123_T29UMT_20181028T175230
S2B_MSIL2A_20181028T114349_N0209_R123_T29UMA_20181028T175230
S2B_MSIL2A_20181028T114349_N0209_R123_T29ULT_20181028T175230
S2B_MSIL2A_20181021T115359_N0209_R023_T29UNV_20181021T174705

Sentinel-2 Satellite Images used in Chapter 3 comparative assessment [continued].

S2B_MSIL2A_20181021T115359_N0209_R023_T29UNU_20181021T174705
S2B_MSIL2A_20181021T115359_N0209_R023_T29UNB_20181021T174705
S2B_MSIL2A_20181021T115359_N0209_R023_T29UMU_20181021T174705
S2B_MSIL2A_20181018T114349_N0209_R123_T30UUF_20181018T143222
S2B_MSIL2A_20181018T114349_N0209_R123_T29UPV_20181018T143222
S2B_MSIL2A_20181018T114349_N0209_R123_T29UPU_20181018T143222
S2B_MSIL2A_20181018T114349_N0209_R123_T29UPT_20181018T143222
S2B_MSIL2A_20181018T114349_N0209_R123_T29UPB_20181018T143222
S2B_MSIL2A_20181018T114349_N0209_R123_T29UPA_20181018T143222
S2B_MSIL2A_20181018T114349_N0209_R123_T29UNV_20181018T143222
S2B_MSIL2A_20181018T114349_N0209_R123_T29UNU_20181018T143222
S2B_MSIL2A_20181018T114349_N0209_R123_T29UNT_20181018T143222
S2B_MSIL2A_20181018T114349_N0209_R123_T29UNA_20181018T143222
S2B_MSIL2A_20181018T114349_N0209_R123_T29UMV_20181018T143222
S2B_MSIL2A_20181018T114349_N0209_R123_T29UMU_20181018T143222
S2B_MSIL2A_20181018T114349_N0209_R123_T29UMT_20181018T143222
S2B_MSIL2A_20181015T113319_N0209_R080_T30UUG_20181015T163033
S2B_MSIL2A_20181015T113319_N0209_R080_T30UUF_20181015T163033
S2B_MSIL2A_20181015T113319_N0209_R080_T29UPV_20181015T163033
S2B_MSIL2A_20181015T113319_N0209_R080_T29UPU_20181015T163033
S2B_MSIL2A_20181015T113319_N0209_R080_T29UPB_20181015T163033
S2B_MSIL2A_20181015T113319_N0209_R080_T29UPA_20181015T163033
S2B_MSIL2A_20181015T113319_N0209_R080_T29UNU_20181015T163033
S2B_MSIL2A_20181015T113319_N0209_R080_T29UNT_20181015T163033
S2B_MSIL2A_20181011T115359_N0209_R023_T29UMT_20181011T161453
S2B_MSIL2A_20181011T115359_N0209_R023_T29ULT_20181011T161453
S2B_MSIL2A_20181005T113319_N0208_R080_T30UUG_20181005T175906

Sentinel-2 Satellite Images used in Chapter 3 comparative assessment [continued].

S2B_MSIL2A_20181005T113319_N0208_R080_T30UUF_20181005T175906
S2B_MSIL2A_20180928T114349_N0208_R123_T29UPU_20180928T192024
S2B_MSIL2A_20180928T114349_N0208_R123_T29UNV_20180928T192024
S2B_MSIL2A_20180928T114349_N0208_R123_T29UNU_20180928T192024
S2B_MSIL2A_20180928T114349_N0208_R123_T29UMU_20180928T192024
S2B_MSIL2A_20180928T114349_N0208_R123_T29UMT_20180928T192024
S2B_MSIL2A_20180921T115349_N0208_R023_T29UPA_20180921T194601
S2B_MSIL2A_20180921T115349_N0208_R023_T29UNV_20180921T194601
S2B_MSIL2A_20180921T115349_N0208_R023_T29UNU_20180921T194601
S2B_MSIL2A_20180921T115349_N0208_R023_T29UNB_20180921T194601
S2B_MSIL2A_20180921T115349_N0208_R023_T29UNA_20180921T194601
S2B_MSIL2A_20180921T115349_N0208_R023_T29UMV_20180921T194601
S2B_MSIL2A_20180921T115349_N0208_R023_T29UMT_20180921T194601
S2B_MSIL2A_20180918T114339_N0208_R123_T29UPV_20180918T155828
S2B_MSIL2A_20180918T114339_N0208_R123_T29UPU_20180918T155828
S2B_MSIL2A_20180918T114339_N0208_R123_T29UNU_20180918T155828
S2B_MSIL2A_20180918T114339_N0208_R123_T29UNT_20180918T155828
S2B_MSIL2A_20180905T113309_N0208_R080_T29UPV_20180905T175148
S2B_MSIL2A_20180905T113309_N0208_R080_T29UPU_20180905T175148
S2B_MSIL2A_20180905T113309_N0208_R080_T29UPT_20180905T175148
S2B_MSIL2A_20180901T115349_N0208_R023_T29UNU_20180901T201240
S2B_MSIL2A_20180901T115349_N0208_R023_T29UNT_20180901T201240
S2B_MSIL2A_20180901T115349_N0208_R023_T29UMU_20180901T201240
S2B_MSIL2A_20180901T115349_N0208_R023_T29UMT_20180901T201240
S2B_MSIL2A_20180829T114339_N0208_R123_T30UUF_20180829T204905
S2B_MSIL2A_20180829T114339_N0208_R123_T29UPV_20180829T204905
S2B_MSIL2A_20180829T114339_N0208_R123_T29UPU_20180829T204905

Sentinel-2 Satellite Images used in Chapter 3 comparative assessment [continued].

S2B_MSIL2A_20180829T114339_N0208_R123_T29UPA_20180829T204905
S2B_MSIL2A_20180829T114339_N0208_R123_T29UNV_20180829T204905
S2B_MSIL2A_20180829T114339_N0208_R123_T29UNU_20180829T204905
S2B_MSIL2A_20180829T114339_N0208_R123_T29UNB_20180829T204905
S2B_MSIL2A_20180829T114339_N0208_R123_T29UNA_20180829T204905
S2B_MSIL2A_20180819T114339_N0208_R123_T29UPT_20180819T180914
S2B_MSIL2A_20180819T114339_N0208_R123_T29UNT_20180819T180914
S2B_MSIL2A_20180816T113309_N0208_R080_T29UPU_20180816T170436
S2B_MSIL2A_20180812T115359_N0208_R023_T29UNA_20180812T175844
S2B_MSIL2A_20180809T114349_N0208_R123_T30UG_20180809T181140
S2B_MSIL2A_20180809T114349_N0208_R123_T30UUF_20180809T181140
S2B_MSIL2A_20180809T114349_N0208_R123_T29UPV_20180809T181140
S2B_MSIL2A_20180809T114349_N0208_R123_T29UPA_20180809T181140
S2B_MSIL2A_20180809T114349_N0208_R123_T29UNV_20180809T181140
S2B_MSIL2A_20180809T114349_N0208_R123_T29UMU_20180809T181140
S2B_MSIL2A_20180809T114349_N0208_R123_T29UMT_20180809T181140
S2B_MSIL2A_20180730T114349_N0208_R123_T29UPV_20180730T193722
S2B_MSIL2A_20180730T114349_N0208_R123_T29UNV_20180730T193722
S2B_MSIL2A_20180730T114349_N0208_R123_T29UNB_20180730T193722
S2B_MSIL2A_20180730T114349_N0208_R123_T29UMT_20180730T193722
S2B_MSIL2A_20180713T115359_N0208_R023_T29UMU_20180713T174201
S2B_MSIL2A_20180713T115359_N0208_R023_T29UMT_20180713T174201
S2B_MSIL2A_20180710T114349_N0208_R123_T30UG_20180710T173033
S2B_MSIL2A_20180710T114349_N0208_R123_T29UPV_20180710T173033
S2B_MSIL2A_20180710T114349_N0208_R123_T29UPU_20180710T173033
S2B_MSIL2A_20180710T114349_N0208_R123_T29UPT_20180710T173033
S2B_MSIL2A_20180710T114349_N0208_R123_T29UPB_20180710T173033

Sentinel-2 Satellite Images used in Chapter 3 comparative assessment [continued].

S2B_MSIL2A_20180710T114349_N0208_R123_T29UPA_20180710T173033
S2B_MSIL2A_20180710T114349_N0208_R123_T29UNV_20180710T173033
S2B_MSIL2A_20180710T114349_N0208_R123_T29UNU_20180710T173033
S2B_MSIL2A_20180710T114349_N0208_R123_T29UNT_20180710T173033
S2B_MSIL2A_20180710T114349_N0208_R123_T29UMV_20180710T173033
S2B_MSIL2A_20180710T114349_N0208_R123_T29UMU_20180710T173033
S2B_MSIL2A_20180710T114349_N0208_R123_T29UMT_20180710T173033
S2B_MSIL2A_20180707T113319_N0208_R080_T29UPU_20180707T154927
S2B_MSIL2A_20180707T113319_N0208_R080_T29UPT_20180707T154927
S2B_MSIL2A_20180703T115359_N0208_R023_T29UPB_20180703T180433
S2B_MSIL2A_20180703T115359_N0208_R023_T29UPA_20180703T180433
S2B_MSIL2A_20180703T115359_N0208_R023_T29UNV_20180703T180433
S2B_MSIL2A_20180703T115359_N0208_R023_T29UNU_20180703T180433
S2B_MSIL2A_20180703T115359_N0208_R023_T29UNT_20180703T180433
S2B_MSIL2A_20180703T115359_N0208_R023_T29UNB_20180703T180433
S2B_MSIL2A_20180703T115359_N0208_R023_T29UNA_20180703T180433
S2B_MSIL2A_20180703T115359_N0208_R023_T29UMV_20180703T180433
S2B_MSIL2A_20180703T115359_N0208_R023_T29UMU_20180703T180433
S2B_MSIL2A_20180703T115359_N0208_R023_T29UMT_20180703T180433
S2B_MSIL2A_20180703T115359_N0208_R023_T29ULT_20180703T180433
S2B_MSIL2A_20180630T114349_N0208_R123_T30UUG_20180630T173428
S2B_MSIL2A_20180630T114349_N0208_R123_T30UUF_20180630T173428
S2B_MSIL2A_20180630T114349_N0208_R123_T29UPV_20180630T173428
S2B_MSIL2A_20180630T114349_N0208_R123_T29UPU_20180630T173428
S2B_MSIL2A_20180630T114349_N0208_R123_T29UPT_20180630T173428
S2B_MSIL2A_20180630T114349_N0208_R123_T29UPB_20180630T173428
S2B_MSIL2A_20180630T114349_N0208_R123_T29UPA_20180630T173428

Sentinel-2 Satellite Images used in Chapter 3 comparative assessment [continued].

S2B_MSIL2A_20180630T114349_N0208_R123_T29UNV_20180630T173428
S2B_MSIL2A_20180630T114349_N0208_R123_T29UNU_20180630T173428
S2B_MSIL2A_20180630T114349_N0208_R123_T29UNT_20180630T173428
S2B_MSIL2A_20180630T114349_N0208_R123_T29UNB_20180630T173428
S2B_MSIL2A_20180630T114349_N0208_R123_T29UNA_20180630T173428
S2B_MSIL2A_20180630T114349_N0208_R123_T29UMV_20180630T173428
S2B_MSIL2A_20180630T114349_N0208_R123_T29UMU_20180630T173428
S2B_MSIL2A_20180630T114349_N0208_R123_T29UMT_20180630T173428
S2B_MSIL2A_20180630T114349_N0208_R123_T29UMA_20180630T173428
S2B_MSIL2A_20180627T113319_N0208_R080_T30UUF_20180627T145107
S2B_MSIL2A_20180627T113319_N0208_R080_T29UPV_20180627T145107
S2B_MSIL2A_20180627T113319_N0208_R080_T29UPU_20180627T145107
S2B_MSIL2A_20180627T113319_N0208_R080_T29UPT_20180627T145107
S2B_MSIL2A_20180627T113319_N0208_R080_T29UPB_20180627T145107
S2B_MSIL2A_20180627T113319_N0208_R080_T29UPA_20180627T145107
S2B_MSIL2A_20180627T113319_N0208_R080_T29UNU_20180627T145107
S2B_MSIL2A_20180627T113319_N0208_R080_T29UNT_20180627T145107
S2B_MSIL2A_20180623T115359_N0208_R023_T29UPV_20180623T160332
S2B_MSIL2A_20180623T115359_N0208_R023_T29UPA_20180623T160332
S2B_MSIL2A_20180623T115359_N0208_R023_T29UNV_20180623T160332
S2B_MSIL2A_20180623T115359_N0208_R023_T29UNU_20180623T160332
S2B_MSIL2A_20180623T115359_N0208_R023_T29UNT_20180623T160332
S2B_MSIL2A_20180623T115359_N0208_R023_T29UNB_20180623T160332
S2B_MSIL2A_20180623T115359_N0208_R023_T29UNA_20180623T160332
S2B_MSIL2A_20180623T115359_N0208_R023_T29UMV_20180623T160332
S2B_MSIL2A_20180623T115359_N0208_R023_T29UMU_20180623T160332
S2B_MSIL2A_20180623T115359_N0208_R023_T29UMT_20180623T160332

Sentinel-2 Satellite Images used in Chapter 3 comparative assessment [continued].

S2B_MSIL2A_20180623T115359_N0208_R023_T29UMA_20180623T160332
S2B_MSIL2A_20180623T115359_N0208_R023_T29ULT_20180623T160332
S2B_MSIL2A_20180610T114349_N0208_R123_T30UUF_20180610T141940
S2B_MSIL2A_20180607T113319_N0208_R080_T30UUF_20180607T141809
S2B_MSIL2A_20180607T113319_N0208_R080_T29UPV_20180607T141809
S2B_MSIL2A_20180607T113319_N0208_R080_T29UPU_20180607T141809
S2B_MSIL2A_20180607T113319_N0208_R080_T29UPB_20180607T141809
S2B_MSIL2A_20180607T113319_N0208_R080_T29UPA_20180607T141809
S2B_MSIL2A_20180607T113319_N0208_R080_T29UNU_20180607T141809
S2B_MSIL2A_20180603T115359_N0208_R023_T29UPB_20180603T131029
S2B_MSIL2A_20180603T115359_N0208_R023_T29UPA_20180603T131029
S2B_MSIL2A_20180603T115359_N0208_R023_T29UNU_20180603T131029
S2B_MSIL2A_20180603T115359_N0208_R023_T29UNA_20180603T131029
S2B_MSIL2A_20180603T115359_N0208_R023_T29UMU_20180603T131029
S2B_MSIL2A_20180531T114349_N0208_R123_T29UNV_20180531T141540
S2B_MSIL2A_20180531T114349_N0208_R123_T29UNU_20180531T141540
S2B_MSIL2A_20180531T114349_N0208_R123_T29UMU_20180531T141540
S2B_MSIL2A_20180528T113319_N0208_R080_T30UUF_20180528T125036
S2B_MSIL2A_20180528T113319_N0208_R080_T29UPV_20180528T125036
S2B_MSIL2A_20180528T113319_N0208_R080_T29UPU_20180528T125036
S2B_MSIL2A_20180528T113319_N0208_R080_T29UPB_20180528T125036
S2B_MSIL2A_20180528T113319_N0208_R080_T29UPA_20180528T125036
S2B_MSIL2A_20180524T115359_N0208_R023_T29UPB_20180524T180956
S2B_MSIL2A_20180524T115359_N0208_R023_T29UPA_20180524T180956
S2B_MSIL2A_20180524T115359_N0208_R023_T29UNV_20180524T180956
S2B_MSIL2A_20180524T115359_N0208_R023_T29UNU_20180524T180956
S2B_MSIL2A_20180524T115359_N0208_R023_T29UNT_20180524T180956

Sentinel-2 Satellite Images used in Chapter 3 comparative assessment [continued].

S2B_MSIL2A_20180524T115359_N0208_R023_T29UNB_20180524T180956
S2B_MSIL2A_20180524T115359_N0208_R023_T29UNA_20180524T180956
S2B_MSIL2A_20180524T115359_N0208_R023_T29UMV_20180524T180956
S2B_MSIL2A_20180524T115359_N0208_R023_T29UMU_20180524T180956
S2B_MSIL2A_20180524T115359_N0208_R023_T29UMT_20180524T180956
S2B_MSIL2A_20180524T115359_N0208_R023_T29UMA_20180524T180956
S2B_MSIL2A_20180524T115359_N0208_R023_T29ULT_20180524T180956
S2B_MSIL2A_20180518T113319_N0207_R080_T29UPU_20180518T133554
S2B_MSIL2A_20180518T113319_N0207_R080_T29UPT_20180518T133554
S2B_MSIL2A_20180518T113319_N0207_R080_T29UNT_20180518T133554
S2B_MSIL2A_20180511T114349_N0207_R123_T29UNU_20180511T151544
S2B_MSIL2A_20180511T114349_N0207_R123_T29UNT_20180511T151544
S2B_MSIL2A_20180511T114349_N0207_R123_T29UMU_20180511T151544
S2B_MSIL2A_20180511T114349_N0207_R123_T29UMT_20180511T151544
S2B_MSIL2A_20180508T113319_N0207_R080_T29UPV_20180508T171644
S2B_MSIL2A_20180508T113319_N0207_R080_T29UPU_20180508T171644
S2B_MSIL2A_20180428T113319_N0207_R080_T30UUF_20180428T115508
S2B_MSIL2A_20180428T113319_N0207_R080_T29UPV_20180428T115508
S2B_MSIL2A_20180428T113319_N0207_R080_T29UPU_20180428T115508
S2B_MSIL2A_20180428T113319_N0207_R080_T29UPA_20180428T115508
S2B_MSIL2A_20180421T114349_N0207_R123_T30UUF_20180421T134219
S2B_MSIL2A_20180421T114349_N0207_R123_T30UUF_20180421T120446
S2B_MSIL2A_20180421T114349_N0207_R123_T29UPV_20180421T134219
S2B_MSIL2A_20180421T114349_N0207_R123_T29UPU_20180421T134219
S2B_MSIL2A_20180421T114349_N0207_R123_T29UPT_20180421T134219
S2B_MSIL2A_20180421T114349_N0207_R123_T29UPB_20180421T120446
S2B_MSIL2A_20180421T114349_N0207_R123_T29UPA_20180421T134219

Sentinel-2 Satellite Images used in Chapter 3 comparative assessment [continued].

S2B_MSIL2A_20180421T114349_N0207_R123_T29UPA_20180421T120446
S2B_MSIL2A_20180421T114349_N0207_R123_T29UNV_20180421T134219
S2B_MSIL2A_20180421T114349_N0207_R123_T29UNU_20180421T134219
S2B_MSIL2A_20180421T114349_N0207_R123_T29UNT_20180421T134219
S2B_MSIL2A_20180421T114349_N0207_R123_T29UNA_20180421T134219
S2B_MSIL2A_20180421T114349_N0207_R123_T29UNA_20180421T120446
S2B_MSIL2A_20180421T114349_N0207_R123_T29UMV_20180421T134219
S2B_MSIL2A_20180421T114349_N0207_R123_T29UMU_20180421T134219
S2B_MSIL2A_20180421T114349_N0207_R123_T29UMT_20180421T134219
S2B_MSIL2A_20180418T113319_N0207_R080_T29UPU_20180418T115417
S2B_MSIL2A_20180404T115359_N0207_R023_T29UMT_20180404T121623
S2A_MSIL2A_20181222T114501_N0211_R123_T30UUF_20181222T124907
S2A_MSIL2A_20181222T114501_N0211_R123_T30UUE_20181222T124907
S2A_MSIL2A_20181222T114501_N0211_R123_T29UPT_20181222T124907
S2A_MSIL2A_20181222T114501_N0211_R123_T29UPA_20181222T124907
S2A_MSIL2A_20181222T114501_N0211_R123_T29UNT_20181222T124907
S2A_MSIL2A_20181222T114501_N0211_R123_T29UNA_20181222T124907
S2A_MSIL2A_20181222T114501_N0211_R123_T29UMT_20181222T124907
S2A_MSIL2A_20181209T113441_N0211_R080_T30UUF_20181209T123027
S2A_MSIL2A_20181209T113441_N0211_R080_T29UPV_20181209T123027
S2A_MSIL2A_20181209T113441_N0211_R080_T29UPU_20181209T123027
S2A_MSIL2A_20181209T113441_N0211_R080_T29UPT_20181209T123027
S2A_MSIL2A_20181209T113441_N0211_R080_T29UNU_20181209T123027
S2A_MSIL2A_20181129T113421_N0211_R080_T29UPV_20181129T123450
S2A_MSIL2A_20181129T113421_N0211_R080_T29UPU_20181129T123450
S2A_MSIL2A_20181125T115411_N0211_R023_T29UNV_20181125T123933
S2A_MSIL2A_20181125T115411_N0211_R023_T29UNU_20181125T123933

Sentinel-2 Satellite Images used in Chapter 3 comparative assessment [continued].

S2A_MSIL2A_20181125T115411_N0211_R023_T29UNT_20181125T123933
S2A_MSIL2A_20181125T115411_N0211_R023_T29UNB_20181125T123933
S2A_MSIL2A_20181125T115411_N0211_R023_T29UNA_20181125T123933
S2A_MSIL2A_20181125T115411_N0211_R023_T29UMV_20181125T123933
S2A_MSIL2A_20181125T115411_N0211_R023_T29UMU_20181125T123933
S2A_MSIL2A_20181125T115411_N0211_R023_T29UMT_20181125T123933
S2A_MSIL2A_20181125T115411_N0211_R023_T29ULT_20181125T123933
S2A_MSIL2A_20181122T114401_N0211_R123_T30UUF_20181122T125119
S2A_MSIL2A_20181122T114401_N0211_R123_T29UPV_20181122T125119
S2A_MSIL2A_20181122T114401_N0211_R123_T29UPB_20181122T125119
S2A_MSIL2A_20181122T114401_N0211_R123_T29UPA_20181122T125119
S2A_MSIL2A_20181122T114401_N0211_R123_T29UNV_20181122T125119
S2A_MSIL2A_20181122T114401_N0211_R123_T29UNB_20181122T125119
S2A_MSIL2A_20181122T114401_N0211_R123_T29UNA_20181122T125119
S2A_MSIL2A_20181122T114401_N0211_R123_T29UMV_20181122T125119
S2A_MSIL2A_20181112T114341_N0210_R123_T29UPV_20181112T130301
S2A_MSIL2A_20181112T114341_N0210_R123_T29UPU_20181112T130301
S2A_MSIL2A_20181112T114341_N0210_R123_T29UNV_20181112T130301
S2A_MSIL2A_20181112T114341_N0210_R123_T29UNU_20181112T130301
S2A_MSIL2A_20181105T115401_N0209_R023_T29UMT_20181105T124023
S2A_MSIL2A_20181030T113321_N0209_R080_T30UUF_20181030T122802
S2A_MSIL2A_20181030T113321_N0209_R080_T30UUD_20181030T122802
S2A_MSIL2A_20181030T113321_N0209_R080_T29UPV_20181030T122802
S2A_MSIL2A_20181030T113321_N0209_R080_T29UPU_20181030T122802
S2A_MSIL2A_20181030T113321_N0209_R080_T29UPB_20181030T122802
S2A_MSIL2A_20181030T113321_N0209_R080_T29UPA_20181030T122802
S2A_MSIL2A_20181030T113321_N0209_R080_T29UNU_20181030T122802

Sentinel-2 Satellite Images used in Chapter 3 comparative assessment [continued].

S2A_MSIL2A_20181026T115401_N0209_R023_T29UPA_20181026T124013
S2A_MSIL2A_20181026T115401_N0209_R023_T29UNV_20181026T124013
S2A_MSIL2A_20181026T115401_N0209_R023_T29UNU_20181026T124013
S2A_MSIL2A_20181026T115401_N0209_R023_T29UNT_20181026T124013
S2A_MSIL2A_20181026T115401_N0209_R023_T29UNA_20181026T124013
S2A_MSIL2A_20181026T115401_N0209_R023_T29UMV_20181026T124013
S2A_MSIL2A_20181026T115401_N0209_R023_T29UMU_20181026T124013
S2A_MSIL2A_20181026T115401_N0209_R023_T29UMT_20181026T124013
S2A_MSIL2A_20181020T113321_N0209_R080_T29UPU_20181020T123439
S2A_MSIL2A_20181016T115401_N0209_R023_T29UNV_20181016T143216
S2A_MSIL2A_20181016T115401_N0209_R023_T29UNU_20181016T143216
S2A_MSIL2A_20181016T115401_N0209_R023_T29UNB_20181016T143216
S2A_MSIL2A_20181016T115401_N0209_R023_T29UNA_20181016T143216
S2A_MSIL2A_20181016T115401_N0209_R023_T29UMU_20181016T143216
S2A_MSIL2A_20181016T115401_N0209_R023_T29UMT_20181016T143216
S2A_MSIL2A_20181016T115401_N0209_R023_T29ULT_20181016T143216
S2A_MSIL2A_20181010T113321_N0209_R080_T30UUF_20181010T141708
S2A_MSIL2A_20181010T113321_N0209_R080_T29UPV_20181010T141708
S2A_MSIL2A_20181010T113321_N0209_R080_T29UPU_20181010T141708
S2A_MSIL2A_20181010T113321_N0209_R080_T29UPT_20181010T141708
S2A_MSIL2A_20181010T113321_N0209_R080_T29UPB_20181010T141708
S2A_MSIL2A_20181010T113321_N0209_R080_T29UPA_20181010T141708
S2A_MSIL2A_20181010T113321_N0209_R080_T29UNU_20181010T141708
S2A_MSIL2A_20181010T113321_N0209_R080_T29UNT_20181010T141708
S2A_MSIL2A_20181006T115401_N0208_R023_T29UPB_20181006T125746
S2A_MSIL2A_20181006T115401_N0208_R023_T29UPA_20181006T125746
S2A_MSIL2A_20181006T115401_N0208_R023_T29UNV_20181006T125746

Sentinel-2 Satellite Images used in Chapter 3 comparative assessment [continued].

S2A_MSIL2A_20181006T115401_N0208_R023_T29UNT_20181006T125746
S2A_MSIL2A_20181006T115401_N0208_R023_T29UNB_20181006T125746
S2A_MSIL2A_20181006T115401_N0208_R023_T29UNA_20181006T125746
S2A_MSIL2A_20181006T115401_N0208_R023_T29UMV_20181006T125746
S2A_MSIL2A_20181006T115401_N0208_R023_T29UMU_20181006T125746
S2A_MSIL2A_20181006T115401_N0208_R023_T29UMT_20181006T125746
S2A_MSIL2A_20181006T115401_N0208_R023_T29UMA_20181006T125746
S2A_MSIL2A_20180923T114341_N0208_R123_T30UUF_20180923T143521
S2A_MSIL2A_20180923T114341_N0208_R123_T29UPV_20180923T143521
S2A_MSIL2A_20180923T114341_N0208_R123_T29UPA_20180923T143521
S2A_MSIL2A_20180923T114341_N0208_R123_T29UNV_20180923T143521
S2A_MSIL2A_20180923T114341_N0208_R123_T29UNU_20180923T143521
S2A_MSIL2A_20180923T114341_N0208_R123_T29UNT_20180923T143521
S2A_MSIL2A_20180923T114341_N0208_R123_T29UNB_20180923T143521
S2A_MSIL2A_20180923T114341_N0208_R123_T29UNA_20180923T143521
S2A_MSIL2A_20180923T114341_N0208_R123_T29UMV_20180923T143521
S2A_MSIL2A_20180923T114341_N0208_R123_T29UMU_20180923T143521
S2A_MSIL2A_20180923T114341_N0208_R123_T29UMT_20180923T143521
S2A_MSIL2A_20180913T114351_N0208_R123_T29UPT_20180913T144400
S2A_MSIL2A_20180903T114351_N0208_R123_T30UUF_20180903T143544
S2A_MSIL2A_20180903T114351_N0208_R123_T29UPV_20180903T143544
S2A_MSIL2A_20180903T114351_N0208_R123_T29UPU_20180903T143544
S2A_MSIL2A_20180903T114351_N0208_R123_T29UPT_20180903T143544
S2A_MSIL2A_20180903T114351_N0208_R123_T29UPA_20180903T143544
S2A_MSIL2A_20180903T114351_N0208_R123_T29UNV_20180903T143544
S2A_MSIL2A_20180903T114351_N0208_R123_T29UNU_20180903T143544
S2A_MSIL2A_20180903T114351_N0208_R123_T29UNT_20180903T143544

Sentinel-2 Satellite Images used in Chapter 3 comparative assessment [continued].

S2A_MSIL2A_20180903T114351_N0208_R123_T29UMT_20180903T143544
S2A_MSIL2A_20180831T113321_N0208_R080_T30UUF_20180831T150101
S2A_MSIL2A_20180831T113321_N0208_R080_T30UUF_20180831T145610
S2A_MSIL2A_20180831T113321_N0208_R080_T29UPB_20180831T150101
S2A_MSIL2A_20180831T113321_N0208_R080_T29UPB_20180831T145610
S2A_MSIL2A_20180831T113321_N0208_R080_T29UPA_20180831T150101
S2A_MSIL2A_20180824T114351_N0208_R123_T29UPV_20180824T150935
S2A_MSIL2A_20180824T114351_N0208_R123_T29UPU_20180824T150935
S2A_MSIL2A_20180824T114351_N0208_R123_T29UPA_20180824T150935
S2A_MSIL2A_20180824T114351_N0208_R123_T29UNV_20180824T150935
S2A_MSIL2A_20180824T114351_N0208_R123_T29UNA_20180824T150935
S2A_MSIL2A_20180824T114351_N0208_R123_T29UMV_20180824T150935
S2A_MSIL2A_20180728T115401_N0208_R023_T29UMT_20180728T150735
S2A_MSIL2A_20180725T114351_N0208_R123_T30UUF_20180725T140825
S2A_MSIL2A_20180725T114351_N0208_R123_T29UPV_20180725T140825
S2A_MSIL2A_20180725T114351_N0208_R123_T29UPU_20180725T140825
S2A_MSIL2A_20180725T114351_N0208_R123_T29UPB_20180725T140825
S2A_MSIL2A_20180725T114351_N0208_R123_T29UPA_20180725T140825
S2A_MSIL2A_20180725T114351_N0208_R123_T29UNT_20180725T140825
S2A_MSIL2A_20180725T114351_N0208_R123_T29UNB_20180725T140825
S2A_MSIL2A_20180725T114351_N0208_R123_T29UNA_20180725T140825
S2A_MSIL2A_20180712T113321_N0208_R080_T29UNT_20180712T141314
S2A_MSIL2A_20180705T114351_N0208_R123_T30UUG_20180705T142104
S2A_MSIL2A_20180705T114351_N0208_R123_T29UPU_20180705T142104
S2A_MSIL2A_20180705T114351_N0208_R123_T29UPT_20180705T142104
S2A_MSIL2A_20180705T114351_N0208_R123_T29UNU_20180705T142104
S2A_MSIL2A_20180705T114351_N0208_R123_T29UNT_20180705T142104

Sentinel-2 Satellite Images used in Chapter 3 comparative assessment [continued].

S2A_MSIL2A_20180705T114351_N0208_R123_T29UNB_20180705T142104
S2A_MSIL2A_20180705T114351_N0208_R123_T29UNA_20180705T142104
S2A_MSIL2A_20180705T114351_N0208_R123_T29UMT_20180705T142104
S2A_MSIL2A_20180702T113321_N0208_R080_T30UG_20180702T141901
S2A_MSIL2A_20180702T113321_N0208_R080_T30UUF_20180702T141901
S2A_MSIL2A_20180702T113321_N0208_R080_T29UPV_20180702T141901
S2A_MSIL2A_20180702T113321_N0208_R080_T29UPU_20180702T141901
S2A_MSIL2A_20180702T113321_N0208_R080_T29UPT_20180702T141901
S2A_MSIL2A_20180702T113321_N0208_R080_T29UPB_20180702T141901
S2A_MSIL2A_20180702T113321_N0208_R080_T29UPA_20180702T141901
S2A_MSIL2A_20180702T113321_N0208_R080_T29UNU_20180702T141901
S2A_MSIL2A_20180628T115401_N0208_R023_T29UPV_20180628T125228
S2A_MSIL2A_20180628T115401_N0208_R023_T29UPB_20180628T125228
S2A_MSIL2A_20180628T115401_N0208_R023_T29UPA_20180628T125228
S2A_MSIL2A_20180628T115401_N0208_R023_T29UNV_20180628T125228
S2A_MSIL2A_20180628T115401_N0208_R023_T29UNU_20180628T125228
S2A_MSIL2A_20180628T115401_N0208_R023_T29UNT_20180628T125228
S2A_MSIL2A_20180628T115401_N0208_R023_T29UNB_20180628T125228
S2A_MSIL2A_20180628T115401_N0208_R023_T29UNA_20180628T125228
S2A_MSIL2A_20180628T115401_N0208_R023_T29UMV_20180628T125228
S2A_MSIL2A_20180628T115401_N0208_R023_T29UMU_20180628T125228
S2A_MSIL2A_20180628T115401_N0208_R023_T29UMT_20180628T125228
S2A_MSIL2A_20180628T115401_N0208_R023_T29UMA_20180628T125228
S2A_MSIL2A_20180628T115401_N0208_R023_T29ULT_20180628T125228
S2A_MSIL2A_20180625T114351_N0208_R123_T30UUF_20180625T173707
S2A_MSIL2A_20180625T114351_N0208_R123_T29UPV_20180625T173707
S2A_MSIL2A_20180625T114351_N0208_R123_T29UPU_20180625T173707

Sentinel-2 Satellite Images used in Chapter 3 comparative assessment [continued].

S2A_MSIL2A_20180625T114351_N0208_R123_T29UPB_20180625T173707
S2A_MSIL2A_20180625T114351_N0208_R123_T29UPA_20180625T173707
S2A_MSIL2A_20180625T114351_N0208_R123_T29UNV_20180625T173707
S2A_MSIL2A_20180625T114351_N0208_R123_T29UNU_20180625T173707
S2A_MSIL2A_20180625T114351_N0208_R123_T29UNT_20180625T173707
S2A_MSIL2A_20180625T114351_N0208_R123_T29UNB_20180625T173707
S2A_MSIL2A_20180625T114351_N0208_R123_T29UNA_20180625T173707
S2A_MSIL2A_20180625T114351_N0208_R123_T29UMV_20180625T173707
S2A_MSIL2A_20180625T114351_N0208_R123_T29UMU_20180625T173707
S2A_MSIL2A_20180625T114351_N0208_R123_T29UMT_20180625T173707
S2A_MSIL2A_20180625T114351_N0208_R123_T29UMA_20180625T173707
S2A_MSIL2A_20180622T113321_N0208_R080_T30UUF_20180622T123307
S2A_MSIL2A_20180622T113321_N0208_R080_T29UPV_20180622T123307
S2A_MSIL2A_20180622T113321_N0208_R080_T29UPU_20180622T123307
S2A_MSIL2A_20180622T113321_N0208_R080_T29UPT_20180622T123307
S2A_MSIL2A_20180622T113321_N0208_R080_T29UPB_20180622T123307
S2A_MSIL2A_20180622T113321_N0208_R080_T29UPA_20180622T123307
S2A_MSIL2A_20180622T113321_N0208_R080_T29UNU_20180622T123307
S2A_MSIL2A_20180622T113321_N0208_R080_T29UNT_20180622T123307
S2A_MSIL2A_20180612T113321_N0208_R080_T29UPU_20180612T143029
S2A_MSIL2A_20180608T115401_N0208_R023_T29UPV_20180608T160042
S2A_MSIL2A_20180608T115401_N0208_R023_T29UPB_20180608T160042
S2A_MSIL2A_20180608T115401_N0208_R023_T29UPA_20180608T160042
S2A_MSIL2A_20180608T115401_N0208_R023_T29UNV_20180608T160042
S2A_MSIL2A_20180608T115401_N0208_R023_T29UNA_20180608T160042
S2A_MSIL2A_20180608T115401_N0208_R023_T29UMV_20180608T160042
S2A_MSIL2A_20180608T115401_N0208_R023_T29UMU_20180608T160042

Sentinel-2 Satellite Images used in Chapter 3 comparative assessment [continued].

S2A_MSIL2A_20180608T115401_N0208_R023_T29ULT_20180608T160042
S2A_MSIL2A_20180605T114351_N0208_R123_T30UUG_20180605T124913
S2A_MSIL2A_20180605T114351_N0208_R123_T29UMT_20180605T124913
S2A_MSIL2A_20180529T115401_N0208_R023_T29UPV_20180529T125059
S2A_MSIL2A_20180529T115401_N0208_R023_T29UPB_20180529T125059
S2A_MSIL2A_20180529T115401_N0208_R023_T29UPA_20180529T125059
S2A_MSIL2A_20180529T115401_N0208_R023_T29UNV_20180529T125059
S2A_MSIL2A_20180529T115401_N0208_R023_T29UNU_20180529T125059
S2A_MSIL2A_20180529T115401_N0208_R023_T29UNB_20180529T125059
S2A_MSIL2A_20180529T115401_N0208_R023_T29UNA_20180529T125059
S2A_MSIL2A_20180529T115401_N0208_R023_T29UMV_20180529T125059
S2A_MSIL2A_20180529T115401_N0208_R023_T29UMU_20180529T125059
S2A_MSIL2A_20180529T115401_N0208_R023_T29UMT_20180529T125059
S2A_MSIL2A_20180529T115401_N0208_R023_T29ULT_20180529T125059
S2A_MSIL2A_20180526T114351_N0208_R123_T29UPV_20180526T173701
S2A_MSIL2A_20180526T114351_N0208_R123_T29UPB_20180526T173701
S2A_MSIL2A_20180526T114351_N0208_R123_T29UPA_20180526T173701
S2A_MSIL2A_20180526T114351_N0208_R123_T29UNV_20180526T173701
S2A_MSIL2A_20180526T114351_N0208_R123_T29UNB_20180526T173701
S2A_MSIL2A_20180526T114351_N0208_R123_T29UNA_20180526T173701
S2A_MSIL2A_20180526T114351_N0208_R123_T29UMV_20180526T173701
S2A_MSIL2A_20180526T114351_N0208_R123_T29UMA_20180526T173701
S2A_MSIL2A_20180523T113321_N0208_R080_T30UUF_20180523T181029
S2A_MSIL2A_20180523T113321_N0208_R080_T29UPV_20180523T181029
S2A_MSIL2A_20180523T113321_N0208_R080_T29UPU_20180523T181029
S2A_MSIL2A_20180523T113321_N0208_R080_T29UPT_20180523T181029
S2A_MSIL2A_20180523T113321_N0208_R080_T29UPB_20180523T181029

Sentinel-2 Satellite Images used in Chapter 3 comparative assessment [continued].

S2A_MSIL2A_20180523T113321_N0208_R080_T29UPA_20180523T181029
S2A_MSIL2A_20180523T113321_N0208_R080_T29UNU_20180523T181029
S2A_MSIL2A_20180523T113321_N0208_R080_T29UNT_20180523T181029
S2A_MSIL2A_20180519T115401_N0207_R023_T29UNU_20180519T154451
S2A_MSIL2A_20180519T115401_N0207_R023_T29UMT_20180519T154451
S2A_MSIL2A_20180516T114351_N0207_R123_T30UUF_20180516T120702
S2A_MSIL2A_20180516T114351_N0207_R123_T29UPV_20180516T120702
S2A_MSIL2A_20180516T114351_N0207_R123_T29UPU_20180516T120702
S2A_MSIL2A_20180516T114351_N0207_R123_T29UPT_20180516T120702
S2A_MSIL2A_20180516T114351_N0207_R123_T29UPB_20180516T120702
S2A_MSIL2A_20180516T114351_N0207_R123_T29UPA_20180516T120702
S2A_MSIL2A_20180516T114351_N0207_R123_T29UNV_20180516T120702
S2A_MSIL2A_20180516T114351_N0207_R123_T29UNU_20180516T120702
S2A_MSIL2A_20180516T114351_N0207_R123_T29UNT_20180516T120702
S2A_MSIL2A_20180516T114351_N0207_R123_T29UNB_20180516T120702
S2A_MSIL2A_20180516T114351_N0207_R123_T29UNA_20180516T120702
S2A_MSIL2A_20180516T114351_N0207_R123_T29UMV_20180516T120702
S2A_MSIL2A_20180516T114351_N0207_R123_T29UMU_20180516T120702
S2A_MSIL2A_20180516T114351_N0207_R123_T29UMT_20180516T120702
S2A_MSIL2A_20180516T114351_N0207_R123_T29UMA_20180516T120702
S2A_MSIL2A_20180516T114351_N0207_R123_T29ULT_20180516T120702
S2A_MSIL2A_20180513T113321_N0207_R080_T30UUG_20180513T133943
S2A_MSIL2A_20180513T113321_N0207_R080_T30UUF_20180513T133943
S2A_MSIL2A_20180513T113321_N0207_R080_T29UPU_20180513T133943
S2A_MSIL2A_20180513T113321_N0207_R080_T29UPT_20180513T133943
S2A_MSIL2A_20180513T113321_N0207_R080_T29UPA_20180513T133943
S2A_MSIL2A_20180506T114351_N0207_R123_T29UPV_20180506T120844

Sentinel-2 Satellite Images used in Chapter 3 comparative assessment [continued].

S2A_MSIL2A_20180506T114351_N0207_R123_T29UPU_20180506T120844
S2A_MSIL2A_20180506T114351_N0207_R123_T29UPA_20180506T120844
S2A_MSIL2A_20180506T114351_N0207_R123_T29UNV_20180506T120844
S2A_MSIL2A_20180506T114351_N0207_R123_T29UNU_20180506T120844
S2A_MSIL2A_20180506T114351_N0207_R123_T29UNT_20180506T120844
S2A_MSIL2A_20180506T114351_N0207_R123_T29UNA_20180506T120844
S2A_MSIL2A_20180506T114351_N0207_R123_T29UMV_20180506T120844
S2A_MSIL2A_20180506T114351_N0207_R123_T29UMU_20180506T120844
S2A_MSIL2A_20180506T114351_N0207_R123_T29UMT_20180506T120844
S2A_MSIL2A_20180429T115401_N0207_R023_T29UNV_20180429T121704
S2A_MSIL2A_20180429T115401_N0207_R023_T29UNU_20180429T121704
S2A_MSIL2A_20180429T115401_N0207_R023_T29UNT_20180429T121704
S2A_MSIL2A_20180429T115401_N0207_R023_T29UMU_20180429T121704
S2A_MSIL2A_20180429T115401_N0207_R023_T29UMT_20180429T121704
S2A_MSIL2A_20180429T115401_N0207_R023_T29UMA_20180429T121704
S2A_MSIL2A_20180426T114351_N0207_R123_T29UPV_20180426T134253
S2A_MSIL2A_20180426T114351_N0207_R123_T29UPU_20180426T134253
S2A_MSIL2A_20180426T114351_N0207_R123_T29UPB_20180426T134253
S2A_MSIL2A_20180426T114351_N0207_R123_T29UPB_20180426T120422
S2A_MSIL2A_20180426T114351_N0207_R123_T29UPA_20180426T134253
S2A_MSIL2A_20180426T114351_N0207_R123_T29UNV_20180426T134253
S2A_MSIL2A_20180426T114351_N0207_R123_T29UNB_20180426T134253
S2A_MSIL2A_20180426T114351_N0207_R123_T29UNA_20180426T134253
S2A_MSIL2A_20180419T115401_N0207_R023_T29UMV_20180419T121634
S2A_MSIL2A_20180419T115401_N0207_R023_T29UMU_20180419T121634
S2A_MSIL2A_20180419T115401_N0207_R023_T29UMT_20180419T121634
S2A_MSIL2A_20180419T115401_N0207_R023_T29ULT_20180419T121634

Sentinel-2 Satellite Images used in Chapter 3 comparative assessment [continued].

S2A_MSIL2A_20180403T113321_N0207_R080_T29UPT_20180403T151646
S2B_MSIL2A_20180630T114349_N0208_R123_T29UMT_20180630T173428
S2B_MSIL2A_20180630T114349_N0208_R123_T29UMA_20180630T173428
S2B_MSIL2A_20180627T113319_N0208_R080_T30UUF_20180627T145107
S2B_MSIL2A_20180627T113319_N0208_R080_T29UPV_20180627T145107
S2B_MSIL2A_20180627T113319_N0208_R080_T29UPU_20180627T145107
S2B_MSIL2A_20180627T113319_N0208_R080_T29UPT_20180627T145107
S2B_MSIL2A_20180627T113319_N0208_R080_T29UPB_20180627T145107
S2B_MSIL2A_20180627T113319_N0208_R080_T29UPA_20180627T145107
S2B_MSIL2A_20180627T113319_N0208_R080_T29UNU_20180627T145107
S2B_MSIL2A_20180627T113319_N0208_R080_T29UNT_20180627T145107
S2B_MSIL2A_20180623T115359_N0208_R023_T29UPV_20180623T160332
S2B_MSIL2A_20180623T115359_N0208_R023_T29UPA_20180623T160332
S2B_MSIL2A_20180623T115359_N0208_R023_T29UNV_20180623T160332
S2B_MSIL2A_20180623T115359_N0208_R023_T29UNU_20180623T160332
S2B_MSIL2A_20180623T115359_N0208_R023_T29UNT_20180623T160332
S2B_MSIL2A_20180623T115359_N0208_R023_T29UNB_20180623T160332
S2B_MSIL2A_20180623T115359_N0208_R023_T29UNA_20180623T160332
S2B_MSIL2A_20180623T115359_N0208_R023_T29UMV_20180623T160332
S2B_MSIL2A_20180623T115359_N0208_R023_T29UMU_20180623T160332
S2B_MSIL2A_20180623T115359_N0208_R023_T29UMT_20180623T160332
S2B_MSIL2A_20180623T115359_N0208_R023_T29UMA_20180623T160332
S2B_MSIL2A_20180623T115359_N0208_R023_T29ULT_20180623T160332
S2B_MSIL2A_20180610T114349_N0208_R123_T30UUF_20180610T141940
S2B_MSIL2A_20180607T113319_N0208_R080_T30UUF_20180607T141809
S2B_MSIL2A_20180607T113319_N0208_R080_T29UPV_20180607T141809
S2B_MSIL2A_20180607T113319_N0208_R080_T29UPU_20180607T141809

Sentinel-2 Satellite Images used in Chapter 3 comparative assessment [continued].

S2B_MSIL2A_20180607T113319_N0208_R080_T29UPB_20180607T141809
S2B_MSIL2A_20180607T113319_N0208_R080_T29UPA_20180607T141809
S2B_MSIL2A_20180607T113319_N0208_R080_T29UNU_20180607T141809
S2B_MSIL2A_20180603T115359_N0208_R023_T29UPB_20180603T131029
S2B_MSIL2A_20180603T115359_N0208_R023_T29UPA_20180603T131029
S2B_MSIL2A_20180603T115359_N0208_R023_T29UNU_20180603T131029
S2B_MSIL2A_20180603T115359_N0208_R023_T29UNA_20180603T131029
S2B_MSIL2A_20180603T115359_N0208_R023_T29UMU_20180603T131029
S2B_MSIL2A_20180531T114349_N0208_R123_T29UNV_20180531T141540
S2B_MSIL2A_20180531T114349_N0208_R123_T29UNU_20180531T141540
S2B_MSIL2A_20180531T114349_N0208_R123_T29UMU_20180531T141540
S2B_MSIL2A_20180528T113319_N0208_R080_T30UUF_20180528T125036
S2B_MSIL2A_20180528T113319_N0208_R080_T29UPV_20180528T125036
S2B_MSIL2A_20180528T113319_N0208_R080_T29UPU_20180528T125036
S2B_MSIL2A_20180528T113319_N0208_R080_T29UPB_20180528T125036
S2B_MSIL2A_20180528T113319_N0208_R080_T29UPA_20180528T125036
S2B_MSIL2A_20180524T115359_N0208_R023_T29UPB_20180524T180956
S2B_MSIL2A_20180524T115359_N0208_R023_T29UPA_20180524T180956
S2B_MSIL2A_20180524T115359_N0208_R023_T29UNV_20180524T180956
S2B_MSIL2A_20180524T115359_N0208_R023_T29UNU_20180524T180956
S2B_MSIL2A_20180524T115359_N0208_R023_T29UNT_20180524T180956
S2B_MSIL2A_20180524T115359_N0208_R023_T29UNB_20180524T180956
S2B_MSIL2A_20180524T115359_N0208_R023_T29UNA_20180524T180956
S2B_MSIL2A_20180524T115359_N0208_R023_T29UMV_20180524T180956
S2B_MSIL2A_20180524T115359_N0208_R023_T29UMU_20180524T180956
S2B_MSIL2A_20180524T115359_N0208_R023_T29UMT_20180524T180956
S2B_MSIL2A_20180524T115359_N0208_R023_T29UMA_20180524T180956

Sentinel-2 Satellite Images used in Chapter 3 comparative assessment [continued].

S2B_MSIL2A_20180524T115359_N0208_R023_T29ULT_20180524T180956
S2B_MSIL2A_20180518T113319_N0207_R080_T29UPU_20180518T133554
S2B_MSIL2A_20180518T113319_N0207_R080_T29UPT_20180518T133554
S2B_MSIL2A_20180518T113319_N0207_R080_T29UNT_20180518T133554
S2B_MSIL2A_20180511T114349_N0207_R123_T29UNU_20180511T151544
S2B_MSIL2A_20180511T114349_N0207_R123_T29UNT_20180511T151544
S2B_MSIL2A_20180511T114349_N0207_R123_T29UMU_20180511T151544
S2B_MSIL2A_20180511T114349_N0207_R123_T29UMT_20180511T151544
S2B_MSIL2A_20180508T113319_N0207_R080_T29UPV_20180508T171644
S2B_MSIL2A_20180508T113319_N0207_R080_T29UPU_20180508T171644
S2B_MSIL2A_20180428T113319_N0207_R080_T30UUF_20180428T115508
S2B_MSIL2A_20180428T113319_N0207_R080_T29UPV_20180428T115508
S2B_MSIL2A_20180428T113319_N0207_R080_T29UPU_20180428T115508
S2B_MSIL2A_20180428T113319_N0207_R080_T29UPA_20180428T115508
S2B_MSIL2A_20180421T114349_N0207_R123_T30UUF_20180421T134219
S2B_MSIL2A_20180421T114349_N0207_R123_T30UUF_20180421T120446
S2B_MSIL2A_20180421T114349_N0207_R123_T29UPV_20180421T134219
S2B_MSIL2A_20180421T114349_N0207_R123_T29UPU_20180421T134219
S2B_MSIL2A_20180421T114349_N0207_R123_T29UPT_20180421T134219
S2B_MSIL2A_20180421T114349_N0207_R123_T29UPB_20180421T120446
S2B_MSIL2A_20180421T114349_N0207_R123_T29UPA_20180421T134219
S2B_MSIL2A_20180421T114349_N0207_R123_T29UPA_20180421T120446
S2B_MSIL2A_20180421T114349_N0207_R123_T29UNV_20180421T134219
S2B_MSIL2A_20180421T114349_N0207_R123_T29UNU_20180421T134219
S2B_MSIL2A_20180421T114349_N0207_R123_T29UNT_20180421T134219
S2B_MSIL2A_20180421T114349_N0207_R123_T29UNA_20180421T134219
S2B_MSIL2A_20180421T114349_N0207_R123_T29UNA_20180421T120446

Sentinel-2 Satellite Images used in Chapter 3 comparative assessment [continued].

S2B_MSIL2A_20180421T114349_N0207_R123_T29UMV_20180421T134219
S2B_MSIL2A_20180421T114349_N0207_R123_T29UMU_20180421T134219
S2B_MSIL2A_20180421T114349_N0207_R123_T29UMT_20180421T134219
S2B_MSIL2A_20180418T113319_N0207_R080_T29UPU_20180418T115417
S2B_MSIL2A_20180404T115359_N0207_R023_T29UMT_20180404T121623
S2A_MSIL2A_20181222T114501_N0211_R123_T30UUF_20181222T124907
S2A_MSIL2A_20181222T114501_N0211_R123_T30UUE_20181222T124907
S2A_MSIL2A_20181222T114501_N0211_R123_T29UPT_20181222T124907
S2A_MSIL2A_20181222T114501_N0211_R123_T29UPA_20181222T124907
S2A_MSIL2A_20181222T114501_N0211_R123_T29UNT_20181222T124907
S2A_MSIL2A_20181222T114501_N0211_R123_T29UNA_20181222T124907
S2A_MSIL2A_20181222T114501_N0211_R123_T29UMT_20181222T124907
S2A_MSIL2A_20181209T113441_N0211_R080_T30UUF_20181209T123027
S2A_MSIL2A_20181209T113441_N0211_R080_T29UPV_20181209T123027
S2A_MSIL2A_20181209T113441_N0211_R080_T29UPU_20181209T123027
S2A_MSIL2A_20181209T113441_N0211_R080_T29UPT_20181209T123027
S2A_MSIL2A_20181209T113441_N0211_R080_T29UNU_20181209T123027
S2A_MSIL2A_20181129T113421_N0211_R080_T29UPV_20181129T123450
S2A_MSIL2A_20181129T113421_N0211_R080_T29UPU_20181129T123450
S2A_MSIL2A_20181125T115411_N0211_R023_T29UNV_20181125T123933
S2A_MSIL2A_20181125T115411_N0211_R023_T29UNU_20181125T123933
S2A_MSIL2A_20181125T115411_N0211_R023_T29UNT_20181125T123933
S2A_MSIL2A_20181125T115411_N0211_R023_T29UNB_20181125T123933
S2A_MSIL2A_20181125T115411_N0211_R023_T29UNA_20181125T123933
S2A_MSIL2A_20181125T115411_N0211_R023_T29UMV_20181125T123933
S2A_MSIL2A_20181125T115411_N0211_R023_T29UMU_20181125T123933
S2A_MSIL2A_20181125T115411_N0211_R023_T29UMT_20181125T123933

Sentinel-2 Satellite Images used in Chapter 3 comparative assessment [continued].

S2A_MSIL2A_20181125T115411_N0211_R023_T29ULT_20181125T123933
S2A_MSIL2A_20181122T114401_N0211_R123_T30UUF_20181122T125119
S2A_MSIL2A_20181122T114401_N0211_R123_T29UPV_20181122T125119
S2A_MSIL2A_20181122T114401_N0211_R123_T29UPB_20181122T125119
S2A_MSIL2A_20181122T114401_N0211_R123_T29UPA_20181122T125119
S2A_MSIL2A_20181122T114401_N0211_R123_T29UNV_20181122T125119
S2A_MSIL2A_20181122T114401_N0211_R123_T29UNB_20181122T125119
S2A_MSIL2A_20181122T114401_N0211_R123_T29UNA_20181122T125119
S2A_MSIL2A_20181122T114401_N0211_R123_T29UMV_20181122T125119
S2A_MSIL2A_20181112T114341_N0210_R123_T29UPV_20181112T130301
S2A_MSIL2A_20181112T114341_N0210_R123_T29UPU_20181112T130301
S2A_MSIL2A_20181112T114341_N0210_R123_T29UNV_20181112T130301
S2A_MSIL2A_20181112T114341_N0210_R123_T29UNU_20181112T130301
S2A_MSIL2A_20181105T115401_N0209_R023_T29UMT_20181105T124023
S2A_MSIL2A_20181030T113321_N0209_R080_T30UUF_20181030T122802
S2A_MSIL2A_20181030T113321_N0209_R080_T30UUD_20181030T122802
S2A_MSIL2A_20181030T113321_N0209_R080_T29UPV_20181030T122802
S2A_MSIL2A_20181030T113321_N0209_R080_T29UPU_20181030T122802
S2A_MSIL2A_20181030T113321_N0209_R080_T29UPB_20181030T122802
S2A_MSIL2A_20181030T113321_N0209_R080_T29UPA_20181030T122802
S2A_MSIL2A_20181030T113321_N0209_R080_T29UNU_20181030T122802
S2A_MSIL2A_20181026T115401_N0209_R023_T29UPA_20181026T124013
S2A_MSIL2A_20181026T115401_N0209_R023_T29UNV_20181026T124013
S2A_MSIL2A_20181026T115401_N0209_R023_T29UNU_20181026T124013
S2A_MSIL2A_20181026T115401_N0209_R023_T29UNT_20181026T124013
S2A_MSIL2A_20181026T115401_N0209_R023_T29UNA_20181026T124013
S2A_MSIL2A_20181026T115401_N0209_R023_T29UMV_20181026T124013

Sentinel-2 Satellite Images used in Chapter 3 comparative assessment [continued].

S2A_MSIL2A_20181026T115401_N0209_R023_T29UMU_20181026T124013
S2A_MSIL2A_20181026T115401_N0209_R023_T29UMT_20181026T124013
S2A_MSIL2A_20181020T113321_N0209_R080_T29UPU_20181020T123439
S2A_MSIL2A_20181016T115401_N0209_R023_T29UNV_20181016T143216
S2A_MSIL2A_20181016T115401_N0209_R023_T29UNU_20181016T143216
S2A_MSIL2A_20181016T115401_N0209_R023_T29UNB_20181016T143216
S2A_MSIL2A_20181016T115401_N0209_R023_T29UNA_20181016T143216
S2A_MSIL2A_20181016T115401_N0209_R023_T29UMU_20181016T143216
S2A_MSIL2A_20181016T115401_N0209_R023_T29UMT_20181016T143216
S2A_MSIL2A_20181016T115401_N0209_R023_T29ULT_20181016T143216
S2A_MSIL2A_20181010T113321_N0209_R080_T30UUF_20181010T141708
S2A_MSIL2A_20181010T113321_N0209_R080_T29UPV_20181010T141708
S2A_MSIL2A_20181010T113321_N0209_R080_T29UPU_20181010T141708
S2A_MSIL2A_20181010T113321_N0209_R080_T29UPT_20181010T141708
S2A_MSIL2A_20181010T113321_N0209_R080_T29UPB_20181010T141708
S2A_MSIL2A_20181010T113321_N0209_R080_T29UPA_20181010T141708
S2A_MSIL2A_20181010T113321_N0209_R080_T29UNU_20181010T141708
S2A_MSIL2A_20181010T113321_N0209_R080_T29UNT_20181010T141708
S2A_MSIL2A_20181006T115401_N0208_R023_T29UPB_20181006T125746
S2A_MSIL2A_20181006T115401_N0208_R023_T29UPA_20181006T125746
S2A_MSIL2A_20181006T115401_N0208_R023_T29UNV_20181006T125746
S2A_MSIL2A_20181006T115401_N0208_R023_T29UNT_20181006T125746
S2A_MSIL2A_20181006T115401_N0208_R023_T29UNB_20181006T125746
S2A_MSIL2A_20181006T115401_N0208_R023_T29UNA_20181006T125746
S2A_MSIL2A_20181006T115401_N0208_R023_T29UMV_20181006T125746
S2A_MSIL2A_20181006T115401_N0208_R023_T29UMU_20181006T125746
S2A_MSIL2A_20181006T115401_N0208_R023_T29UMT_20181006T125746

Sentinel-2 Satellite Images used in Chapter 3 comparative assessment [continued].

S2A_MSIL2A_20181006T115401_N0208_R023_T29UMA_20181006T125746
S2A_MSIL2A_20180923T114341_N0208_R123_T30UUF_20180923T143521
S2A_MSIL2A_20180923T114341_N0208_R123_T29UPV_20180923T143521
S2A_MSIL2A_20180923T114341_N0208_R123_T29UPA_20180923T143521
S2A_MSIL2A_20180923T114341_N0208_R123_T29UNV_20180923T143521
S2A_MSIL2A_20180923T114341_N0208_R123_T29UNU_20180923T143521
S2A_MSIL2A_20180923T114341_N0208_R123_T29UNT_20180923T143521
S2A_MSIL2A_20180923T114341_N0208_R123_T29UNB_20180923T143521
S2A_MSIL2A_20180923T114341_N0208_R123_T29UNA_20180923T143521
S2A_MSIL2A_20180923T114341_N0208_R123_T29UMV_20180923T143521
S2A_MSIL2A_20180923T114341_N0208_R123_T29UMU_20180923T143521
S2A_MSIL2A_20180923T114341_N0208_R123_T29UMT_20180923T143521
S2A_MSIL2A_20180913T114351_N0208_R123_T29UPT_20180913T144400
S2A_MSIL2A_20180903T114351_N0208_R123_T30UUF_20180903T143544
S2A_MSIL2A_20180903T114351_N0208_R123_T29UPV_20180903T143544
S2A_MSIL2A_20180903T114351_N0208_R123_T29UPU_20180903T143544
S2A_MSIL2A_20180903T114351_N0208_R123_T29UPT_20180903T143544
S2A_MSIL2A_20180903T114351_N0208_R123_T29UPA_20180903T143544
S2A_MSIL2A_20180903T114351_N0208_R123_T29UNV_20180903T143544
S2A_MSIL2A_20180903T114351_N0208_R123_T29UNU_20180903T143544
S2A_MSIL2A_20180903T114351_N0208_R123_T29UNT_20180903T143544
S2A_MSIL2A_20180903T114351_N0208_R123_T29UMT_20180903T143544
S2A_MSIL2A_20180831T113321_N0208_R080_T30UUF_20180831T150101
S2A_MSIL2A_20180831T113321_N0208_R080_T30UUF_20180831T145610
S2A_MSIL2A_20180831T113321_N0208_R080_T29UPB_20180831T150101
S2A_MSIL2A_20180831T113321_N0208_R080_T29UPB_20180831T145610
S2A_MSIL2A_20180831T113321_N0208_R080_T29UPA_20180831T150101

Sentinel-2 Satellite Images used in Chapter 3 comparative assessment [continued].

S2A_MSIL2A_20180824T114351_N0208_R123_T29UPV_20180824T150935
S2A_MSIL2A_20180824T114351_N0208_R123_T29UPU_20180824T150935
S2A_MSIL2A_20180824T114351_N0208_R123_T29UPA_20180824T150935
S2A_MSIL2A_20180824T114351_N0208_R123_T29UNV_20180824T150935
S2A_MSIL2A_20180824T114351_N0208_R123_T29UNA_20180824T150935
S2A_MSIL2A_20180824T114351_N0208_R123_T29UMV_20180824T150935
S2A_MSIL2A_20180728T115401_N0208_R023_T29UMT_20180728T150735
S2A_MSIL2A_20180725T114351_N0208_R123_T30UUF_20180725T140825
S2A_MSIL2A_20180725T114351_N0208_R123_T29UPV_20180725T140825
S2A_MSIL2A_20180725T114351_N0208_R123_T29UPU_20180725T140825
S2A_MSIL2A_20180725T114351_N0208_R123_T29UPB_20180725T140825
S2A_MSIL2A_20180725T114351_N0208_R123_T29UPA_20180725T140825
S2A_MSIL2A_20180725T114351_N0208_R123_T29UNT_20180725T140825
S2A_MSIL2A_20180725T114351_N0208_R123_T29UNB_20180725T140825
S2A_MSIL2A_20180725T114351_N0208_R123_T29UNA_20180725T140825
S2A_MSIL2A_20180712T113321_N0208_R080_T29UNT_20180712T141314
S2A_MSIL2A_20180705T114351_N0208_R123_T30UUG_20180705T142104
S2A_MSIL2A_20180705T114351_N0208_R123_T29UPU_20180705T142104
S2A_MSIL2A_20180705T114351_N0208_R123_T29UPT_20180705T142104
S2A_MSIL2A_20180705T114351_N0208_R123_T29UNU_20180705T142104
S2A_MSIL2A_20180705T114351_N0208_R123_T29UNT_20180705T142104
S2A_MSIL2A_20180705T114351_N0208_R123_T29UNB_20180705T142104
S2A_MSIL2A_20180705T114351_N0208_R123_T29UNA_20180705T142104
S2A_MSIL2A_20180705T114351_N0208_R123_T29UMT_20180705T142104
S2A_MSIL2A_20180702T113321_N0208_R080_T30UUG_20180702T141901
S2A_MSIL2A_20180702T113321_N0208_R080_T30UUF_20180702T141901
S2A_MSIL2A_20180702T113321_N0208_R080_T29UPV_20180702T141901

Sentinel-2 Satellite Images used in Chapter 3 comparative assessment [continued].

S2A_MSIL2A_20180702T113321_N0208_R080_T29UPU_20180702T141901
S2A_MSIL2A_20180702T113321_N0208_R080_T29UPT_20180702T141901
S2A_MSIL2A_20180702T113321_N0208_R080_T29UPB_20180702T141901
S2A_MSIL2A_20180702T113321_N0208_R080_T29UPA_20180702T141901
S2A_MSIL2A_20180702T113321_N0208_R080_T29UNU_20180702T141901
S2A_MSIL2A_20180628T115401_N0208_R023_T29UPV_20180628T125228
S2A_MSIL2A_20180628T115401_N0208_R023_T29UPB_20180628T125228
S2A_MSIL2A_20180628T115401_N0208_R023_T29UPA_20180628T125228
S2A_MSIL2A_20180628T115401_N0208_R023_T29UNV_20180628T125228
S2A_MSIL2A_20180628T115401_N0208_R023_T29UNU_20180628T125228
S2A_MSIL2A_20180628T115401_N0208_R023_T29UNT_20180628T125228
S2A_MSIL2A_20180628T115401_N0208_R023_T29UNB_20180628T125228
S2A_MSIL2A_20180628T115401_N0208_R023_T29UNA_20180628T125228
S2A_MSIL2A_20180628T115401_N0208_R023_T29UMV_20180628T125228
S2A_MSIL2A_20180628T115401_N0208_R023_T29UMU_20180628T125228
S2A_MSIL2A_20180628T115401_N0208_R023_T29UMT_20180628T125228
S2A_MSIL2A_20180628T115401_N0208_R023_T29UMA_20180628T125228
S2A_MSIL2A_20180628T115401_N0208_R023_T29ULT_20180628T125228
S2A_MSIL2A_20180625T114351_N0208_R123_T30UUF_20180625T173707
S2A_MSIL2A_20180625T114351_N0208_R123_T29UPV_20180625T173707
S2A_MSIL2A_20180625T114351_N0208_R123_T29UPU_20180625T173707
S2A_MSIL2A_20180625T114351_N0208_R123_T29UPB_20180625T173707
S2A_MSIL2A_20180625T114351_N0208_R123_T29UPA_20180625T173707
S2A_MSIL2A_20180625T114351_N0208_R123_T29UNV_20180625T173707
S2A_MSIL2A_20180625T114351_N0208_R123_T29UNU_20180625T173707
S2A_MSIL2A_20180625T114351_N0208_R123_T29UNT_20180625T173707
S2A_MSIL2A_20180625T114351_N0208_R123_T29UNB_20180625T173707

Sentinel-2 Satellite Images used in Chapter 3 comparative assessment [continued].

S2A_MSIL2A_20180625T114351_N0208_R123_T29UNA_20180625T173707
S2A_MSIL2A_20180625T114351_N0208_R123_T29UMV_20180625T173707
S2A_MSIL2A_20180625T114351_N0208_R123_T29UMU_20180625T173707
S2A_MSIL2A_20180625T114351_N0208_R123_T29UMT_20180625T173707
S2A_MSIL2A_20180625T114351_N0208_R123_T29UMA_20180625T173707
S2A_MSIL2A_20180622T113321_N0208_R080_T30UUF_20180622T123307
S2A_MSIL2A_20180622T113321_N0208_R080_T29UPV_20180622T123307
S2A_MSIL2A_20180622T113321_N0208_R080_T29UPU_20180622T123307
S2A_MSIL2A_20180622T113321_N0208_R080_T29UPT_20180622T123307
S2A_MSIL2A_20180622T113321_N0208_R080_T29UPB_20180622T123307
S2A_MSIL2A_20180622T113321_N0208_R080_T29UPA_20180622T123307
S2A_MSIL2A_20180622T113321_N0208_R080_T29UNU_20180622T123307
S2A_MSIL2A_20180622T113321_N0208_R080_T29UNT_20180622T123307
S2A_MSIL2A_20180612T113321_N0208_R080_T29UPU_20180612T143029
S2A_MSIL2A_20180608T115401_N0208_R023_T29UPV_20180608T160042
S2A_MSIL2A_20180608T115401_N0208_R023_T29UPB_20180608T160042
S2A_MSIL2A_20180608T115401_N0208_R023_T29UPA_20180608T160042
S2A_MSIL2A_20180608T115401_N0208_R023_T29UNV_20180608T160042
S2A_MSIL2A_20180608T115401_N0208_R023_T29UNA_20180608T160042
S2A_MSIL2A_20180608T115401_N0208_R023_T29UMV_20180608T160042
S2A_MSIL2A_20180608T115401_N0208_R023_T29UMU_20180608T160042
S2A_MSIL2A_20180608T115401_N0208_R023_T29ULT_20180608T160042
S2A_MSIL2A_20180605T114351_N0208_R123_T30UG_20180605T124913
S2A_MSIL2A_20180605T114351_N0208_R123_T29UMT_20180605T124913
S2A_MSIL2A_20180529T115401_N0208_R023_T29UPV_20180529T125059
S2A_MSIL2A_20180529T115401_N0208_R023_T29UPB_20180529T125059
S2A_MSIL2A_20180529T115401_N0208_R023_T29UPA_20180529T125059

Sentinel-2 Satellite Images used in Chapter 3 comparative assessment [continued].

S2A_MSIL2A_20180529T115401_N0208_R023_T29UNV_20180529T125059
S2A_MSIL2A_20180529T115401_N0208_R023_T29UNU_20180529T125059
S2A_MSIL2A_20180529T115401_N0208_R023_T29UNB_20180529T125059
S2A_MSIL2A_20180529T115401_N0208_R023_T29UNA_20180529T125059
S2A_MSIL2A_20180529T115401_N0208_R023_T29UMV_20180529T125059
S2A_MSIL2A_20180529T115401_N0208_R023_T29UMU_20180529T125059
S2A_MSIL2A_20180529T115401_N0208_R023_T29UMT_20180529T125059
S2A_MSIL2A_20180529T115401_N0208_R023_T29ULT_20180529T125059
S2A_MSIL2A_20180526T114351_N0208_R123_T29UPV_20180526T173701
S2A_MSIL2A_20180526T114351_N0208_R123_T29UPB_20180526T173701
S2A_MSIL2A_20180526T114351_N0208_R123_T29UPA_20180526T173701
S2A_MSIL2A_20180526T114351_N0208_R123_T29UNV_20180526T173701
S2A_MSIL2A_20180526T114351_N0208_R123_T29UNB_20180526T173701
S2A_MSIL2A_20180526T114351_N0208_R123_T29UNA_20180526T173701
S2A_MSIL2A_20180526T114351_N0208_R123_T29UMV_20180526T173701
S2A_MSIL2A_20180526T114351_N0208_R123_T29UMA_20180526T173701
S2A_MSIL2A_20180523T113321_N0208_R080_T30UUF_20180523T181029
S2A_MSIL2A_20180523T113321_N0208_R080_T29UPV_20180523T181029
S2A_MSIL2A_20180523T113321_N0208_R080_T29UPU_20180523T181029
S2A_MSIL2A_20180523T113321_N0208_R080_T29UPT_20180523T181029
S2A_MSIL2A_20180523T113321_N0208_R080_T29UPB_20180523T181029
S2A_MSIL2A_20180523T113321_N0208_R080_T29UPA_20180523T181029
S2A_MSIL2A_20180523T113321_N0208_R080_T29UNU_20180523T181029
S2A_MSIL2A_20180523T113321_N0208_R080_T29UNT_20180523T181029
S2A_MSIL2A_20180519T115401_N0207_R023_T29UNU_20180519T154451
S2A_MSIL2A_20180519T115401_N0207_R023_T29UMT_20180519T154451
S2A_MSIL2A_20180516T114351_N0207_R123_T30UUF_20180516T120702

Sentinel-2 Satellite Images used in Chapter 3 comparative assessment [continued].

S2A_MSIL2A_20180516T114351_N0207_R123_T29UPV_20180516T120702
S2A_MSIL2A_20180516T114351_N0207_R123_T29UPU_20180516T120702
S2A_MSIL2A_20180516T114351_N0207_R123_T29UPT_20180516T120702
S2A_MSIL2A_20180516T114351_N0207_R123_T29UPB_20180516T120702
S2A_MSIL2A_20180516T114351_N0207_R123_T29UPA_20180516T120702
S2A_MSIL2A_20180516T114351_N0207_R123_T29UNV_20180516T120702
S2A_MSIL2A_20180516T114351_N0207_R123_T29UNU_20180516T120702
S2A_MSIL2A_20180516T114351_N0207_R123_T29UNT_20180516T120702
S2A_MSIL2A_20180516T114351_N0207_R123_T29UNB_20180516T120702
S2A_MSIL2A_20180516T114351_N0207_R123_T29UNA_20180516T120702
S2A_MSIL2A_20180516T114351_N0207_R123_T29UMV_20180516T120702
S2A_MSIL2A_20180516T114351_N0207_R123_T29UMU_20180516T120702
S2A_MSIL2A_20180516T114351_N0207_R123_T29UMT_20180516T120702
S2A_MSIL2A_20180516T114351_N0207_R123_T29UMA_20180516T120702
S2A_MSIL2A_20180516T114351_N0207_R123_T29ULT_20180516T120702
S2A_MSIL2A_20180513T113321_N0207_R080_T30UUG_20180513T133943
S2A_MSIL2A_20180513T113321_N0207_R080_T30UUF_20180513T133943
S2A_MSIL2A_20180513T113321_N0207_R080_T29UPU_20180513T133943
S2A_MSIL2A_20180513T113321_N0207_R080_T29UPT_20180513T133943
S2A_MSIL2A_20180513T113321_N0207_R080_T29UPA_20180513T133943
S2A_MSIL2A_20180506T114351_N0207_R123_T29UPV_20180506T120844
S2A_MSIL2A_20180506T114351_N0207_R123_T29UPU_20180506T120844
S2A_MSIL2A_20180506T114351_N0207_R123_T29UPA_20180506T120844
S2A_MSIL2A_20180506T114351_N0207_R123_T29UNV_20180506T120844
S2A_MSIL2A_20180506T114351_N0207_R123_T29UNU_20180506T120844
S2A_MSIL2A_20180506T114351_N0207_R123_T29UNT_20180506T120844
S2A_MSIL2A_20180506T114351_N0207_R123_T29UNA_20180506T120844

Sentinel-2 Satellite Images used in Chapter 3 comparative assessment [continued].

S2A_MSIL2A_20180506T114351_N0207_R123_T29UMV_20180506T120844
S2A_MSIL2A_20180506T114351_N0207_R123_T29UMU_20180506T120844
S2A_MSIL2A_20180506T114351_N0207_R123_T29UMT_20180506T120844
S2A_MSIL2A_20180429T115401_N0207_R023_T29UNV_20180429T121704
S2A_MSIL2A_20180429T115401_N0207_R023_T29UNU_20180429T121704
S2A_MSIL2A_20180429T115401_N0207_R023_T29UNT_20180429T121704
S2A_MSIL2A_20180429T115401_N0207_R023_T29UMU_20180429T121704
S2A_MSIL2A_20180429T115401_N0207_R023_T29UMT_20180429T121704
S2A_MSIL2A_20180429T115401_N0207_R023_T29UMA_20180429T121704
S2A_MSIL2A_20180426T114351_N0207_R123_T29UPV_20180426T134253
S2A_MSIL2A_20180426T114351_N0207_R123_T29UPU_20180426T134253
S2A_MSIL2A_20180426T114351_N0207_R123_T29UPB_20180426T134253
S2A_MSIL2A_20180426T114351_N0207_R123_T29UPB_20180426T120422
S2A_MSIL2A_20180426T114351_N0207_R123_T29UPA_20180426T134253
S2A_MSIL2A_20180426T114351_N0207_R123_T29UNV_20180426T134253
S2A_MSIL2A_20180426T114351_N0207_R123_T29UNB_20180426T134253
S2A_MSIL2A_20180426T114351_N0207_R123_T29UNA_20180426T134253
S2A_MSIL2A_20180419T115401_N0207_R023_T29UMV_20180419T121634
S2A_MSIL2A_20180419T115401_N0207_R023_T29UMU_20180419T121634
S2A_MSIL2A_20180419T115401_N0207_R023_T29UMT_20180419T121634
S2A_MSIL2A_20180419T115401_N0207_R023_T29ULT_20180419T121634
S2A_MSIL2A_20180403T113321_N0207_R080_T29UPT_20180403T151646

A.3 Landsat-8 Images

Table A.3: Landsat-8 Satellite Images used in Chapter 3 comparative assessment.

LC08.L2SP.207022.20180607.20200831.02.T1
LC08.L2SP.207022.20180420.20200901.02.T1
LC08.L2SP.205022.20180217.20200902.02.T1
LC08.L2SP.207022.20180725.20200831.02.T1
LC08.L2SP.206022.20180429.20200901.02.T1
LC08.L2SP.207022.20180215.20200902.02.T1
LC08.L2SP.207022.20180506.20200901.02.T1
LC08.L2SP.205022.20180625.20200831.02.T1
LC08.L2SP.205022.20180524.20200901.02.T1
LC08.L2SP.207022.20180319.20200901.02.T1
LC08.L2SP.206022.20181022.20200830.02.T1
LC08.L2SP.206022.20181123.20200830.02.T1
LC08.L2SP.206022.20180904.20200831.02.T1
LC08.L2SP.206022.20180702.20200831.02.T1
LC08.L2SP.207022.20180810.20200831.02.T1
LC08.L2SP.205022.20180201.20200902.02.T1
LC08.L2SP.205022.20180929.20200830.02.T1
LC08.L2SP.206022.20181006.20200830.02.T1
LC08.L2SP.206022.20180616.20200831.02.T1
LC08.L2SP.207023.20180522.20200901.02.T1
LC08.L2SP.208023.20180222.20200902.02.T1
LC08.L2SP.207023.20180506.20200901.02.T1
LC08.L2SP.208022.20180427.20200901.02.T1
LC08.L2SP.207023.20181130.20200830.02.T1
LC08.L2SP.207023.20180810.20200831.02.T1

Landsat-8 Satellite Images used in Chapter 3 comparative assessment [continued].

LC08_L2SP_208023_20180630_20200831_02_T1
LC08_L2SP_208023_20180529_20200901_02_T1
LC08_L2SP_207023_20180607_20200831_02_T1
LC08_L2SP_208022_20180630_20200831_02_T1
LC08_L2SP_208022_20180529_20200901_02_T1
LC08_L2SP_208023_20180206_20200902_02_T1
LC08_L2SP_207023_20180404_20200901_02_T1
LC08_L2SP_208023_20180513_20200901_02_T1
LC08_L2SP_207023_20180623_20200831_02_T1
LC08_L2SP_207023_20180420_20200901_02_T1
LC08_L2SP_207023_20180215_20200902_02_T1
LC08_L2SP_208023_20180614_20200831_02_T1
LC08_L2SP_206023_20180429_20200901_02_T1
LC08_L2SP_207024_20181130_20200830_02_T1
LC08_L2SP_206024_20181022_20200830_02_T1
LC08_L2SP_208023_20180614_20200831_02_T1
LC08_L2SP_206024_20181006_20200830_02_T1
LC08_L2SP_207023_20180215_20200902_02_T1
LC08_L2SP_207023_20180927_20200830_02_T1
LC08_L2SP_207024_20180506_20200901_02_T1
LC08_L2SP_207024_20180404_20200901_02_T1
LC08_L2SP_207023_20181130_20200830_02_T1
LC08_L2SP_208023_20180529_20200901_02_T1
LC08_L2SP_208023_20180206_20200902_02_T1
LC08_L2SP_206024_20180429_20200901_02_T1
LC08_L2SP_207023_20180506_20200901_02_T1
LC08_L2SP_208023_20180222_20200902_02_T1

Landsat-8 Satellite Images used in Chapter 3 comparative assessment [continued].

LC08.L2SP_207023_20180810_20200831_02_T1
LC08.L2SP_207024_20180725_20200831_02_T1
LC08.L2SP_207024_20180623_20200831_02_T1
LC08.L2SP_207023_20180623_20200831_02_T1
LC08.L2SP_206024_20180702_20200831_02_T1
LC08.L2SP_206023_20181022_20200830_02_T1
LC08.L2SP_207023_20180420_20200901_02_T1
LC08.L2SP_207023_20180725_20200831_02_T1
LC08.L2SP_208023_20180630_20200831_02_T1
LC08.L2SP_207023_20180522_20200901_02_T1
LC08.L2SP_206023_20181006_20200830_02_T1
LC08.L2SP_207024_20180522_20200901_02_T1
LC08.L2SP_207023_20180607_20200831_02_T1
LC08.L2SP_207024_20180607_20200831_02_T1
LC08.L2SP_206023_20180702_20200831_02_T1
LC08.L2SP_207024_20180420_20201015_02_T1
LC08.L2SP_208023_20180513_20200901_02_T1
LC08.L2SP_207024_20180810_20200831_02_T1
LC08.L2SP_206024_20180107_20200902_02_T1
LC08.L2SP_207023_20180404_20200901_02_T1
LC08.L2SP_207024_20180927_20200830_02_T1
LC08.L2SP_207022_20180319_20200901_02_T1
LC08.L2SP_208022_20180206_20200902_02_T1
LC08.L2SP_207022_20180506_20200901_02_T1
LC08.L2SP_208022_20180427_20200901_02_T1
LC08.L2SP_208022_20180529_20200901_02_T1
LC08.L2SP_208022_20180630_20200831_02_T1

Landsat-8 Satellite Images used in Chapter 3 comparative assessment [continued].

LC08_L2SP_207022_20180725_20200831_02_T1
LC08_L2SP_208022_20180614_20200831_02_T1
LC08_L2SP_208022_20180513_20200901_02_T1
LC08_L2SP_207022_20180522_20201015_02_T1
LC08_L2SP_207022_20180623_20200831_02_T1
LC08_L2SP_207022_20180420_20200901_02_T1
LC08_L2SP_207022_20180810_20200831_02_T1
LC08_L2SP_207023_20181130_20200830_02_T1
LC08_L2SP_206024_20180107_20200902_02_T1
LC08_L2SP_206024_20181107_20200830_02_T1
LC08_L2SP_207023_20180725_20200831_02_T1
LC08_L2SP_206023_20180328_20200901_02_T1
LC08_L2SP_207024_20180623_20200831_02_T1
LC08_L2SP_206024_20180702_20200831_02_T1
LC08_L2SP_206023_20180803_20200831_02_T1
LC08_L2SP_206024_20180904_20200831_02_T1
LC08_L2SP_207024_20180420_20201015_02_T1
LC08_L2SP_207023_20180607_20200831_02_T1
LC08_L2SP_206024_20181006_20200830_02_T1
LC08_L2SP_206024_20181022_20200830_02_T1
LC08_L2SP_207023_20180623_20200831_02_T1
LC08_L2SP_207024_20181130_20200830_02_T1
LC08_L2SP_207024_20180927_20200830_02_T1
LC08_L2SP_206023_20181022_20200830_02_T1
LC08_L2SP_206023_20180429_20200901_02_T1
LC08_L2SP_206024_20180819_20200831_02_T1
LC08_L2SP_207023_20180215_20200902_02_T1

Landsat-8 Satellite Images used in Chapter 3 comparative assessment [continued].

LC08_L2SP_206023_20180904_20200831_02_T1
LC08_L2SP_207024_20180522_20200901_02_T1
LC08_L2SP_206023_20180819_20200831_02_T1
LC08_L2SP_206024_20180429_20200901_02_T1
LC08_L2SP_207024_20180215_20200902_02_T1
LC08_L2SP_207023_20180420_20200901_02_T1
LC08_L2SP_207024_20180607_20200831_02_T1
LC08_L2SP_207024_20180725_20200831_02_T1
LC08_L2SP_206024_20180803_20200831_02_T1
LC08_L2SP_207023_20180506_20200901_02_T1
LC08_L2SP_207024_20180506_20200901_02_T1
LC08_L2SP_207024_20180810_20200831_02_T1
LC08_L2SP_206023_20180702_20200831_02_T1
LC08_L2SP_206024_20180328_20200901_02_T1
LC08_L2SP_206024_20181209_20200830_02_T1
LC08_L2SP_207024_20180404_20200901_02_T1
LC08_L2SP_207023_20180810_20200831_02_T1
LC08_L2SP_207023_20180404_20200901_02_T1
LC08_L2SP_206023_20181006_20200830_02_T1
LC08_L2SP_207023_20180927_20200830_02_T1
LC08_L2SP_207023_20180522_20200901_02_T1
LC08_L2SP_207023_20180506_20200901_02_T1
LC08_L2SP_207023_20180215_20200902_02_T1
LC08_L2SP_207024_20180927_20200830_02_T1
LC08_L2SP_206024_20180904_20200831_02_T1
LC08_L2SP_207024_20180607_20200831_02_T1
LC08_L2SP_206024_20180429_20200901_02_T1

Landsat-8 Satellite Images used in Chapter 3 comparative assessment [continued].

LC08_L2SP_207023_20180623_20200831_02_T1
LC08_L2SP_207023_20180810_20200831_02_T1
LC08_L2SP_208024_20180716_20200831_02_T1
LC08_L2SP_206024_20180803_20200831_02_T1
LC08_L2SP_207023_20180420_20200901_02_T1
LC08_L2SP_207023_20180522_20200901_02_T1
LC08_L2SP_208024_20180630_20200831_02_T1
LC08_L2SP_208023_20180614_20200831_02_T1
LC08_L2SP_208024_20180206_20200902_02_T1
LC08_L2SP_207024_20180522_20200901_02_T1
LC08_L2SP_206024_20181022_20200830_02_T1
LC08_L2SP_207024_20180506_20200901_02_T1
LC08_L2SP_207024_20180623_20200831_02_T1
LC08_L2SP_206024_20180819_20200831_02_T1
LC08_L2SP_206024_20181006_20200830_02_T1
LC08_L2SP_207024_20180725_20200831_02_T1
LC08_L2SP_207023_20180607_20200831_02_T1
LC08_L2SP_207024_20180215_20200902_02_T1
LC08_L2SP_207024_20180810_20200831_02_T1
LC08_L2SP_207023_20180725_20200831_02_T1
LC08_L2SP_206024_20181209_20200830_02_T1
LC08_L2SP_207024_20180420_20201015_02_T1
LC08_L2SP_208023_20180206_20200902_02_T1
LC08_L2SP_208023_20180630_20200831_02_T1
LC08_L2SP_207024_20180404_20200901_02_T1
LC08_L2SP_207024_20181130_20200830_02_T1
LC08_L2SP_207023_20180927_20200830_02_T1

Landsat-8 Satellite Images used in Chapter 3 comparative assessment [continued].

LC08.L2SP_206024_20180702_20200831_02_T1
LC08.L2SP_207024_20180215_20200902_02_T1
LC08.L2SP_207024_20181130_20200830_02_T1
LC08.L2SP_208024_20181105_20200830_02_T1
LC08.L2SP_207024_20180404_20200901_02_T1
LC08.L2SP_208024_20180206_20200902_02_T1
LC08.L2SP_207024_20180420_20201015_02_T1
LC08.L2SP_208024_20180614_20200831_02_T1
LC08.L2SP_207024_20180607_20200831_02_T1
LC08.L2SP_208024_20180529_20200901_02_T1
LC08.L2SP_207024_20180522_20200901_02_T1
LC08.L2SP_208024_20180513_20201015_02_T1
LC08.L2SP_208024_20181121_20200830_02_T1
LC08.L2SP_207024_20180927_20200830_02_T1
LC08.L2SP_207024_20180810_20200831_02_T1
LC08.L2SP_207024_20180506_20200901_02_T1
LC08.L2SP_207024_20180725_20200831_02_T1
LC08.L2SP_207024_20180623_20200831_02_T1
LC08.L2SP_208024_20180716_20200831_02_T1
LC08.L2SP_208024_20180630_20200831_02_T1
LC08.L2SP_207024_20180709_20200831_02_T1
LC08.L2SP_205023_20180625_20200831_02_T1
LC08.L2SP_206023_20180718_20200831_02_T1
LC08.L2SP_206022_20180531_20200831_02_T1
LC08.L2SP_205023_20180201_20200902_02_T1
LC08.L2SP_206023_20180531_20200831_02_T1
LC08.L2SP_205023_20180711_20200831_02_T1

Appendix B

Chapter 3 Results

Contents

B.1 Sentinel-1 Results	292
B.2 Sentinel-2 Results	295
B.3 Landsat-8 Results	304
B.4 Sentinel-1 Results With Shrub	306
B.5 Sentinel-2 Results With Shrub	308
B.6 Landsat-8 Results With Shrub	312

All results presented in this section are calculated using all label data available to each model and, therefore, may differ from those presented as part of the comparative assessment undertaken in Chapter 3.

B.1 Sentinel-1 Results

Table B.1: Sentinel-1 Model Results.

		Sealed	Coniferous Forest	Broadleaved Forest	Permanent Herbaceous	Periodically Herbaceous	Sparsely Vegetated	Non-vegetated	Water	Weighted F1	OA%
ANN Single Date	Train	0.320	0.490	0.223	0.385	0.117	0.359	0.024	0.909	0.362	0.400
	Validation	0.284	0.401	0.270	0.361	0.104	0.340	0.024	0.904	0.344	0.377
	Test	0.317	0.470	0.219	0.358	0.106	0.272	0.025	0.933	0.345	0.380
RF Single Date	Train	0.318	0.499	0.305	0.383	0.200	0.359	0.174	0.908	0.399	0.419
	Validation	0.273	0.443	0.335	0.382	0.181	0.368	0.192	0.929	0.393	0.412
	Test	0.284	0.450	0.263	0.317	0.076	0.254	0.183	0.928	0.349	0.367
SVM Single Date	Train	0.299	0.456	0.281	0.386	0.116	0.327	0.186	0.904	0.374	0.395
	Validation	0.244	0.464	0.287	0.294	0.143	0.385	0.278	0.907	0.378	0.392
	Test	0.302	0.456	0.284	0.370	0.122	0.246	0.164	0.939	0.366	0.385
ANN Annual Average	Train	0.461	0.604	0.271	0.473	0.290	0.297	0.417	0.963	0.473	0.490
	Validation	0.387	0.554	0.244	0.408	0.292	0.270	0.382	0.966	0.439	0.453
	Test	0.492	0.614	0.266	0.433	0.275	0.195	0.396	0.974	0.457	0.479
RF Annual Average	Train	0.456	0.584	0.462	0.496	0.341	0.449	0.321	0.954	0.513	0.520
	Validation	0.413	0.498	0.459	0.518	0.344	0.459	0.339	0.971	0.504	0.511
	Test	0.489	0.594	0.505	0.447	0.270	0.224	0.266	0.975	0.477	0.482
SVM Annual Average	Train	0.436	0.583	0.408	0.482	0.291	0.409	0.258	0.952	0.483	0.495
	Validation	0.405	0.525	0.387	0.480	0.323	0.396	0.209	0.966	0.468	0.479
	Test	0.453	0.561	0.441	0.464	0.216	0.192	0.231	0.973	0.447	0.455

Sentinel-1 Model Results [continued].

		Sealed	Coniferous Forest	Broadleaved Forest	Permanent Herbaceous	Periodically Herbaceous	Sparsely Vegetated	Non-vegetated	Water	Weighted F1	OA%
ANN Half-Year Average	Train	0.432	0.611	0.473	0.472	0.302	0.439	0.354	0.963	0.510	0.518
	Validation	0.374	0.563	0.482	0.459	0.270	0.425	0.362	0.971	0.491	0.501
	Test	0.469	0.669	0.487	0.438	0.334	0.220	0.329	0.978	0.495	0.505
RF Half-Year Average	Train	0.487	0.675	0.543	0.489	0.477	0.489	0.350	0.963	0.564	0.569
	Validation	0.396	0.596	0.484	0.456	0.458	0.477	0.365	0.971	0.529	0.534
	Test	0.505	0.709	0.519	0.471	0.392	0.280	0.274	0.979	0.522	0.533
SVM Half-Year Average	Train	0.473	0.640	0.528	0.467	0.437	0.450	0.274	0.954	0.534	0.543
	Validation	0.405	0.623	0.516	0.469	0.454	0.460	0.303	0.966	0.530	0.539
	Test	0.484	0.732	0.575	0.465	0.480	0.263	0.256	0.975	0.536	0.545
ANN Season Average	Train	0.502	0.755	0.579	0.468	0.348	0.352	0.469	0.970	0.558	0.568
	Validation	0.420	0.720	0.525	0.429	0.318	0.373	0.461	0.945	0.525	0.535
	Test	0.537	0.759	0.646	0.466	0.407	0.186	0.398	0.976	0.551	0.569
RF Season Average	Train	0.498	0.765	0.625	0.506	0.500	0.498	0.413	0.963	0.601	0.605
	Validation	0.446	0.723	0.634	0.478	0.503	0.532	0.412	0.971	0.592	0.597
	Test	0.509	0.765	0.643	0.457	0.416	0.256	0.391	0.980	0.556	0.563
SVM Season Average	Train	0.500	0.768	0.615	0.470	0.490	0.501	0.440	0.964	0.598	0.600
	Validation	0.452	0.747	0.619	0.449	0.497	0.512	0.478	0.966	0.593	0.597
	Test	0.545	0.784	0.661	0.480	0.498	0.323	0.451	0.978	0.593	0.599
1DCNN Season Average	Train	0.536	0.782	0.632	0.479	0.557	0.511	0.505	0.973	0.625	0.626
	Validation	0.437	0.767	0.627	0.484	0.552	0.567	0.541	0.971	0.620	0.623
	Test	0.553	0.788	0.655	0.504	0.628	0.322	0.503	0.980	0.620	0.629

Sentinel-1 Model Results [continued].

		Sealed	Coniferous Forest	Broadleaved Forest	Permanent Herbaceous	Periodically Herbaceous	Sparsely Vegetated	Non-vegetated	Water	Weighted F1	OA%
ANN Monthly Average	Train	0.666	0.810	0.683	0.632	0.735	0.775	0.770	0.994	0.758	0.758
	Validation	0.488	0.815	0.592	0.371	0.565	0.685	0.586	0.980	0.637	0.642
	Test	0.559	0.806	0.668	0.421	0.635	0.410	0.364	0.958	0.609	0.606
RF Monthly Average	Train	0.544	0.789	0.646	0.548	0.597	0.595	0.461	0.968	0.647	0.651
	Validation	0.460	0.761	0.673	0.495	0.552	0.590	0.419	0.971	0.620	0.626
	Test	0.509	0.781	0.673	0.467	0.538	0.366	0.413	0.978	0.595	0.602
SVM Monthly Average	Train	0.598	0.805	0.654	0.539	0.639	0.643	0.578	0.975	0.681	0.681
	Validation	0.517	0.800	0.673	0.521	0.602	0.725	0.658	0.980	0.686	0.689
	Test	0.536	0.802	0.691	0.506	0.672	0.484	0.416	0.976	0.641	0.645
LSTM Monthly Average	Train	0.522	0.767	0.615	0.492	0.525	0.504	0.436	0.965	0.607	0.609
	Validation	0.483	0.740	0.597	0.490	0.543	0.526	0.427	0.966	0.602	0.604
	Test	0.537	0.773	0.642	0.475	0.527	0.425	0.409	0.978	0.600	0.602
1DCNN Monthly Average	Train	0.670	0.827	0.676	0.610	0.681	0.769	0.731	0.989	0.744	0.744
	Validation	0.577	0.833	0.625	0.571	0.576	0.754	0.593	0.975	0.691	0.694
	Test	0.544	0.800	0.663	0.558	0.649	0.639	0.405	0.925	0.654	0.653

B.2 Sentinel-2 Results

Table B.2: Sentinel-2 Model Results.

		Sealed	Woody Coniferous	Woody Broadleaved	Permanent Herbaceous	Periodically Herbaceous	Sparsely Vegetated	Non- vegetated	Water	Weighted F1	OA%
ANN Annual Average 10m bands	Train	0.587	0.772	0.628	0.533	0.386	0.590	0.428	0.969	0.616	0.625
	Validation	0.547	0.778	0.562	0.507	0.338	0.605	0.397	0.966	0.593	0.609
	Test	0.558	0.766	0.680	0.580	0.229	0.531	0.339	0.980	0.586	0.600
ANN Annual Average 10m and 20m bands	Train	0.694	0.848	0.698	0.555	0.598	0.761	0.488	0.981	0.708	0.713
	Validation	0.640	0.885	0.726	0.516	0.613	0.731	0.427	0.971	0.695	0.703
	Test	0.649	0.877	0.741	0.636	0.631	0.794	0.394	0.986	0.720	0.728
ANN Annual Average All bands	Train	0.701	0.863	0.700	0.527	0.598	0.758	0.577	0.982	0.716	0.722
	Validation	0.649	0.880	0.687	0.508	0.602	0.733	0.504	0.970	0.697	0.704
	Test	0.625	0.879	0.745	0.596	0.583	0.803	0.462	0.985	0.714	0.721
RF Annual Average 10m bands	Train	0.547	0.749	0.623	0.552	0.442	0.565	0.439	0.962	0.614	0.617
	Validation	0.524	0.778	0.574	0.514	0.405	0.595	0.481	0.960	0.608	0.613
	Test	0.558	0.784	0.670	0.583	0.337	0.544	0.505	0.979	0.621	0.621
RF Annual Average 10m and 20m bands	Train	0.600	0.844	0.696	0.569	0.500	0.698	0.421	0.961	0.667	0.673
	Validation	0.551	0.884	0.693	0.502	0.478	0.701	0.484	0.975	0.663	0.670
	Test	0.563	0.874	0.732	0.612	0.443	0.671	0.466	0.980	0.670	0.676
RF Annual Average All bands	Train	0.615	0.839	0.698	0.582	0.497	0.714	0.457	0.960	0.675	0.681
	Validation	0.557	0.874	0.694	0.524	0.457	0.706	0.524	0.975	0.667	0.674
	Test	0.573	0.883	0.750	0.614	0.412	0.663	0.490	0.979	0.672	0.677
SVM Annual Average 10m bands	Train	0.593	0.712	0.553	0.523	0.434	0.612	0.298	0.880	0.582	0.599
	Validation	0.549	0.769	0.529	0.512	0.384	0.626	0.286	0.910	0.578	0.600
	Test	0.588	0.761	0.622	0.561	0.341	0.593	0.439	0.952	0.610	0.618
SVM Annual Average 10m and 20m bands	Train	0.662	0.818	0.685	0.533	0.614	0.758	0.465	0.900	0.684	0.690
	Validation	0.632	0.857	0.673	0.487	0.651	0.731	0.487	0.922	0.685	0.692
	Test	0.626	0.873	0.759	0.631	0.613	0.796	0.555	0.969	0.731	0.734
SVM Annual Average All bands	Train	0.652	0.829	0.686	0.547	0.612	0.770	0.478	0.902	0.689	0.695
	Validation	0.628	0.859	0.680	0.497	0.678	0.742	0.506	0.931	0.695	0.701
	Test	0.604	0.869	0.752	0.637	0.621	0.802	0.529	0.969	0.726	0.729

Sentinel-2 Model Results [continued].

		Sealed	Woody Coniferous	Woody Broadleaved	Permanent Herbaceous	Periodically Herbaceous	Sparsely Vegetated	Non- vegetated	Water	Weighted F1	OA%
LCNN3×3 Annual Average 10m bands	Train	0.283	0.733	0.602	0.511	0.415	0.465	0.420	0.932	0.548	0.557
	Validation	0.269	0.763	0.575	0.520	0.419	0.544	0.438	0.928	0.561	0.572
	Test	0.323	0.772	0.662	0.547	0.345	0.327	0.508	0.971	0.555	0.552
LCNN3×3 Annual Average 10m and 20m bands	Train	0.587	0.846	0.660	0.523	0.520	0.732	0.379	0.957	0.657	0.664
	Validation	0.549	0.876	0.706	0.524	0.535	0.735	0.414	0.962	0.670	0.678
	Test	0.577	0.889	0.726	0.604	0.536	0.748	0.410	0.982	0.689	0.695
LCNN3×3 Annual Average all bands	Train	0.581	0.843	0.671	0.541	0.515	0.721	0.394	0.956	0.659	0.664
	Validation	0.603	0.876	0.703	0.526	0.543	0.723	0.439	0.967	0.679	0.685
	Test	0.571	0.876	0.725	0.610	0.495	0.712	0.467	0.983	0.683	0.685
LCNN5×5 Annual Average 10m bands	Train	0.530	0.751	0.593	0.526	0.421	0.499	0.449	0.954	0.594	0.595
	Validation	0.519	0.790	0.589	0.498	0.420	0.539	0.481	0.965	0.604	0.606
	Test	0.572	0.802	0.659	0.568	0.295	0.386	0.463	0.977	0.590	0.587
LCNN5×5 Annual Average 10m and 20m bands	Train	0.613	0.848	0.666	0.520	0.563	0.738	0.467	0.967	0.678	0.681
	Validation	0.598	0.888	0.713	0.530	0.607	0.739	0.464	0.971	0.695	0.700
	Test	0.595	0.891	0.737	0.602	0.504	0.735	0.530	0.980	0.699	0.700
LCNN5×5 Annual Average all bands	Train	0.462	0.834	0.621	0.496	0.357	0.679	0.307	0.939	0.593	0.603
	Validation	0.486	0.862	0.649	0.488	0.390	0.723	0.274	0.943	0.611	0.625
	Test	0.470	0.883	0.696	0.610	0.290	0.650	0.474	0.979	0.633	0.632
LCNN9×9 Annual Average 10m bands	Train	0.757	0.787	0.670	0.581	0.494	0.670	0.606	0.973	0.694	0.695
	Validation	0.707	0.815	0.664	0.539	0.527	0.695	0.585	0.990	0.693	0.696
	Test	0.709	0.816	0.704	0.611	0.445	0.593	0.562	0.986	0.680	0.680
LCNN9×9 Annual Average 10and20m bands	Train	0.733	0.857	0.663	0.504	0.606	0.769	0.633	0.964	0.718	0.721
	Validation	0.773	0.896	0.686	0.464	0.597	0.757	0.676	0.970	0.729	0.735
	Test	0.679	0.878	0.706	0.565	0.654	0.810	0.544	0.982	0.731	0.736
LCNN9×9 Annual Average all bands	Train	0.577	0.831	0.627	0.536	0.359	0.729	0.394	0.965	0.632	0.649
	Validation	0.605	0.876	0.621	0.487	0.400	0.732	0.365	0.980	0.641	0.660
	Test	0.526	0.872	0.693	0.606	0.275	0.763	0.336	0.984	0.637	0.661
LCNN15×15 Annual Average 10m bands	Train	0.750	0.797	0.650	0.566	0.500	0.648	0.544	0.971	0.681	0.685
	Validation	0.751	0.827	0.652	0.529	0.488	0.644	0.496	0.976	0.675	0.685
	Test	0.731	0.821	0.693	0.620	0.469	0.574	0.461	0.979	0.672	0.677
LCNN15×15 Annual Average 10and20m	Train	0.700	0.852	0.666	0.561	0.592	0.739	0.609	0.968	0.713	0.716
	Validation	0.713	0.864	0.657	0.521	0.597	0.752	0.657	0.971	0.718	0.723
	Test	0.656	0.882	0.735	0.601	0.586	0.832	0.546	0.984	0.731	0.735
LCNN15×15 Annual Average all bands	Train	0.606	0.835	0.611	0.474	0.443	0.745	0.407	0.963	0.640	0.650
	Validation	0.629	0.873	0.647	0.441	0.446	0.724	0.459	0.980	0.655	0.667
	Test	0.589	0.886	0.689	0.547	0.416	0.723	0.382	0.983	0.657	0.666

Sentinel-2 Model Results [continued].

		Scaled	Woody Coniferous	Woody Broadleaved	Permanent Herbaceous	Periodically Herbaceous	Sparsely Vegetated	Non- vegetated	Water	Weighted F1	OA%
LCNN17×17 Annual Average 10m bands	Train	0.710	0.793	0.652	0.562	0.482	0.659	0.603	0.968	0.680	0.682
	Validation	0.726	0.809	0.655	0.541	0.466	0.702	0.594	0.975	0.686	0.692
	Test	0.724	0.824	0.706	0.611	0.400	0.565	0.612	0.982	0.677	0.679
LCNN17×17 Annual Average 10and20m bands	Train	0.672	0.840	0.656	0.566	0.559	0.757	0.568	0.972	0.702	0.704
	Validation	0.658	0.883	0.705	0.530	0.536	0.765	0.603	0.980	0.710	0.714
	Test	0.622	0.882	0.729	0.636	0.563	0.795	0.385	0.982	0.706	0.713
LCNN17×17 Annual Average all bands	Train	0.700	0.851	0.664	0.555	0.553	0.752	0.555	0.969	0.703	0.709
	Validation	0.727	0.875	0.691	0.514	0.575	0.739	0.583	0.966	0.712	0.721
	Test	0.624	0.871	0.710	0.607	0.537	0.763	0.405	0.979	0.693	0.704

Sentinel-2 Model Results [continued].

		Sealed	Woody Coniferous	Woody Broadleaved	Permanent Herbaceous	Periodically Herbaceous	Sparsely Vegetated	Non- vegetated	Water	Weighted F1	OA%
ANN Half-Year Average 10m bands	Train	0.676	0.802	0.665	0.559	0.576	0.707	0.547	0.976	0.690	0.693
	Validation	0.554	0.794	0.635	0.509	0.605	0.732	0.547	0.977	0.668	0.673
	Test	0.635	0.779	0.669	0.643	0.630	0.342	0.507	0.986	0.695	0.694
ANN Half-Year Average 10m and 20m bands	Train	0.697	0.844	0.722	0.559	0.603	0.766	0.630	0.985	0.726	0.729
	Validation	0.650	0.857	0.747	0.497	0.641	0.732	0.592	0.965	0.709	0.713
	Test	0.673	0.825	0.724	0.640	0.712	0.270	0.593	0.986	0.734	0.721
ANN Half-Year Average all bands	Train	0.787	0.861	0.745	0.601	0.617	0.818	0.795	0.992	0.776	0.777
	Validation	0.686	0.839	0.703	0.512	0.615	0.715	0.681	0.976	0.713	0.714
	Test	0.706	0.821	0.709	0.653	0.706	0.172	0.586	0.986	0.736	0.725
RF Half-Year Average 10m bands	Train	0.553	0.756	0.658	0.551	0.532	0.619	0.493	0.963	0.641	0.643
	Validation	0.480	0.787	0.641	0.524	0.434	0.628	0.492	0.959	0.616	0.622
	Test	0.569	0.710	0.651	0.594	0.552	0.174	0.464	0.980	0.647	0.636
RF Half-Year Average 10m and 20m bands	Train	0.644	0.818	0.705	0.570	0.563	0.714	0.482	0.964	0.683	0.688
	Validation	0.582	0.872	0.730	0.494	0.561	0.724	0.543	0.970	0.681	0.687
	Validation	0.606	0.857	0.726	0.506	0.540	0.727	0.548	0.976	0.684	0.690
RF Half-Year Average all bands	Train	0.656	0.825	0.705	0.589	0.585	0.723	0.525	0.961	0.695	0.699
	Validation	0.617	0.867	0.730	0.506	0.536	0.731	0.569	0.975	0.688	0.693
	Test	0.660	0.825	0.699	0.630	0.603	0.167	0.485	0.980	0.691	0.678
SVM Half-Year Average 10m bands	Train	0.563	0.764	0.655	0.522	0.502	0.623	0.455	0.960	0.631	0.635
	Validation	0.537	0.766	0.644	0.524	0.511	0.630	0.550	0.959	0.639	0.642
	Test	0.596	0.717	0.634	0.596	0.556	0.182	0.462	0.981	0.651	0.641
SVM Half-Year Average 10m and 20m bands	Train	0.672	0.821	0.708	0.553	0.637	0.771	0.519	0.914	0.700	0.704
	Validation	0.635	0.829	0.701	0.547	0.695	0.762	0.547	0.927	0.704	0.709
	Test	0.663	0.838	0.723	0.684	0.723	0.366	0.563	0.973	0.736	0.734
SVM Half-Year Average all bands	Train	0.678	0.825	0.705	0.559	0.651	0.780	0.547	0.914	0.707	0.711
	Validation	0.617	0.838	0.701	0.533	0.699	0.740	0.568	0.937	0.701	0.706
	Test	0.645	0.834	0.732	0.675	0.718	0.309	0.557	0.977	0.730	0.727

Sentinel-2 Model Results [continued].

		Sealed	Woody Coniferous	Woody Broadleaved	Permanent Herbaceous	Periodically Herbaceous	Sparsely Vegetated	Non- vegetated	Water	Weighted F1	OA%
3DLCNN3×3 Half-Year Average 10m bands	Train	0.453	0.804	0.656	0.520	0.449	0.500	0.393	0.941	0.593	0.599
	Validation	0.409	0.854	0.672	0.492	0.434	0.540	0.438	0.931	0.599	0.606
	Test	0.407	0.818	0.686	0.566	0.447	0.181	0.342	0.977	0.569	0.571
3DLCNN3×3 Half-Year Average 10m and 20m bands	Train	0.640	0.850	0.682	0.561	0.509	0.735	0.419	0.963	0.674	0.685
	Validation	0.611	0.874	0.699	0.537	0.507	0.738	0.437	0.975	0.677	0.689
	Test	0.648	0.885	0.725	0.665	0.627	0.711	0.504	0.982	0.721	0.726
3DLCNN3×3 Half-Year Average allm bands	Train	0.621	0.822	0.675	0.549	0.570	0.755	0.404	0.959	0.670	0.681
	Validation	0.628	0.846	0.732	0.557	0.606	0.760	0.487	0.961	0.697	0.706
	Test	0.642	0.853	0.692	0.668	0.653	0.323	0.426	0.981	0.700	0.701
3DLCNN5×5 Half-Year Average 10m bands	Train	0.628	0.825	0.672	0.528	0.555	0.643	0.453	0.955	0.661	0.664
	Validation	0.598	0.828	0.670	0.469	0.556	0.657	0.496	0.959	0.658	0.661
	Test	0.655	0.835	0.706	0.571	0.608	0.609	0.421	0.967	0.678	0.683
3DLFCNN5×5 Half-Year Average 10m and 20m bands	Train	0.698	0.861	0.690	0.566	0.613	0.764	0.552	0.968	0.717	0.719
	Validation	0.696	0.888	0.701	0.536	0.663	0.757	0.543	0.975	0.724	0.728
	Test	0.704	0.897	0.767	0.651	0.686	0.779	0.554	0.982	0.753	0.756
3DLCNN5×5 Half-Year Average all bands	Train	0.700	0.857	0.687	0.511	0.614	0.766	0.506	0.965	0.704	0.712
	Validation	0.698	0.878	0.700	0.548	0.648	0.739	0.496	0.970	0.715	0.723
	Test	0.707	0.889	0.748	0.595	0.681	0.755	0.562	0.983	0.741	0.747
3DLCNN9×9 Half-Year Average 10m bands	Train	0.760	0.842	0.670	0.570	0.591	0.741	0.625	0.972	0.723	0.725
	Validation	0.716	0.874	0.693	0.553	0.624	0.769	0.610	0.970	0.729	0.733
	Test	0.718	0.845	0.708	0.618	0.671	0.859	0.553	0.986	0.743	0.747
3DLCNN9×9 Half-Year Average 10m and 20m bands	Train	0.789	0.852	0.691	0.584	0.627	0.788	0.642	0.966	0.744	0.745
	Validation	0.779	0.879	0.754	0.578	0.659	0.749	0.605	0.974	0.751	0.753
	Test	0.760	0.885	0.757	0.676	0.735	0.707	0.569	0.980	0.764	0.765
3DLCNN9×9 Half-Year Average all bands	Train	0.714	0.864	0.674	0.553	0.600	0.779	0.618	0.971	0.722	0.727
	Validation	0.723	0.888	0.688	0.554	0.662	0.781	0.628	0.970	0.739	0.745
	Test	0.711	0.887	0.747	0.640	0.710	0.826	0.547	0.986	0.757	0.763
3DLCNN3×3 Half-Year Average 10m and 20m bands	Train	0.598	0.849	0.605	0.442	0.489	0.686	0.380	0.957	0.629	0.643
	Validation	0.590	0.883	0.631	0.403	0.476	0.704	0.360	0.975	0.633	0.651
	Test	0.626	0.871	0.642	0.384	0.540	0.527	0.275	0.984	0.614	0.631
3DLCNN15×15 Half-Year Average 10m and 20m bands	Train	0.688	0.854	0.631	0.536	0.538	0.765	0.594	0.967	0.697	0.700
	Validation	0.645	0.884	0.672	0.510	0.524	0.765	0.603	0.980	0.699	0.705
	Test	0.709	0.873	0.686	0.638	0.642	0.785	0.564	0.982	0.735	0.738
3DLCNN15×15 Half-Year Average allm bands	Train	0.509	0.841	0.631	0.529	0.434	0.635	0.421	0.963	0.623	0.631
	Validation	0.511	0.883	0.635	0.460	0.440	0.658	0.479	0.975	0.632	0.639
	Test	0.485	0.879	0.692	0.615	0.547	0.466	0.293	0.985	0.629	0.635

Sentinel-2 Model Results [continued].

		Sealed	Woody Coniferous	Woody Broadleaved	Permanent Herbaceous	Periodically Herbaceous	Sparsely Vegetated	Non- vegetated	Water	Weighted F1	OA%
ANN Season Average 10m bands	Train	0.759	0.834	0.720	0.615	0.656	0.751	0.699	0.990	0.755	0.754
	Validation	0.625	0.844	0.681	0.560	0.596	0.735	0.522	0.953	0.693	0.694
	Test	0.635	0.823	0.713	0.584	0.671	0.677	0.554	0.980	0.711	0.711
ANN Season Average 10m and 20m bands	Train	0.789	0.863	0.730	0.599	0.687	0.801	0.774	0.988	0.779	0.778
	Validation	0.663	0.899	0.714	0.587	0.637	0.767	0.618	0.963	0.732	0.734
	Test	0.690	0.872	0.752	0.613	0.697	0.804	0.659	0.985	0.761	0.762
ANN Season Average all bands	Train	0.702	0.843	0.711	0.557	0.671	0.738	0.585	0.983	0.726	0.729
	Validation	0.642	0.894	0.738	0.510	0.671	0.739	0.508	0.968	0.712	0.719
	Test	0.624	0.888	0.745	0.617	0.705	0.748	0.566	0.981	0.737	0.741
RF Season Average 10m bands	Train	0.618	0.759	0.667	0.554	0.588	0.671	0.436	0.962	0.662	0.666
	Validation	0.584	0.809	0.692	0.543	0.597	0.692	0.449	0.962	0.671	0.676
	Test	0.609	0.792	0.698	0.593	0.565	0.674	0.456	0.980	0.678	0.683
RF Season Average 10m and 20m bands	Train	0.677	0.825	0.714	0.583	0.610	0.736	0.476	0.961	0.702	0.707
	Validation	0.627	0.868	0.727	0.554	0.627	0.759	0.491	0.962	0.705	0.712
	Test	0.667	0.867	0.761	0.634	0.648	0.690	0.491	0.979	0.723	0.729
RF Season Average all bands	Train	0.679	0.830	0.704	0.582	0.627	0.736	0.508	0.963	0.706	0.711
	Validation	0.629	0.877	0.753	0.531	0.609	0.754	0.505	0.962	0.705	0.711
	Test	0.660	0.877	0.763	0.637	0.661	0.656	0.490	0.979	0.722	0.727
SVM Season Average 10m bands	Train	0.634	0.780	0.662	0.534	0.583	0.683	0.459	0.961	0.666	0.670
	Validation	0.595	0.786	0.670	0.497	0.625	0.705	0.509	0.963	0.674	0.677
	Test	0.642	0.769	0.664	0.606	0.619	0.729	0.460	0.980	0.691	0.696
SVM Season Average 10m and 20m bands	Train	0.706	0.822	0.693	0.557	0.611	0.773	0.561	0.964	0.714	0.717
	Validation	0.718	0.855	0.725	0.541	0.653	0.802	0.610	0.957	0.736	0.739
	Test	0.695	0.879	0.743	0.661	0.701	0.845	0.535	0.982	0.757	0.760
SVM Season Average all bands	Train	0.712	0.816	0.695	0.565	0.617	0.772	0.583	0.965	0.718	0.720
	Validation	0.710	0.844	0.720	0.532	0.635	0.794	0.559	0.962	0.723	0.728
	Test	0.694	0.881	0.736	0.666	0.684	0.834	0.568	0.984	0.757	0.760

Sentinel-2 Model Results [continued].

		Sealed	Woody Coniferous	Woody Broadleaved	Permanent Herbaceous	Periodically Herbaceous	Sparsely Vegetated	Non- vegetated	Water	Weighted F1	OA%
3DLCNN3×3 Season Average 10m bands	Train	0.665	0.794	0.679	0.514	0.581	0.642	0.492	0.954	0.669	0.671
	Validation	0.711	0.821	0.713	0.524	0.650	0.663	0.513	0.957	0.701	0.706
	Test	0.634	0.806	0.693	0.570	0.597	0.655	0.540	0.977	0.691	0.693
3DLCNN3×3 Season Average 10m and 20m bands	Train	0.685	0.812	0.665	0.540	0.602	0.743	0.362	0.954	0.676	0.686
	Validation	0.700	0.886	0.718	0.513	0.632	0.789	0.404	0.963	0.708	0.716
	Test	0.671	0.875	0.752	0.624	0.668	0.806	0.366	0.983	0.722	0.733
3DLCNN3×3 Season Average all bands	Train	0.689	0.823	0.656	0.549	0.599	0.764	0.469	0.968	0.694	0.700
	Validation	0.711	0.865	0.710	0.560	0.711	0.779	0.514	0.979	0.735	0.739
	Test	0.668	0.877	0.726	0.654	0.630	0.810	0.528	0.980	0.736	0.742
3DLCNN5×5 Season Average 10m bands	Train	0.679	0.804	0.661	0.534	0.526	0.674	0.469	0.962	0.668	0.671
	Validation	0.652	0.838	0.692	0.558	0.593	0.702	0.477	0.967	0.690	0.693
	Test	0.692	0.828	0.703	0.588	0.535	0.532	0.490	0.977	0.679	0.684
3DLCNN5×5 Season Average 10m and 20m bands	Train	0.726	0.834	0.694	0.535	0.633	0.762	0.532	0.968	0.714	0.718
	Validation	0.757	0.857	0.710	0.554	0.675	0.781	0.559	0.973	0.738	0.743
	Test	0.725	0.883	0.757	0.636	0.692	0.799	0.580	0.984	0.761	0.763
3DLCNN5×5 Season Average all bands	Train	0.610	0.818	0.630	0.515	0.576	0.758	0.277	0.960	0.649	0.666
	Validation	0.642	0.841	0.702	0.480	0.608	0.778	0.280	0.968	0.671	0.690
	Test	0.617	0.867	0.691	0.656	0.579	0.803	0.452	0.979	0.707	0.715
3DLCNN9×9 Season Average 10m bands	Train	0.752	0.816	0.666	0.536	0.650	0.736	0.607	0.972	0.720	0.724
	Validation	0.712	0.865	0.704	0.517	0.667	0.811	0.587	0.963	0.732	0.740
	Test	0.734	0.804	0.676	0.599	0.678	0.783	0.608	0.978	0.738	0.743
3DLCNN9×9 Season Average 10m and 20m bands	Train	0.790	0.848	0.685	0.585	0.625	0.785	0.674	0.978	0.748	0.751
	Validation	0.777	0.901	0.772	0.566	0.676	0.782	0.633	0.967	0.763	0.766
	Test	0.778	0.884	0.760	0.684	0.736	0.818	0.677	0.981	0.794	0.795
3DLCNN9×9 Season Average all bands	Train	0.695	0.845	0.661	0.497	0.650	0.776	0.593	0.964	0.712	0.717
	Validation	0.739	0.879	0.711	0.479	0.667	0.777	0.614	0.979	0.734	0.740
	Test	0.696	0.897	0.748	0.546	0.693	0.813	0.613	0.987	0.752	0.757
3DLCNN15×15 Season Average 10m bands	Train	0.749	0.815	0.642	0.496	0.611	0.715	0.599	0.969	0.702	0.708
	Validation	0.723	0.836	0.709	0.500	0.638	0.749	0.633	0.967	0.723	0.729
	Test	0.728	0.830	0.660	0.537	0.675	0.698	0.619	0.980	0.724	0.730
3DLCNN15×15 Season Average 10m and 20m bands	Train	0.763	0.847	0.652	0.579	0.614	0.785	0.681	0.973	0.738	0.738
	Validation	0.809	0.899	0.717	0.588	0.699	0.765	0.635	0.956	0.762	0.760
	Test	0.723	0.878	0.724	0.678	0.713	0.759	0.595	0.982	0.762	0.762
3DLCNN15×15 Season Average all bands	Train	0.716	0.834	0.647	0.561	0.627	0.791	0.620	0.977	0.724	0.726
	Validation	0.774	0.868	0.693	0.509	0.644	0.778	0.621	0.978	0.737	0.740
	Test	0.710	0.880	0.729	0.669	0.713	0.733	0.467	0.983	0.743	0.747

Sentinel-2 Model Results [continued].

		Sealed	Woody Coniferous	Woody Broadleaved	Permanent Herbaceous	Periodically Herbaceous	Sparsely Vegetated	Non- vegetated	Water	Weighted F1	OA%
ANN Six Monthly Average 10m bands	Train	0.746	0.749	0.481	0.597	0.709	0.784	0.441	0.907	0.681	0.697
	Validation	0.641	0.725	0.439	0.466	0.635	0.700	0.320	0.855	0.599	0.618
	Test	0.663	0.687	0.325	0.514	0.725	0.652	0.466	0.956	0.690	0.707
ANN Six Monthly Average 10m and 20m bands	Train	0.777	0.894	0.770	0.646	0.769	0.824	0.569	0.991	0.783	0.785
	Validation	0.671	0.870	0.741	0.531	0.640	0.758	0.432	0.955	0.702	0.709
	Test	0.706	0.815	0.703	0.554	0.748	0.634	0.308	0.987	0.746	0.756
ANN Six Monthly Average all bands	Train	0.841	0.811	0.727	0.604	0.733	0.769	0.780	0.994	0.781	0.780
	Validation	0.699	0.789	0.676	0.474	0.607	0.694	0.615	0.983	0.691	0.692
	Test	0.688	0.761	0.670	0.506	0.750	0.567	0.493	0.985	0.744	0.741
RF Six Monthly Average 10m bands	Train	0.649	0.792	0.661	0.592	0.663	0.712	0.353	0.951	0.676	0.684
	Validation	0.581	0.825	0.727	0.533	0.687	0.722	0.358	0.939	0.677	0.685
	Test	0.685	0.810	0.682	0.524	0.681	0.408	0.459	0.985	0.732	0.735
RF Six Monthly Average 10m and 20m bands	Train	0.705	0.853	0.714	0.620	0.692	0.760	0.389	0.962	0.717	0.726
	Validation	0.649	0.862	0.748	0.576	0.696	0.832	0.451	0.946	0.721	0.728
	Test	0.724	0.869	0.750	0.544	0.674	0.400	0.427	0.985	0.747	0.753
RF Six Monthly Average all bands	Train	0.706	0.851	0.718	0.618	0.679	0.760	0.383	0.958	0.713	0.722
	Validation	0.689	0.862	0.753	0.586	0.681	0.816	0.507	0.955	0.732	0.738
	Test	0.734	0.880	0.756	0.567	0.664	0.368	0.411	0.986	0.748	0.753
SVM Six Monthly Average 10m bands	Train	0.683	0.800	0.655	0.550	0.677	0.711	0.364	0.890	0.672	0.682
	Validation	0.638	0.774	0.685	0.518	0.662	0.750	0.239	0.868	0.648	0.666
	Test	0.721	0.774	0.654	0.511	0.724	0.130	0.519	0.976	0.727	0.735
SVM Six Monthly Average 10m and 20m bands	Train	0.713	0.842	0.690	0.577	0.685	0.812	0.548	0.963	0.728	0.731
	Validation	0.741	0.850	0.720	0.512	0.646	0.820	0.636	0.956	0.732	0.734
	Test	0.744	0.890	0.723	0.617	0.742	0.651	0.561	0.985	0.790	0.789
SVM Six Monthly Average all bands	Train	0.772	0.852	0.709	0.611	0.753	0.835	0.584	0.902	0.754	0.758
	Validation	0.794	0.833	0.747	0.554	0.727	0.808	0.605	0.875	0.745	0.750
	Test	0.715	0.866	0.761	0.570	0.749	0.632	0.604	0.972	0.783	0.785
LSTM Six Monthly Average 10m bands	Train	0.663	0.760	0.661	0.492	0.661	0.706	0.522	0.962	0.680	0.681
	Validation	0.609	0.785	0.713	0.485	0.662	0.655	0.449	0.948	0.669	0.672
	Test	0.667	0.753	0.692	0.442	0.593	0.229	0.551	0.987	0.706	0.707
LSTM Six Monthly Average 10m and 20m bands	Train	0.708	0.863	0.686	0.547	0.659	0.785	0.429	0.983	0.710	0.717
	Validation	0.638	0.848	0.747	0.500	0.638	0.793	0.348	0.965	0.687	0.699
	Test	0.707	0.839	0.756	0.576	0.640	0.661	0.416	0.987	0.752	0.758
LSTM Six Monthly Average all bands	Train	0.774	0.858	0.693	0.558	0.696	0.817	0.729	0.988	0.760	0.762
	Validation	0.696	0.875	0.720	0.482	0.630	0.792	0.667	0.982	0.727	0.731
	Test	0.735	0.833	0.709	0.600	0.698	0.708	0.541	0.985	0.775	0.775

Sentinel-2 Model Results [continued].

		Sealed	Woody Coniferous	Woody Broadleaved	Permanent Herbaceous	Periodically Herbaceous	Sparsely Vegetated	Non- vegetated	Water	Weighted F1	OA%
1DCNN6 Six Monthly Average 10m bands	Train	0.730	0.838	0.679	0.585	0.660	0.732	0.461	0.964	0.710	0.713
	Validation	0.667	0.810	0.671	0.560	0.623	0.772	0.598	0.947	0.703	0.705
	Test	0.718	0.823	0.700	0.535	0.713	0.638	0.554	0.990	0.767	0.766
1DCNN6 Six Monthly Average 10m and 20m bands	Train	0.851	0.869	0.746	0.635	0.755	0.864	0.820	0.993	0.814	0.811
	Validation	0.733	0.850	0.736	0.587	0.702	0.809	0.687	0.974	0.757	0.755
	Test	0.755	0.831	0.696	0.579	0.757	0.667	0.643	0.985	0.791	0.789
1DCNN6 Six Monthly Average all bands	Train	0.869	0.884	0.757	0.645	0.729	0.836	0.807	0.992	0.813	0.811
	Validation	0.748	0.894	0.727	0.578	0.617	0.762	0.682	0.974	0.745	0.746
	Test	0.714	0.874	0.734	0.561	0.740	0.661	0.540	0.985	0.778	0.777

B.3 Landsat-8 Results

Table B.3: Landsat-8 Model Results.

		Sealed	Coniferous Forest	Broadleaved Forest	Permanent Herbaceous	Periodically Herbaceous	Sparsely Vegetated	Non-vegetated	Water	Weighted F1	OA%
ANN Annual Average	Train	0.577	0.832	0.492	0.409	0.471	0.734	0.610	0.977	0.638	0.644
	Validation	0.532	0.844	0.503	0.388	0.450	0.730	0.577	0.990	0.628	0.635
	Test	0.566	0.853	0.656	0.426	0.489	0.737	0.481	0.978	0.652	0.652
RF Annual Average	Train	0.590	0.799	0.583	0.518	0.362	0.658	0.410	0.955	0.614	0.626
	Validation	0.564	0.815	0.604	0.510	0.322	0.633	0.466	0.970	0.614	0.628
	Test	0.565	0.794	0.586	0.521	0.384	0.451	0.444	0.977	0.595	0.603
SVM Annual Average	Train	0.569	0.801	0.570	0.509	0.374	0.687	0.448	0.959	0.619	0.626
	Validation	0.591	0.845	0.577	0.454	0.360	0.681	0.460	0.971	0.621	0.633
	Test	0.561	0.840	0.639	0.515	0.462	0.562	0.531	0.983	0.640	0.642
LCNN3×3 Annual Average	Train	0.499	0.784	0.534	0.459	0.283	0.673	0.439	0.951	0.581	0.590
	Validation	0.526	0.800	0.522	0.429	0.400	0.634	0.471	0.980	0.598	0.606
	Test	0.491	0.830	0.596	0.477	0.326	0.547	0.539	0.982	0.600	0.606
LCNN5×5 Annual Average	Train	0.545	0.808	0.548	0.449	0.366	0.689	0.497	0.955	0.610	0.618
	Validation	0.554	0.804	0.546	0.402	0.486	0.678	0.481	0.966	0.618	0.628
	Test	0.511	0.826	0.590	0.537	0.353	0.650	0.418	0.985	0.613	0.623
LCNN9×9 Annual Average	Train	0.727	0.836	0.646	0.479	0.558	0.748	0.665	0.974	0.705	0.707
	Validation	0.667	0.817	0.610	0.462	0.515	0.738	0.606	0.985	0.677	0.681
	Test	0.643	0.838	0.669	0.474	0.558	0.710	0.527	0.982	0.678	0.680
LCNN15×15 Annual Average	Train	0.518	0.769	0.456	0.380	0.280	0.702	0.608	0.963	0.583	0.597
	Validation	0.486	0.805	0.449	0.320	0.322	0.655	0.605	0.980	0.576	0.592
	Test	0.483	0.783	0.418	0.213	0.350	0.578	0.516	0.980	0.538	0.557

Landsat-8 Model Results [continued].

		Sealed	Coniferous Forest	Broadleaved Forest	Permanent Herbaceous	Periodically Herbaceous	Sparsely Vegetated	Non-vegetated	Water	Weighted F1	OA%
ANN Half-Year Average	Train	0.730	0.858	0.547	0.532	0.593	0.765	0.649	0.975	0.714	0.719
	Validation	0.676	0.812	0.495	0.490	0.525	0.714	0.571	0.988	0.665	0.676
	Test	0.674	0.812	0.597	0.605	0.688	0.180	0.330	0.973	0.680	0.680
RF Half-Year Average	Train	0.643	0.808	0.636	0.529	0.546	0.684	0.394	0.969	0.664	0.674
	Validation	0.705	0.771	0.627	0.492	0.576	0.720	0.460	0.971	0.674	0.687
	Test	0.669	0.793	0.692	0.569	0.593	0.030	0.288	0.986	0.667	0.658
SVM Half-Year Average	Train	0.619	0.802	0.615	0.520	0.577	0.765	0.401	0.874	0.657	0.668
	Validation	0.701	0.826	0.637	0.613	0.636	0.772	0.491	0.896	0.702	0.710
	Test	0.617	0.792	0.666	0.669	0.692	0.177	0.463	0.952	0.699	0.702
3DLFCNN3×3 Half-Year Average	Train	0.672	0.828	0.601	0.505	0.572	0.768	0.535	0.973	0.692	0.694
	Validation	0.699	0.841	0.630	0.507	0.589	0.777	0.558	0.988	0.706	0.710
	Test	0.676	0.831	0.694	0.636	0.703	0.224	0.435	0.983	0.717	0.718
3DLFCNN5×5 Half-Year Average	Train	0.591	0.800	0.584	0.405	0.555	0.711	0.547	0.965	0.656	0.659
	Validation	0.633	0.800	0.589	0.321	0.568	0.739	0.534	0.977	0.655	0.660
	Test	0.593	0.778	0.652	0.368	0.583	0.000	0.377	0.981	0.630	0.644
3DLFCNN9×9 Half-Year Average	Train	0.693	0.826	0.593	0.489	0.555	0.764	0.572	0.966	0.692	0.700
	Validation	0.759	0.820	0.596	0.517	0.619	0.740	0.604	0.988	0.712	0.720
	Test	0.695	0.841	0.675	0.626	0.694	0.177	0.525	0.986	0.726	0.715

B.4 Sentinel-1 Results With Shrub

Table B.4: Sentinel-1 Model Results including shrub class.

		Broadleaved Forest	Coniferous Forest	Periodically Herbaceous	Permanent Herbaceous	Non-vegetated	Sparsely Vegetated	Sealed	Water	Shrub	Weighted F1	OA%
ANN Annual Average	Train	0.389	0.582	0.238	0.406	0.393	0.435	0.415	0.813	0.260	0.437	0.446
	Validation	0.382	0.562	0.234	0.411	0.382	0.438	0.424	0.812	0.276	0.436	0.446
	Test	0.476	0.611	0.297	0.457	0.377	0.108	0.410	0.844	0.298	0.442	0.458
RF Annual Average	Train	0.408	0.598	0.296	0.422	0.503	0.456	0.424	0.819	0.292	0.469	0.473
	Validation	0.382	0.555	0.271	0.400	0.495	0.439	0.411	0.826	0.269	0.450	0.453
	Test	0.460	0.590	0.228	0.434	0.419	0.131	0.413	0.836	0.287	0.432	0.441
SVM Annual Average	Train	0.322	0.569	0.222	0.403	0.373	0.336	0.382	0.801	0.250	0.409	0.423
	Validation	0.330	0.565	0.240	0.414	0.359	0.325	0.387	0.805	0.264	0.413	0.427
	Test	0.345	0.561	0.196	0.446	0.249	0.119	0.380	0.797	0.263	0.381	0.407
ANN Half-Year Average	Train	0.523	0.735	0.380	0.372	0.567	0.491	0.448	0.855	0.266	0.516	0.515
	Validation	0.521	0.723	0.402	0.389	0.562	0.495	0.462	0.857	0.283	0.522	0.521
	Test	0.631	0.788	0.512	0.412	0.586	0.277	0.475	0.908	0.312	0.554	0.555
RF Half-Year Average	Train	0.544	0.740	0.431	0.426	0.589	0.490	0.460	0.862	0.318	0.542	0.542
	Validation	0.519	0.715	0.411	0.401	0.568	0.470	0.448	0.861	0.302	0.523	0.523
	Test	0.618	0.764	0.497	0.422	0.491	0.243	0.463	0.861	0.315	0.528	0.536
SVM Half-Year Average	Train	0.522	0.728	0.359	0.375	0.548	0.466	0.423	0.848	0.260	0.504	0.506
	Validation	0.523	0.711	0.374	0.386	0.561	0.464	0.431	0.861	0.273	0.511	0.511
	Test	0.619	0.769	0.494	0.441	0.584	0.247	0.449	0.910	0.313	0.546	0.550

Sentinel-1 Model Results including shrub class [continued].

		Broadleaved Forest	Coniferous Forest	Periodically Herbaceous	Permanent Herbaceous	Non-vegetated	Sparsely Vegetated	Sealed	Water	Shrub	Weighted F1	OA%
ANN Season Average	Train	0.544	0.762	0.457	0.386	0.639	0.502	0.472	0.890	0.279	0.549	0.551
	Validation	0.537	0.751	0.455	0.385	0.635	0.496	0.483	0.891	0.300	0.550	0.551
	Test	0.655	0.794	0.533	0.412	0.582	0.197	0.469	0.878	0.300	0.547	0.558
RF Season Average	Train	0.570	0.769	0.466	0.450	0.651	0.521	0.503	0.887	0.328	0.573	0.574
	Validation	0.540	0.747	0.435	0.416	0.629	0.485	0.472	0.887	0.296	0.547	0.547
	Test	0.663	0.787	0.533	0.454	0.613	0.217	0.473	0.911	0.328	0.564	0.571
SVM Season Average	Train	0.544	0.760	0.399	0.396	0.610	0.470	0.467	0.864	0.272	0.533	0.535
	Validation	0.537	0.748	0.423	0.404	0.619	0.452	0.480	0.876	0.286	0.539	0.539
	Test	0.656	0.788	0.532	0.450	0.609	0.229	0.457	0.901	0.351	0.563	0.568
ANN Monthly Average	Train	0.550	0.787	0.546	0.417	0.674	0.667	0.559	0.878	0.374	0.604	0.605
	Validation	0.533	0.744	0.499	0.369	0.631	0.634	0.527	0.864	0.352	0.570	0.571
	Test	0.622	0.796	0.557	0.383	0.548	0.344	0.511	0.884	0.279	0.553	0.562
RF Monthly Average	Train	0.612	0.826	0.647	0.520	0.698	0.600	0.598	0.935	0.400	0.650	0.652
	Validation	0.554	0.769	0.545	0.401	0.641	0.544	0.529	0.925	0.297	0.575	0.577
	Test	0.618	0.783	0.556	0.412	0.387	0.151	0.502	0.828	0.262	0.511	0.536
SVM Monthly Average	Train	0.537	0.796	0.515	0.379	0.638	0.533	0.517	0.917	0.271	0.566	0.569
	Validation	0.542	0.769	0.505	0.356	0.620	0.544	0.517	0.913	0.270	0.554	0.558
	Test	0.619	0.790	0.551	0.394	0.520	0.303	0.490	0.877	0.325	0.548	0.560
LSTM Monthly Average	Train	0.567	0.815	0.511	0.436	0.662	0.548	0.533	0.916	0.286	0.585	0.581
	Validation	0.541	0.775	0.513	0.452	0.641	0.542	0.524	0.907	0.292	0.572	0.568
	Test	0.607	0.805	0.582	0.454	0.472	0.243	0.503	0.850	0.263	0.540	0.552

B.5 Sentinel-2 Results With Shrub

Sentinel-2 Model Results including shrub class.

		Broadleaved Forest	Coniferous Forest	Periodically Herbaceous	Permanent Herbaceous	Non-vegetated	Sparsely Vegetated	Sealed	Water	Shrub	Weighted F1	OA%
ANN Annual Average 10m res bands	Train	0.501	0.664	0.299	0.422	0.690	0.506	0.478	0.928	0.328	0.536	0.536
	Validation	0.469	0.651	0.309	0.427	0.685	0.499	0.474	0.935	0.320	0.531	0.531
	Test	0.584	0.739	0.366	0.474	0.677	0.263	0.512	0.885	0.317	0.544	0.540
ANN Annual Average 10m and 20m res bands	Train	0.577	0.810	0.493	0.462	0.798	0.692	0.676	0.941	0.429	0.652	0.653
	Validation	0.552	0.795	0.479	0.460	0.766	0.681	0.650	0.926	0.440	0.637	0.638
	Test	0.665	0.848	0.616	0.488	0.712	0.564	0.625	0.859	0.435	0.648	0.645
ANN Annual Average All bands	Train	0.613	0.836	0.532	0.475	0.827	0.732	0.717	0.949	0.417	0.675	0.678
	Validation	0.561	0.803	0.496	0.460	0.779	0.712	0.684	0.936	0.403	0.646	0.648
	Test	0.671	0.858	0.590	0.501	0.716	0.571	0.634	0.921	0.379	0.651	0.654
RF Annual Average 10m bands	Train	0.520	0.684	0.409	0.443	0.706	0.565	0.528	0.932	0.353	0.571	0.573
	Validation	0.464	0.661	0.377	0.424	0.691	0.519	0.496	0.938	0.328	0.545	0.547
	Test	0.590	0.765	0.414	0.461	0.626	0.273	0.514	0.722	0.285	0.525	0.528
RF Annual Average 10m and 20m bands	Train	0.578	0.787	0.473	0.460	0.737	0.664	0.609	0.929	0.410	0.626	0.627
	Validation	0.540	0.765	0.438	0.430	0.728	0.635	0.586	0.931	0.386	0.603	0.605
	Test	0.675	0.863	0.484	0.499	0.636	0.550	0.567	0.851	0.411	0.617	0.615
RF Annual Average all bands	Train	0.603	0.809	0.544	0.519	0.769	0.695	0.652	0.935	0.452	0.663	0.663
	Validation	0.549	0.774	0.451	0.438	0.745	0.649	0.626	0.936	0.394	0.617	0.617
	Test	0.682	0.861	0.500	0.495	0.665	0.524	0.586	0.857	0.417	0.623	0.621
SVM Annual Average 10m bands	Train	0.459	0.648	0.301	0.392	0.660	0.541	0.505	0.915	0.313	0.525	0.532
	Validation	0.427	0.631	0.313	0.420	0.666	0.560	0.512	0.923	0.310	0.528	0.535
	Test	0.531	0.720	0.375	0.508	0.711	0.417	0.538	0.937	0.252	0.559	0.563
SVM Annual Average 10m and 20m bands	Train	0.560	0.773	0.401	0.410	0.710	0.648	0.623	0.915	0.377	0.600	0.604
	Validation	0.531	0.756	0.393	0.435	0.708	0.653	0.628	0.923	0.380	0.599	0.604
	Test	0.675	0.864	0.553	0.523	0.699	0.590	0.603	0.924	0.376	0.647	0.647
SVM Annual Average all bands	Train	0.563	0.774	0.418	0.414	0.731	0.651	0.636	0.915	0.381	0.608	0.612
	Validation	0.541	0.752	0.424	0.440	0.729	0.658	0.652	0.927	0.397	0.612	0.616
	Test	0.681	0.862	0.543	0.520	0.694	0.583	0.589	0.922	0.396	0.645	0.645

Sentinel-2 Model Results including shrub class [continued].

		Broadleaved Forest	Coniferous Forest	Periodically Herbaceous	Permanent Herbaceous	Non-vegetated	Sparsely Vegetated	Sealed	Water	Shrub	Weighted F1	OA%
ANN Half Year Average 10m bands	Train	0.591	0.799	0.468	0.466	0.785	0.612	0.638	0.952	0.408	0.636	0.632
	Validation	0.553	0.766	0.463	0.469	0.766	0.591	0.619	0.953	0.403	0.622	0.618
	Test	0.617	0.807	0.539	0.505	0.648	0.152	0.597	0.732	0.337	0.562	0.574
ANN Half Year Average 10mand20m bands	Train	0.575	0.815	0.574	0.404	0.814	0.724	0.712	0.942	0.429	0.663	0.672
	Validation	0.548	0.799	0.563	0.390	0.777	0.703	0.681	0.938	0.436	0.647	0.655
	Test	0.628	0.834	0.614	0.428	0.762	0.547	0.633	0.962	0.359	0.644	0.654
ANN Half Year Average all bands	Train	0.587	0.848	0.526	0.461	0.843	0.733	0.714	0.954	0.468	0.680	0.683
	Validation	0.551	0.816	0.527	0.472	0.800	0.707	0.701	0.946	0.466	0.664	0.667
	Test	0.670	0.867	0.620	0.536	0.626	0.530	0.639	0.621	0.414	0.617	0.618
RF Half Year Average 10m bands	Train	0.582	0.749	0.481	0.470	0.734	0.595	0.567	0.931	0.387	0.611	0.612
	Validation	0.537	0.726	0.430	0.439	0.725	0.561	0.550	0.933	0.355	0.585	0.586
	Test	0.609	0.802	0.546	0.442	0.649	0.449	0.532	0.788	0.328	0.576	0.577
RF Half Year Average 10and20m bands	Train	0.604	0.812	0.505	0.486	0.758	0.681	0.640	0.928	0.429	0.648	0.649
	Validation	0.563	0.785	0.478	0.452	0.738	0.640	0.623	0.931	0.415	0.625	0.626
	Test	0.663	0.870	0.583	0.482	0.680	0.567	0.608	0.841	0.410	0.636	0.633
RF Half Year Average all bands	Train	0.591	0.780	0.447	0.456	0.745	0.649	0.628	0.925	0.403	0.624	0.625
	Validation	0.546	0.755	0.427	0.429	0.729	0.635	0.612	0.927	0.385	0.604	0.605
	Test	0.685	0.848	0.516	0.470	0.703	0.300	0.597	0.882	0.381	0.608	0.610
SVM Half Year Average 10m bands	Train	0.551	0.738	0.409	0.402	0.697	0.573	0.555	0.917	0.326	0.574	0.579
	Validation	0.527	0.713	0.427	0.426	0.695	0.579	0.553	0.921	0.317	0.573	0.577
	Test	0.590	0.785	0.583	0.454	0.725	0.442	0.551	0.951	0.280	0.601	0.606
SVM Half Year Average 10and20m bands	Train	0.593	0.802	0.453	0.420	0.741	0.663	0.663	0.915	0.398	0.626	0.629
	Validation	0.574	0.780	0.479	0.452	0.732	0.664	0.663	0.921	0.416	0.630	0.632
	Test	0.698	0.876	0.624	0.517	0.714	0.603	0.637	0.928	0.393	0.668	0.668
SVM Half Year Average all bands	Train	0.590	0.805	0.458	0.427	0.755	0.664	0.673	0.916	0.401	0.631	0.634
	Validation	0.571	0.787	0.479	0.451	0.742	0.665	0.677	0.924	0.418	0.634	0.636
	Test	0.701	0.870	0.628	0.515	0.706	0.570	0.623	0.927	0.404	0.663	0.663

Sentinel-2 Model Results including shrub class [continued].

		Broadleaved Forest	Coniferous Forest	Periodically Herbaceous	Permanent Herbaceous	Non-vegetated	Sparsely Vegetated	Sealed	Water	Shrub	Weighted F1	OA%
ANN Season Average 10 and 20m bands	Train	0.653	0.867	0.604	0.504	0.844	0.731	0.747	0.943	0.458	0.703	0.703
	Validation	0.609	0.835	0.562	0.481	0.788	0.638	0.699	0.927	0.434	0.666	0.666
	Test	0.700	0.883	0.642	0.508	0.740	0.501	0.648	0.927	0.337	0.660	0.661
RF Season Average 10m bands	Train	0.566	0.755	0.425	0.462	0.710	0.506	0.532	0.906	0.337	0.579	0.579
	Validation	0.522	0.739	0.409	0.473	0.711	0.476	0.515	0.916	0.333	0.571	0.571
	Test	0.652	0.812	0.566	0.489	0.710	0.491	0.530	0.916	0.329	0.615	0.615
RF Season Average 10 and 20m bands	Train	0.673	0.854	0.632	0.580	0.812	0.713	0.701	0.932	0.497	0.709	0.707
	Validation	0.608	0.830	0.512	0.506	0.790	0.652	0.641	0.932	0.416	0.654	0.653
	Test	0.704	0.880	0.619	0.524	0.720	0.639	0.629	0.893	0.406	0.670	0.667
RF Season Average all bands	Train	0.647	0.844	0.561	0.536	0.801	0.676	0.682	0.923	0.447	0.678	0.677
	Validation	0.608	0.823	0.487	0.509	0.790	0.629	0.652	0.931	0.412	0.650	0.650
	Test	0.711	0.878	0.601	0.518	0.723	0.641	0.625	0.895	0.401	0.667	0.665
SVM Season Average 10 and 20m bands	Train	0.622	0.785	0.513	0.469	0.781	0.635	0.678	0.889	0.385	0.638	0.638
	Validation	0.573	0.765	0.505	0.481	0.792	0.619	0.693	0.902	0.392	0.642	0.640
	Test	0.688	0.837	0.672	0.581	0.761	0.000	0.652	0.909	0.392	0.681	0.683
SVM Season Average 10 and 20m bands no winter data	Train	0.618	0.836	0.497	0.471	0.756	0.652	0.677	0.897	0.377	0.640	0.641
	Validation	0.611	0.829	0.504	0.508	0.764	0.645	0.677	0.911	0.411	0.652	0.652
	Test	0.700	0.881	0.643	0.547	0.726	0.683	0.647	0.937	0.382	0.683	0.683

Sentinel-2 Model Results including shrub class [continued].

		Broadleaved Forest	Coniferous Forest	Periodically Herbaceous	Permanent Herbaceous	Non-vegetated	Sparsely Vegetated	Sealed	Water	Shrub	Weighted F1	OA%
LCNN3×3 Annual Average 10m bands	Train	0.517	0.729	0.277	0.424	0.692	0.515	0.559	0.927	0.325	0.553	0.552
	Validation	0.500	0.711	0.297	0.450	0.691	0.536	0.562	0.928	0.327	0.557	0.557
	Test	0.604	0.776	0.338	0.515	0.660	0.295	0.594	0.827	0.365	0.560	0.556
LCNN3×3 Annual Average 10m and 20m bands	Train	0.589	0.828	0.454	0.425	0.743	0.657	0.662	0.933	0.378	0.629	0.631
	Validation	0.585	0.820	0.468	0.458	0.744	0.654	0.672	0.937	0.409	0.638	0.640
	Test	0.691	0.862	0.583	0.502	0.577	0.576	0.616	0.742	0.356	0.611	0.611
LCNN5×5 Annual Average 10m bands	Train	0.469	0.743	0.304	0.378	0.691	0.489	0.530	0.904	0.341	0.541	0.543
	Validation	0.464	0.741	0.311	0.407	0.695	0.518	0.550	0.904	0.363	0.552	0.555
	Test	0.575	0.772	0.315	0.474	0.633	0.212	0.545	0.762	0.387	0.528	0.529
LCNN5×5 Annual Average 10m and 20m bands	Train	0.562	0.819	0.364	0.409	0.738	0.631	0.625	0.929	0.334	0.600	0.607
	Validation	0.544	0.811	0.364	0.442	0.739	0.636	0.632	0.934	0.335	0.603	0.609
	Test	0.672	0.863	0.447	0.501	0.656	0.598	0.564	0.805	0.353	0.605	0.607
LCNN9×9 Annual Average 10and20m	Train	0.614	0.857	0.504	0.479	0.803	0.678	0.738	0.937	0.435	0.672	0.674
	Validation	0.599	0.838	0.514	0.479	0.807	0.671	0.757	0.945	0.469	0.676	0.677
	Test	0.722	0.880	0.648	0.471	0.657	0.419	0.673	0.853	0.412	0.643	0.648
LCNN15×15 Annual Average 10m	Train	0.591	0.827	0.525	0.402	0.829	0.658	0.775	0.946	0.434	0.666	0.675
	Validation	0.545	0.798	0.502	0.397	0.819	0.646	0.762	0.949	0.414	0.649	0.658
	Test	0.629	0.818	0.549	0.419	0.813	0.499	0.708	0.960	0.420	0.651	0.660
LCNN15×15 Annual Average 10and20m	Train	0.634	0.857	0.449	0.508	0.830	0.705	0.783	0.943	0.431	0.682	0.686
	Validation	0.599	0.832	0.443	0.512	0.818	0.699	0.770	0.942	0.432	0.671	0.676
	Test	0.721	0.862	0.665	0.499	0.774	0.267	0.709	0.917	0.412	0.658	0.667

B.6 Landsat-8 Results With Shrub

Table B.5: Landsat-8 Model Results including shrub class.

		Broadleaved Forest	Coniferous Forest	Periodically Herbaceous	Permanent Herbaceous	Non-vegetated	Sparsely Vegetated	Sealed	Water	Shrub	Weighted F1	OA%
ANN Annual Average	Train	0.512	0.777	0.349	0.423	0.730	0.594	0.615	0.930	0.349	0.588	0.596
	Validation	0.517	0.768	0.377	0.453	0.726	0.575	0.614	0.931	0.349	0.593	0.600
	Test	0.630	0.772	0.473	0.500	0.670	0.148	0.554	0.906	0.317	0.595	0.600
RF Annual Average	Train	0.561	0.805	0.468	0.484	0.740	0.626	0.603	0.929	0.412	0.627	0.626
	Validation	0.508	0.785	0.394	0.450	0.714	0.576	0.549	0.928	0.334	0.584	0.584
	Test	0.650	0.825	0.455	0.479	0.654	0.058	0.520	0.890	0.327	0.588	0.591
SVM Annual Average	Train	0.508	0.783	0.328	0.399	0.706	0.571	0.564	0.918	0.320	0.568	0.571
	Validation	0.498	0.770	0.364	0.440	0.703	0.562	0.571	0.925	0.318	0.575	0.578
	Test	0.632	0.813	0.403	0.496	0.573	0.094	0.527	0.862	0.303	0.564	0.575
ANN Half Year Average	Train	0.594	0.833	0.529	0.467	0.789	0.722	0.679	0.966	0.412	0.662	0.660
	Validation	0.570	0.790	0.501	0.476	0.736	0.698	0.648	0.957	0.381	0.633	0.632
	Test	0.681	0.849	0.581	0.493	0.759	0.026	0.624	0.941	0.318	0.658	0.664
RF Half Year Average	Train	0.619	0.829	0.610	0.549	0.745	0.698	0.662	0.955	0.495	0.684	0.683
	Validation	0.572	0.783	0.495	0.462	0.687	0.657	0.602	0.957	0.369	0.615	0.615
	Test	0.676	0.844	0.564	0.523	0.690	0.073	0.588	0.906	0.350	0.642	0.640
SVM Half Year Average	Train	0.540	0.812	0.437	0.422	0.674	0.647	0.620	0.938	0.351	0.602	0.603
	Validation	0.552	0.786	0.456	0.477	0.679	0.637	0.622	0.953	0.360	0.608	0.609
	Test	0.660	0.856	0.565	0.540	0.606	0.140	0.611	0.869	0.336	0.626	0.633

Landsat-8 Model Results including shrub class [continued].

		Broadleaved Forest	Coniferous Forest	Periodically Herbaceous	Permanent Herbaceous	Non- vegetated	Sparsely Vegetated	Sealed	Water	Shrub	Weighted F1	OA%
LCNN3×3 Annual Average	Train	0.504	0.794	0.367	0.249	0.736	0.601	0.563	0.915	0.320	0.562	0.568
	Validation	0.508	0.785	0.368	0.287	0.742	0.602	0.562	0.926	0.329	0.569	0.573
	Test	0.660	0.816	0.372	0.399	0.572	0.113	0.491	0.861	0.293	0.546	0.552
LCNN5×5 Annual Average	Train	0.488	0.792	0.329	0.372	0.756	0.611	0.595	0.915	0.309	0.574	0.575
	Validation	0.491	0.779	0.337	0.421	0.773	0.606	0.605	0.925	0.324	0.586	0.586
	Test	0.660	0.800	0.415	0.456	0.641	0.138	0.532	0.829	0.276	0.565	0.562
LCNN9×9 Annual Average	Train	0.562	0.815	0.431	0.436	0.832	0.634	0.705	0.945	0.399	0.642	0.645
	Validation	0.532	0.799	0.409	0.451	0.813	0.605	0.685	0.941	0.378	0.627	0.629
	Test	0.649	0.810	0.483	0.416	0.741	0.046	0.637	0.913	0.309	0.611	0.617
LCNN15×15 Annual Average	Train	0.609	0.848	0.580	0.422	0.865	0.738	0.763	0.951	0.437	0.691	0.703
	Validation	0.539	0.812	0.524	0.360	0.834	0.674	0.736	0.941	0.379	0.646	0.660
	Test	0.641	0.821	0.608	0.376	0.764	0.153	0.670	0.915	0.330	0.635	0.653

Appendix C

Chapter 4 Results

Contents

C.1 Sensor Fusion Comparative Results	314
C.1.1 Pixel-Level fusion	315
C.1.2 Decision-Level Fusion	325
C.2 Variable Data Fusion Assessment Results	347

C.1 Sensor Fusion Comparative Results

The weighted F1 and OA of each model was calculated to assess the accuracy of both pixel-level fusion and decision-level fusion techniques. Additionally, the difference in Weighted F1 and OA relative to mono-sensor models trained in Chapter 3 was calculated. The results indicating the difference in F1 and OA will denote by Δ . For each pixel-level fused model, Δ F1 and OA was calculated relative to the best mono-sensor model prepared using the same temporal splits. For the decision-level fusion models, the Δ F1 and OA was calculated relative to the highest accuracy Sentinel-2 prior model used in the fusion.

C.1.1 Pixel-Level fusion

C.1.1.1 Fusion with Annually Averaged data

Table C.1: Results of Pixel-level Fusion using Annually Averaged data. Δ result calculated relative to LFCNN9 \times 9 using Annually Averaged Sentinel-2 data.

		Sealed	Woody Coniferous	Woody Broadleaved	Permanent Herbaceous	Periodically Herbaceous	Sparsely Vegetated	Non- vegetated	Water	Weighted F1	OA%
ANN S1, and S2 10m and 20m bands	Train	0.637	0.858	0.742	0.544	0.564	0.778	0.643	0.975	0.719	0.718
	Train Δ	-0.096	+0.001	+0.079	+0.040	-0.043	+0.009	+0.011	+0.011	+0.001	-0.003
	Validation	0.564	0.883	0.742	0.511	0.553	0.753	0.612	0.975	0.701	0.704
	Validation Δ	-0.209	-0.013	+0.056	+0.047	-0.044	-0.004	-0.063	+0.006	-0.028	-0.031
	Test	0.638	0.881	0.762	0.631	0.565	0.811	0.606	0.986	0.737	0.733
	Test Δ	-0.041	+0.003	+0.056	+0.066	-0.089	+0.001	+0.061	+0.004	+0.005	-0.003
ANN L8 and S2 10m and 20m bands	Train	0.784	0.875	0.721	0.605	0.617	0.833	0.745	0.991	0.772	0.776
	Train Δ	+0.050	+0.019	+0.058	+0.101	+0.011	+0.064	+0.111	+0.027	+0.054	+0.055
	Validation	0.720	0.878	0.692	0.529	0.613	0.755	0.585	0.970	0.722	0.727
	Validation Δ	-0.053	-0.018	+0.008	+0.062	+0.016	-0.002	-0.090	+0.001	-0.008	-0.008
	Test	0.661	0.881	0.739	0.598	0.627	0.752	0.505	0.987	0.723	0.725
	Test Δ	-0.017	+0.004	+0.034	+0.029	-0.026	-0.051	-0.039	+0.006	-0.007	-0.010
ANN S1 and L8	Train	0.658	0.831	0.680	0.572	0.465	0.715	0.602	0.982	0.690	0.694
	Train Δ	-0.076	-0.025	+0.017	+0.068	-0.141	-0.054	-0.032	+0.017	-0.028	-0.027
	Validation	0.606	0.859	0.708	0.539	0.430	0.690	0.556	0.970	0.673	0.678
	Validation Δ	-0.167	-0.037	+0.024	+0.073	-0.167	-0.067	-0.120	+0.001	-0.056	-0.057
	Test	0.596	0.859	0.707	0.521	0.509	0.575	0.506	0.983	0.659	0.657
	Test Δ	-0.082	-0.018	+0.003	-0.047	-0.144	-0.228	-0.039	+0.001	-0.070	-0.077
ANN S1, L8 and S2 10m and 20m bands	Train	0.770	0.861	0.721	0.498	0.638	0.816	0.738	0.989	0.754	0.758
	Train Δ	+0.036	+0.005	+0.058	-0.007	+0.032	+0.047	+0.104	+0.024	+0.036	+0.037
	Validation	0.693	0.861	0.681	0.494	0.622	0.759	0.577	0.971	0.711	0.718
	Validation Δ	-0.080	-0.035	-0.003	+0.027	+0.025	+0.002	-0.098	+0.001	-0.018	-0.017
	Test	0.697	0.874	0.742	0.556	0.625	0.750	0.572	0.988	0.728	0.730
	Test Δ	+0.019	-0.004	+0.038	-0.012	-0.028	-0.053	+0.028	+0.007	-0.002	-0.004

Results of Pixel-level Fusion using Annually Averaged data. Δ result calculated relative to LFCNN9 \times 9 using Annually Averaged Sentinel-2 data [Continued].

		Sealed	Woody Coniferous	Woody Broadleaved	Permanent Herbaceous	Periodically Herbaceous	Sparsely Vegetated	Non-vegetated	Water	Weighted F1	OA%
SVM S1, and S2 10m and 20m bands	Train	0.727	0.851	0.721	0.564	0.601	0.767	0.615	0.967	0.729	0.731
	Train Δ	-0.005	-0.006	+0.057	+0.059	-0.006	-0.003	-0.018	+0.003	+0.011	+0.010
	Validation	0.692	0.869	0.698	0.549	0.671	0.740	0.604	0.961	0.726	0.728
	Validation Δ	-0.081	-0.027	+0.012	+0.085	+0.073	-0.017	-0.071	-0.008	-0.003	-0.006
	Test	0.712	0.886	0.775	0.655	0.647	0.814	0.593	0.986	0.762	0.763
	Test Δ	+0.033	+0.008	+0.069	+0.090	-0.007	+0.004	+0.049	+0.005	+0.030	+0.028
SVM L8 and S2 10m and 20m bands	Train	0.671	0.836	0.690	0.552	0.608	0.764	0.480	0.917	0.695	0.700
	Train Δ	-0.062	-0.020	+0.027	+0.048	+0.002	-0.005	-0.154	-0.048	-0.024	-0.021
	Validation	0.650	0.852	0.683	0.521	0.671	0.758	0.497	0.940	0.701	0.708
	Validation Δ	-0.123	-0.044	-0.001	+0.054	+0.073	+0.000	-0.179	-0.030	-0.028	-0.027
	Test	0.603	0.879	0.756	0.636	0.611	0.778	0.565	0.974	0.727	0.729
	Test Δ	-0.075	+0.002	+0.052	+0.067	-0.042	-0.025	+0.021	-0.008	-0.002	-0.005
SVM S1 and L8	Train	0.672	0.828	0.675	0.564	0.423	0.699	0.534	0.963	0.673	0.678
	Train Δ	-0.062	-0.028	+0.012	+0.060	-0.183	-0.070	-0.100	-0.001	-0.046	-0.044
	Validation	0.633	0.859	0.700	0.545	0.444	0.658	0.559	0.966	0.674	0.678
	Validation Δ	-0.140	-0.037	+0.017	+0.078	-0.153	-0.100	-0.116	-0.004	-0.056	-0.057
	Test	0.671	0.858	0.715	0.554	0.572	0.621	0.573	0.987	0.696	0.694
	Test Δ	-0.007	-0.020	+0.010	-0.015	-0.081	-0.182	+0.028	+0.006	-0.034	-0.040
SVM S1, L8 and S2 10m and 20m bands	Train	0.740	0.854	0.715	0.571	0.596	0.766	0.619	0.966	0.731	0.733
	Train Δ	+0.006	-0.002	+0.052	+0.067	-0.011	-0.003	-0.015	+0.001	+0.012	+0.012
	Validation	0.702	0.863	0.689	0.573	0.632	0.738	0.604	0.961	0.724	0.726
	Validation Δ	-0.071	-0.033	+0.006	+0.106	+0.035	-0.020	-0.071	-0.008	-0.006	-0.009
	Test	0.709	0.894	0.780	0.651	0.638	0.788	0.608	0.985	0.759	0.760
	Test Δ	+0.031	+0.017	+0.075	+0.082	-0.015	-0.015	+0.063	+0.003	+0.029	+0.026

Results of Pixel-level Fusion using Annually Averaged data. Δ result calculated relative to LFCNN9 \times 9 using Annually Averaged Sentinel-2 data [Continued].

		Sealed	Woody Coniferous	Woody Broadleaved	Permanent Herbaceous	Periodically Herbaceous	Sparsely Vegetated	Non-vegetated	Water	Weighted F1	OA%
RF S1, and S2 10m and 20m bands	Train	0.659	0.844	0.723	0.589	0.519	0.722	0.556	0.961	0.700	0.702
	Train Δ	-0.073	-0.013	+0.060	+0.085	-0.088	-0.048	-0.077	-0.004	-0.018	-0.019
	Validation	0.609	0.884	0.729	0.548	0.506	0.739	0.594	0.980	0.701	0.706
	Validation Δ	-0.164	-0.012	+0.043	+0.084	-0.091	-0.018	-0.081	+0.011	-0.027	-0.028
	Test	0.663	0.876	0.754	0.626	0.497	0.689	0.513	0.980	0.702	0.706
	Test Δ	-0.015	-0.003	+0.048	+0.060	-0.157	-0.121	-0.031	-0.002	-0.029	-0.030
RF L8 and S2 10m and 20m bands	Train	0.626	0.846	0.697	0.574	0.501	0.710	0.431	0.962	0.674	0.681
	Train Δ	-0.107	-0.010	+0.034	+0.070	-0.106	-0.059	-0.203	-0.003	-0.045	-0.040
	Validation	0.591	0.869	0.706	0.515	0.463	0.716	0.504	0.975	0.672	0.680
	Validation Δ	-0.182	-0.027	+0.022	+0.048	-0.134	-0.042	-0.171	+0.005	-0.057	-0.055
	Test	0.573	0.883	0.745	0.621	0.425	0.663	0.444	0.980	0.670	0.676
	Test Δ	-0.105	+0.006	+0.040	+0.053	-0.228	-0.140	-0.100	-0.002	-0.060	-0.058
RF S1 and L8	Train	0.621	0.805	0.666	0.580	0.444	0.666	0.532	0.963	0.662	0.668
	Train Δ	-0.113	-0.051	+0.003	+0.075	-0.162	-0.103	-0.102	-0.002	-0.056	-0.053
	Validation	0.586	0.833	0.696	0.551	0.442	0.667	0.518	0.970	0.662	0.669
	Validation Δ	-0.187	-0.062	+0.013	+0.084	-0.156	-0.091	-0.158	+0.001	-0.067	-0.066
	Test	0.644	0.804	0.678	0.521	0.460	0.495	0.457	0.980	0.633	0.634
	Test Δ	-0.034	-0.074	-0.027	-0.047	-0.194	-0.309	-0.087	-0.002	-0.096	-0.100
RF S1, L8 and S2 10m and 20m bands	Train	0.669	0.849	0.723	0.590	0.519	0.721	0.551	0.962	0.701	0.704
	Train Δ	-0.064	-0.007	+0.060	+0.086	-0.088	-0.049	-0.083	-0.002	-0.017	-0.017
	Validation	0.640	0.883	0.729	0.538	0.491	0.728	0.588	0.975	0.700	0.705
	Validation Δ	-0.133	-0.013	+0.045	+0.071	-0.106	-0.029	-0.087	+0.005	-0.030	-0.030
	Test	0.648	0.880	0.760	0.635	0.487	0.676	0.517	0.981	0.701	0.704
	Test Δ	-0.030	+0.002	+0.055	+0.067	-0.166	-0.128	-0.027	-0.001	-0.029	-0.030

Results of Pixel-level Fusion using Annually Averaged data. Δ result calculated relative to LFCNN9 \times 9 using Annually Averaged Sentinel-2 data [Continued].

		Sealed	Woody Coniferous	Woody Broadleaved	Permanent Herbaceous	Periodically Herbaceous	Sparsely Vegetated	Non-vegetated	Water	Weighted F1	OA%
LFCNN9 \times 9 S1 and S2 10m and 20m bands	Train	0.708	0.796	0.703	0.595	0.502	0.772	0.619	0.964	0.706	0.709
	Train Δ	-0.025	-0.051	+0.041	+0.084	-0.082	+0.001	-0.019	+0.000	-0.005	-0.005
	Validation	0.663	0.846	0.726	0.594	0.529	0.740	0.622	0.974	0.707	0.711
	Validation Δ	-0.096	-0.063	+0.037	+0.118	-0.067	-0.015	-0.044	+0.013	-0.012	-0.016
	Test	0.683	0.809	0.709	0.646	0.551	0.818	0.587	0.982	0.726	0.728
	Test Δ	+0.004	-0.070	+0.003	+0.081	-0.103	+0.008	+0.043	+0.000	-0.005	-0.008
LFCNN9 \times 9 L8 and S2 10m and 20m bands	Train	0.703	0.846	0.710	0.581	0.539	0.783	0.520	0.979	0.707	0.716
	Train Δ	-0.029	-0.001	+0.048	+0.071	-0.045	+0.012	-0.118	+0.015	-0.004	+0.002
	Validation	0.707	0.891	0.758	0.538	0.594	0.747	0.419	0.975	0.699	0.715
	Validation Δ	-0.052	-0.019	+0.069	+0.062	-0.002	-0.009	-0.248	+0.014	-0.020	-0.012
	Test	0.668	0.869	0.732	0.622	0.661	0.805	0.423	0.982	0.727	0.734
	Test Δ	-0.011	-0.009	+0.026	+0.057	+0.008	-0.005	-0.122	+0.000	-0.004	-0.001
LFCNN9 \times 9 S1 and L8	Train	0.646	0.781	0.656	0.548	0.367	0.692	0.554	0.971	0.650	0.657
	Train Δ	-0.086	-0.066	-0.005	+0.037	-0.217	-0.079	-0.084	+0.007	-0.061	-0.057
	Validation	0.590	0.853	0.720	0.512	0.408	0.669	0.534	0.975	0.651	0.659
	Validation Δ	-0.169	-0.056	+0.031	+0.036	-0.187	-0.086	-0.132	+0.014	-0.068	-0.067
	Test	0.636	0.832	0.687	0.475	0.458	0.626	0.509	0.986	0.653	0.656
	Test Δ	-0.042	-0.047	-0.019	-0.090	-0.196	-0.184	-0.035	+0.004	-0.078	-0.080
LFCNN9 \times 9 S1, L8 and S2 10m and 20m bands	Train	0.661	0.815	0.713	0.539	0.515	0.767	0.608	0.968	0.696	0.699
	Train Δ	-0.071	-0.032	+0.051	+0.029	-0.069	-0.004	-0.030	+0.003	-0.015	-0.016
	Validation	0.601	0.881	0.755	0.516	0.565	0.742	0.576	0.969	0.693	0.700
	Validation Δ	-0.158	-0.028	+0.066	+0.040	-0.030	-0.014	-0.091	+0.007	-0.026	-0.026
	Test	0.670	0.852	0.740	0.599	0.582	0.803	0.606	0.986	0.732	0.733
	Test Δ	-0.008	-0.026	+0.034	+0.034	-0.072	-0.007	+0.062	+0.004	+0.001	-0.002

C.1.1.2 Fusion with Half-Yearly Averaged data

Table C.2: Results of Pixel-level Fusion using Half-Yearly Averaged data. Δ result calculated relative to 3DLCNN 9×9 using Half-Yearly averaged S2 data.

		Sealed	Woody Coniferous	Woody Broadleaved	Permanent Herbaceous	Periodically Herbaceous	Sparsely Vegetated	Non- vegetated	Water	Weighted F1	OA%
ANN S1 and S2 10m and 20m bands	Train	0.769	0.870	0.751	0.620	0.606	0.816	0.742	0.990	0.770	0.773
	Train Δ	-0.020	+0.018	+0.060	+0.035	-0.020	+0.028	+0.100	+0.025	+0.026	+0.028
	Validation	0.697	0.865	0.718	0.556	0.613	0.752	0.612	0.965	0.725	0.729
	Validation Δ	-0.082	-0.014	-0.036	-0.021	-0.045	+0.003	+0.007	-0.009	-0.026	-0.024
	Test	0.730	0.884	0.768	0.653	0.704	0.798	0.618	0.986	0.768	0.771
	Test Δ	-0.029	-0.002	+0.011	-0.023	-0.030	+0.091	+0.049	+0.007	+0.004	+0.006
ANN L8 and S2 10m and 20m bands	Train	0.691	0.887	0.705	0.555	0.636	0.792	0.679	0.988	0.742	0.745
	Train Δ	-0.099	+0.036	+0.014	-0.029	+0.010	+0.003	+0.036	+0.021	-0.002	+0.000
	Validation	0.578	0.870	0.661	0.515	0.601	0.736	0.558	0.975	0.689	0.696
	Validation Δ	-0.201	-0.010	-0.088	-0.058	-0.057	-0.013	-0.047	+0.001	-0.060	-0.056
	Test	0.635	0.881	0.729	0.579	0.686	0.668	0.602	0.950	0.718	0.717
	Test Δ	-0.125	-0.004	-0.028	-0.098	-0.048	-0.039	+0.032	-0.030	-0.046	-0.048
ANN S1, L8 and S2 10m and 20m bands	Train	0.709	0.845	0.705	0.630	0.592	0.826	0.749	0.986	0.754	0.754
	Train Δ	-0.080	-0.006	+0.014	+0.046	-0.035	+0.037	+0.106	+0.020	+0.010	+0.009
	Validation	0.621	0.853	0.671	0.566	0.573	0.756	0.638	0.970	0.707	0.710
	Validation Δ	-0.159	-0.026	-0.078	-0.007	-0.086	+0.007	+0.033	-0.004	-0.043	-0.042
	Test	0.700	0.855	0.719	0.609	0.639	0.478	0.577	0.987	0.707	0.709
	Test Δ	-0.059	-0.030	-0.038	-0.068	-0.096	-0.228	+0.007	+0.008	-0.057	-0.056
ANN S1 and L8	Train	0.727	0.843	0.648	0.569	0.590	0.783	0.682	0.978	0.727	0.729
	Train Δ	-0.062	-0.008	-0.043	-0.015	-0.037	-0.006	+0.038	+0.012	-0.017	-0.016
	Validation	0.701	0.856	0.634	0.500	0.540	0.781	0.599	0.960	0.698	0.707
	Validation Δ	-0.079	-0.023	-0.115	-0.073	-0.119	+0.032	-0.007	-0.014	-0.052	-0.045
	Test	0.692	0.871	0.706	0.543	0.697	0.296	0.514	0.986	0.682	0.692
	Test Δ	-0.067	-0.013	-0.051	-0.134	-0.037	-0.410	-0.056	+0.007	-0.082	-0.073

Results of Pixel-level Fusion using Half-Yearly Averaged data. Δ result calculated relative to 3DLCNN9 \times 9 using Half-Yearly averaged S2 data [Continued].

		Sealed	Woody Coniferous	Woody Broadleaved	Permanent Herbaceous	Periodically Herbaceous	Sparsely Vegetated	Non- vegetated	Water	Weighted F1	OA%
SVM S1 and S2 10m and 20m bands	Train	0.737	0.858	0.731	0.583	0.632	0.776	0.636	0.964	0.741	0.743
	Train Δ	-0.051	+0.005	+0.040	-0.001	+0.005	-0.011	-0.005	-0.001	-0.002	-0.002
	Validation	0.695	0.862	0.696	0.567	0.682	0.758	0.624	0.960	0.733	0.736
	Validation Δ	-0.085	-0.017	-0.058	-0.010	+0.023	+0.009	+0.019	-0.014	-0.018	-0.017
	Test	0.748	0.884	0.768	0.680	0.701	0.822	0.653	0.985	0.780	0.781
	Test Δ	-0.012	-0.001	+0.012	+0.004	-0.033	+0.115	+0.084	+0.006	+0.016	+0.016
SVM L8 and S2 10m and 20m bands	Train	0.638	0.840	0.706	0.571	0.617	0.773	0.515	0.927	0.701	0.705
	Train Δ	-0.151	-0.011	+0.016	-0.013	-0.009	-0.016	-0.129	-0.039	-0.043	-0.040
	Validation	0.667	0.871	0.683	0.564	0.619	0.761	0.550	0.947	0.711	0.716
	Validation Δ	-0.113	-0.008	-0.066	-0.009	-0.040	+0.012	-0.055	-0.027	-0.039	-0.036
	Test	0.611	0.875	0.753	0.645	0.695	0.669	0.550	0.978	0.726	0.728
	Test Δ	-0.148	-0.009	-0.004	-0.032	-0.039	-0.037	-0.020	-0.002	-0.038	-0.037
SVM S1, L8 and S2 10m and 20m bands	Train	0.731	0.858	0.737	0.594	0.615	0.779	0.650	0.964	0.742	0.744
	Train Δ	-0.058	+0.007	+0.047	+0.010	-0.012	-0.010	+0.006	-0.002	-0.002	-0.001
	Validation	0.722	0.871	0.683	0.594	0.644	0.773	0.635	0.960	0.737	0.740
	Validation Δ	-0.058	-0.008	-0.066	+0.021	-0.015	+0.024	+0.030	-0.014	-0.012	-0.012
	Test	0.737	0.890	0.776	0.658	0.693	0.666	0.627	0.987	0.759	0.760
	Test Δ	-0.022	+0.005	+0.019	-0.019	-0.041	-0.041	+0.058	+0.008	-0.005	-0.006
SVM S1 and L8	Train	0.662	0.838	0.678	0.582	0.518	0.721	0.565	0.963	0.692	0.695
	Train Δ	-0.127	-0.013	-0.013	-0.002	-0.108	-0.068	-0.079	-0.003	-0.051	-0.050
	Validation	0.601	0.862	0.711	0.547	0.521	0.723	0.568	0.960	0.688	0.692
	Validation Δ	-0.178	-0.017	-0.037	-0.026	-0.138	-0.026	-0.038	-0.014	-0.061	-0.060
	Test	0.702	0.867	0.718	0.597	0.568	0.282	0.595	0.986	0.682	0.685
	Test Δ	-0.057	-0.018	-0.039	-0.080	-0.166	-0.424	+0.026	+0.007	-0.082	-0.080

Results of Pixel-level Fusion using Half-Yearly Averaged data. Δ result calculated relative to 3DLCNN9 \times 9 using Half-Yearly averaged S2 data [Continued].

		Sealed	Woody Coniferous	Woody Broadleaved	Permanent Herbaceous	Periodically Herbaceous	Sparsely Vegetated	Non-vegetated	Water	Weighted F1	OA%
RF S1 and S2 10m and 20m bands	Train	0.676	0.847	0.734	0.592	0.582	0.708	0.577	0.967	0.712	0.714
	Train Δ	-0.113	-0.006	+0.043	+0.008	-0.045	-0.080	-0.065	+0.001	-0.031	-0.031
	Validation	0.613	0.872	0.744	0.549	0.533	0.733	0.590	0.975	0.703	0.708
	Validation Δ	-0.166	-0.008	-0.010	-0.028	-0.126	-0.016	-0.015	+0.001	-0.048	-0.045
	Test	0.704	0.876	0.764	0.660	0.621	0.659	0.509	0.984	0.727	0.730
	Test Δ	-0.056	-0.009	+0.007	-0.017	-0.114	-0.048	-0.060	+0.004	-0.037	-0.036
RF L8 and S2 10m and 20m bands	Train	0.652	0.845	0.707	0.581	0.579	0.724	0.451	0.960	0.691	0.698
	Train Δ	-0.138	-0.006	+0.017	-0.004	-0.048	-0.065	-0.193	-0.006	-0.053	-0.047
	Validation	0.618	0.883	0.716	0.486	0.547	0.725	0.500	0.965	0.683	0.691
	Validation Δ	-0.162	+0.004	-0.033	-0.087	-0.112	-0.024	-0.105	-0.009	-0.066	-0.061
	Test	0.643	0.871	0.732	0.626	0.586	0.625	0.438	0.980	0.693	0.699
	Test Δ	-0.116	-0.014	-0.025	-0.051	-0.148	-0.081	-0.131	+0.000	-0.071	-0.066
RF S1, L8 and S2 10m and 20m bands	Train	0.689	0.844	0.732	0.606	0.589	0.720	0.559	0.965	0.715	0.718
	Train Δ	-0.100	-0.007	+0.041	+0.022	-0.038	-0.069	-0.085	-0.001	-0.028	-0.027
	Validation	0.640	0.873	0.733	0.541	0.556	0.736	0.613	0.980	0.711	0.715
	Validation Δ	-0.140	-0.006	-0.015	-0.032	-0.103	-0.012	+0.008	+0.005	-0.039	-0.037
	Test	0.694	0.875	0.757	0.668	0.623	0.614	0.484	0.982	0.719	0.721
	Test Δ	-0.065	-0.010	+0.000	-0.010	-0.111	-0.093	-0.085	+0.002	-0.045	-0.044
RF S1 and L8	Train	0.644	0.820	0.683	0.590	0.524	0.649	0.497	0.965	0.674	0.678
	Train Δ	-0.145	-0.031	-0.008	+0.006	-0.103	-0.140	-0.146	-0.002	-0.069	-0.067
	Validation	0.621	0.832	0.688	0.551	0.500	0.689	0.496	0.970	0.672	0.678
	Validation Δ	-0.158	-0.047	-0.060	-0.022	-0.159	-0.060	-0.109	-0.004	-0.078	-0.074
	Test	0.696	0.818	0.690	0.571	0.518	0.155	0.358	0.983	0.623	0.627
	Test Δ	-0.063	-0.066	-0.067	-0.106	-0.216	-0.551	-0.212	+0.004	-0.141	-0.138

Results of Pixel-level Fusion using Half-Yearly Averaged data. Δ result calculated relative to 3DLCNN9 \times 9 using Half-Yearly averaged S2 data [Continued].

		Sealed	Woody Coniferous	Woody Broadleaved	Permanent Herbaceous	Periodically Herbaceous	Sparsely Vegetated	Non- vegetated	Water	Weighted F1	OA%
3DLFCNN9 \times 9 S1 and S2 10m and 20m bands	Train	0.757	0.853	0.718	0.595	0.543	0.780	0.640	0.968	0.728	0.734
	Train Δ	-0.030	+0.008	+0.025	+0.009	-0.055	-0.008	-0.013	+0.001	-0.008	-0.005
	Validation	0.762	0.875	0.744	0.578	0.605	0.766	0.657	0.962	0.738	0.744
	Validation Δ	-0.018	-0.006	-0.018	-0.015	-0.052	+0.020	+0.058	-0.006	-0.005	-0.003
	Test	0.773	0.887	0.769	0.664	0.688	0.769	0.630	0.985	0.773	0.775
	Test Δ	+0.013	+0.002	+0.013	-0.012	-0.047	+0.062	+0.061	+0.006	+0.009	+0.010
3DLFCNN9 \times 9 L8 and S2 10m and 20m bands	Train	0.709	0.854	0.685	0.591	0.569	0.760	0.590	0.967	0.712	0.716
	Train Δ	-0.078	+0.009	-0.008	+0.005	-0.029	-0.029	-0.063	+0.000	-0.025	-0.024
	Validation	0.731	0.889	0.710	0.541	0.619	0.729	0.628	0.981	0.722	0.725
	Validation Δ	-0.048	+0.008	-0.052	-0.052	-0.038	-0.017	+0.029	+0.014	-0.022	-0.021
	Test	0.686	0.897	0.728	0.650	0.710	0.730	0.599	0.984	0.750	0.752
	Test Δ	-0.073	+0.012	-0.029	-0.026	-0.025	+0.023	+0.030	+0.005	-0.014	-0.013
3DLFCNN9 \times 9 S1, L8 and S2 10m and 20m bands	Train	0.716	0.834	0.714	0.606	0.540	0.790	0.662	0.969	0.725	0.729
	Train Δ	-0.072	-0.011	+0.021	+0.020	-0.058	+0.001	+0.009	+0.002	-0.012	-0.010
	Validation	0.710	0.908	0.785	0.570	0.605	0.770	0.647	0.974	0.739	0.745
	Validation Δ	-0.069	+0.027	+0.023	-0.023	-0.052	+0.024	+0.048	+0.007	-0.004	-0.001
	Test	0.735	0.879	0.766	0.656	0.710	0.740	0.625	0.985	0.765	0.766
	Test Δ	-0.025	-0.006	+0.010	-0.020	-0.025	+0.033	+0.056	+0.006	+0.001	+0.001
3DLFCNN9 \times 9 S1 and L8	Train	0.669	0.815	0.686	0.577	0.451	0.741	0.577	0.971	0.682	0.690
	Train Δ	-0.118	-0.029	-0.007	-0.009	-0.147	-0.048	-0.076	+0.004	-0.055	-0.049
	Validation	0.656	0.868	0.687	0.586	0.492	0.737	0.582	0.974	0.691	0.700
	Validation Δ	-0.123	-0.012	-0.075	-0.007	-0.166	-0.010	-0.016	+0.007	-0.052	-0.047
	Test	0.697	0.843	0.719	0.570	0.633	0.324	0.592	0.987	0.687	0.686
	Test Δ	-0.063	-0.042	-0.038	-0.106	-0.102	-0.383	+0.024	+0.008	-0.077	-0.079

C.1.1.3 Fusion with Seasonally Averaged data

Table C.3: Results of Pixel-level Fusion using Seasonally Averaged data. Δ result calculated relative to 3DLCNN9 \times 9 using Seasonally averaged S2 data.

		Sealed	Woody Coniferous	Woody Broadleaved	Permanent Herbaceous	Periodically Herbaceous	Sparsely Vegetated	Non-vegetated	Water	Weighted F1	OA%
ANN S1 and S2 10m and 20m bands	Train	0.844	0.855	0.745	0.610	0.702	0.838	0.809	0.992	0.800	0.800
	Train Δ	+0.054	+0.007	+0.059	+0.025	+0.077	+0.053	+0.136	+0.014	+0.052	+0.049
	Validation	0.726	0.867	0.700	0.563	0.642	0.825	0.695	0.968	0.749	0.752
	Validation Δ	-0.051	-0.034	-0.072	-0.003	-0.034	+0.043	+0.062	+0.001	-0.013	-0.014
	Test	0.734	0.868	0.760	0.641	0.725	0.816	0.582	0.987	0.768	0.771
	Test Δ	-0.045	-0.015	+0.000	-0.043	-0.010	-0.003	-0.095	+0.007	-0.025	-0.024
SVM S1 and S2 10m and 20m bands	Train	0.771	0.847	0.720	0.593	0.660	0.790	0.687	0.971	0.756	0.758
	Train Δ	-0.020	-0.002	+0.035	+0.008	+0.035	+0.005	+0.014	-0.006	+0.008	+0.007
	Validation	0.747	0.878	0.707	0.565	0.667	0.811	0.688	0.963	0.755	0.757
	Validation Δ	-0.030	-0.023	-0.065	-0.002	-0.009	+0.029	+0.056	-0.005	-0.008	-0.009
	Test	0.759	0.872	0.754	0.681	0.726	0.855	0.643	0.986	0.787	0.788
	Test Δ	-0.020	-0.012	-0.006	-0.003	-0.010	+0.037	-0.035	+0.005	-0.006	-0.007
RF S1 and S2 10m and 20m bands	Train	0.729	0.834	0.726	0.603	0.632	0.742	0.593	0.974	0.732	0.733
	Train Δ	-0.062	-0.014	+0.040	+0.018	+0.007	-0.043	-0.080	-0.004	-0.016	-0.018
	Validation	0.692	0.872	0.744	0.546	0.605	0.774	0.610	0.968	0.728	0.732
	Validation Δ	-0.086	-0.029	-0.028	-0.021	-0.071	-0.008	-0.022	+0.000	-0.034	-0.033
	Test	0.724	0.878	0.771	0.641	0.672	0.655	0.526	0.983	0.740	0.741
	Test Δ	-0.054	-0.005	+0.011	-0.043	-0.063	-0.163	-0.152	+0.002	-0.054	-0.054
3DLCNN9 \times 9 S1 and S2 10m and 20m bands	Train	0.778	0.847	0.715	0.591	0.639	0.792	0.728	0.973	0.756	0.759
	Train Δ	-0.013	-0.005	+0.024	-0.002	+0.037	+0.007	+0.052	-0.001	+0.012	+0.011
	Validation	0.787	0.899	0.787	0.549	0.662	0.814	0.672	0.961	0.764	0.769
	Validation Δ	+0.012	-0.015	-0.001	-0.041	-0.016	+0.037	+0.047	+0.001	+0.003	+0.003
	Test	0.782	0.877	0.749	0.697	0.728	0.816	0.642	0.986	0.789	0.791
	Test Δ	+0.003	-0.007	-0.011	+0.013	-0.008	-0.002	-0.036	+0.005	-0.004	-0.004

C.1.1.4 Fusion with Monthly Averaged data

Table C.4: Results of Pixel-level Fusion using Monthly Averaged data. Δ result calculated relative to 1DCNN6 using Monthly averaged S2.

		Sealed	Woody Coniferous	Woody Broadleaved	Permanent Herbaceous	Periodically Herbaceous	Sparsely Vegetated	Non- vegetated	Water	Weighted F1	OA%
ANN S1 and S2 10m and 20m bands	Train	0.730	0.838	0.724	0.588	0.780	0.837	0.708	0.990	0.772	0.773
	Train Δ	-0.105	+0.003	+0.003	-0.042	-0.008	-0.027	-0.097	+0.000	-0.034	-0.029
	Validation	0.585	0.845	0.667	0.561	0.743	0.773	0.659	0.974	0.728	0.730
	Validation Δ	-0.072	+0.057	-0.019	-0.014	-0.033	-0.045	-0.057	-0.013	-0.026	-0.019
	Test	0.746	0.884	0.766	0.541	0.743	0.612	0.511	0.987	0.781	0.775
	Test Δ	-0.009	+0.054	+0.070	-0.038	-0.014	-0.054	-0.132	+0.002	-0.009	-0.013
SVM S1 and S2 10m and 20m bands	Train	0.793	0.835	0.713	0.621	0.778	0.850	0.724	0.964	0.783	0.783
	Train Δ	-0.042	-0.001	-0.007	-0.009	-0.010	-0.014	-0.080	-0.025	-0.023	-0.019
	Validation	0.709	0.817	0.673	0.576	0.800	0.800	0.744	0.974	0.766	0.764
	Validation Δ	+0.052	+0.029	-0.012	+0.001	+0.025	-0.018	+0.028	-0.013	+0.012	+0.016
	Test	0.759	0.846	0.717	0.611	0.748	0.621	0.603	0.987	0.790	0.788
	Test Δ	+0.004	+0.015	+0.021	+0.032	-0.008	-0.046	-0.040	+0.002	+0.000	+0.000
RF S1 and S2 10m and 20m bands	Train	0.764	0.836	0.725	0.671	0.796	0.792	0.616	0.975	0.772	0.774
	Train Δ	-0.071	+0.000	+0.004	+0.041	+0.008	-0.072	-0.189	-0.015	-0.033	-0.028
	Validation	0.684	0.818	0.727	0.607	0.782	0.838	0.677	0.974	0.766	0.767
	Validation Δ	+0.027	+0.030	+0.042	+0.032	+0.006	+0.020	-0.040	-0.013	+0.013	+0.019
	Test	0.779	0.863	0.764	0.600	0.683	0.317	0.372	0.985	0.754	0.753
	Test Δ	+0.024	+0.033	+0.068	+0.021	-0.074	-0.350	-0.271	+0.000	-0.036	-0.035
LSTM S1 and S2 10m and 20m bands	Train	0.741	0.807	0.655	0.179	0.669	0.523	0.584	0.977	0.642	0.669
	Train Δ	-0.094	-0.028	-0.065	-0.451	-0.119	-0.341	-0.221	-0.013	-0.163	-0.133
	Validation	0.575	0.784	0.540	0.216	0.740	0.531	0.538	0.974	0.630	0.645
	Validation Δ	-0.082	-0.004	-0.146	-0.359	-0.035	-0.288	-0.178	-0.013	-0.124	-0.104
	Test	0.765	0.840	0.700	0.000	0.568	0.230	0.478	0.980	0.679	0.708
	Test Δ	+0.010	+0.009	+0.004	-0.579	-0.188	-0.437	-0.165	-0.005	-0.111	-0.080
1DCNN6 S1 and S2 10m and 20m bands	Train	0.754	0.830	0.694	0.602	0.744	0.824	0.670	0.975	0.759	0.758
	Train Δ	-0.081	-0.005	-0.027	-0.028	-0.044	-0.040	-0.134	-0.015	-0.047	-0.044
	Validation	0.667	0.829	0.673	0.531	0.729	0.822	0.685	0.987	0.743	0.739
	Validation Δ	+0.010	+0.041	-0.013	-0.044	-0.046	+0.004	-0.031	+0.000	-0.011	-0.009
	Test	0.773	0.877	0.736	0.593	0.715	0.769	0.583	0.990	0.797	0.794
	Test Δ	+0.018	+0.046	+0.040	+0.014	-0.041	+0.103	-0.060	+0.005	+0.007	+0.007

C.1.2 Decision-Level Fusion

Table C.5: Prior Model List.

Platform	Model	Acronyms
Sentinel-2	Annually Averaged 10m and 20m bands 3DLFCNN9×9	S2AN
Sentinel-2	Half-Yearly Averaged 10m and 20m bands 3DLFCNN9×9	S2HY
Sentinel-2	Seasonally Averaged 10m and 20m bands 3DLFCNN9×9	S2SE
Sentinel-2	Six-Monthly Averaged 10m and 20m bands 3DLFCNN9×9	S2MO
Landsat-8	Annually Averaged All Bands LFCNN9×9	L8AN
Landsat-8	Half-Yearly Averaged All Bands 3DLFCNN9×9	L8HY
Sentinel-1	Monthly Averaged All Bands 1DCNN12	S1MO

C.1.2.1 Preliminary analysis of Decision-Level fusion techniques

Table C.6: Preliminary analysis of decision-level fusion methodologies using all prior models

		Sealed	Woody Coniferous	Woody Broadleaved	Permanent Herbaceous	Periodically Herbaceous	Sparsely Vegetated	Non- vegetated	Water	Weighted F1	OA%
Weighted Voting	Train	0.822	0.844	0.712	0.610	0.657	0.816	0.708	0.987	0.778	0.781
	Validation	0.783	0.861	0.733	0.612	0.678	0.830	0.719	0.987	0.782	0.783
	Test	0.790	0.846	0.751	0.694	0.769	0.157	0.624	0.988	0.788	0.786
Max Probability	Train	0.805	0.853	0.712	0.604	0.690	0.822	0.761	0.992	0.788	0.790
	Validation	0.735	0.905	0.752	0.655	0.667	0.813	0.705	0.987	0.782	0.786
	Test	0.760	0.818	0.741	0.678	0.780	0.233	0.574	0.987	0.774	0.772
Average Probability	Train	0.830	0.852	0.716	0.622	0.688	0.821	0.747	0.991	0.792	0.794
	Validation	0.776	0.875	0.733	0.650	0.679	0.822	0.717	0.987	0.786	0.788
	Test	0.784	0.844	0.761	0.705	0.789	0.244	0.646	0.988	0.797	0.795
ANN	Train	0.973	0.911	0.880	0.828	0.863	0.924	0.904	0.999	0.914	0.914
	Validation	0.739	0.881	0.689	0.603	0.711	0.832	0.702	0.994	0.776	0.777
	Test	0.788	0.827	0.722	0.651	0.741	0.203	0.613	0.984	0.772	0.773
RF	Train	0.835	0.858	0.713	0.585	0.740	0.832	0.765	0.990	0.798	0.800
	Validation	0.793	0.864	0.733	0.519	0.683	0.825	0.710	0.981	0.771	0.773
	Test	0.800	0.847	0.748	0.638	0.764	0.256	0.678	0.987	0.790	0.789
SVM	Train	0.860	0.868	0.746	0.640	0.769	0.862	0.841	0.995	0.830	0.830
	Validation	0.819	0.902	0.758	0.582	0.708	0.851	0.792	0.987	0.805	0.805
	Test	0.794	0.853	0.771	0.661	0.754	0.346	0.691	0.985	0.796	0.797

C.1.2.2 Sentinel-2 and Sentinel-1

Table C.7: Results of Decision-level Fusion Sentinel-2 and Sentinel-1 prior models using an SVM.

		Sealed	Woody Coniferous	Woody Broadleaved	Permanent Herbaceous	Periodically Herbaceous	Sparsely Vegetated	Non- vegetated	Water	Weighted F1	OA%
S2AN and S1MO	Train	0.809	0.866	0.727	0.626	0.721	0.811	0.775	0.990	0.791	0.790
	Train Δ	+0.076	+0.009	+0.064	+0.122	+0.114	+0.042	+0.142	+0.026	+0.073	+0.069
	Validation	0.771	0.883	0.721	0.549	0.629	0.794	0.680	0.975	0.752	0.754
	Validation Δ	-0.002	-0.013	+0.035	+0.085	+0.032	+0.037	+0.004	+0.005	+0.024	+0.019
	Test	0.709	0.897	0.778	0.599	0.690	0.754	0.545	0.954	0.745	0.742
	Test Δ	+0.031	+0.019	+0.072	+0.034	+0.037	-0.056	+0.001	-0.028	+0.013	+0.007
S2HY and S1MO	Train	0.839	0.864	0.743	0.641	0.756	0.841	0.830	0.991	0.814	0.814
	Train Δ	+0.051	+0.029	+0.046	+0.056	+0.135	+0.047	+0.176	+0.024	+0.070	+0.069
	Validation	0.760	0.855	0.728	0.544	0.640	0.807	0.690	0.970	0.749	0.750
	Validation Δ	-0.014	+0.000	-0.041	-0.052	-0.017	+0.048	+0.069	+0.000	-0.001	-0.002
	Test	0.793	0.840	0.722	0.646	0.735	0.482	0.649	0.981	0.770	0.771
	Test Δ	+0.018	-0.008	+0.005	-0.055	-0.021	+0.168	+0.049	+0.000	+0.001	+0.008
S2SE and S1MO	Train	0.838	0.871	0.735	0.643	0.736	0.828	0.827	0.992	0.809	0.810
	Train Δ	+0.048	+0.023	+0.050	+0.058	+0.112	+0.044	+0.153	+0.014	+0.061	+0.059
	Validation	0.783	0.901	0.731	0.526	0.663	0.819	0.682	0.973	0.762	0.764
	Validation Δ	+0.006	+0.001	-0.040	-0.041	-0.013	+0.037	+0.049	+0.005	-0.001	-0.001
	Test	0.770	0.882	0.773	0.617	0.730	0.786	0.657	0.957	0.776	0.775
	Test Δ	-0.008	-0.002	+0.013	-0.067	-0.006	-0.032	-0.020	-0.023	-0.018	-0.021
S2MO and S1MO	Train	0.858	0.853	0.747	0.643	0.799	0.880	0.860	0.989	0.826	0.823
	Train Δ	+0.023	+0.017	+0.026	+0.013	+0.012	+0.016	+0.055	-0.001	+0.020	+0.020
	Validation	0.622	0.806	0.679	0.543	0.729	0.836	0.675	0.975	0.737	0.731
	Validation Δ	-0.035	+0.018	-0.006	-0.032	-0.046	+0.018	-0.041	-0.013	-0.019	-0.019
	Test	0.756	0.863	0.735	0.591	0.766	0.723	0.631	0.980	0.800	0.796
	Test Δ	+0.001	+0.033	+0.039	+0.012	+0.010	+0.056	-0.012	-0.005	+0.009	+0.007

Results of Decision-level Fusion Sentinel-2 and Sentinel-1 prior models using an SVM [Continued].

		Sealed	Woody Coniferous	Woody Broadleaved	Permanent Herbaceous	Periodically Herbaceous	Sparsely Vegetated	Non- vegetated	Water	Weighted F1	OA%
S2HY,S2AN and S1MO	Train	0.833	0.852	0.742	0.624	0.731	0.834	0.822	0.990	0.804	0.804
	Train Δ	+0.045	+0.017	+0.045	+0.040	+0.110	+0.039	+0.168	+0.023	+0.061	+0.059
	Validation	0.768	0.860	0.736	0.542	0.657	0.776	0.681	0.970	0.749	0.749
	Validation Δ	-0.006	+0.005	-0.034	-0.054	+0.000	+0.017	+0.060	+0.000	-0.002	-0.003
	Test	0.790	0.844	0.721	0.667	0.756	0.495	0.663	0.960	0.775	0.773
	Test Δ	+0.014	-0.005	+0.004	-0.034	+0.000	+0.182	+0.063	-0.020	+0.005	+0.010
S2SE,S2AN and S1MO	Train	0.835	0.859	0.726	0.632	0.726	0.816	0.814	0.991	0.801	0.800
	Train Δ	+0.045	+0.010	+0.040	+0.047	+0.101	+0.031	+0.140	+0.013	+0.052	+0.049
	Validation	0.794	0.884	0.743	0.554	0.662	0.816	0.712	0.973	0.769	0.770
	Validation Δ	+0.016	-0.017	-0.029	-0.012	-0.014	+0.034	+0.080	+0.005	+0.007	+0.005
	Test	0.781	0.893	0.779	0.655	0.745	0.836	0.667	0.959	0.792	0.791
	Test Δ	+0.003	+0.009	+0.019	-0.029	+0.010	+0.018	-0.011	-0.021	-0.001	-0.004
S2MO,S2AN and S1MO	Train	0.869	0.856	0.756	0.685	0.839	0.888	0.871	0.994	0.844	0.844
	Train Δ	+0.034	+0.021	+0.035	+0.055	+0.052	+0.024	+0.067	+0.004	+0.037	+0.042
	Validation	0.740	0.841	0.692	0.517	0.766	0.806	0.732	0.975	0.765	0.763
	Validation Δ	+0.083	+0.053	+0.007	-0.058	-0.009	-0.012	+0.016	-0.013	+0.010	+0.013
	Test	0.802	0.872	0.751	0.600	0.743	0.778	0.698	0.987	0.819	0.818
	Test Δ	+0.047	+0.041	+0.055	+0.021	-0.014	+0.111	+0.055	+0.002	+0.028	+0.030
S2SE,S2HY and S1MO	Train	0.854	0.859	0.736	0.651	0.759	0.850	0.858	0.992	0.822	0.822
	Train Δ	+0.057	+0.025	+0.049	+0.069	+0.144	+0.061	+0.180	+0.015	+0.074	+0.072
	Validation	0.821	0.879	0.742	0.552	0.712	0.846	0.748	0.969	0.786	0.787
	Validation Δ	+0.040	+0.001	-0.041	-0.045	+0.040	+0.055	+0.117	+0.006	+0.022	+0.019
	Test	0.800	0.841	0.735	0.643	0.747	0.575	0.708	0.981	0.786	0.787
	Test Δ	+0.012	+0.001	+0.010	-0.052	-0.004	+0.187	+0.021	-0.002	+0.001	+0.006
S2MO, S2HY and S1MO	Train	0.869	0.847	0.744	0.672	0.815	0.894	0.872	0.993	0.837	0.835
	Train Δ	+0.030	+0.016	+0.020	+0.044	+0.041	+0.028	+0.070	+0.003	+0.032	+0.034
	Validation	0.722	0.849	0.705	0.448	0.717	0.853	0.747	0.971	0.757	0.753
	Validation Δ	+0.076	+0.055	+0.013	-0.123	-0.038	+0.040	+0.038	-0.014	+0.009	+0.010
	Test	0.811	0.841	0.701	0.588	0.782	0.677	0.698	0.988	0.817	0.816
	Test Δ	+0.059	+0.038	+0.031	+0.005	+0.022	+0.081	+0.052	+0.003	+0.029	+0.029
S2MO,S2SE and S1MO	Train	0.868	0.848	0.749	0.684	0.834	0.897	0.873	0.994	0.842	0.843
	Train Δ	+0.033	+0.014	+0.028	+0.054	+0.047	+0.033	+0.069	+0.004	+0.036	+0.040
	Validation	0.744	0.841	0.692	0.500	0.748	0.824	0.734	0.987	0.765	0.763
	Validation Δ	+0.086	+0.053	+0.007	-0.075	-0.028	+0.005	+0.018	+0.000	+0.010	+0.013
	Test	0.816	0.862	0.752	0.588	0.733	0.764	0.711	0.985	0.818	0.817
	Test Δ	+0.061	+0.031	+0.056	+0.009	-0.024	+0.097	+0.068	+0.000	+0.027	+0.029

Results of Decision-level Fusion Sentinel-2 and Sentinel-1 prior models using an SVM [Continued].

		Sealed	Woody Coniferous	Woody Broadleaved	Permanent Herbaceous	Periodically Herbaceous	Sparsely Vegetated	Non- vegetated	Water	Weighted F1	OA%
S2SE,S2HY,S2AN and S1MO	Train	0.852	0.858	0.745	0.649	0.729	0.845	0.845	0.990	0.816	0.816
	Train Δ	+0.056	+0.023	+0.058	+0.067	+0.114	+0.057	+0.168	+0.014	+0.069	+0.065
	Validation	0.805	0.857	0.741	0.579	0.657	0.844	0.746	0.969	0.777	0.776
	Validation Δ	+0.023	-0.020	-0.042	-0.018	-0.015	+0.053	+0.115	+0.006	+0.012	+0.009
	Test	0.807	0.837	0.718	0.686	0.761	0.558	0.680	0.945	0.782	0.781
	Test Δ	+0.019	-0.003	-0.006	-0.009	+0.009	+0.170	-0.008	-0.037	-0.003	+0.000
S2MO,S2HY,S2AN and S1MO	Train	0.865	0.850	0.754	0.677	0.818	0.899	0.867	0.993	0.839	0.838
	Train Δ	+0.025	+0.019	+0.031	+0.049	+0.043	+0.032	+0.066	+0.003	+0.034	+0.037
	Validation	0.732	0.866	0.699	0.500	0.747	0.836	0.727	0.971	0.764	0.759
	Validation Δ	+0.086	+0.072	+0.007	-0.071	-0.008	+0.023	+0.018	-0.014	+0.016	+0.017
	Test	0.799	0.841	0.708	0.594	0.782	0.677	0.698	0.987	0.816	0.815
	Test Δ	+0.046	+0.038	+0.038	+0.011	+0.022	+0.081	+0.052	+0.002	+0.027	+0.028
S2MO,S2SE,S2HY and S1MO	Train	0.860	0.845	0.747	0.678	0.815	0.896	0.868	0.993	0.836	0.835
	Train Δ	+0.021	+0.014	+0.023	+0.050	+0.041	+0.030	+0.067	+0.003	+0.031	+0.034
	Validation	0.732	0.836	0.667	0.475	0.731	0.836	0.727	0.971	0.751	0.746
	Validation Δ	+0.086	+0.042	-0.026	-0.097	-0.024	+0.023	+0.018	-0.014	+0.003	+0.003
	Test	0.810	0.841	0.705	0.576	0.774	0.698	0.718	0.985	0.817	0.816
	Test Δ	+0.057	+0.038	+0.035	-0.007	+0.014	+0.102	+0.072	+0.000	+0.029	+0.029
S2MO,S2SE,S2HY,S2AN and S1MO	Train	0.853	0.843	0.741	0.659	0.801	0.879	0.847	0.993	0.826	0.825
	Train Δ	+0.014	+0.012	+0.018	+0.031	+0.027	+0.013	+0.046	+0.003	+0.021	+0.024
	Validation	0.704	0.836	0.706	0.508	0.747	0.818	0.711	0.971	0.755	0.749
	Validation Δ	+0.058	+0.042	+0.014	-0.063	-0.008	+0.006	+0.002	-0.014	+0.007	+0.007
	Test	0.819	0.850	0.736	0.580	0.789	0.687	0.725	0.985	0.825	0.825
	Test Δ	+0.066	+0.047	+0.066	-0.003	+0.029	+0.090	+0.079	+0.000	+0.036	+0.038

C.1.2.3 Sentinel-2 and Landsat-8

Table C.8: Results of Decision-level Fusion Sentinel-2 and Landsat-8 prior models using an SVM.

		Sealed	Woody Coniferous	Woody Broadleaved	Permanent Herbaceous	Periodically Herbaceous	Sparsely Vegetated	Non-vegetated	Water	Weighted F1	OA%
S2AN and L8AN	Train	0.816	0.874	0.712	0.567	0.632	0.786	0.716	0.980	0.761	0.763
	Train Δ	+0.083	+0.018	+0.050	+0.062	+0.026	+0.016	+0.082	+0.016	+0.043	+0.043
	Validation	0.772	0.871	0.677	0.535	0.588	0.754	0.671	0.980	0.733	0.737
	Validation Δ	-0.001	-0.025	-0.007	+0.065	-0.010	-0.003	-0.004	+0.010	+0.003	+0.001
	Test	0.742	0.879	0.731	0.630	0.665	0.818	0.674	0.984	0.766	0.768
	Test Δ	+0.064	+0.001	+0.027	+0.062	+0.012	+0.014	+0.130	+0.002	+0.037	+0.035
S2HY and L8AN	Train	0.829	0.860	0.730	0.587	0.657	0.812	0.776	0.981	0.779	0.780
	Train Δ	+0.041	+0.026	+0.033	+0.002	+0.036	+0.017	+0.120	+0.013	+0.035	+0.035
	Validation	0.807	0.872	0.740	0.581	0.638	0.775	0.736	0.970	0.765	0.768
	Validation Δ	+0.028	+0.017	-0.028	-0.010	-0.019	+0.016	+0.115	+0.000	+0.014	+0.016
	Test	0.791	0.828	0.702	0.670	0.751	0.400	0.682	0.987	0.776	0.773
	Test Δ	+0.016	-0.020	-0.017	-0.032	-0.005	+0.086	+0.082	+0.007	+0.008	+0.010
S2SE and L8AN	Train	0.806	0.823	0.688	0.499	0.651	0.784	0.694	0.983	0.743	0.744
	Train Δ	+0.013	-0.024	+0.003	-0.088	+0.026	-0.002	+0.019	+0.006	-0.006	-0.007
	Validation	0.794	0.886	0.759	0.531	0.714	0.796	0.625	0.973	0.765	0.767
	Validation Δ	+0.013	-0.015	-0.012	-0.039	+0.038	+0.010	-0.007	+0.005	+0.000	+0.000
	Test	0.776	0.862	0.749	0.635	0.708	0.836	0.700	0.987	0.784	0.785
	Test Δ	-0.002	-0.021	-0.010	-0.049	-0.028	+0.019	+0.023	+0.007	-0.008	-0.009
S2MO and L8AN	Train	0.872	0.860	0.763	0.635	0.799	0.875	0.861	0.991	0.830	0.829
	Train Δ	+0.035	+0.026	+0.043	+0.003	+0.012	+0.012	+0.055	+0.001	+0.023	+0.026
	Validation	0.701	0.776	0.654	0.525	0.753	0.824	0.781	0.988	0.756	0.752
	Validation Δ	+0.044	-0.012	-0.026	-0.051	-0.023	+0.005	+0.064	+0.000	+0.001	+0.003
	Test	0.788	0.876	0.767	0.556	0.749	0.787	0.688	0.986	0.814	0.814
	Test Δ	+0.033	+0.046	+0.071	-0.023	-0.007	+0.121	+0.046	+0.002	+0.024	+0.027

Results of Decision-level Fusion Sentinel-2 and Landsat-8 prior models using an SVM [Continued].

		Sealed	Woody Coniferous	Woody Broadleaved	Permanent Herbaceous	Periodically Herbaceous	Sparsely Vegetated	Non- vegetated	Water	Weighted F1	OA%
S2AN and L8HY	Train	0.808	0.840	0.698	0.558	0.663	0.795	0.673	0.980	0.760	0.760
	Train Δ	+0.076	+0.001	+0.020	+0.054	+0.027	+0.014	+0.059	+0.007	+0.031	+0.030
	Validation	0.785	0.884	0.699	0.519	0.618	0.784	0.649	0.988	0.745	0.747
	Validation Δ	+0.007	-0.009	-0.017	+0.072	+0.001	+0.009	-0.040	+0.006	+0.004	+0.002
	Test	0.779	0.882	0.762	0.656	0.726	0.291	0.651	0.988	0.781	0.778
	Test Δ	+0.076	+0.015	+0.044	+0.057	+0.041	+0.019	+0.111	+0.002	+0.048	+0.046
S2HY and L8HY	Train	0.825	0.842	0.724	0.575	0.680	0.830	0.738	0.980	0.782	0.782
	Train Δ	+0.025	+0.011	+0.020	-0.004	+0.039	+0.009	+0.062	+0.008	+0.021	+0.021
	Validation	0.810	0.872	0.766	0.631	0.667	0.782	0.734	0.986	0.782	0.784
	Validation Δ	+0.041	+0.003	-0.011	+0.039	+0.032	+0.024	+0.127	+0.000	+0.032	+0.032
	Test	0.814	0.833	0.721	0.671	0.770	0.065	0.648	0.985	0.795	0.784
	Test Δ	+0.009	-0.010	-0.010	-0.035	-0.004	-0.034	+0.050	+0.002	+0.002	+0.002
S2SE and L8HY	Train	0.820	0.840	0.687	0.572	0.668	0.818	0.741	0.983	0.775	0.775
	Train Δ	+0.016	+0.004	+0.000	-0.015	+0.025	+0.013	+0.074	+0.000	+0.014	+0.012
	Validation	0.771	0.883	0.772	0.567	0.655	0.814	0.708	0.981	0.775	0.775
	Validation Δ	-0.014	-0.023	-0.019	-0.022	-0.017	+0.017	+0.057	+0.000	-0.003	-0.004
	Test	0.818	0.875	0.778	0.693	0.757	0.297	0.704	0.989	0.809	0.807
	Test Δ	+0.015	+0.012	+0.013	+0.022	+0.013	+0.075	+0.037	+0.002	+0.016	+0.019
S2MO and L8HY	Train	0.865	0.836	0.735	0.629	0.796	0.876	0.854	0.990	0.826	0.823
	Train Δ	+0.017	+0.014	+0.005	+0.003	+0.002	+0.005	+0.044	+0.000	+0.010	+0.012
	Validation	0.682	0.800	0.691	0.520	0.775	0.853	0.813	1.000	0.783	0.780
	Validation Δ	+0.015	-0.016	-0.040	-0.051	-0.045	+0.014	+0.000	+0.000	-0.017	-0.016
	Test	0.788	0.911	0.790	0.576	0.769	0.118	0.667	0.985	0.818	0.822
	Test Δ	+0.022	+0.069	+0.068	+0.006	+0.001	+0.000	+0.010	+0.000	+0.016	+0.018
S2AN and L8HY,L8AN	Train	0.834	0.869	0.723	0.577	0.681	0.810	0.711	0.984	0.781	0.782
	Train Δ	+0.102	+0.031	+0.045	+0.073	+0.045	+0.029	+0.097	+0.012	+0.052	+0.051
	Validation	0.803	0.866	0.695	0.523	0.641	0.773	0.673	0.988	0.750	0.753
	Validation Δ	+0.025	-0.028	-0.021	+0.077	+0.024	-0.002	-0.016	+0.006	+0.009	+0.007
	Test	0.769	0.850	0.745	0.669	0.741	0.282	0.669	0.989	0.780	0.775
	Test Δ	+0.066	-0.017	+0.027	+0.070	+0.056	+0.010	+0.130	+0.004	+0.047	+0.044
S2HY and L8HY,L8AN	Train	0.845	0.864	0.752	0.596	0.694	0.845	0.787	0.983	0.802	0.803
	Train Δ	+0.045	+0.033	+0.048	+0.018	+0.053	+0.024	+0.111	+0.011	+0.042	+0.042
	Validation	0.842	0.872	0.729	0.655	0.673	0.779	0.754	0.986	0.787	0.789
	Validation Δ	+0.073	+0.003	-0.048	+0.064	+0.039	+0.022	+0.147	+0.000	+0.037	+0.036
	Test	0.815	0.810	0.697	0.676	0.776	0.095	0.670	0.990	0.797	0.788
	Test Δ	+0.010	-0.033	-0.034	-0.030	+0.001	-0.004	+0.072	+0.007	+0.004	+0.006

Results of Decision-level Fusion Sentinel-2 and Landsat-8 prior models using an SVM [Continued].

		Sealed	Woody Coniferous	Woody Broadleaved	Permanent Herbaceous	Periodically Herbaceous	Sparsely Vegetated	Non- vegetated	Water	Weighted F1	OA%
S2SE and L8HY,L8AN	Train	0.834	0.850	0.711	0.591	0.679	0.826	0.768	0.984	0.788	0.788
	Train Δ	+0.030	+0.013	+0.023	+0.004	+0.036	+0.021	+0.101	+0.001	+0.027	+0.025
	Validation	0.797	0.861	0.738	0.557	0.678	0.837	0.723	0.987	0.780	0.779
	Validation Δ	+0.011	-0.046	-0.053	-0.031	+0.006	+0.040	+0.072	+0.006	+0.002	+0.000
	Test	0.812	0.865	0.773	0.687	0.758	0.286	0.713	0.989	0.807	0.805
	Test Δ	+0.010	+0.002	+0.008	+0.017	+0.014	+0.064	+0.046	+0.002	+0.014	+0.017
S2MO and L8HY,L8AN	Train	0.885	0.850	0.763	0.627	0.810	0.887	0.881	0.991	0.840	0.839
	Train Δ	+0.037	+0.028	+0.034	+0.001	+0.017	+0.016	+0.070	+0.002	+0.024	+0.028
	Validation	0.727	0.800	0.682	0.488	0.747	0.857	0.844	1.000	0.783	0.784
	Validation Δ	+0.061	-0.016	-0.049	-0.084	-0.073	+0.018	+0.031	+0.000	-0.017	-0.012
	Test	0.814	0.875	0.750	0.534	0.761	0.105	0.696	0.985	0.815	0.819
	Test Δ	+0.048	+0.033	+0.028	-0.035	-0.007	-0.012	+0.040	+0.000	+0.013	+0.016
S2HY,S2AN and L8AN	Train	0.826	0.850	0.724	0.592	0.641	0.807	0.756	0.980	0.772	0.773
	Train Δ	+0.038	+0.016	+0.026	+0.007	+0.020	+0.011	+0.100	+0.012	+0.029	+0.028
	Validation	0.802	0.872	0.740	0.585	0.662	0.781	0.709	0.970	0.765	0.766
	Validation Δ	+0.024	+0.017	-0.028	-0.006	+0.005	+0.022	+0.089	+0.000	+0.015	+0.014
	Test	0.793	0.848	0.730	0.691	0.763	0.439	0.701	0.986	0.789	0.786
	Test Δ	+0.017	-0.001	+0.012	-0.011	+0.006	+0.125	+0.101	+0.006	+0.020	+0.023
S2SE,S2AN and L8AN	Train	0.836	0.873	0.723	0.595	0.691	0.812	0.774	0.984	0.786	0.788
	Train Δ	+0.043	+0.026	+0.039	+0.007	+0.066	+0.025	+0.099	+0.006	+0.038	+0.037
	Validation	0.810	0.874	0.737	0.541	0.693	0.798	0.672	0.973	0.766	0.769
	Validation Δ	+0.029	-0.027	-0.034	-0.029	+0.017	+0.012	+0.040	+0.005	+0.002	+0.002
	Test	0.798	0.883	0.756	0.672	0.725	0.861	0.724	0.987	0.803	0.804
	Test Δ	+0.020	+0.000	-0.003	-0.012	-0.010	+0.045	+0.047	+0.007	+0.010	+0.010
S2MO,S2AN and L8AN	Train	0.857	0.826	0.735	0.642	0.796	0.849	0.837	0.990	0.815	0.812
	Train Δ	+0.020	-0.008	+0.014	+0.010	+0.009	-0.015	+0.031	+0.000	+0.008	+0.009
	Validation	0.732	0.788	0.673	0.587	0.796	0.794	0.744	0.975	0.767	0.759
	Validation Δ	+0.075	+0.000	-0.006	+0.011	+0.020	-0.024	+0.028	-0.013	+0.012	+0.009
	Test	0.813	0.818	0.746	0.605	0.768	0.787	0.701	0.986	0.818	0.818
	Test Δ	+0.058	-0.013	+0.050	+0.027	+0.012	+0.120	+0.058	+0.002	+0.029	+0.031
S2SE,S2HY and L8AN	Train	0.840	0.855	0.725	0.592	0.683	0.818	0.804	0.983	0.789	0.790
	Train Δ	+0.041	+0.023	+0.037	+0.008	+0.068	+0.029	+0.124	+0.007	+0.041	+0.039
	Validation	0.809	0.852	0.739	0.618	0.718	0.840	0.733	0.969	0.788	0.789
	Validation Δ	+0.023	-0.026	-0.044	+0.016	+0.045	+0.044	+0.103	+0.006	+0.021	+0.019
	Test	0.801	0.837	0.717	0.666	0.757	0.456	0.712	0.987	0.788	0.787
	Test Δ	+0.013	-0.003	-0.007	-0.029	+0.006	+0.068	+0.024	+0.005	+0.003	+0.007

Results of Decision-level Fusion Sentinel-2 and Landsat-8 prior models using an SVM [Continued].

		Sealed	Woody Coniferous	Woody Broadleaved	Permanent Herbaceous	Periodically Herbaceous	Sparsely Vegetated	Non- vegetated	Water	Weighted F1	OA%
S2MO,S2HY and L8AN	Train	0.876	0.850	0.762	0.642	0.790	0.882	0.860	0.990	0.829	0.828
	Train Δ	+0.034	+0.019	+0.039	+0.013	+0.016	+0.016	+0.058	+0.000	+0.024	+0.026
	Validation	0.747	0.781	0.687	0.516	0.733	0.836	0.790	0.986	0.763	0.758
	Validation Δ	+0.101	-0.012	+0.001	-0.055	-0.022	+0.023	+0.081	+0.000	+0.016	+0.017
	Test	0.795	0.837	0.735	0.602	0.771	0.735	0.692	0.986	0.817	0.816
	Test Δ	+0.043	+0.034	+0.066	+0.020	+0.011	+0.139	+0.047	+0.002	+0.030	+0.031
S2MO,S2SE and L8AN	Train	0.872	0.857	0.768	0.646	0.804	0.881	0.867	0.991	0.833	0.833
	Train Δ	+0.035	+0.022	+0.047	+0.014	+0.017	+0.017	+0.061	+0.001	+0.026	+0.030
	Validation	0.692	0.794	0.667	0.585	0.772	0.824	0.775	0.987	0.766	0.762
	Validation Δ	+0.035	+0.006	-0.013	+0.009	-0.003	+0.005	+0.059	+0.000	+0.011	+0.013
	Test	0.806	0.872	0.753	0.599	0.753	0.774	0.704	0.985	0.820	0.819
	Test Δ	+0.051	+0.041	+0.057	+0.020	-0.003	+0.108	+0.061	+0.000	+0.030	+0.032
S2HY,S2AN and L8HY	Train	0.824	0.853	0.733	0.576	0.678	0.836	0.751	0.981	0.786	0.787
	Train Δ	+0.023	+0.022	+0.028	-0.002	+0.038	+0.015	+0.075	+0.009	+0.026	+0.026
	Validation	0.800	0.861	0.756	0.606	0.685	0.771	0.748	0.986	0.779	0.780
	Validation Δ	+0.031	-0.008	-0.021	+0.014	+0.051	+0.014	+0.141	+0.000	+0.028	+0.028
	Test	0.828	0.841	0.726	0.679	0.781	0.067	0.655	0.988	0.802	0.793
	Test Δ	+0.023	-0.002	-0.005	-0.027	+0.007	-0.032	+0.057	+0.005	+0.010	+0.011
S2SE,S2AN and L8HY	Train	0.834	0.854	0.716	0.586	0.713	0.828	0.773	0.984	0.794	0.794
	Train Δ	+0.030	+0.018	+0.029	-0.001	+0.070	+0.023	+0.106	+0.001	+0.033	+0.031
	Validation	0.832	0.850	0.714	0.564	0.711	0.814	0.729	0.987	0.783	0.783
	Validation Δ	+0.047	-0.057	-0.076	-0.025	+0.038	+0.017	+0.078	+0.006	+0.005	+0.004
	Test	0.803	0.868	0.771	0.672	0.763	0.306	0.696	0.985	0.802	0.801
	Test Δ	+0.000	+0.005	+0.007	+0.002	+0.020	+0.083	+0.029	-0.001	+0.009	+0.013
S2MO,S2AN and L8HY	Train	0.869	0.834	0.736	0.631	0.808	0.887	0.868	0.991	0.831	0.830
	Train Δ	+0.021	+0.012	+0.006	+0.005	+0.015	+0.016	+0.058	+0.002	+0.016	+0.019
	Validation	0.744	0.800	0.691	0.520	0.775	0.839	0.844	1.000	0.791	0.787
	Validation Δ	+0.078	-0.016	-0.040	-0.051	-0.045	+0.000	+0.031	+0.000	-0.009	-0.008
	Test	0.791	0.912	0.778	0.546	0.764	0.095	0.663	0.985	0.814	0.817
	Test Δ	+0.025	+0.070	+0.056	-0.024	-0.005	-0.022	+0.007	+0.000	+0.012	+0.013
S2SE,S2HY and L8HY	Train	0.832	0.853	0.720	0.575	0.704	0.833	0.770	0.984	0.793	0.793
	Train Δ	+0.026	+0.020	+0.029	-0.009	+0.078	+0.025	+0.106	+0.002	+0.034	+0.032
	Validation	0.804	0.841	0.733	0.600	0.699	0.818	0.756	0.985	0.785	0.786
	Validation Δ	+0.004	-0.052	-0.057	+0.000	+0.032	+0.038	+0.113	+0.007	+0.012	+0.012
	Test	0.827	0.847	0.725	0.651	0.782	0.032	0.668	0.985	0.802	0.797
	Test Δ	+0.011	+0.011	-0.003	-0.023	+0.026	+0.032	-0.003	-0.001	+0.004	+0.007

Results of Decision-level Fusion Sentinel-2 and Landsat-8 prior models using an SVM [Continued].

		Sealed	Woody Coniferous	Woody Broadleaved	Permanent Herbaceous	Periodically Herbaceous	Sparsely Vegetated	Non- vegetated	Water	Weighted F1	OA%
S2MO,S2HY and L8HY	Train	0.879	0.829	0.739	0.619	0.797	0.892	0.872	0.991	0.831	0.830
	Train Δ	+0.025	+0.012	+0.006	-0.004	+0.019	+0.019	+0.064	+0.002	+0.017	+0.020
	Validation	0.744	0.792	0.707	0.524	0.778	0.820	0.839	1.000	0.788	0.787
	Validation Δ	+0.078	-0.017	-0.024	-0.042	-0.022	-0.014	+0.032	+0.000	-0.003	+0.000
	Test	0.804	0.889	0.750	0.567	0.781	0.174	0.644	0.985	0.818	0.819
	Test Δ	+0.041	+0.067	+0.044	-0.017	+0.011	+0.174	-0.009	+0.000	+0.017	+0.015
S2MO,S2SE and L8HY	Train	0.878	0.842	0.745	0.644	0.810	0.888	0.876	0.991	0.837	0.837
	Train Δ	+0.030	+0.020	+0.015	+0.019	+0.017	+0.018	+0.065	+0.002	+0.022	+0.025
	Validation	0.756	0.800	0.707	0.512	0.762	0.839	0.844	1.000	0.792	0.791
	Validation Δ	+0.089	-0.016	-0.024	-0.060	-0.059	+0.000	+0.031	+0.000	-0.008	-0.004
	Test	0.807	0.912	0.783	0.578	0.764	0.100	0.685	0.985	0.822	0.825
	Test Δ	+0.041	+0.070	+0.061	+0.008	-0.005	-0.018	+0.029	+0.000	+0.020	+0.021
S2HY,S2AN and L8HY,L8AN	Train	0.834	0.855	0.743	0.590	0.671	0.842	0.767	0.981	0.792	0.792
	Train Δ	+0.034	+0.024	+0.038	+0.011	+0.031	+0.020	+0.091	+0.009	+0.031	+0.031
	Validation	0.804	0.872	0.719	0.591	0.634	0.756	0.741	0.986	0.764	0.765
	Validation Δ	+0.034	+0.003	-0.058	+0.000	-0.001	-0.001	+0.134	+0.000	+0.013	+0.013
	Test	0.827	0.808	0.713	0.684	0.785	0.071	0.670	0.989	0.802	0.794
	Test Δ	+0.022	-0.035	-0.018	-0.022	+0.011	-0.028	+0.072	+0.006	+0.010	+0.011
S2SE,S2AN and L8HY,L8AN	Train	0.840	0.864	0.724	0.601	0.720	0.840	0.789	0.987	0.803	0.804
	Train Δ	+0.036	+0.027	+0.037	+0.014	+0.077	+0.035	+0.122	+0.004	+0.042	+0.041
	Validation	0.810	0.861	0.740	0.571	0.683	0.811	0.731	0.987	0.781	0.783
	Validation Δ	+0.025	-0.046	-0.050	-0.017	+0.010	+0.014	+0.080	+0.006	+0.004	+0.004
	Test	0.809	0.853	0.755	0.665	0.757	0.275	0.712	0.990	0.801	0.799
	Test Δ	+0.007	-0.009	-0.009	-0.006	+0.013	+0.053	+0.045	+0.003	+0.008	+0.012
S2MO,S2AN and L8HY,L8AN	Train	0.893	0.855	0.768	0.640	0.813	0.889	0.877	0.991	0.844	0.844
	Train Δ	+0.045	+0.033	+0.039	+0.014	+0.020	+0.019	+0.066	+0.002	+0.028	+0.032
	Validation	0.711	0.800	0.706	0.558	0.781	0.857	0.871	1.000	0.800	0.799
	Validation Δ	+0.044	-0.016	-0.026	-0.013	-0.040	+0.018	+0.059	+0.000	+0.000	+0.004
	Test	0.815	0.853	0.744	0.558	0.779	0.095	0.674	0.985	0.816	0.819
	Test Δ	+0.049	+0.011	+0.022	-0.011	+0.010	-0.022	+0.018	+0.000	+0.014	+0.016
S2SE,S2HY and L8HY,L8AN	Train	0.844	0.857	0.729	0.592	0.707	0.844	0.809	0.985	0.804	0.805
	Train Δ	+0.039	+0.025	+0.038	+0.008	+0.081	+0.036	+0.145	+0.004	+0.045	+0.043
	Validation	0.835	0.841	0.727	0.626	0.706	0.806	0.753	0.985	0.790	0.791
	Validation Δ	+0.035	-0.052	-0.063	+0.026	+0.039	+0.026	+0.110	+0.007	+0.017	+0.016
	Test	0.825	0.816	0.707	0.655	0.770	0.064	0.675	0.990	0.798	0.794
	Test Δ	+0.010	-0.019	-0.021	-0.019	+0.013	+0.064	+0.004	+0.003	+0.000	+0.004

Results of Decision-level Fusion Sentinel-2 and Landsat-8 prior models using an SVM [Continued].

		Sealed	Woody Coniferous	Woody Broadleaved	Permanent Herbaceous	Periodically Herbaceous	Sparsely Vegetated	Non- vegetated	Water	Weighted F1	OA%
S2MO,S2HY and L8HY,L8AN	Train	0.885	0.843	0.770	0.641	0.788	0.891	0.874	0.989	0.838	0.837
	Train Δ	+0.030	+0.027	+0.036	+0.018	+0.010	+0.018	+0.066	+0.000	+0.024	+0.027
	Validation	0.773	0.792	0.723	0.558	0.761	0.853	0.867	1.000	0.801	0.799
	Validation Δ	+0.106	-0.017	-0.009	-0.008	-0.039	+0.019	+0.060	+0.000	+0.010	+0.013
	Test	0.822	0.866	0.757	0.606	0.773	0.000	0.674	0.986	0.824	0.826
	Test Δ	+0.059	+0.044	+0.051	+0.022	+0.003	+0.000	+0.022	+0.002	+0.022	+0.022
S2MO,S2SE and L8HY,L8AN	Train	0.876	0.852	0.757	0.630	0.809	0.881	0.883	0.991	0.838	0.837
	Train Δ	+0.029	+0.030	+0.027	+0.004	+0.015	+0.011	+0.072	+0.002	+0.022	+0.026
	Validation	0.739	0.800	0.699	0.524	0.771	0.839	0.844	1.000	0.791	0.791
	Validation Δ	+0.073	-0.016	-0.033	-0.048	-0.049	+0.000	+0.031	+0.000	-0.008	-0.004
	Test	0.825	0.882	0.771	0.591	0.764	0.100	0.703	0.985	0.825	0.828
	Test Δ	+0.059	+0.040	+0.049	+0.022	-0.005	-0.018	+0.047	+0.000	+0.023	+0.024
S2SE,S2HY,S2AN and L8AN	Train	0.840	0.848	0.719	0.595	0.656	0.815	0.783	0.982	0.781	0.782
	Train Δ	+0.040	+0.015	+0.031	+0.011	+0.041	+0.025	+0.103	+0.006	+0.033	+0.031
	Validation	0.796	0.852	0.745	0.589	0.704	0.847	0.738	0.975	0.784	0.784
	Validation Δ	+0.009	-0.026	-0.037	-0.012	+0.032	+0.051	+0.107	+0.012	+0.017	+0.014
	Test	0.807	0.847	0.737	0.698	0.768	0.477	0.732	0.986	0.801	0.799
	Test Δ	+0.018	+0.007	+0.013	+0.003	+0.017	+0.089	+0.045	+0.003	+0.016	+0.019
S2MO,S2HY,S2AN and L8AN	Train	0.861	0.851	0.740	0.624	0.787	0.880	0.855	0.991	0.821	0.820
	Train Δ	+0.020	+0.020	+0.016	-0.005	+0.013	+0.014	+0.052	+0.002	+0.016	+0.019
	Validation	0.737	0.813	0.701	0.546	0.756	0.831	0.773	0.986	0.771	0.765
	Validation Δ	+0.091	+0.019	+0.015	-0.026	+0.000	+0.018	+0.065	+0.000	+0.024	+0.023
	Test	0.801	0.859	0.755	0.622	0.783	0.722	0.679	0.985	0.822	0.822
	Test Δ	+0.049	+0.056	+0.085	+0.039	+0.023	+0.126	+0.034	+0.000	+0.036	+0.037
S2MO,S2SE,S2HY and L8AN	Train	0.868	0.826	0.737	0.651	0.785	0.879	0.851	0.993	0.822	0.819
	Train Δ	+0.026	-0.005	+0.013	+0.021	+0.011	+0.013	+0.049	+0.003	+0.016	+0.018
	Validation	0.711	0.807	0.707	0.571	0.777	0.831	0.753	0.971	0.769	0.762
	Validation Δ	+0.064	+0.013	+0.021	+0.000	+0.021	+0.018	+0.044	-0.014	+0.022	+0.020
	Test	0.801	0.816	0.743	0.622	0.781	0.677	0.687	0.986	0.817	0.816
	Test Δ	+0.049	+0.014	+0.073	+0.039	+0.020	+0.080	+0.041	+0.002	+0.030	+0.031
S2MO,S2SE,S2HY,S2AN and L8AN	Train	0.876	0.857	0.775	0.641	0.796	0.881	0.874	0.991	0.834	0.834
	Train Δ	+0.034	+0.026	+0.051	+0.012	+0.022	+0.016	+0.071	+0.002	+0.029	+0.032
	Validation	0.753	0.781	0.688	0.500	0.783	0.849	0.785	1.000	0.773	0.768
	Validation Δ	+0.107	-0.012	+0.001	-0.071	+0.027	+0.036	+0.076	+0.014	+0.026	+0.027
	Test	0.808	0.841	0.737	0.582	0.777	0.685	0.683	0.986	0.816	0.816
	Test Δ	+0.056	+0.038	+0.068	-0.001	+0.017	+0.088	+0.038	+0.002	+0.029	+0.031

Results of Decision-level Fusion Sentinel-2 and Landsat-8 prior models using an SVM [Continued].

		Sealed	Woody Coniferous	Woody Broadleaved	Permanent Herbaceous	Periodically Herbaceous	Sparsely Vegetated	Non- vegetated	Water	Weighted F1	OA%
S2SE,S2HY,S2AN, and L8HY	Train	0.833	0.854	0.726	0.588	0.703	0.831	0.767	0.984	0.794	0.796
	Train Δ	+0.027	+0.022	+0.035	+0.004	+0.077	+0.023	+0.103	+0.002	+0.035	+0.034
	Validation	0.843	0.841	0.740	0.654	0.713	0.806	0.764	0.978	0.797	0.798
	Validation Δ	+0.043	-0.052	-0.050	+0.054	+0.046	+0.026	+0.121	+0.000	+0.024	+0.024
	Test	0.827	0.843	0.726	0.681	0.789	0.030	0.679	0.989	0.809	0.802
	Test Δ	+0.011	+0.007	-0.002	+0.007	+0.032	+0.030	+0.008	+0.002	+0.010	+0.013
S2AN,S2HY,S2MO and L8HY	Train	0.849	0.829	0.731	0.632	0.797	0.888	0.854	0.989	0.825	0.824
	Train Δ	-0.005	+0.012	-0.002	+0.009	+0.019	+0.015	+0.046	+0.000	+0.011	+0.014
	Validation	0.756	0.816	0.709	0.522	0.771	0.853	0.867	1.000	0.799	0.795
	Validation Δ	+0.089	+0.008	-0.023	-0.044	-0.029	+0.019	+0.060	+0.000	+0.007	+0.008
	Test	0.810	0.878	0.745	0.631	0.785	0.091	0.648	0.985	0.823	0.824
	Test Δ	+0.047	+0.055	+0.039	+0.047	+0.015	+0.091	-0.004	+0.000	+0.022	+0.020
S2HY,S2SE,S2MO and L8HY	Train	0.864	0.813	0.737	0.625	0.779	0.877	0.858	0.991	0.822	0.820
	Train Δ	+0.010	-0.004	+0.003	+0.002	+0.001	+0.004	+0.050	+0.002	+0.008	+0.010
	Validation	0.773	0.851	0.741	0.549	0.776	0.833	0.833	1.000	0.806	0.799
	Validation Δ	+0.106	+0.043	+0.009	-0.017	-0.024	+0.000	+0.027	+0.000	+0.015	+0.013
	Test	0.808	0.857	0.764	0.606	0.791	0.000	0.652	0.986	0.821	0.823
	Test Δ	+0.045	+0.035	+0.058	+0.022	+0.021	+0.000	-0.001	+0.002	+0.020	+0.019
S2MO,S2SE,S2HY,S2AN and L8HY	Train	0.871	0.834	0.744	0.623	0.794	0.885	0.867	0.991	0.830	0.830
	Train Δ	+0.017	+0.017	+0.010	+0.000	+0.016	+0.012	+0.058	+0.002	+0.016	+0.019
	Validation	0.800	0.792	0.691	0.522	0.771	0.839	0.825	1.000	0.791	0.787
	Validation Δ	+0.133	-0.017	-0.040	-0.044	-0.029	+0.005	+0.019	+0.000	-0.001	+0.000
	Test	0.816	0.909	0.770	0.558	0.777	0.000	0.682	0.986	0.824	0.826
	Test Δ	+0.053	+0.087	+0.065	-0.026	+0.006	+0.000	+0.029	+0.002	+0.022	+0.022
S2SE,S2HY,S2AN and L8HY,L8AN	Train	0.847	0.863	0.731	0.600	0.715	0.848	0.809	0.985	0.808	0.808
	Train Δ	+0.042	+0.030	+0.040	+0.016	+0.088	+0.040	+0.146	+0.004	+0.049	+0.047
	Validation	0.835	0.829	0.740	0.633	0.699	0.800	0.753	0.985	0.790	0.791
	Validation Δ	+0.035	-0.064	-0.050	+0.033	+0.032	+0.020	+0.110	+0.007	+0.017	+0.016
	Test	0.829	0.813	0.706	0.650	0.772	0.063	0.675	0.990	0.798	0.794
	Test Δ	+0.013	-0.022	-0.022	-0.024	+0.015	+0.063	+0.004	+0.003	+0.000	+0.004
S2MO,S2HY,S2AN and L8HY,L8AN	Train	0.889	0.851	0.775	0.650	0.797	0.891	0.878	0.991	0.843	0.843
	Train Δ	+0.035	+0.034	+0.042	+0.027	+0.019	+0.018	+0.070	+0.002	+0.029	+0.032
	Validation	0.744	0.792	0.732	0.500	0.800	0.839	0.867	1.000	0.800	0.799
	Validation Δ	+0.078	-0.017	+0.000	-0.066	+0.000	+0.005	+0.060	+0.000	+0.008	+0.013
	Test	0.826	0.845	0.717	0.581	0.784	0.000	0.678	0.986	0.821	0.822
	Test Δ	+0.063	+0.023	+0.011	-0.003	+0.014	+0.000	+0.025	+0.002	+0.019	+0.017

Results of Decision-level Fusion Sentinel-2 and Landsat-8 prior models using an SVM [Continued].

		Sealed	Woody Coniferous	Woody Broadleaved	Permanent Herbaceous	Periodically Herbaceous	Sparsely Vegetated	Non- vegetated	Water	Weighted F1	OA%
S2MO,S2SE,S2HY and L8HY,L8AN	Train	0.889	0.843	0.769	0.639	0.789	0.891	0.883	0.989	0.840	0.839
	Train Δ	+0.034	+0.027	+0.035	+0.016	+0.011	+0.018	+0.075	+0.000	+0.026	+0.028
	Validation	0.727	0.816	0.716	0.558	0.778	0.839	0.848	1.000	0.797	0.795
	Validation Δ	+0.061	+0.008	-0.016	-0.008	-0.022	+0.005	+0.041	+0.000	+0.006	+0.008
	Test	0.826	0.866	0.755	0.574	0.769	0.000	0.682	0.986	0.822	0.824
	Test Δ	+0.063	+0.044	+0.049	-0.010	-0.001	+0.000	+0.029	+0.002	+0.021	+0.020
S2MO,S2SE,S2HY,S2AN and L8HY,L8AN	Train	0.880	0.804	0.748	0.641	0.797	0.879	0.872	0.991	0.831	0.829
	Train Δ	+0.026	-0.013	+0.014	+0.018	+0.019	+0.006	+0.064	+0.002	+0.017	+0.019
	Validation	0.727	0.826	0.732	0.560	0.765	0.825	0.807	1.000	0.792	0.787
	Validation Δ	+0.061	+0.018	+0.000	-0.006	-0.035	-0.008	+0.001	+0.000	+0.001	+0.000
	Test	0.834	0.832	0.753	0.618	0.799	0.000	0.667	0.986	0.828	0.831
	Test Δ	+0.072	+0.009	+0.048	+0.034	+0.028	+0.000	+0.014	+0.002	+0.026	+0.027

C.1.2.4 Landsat-8 and Sentinel-1

Table C.9: Results of Decision-level Fusion Landsat-8 and Sentinel-1 prior models using an SVM.

		Sealed	Woody Coniferous	Woody Broadleaved	Permanent Herbaceous	Periodically Herbaceous	Sparsely Vegetated	Non- vegetated	Water	Weighted F1	OA%
L8AN and S1MO	Train	0.812	0.872	0.725	0.634	0.715	0.810	0.801	0.991	0.795	0.796
	Train Δ	+0.085	+0.036	+0.079	+0.156	+0.157	+0.062	+0.136	+0.017	+0.090	+0.089
	Validation	0.726	0.847	0.667	0.536	0.622	0.800	0.715	0.975	0.737	0.739
	Validation Δ	+0.060	+0.030	+0.056	+0.075	+0.107	+0.062	+0.109	-0.010	+0.060	+0.059
	Test	0.723	0.859	0.731	0.579	0.669	0.710	0.610	0.954	0.732	0.731
	Test Δ	+0.081	+0.021	+0.062	+0.105	+0.110	-0.001	+0.083	-0.028	+0.054	+0.051
L8HY and S1MO	Train	0.798	0.860	0.721	0.601	0.734	0.841	0.781	0.992	0.798	0.797
	Train Δ	+0.105	+0.034	+0.128	+0.112	+0.179	+0.077	+0.209	+0.026	+0.106	+0.097
	Validation	0.724	0.860	0.642	0.552	0.638	0.800	0.694	0.988	0.743	0.743
	Validation Δ	-0.034	+0.040	+0.047	+0.035	+0.019	+0.060	+0.090	+0.000	+0.031	+0.024
	Test	0.724	0.850	0.749	0.672	0.728	0.167	0.564	0.963	0.753	0.753
	Test Δ	+0.029	+0.010	+0.074	+0.046	+0.033	-0.010	+0.038	-0.023	+0.027	+0.038
L8AN,L8HY and S1MO	Train	0.827	0.860	0.734	0.615	0.734	0.836	0.801	0.992	0.806	0.806
	Train Δ	+0.134	+0.034	+0.141	+0.126	+0.179	+0.073	+0.229	+0.026	+0.115	+0.106
	Validation	0.734	0.840	0.671	0.569	0.657	0.831	0.732	0.988	0.759	0.760
	Validation Δ	-0.024	+0.020	+0.076	+0.052	+0.038	+0.092	+0.128	+0.000	+0.048	+0.040
	Test	0.765	0.847	0.766	0.672	0.737	0.212	0.631	0.974	0.774	0.774
	Test Δ	+0.070	+0.006	+0.091	+0.046	+0.042	+0.035	+0.106	-0.011	+0.048	+0.059

C.1.2.5 Sentinel-2 Landsat-8 and Sentinel-1

Table C.10: Results of Decision-level Fusion of Sentinel-2 Landsat-8 and Sentinel-1 prior models using SVM.

		Sealed	Woody Coniferous	Woody Broadleaved	Permanent Herbaceous	Periodically Herbaceous	Sparsely Vegetated	Non- vegetated	Water	Weighted F1	OA%
S2AN,L8AN and S1MO	Train	0.835	0.878	0.744	0.637	0.725	0.818	0.798	0.990	0.803	0.803
	Train Δ	+0.102	+0.022	+0.082	+0.132	+0.119	+0.048	+0.164	+0.026	+0.085	+0.082
	Validation	0.800	0.878	0.694	0.534	0.625	0.794	0.732	0.975	0.755	0.756
	Validation Δ	+0.027	-0.018	+0.010	+0.065	+0.028	+0.037	+0.057	+0.005	+0.026	+0.021
	Test	0.756	0.887	0.771	0.605	0.703	0.768	0.638	0.960	0.763	0.760
	Test Δ	+0.077	+0.010	+0.066	+0.037	+0.050	-0.035	+0.094	-0.021	+0.034	+0.027
S2HY,L8AN and S1MO	Train	0.853	0.866	0.756	0.654	0.766	0.855	0.852	0.992	0.825	0.825
	Train Δ	+0.065	+0.032	+0.059	+0.069	+0.145	+0.060	+0.195	+0.024	+0.081	+0.080
	Validation	0.798	0.885	0.737	0.562	0.667	0.802	0.726	0.970	0.768	0.769
	Validation Δ	+0.019	+0.031	-0.031	-0.029	+0.010	+0.043	+0.105	+0.000	+0.018	+0.017
	Test	0.806	0.824	0.715	0.664	0.747	0.500	0.696	0.981	0.781	0.781
	Test Δ	+0.031	-0.025	-0.003	-0.038	-0.009	+0.186	+0.096	+0.001	+0.012	+0.018
S2SE,L8AN and S1MO	Train	0.854	0.863	0.733	0.638	0.733	0.819	0.817	0.991	0.807	0.807
	Train Δ	+0.061	+0.016	+0.049	+0.051	+0.108	+0.033	+0.142	+0.014	+0.058	+0.055
	Validation	0.791	0.882	0.744	0.558	0.671	0.819	0.733	0.973	0.773	0.773
	Validation Δ	+0.010	-0.018	-0.027	-0.012	-0.005	+0.033	+0.100	+0.005	+0.009	+0.006
	Test	0.787	0.876	0.764	0.646	0.753	0.842	0.697	0.960	0.793	0.791
	Test Δ	+0.009	-0.007	+0.005	-0.038	+0.018	+0.026	+0.019	-0.021	+0.000	-0.003
S2MO,L8AN and S1MO	Train	0.876	0.855	0.761	0.681	0.821	0.892	0.883	0.993	0.843	0.841
	Train Δ	+0.039	+0.020	+0.040	+0.050	+0.034	+0.028	+0.077	+0.003	+0.036	+0.039
	Validation	0.727	0.812	0.647	0.500	0.745	0.836	0.753	0.975	0.755	0.749
	Validation Δ	+0.070	+0.024	-0.033	-0.075	-0.030	+0.018	+0.037	-0.013	+0.000	+0.000
	Test	0.846	0.866	0.775	0.623	0.765	0.773	0.731	0.986	0.834	0.834
	Test Δ	+0.090	+0.035	+0.079	+0.044	+0.008	+0.106	+0.088	+0.002	+0.045	+0.047

Results of Decision-level Fusion of Sentinel-2 Landsat-8 and Sentinel-1 prior models using SVM [Continued].

		Sealed	Woody Coniferous	Woody Broadleaved	Permanent Herbaceous	Periodically Herbaceous	Sparsely Vegetated	Non-vegetated	Water	Weighted F1	OA%
S2AN,L8HY and S1MO	Train	0.829	0.859	0.743	0.615	0.753	0.831	0.790	0.992	0.808	0.807
	Train Δ	+0.097	+0.021	+0.065	+0.111	+0.117	+0.050	+0.175	+0.020	+0.079	+0.077
	Validation	0.781	0.880	0.726	0.571	0.682	0.827	0.711	0.988	0.776	0.777
	Validation Δ	+0.004	-0.014	+0.010	+0.125	+0.065	+0.053	+0.022	+0.006	+0.035	+0.031
	Test	0.755	0.885	0.792	0.670	0.749	0.303	0.628	0.984	0.783	0.784
	Test Δ	+0.052	+0.017	+0.074	+0.071	+0.063	+0.031	+0.089	-0.001	+0.050	+0.053
S2HY,L8HY and S1MO	Train	0.850	0.854	0.763	0.630	0.760	0.867	0.827	0.992	0.825	0.825
	Train Δ	+0.049	+0.023	+0.058	+0.052	+0.120	+0.045	+0.151	+0.020	+0.065	+0.064
	Validation	0.750	0.850	0.726	0.551	0.650	0.819	0.767	0.986	0.766	0.767
	Validation Δ	-0.019	-0.018	-0.051	-0.041	+0.015	+0.062	+0.160	+0.000	+0.016	+0.015
	Test	0.824	0.826	0.725	0.694	0.782	0.128	0.686	0.983	0.806	0.803
	Test Δ	+0.020	-0.017	-0.006	-0.012	+0.007	+0.029	+0.088	+0.000	+0.013	+0.021
S2SE,L8HY and S1MO	Train	0.860	0.868	0.746	0.645	0.771	0.862	0.842	0.995	0.831	0.831
	Train Δ	+0.056	+0.031	+0.059	+0.058	+0.128	+0.057	+0.175	+0.012	+0.069	+0.068
	Validation	0.819	0.902	0.758	0.556	0.697	0.851	0.792	0.987	0.800	0.800
	Validation Δ	+0.034	-0.004	-0.033	-0.033	+0.024	+0.053	+0.140	+0.006	+0.023	+0.021
	Test	0.794	0.853	0.773	0.658	0.751	0.346	0.689	0.984	0.795	0.796
	Test Δ	-0.009	-0.010	+0.008	-0.012	+0.008	+0.124	+0.023	-0.002	+0.002	+0.008
S2MO,L8HY,L8AN and S1MO	Train	0.874	0.847	0.760	0.676	0.844	0.901	0.892	0.991	0.852	0.852
	Train Δ	+0.027	+0.025	+0.031	+0.051	+0.051	+0.031	+0.082	+0.002	+0.037	+0.040
	Validation	0.783	0.863	0.753	0.526	0.767	0.807	0.807	1.000	0.802	0.803
	Validation Δ	+0.116	+0.046	+0.021	-0.045	-0.053	-0.032	-0.006	+0.000	+0.002	+0.008
	Test	0.834	0.878	0.762	0.578	0.757	0.125	0.715	0.985	0.825	0.828
	Test Δ	+0.068	+0.036	+0.040	+0.008	-0.012	+0.007	+0.059	+0.000	+0.023	+0.024
S2AN,L8HY,L8AN and S1MO	Train	0.844	0.863	0.746	0.617	0.749	0.833	0.809	0.993	0.813	0.812
	Train Δ	+0.112	+0.025	+0.067	+0.113	+0.113	+0.052	+0.194	+0.021	+0.084	+0.082
	Validation	0.769	0.878	0.711	0.559	0.657	0.838	0.744	0.988	0.773	0.773
	Validation Δ	-0.008	-0.016	-0.005	+0.113	+0.040	+0.063	+0.055	+0.006	+0.032	+0.028
	Test	0.768	0.877	0.789	0.678	0.750	0.308	0.654	0.987	0.789	0.790
	Test Δ	+0.065	+0.009	+0.071	+0.079	+0.064	+0.036	+0.115	+0.001	+0.056	+0.059
S2HY,L8HY,L8AN and S1MO	Train	0.859	0.865	0.767	0.638	0.775	0.876	0.856	0.994	0.836	0.836
	Train Δ	+0.059	+0.034	+0.062	+0.060	+0.135	+0.054	+0.180	+0.022	+0.075	+0.075
	Validation	0.807	0.850	0.719	0.589	0.690	0.803	0.786	0.986	0.782	0.782
	Validation Δ	+0.038	-0.018	-0.058	-0.002	+0.056	+0.045	+0.179	+0.000	+0.032	+0.030
	Test	0.823	0.824	0.718	0.671	0.773	0.115	0.671	0.985	0.799	0.797
	Test Δ	+0.018	-0.019	-0.013	-0.035	-0.002	+0.016	+0.074	+0.002	+0.006	+0.014

Results of Decision-level Fusion of Sentinel-2 Landsat-8 and Sentinel-1 prior models using SVM [Continued].

		Sealed	Woody Coniferous	Woody Broadleaved	Permanent Herbaceous	Periodically Herbaceous	Sparsely Vegetated	Non- vegetated	Water	Weighted F1	OA%
S2SE, L8AN,L8HY and S1MO	Train	0.871	0.866	0.751	0.654	0.770	0.863	0.848	0.994	0.834	0.834
	Train Δ	+0.067	+0.030	+0.064	+0.067	+0.127	+0.058	+0.181	+0.011	+0.073	+0.071
	Validation	0.811	0.861	0.740	0.607	0.709	0.851	0.812	0.987	0.803	0.803
	Validation Δ	+0.026	-0.046	-0.050	+0.019	+0.036	+0.053	+0.160	+0.006	+0.026	+0.023
	Test	0.798	0.853	0.767	0.669	0.764	0.314	0.700	0.987	0.800	0.801
	Test Δ	-0.004	-0.009	+0.003	-0.001	+0.020	+0.092	+0.034	+0.000	+0.007	+0.014
S2MO, L8AN,L8HY and S1MO	Train	0.876	0.829	0.762	0.660	0.819	0.887	0.889	0.993	0.843	0.841
	Train Δ	+0.028	+0.007	+0.032	+0.034	+0.026	+0.017	+0.078	+0.003	+0.027	+0.029
	Validation	0.708	0.840	0.738	0.583	0.805	0.825	0.800	1.000	0.803	0.799
	Validation Δ	+0.042	+0.024	+0.006	+0.012	-0.015	-0.013	-0.012	+0.000	+0.003	+0.004
	Test	0.837	0.869	0.800	0.617	0.799	0.118	0.696	0.988	0.837	0.839
	Test Δ	+0.070	+0.027	+0.078	+0.048	+0.030	+0.000	+0.039	+0.003	+0.034	+0.036
S2AN,S2HY, L8AN and S1MO	Train	0.845	0.862	0.748	0.622	0.729	0.836	0.828	0.990	0.808	0.807
	Train Δ	+0.057	+0.028	+0.050	+0.037	+0.108	+0.040	+0.172	+0.022	+0.064	+0.063
	Validation	0.796	0.850	0.726	0.556	0.648	0.793	0.733	0.970	0.760	0.760
	Validation Δ	+0.017	-0.005	-0.042	-0.036	-0.009	+0.034	+0.113	+0.000	+0.009	+0.008
	Test	0.807	0.835	0.724	0.683	0.768	0.519	0.730	0.982	0.794	0.793
	Test Δ	+0.031	-0.013	+0.006	-0.018	+0.012	+0.205	+0.130	+0.002	+0.025	+0.030
S2AN,S2SE, L8AN and S1MO	Train	0.856	0.863	0.730	0.631	0.734	0.817	0.818	0.990	0.806	0.806
	Train Δ	+0.063	+0.016	+0.046	+0.044	+0.109	+0.030	+0.143	+0.013	+0.057	+0.054
	Validation	0.813	0.874	0.736	0.549	0.671	0.809	0.727	0.973	0.772	0.772
	Validation Δ	+0.032	-0.027	-0.035	-0.021	-0.005	+0.024	+0.095	+0.005	+0.008	+0.005
	Test	0.790	0.881	0.766	0.654	0.757	0.855	0.715	0.983	0.802	0.802
	Test Δ	+0.012	-0.002	+0.007	-0.030	+0.021	+0.039	+0.037	+0.002	+0.010	+0.008
S2AN,S2MO, L8AN and S1MO	Train	0.880	0.862	0.773	0.694	0.831	0.900	0.891	0.993	0.851	0.850
	Train Δ	+0.042	+0.028	+0.052	+0.062	+0.044	+0.036	+0.085	+0.003	+0.044	+0.047
	Validation	0.769	0.812	0.667	0.531	0.768	0.836	0.760	0.975	0.770	0.765
	Validation Δ	+0.112	+0.024	-0.013	-0.044	-0.008	+0.018	+0.043	-0.013	+0.016	+0.016
	Test	0.842	0.862	0.764	0.634	0.773	0.773	0.712	0.986	0.833	0.832
	Test Δ	+0.086	+0.031	+0.068	+0.056	+0.017	+0.106	+0.069	+0.002	+0.043	+0.045
S2HY,S2SE, L8AN and S1MO	Train	0.861	0.856	0.740	0.632	0.739	0.838	0.844	0.990	0.814	0.815
	Train Δ	+0.061	+0.024	+0.052	+0.047	+0.123	+0.049	+0.165	+0.014	+0.066	+0.064
	Validation	0.798	0.854	0.758	0.576	0.671	0.839	0.756	0.969	0.780	0.780
	Validation Δ	+0.012	-0.023	-0.024	-0.026	-0.001	+0.043	+0.125	+0.006	+0.014	+0.011
	Test	0.816	0.839	0.727	0.679	0.770	0.591	0.741	0.982	0.801	0.800
	Test Δ	+0.027	-0.002	+0.003	-0.016	+0.019	+0.203	+0.053	+0.000	+0.016	+0.020

Results of Decision-level Fusion of Sentinel-2 Landsat-8 and Sentinel-1 prior models using SVM [Continued].

		Sealed	Woody Coniferous	Woody Broadleaved	Permanent Herbaceous	Periodically Herbaceous	Sparsely Vegetated	Non- vegetated	Water	Weighted F1	OA%
S2HY,S2MO, L8AN and S1MO	Train	0.870	0.845	0.748	0.663	0.811	0.887	0.870	0.993	0.834	0.833
	Train Δ	+0.029	+0.014	+0.024	+0.033	+0.037	+0.022	+0.067	+0.003	+0.029	+0.032
	Validation	0.703	0.818	0.686	0.533	0.756	0.818	0.737	0.971	0.756	0.752
	Validation Δ	+0.057	+0.025	+0.000	-0.038	+0.000	+0.006	+0.028	-0.014	+0.009	+0.010
	Test	0.839	0.850	0.737	0.585	0.785	0.758	0.705	0.986	0.828	0.827
	Test Δ	+0.086	+0.047	+0.067	+0.002	+0.024	+0.161	+0.059	+0.002	+0.041	+0.042
S2SE,S2MO, L8AN and S1MO	Train	0.880	0.864	0.776	0.686	0.825	0.886	0.886	0.993	0.848	0.846
	Train Δ	+0.043	+0.030	+0.056	+0.055	+0.038	+0.022	+0.080	+0.003	+0.041	+0.044
	Validation	0.760	0.812	0.654	0.508	0.753	0.836	0.769	0.975	0.764	0.759
	Validation Δ	+0.102	+0.024	-0.026	-0.067	-0.023	+0.018	+0.053	-0.013	+0.009	+0.009
	Test	0.847	0.856	0.758	0.623	0.779	0.756	0.734	0.986	0.833	0.833
	Test Δ	+0.091	+0.025	+0.062	+0.044	+0.022	+0.089	+0.091	+0.002	+0.044	+0.046
S2AN,S2HY, L8HY and S1MO	Train	0.856	0.854	0.759	0.641	0.781	0.869	0.846	0.994	0.832	0.832
	Train Δ	+0.055	+0.023	+0.055	+0.063	+0.141	+0.048	+0.170	+0.022	+0.072	+0.071
	Validation	0.800	0.878	0.724	0.598	0.718	0.800	0.780	0.986	0.788	0.789
	Validation Δ	+0.031	+0.010	-0.052	+0.007	+0.083	+0.042	+0.173	+0.000	+0.037	+0.036
	Test	0.832	0.827	0.722	0.680	0.766	0.133	0.689	0.985	0.804	0.802
	Test Δ	+0.027	-0.016	-0.009	-0.026	-0.009	+0.034	+0.091	+0.002	+0.011	+0.020
S2AN,S2SE, L8HY and S1MO	Train	0.857	0.868	0.746	0.644	0.774	0.861	0.850	0.995	0.831	0.832
	Train Δ	+0.053	+0.032	+0.059	+0.057	+0.131	+0.056	+0.183	+0.012	+0.070	+0.069
	Validation	0.844	0.902	0.732	0.600	0.719	0.844	0.788	0.987	0.807	0.807
	Validation Δ	+0.059	-0.004	-0.059	+0.012	+0.046	+0.047	+0.136	+0.006	+0.029	+0.028
	Test	0.805	0.859	0.778	0.651	0.755	0.346	0.691	0.985	0.798	0.800
	Test Δ	+0.003	-0.004	+0.013	-0.019	+0.011	+0.124	+0.024	-0.001	+0.005	+0.012
S2AN,S2MO, L8HY and S1MO	Train	0.873	0.845	0.763	0.677	0.840	0.906	0.897	0.993	0.853	0.851
	Train Δ	+0.025	+0.023	+0.033	+0.051	+0.047	+0.036	+0.086	+0.003	+0.037	+0.040
	Validation	0.727	0.840	0.714	0.522	0.815	0.857	0.807	1.000	0.802	0.799
	Validation Δ	+0.061	+0.024	-0.017	-0.050	-0.006	+0.018	-0.006	+0.000	+0.002	+0.004
	Test	0.827	0.885	0.781	0.593	0.781	0.118	0.717	0.988	0.832	0.835
	Test Δ	+0.061	+0.043	+0.058	+0.024	+0.013	+0.000	+0.061	+0.003	+0.030	+0.031
S2HY,S2SE, L8HY and S1MO	Train	0.865	0.855	0.748	0.648	0.782	0.872	0.861	0.994	0.836	0.836
	Train Δ	+0.060	+0.023	+0.057	+0.064	+0.156	+0.065	+0.198	+0.012	+0.077	+0.075
	Validation	0.825	0.889	0.759	0.606	0.713	0.836	0.800	0.985	0.805	0.805
	Validation Δ	+0.025	-0.003	-0.031	+0.006	+0.046	+0.056	+0.157	+0.007	+0.032	+0.031
	Test	0.825	0.822	0.720	0.658	0.775	0.121	0.714	0.985	0.806	0.805
	Test Δ	+0.009	-0.014	-0.008	-0.017	+0.019	+0.121	+0.043	-0.001	+0.007	+0.015

Results of Decision-level Fusion of Sentinel-2 Landsat-8 and Sentinel-1 prior models using SVM [Continued].

		Sealed	Woody Coniferous	Woody Broadleaved	Permanent Herbaceous	Periodically Herbaceous	Sparsely Vegetated	Non- vegetated	Water	Weighted F1	OA%
S2HY,S2MO L8HY and S1MO	Train	0.871	0.824	0.757	0.648	0.812	0.888	0.869	0.992	0.837	0.836
	Train Δ	+0.016	+0.007	+0.024	+0.025	+0.034	+0.015	+0.061	+0.003	+0.023	+0.025
	Validation	0.727	0.816	0.714	0.565	0.765	0.853	0.814	0.985	0.791	0.787
	Validation Δ	+0.061	+0.008	-0.017	-0.001	-0.035	+0.019	+0.007	-0.015	-0.001	+0.000
	Test	0.840	0.845	0.741	0.601	0.797	0.000	0.701	0.986	0.831	0.833
	Test Δ	+0.077	+0.023	+0.035	+0.018	+0.027	+0.000	+0.048	+0.002	+0.029	+0.029
S2SE,S2MO, L8HY and S1MO	Train	0.878	0.849	0.762	0.674	0.828	0.896	0.887	0.993	0.849	0.848
	Train Δ	+0.030	+0.027	+0.032	+0.049	+0.035	+0.026	+0.076	+0.003	+0.034	+0.037
	Validation	0.711	0.863	0.747	0.565	0.781	0.857	0.820	0.987	0.805	0.803
	Validation Δ	+0.044	+0.046	+0.015	-0.006	-0.040	+0.018	+0.007	-0.013	+0.006	+0.008
	Test	0.833	0.878	0.773	0.603	0.783	0.111	0.729	0.986	0.834	0.836
	Test Δ	+0.067	+0.036	+0.051	+0.033	+0.014	-0.006	+0.073	+0.002	+0.032	+0.032
S2AN,S2HY and L8AN,L8HY, S1MO	Train	0.858	0.864	0.770	0.655	0.783	0.876	0.853	0.991	0.838	0.838
	Train Δ	+0.057	+0.033	+0.065	+0.076	+0.142	+0.055	+0.178	+0.019	+0.077	+0.077
	Validation	0.800	0.850	0.713	0.569	0.678	0.803	0.776	0.986	0.775	0.776
	Validation Δ	+0.031	-0.018	-0.064	-0.022	+0.044	+0.045	+0.169	+0.000	+0.025	+0.023
	Test	0.827	0.819	0.725	0.665	0.774	0.128	0.685	0.985	0.802	0.800
	Test Δ	+0.022	-0.024	-0.006	-0.041	-0.001	+0.029	+0.087	+0.002	+0.009	+0.018
S2AN,S2SE and L8AN,L8HY, S1MO	Train	0.864	0.857	0.743	0.644	0.746	0.852	0.829	0.992	0.823	0.823
	Train Δ	+0.060	+0.021	+0.056	+0.057	+0.103	+0.046	+0.162	+0.009	+0.062	+0.060
	Validation	0.826	0.861	0.750	0.602	0.694	0.859	0.776	0.987	0.801	0.800
	Validation Δ	+0.041	-0.046	-0.041	+0.014	+0.021	+0.062	+0.124	+0.006	+0.023	+0.021
	Test	0.806	0.856	0.779	0.686	0.778	0.275	0.667	0.961	0.797	0.797
	Test Δ	+0.004	-0.007	+0.015	+0.015	+0.035	+0.052	+0.000	-0.025	+0.004	+0.010
S2AN,S2MO and L8AN,L8HY, S1MO	Train	0.897	0.854	0.777	0.682	0.833	0.908	0.899	0.993	0.858	0.857
	Train Δ	+0.049	+0.032	+0.048	+0.056	+0.040	+0.038	+0.089	+0.003	+0.043	+0.046
	Validation	0.766	0.840	0.744	0.609	0.810	0.857	0.848	1.000	0.821	0.819
	Validation Δ	+0.099	+0.024	+0.013	+0.037	-0.010	+0.018	+0.035	+0.000	+0.022	+0.024
	Test	0.852	0.887	0.793	0.620	0.796	0.118	0.719	0.988	0.842	0.846
	Test Δ	+0.086	+0.045	+0.070	+0.050	+0.027	+0.000	+0.063	+0.003	+0.040	+0.042
S2HY,S2SE and L8AN,L8HY, S1MO	Train	0.877	0.864	0.756	0.655	0.775	0.874	0.879	0.994	0.842	0.842
	Train Δ	+0.072	+0.032	+0.065	+0.071	+0.149	+0.067	+0.215	+0.012	+0.083	+0.081
	Validation	0.837	0.857	0.740	0.647	0.734	0.839	0.809	0.985	0.810	0.810
	Validation Δ	+0.037	-0.035	-0.050	+0.047	+0.067	+0.059	+0.166	+0.007	+0.037	+0.035
	Test	0.828	0.807	0.707	0.660	0.775	0.111	0.702	0.985	0.803	0.802
	Test Δ	+0.012	-0.029	-0.021	-0.014	+0.019	+0.111	+0.031	-0.001	+0.004	+0.012

Results of Decision-level Fusion of Sentinel-2 Landsat-8 and Sentinel-1 prior models using SVM [Continued].

		Sealed	Woody Coniferous	Woody Broadleaved	Permanent Herbaceous	Periodically Herbaceous	Sparsely Vegetated	Non- vegetated	Water	Weighted F1	OA%
S2HY,S2MO and L8AN,L8HY, S1MO	Train	0.895	0.858	0.780	0.687	0.843	0.904	0.901	0.994	0.861	0.862
	Train Δ	+0.041	+0.041	+0.047	+0.064	+0.065	+0.031	+0.093	+0.005	+0.047	+0.051
	Validation	0.800	0.863	0.756	0.541	0.773	0.820	0.814	1.000	0.807	0.808
	Validation Δ	+0.133	+0.054	+0.024	-0.025	-0.027	-0.014	+0.007	+0.000	+0.016	+0.021
	Test	0.840	0.863	0.742	0.606	0.788	0.111	0.715	0.990	0.835	0.838
	Test Δ	+0.077	+0.041	+0.037	+0.022	+0.018	+0.111	+0.063	+0.005	+0.034	+0.034
S2SE,S2MO and L8AN,L8HY, S1MO	Train	0.888	0.851	0.769	0.673	0.835	0.893	0.895	0.993	0.853	0.852
	Train Δ	+0.040	+0.029	+0.040	+0.047	+0.042	+0.023	+0.084	+0.003	+0.037	+0.040
	Validation	0.723	0.840	0.723	0.533	0.781	0.857	0.820	0.987	0.798	0.795
	Validation Δ	+0.057	+0.024	-0.009	-0.038	-0.040	+0.018	+0.007	-0.013	-0.002	+0.000
	Test	0.844	0.887	0.788	0.610	0.777	0.100	0.711	0.988	0.836	0.838
	Test Δ	+0.078	+0.045	+0.065	+0.041	+0.009	-0.018	+0.055	+0.003	+0.034	+0.034
S2AN,S2HY,S2SE and L8AN, S1MO	Train	0.856	0.855	0.741	0.628	0.737	0.837	0.843	0.990	0.813	0.813
	Train Δ	+0.056	+0.023	+0.053	+0.044	+0.122	+0.048	+0.163	+0.013	+0.065	+0.062
	Validation	0.826	0.843	0.744	0.578	0.672	0.839	0.762	0.969	0.782	0.782
	Validation Δ	+0.040	-0.034	-0.039	-0.024	-0.001	+0.043	+0.131	+0.006	+0.016	+0.012
	Test	0.815	0.838	0.727	0.674	0.765	0.584	0.745	0.982	0.799	0.799
	Test Δ	+0.026	-0.003	+0.003	-0.021	+0.014	+0.196	+0.058	+0.000	+0.015	+0.019
S2AN,S2HY,S2MO and L8AN, S1MO	Train	0.874	0.831	0.756	0.659	0.802	0.883	0.872	0.993	0.832	0.830
	Train Δ	+0.032	+0.000	+0.032	+0.030	+0.028	+0.017	+0.069	+0.003	+0.027	+0.028
	Validation	0.712	0.807	0.673	0.548	0.764	0.831	0.711	0.971	0.755	0.748
	Validation Δ	+0.066	+0.013	-0.013	-0.023	+0.009	+0.018	+0.002	-0.014	+0.008	+0.007
	Test	0.825	0.819	0.736	0.580	0.788	0.719	0.702	0.988	0.822	0.820
	Test Δ	+0.072	+0.016	+0.067	-0.003	+0.027	+0.122	+0.057	+0.003	+0.035	+0.035
S2HY,S2SE,S2MO and L8AN, S1MO	Train	0.865	0.846	0.743	0.657	0.803	0.886	0.862	0.991	0.830	0.829
	Train Δ	+0.024	+0.015	+0.019	+0.027	+0.029	+0.021	+0.059	+0.002	+0.024	+0.028
	Validation	0.730	0.781	0.673	0.484	0.739	0.831	0.737	0.971	0.748	0.742
	Validation Δ	+0.084	-0.012	-0.013	-0.088	-0.016	+0.018	+0.028	-0.014	+0.001	+0.000
	Test	0.837	0.850	0.754	0.607	0.784	0.708	0.725	0.986	0.831	0.831
	Test Δ	+0.085	+0.047	+0.084	+0.024	+0.023	+0.111	+0.079	+0.002	+0.044	+0.046
S2AN,S2HY,S2SE,S2MO and L8AN, S1MO	Train	0.861	0.844	0.738	0.662	0.805	0.885	0.860	0.991	0.829	0.828
	Train Δ	+0.019	+0.013	+0.014	+0.032	+0.031	+0.020	+0.058	+0.002	+0.024	+0.027
	Validation	0.730	0.800	0.687	0.500	0.747	0.831	0.737	0.971	0.755	0.748
	Validation Δ	+0.084	+0.006	+0.001	-0.071	-0.008	+0.018	+0.028	-0.014	+0.008	+0.007
	Test	0.836	0.850	0.754	0.599	0.784	0.716	0.740	0.986	0.832	0.832
	Test Δ	+0.084	+0.047	+0.084	+0.016	+0.023	+0.120	+0.095	+0.002	+0.045	+0.047

Results of Decision-level Fusion of Sentinel-2 Landsat-8 and Sentinel-1 prior models using SVM [Continued].

		Sealed	Woody Coniferous	Woody Broadleaved	Permanent Herbaceous	Periodically Herbaceous	Sparsely Vegetated	Non- vegetated	Water	Weighted F1	OA%
S2AN,S2HY,S2SE and L8HY, S1MO	Train	0.856	0.871	0.761	0.657	0.778	0.869	0.865	0.994	0.839	0.840
	Train Δ	+0.051	+0.038	+0.070	+0.073	+0.151	+0.062	+0.202	+0.012	+0.080	+0.078
	Validation	0.832	0.889	0.754	0.612	0.732	0.839	0.800	0.985	0.809	0.810
	Validation Δ	+0.032	-0.003	-0.035	+0.012	+0.066	+0.059	+0.157	+0.007	+0.036	+0.035
	Test	0.832	0.823	0.719	0.660	0.771	0.054	0.707	0.985	0.805	0.805
	Test Δ	+0.016	-0.013	-0.010	-0.014	+0.015	+0.054	+0.036	-0.001	+0.007	+0.015
S2AN,S2HY,S2MO and L8HY, S1MO	Train	0.869	0.812	0.759	0.651	0.804	0.885	0.869	0.992	0.835	0.833
	Train Δ	+0.014	-0.005	+0.025	+0.028	+0.026	+0.012	+0.061	+0.003	+0.021	+0.023
	Validation	0.714	0.816	0.699	0.511	0.754	0.871	0.814	0.985	0.783	0.778
	Validation Δ	+0.048	+0.008	-0.033	-0.055	-0.046	+0.038	+0.007	-0.015	-0.008	-0.008
	Test	0.833	0.854	0.750	0.582	0.794	0.000	0.700	0.985	0.828	0.831
	Test Δ	+0.070	+0.032	+0.044	-0.002	+0.024	+0.000	+0.047	+0.000	+0.026	+0.027
S2HY,S2SE,S2MO and L8HY, S1MO	Train	0.877	0.863	0.771	0.687	0.833	0.911	0.892	0.994	0.857	0.858
	Train Δ	+0.023	+0.046	+0.037	+0.064	+0.055	+0.038	+0.084	+0.005	+0.043	+0.047
	Validation	0.800	0.863	0.741	0.541	0.763	0.839	0.828	1.000	0.807	0.808
	Validation Δ	+0.133	+0.054	+0.009	-0.025	-0.037	+0.005	+0.021	+0.000	+0.016	+0.021
	Test	0.830	0.891	0.746	0.563	0.781	0.000	0.723	0.988	0.829	0.832
	Test Δ	+0.067	+0.069	+0.040	-0.021	+0.010	+0.000	+0.071	+0.003	+0.028	+0.028
S2AN,S2HY,S2SE,S2MO and L8HY, S1MO	Train	0.869	0.816	0.752	0.651	0.801	0.883	0.865	0.992	0.833	0.832
	Train Δ	+0.014	-0.001	+0.019	+0.028	+0.023	+0.010	+0.057	+0.003	+0.019	+0.021
	Validation	0.744	0.792	0.706	0.578	0.783	0.857	0.828	0.985	0.794	0.791
	Validation Δ	+0.078	-0.017	-0.026	+0.012	-0.017	+0.024	+0.021	-0.015	+0.003	+0.004
	Test	0.840	0.872	0.763	0.580	0.788	0.000	0.722	0.985	0.832	0.836
	Test Δ	+0.077	+0.050	+0.057	-0.004	+0.018	+0.000	+0.070	+0.000	+0.031	+0.031
S2AN,S2HY,S2SE and L8AN,L8HY, S1MO	Train	0.855	0.855	0.752	0.632	0.748	0.862	0.841	0.991	0.825	0.825
	Train Δ	+0.050	+0.023	+0.062	+0.048	+0.121	+0.054	+0.178	+0.010	+0.066	+0.064
	Validation	0.816	0.841	0.730	0.623	0.692	0.832	0.809	0.985	0.796	0.796
	Validation Δ	+0.016	-0.052	-0.059	+0.023	+0.026	+0.052	+0.166	+0.007	+0.023	+0.021
	Test	0.832	0.827	0.731	0.676	0.791	0.100	0.715	0.988	0.813	0.811
	Test Δ	+0.016	-0.009	+0.003	+0.002	+0.034	+0.100	+0.044	+0.001	+0.015	+0.022
S2AN,S2HY,S2MO and L8AN,L8HY, S1MO	Train	0.885	0.826	0.773	0.659	0.812	0.890	0.878	0.992	0.844	0.842
	Train Δ	+0.030	+0.009	+0.039	+0.036	+0.034	+0.017	+0.070	+0.003	+0.029	+0.032
	Validation	0.696	0.792	0.714	0.512	0.771	0.853	0.814	0.985	0.782	0.778
	Validation Δ	+0.029	-0.017	-0.017	-0.054	-0.029	+0.019	+0.007	-0.015	-0.010	-0.008
	Test	0.842	0.854	0.776	0.599	0.794	0.000	0.700	0.986	0.833	0.837
	Test Δ	+0.079	+0.032	+0.070	+0.015	+0.024	+0.000	+0.047	+0.002	+0.032	+0.032

Results of Decision-level Fusion of Sentinel-2 Landsat-8 and Sentinel-1 prior models using SVM [Continued].

		Sealed	Woody Coniferous	Woody Broadleaved	Permanent Herbaceous	Periodically Herbaceous	Sparsely Vegetated	Non- vegetated	Water	Weighted F1	OA%
S2HY,S2SE,S2MO and L8AN,L8HY, S1MO	Train	0.886	0.848	0.760	0.690	0.835	0.910	0.901	0.991	0.856	0.856
	Train Δ	+0.032	+0.031	+0.027	+0.067	+0.057	+0.037	+0.093	+0.002	+0.042	+0.045
	Validation	0.727	0.840	0.762	0.556	0.790	0.820	0.814	1.000	0.802	0.803
	Validation Δ	+0.061	+0.032	+0.030	-0.010	-0.010	-0.014	+0.007	+0.000	+0.011	+0.017
	Test	0.837	0.860	0.739	0.585	0.769	0.000	0.718	0.988	0.828	0.831
	Test Δ	+0.074	+0.038	+0.033	+0.001	-0.001	+0.000	+0.066	+0.003	+0.026	+0.027
S2AN,S2HY,S2SE,S2MO and L8AN,L8HY, S1MO	Train	0.884	0.848	0.764	0.698	0.839	0.915	0.912	0.991	0.860	0.860
	Train Δ	+0.030	+0.031	+0.030	+0.075	+0.061	+0.043	+0.104	+0.002	+0.045	+0.049
	Validation	0.762	0.833	0.767	0.579	0.784	0.820	0.820	1.000	0.808	0.808
	Validation Δ	+0.095	+0.025	+0.036	+0.013	-0.016	-0.014	+0.013	+0.000	+0.016	+0.021
	Test	0.834	0.860	0.730	0.567	0.773	0.000	0.718	0.988	0.826	0.829
	Test Δ	+0.071	+0.038	+0.024	-0.017	+0.003	+0.000	+0.066	+0.003	+0.024	+0.024

C.2 Variable Data Fusion Assessment Results

Table C.11: Results of Decision-level Fusion using the Sentinel Only Fusion Set on S2AN-reduced dataset.

		Sealed	Woody Coniferous	Woody Broadleaved	Permanent Herbaceous	Periodically Herbaceous	Sparsely Vegetated	Non- vegetated	Water	Weighted F1	OA%
F1 Ordered	Train	0.779	0.859	0.696	0.579	0.619	0.795	0.649	0.968	0.745	0.747
	Validation	0.776	0.875	0.735	0.564	0.642	0.763	0.623	0.975	0.747	0.750
	Test	0.754	0.891	0.750	0.637	0.724	0.806	0.586	0.977	0.770	0.773
OA Ordered	Train	0.815	0.868	0.725	0.592	0.674	0.802	0.723	0.981	0.774	0.774
	Validation	0.774	0.884	0.713	0.558	0.683	0.764	0.640	0.975	0.752	0.753
	Test	0.735	0.878	0.734	0.631	0.719	0.832	0.649	0.984	0.773	0.774
Class F1 Ordered	Train	0.791	0.852	0.674	0.582	0.685	0.808	0.669	0.984	0.758	0.759
	Validation	0.810	0.887	0.718	0.557	0.679	0.800	0.703	0.985	0.769	0.772
	Test	0.727	0.869	0.717	0.649	0.732	0.819	0.547	0.989	0.761	0.765
PTO	Train	0.805	0.865	0.703	0.579	0.657	0.799	0.715	0.978	0.764	0.766
	Validation	0.781	0.881	0.700	0.553	0.704	0.770	0.667	0.975	0.756	0.759
	Test	0.730	0.888	0.747	0.611	0.744	0.816	0.594	0.985	0.768	0.773
Weighted Voting	Train	0.803	0.861	0.713	0.592	0.637	0.806	0.707	0.975	0.763	0.765
	Validation	0.781	0.895	0.726	0.570	0.679	0.774	0.667	0.975	0.761	0.763
	Test	0.766	0.893	0.749	0.638	0.725	0.823	0.656	0.981	0.782	0.784
Max Probability	Train	0.810	0.866	0.708	0.584	0.677	0.804	0.731	0.979	0.771	0.773
	Validation	0.791	0.885	0.699	0.540	0.699	0.770	0.652	0.966	0.753	0.756
	Test	0.742	0.889	0.747	0.617	0.750	0.818	0.599	0.985	0.772	0.777
Model F1 Weighted Max Probability	Train	0.813	0.869	0.710	0.586	0.675	0.803	0.734	0.980	0.772	0.774
	Validation	0.794	0.885	0.699	0.547	0.704	0.770	0.648	0.966	0.754	0.758
	Test	0.744	0.888	0.745	0.620	0.750	0.817	0.611	0.985	0.774	0.778
Class F1 Weighted Max Probability	Train	0.798	0.870	0.697	0.544	0.690	0.796	0.701	0.979	0.761	0.766
	Validation	0.811	0.891	0.704	0.485	0.686	0.759	0.621	0.966	0.743	0.753
	Test	0.739	0.894	0.733	0.594	0.745	0.826	0.574	0.985	0.766	0.774
Average Probability	Train	0.806	0.865	0.718	0.592	0.656	0.804	0.720	0.975	0.768	0.770
	Validation	0.817	0.885	0.733	0.557	0.667	0.777	0.700	0.980	0.766	0.769
	Test	0.754	0.888	0.756	0.646	0.742	0.828	0.644	0.983	0.783	0.786
Model F1 Weighted Average Probability	Train	0.807	0.864	0.716	0.592	0.656	0.805	0.721	0.975	0.768	0.770
	Validation	0.817	0.885	0.733	0.564	0.667	0.783	0.695	0.980	0.768	0.771
	Test	0.755	0.888	0.756	0.646	0.741	0.829	0.644	0.983	0.783	0.786
Class F1 Weighted Average Probability	Train	0.796	0.868	0.708	0.562	0.687	0.802	0.717	0.979	0.766	0.770
	Validation	0.815	0.891	0.727	0.539	0.707	0.769	0.687	0.970	0.765	0.771
	Test	0.756	0.894	0.743	0.614	0.745	0.831	0.623	0.982	0.777	0.783

Table C.12: Results of Decision-level Fusion using the Mono-Platform Fusion Set on S2AN-reduced dataset.

		Sealed	Woody Coniferous	Woody Broadleaved	Permanent Herbaceous	Periodically Herbaceous	Sparsely Vegetated	Non- vegetated	Water	Weighted F1	OA%
F1 Ordered	Train	0.815	0.868	0.725	0.592	0.674	0.802	0.723	0.981	0.774	0.774
	Validation	0.774	0.884	0.713	0.558	0.683	0.764	0.640	0.975	0.752	0.753
	Test	0.735	0.878	0.734	0.631	0.719	0.832	0.649	0.984	0.773	0.774
OA Ordered	Train	0.784	0.863	0.700	0.575	0.621	0.790	0.657	0.974	0.748	0.751
	Validation	0.779	0.895	0.742	0.557	0.667	0.764	0.603	0.970	0.751	0.755
	Test	0.763	0.889	0.754	0.638	0.717	0.829	0.656	0.980	0.781	0.783
Class F1 Ordered	Train	0.790	0.863	0.700	0.599	0.694	0.779	0.728	0.984	0.768	0.768
	Validation	0.794	0.895	0.735	0.569	0.691	0.777	0.703	0.980	0.770	0.771
	Test	0.737	0.886	0.766	0.644	0.704	0.768	0.551	0.943	0.754	0.754
PTO	Test	0.737	0.886	0.766	0.644	0.704	0.768	0.551	0.943	0.754	0.754
	Validation	0.783	0.878	0.679	0.582	0.702	0.790	0.676	0.970	0.760	0.763
	Test	0.750	0.877	0.751	0.625	0.726	0.797	0.584	0.983	0.765	0.769
Weighted Voting	Train	0.811	0.867	0.719	0.600	0.640	0.812	0.735	0.977	0.771	0.773
	Validation	0.800	0.885	0.738	0.591	0.662	0.780	0.681	0.975	0.766	0.769
	Test	0.766	0.891	0.753	0.647	0.734	0.825	0.656	0.982	0.785	0.787
Max Probability	Train	0.823	0.870	0.723	0.622	0.711	0.814	0.791	0.987	0.793	0.795
	Validation	0.755	0.874	0.676	0.591	0.691	0.778	0.647	0.970	0.750	0.754
	Test	0.751	0.882	0.758	0.631	0.731	0.791	0.591	0.985	0.769	0.772
Model F1 Weighted Max Probability	Train	0.825	0.873	0.724	0.615	0.703	0.814	0.782	0.983	0.790	0.792
	Validation	0.777	0.874	0.673	0.592	0.687	0.790	0.652	0.966	0.754	0.758
	Test	0.748	0.885	0.754	0.636	0.734	0.803	0.603	0.983	0.772	0.775
Class F1 Weighted Max Probability	Train	0.809	0.875	0.709	0.587	0.707	0.803	0.728	0.978	0.776	0.781
	Validation	0.815	0.873	0.673	0.538	0.694	0.766	0.615	0.966	0.746	0.754
	Test	0.741	0.883	0.730	0.607	0.736	0.796	0.531	0.981	0.756	0.764
Average Probability	Train	0.828	0.872	0.731	0.631	0.683	0.819	0.781	0.980	0.791	0.792
	Validation	0.816	0.876	0.713	0.589	0.671	0.781	0.690	0.975	0.766	0.768
	Test	0.762	0.896	0.778	0.652	0.744	0.821	0.660	0.983	0.790	0.791
Model F1 Weighted Average Probability	Train	0.830	0.872	0.732	0.633	0.683	0.819	0.777	0.981	0.791	0.792
	Validation	0.820	0.876	0.716	0.595	0.671	0.786	0.704	0.975	0.770	0.772
	Test	0.761	0.898	0.778	0.648	0.743	0.823	0.659	0.984	0.789	0.791
Class F1 Weighted Average Probability	Train	0.823	0.879	0.728	0.616	0.709	0.815	0.768	0.986	0.791	0.793
	Validation	0.809	0.884	0.713	0.575	0.683	0.780	0.677	0.975	0.764	0.769
	Test	0.760	0.893	0.756	0.648	0.745	0.824	0.637	0.982	0.784	0.788

Table C.13: Results of Decision-level Fusion using the SVM Fused Fusion Set on the S2AN-reduced dataset.

		Sealed	Woody Coniferous	Woody Broadleaved	Permanent Herbaceous	Periodically Herbaceous	Sparsely Vegetated	Non- vegetated	Water	Weighted F1	OA%
F1 Ordered	Train	0.863	0.889	0.764	0.652	0.758	0.855	0.840	0.989	0.826	0.826
	Validation	0.806	0.882	0.710	0.585	0.715	0.802	0.712	0.975	0.775	0.777
	Test	0.779	0.889	0.769	0.626	0.723	0.833	0.713	0.984	0.791	0.791
OA Ordered	Train	0.873	0.889	0.767	0.671	0.778	0.860	0.866	0.992	0.836	0.837
	Validation	0.847	0.886	0.724	0.580	0.678	0.798	0.740	0.975	0.780	0.782
	Test	0.780	0.887	0.754	0.601	0.711	0.774	0.716	0.985	0.777	0.776
Class F1 Ordered	Train	0.846	0.888	0.729	0.623	0.757	0.826	0.832	0.989	0.811	0.811
	Validation	0.811	0.905	0.759	0.636	0.715	0.805	0.716	0.975	0.792	0.795
	Test	0.771	0.895	0.757	0.586	0.717	0.694	0.710	0.985	0.765	0.765
PTO	Train	0.849	0.887	0.751	0.628	0.747	0.835	0.833	0.992	0.815	0.817
	Validation	0.851	0.869	0.704	0.595	0.667	0.800	0.723	0.975	0.774	0.778
	Test	0.784	0.887	0.766	0.648	0.744	0.836	0.720	0.983	0.798	0.799
Weighted Voting	Train	0.861	0.881	0.758	0.647	0.744	0.846	0.842	0.991	0.821	0.821
	Validation	0.813	0.873	0.714	0.576	0.682	0.802	0.737	0.975	0.773	0.774
	Test	0.795	0.895	0.782	0.640	0.739	0.808	0.737	0.985	0.799	0.798
Max Probability	Train	0.853	0.887	0.752	0.631	0.748	0.834	0.835	0.991	0.816	0.818
	Validation	0.849	0.876	0.723	0.582	0.674	0.800	0.732	0.975	0.778	0.782
	Test	0.779	0.882	0.758	0.643	0.743	0.835	0.717	0.983	0.794	0.795
Model F1 Weighted Max Probability	Train	0.853	0.886	0.753	0.628	0.749	0.838	0.840	0.991	0.817	0.819
	Validation	0.853	0.870	0.720	0.590	0.671	0.796	0.727	0.975	0.777	0.781
	Test	0.786	0.885	0.765	0.640	0.741	0.839	0.729	0.984	0.798	0.799
Class F1 Weighted Max Probability	Train	0.843	0.885	0.738	0.576	0.751	0.832	0.828	0.988	0.805	0.810
	Validation	0.827	0.877	0.705	0.503	0.678	0.784	0.680	0.971	0.755	0.764
	Test	0.770	0.888	0.754	0.607	0.734	0.852	0.693	0.982	0.787	0.792
Average Probability	Train	0.859	0.881	0.758	0.655	0.748	0.845	0.842	0.991	0.822	0.822
	Validation	0.816	0.873	0.726	0.589	0.693	0.811	0.740	0.975	0.779	0.781
	Test	0.798	0.896	0.779	0.655	0.744	0.831	0.742	0.985	0.805	0.805
Model F1 Weighted Average Probability	Train	0.858	0.881	0.758	0.655	0.749	0.845	0.842	0.991	0.822	0.822
	Validation	0.816	0.873	0.726	0.589	0.693	0.811	0.740	0.975	0.779	0.781
	Test	0.800	0.896	0.779	0.655	0.744	0.831	0.744	0.985	0.805	0.805
Class F1 Weighted Average Probability	Train	0.858	0.883	0.754	0.636	0.765	0.841	0.844	0.991	0.821	0.823
	Validation	0.830	0.879	0.730	0.531	0.670	0.805	0.724	0.975	0.769	0.774
	Test	0.796	0.893	0.776	0.647	0.738	0.858	0.738	0.984	0.805	0.807
Multi-ML model	Train	0.865	0.879	0.752	0.655	0.755	0.852	0.853	0.990	0.825	0.825
	Validation	0.816	0.873	0.711	0.573	0.685	0.802	0.719	0.975	0.771	0.773
	Test	0.780	0.893	0.770	0.632	0.728	0.815	0.728	0.985	0.793	0.792

Table C.14: Results of Decision-level Fusion using the Mono-Platform Fusion Set on the 25%-reduced dataset.

		Sealed	Woody Coniferous	Woody Broadleaved	Permanent Herbaceous	Periodically Herbaceous	Sparsely Vegetated	Non- vegetated	Water	Weighted F1	OA%
F1 Ordered	Train	0.772	0.849	0.701	0.584	0.641	0.787	0.694	0.976	0.752	0.753
	Validation	0.739	0.853	0.705	0.560	0.639	0.761	0.557	0.970	0.727	0.731
	Test	0.720	0.872	0.714	0.621	0.716	0.813	0.611	0.985	0.760	0.761
OA Ordered	Train	0.757	0.850	0.688	0.575	0.625	0.786	0.668	0.972	0.742	0.744
	Validation	0.750	0.853	0.732	0.562	0.639	0.777	0.596	0.970	0.738	0.742
	Test	0.736	0.880	0.731	0.623	0.711	0.813	0.606	0.982	0.764	0.765
Class F1 Ordered	Train	0.759	0.848	0.697	0.592	0.658	0.756	0.676	0.984	0.748	0.748
	Validation	0.767	0.854	0.718	0.574	0.624	0.780	0.657	0.980	0.747	0.750
	Test	0.712	0.875	0.753	0.610	0.695	0.720	0.527	0.944	0.734	0.732
PTO	Train	0.793	0.864	0.699	0.608	0.669	0.796	0.754	0.986	0.772	0.773
	Validation	0.757	0.850	0.689	0.556	0.655	0.764	0.643	0.970	0.738	0.741
	Test	0.728	0.871	0.733	0.607	0.714	0.761	0.544	0.965	0.745	0.747
Weighted Voting	Train	0.775	0.860	0.700	0.586	0.636	0.798	0.723	0.974	0.757	0.759
	Validation	0.755	0.853	0.718	0.573	0.638	0.785	0.653	0.975	0.746	0.749
	Test	0.735	0.876	0.726	0.634	0.723	0.812	0.614	0.981	0.766	0.768
Max Probability	Train	0.788	0.858	0.706	0.611	0.688	0.796	0.768	0.986	0.775	0.777
	Validation	0.726	0.843	0.664	0.550	0.628	0.773	0.624	0.970	0.725	0.728
	Test	0.727	0.877	0.740	0.600	0.714	0.738	0.548	0.978	0.744	0.747
Model F1 Weighted Max Probability	Train	0.792	0.858	0.705	0.610	0.684	0.794	0.760	0.983	0.774	0.775
	Validation	0.743	0.843	0.670	0.547	0.635	0.779	0.604	0.966	0.727	0.731
	Test	0.726	0.877	0.734	0.600	0.714	0.752	0.547	0.977	0.745	0.748
Class F1 Weighted Max Probability	Train	0.785	0.862	0.695	0.588	0.687	0.788	0.724	0.979	0.765	0.769
	Validation	0.778	0.847	0.660	0.514	0.620	0.751	0.598	0.966	0.720	0.728
	Test	0.715	0.871	0.713	0.580	0.716	0.768	0.491	0.980	0.735	0.743
Average Probability	Train	0.801	0.861	0.714	0.620	0.682	0.800	0.764	0.980	0.778	0.779
	Validation	0.766	0.845	0.699	0.588	0.639	0.789	0.662	0.975	0.748	0.750
	Test	0.735	0.883	0.745	0.629	0.729	0.767	0.609	0.978	0.762	0.763
Model F1 Weighted Average Probability	Train	0.800	0.861	0.713	0.621	0.680	0.800	0.760	0.980	0.777	0.778
	Validation	0.766	0.850	0.695	0.588	0.639	0.789	0.662	0.975	0.748	0.750
	Test	0.734	0.883	0.745	0.627	0.729	0.770	0.609	0.979	0.763	0.763
Class F1 Weighted Average Probability	Train	0.798	0.867	0.714	0.607	0.692	0.800	0.755	0.987	0.778	0.781
	Validation	0.771	0.850	0.689	0.534	0.635	0.765	0.632	0.975	0.734	0.740
	Test	0.730	0.882	0.739	0.623	0.733	0.787	0.581	0.977	0.761	0.764

Table C.15: Results of Decision-level Fusion using the SVM Fused and Mono Platform Fusion Set on the 25%-reduced dataset.

		Sealed	Woody Coniferous	Woody Broadleaved	Permanent Herbaceous	Periodically Herbaceous	Sparsely Vegetated	Non- vegetated	Water	Weighted F1	OA%
F1 Ordered	Train	0.836	0.878	0.750	0.643	0.743	0.840	0.833	0.988	0.814	0.814
	Validation	0.776	0.856	0.692	0.577	0.692	0.789	0.690	0.975	0.758	0.759
	Test	0.763	0.882	0.748	0.624	0.719	0.818	0.692	0.982	0.780	0.780
OA Ordered	Train	0.821	0.876	0.738	0.639	0.740	0.831	0.824	0.988	0.807	0.807
	Validation	0.781	0.869	0.707	0.566	0.685	0.781	0.680	0.970	0.757	0.759
	Test	0.770	0.885	0.748	0.617	0.716	0.813	0.681	0.979	0.778	0.778
Class F1 Ordered	Train	0.808	0.871	0.706	0.616	0.741	0.819	0.820	0.988	0.796	0.796
	Validation	0.775	0.882	0.734	0.621	0.705	0.796	0.685	0.975	0.774	0.776
	Test	0.749	0.888	0.741	0.621	0.726	0.781	0.669	0.980	0.771	0.772
PTO	Train	0.821	0.872	0.734	0.615	0.721	0.819	0.812	0.989	0.798	0.799
	Validation	0.800	0.856	0.705	0.577	0.644	0.784	0.667	0.970	0.753	0.756
	Test	0.763	0.876	0.743	0.635	0.730	0.793	0.664	0.985	0.776	0.778
Weighted Voting	Train	0.833	0.873	0.741	0.640	0.730	0.828	0.833	0.989	0.808	0.808
	Validation	0.783	0.847	0.696	0.585	0.674	0.785	0.693	0.975	0.757	0.758
	Test	0.780	0.884	0.752	0.642	0.736	0.804	0.708	0.983	0.788	0.787
Max Probability	Train	0.828	0.875	0.739	0.622	0.732	0.819	0.824	0.990	0.803	0.805
	Validation	0.815	0.840	0.696	0.586	0.648	0.774	0.676	0.970	0.753	0.756
	Test	0.766	0.878	0.742	0.631	0.733	0.796	0.686	0.982	0.779	0.780
Model F1 Weighted Max Probability	Train	0.831	0.874	0.739	0.618	0.734	0.821	0.826	0.988	0.804	0.805
	Validation	0.815	0.844	0.692	0.594	0.644	0.774	0.671	0.970	0.753	0.756
	Test	0.769	0.879	0.742	0.636	0.732	0.819	0.701	0.982	0.784	0.786
Class F1 Weighted Max Probability	Train	0.821	0.871	0.724	0.578	0.735	0.821	0.819	0.986	0.794	0.798
	Validation	0.800	0.853	0.689	0.514	0.648	0.756	0.653	0.971	0.738	0.745
	Test	0.760	0.875	0.731	0.602	0.726	0.817	0.660	0.980	0.771	0.776
Average Probability	Train	0.834	0.871	0.740	0.640	0.733	0.828	0.831	0.989	0.808	0.808
	Validation	0.781	0.841	0.705	0.581	0.678	0.793	0.711	0.975	0.759	0.760
	Test	0.781	0.886	0.755	0.652	0.737	0.810	0.708	0.983	0.791	0.791
Model F1 Weighted Average Probability	Train	0.833	0.872	0.741	0.640	0.734	0.828	0.831	0.989	0.808	0.808
	Validation	0.781	0.841	0.705	0.581	0.678	0.793	0.711	0.975	0.759	0.760
	Test	0.780	0.885	0.754	0.652	0.737	0.811	0.708	0.983	0.791	0.790
Class F1 Weighted Average Probability	Train	0.831	0.872	0.743	0.630	0.747	0.824	0.832	0.991	0.808	0.809
	Validation	0.794	0.854	0.709	0.561	0.667	0.782	0.689	0.975	0.756	0.759
	Test	0.780	0.880	0.750	0.642	0.733	0.838	0.709	0.982	0.791	0.792
Multi-ML model	Train	0.836	0.873	0.741	0.646	0.744	0.837	0.841	0.989	0.813	0.813
	Validation	0.774	0.847	0.693	0.570	0.670	0.783	0.680	0.975	0.751	0.753
	Test	0.764	0.884	0.748	0.628	0.720	0.797	0.704	0.983	0.780	0.779

Appendix D

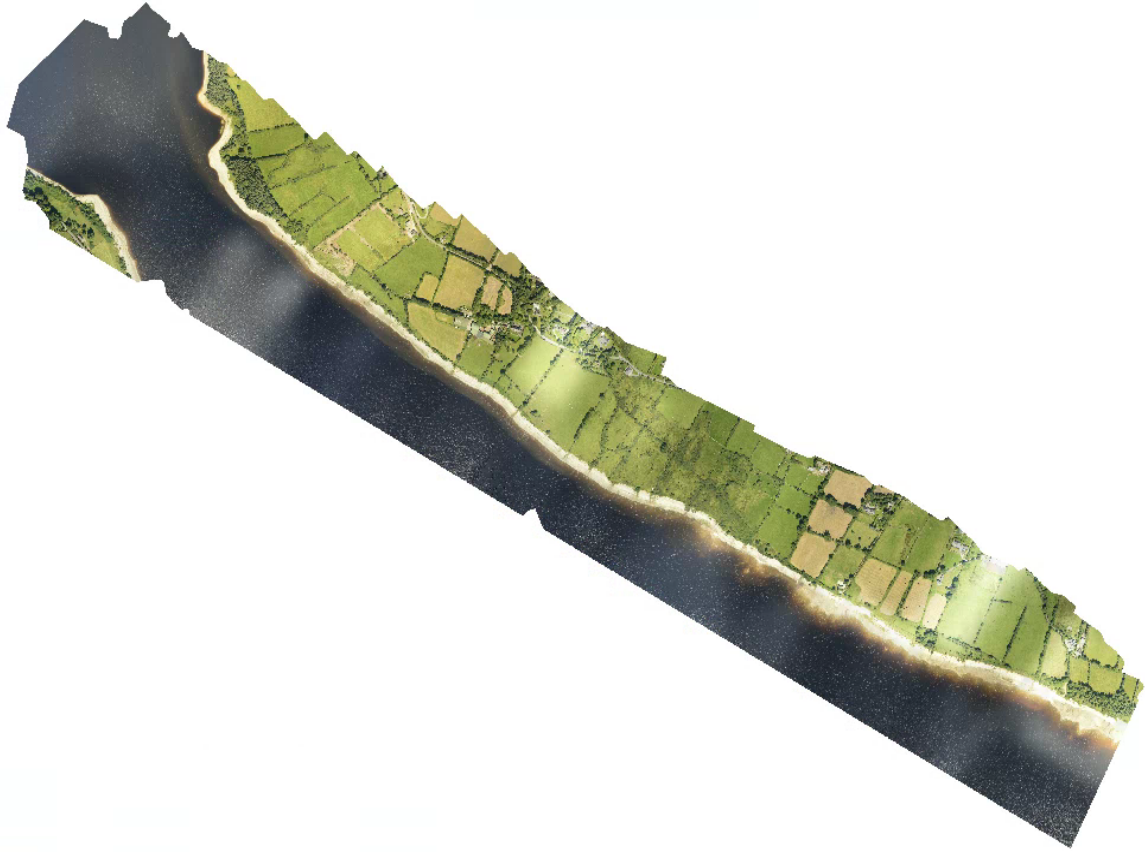
Chapter 5 Aerial Surveys



(a) Twomilebridge



(b) Rathdown Upper



(c) Sroughan



(d) Horsepasstown